INTERNATIONAL DOCTORAL
SCHOOL OF THE USC

Daniel
Fernández Fernández

PhD Thesis

High-energy fission and the onset of quasi-fission

Santiago de Compostela, 2023

Doctoral Programme in Nuclear and Particles Physics

USC
UNIVERSIDADE
DE SANTIAGO
DE COMPOSTELA

ESCOLA DE DOUTORAMENTO
INTERNACIONAL DA USC

DOCTORAL THESIS

HIGH-ENERGY FISSION AND THE ONSET OF QUASI-FISSION

Author

Daniel Fernández Fernández

Supervisors: Manuel Caamaño Fresco and Diego Ramos Doval

Tutor: Manuel Caamaño Fresco

PHD PROGRAMME IN NUCLEAR AND PARTICLE PHYSICS

SANTIAGO DE COMPOSTELA
17 december 2023

"A todos los que la presente vieren y entendieren"

Inicio de las Leyes Orgánicas
Juan Carlos I.

USC
UNIVERSIDADE DE SANTIAGO DE COMPOSTELA

USC
UNIVERSIDADE
DE SANTIAGO
DE COMPOSTELA

Acknowledgements

Durante estos años, el desarrollo de mi trabajo habría sido considerablemente más complejo sin el apoyo, la ayuda y los sabios consejos de numerosas personas, tanto dentro como fuera del entorno laboral. En este momento, deseo expresar mi sincero agradecimiento a todos ellos. Aunque procuraré ser breve y conciso, ésta es una oportunidad única para expresar mis pensamientos sin omitir a nadie; me comprometo a no ser demasiado intenso.

Quiero comenzar reconociendo el inmenso trabjo de mis dos directores de tesis, Manu y Diego (el bueno), quienes desplegaron incansables esfuerzos para llevar este proyecto a buen puerto. Les agradezco profundamente las incontables horas dedicadas, la confianza depositada en mí y el trato cordial que siempre me dispensaron. Con el permiso de Diego, deseo resaltar la labor de Manu. Principalmente, agradezco su paciencia, permitirme realizar múltiples proyectos simultáneos y resistir durante años la travesía de realizar una tesis en Python y conmigo. Su dedicación es digna de elogio. Espero que ambos sientan la misma satisfacción con este trabajo que yo y que de vez en cuando recuerden las tonterías que les soltaba y que las echen de menos.

He redactado, tachado y vuelto a escribir este párrafo en varias ocasiones, llegando a la conclusión de que la sencillez supera a una enumeración de agradecimientos individuales. Mi agradecimiento se extiende a Bea, Héctor y Yassid, y mis amigos de despacho, los del *OnlyFans-FICA*, con quienes compartí cervezas, vinos, comidas, cenas, incontables cafés y, sobre todo, risas. A todos, simplemente, gracias. Han hecho feliz a un hombre a lo largo de los años y, como dijo Forrest Gump: "*My mom always said life was like a box of chocolates. You never know what you're gonna get*", son los mejores chocolates que me podían tocar en este férreo pedestal propedéutico educativo que vivimos. Sin lugar a duda, ustedes son la gallina.

I would like to extend my gratitude to the entire VAMOS-GANIL collaboration, also with special thanks to A. Lemasson and T. Roger, as well as all those who participated in the *e753* experiment.

Nesta derradeira parte, pero non menos importante, agradezo ás marabillosas persoas que coñecín en Santiago e que compartiron anos de felicidade e risas entre moitas copas de viño comigo. Vostedes saben quen son e poderán recoñecerse nestas iniciais: V, S, R, F e S. Sacáronme un sorriso en incontables ocasións, fixéronme feliz e axudáronme a ser mellor persoa. Coas miñas inestabilidades e estrés, foron refuxio e escribiron moitas das páxinas máis fermosas da miña vida. A todos débolles moito. Non se imaxinan canto.

Y aquí lo dejo. Conciso y claro. Los animo a seguir leyendo, aunque advierto que no se trata de una lectura ligera. Como escribió Tolkien: "*It's a dangerous business, Frodo, going out your door. You step onto the road, and if you don't keep your feet, there's no knowing where you might be swept off to*". Están advertidos antes de pasar la página.

USC
UNIVERSIDADE
DE SANTIAGO
DE COMPOSTELA

Contents

Contents I

List of Figures V

List of Tables XIII

Introduction 1

1 Theoretical review and motivations 1
- 1.1 The discovery of nuclear fission . . . 1
- 1.2 Fission applications and motivations . . . 2
- 1.3 Fission description and models . . . 3
  - 1.3.1 Stages of the fission process . . . 5
  - 1.3.2 Liquid Drop Model . . . 8
  - 1.3.3 Strutinsky Model: a microscopic-macroscopic approach . . . 11
  - 1.3.4 Scission-Point Model . . . 15
  - 1.3.5 Fission modes and Random Neck Rupture Model . . . 18
  - 1.3.6 Multidimensional Potential - Energy Surface Models . . . 22
  - 1.3.7 Semi-empirical GEF code . . . 25
    - 1.3.7.1 Theory behind GEF . . . 26
- 1.4 Quasi-fission . . . 28
  - 1.4.1 Mass-Angle Distribution and Mass-Energy Distribution . . . 31
- 1.5 Unresolved points in fission . . . 35
- 1.6 Experimental fission observables . . . 36
  - 1.6.1 Inverse kinematics . . . 37
- 1.7 Objectives . . . 38
- 1.8 In this thesis... . . . 39

2 Experimental setup 41
- 2.1 GANIL facility . . . 41
- 2.2 The experiment . . . 43
  - 2.2.1 Experiment coordinate system . . . 45
- 2.3 Target position detection . . . 46
  - 2.3.1 MWPCs Start detector . . . 46
  - 2.3.2 SPIDER detector . . . 48
  - 2.3.3 AGATA detector . . . 49
- 2.4 VAMOS++ spectrometer . . . 49
  - 2.4.1 Mathematics behind VAMOS++ . . . 49
  - 2.4.2 Focal plane in VAMOS++ . . . 53
    - 2.4.2.1 Multi-Wire Parallel Plate Avalanche Counter detector . . . 54

USC UNIVERSIDADE DE SANTIAGO DE COMPOSTELA

2.4.2.2 Drift Chambers . . . 56
2.4.2.3 Ionisation Chamber . . . 57
2.4.3 Reconstruction algorithm . . . 60
2.5 Electronics . . . 61
2.6 Fissioning system tagging . . . 67
2.7 Fissioning system reference frame . . . 70
2.8 Excitation energy reconstruction . . . 71
2.9 Not measured energy estimation . . . 73
2.9.1 Energy lost in the target . . . 75
2.9.2 Energy lost in MWPCs Start detector . . . 76

3 Detectors calibration **77**
3.1 Drift Chamber calibration . . . 77
3.1.1 Induced charge calibration . . . 77
3.1.2 Gain-matching calibration . . . 78
3.1.3 Max charge calibration . . . 80
3.1.4 Drift time calibration . . . 82
3.2 Ionisation Chamber calibration . . . 82
3.2.1 Energy alignment in IC . . . 82
3.3 SPIDER calibration . . . 84
3.4 Multi-Wire chamber calibration . . . 84
3.4.1 MWPCs Start detector angle correction . . . 85

4 Fission-fragment identification **87**
4.1 Fragment atomic number . . . 87
4.1.1 dE vs E_{res} cuts . . . 87
4.1.2 Atomic number selection . . . 89
4.1.3 Atomic number correction . . . 91
4.2 Mass number and charge state . . . 93
4.2.1 ToF correction . . . 94
4.2.2 Correcting charge states . . . 97
4.2.3 Mass dependence . . . 98
4.3 Identification resolution and accuracy . . . 101

5 VAMOS++ acceptance, normalisation and anisotropy **107**
5.1 Phi acceptance $\mathcal{A}\phi_{LAB}$ . . . 108
5.2 Normalisation of the settings . . . 111
5.3 Theta acceptance $\mathcal{A}\theta_{CM}$ . . . 115
5.3.1 Limits in $\cos(\theta^{FF}_{CM})$ distribution . . . 116
5.4 Fission fragment angular distribution . . . 120

6 Calculation of fission yields and fragments velocities **125**
6.1 Fission-fragment yield definition . . . 125
6.2 Charge-states addition and setting merging . . . 126
6.3 Intrinsic efficiency . . . 129
6.3.1 Drift Chamber intrinsic efficiency . . . 129
6.4 Contamination study with aluminium target . . . 132
6.5 Contamination study with boron target . . . 136
6.6 Calculation of boron target isotopic yields . . . 137
6.7 Calculation of isotopic yields from the aluminium target . . . 145

6.8 Fission yields uncertainty . . . 149
6.8.1 Statistical uncertainty . . . 149
6.8.2 Systematical uncertainty . . . 149
6.9 Calculation of fission fragment velocities . . . 151
6.9.1 Fragment velocities from ^{265}Db fission . . . 151
6.9.2 Fragment velocities from ^{249}Bk fission . . . 154

7 Results and interpretations **157**
7.1 Final observables measurements . . . 157
7.2 Fission fragment yields . . . 159
7.2.1 Fusion-induced fission reactions with boron target . . . 160
7.2.2 Fission modes in ^{249}Bk fissioning system . . . 165
7.2.3 Transfer reactions with boron target . . . 167
7.2.4 Fusion-induced fission reactions with aluminium target . . . 169
7.2.5 Fission modes in ^{265}Db fissioning system . . . 175
7.2.6 Transfer reactions with aluminium target . . . 177
7.3 Angular anisotropy . . . 179
7.4 Quasi-fission and experimental MAD . . . 180
7.5 Neutron excess . . . 183
7.6 Neutron evaporation . . . 184
7.7 Even-odd staggering . . . 186
7.8 Fission dynamics . . . 193
7.8.1 Average velocity . . . 199
7.9 Characterization of the scission point . . . 200
7.9.1 Reconstruction of fragment mass at scission . . . 200
7.9.2 Neutron excess at scission . . . 202
7.9.3 Post-scission neutron evaporation . . . 204
7.9.4 Total Kinetic Energy at scission . . . 206
7.9.5 Relative distance between fragments . . . 208
7.9.6 Total Excitation Energy at scission . . . 209

Conclusions **211**

Resume **217**
R.1 Limiar . . . 217
R.2 Obxectivos . . . 219
R.3 Dispositivo experimental . . . 219
R.4 Análise de datos . . . 220
R.5 Discusión de resultados . . . 221

Appendix **225**
A.1 Lorentz Formalism . . . 225
A.2 Legendre polynomials . . . 227
A.3 Isotopic Fission Yields . . . 231
A.3.1 ^{265}Db isotopic fusion-induced fission yields . . . 231
A.3.2 ^{249}Bk isotopic fusion-induced fission yields . . . 237
A.4 Transfer reactions isotopic yields . . . 242
A.4.1 Aluminium target transfer reactions isotopic yields . . . 242
A.4.2 Boron target transfer reactions isotopic yields . . . 251

Erratum . . . 267

USC UNIVERSIDADE DE SANTIAGO DE COMPOSTELA

USC
UNIVERSIDADE
DE SANTIAGO
DE COMPOSTELA

List of Figures

All figures in this work are the creation of the author, unless otherwise noted. References and permissions for reproduced figures are provided.

1.1 The schematic diagram of the fission barrier as a function of elongation 4
1.2 Potential energy landscape of ^{236}U, obtained from a macroscopic-microscopic approach 5
1.3 The schematic diagram of the fission barrier as a function of elongation, depicting the energy distribution throughout the fission process 6
1.4 Principal deformations involved in the fission process include quadrupole ($n = 2$), octupole ($n = 3$), and hexadecapole ($n = 4$) 10
1.5 Potential energy plotted against the quadrupole and hexadecapole deformations . 11
1.6 The single-humped fission barrier in the Liquid Drop Model (LDM) with the double-humped fission barrier 13
1.7 Binding energy of heavy nuclei calculated using the Strutinsky Model (W) compared to the predictions of the Liquid Drop Model (W_{LDM}) as a function of the deformation parameter (β) 14
1.8 The energy potential of ^{240}Pu, calculated using a microscopic-macroscopic model incorporating the Strutinsky approach 15
1.9 Schematic illustration of the triple-humped fission barrier 16
1.10 Shell corrections of the nascent fission-fragment potential as functions of the deformation calculated separately for protons and neutrons using the Scission-Point Model 17
1.11 ^{227}Ra yields calculated with the Scission-Point Model 18
1.12 Schematic representation of the scission point configuration for different fission channels 20
1.13 The scission configuration, as described by Brosa *et al.*, is depicted, showcasing both the pre-scission state and the post-scission situation. 21
1.14 Experimental mass yield distribution for the ^{234}U(n_{th}, f) reaction at an incident neutron energy of 2 MeV 21
1.15 Schematic representation of a fissioning system in a five-dimensional shape parameterisation used for the PES calculation 23
1.16 The relationship between the reduced mass width and the angular momentum characteristics of the reaction related with the width of the fission fragment mass distribution. 29
1.17 Schematic drawing of the three competing processes when two nuclei are accelerated and collided 30
1.18 Illustration of the fundamental principles of the mass-angle distribution (MAD) . 33
1.19 Display of the measured mass-angle distributions (MADs) and their corresponding projections onto the mass ratio (M_R) 33

USC UNIVERSIDADE DE SANTIAGO DE COMPOSTELA

1.20 The mass-energy distributions (MEDs) and mass-angle distributions (MADs) are presented for the reactions of ^{238}U + ^{27}Al and ^{238}U + ^{48}Ca 34
1.21 Scheme of direct kinematics and inverse kinematics 37

2.1 Layout of GANIL facility with VAMOS++ spectrometer 42
2.2 The experimental setup of VAMOS++ spectrometer and SPIDER detector with the uranium beam impinged a target 44
2.3 A graphical representation illustrating the angular relations between the VAMOS++ angular system and the laboratory system is represented 45
2.4 Sketch of the e753 experiment with VAMOS++ experimental setup 46
2.5 Schematic representation of the DPS-MWPC including a zoomed-in view of the wire planes to illustrate their orientations and spacing 47
2.6 Configuration of the SPIDER detector with a transfer-fission event 48
2.7 Top view of a mass spectrometer with a charged particle of velocity v and a magnetic field B 50
2.8 The schematic representation of a magnetic dipole and a comparison between ion paths with different $B\rho$ values 51
2.9 The solid angle of VAMOS++ as a function of the relative magnetic rigidity 53
2.10 Simulation results for the $(B\rho, \theta)$ phase space of fission fragments for two reactions: ^{238}U + ^{nat}B and ^{238}U + ^{27}Al 54
2.11 Schematic diagram of the different detectors comprising the VAMOS++ spectrometer 55
2.12 Illustration of the Ionisation Chamber detector 56
2.13 Illustration of the Drift Chamber detector 57
2.14 Illustration of the Ionisation Chamber detector 58
2.15 The logic electronic chain with the triggers diagram involved in fission fragment detection used during the experiment 63
2.16 The electronic chain of the SPIDER detector 65
2.17 The electronic setup diagram of the detectors involved in fission fragment detection 66
2.18 Isotopic identification of target-like recoil nuclei produced by transfer reactions using the SPIDER detector 68
2.19 Fission-fragments angles and velocities in the two reference frames 71
2.20 The interaction diagram of the uranium beam with a target illustrating the energy loss 72
2.21 The cross-section, excitation energy, and generation location of the ^{265}Db fissioning system estimated with PACEIV 73
2.22 Schematic view of the energy depositions ΔE_i, $i = 0, 1, 2, 3$, of the fission fragments as they pass through all the detectors and Mylar foils placed between them. . . . 74
2.23 The relation between the energy lost in the target by simulated fission fragments of different (Z, A) isotopes and the energy in the first row of the Ionisation Chamber 75
2.24 The correlation plot between the not measured energy in the MWPCs Start detector and the energy loss in the row number zero of the Ionisation Chamber 76

3.1 Adjustment of the linear behaviour between pad number 60 and pad number 21 is illustrated for the first Drift Chamber 78
3.2 Alignment of the pads in the Drift Chamber is achieved by comparing the output signals before and after the alignment process 79
3.3 The alignment of the Drift Chamber pads, before and after the calibration, is depicted in the figure with the maximum charge deposited 81
3.4 Diagram illustrating the arrangement of pads and rows in the Ionisation Chamber 83

3.5 The misalignment for the energy projection in the IC within the $E_{res} \in (200, 250)$ MeV range . . . 83
3.6 The energy E_{res} as a function of the ToF exhibits replicated wrong events spread throughout the ToF . . . 85
3.7 Angular misalignment between the angle θ and the θ_{TP} measured with the target position MWPCs Start detector . . . 86

4.1 Energy loss of fission fragments as a function of the residual energy for $(14°, 21.5°)$ settings . . . 88
4.2 The energy loss of fission fragments is presented as a function of the residual energy for both settings after cut selections . . . 89
4.3 A descriptive scheme is presented for the variables utilised to obtain Z_{float} . . . 90
4.4 The selection of atomic numbers in the (dE, E_{tot}^{IC}) phase space . . . 90
4.5 The atomic numbers are plotted against the total energy, and the projected distribution of the atomic numbers is displayed . . . 91
4.6 The atomic number against the observable Y_{FP} and the distribution after the alignment . . . 92
4.7 The atomic number corrected in Y_{FP} against the observable X_{FP} and the distribution after the alignment . . . 92
4.8 The atomic number, corrected and aligned, is plotted against the E_{tot}^{IC} for all the runs 92
4.9 The pattern of A versus A/q where A and q are integer numbers . . . 94
4.10 The mass-charge state identification and the (A/q) projection. . . . 95
4.11 The (A/q) as a function of the Multi-Wire chamber MWPPAC sections after the *Offset* correction . . . 96
4.12 A descriptive scheme is presented for the variables used to obtain q_{float} . . . 97
4.13 The charge states against the observable ToF and the distribution after the alignment 98
4.14 The charge states corrected in ToF against the observable X_{FP} and the distribution after the alignment . . . 98
4.15 The effect of mass dependence on the identification of atomic number . . . 99
4.16 The mean value of $Z = 42$ is calculated for two extreme masses within that atomic number . . . 99
4.17 The dependence of fragment atomic numbers Z on mass with the trends lines depicted 100
4.18 Scheme of the variables used in the alignment of atomic numbers to correct for mass dependence . . . 100
4.19 The fragment atomic number Z distribution as a function of the mass, after the mass dependence correction . . . 101
4.20 Schematic view of the trajectories of the fission fragments and γ-rays . . . 102
4.21 Isotopic selection of ^{106}Ru and ^{108} from fission fragment identification . . . 103
4.22 Gamma spectra of ^{106}Ru and^{108}Ru . . . 103
4.23 The enveloped fission fragment atomic number distribution for both VAMOS++ settings is depicted, along with its resolution . . . 104
4.24 The enveloped fission fragment charge state distribution for both VAMOS++ settings is depicted, along with its resolution . . . 105
4.25 The enveloped fission fragment mass distribution for both VAMOS++ settings is depicted, along with its resolution . . . 105

5.1 Target position $(\theta_{LAB}^{TP}, \phi_{LAB}^{TP})$ space and δ against θ_{LAB}^{TP} . . . 109
5.2 The $(\theta_{LAB}$ - $\phi)$ space and the ϕ projection, both for $\delta \in (1.009, 1.019)$, are depicted 109
5.3 The 2D $\mathcal{A}\phi_{LAB}$ surfaces obtained for both VAMOS++ settings . . . 110

USC UNIVERSIDADE DE SANTIAGO DE COMPOSTELA

5.4 The 2D $\mathcal{A}_\phi$ interpolated surfaces obtained for both VAMOS++ settings 110
5.5 Simulation of an anisotropic distribution of $\Delta B\rho = B\rho - B\rho_0/(B\rho_0)$ (%) against θ (deg) of particles entering the VAMOS++ spectrometer 111
5.6 The $(\theta^{TP}_{LAB}, B\rho)$ space for both VAMOS++ settings 112
5.7 The θ^{TP}_{LAB} angle distributions in the same $B\rho \in (1.16, 1.19)$ Tm window for the aluminium target with the two VAMOS++ settings 113
5.8 The $(\theta^{TP}_{LAB}, B\rho)$ space and the distribution of the ratio between VAMOS++ settings in aluminium target 114
5.9 The space distribution $(\theta^{TP}_{LAB}, B\rho)$ after applying normalisation and acceptance correction in boron and aluminium targets 114
5.10 The projected velocity v^{FF}_{CM} of Rh ($Z = 45$) and Nd ($Z = 60$) in the centre-of-mass reference frame 115
5.11 The velocity of all fission fragments in the centre-of-mass reference frame for the aluminium target 116
5.12 The distribution of $\cos(\theta^{FF}_{CM})$ for fission fragments with $A = 125$ resulting from the ^{238}U + ^{27}Al reaction 116
5.13 The $\cos(\theta^{FF}_{CM})$ limits, calculated for the entire range of mass numbers, are shown for both VAMOS++ settings 118
5.14 The $\cos(\theta^{FF}_{CM})$ limits of aluminium and boron targets 118
5.15 The $\cos(\theta^{FF}_{CM})$ for fission fragment mass $A = 120$ is shown as a function of the θ^{TP}_{LAB} angle, considering all charge states of the fission fragment mass 119
5.16 The distribution of $\cos(\theta^{FF}_{CM})$ for fission fragments with $A = 125$ resulting from the ^{238}U + ^{27}Al reaction 119
5.17 θ_{CM} (deg) versus fragment mass number A before neutron evaporation for the reaction of ^{238}U + ^{27}Al and VAMOS++ measurement region 120
5.18 Typical fissioning system with a representation of $\vec{J}$, $\vec{M}$, $\vec{K}$ and $\vec{R}$ 121
5.19 Angular distributions of fission fragments are displayed for different combinations of quantum numbers J, K, and M 122
5.20 Experimental angular distribution $W(\theta_{CM})$ versus the angle θ_{CM} (deg) fitted using a sum of Legendre polynomials 122

6.1 The enveloped $\cos(\theta^{FF}_{CM})$ distribution for ^{125}Te^{43+} obtained by combining the contributions from the VAMOS++ settings of $(14°, 21.5°)$ 127
6.2 The distribution of $\cos(\theta^{FF}_{CM})$ for each enveloped charge-state of ^{125}Te in different colours. 127
6.3 The final distribution of $\cos(\theta^{FF}_{CM})$ for ^{125}Te, obtained by combining the individual contributions from different charge states 128
6.4 The $\cos(\theta^{FF}_{CM})$ distribution for ^{125}Te with the red line corresponding to the region where the fitting procedure is applied 129
6.5 The intrinsic efficiency of the Drift Chamber ($\mathcal{E}^{DC}_i$) for two VAMOS++ settings . . 130
6.6 The representation of the spatial coordinate X_{FP} of the Multi-Wire chamber MWPPAC and the energy deposited in the first row of the Ionisation Chamber . . 131
6.7 The isotopic fission yields of ^{265}Db for nuclear charge $Z = 52$ as a function of fragment mass number A. 132
6.8 The fusion-induced fission and transfer events for nuclear charge $Z = 52$ in the (v^{FF}_{CM}, A) space with aluminium target 133
6.9 The scheme of fusion-induced fission and transfer events for generic nuclear charge in the (v^{FF}_{CM}, A) space 134

6.10 Contamination factor evaluated for the aluminium target for each Z and for both VAMOS++ settings . . . 135
6.11 A schematic representation of the $\cos(\theta^{FF}_{CM})$ distribution for each 14° and 21.5° settings 135
6.12 The fusion-induced fission and transfer events for nuclear charge $Z = 52$ in the (v^{FF}_{CM}, A) space with boron target . . . 136
6.13 The contamination factor $\mathcal{C}(Z)$ of the boron target as a function of the nuclear charge Z . . . 137
6.14 The difference between the masses and the average mass for each elemental yield is used to determine the global background with ^{249}Bk . . . 138
6.15 The ratio of fusion-induced fission elemental yields for Z and its complement Z_{comp} is displayed in various colours for different constant contamination factors . . . 139
6.16 The correlation between $(Z/v^{FF}_{LAB})^2$ and Z^2 for fusion-induced fission events in both VAMOS++ settings is depicted for the boron target . . . 140
6.17 Different χ^2_r values obtained from fitting trigger efficiency to elemental yield ratios for various constant initial contamination factors . . . 140
6.18 The intrinsic trigger efficiency is obtained by fitting the ratio of the fusion-induced fission yields and their complementary . . . 141
6.19 The intrinsic efficiency $\mathcal{E}^{trigger}_i$ results for each fragment atomic number Z for boron target . . . 141
6.20 The contamination factors for boron target $\mathcal{C}(Z)_{init}$, $\mathcal{C}(Z)_{evaluated}$ and $\mathcal{C}(Z)_{smooth}$ are depicted . . . 142
6.21 The ratio of yields, $Y^{FuFi}_{corr}(Z)/Y^{FuFi}_{corr}(Z_{comp})$, for $Z < 48.6$ with the efficiency $\mathcal{E}_{rel}(Z)$ 143
6.22 The ratio of the final yields of fusion-induced fission to their complements, $Y(Z)/Y(Z_{comp})$ for the boron target . . . 144
6.23 The elemental yields as a percentage against the fragment atomic number Z for the boron target are presented in different colours . . . 144
6.24 Angular measurements in the centre-of-mass reference frame plotted against fragment mass (A) before evaporation for the ^{238}U + ^{27}Al reaction . . . 145
6.25 Representation of the angular distribution $W(\theta^{FF}_{CM})$ versus the polar angle θ_{CM} (deg) fitted using a sum of Legendre polynomials . . . 146
6.26 The difference between the masses and the average mass for each elemental yield is used to determine the global background with the fissioning system ^{265}Db . . . 147
6.27 The intrinsic efficiency $\mathcal{E}^{trigger}_i$ results for each fragment atomic number Z for aluminium target . . . 148
6.28 The green-shaded region represents the initial selection of a common region between the limits of $\cos(\theta^{FF}_{CM}) \in (0.47, 0.72)$ . . . 148
6.29 The systematic uncertainty of the yields, $\delta_{syst}(Y)$ (%) for each Z evaluated with fusion-induced fission data . . . 150
6.30 The envelopes of the centre-of-mass velocity distributions for both VAMOS++ settings, incorporating fusion-induced fission and transfer events for ^{265}Db and the isotopic selection $(Z = 52, A = 49)$ . . . 151
6.31 The kinematic of the fission reaction is depicted, illustrating the relationships between the centre-of-mass and laboratory reference frames . . . 152
6.32 The centre-of-mass velocity v^{FF}_{CM} is plotted against $\cos(\theta^{FF}_{CM})$ with $(Z = 52, A = 126)$ for fusion-induced fission events of the fissioning system ^{265}Db . . . 152
6.33 The velocity distribution $V^{FF}_{CM}(Z, A)$ of fusion-induced fission events after subtracting the contamination for the $(Z = 52, A = 149)$ fragment in ^{265}Db . . . 153

6.34 The simulated velocity distribution of fission fragments from ^{265}Db as predicted by the GEF model [46] . . . 154
6.35 The distribution resulting from velocities of fusion-induced fission events after subtracting the contamination for the $(Z = 41, A = 101)$ fragment in ^{249}Bk . . . 156
6.36 The simulated velocity distribution of fission fragments from ^{249}Bk as predicted by the GEF model [46] . . . 156

7.1 The fragment mass number A and atomic number Z against the mass over charge (A/q) . . . 158
7.2 The X_{FP} (mm) vs Y_{FP} (mm) and θ_{FP} (mrad) vs ϕ_{FP} (mrad) are represented . . . 158
7.3 The fission fragment yields for the fissioning systems ^{265}Db and ^{249}Bk are depicted on the nuclear chart . . . 159
7.4 The isotopic yields of ^{249}Bk are depicted in the figure with a colour line from each $Z \in (33, 65)$ . . . 160
7.5 The fusion-induced fission isotopic yield distributions as a function of the fragment mass number A resulting from the ^{249}Bk . . . 161
7.6 The fusion-induced fission isotopic yield distributions as a function of the fragment mass number A resulting from the ^{249}Bk . . . 162
7.7 The standard deviation of the isotopic yields $Y(Z, A)$ as a function of Z fragment of fission fragments of the ^{249}Bk fission system is shown . . . 163
7.8 Nuclear charge elemental yields distribution of ^{249}Bk at $E^*_{FS} = 47.7$ MeV . . . 164
7.9 Fragment mass elemental yields distribution of ^{249}Bk at $E^*_{FS} = 47.7$ MeV . . . 164
7.10 Description of the fragment atomic number Z isotopic yield distribution in terms of fission channels for the ^{249}Bk fissioning system . . . 166
7.11 The isotopic yields of the transfer reactions with the boron target are displayed in various colours for each fragment atomic number . . . 167
7.12 The elemental yields of the fragment atomic number distributions $Y(Z)^{Transfer}$ of transfer reactions with the boron target are presented . . . 168
7.13 The elemental yields of the fragment mass number distributions $Y(A)^{Transfer}$ of transfer reactions with the boron target are presented . . . 168
7.14 The elemental yields $Y(Z)^{recoil}$ for each recoil selected with SPIDER telescope detector and generated in the transfer reactions with the boron target and uranium beam . . . 169
7.15 The isotopic yields of ^{265}Db are depicted in the figure with a separate colour line from $Z \in (33, 66)$ . . . 170
7.16 The ratio of yields between complementary fission fragments is shown for the ^{265}Db fissioning system . . . 170
7.17 The fusion-induced fission isotopic yield distributions as a function of the fragment mass number A resulting from the ^{265}Db . . . 171
7.18 The isotopic yield distributions as a function of the neutron number of fragments resulting from the ^{265}Db . . . 172
7.19 The standard deviation of the isotopic yields $Y(Z, A)$ as a function of Z fragment of fission fragments of the ^{265}Db fission system is shown . . . 173
7.20 Fragment atomic number elemental yields distribution of ^{265}Db fissioning system at $E^*_{FS} = 61.2$ MeV . . . 174
7.21 Fragment mass elemental yields distribution of ^{265}Db fissioning system at $E^*_{FS} = 61.2$ MeV . . . 175

7.22 Description of the fragment atomic number Z isotopic yield distribution in terms of fission channels for the ^{265}Db fissioning system . . . 176
7.23 The isotopic yields of the transfer reactions with the aluminium target are displayed in various colours for each fragment atomic number . . . 177
7.24 The elemental yields of the fragment atomic number distributions $Y(Z)^{Transfer}$ of transfer reactions with the aluminium target are presented . . . 178
7.25 The yields of the fragment mass number distributions $Y(A)^{Transfer}$ of transfer reactions with the aluminium target are presented . . . 178
7.26 The elemental yields $Y(Z)^{recoil}$ for each recoil selected with the SPIDER telescope detector and generated in the transfer reactions with the aluminium target and uranium beam . . . 179
7.27 The evolution of the anisotropy factor is shown for each fragment atomic number Z of the ^{265}Db and ^{249}Bk fissioning systems . . . 180
7.28 Mass-Angle contour picture of the double differential cross section for emitted fragments deriving the reaction $^{238} + {}^{27}Al$ from Tōke *et al.* [65] . . . 181
7.29 The elemental yields $Y(Z)$ of the ^{265}Db fissioning system with the quasi-fission components remarked . . . 182
7.30 The neutron excess, $\langle N \rangle / Z$, is shown as a function of fragment atomic number Z for the fissioning systems ^{265}Db and ^{249}Bk . . . 184
7.31 The total neutron evaporation as a function of the fragment atomic number Z for ^{265}Db and ^{249}Bk fissioning systems . . . 185
7.32 Projection for all fragment atomic numbers Z of the even-odd staggering $\delta(Z+1.5)$ from 10.000 distributions of $Y(Z)$ . . . 187
7.33 The local even-odd effect as a function of the atomic number Z for the fission fragments of two fissioning systems, ^{265}Db and ^{249}Bk . . . 188
7.34 Elemental yields $Y(Z)$ of the ^{265}Db fissioning system estimated in the measurement regions $(r_{tot}, r2, r3)$ . . . 189
7.35 The local even-odd effect $\delta(Z+1.5)$ for the fission fragments of ^{265}Db within $(r_{tot}, r2, r3)$ regions in red, green and blue, respectively . . . 190
7.36 The local even-odd effect $\delta(Z+1.5)$ of $Y(Z)$ as a function of the atomic number Z for the heavy component of quasi-fission within $(r_{tot}, r2, r3)$ regions in red, green and blue, respectively . . . 190
7.37 The fragment mass asymmetry $\delta\Delta A(\tau)$ and the asymmetry between proton and neutron numbers $\delta I(\tau)$ as a function of contact time τ . . . 192
7.38 The average neutron excess is shown for each fragment Z for ^{265}Db fissioning system, including comparison with GEF calculations and the estimation of quasi-fission neutron excess . . . 193
7.39 The isotopic velocities of the fission fragments of the ^{265}Db and ^{249}Bk fissioning systems are displayed in various colours for each fragment atomic number . . . 194
7.40 The isotopic centre-of-mass velocities, v_{CM}^{FF} (cm/ns), for fission fragments produced in the fissioning system ^{249}Bk versus A. . . . 195
7.41 The isotopic centre-of-mass velocities, v_{CM}^{FF} (cm/ns), for fission fragments produced in the fissioning system ^{249}Bk versus N. . . . 196
7.42 The isotopic centre-of-mass velocities, v_{CM}^{FF} (cm/ns), for fission fragments produced in the fissioning system ^{265}Db versus A. . . . 197
7.43 The isotopic centre-of-mass velocities, v_{CM}^{FF} (cm/ns), for fission fragments produced in the fissioning system ^{265}Db versus N . . . 198

7.44 The average fragment velocity $\langle V \rangle(Z)$ as a function of the fragment Z for aluminium and boron targets 199
7.45 The average neutron excess post- and pre-evaporation is compared with the GEF for each Z in ^{249}Bk fissioning system 203
7.46 Average neutron multiplicity $\langle \nu \rangle(Z)$ as a function of the fragment Z 205
7.47 Neutron multiplicity $\langle \nu_{total} \rangle(Z)$ and $\langle \nu_{1+2} \rangle(Z)$ as a function of the fragment Z . . 206
7.48 The total kinetic energy $\langle TKE^{*} \rangle$ of the fission fragments at the scission point is presented for the ^{249}Bk fissioning system 207
7.49 Ratio between the distance between fragments at scission and that as spherical touching nuclei for fission of ^{249}Bk fissioning system 208
7.50 The $\langle Q_{g.s} \rangle$, $\langle TKE^{*} \rangle$, $\langle TXE^{*}_{g.s} \rangle$, and the fission fragment yields for each fragment atomic charge Z for ^{249}Bk 210
A.1 The relationship between the centre-of-mass of the fissioning system (CM) and the laboratory reference frame (LAB) is depicted in a schematic view 225
A.2 Legendre polynomials of even order in panel (a) and odd order in panel (b). Their polar representations are depicted in panel (c) and in panel (d). 230

USC
UNIVERSIDADE DE SANTIAGO DE COMPOSTELA

List of Tables

2.1 List of reactions between the ^{238}U beam at 5.88A MeV and the four targets used in the experiment . . . 43
2.2 The list of VAMOS++ configurations along with their corresponding spectrometer orientation . . . 53
2.3 List of transfer reaction channels identified by SPIDER detector . . . 67
2.4 Summary of fissioning system velocity, remaining energy of the uranium beam, and excitation energy of the fissioning system for the four targets . . . 73

5.1 List of the normalisation factors between the two VAMOS++ settings . . . 113

7.1 Parameters of the fission channels, fitted to the fragment atomic number yield distributions . . . 165
7.2 Parameters of the fission channels, fitted to the fragment atomic number yield distributions . . . 176
7.3 The contributions of emitting pre-saddle neutrons and protons from the ^{249}Bk fissioning system . . . 202
A.1 First Legendre polynomials. . . . 228
A.2 ^{265}Db isotopic fusion-induced fission yields . . . 231
A.3 ^{249}Bk isotopic fusion-induced fission yields . . . 237
A.4 Aluminium target transfer reactions isotopic yields . . . 242
A.5 Boron target transfer reactions isotopic yields . . . 251

USC UNIVERSIDADE DE SANTIAGO DE COMPOSTELA

USC
UNIVERSIDADE
DE SANTIAGO
DE COMPOSTELA

Introduction

Nuclear fission is a complex process which involves the interplay of different nuclear properties that shape the characteristics of the emerging fission-fragment distributions, the collective motions of the nucleons and the identity of the fragments, which are strongly affected by the nuclear shell structure.

Fission-fragment distributions are crucial observables for modelling the fission process. Until recently, access to such observables was limited to mass information, where the contributions of protons and neutrons are mixed. However, recent experiments have shown that fission in inverse kinematics is a powerful tool to investigate nuclear fission, giving access to a full isotopic identification of the fission fragments and bypassing some of the limitations of the direct kinematics approach.

A classic approach to facilitate the comprehension of the fission process involves considering it as a pure liquid-drop problem, incorporating shell effects, and other properties such as pairing, as perturbative elements. Empirically, it is observed that these effects, especially those linked to nuclear structure, diminish as the excitation energy of the fissioning system increases. The primary observable employed to study the evolution with excitation energy is the mass distribution of the fragments. Apparently, asymmetrical fission occurs due to the influence of shell effects, whereas symmetrical fission agrees with the expected outcomes of a liquid-drop behaviour. Nonetheless, recent experiments have shown that certain features associated with shell effects may persist even at high excitation energy.

This PhD thesis is part of the fission campaign at VAMOS-GANIL, focusing on the study of fusion-induced fission in highly excited ^{265}Db and ^{249}Bk fissioning systems, with excitation energies of E^*_{FS} = 61.2 MeV and E^*_{FS} = 47.7 MeV, respectively. The experiment was based on the inverse kinematics technique, wherein a ^{238}U beam was accelerated to 5.88A MeV and directed onto a ^{27}Al target and a ^{nat}B target. Additionally, the competition with the quasi-fission mechanism was studied with the ^{27}Al target.

The information on both atomic and mass numbers is crucial to obtain observables sensitive to the structure effects, such as nuclear-charge yield distribution, mass yield distribution, neutron excess, and total neutron evaporation. In addition, the correlation between mass and angle, and nuclear-charge and angle distributions, are derived. The latter can inform on the contribution of dynamical processes such as the quasi-fission mechanism.

USC

The nuclear-charge and mass yield distributions of the studied fissioning systems reflect the collective or microscopic nature of the fission process. If any shell is favoured by the fragments, it will be more populated than others. Nevertheless, in the absence of strong shell effects favouring specific configurations, the resulting distributions tend to exhibit Gaussian-like characteristics,

indicating a fission process primarily driven by liquid-drop properties. In the ^{265}Db fissioning system, an overproduction on the heavy side, which is not compensated on the light-partner side, is observed in both distributions. This effect is ascribed to quasi-fission events generated in ^{238}U + ^{27}Al collisions. This effect does not appear in the ^{249}Bk fissioning system. A comparison of the experimental neutron excess and total neutron evaporation with GEF code predictions was also performed for both systems.

The fission process offers the possibility of producing neutron-rich nuclei, which are a current topic of research in nuclear physics, such as studying the evolution of the shell structure in nuclei far from stability. The fission of the nuclei presented in this work produces neutron-rich fragments from $Z = 26$ to $Z = 66$, which may contribute to the possibility of such investigations.

USC
UNIVERSIDADE DE SANTIAGO DE COMPOSTELA

Chapter 1

Theoretical review and motivations

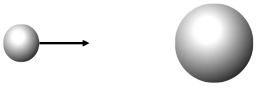

This chapter provides an overview of nuclear fission, including a discussion of the main models and the evolution from a macroscopic to a microscopic description. The GEF code, which was used for comparison with experimental data in Chapter 7, is briefly described. The theory of quasi-fission mechanism and the theory of nuclear shell structure are also introduced. Additionally, some unresolved issues in the description of fission are discussed. Finally, the chapter explores the recent inverse-kinematics technique, which allows for the acquisition of new experimental observables.

1.1 The discovery of nuclear fission

The history of nuclear fission began with the discovery of the neutron by Chadwick in 1932 [1], marking a significant milestone in the field of nuclear physics. This fundamental particle opened up new possibilities and sparked interest among researchers in exploring the potential of producing transuranic elements through the bombardment of uranium with neutrons.

In 1934, Fermi and his associates made a crucial observation that set the nascent field of nuclear physics on the path towards fission and the search for heavier, transuranic elements. They observed the production of artificial, radioactive isotopes resulting from the neutron bombardment of uranium (atomic number $Z = 92$). Fermi believed that he had discovered a transuranic element with $Z = 93$ [2]. However, doubts about this interpretation soon arose.

It was not until 1937 that Meitner, Hahn, and Strassmann replicated the experiments of Fermi and delved deeper into the analysis of the produced radioisotopes [3]. Their investigations revealed at least nine distinct radioactive decay rates, and they assigned six of them to elements beyond uranium. By comparing the chemical properties of these isotopes, they determined that some of them likely had atomic numbers higher than 92. This chemical analysis played a critical role in identifying and assigning atomic numbers to these transuranic elements, which exhibited similarities to the lanthanides.

Amid these groundbreaking discoveries, another hurdle emerged in 1938. Curie and Savitch investigated a new radioisotope produced by neutron-irradiated uranium [4]. Through chemical analysis, they found that this isotope possessed all the chemical properties of rare earths but ruled out the possibility of it being an isotope of actinium ($Z = 89$). Moreover, it did not fit within the region surrounding uranium in the periodic table. This added further complexity to the determination of the atomic numbers of the transuranic isotopes.

The breakthrough in understanding the nature of these processes came in 1939 with the work of Hahn and Strassmann [5], who analysed the assumed "radium isotopes" produced in the neutron bombardment of uranium. During their chemical analysis, they encountered difficulties in separating these isotopes from the barium "carrier". This led them to conclude that the isotope was chemically identical to barium ($Z = 56$). This revelation puzzled the scientific community and called for a comprehensive theoretical explanation.

In the same year, Meitner and Frisch provided the much-needed theoretical understanding of nuclear fission in their seminal work, *"Disintegration of Uranium by Neutrons: A New Type of Nuclear Reaction"* [6]. They employed the nuclear Liquid Drop Model (LDM) [7][8], which described the nucleus as an electrically charged droplet with surface tension responsible for maintaining its shape. By considering the balance between surface tension and the effective charge of the nucleus, they proposed a mechanism for nuclear fission. According to their model, a highly deformed heavy nucleus could split into two fragments of intermediate masses due to the collective motion of nucleons within the nucleus. The Coulomb repulsion between the nascent fragments and the nuclear surface tension were identified as the driving forces behind this process. To describe this phenomenon, they named the new nuclear process *"fission"* after learning that the term *"binary fission"* was used by Barthelemy Dumortier in 1832 in France to refer to the cell division in plants.

Building upon this theoretical foundation, Bohr and Wheeler further developed the description of nuclear fission based on the LDM [9]. They introduced the concept of fissility as a measure of the stability of the liquid drop against deformation. By treating the stability of nuclei in terms of surface tension, they estimated that the surface tension was zero for nuclei with $Z \approx 100$. This insight led them to confirm that uranium nuclei could divide into two nuclei of equal size when receiving excitation energy from the captured neutron binding energy. However these calculations, while capable of demonstrating symmetric fission, could not explain the phenomena of asymmetric fission [10]. The experimental confirmation of Frisch of this asymmetric fission in the same year solidified the incomplete understanding of nuclear fission [11].

Since the early days of the discovery of nuclear fission, a wealth of experimental data has been gathered. Combined with the contributions of Meitner, Frisch, Bohr, and Wheeler, this has led to the development of various models for understanding nuclear fission. These models encompass a range of approaches, from fully microscopic to combinations of micro- and macroscopic perspectives, as well as phenomenological codes which rely on experimental data. The ongoing research in this field continues to deepen our understanding of nuclear fission and its applications.

1.2 Fission applications and motivations

The discovery of fission had profound consequences, both in the field of nuclear physics and in its wider societal implications. It sparked extensive research in nuclear physics and captured public attention due to its relevance to nuclear power generation and nuclear weapons. The discovery of fission not only impacted the study of the nuclear physics field but also justified the continued exploration of nuclear physics as a whole, even in areas with limited societal applications.

The production of electricity through nuclear power plants is one of the foremost applications of nuclear fission worldwide. Presently, nuclear fission constitutes over 10% of the power

generation of the world. Nuclear power plants employ ^{235}U, a fissile isotope of uranium, as fuel. Through fission, ^{235}U releases a significant amount of heat, which is harnessed to boil water and generate steam, subsequently driving turbines to produce electricity. In order to optimise the development and operation of nuclear reactors, a precise understanding of fission cross-sections and fission yields is essential. These parameters play a critical role in determining the behaviour and efficiency of nuclear reactions within reactors, influencing factors such as neutron population, energy production, and fuel depletion. By accurately characterising fission cross sections and yields, scientists and engineers can make informed decisions and design reactors that are safer, more efficient, and economically viable. Additionally, this knowledge is crucial for ensuring the proper handling and management of nuclear fuel and waste, minimising environmental impact.

The production of radioactive beams is another significant application of the fission process. Actinides, due to their higher number of neutrons per nuclear charge compared to lighter nuclei, yield neutron-rich nuclei as fission products. Having accurate knowledge of fission yields enables us to estimate the production rate of specific nuclei, which is crucial for the development and optimisation of radioactive beam facilities.

Another application pertains to the r-process in stellar nucleosynthesis. The generation of elements beyond iron can be attributed to three distinct processes: proton capture (rp-process), slow neutron capture (s-process), and rapid neutron capture (r-process). Each process occupies distinct regions of the nuclear chart and occurs within specific stellar scenarios. To enhance the accuracy of stellar nucleosynthesis models, the acquisition of more precise experimental data, including fission cross-sections and fission yields, becomes imperative.

1.3 Fission description and models

Nuclear fission is a complex process where a highly-deformed heavy nucleus undergoes splitting into two fragments of intermediate masses. This phenomenon is driven by large-scale collective motions of the nucleons within the fissioning system, causing a rearrangement of the nucleons from the initial nucleus configuration to the formation of the fragments. The outcome of this reaction is influenced by several factors, including the initial conditions of the fissioning nucleus, such as its excitation energy, deformation, and angular momentum. Additionally, the path taken by the fissioning system through its intrinsic potential energy surface will define the deformation and mass of the pre-formed fragments. Thus, the path plays a crucial role in determining the final result of the fission process. In a highly simplified manner, the path followed by the fissioning system can be observed in the energy-versus-elongation representation in Fig. 1.1. The characteristics of the fragment distributions are studied to establish a connection between the initial conditions of the fissioning nucleus and the products of the reaction.

To initiate fission, energy must be supplied to the system, which is initially in its ground state, in order to overcome the fission barrier (depicted in yellow in Fig. 1.1). This energy is denoted as E^*_{FS}. The fission barrier is defined as the activation energy needed for a system to undergo fission. During the fission process, the fissioning system undergoes a transition along a path, starting from the top of the energy barrier, which is conventionally referred to as the "*saddle*", and progressing towards the final shape formation of fragments at some point. Consequently, there is a need to clearly separate the fragment formation phase (labelled as pre-fragments) from the fragment acceleration phase during the course of the fission process. The pre-fragments (shaping from the saddle point) are connected by a neck and can exchange nucleons and excitation energy. This

distinct moment in the fission process, at which the separation occurs, is conventionally referred to as the "*scission point*" (depicted in green in Fig. 1.1). During this journey before the scission point, the nascent fragments acquire their individual thermodynamic properties, long before the scission point and after the evaporation of neutrons and gammas from the fissioning system. The properties of the fragments: neutron and proton numbers, kinetic energy, excitation energy, and angular momentum, are fixed[1] at the scission point.

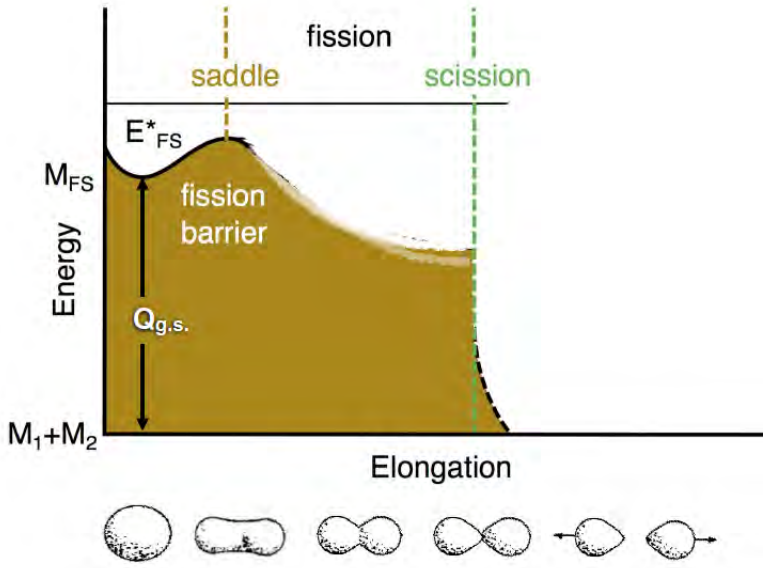

Figure 1.1: *Simplified schematic of the fission barrier representing the energy as a function of elongation for the fissioning system and its subsequent division into two fission fragments. The saddle point and scission point are depicted in yellow and green, respectively.*

This transition involves a transfer of energy within the system among degrees of freedom, resulting in an increased deformation of the nucleus (see Fig 1.1). The process entails a complex interplay between collective and intrinsic degrees of freedom, which shape the characteristics of the resulting fission-fragment distributions. M_1 and M_2 are the masses of the two fragments, M_{FS} is the mass of the fissioning system and E^*_{FS} is the excitation energy of the fissioning system. It is satisfied that:

$$Q_{g.s} = M_{FS} - M_1 - M_2\,, \tag{1.1}$$

where and $Q_{g.s}$ refers to the Q-value of the fundamental state of the fissioning system and the fragments (see Fig 1.1).

An example of the potential energy landscape for the fission process of the ^{236}U system is illustrated in Fig. 1.2. The data, obtained from a macroscopic-microscopic model [13], present the potential energy as a function of the quadrupole momentum (q_2), representing the deformation, and the mass asymmetry (α_g). In order to transition the fissioning system from its ground state (a) to the saddle point (b), which corresponds to the fission barrier dominated by Coulomb repulsion, a minimum amount of excitation energy E^*_{FS} is required. From the saddle point, the fissioning system continues to deform until reaching the scission point (c), where the two fragments are completely separated and emitted in opposite directions with substantial kinetic energy. It is important to note that points (a), (b), and (c) in Fig. 1.2 refer to the path with zero mass

[1]Some articles describe excitation energy sharing beyond scission throughout virtual photons [12].

asymmetry ($\alpha_g = 0$). The figure also depicts the varying shape of the fissioning system at different positions along the path.

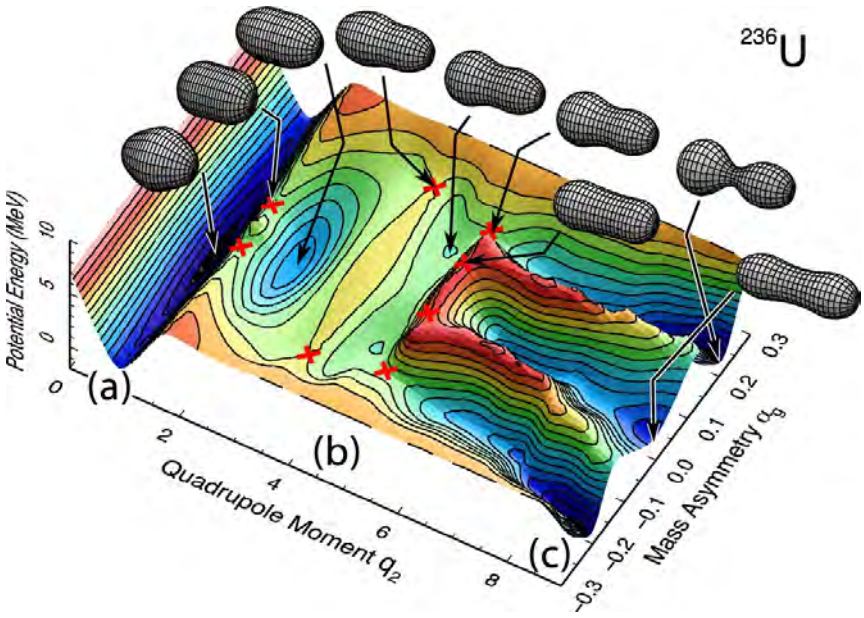

Figure 1.2: *The figure illustrates the potential energy landscape of ^{236}U, obtained from a macroscopic-microscopic approach. The graph depicts the dependence of the potential energy on the quadrupole momentum (q_2) and mass asymmetry (α_g). Notable points along the path with zero mass asymmetry are marked: (a) denotes the ground state of the fissioning system, (b) corresponds to the saddle point, and (c) represents the scission point. The figure also includes visual representations of the nucleus at different positions. Adapted with permission from [13]. Copyright (2012) by the American Physical Society.*

The excitation energy E^*_{FS} can be decomposed into two components:

$$E^*_{FS} = E^*_{coll} + E^*_{int}\,, \tag{1.2}$$

the collective excitation energy (E^*_{coll}) represents the energy associated with collective degrees of freedom, such as deformation and rotation. The intrinsic excitation energy (E^*_{int}) corresponds to the energy invested in intrinsic degrees of freedom, such as single-particle excitation.

The sources of E^*_{int} include the initial energy that the fissioning system possesses above the fission barrier (B_f) and the dissipation of the energy (E_{diss}). The system converts the energy associated with collective degrees of freedom into the energy of intrinsic degrees of freedom and no energy is lost from the system:

$$E^*_{int} = (E^*_{FS} - B_f) + E_{diss}\,. \tag{1.3}$$

This intrinsic excitation energy is distributed between the nascent fragments according to their level density, promoting an intrinsic energy flow from the lighter fragment to the heavier one. The division of E^*_{coll}, on the other hand, is determined by the structural characteristics of the fragments.

1.3.1 Stages of the fission process

The outcome of a single fission decay depends on the initial conditions of the compound nucleus undergoing fission and this is not a static problem, as the evolution of the system is

determined by the inherent dynamic nature of the process, encompassing aspects such as time, scale, dissipation, and inertia.

Before the fission barrier, part of the excitation energy of the fissioning system may be released through the emission of neutrons, which is referred to as neutron evaporation. Additionally, another portion of the excitation energy may be released through γ-ray emission. In the general scenario for the fissioning system, the most probable sequence is the emission of neutrons followed by γ-rays. Once the fissioning system can no longer emit additional neutrons, it might release the remaining energy in the form of γ-ray emission.

The generation, deformation, and split of a fissioning system occur within a timescale of the order of 10^{-21} seconds [14]. The resulting fission fragments are emitted with considerable kinetic energy and excitation energy, and this can be expressed as:

$$Q_{g.s} + E^*_{FS} = TKE + TXE\,, \tag{1.4}$$

where the Total Kinetic Energy (TKE) is the sum of the kinetic energy of the fission fragments and the Total Excitation Energy (TXE) is the sum of the excitation energy of the fission fragments, involving the total energy available in the fission reaction, E_{tot}:

$$E_{tot} = M_{FS} + E^*_{FS}\,, \tag{1.5}$$

which is the sum of the mass of the fissioning system in its ground state and its total excitation energy, E^*_{FS}.

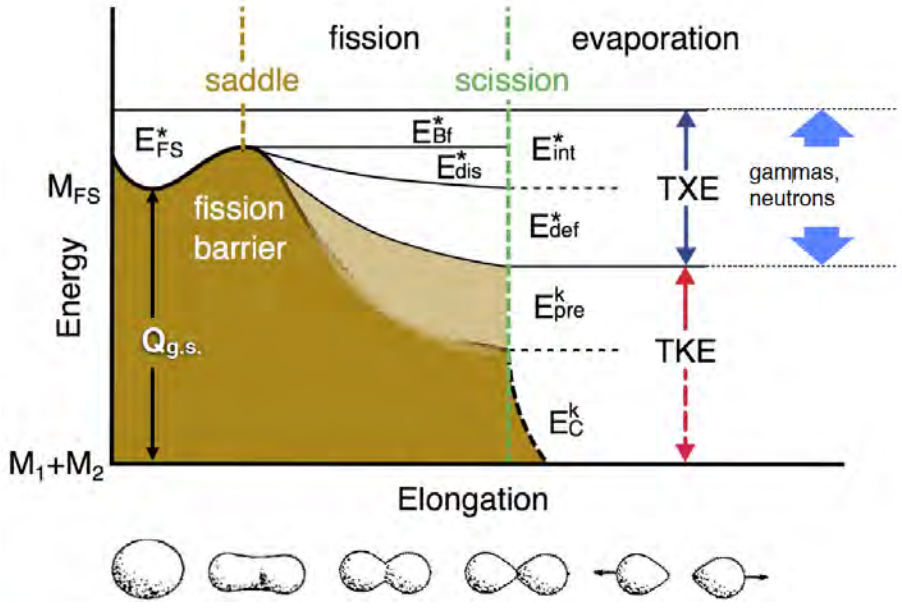

Figure 1.3: *The figure presents a schematic diagram of the fission barrier as a function of elongation, depicting the energy distribution throughout the fission process, from the saddle point to the scission point. The lower part of the figure illustrates the division of the fissioning system and its relation with the barrier, depicted through a diagram.*

The quantities M_{FS} and E^*_{FS} are summarised in Fig. 1.3, where a schematic representation of a simple fissioning system is depicted, illustrating the relationship between elongation and energy. The different sections of the barrier in the lower part of the diagram correspond to specific stages

of the fission process, with the fissioning system and the generation of fission fragments depicted based on the elongation parameter.

The TXE is the sum of the distribution of excitation energies, given by:

$$TXE = \sum(E^*_{col} + E^*_{ind}) = \sum(E^*_{int} + E^*_{def}) \approx \sum(E^*_{Bf} + E^*_{dis} + E^*_{def})\,. \tag{1.6}$$

The excitation energy is classified into two components based on their distribution among the degrees of freedom. E^*_{col} represents the energy acquired in collective degrees of freedom such as global deformation or rotations. The approximation in the equation is due the fact that the rotational energy is ignored. E^*_{int} is the excitation energy associated with single-particle excitations and primarily arises from the energy above the fission barrier and the energy dissipated in the coupling of collective and intrinsic degrees of freedom. Thus, an initial classification based on the behaviour concerning degrees of freedom is done, followed by another classification based on the elements involved in the specific fission process.

After acquiring their individual properties, the nascent fragments are characterised by approximately parallel single-particle levels, resulting in an essentially adiabatic process [15]. Deviations from the adiabatic limit of the microscopic transport theory due to single-particle level crossings near the fission barrier have been recently observed by Tanimura *et al.* [16]. Enhanced one-body dissipation arises shortly before scission (refer to Fig. 1.3), primarily attributed to rapid shape changes linked to the neck rupture. This dissipation-related excitation energy, denoted as E^*_{dis}, arises from the "one-body dissipation": the potential energy between the outer barrier (the final barrier that the fissioning system overcomes) and the scission point, and also emerges as a result of energy level crossings, occurring throughout the entire trajectory between the initial fission barrier and the scission point. In addition to the dissipation energy, there is an extra excitation energy present in the fissioning system above the fission barrier, denoted as E^*_{Bf}. A fissioning system with sufficient energy to surpass the saddle point (the point of no return) is energetically favoured to elongate further. The sum of the barrier energy E^*_{Bf} and the dissipation energy E^*_{dis} is referred to as the intrinsic excitation energy E^*_{int}.

Hence, the energy TXE is closely associated with the excitation energy of the fissioning system and its energy allocation. The allocation of collective excitation energy between the two fragments is directly influenced by the specific nature of the collective mode (angular momentum will not be divided in the same manner as spin momentum). The distribution of intrinsic excitations occurs under the assumption of thermal equilibrium between the intrinsic degrees of freedom of each fragment. Following energy allocation principles, at low energies, it obeys the constant-temperature rule, where the excitation energy is transferred to the fragment with the lower temperature. In other words, E^*_{int} is divided among the still-forming fragments (pre-fragments) according to their level densities, favouring heat flows towards the heavier fragment. Owing to the variations in level densities, a discernible disparity emerges in temperature between the lighter and heavier fragments. This phenomenon establishes a consistent trend where the light fragment exhibits a systematically elevated temperature compared to its heavier counterpart[2]. As a result, the intrinsic energy (heat) tends to be directed towards the nascent heavy fragment. This process, referred to as "*energy sorting*", was initially expounded in [17]. As the initial excitation energy increases, the fragments may traverse into the domain of a

[2]This trend, however, may experience inversion in nearly symmetric fission events due to the influential presence of shell effects

Fermi gas, leading to a gradual attenuation of the energy sorting mechanism. In the asymptotic scenario of elevated excitation energy, the distribution of heat experiences an equitable sharing among the fragments, directly proportional to their respective masses [15].

This excitation energy TXE is distributed between the fragments and, after scission, released with the emission of prompt neutrons (within a time range of $10^{-18} - 10^{-14}$ seconds) and subsequently for the emission of prompt γ-rays (within a time range of $10^{-14} - 10^{-3}$ seconds). In the reference frame of the fissioning system, the nascent fragments are emitted back to back along the so-called "*fission axis*" due to Coulomb repulsion.

The total kinetic energy, TKE, is given by the available kinetic energy of both pre-fission fragments (just at scission point) plus the energy generated by the Coulomb repulsion of the fragments at scission ([18] and references therein), expressed as:

$$TKE = E^k_{pre} + E^k_C \,, \tag{1.7}$$

where the Coulomb repulsion can be expressed in its classical form as:

$$E^k_C = \frac{Z_1\, Z_2\, e^2}{d_f} \,, \tag{1.8}$$

where Z_1 and Z_2 are the atomic number of the fragments, e is the electron charge and d_f is the distance between fragment centres.

There is a balance in the distribution of available energy, $Q_{g.s} + E^*_{FS}$, between kinetic and excitation energy, so that $TKE = Q_{g.s} + E^*_{FS} - TXE$. The TKE reflects the changes in $Q_{g.s}$ due to the different distributions of the fission fragments. This relationship arises from Eq. 1.1. The specific allocation of excitation energies, contingent upon the potential energy surface (refer to Fig. 1.2), produces different *Q-value* as expressed by $Q = (M^{g.s}_{FS} + E^*_{FS}) - (M^{g.s}_{F1} + E^*_{F1}) - (M^{g.s}_{F2} + E^*_{F2})$. Thus, for a TXE with a smooth, unaltered, and approximately constant behaviour, the distribution of TKE mirrors the behaviour of the Q.

The total kinetic energy of the final fission fragments is an important observable that can be used to characterise fission properties. It is related to the elongation of the system upon splitting, and hence to the deformation of the fragments. Furthermore, the TKE reflects the total mass loss, meaning that the TKE after neutron emission provides information about the mass difference of the system before and after scission. In general, the direct measurement of information before scission cannot be achieved directly. It could be directly measured if the fissioning system had excitation energy E^*_{FS} below $B_f + S_n$ by measuring the TKE through the *Time of Flight* (ToF) measurement of both fragments.

To establish a relationship between the initial conditions of the compound nucleus undergoing fission and the final products, the characteristics of the distributions of observable quantities for the fission fragments are studied.

1.3.2 Liquid Drop Model

The Liquid Drop Model (LDM) proposed by G. Gamow in 1928 [7] is a theoretical framework which assumes the nucleus can be treated as a uniform, incompressible liquid drop composed of nucleons bound by the strong force. This model is based on the observation that nuclear matter

has an almost constant density, which is similar to the cohesive forces holding water molecules in a droplet together. According to the LDM, the nucleus is assumed to have a spherical shape in its ground state, with a radius $R = r_0 \cdot A^{1/3}$, where A is the mass number and $r_0 = 1.15$ fm is a constant that expresses the classical nucleon radius related to the mean nuclear interaction distance.

The semi-empirical mass formula, introduced by Weizsacker in 1935 [19], is used to calculate the binding energy of groundstate nuclei, $B(Z, A)$:

$$B(Z,A) = a_v A - a_s A^{2/3} - a_c \frac{Z(Z-1)}{4\pi A^{1/3}} - a_a \frac{(A-2Z)^2}{A} + \delta(Z,A)\,. \tag{1.9}$$

The nucleus can be described as a sphere consisting of nucleons, where the nuclear force acts as a volume force ($a_v A$) that is proportional to the mass of the nucleus. This volume term represents the strong interaction within the nucleus. Additionally, there is a surface contribution, $a_s A^{2/3}$, that accounts for the fact that nucleons on the surface of the nucleus interact with fewer neighbours, resulting in a reduction of the binding energy. The Coulomb term, $a_C \frac{Z(Z-1)}{4\pi A^{1/3}}$, takes into consideration the repulsion between protons within the nucleus, further reducing the binding energy. Moreover, the asymmetry component $a_A \frac{(A-2Z)^2}{A}$ considers the quantum effect of the Pauli exclusion principle, which states that an excess of neutrons in the nucleus occupies higher energy levels, increasing the total energy of the nucleus and reducing its binding energy. In summary, the nucleus is characterised by sphere that has least surface energy and greatest Coulomb energy with nucleons experiencing a volume force, a surface layer of nucleons with decreased binding energy due to reduced interactions, Coulomb repulsion between protons, and the quantum effect of the Pauli exclusion principle. Additionally, the pairing term $\delta(Z, A)$ accounts for the energy required to form pairs of nucleons:

$$\delta(Z,A) = \begin{cases} a_p A^{-3/4} & \text{even-Z, even-N} \\ 0 & \text{odd-A} \\ -a_p A^{-3/4} & \text{odd-Z, odd-N}\,. \end{cases} \tag{1.10}$$

The values of the constants in this formula are adjusted to experimental mass measurements and result in $a_v = 15.5$ MeV, $a_s = 16.8$ MeV, $a_c = 0.72$ MeV, $a_a = 23$ MeV, and $a_p = 34$ MeV.

The LDM was further developed by Bohr and Wheeler [9] in 1935, who extended the description of the model to deformed nuclei. In this case, the radius of the nuclear surface $R(\theta, \phi)$ is dependent on the polar and azimuthal angle, θ and ϕ, and can be parameterised following a multipolar series:

$$R(\theta,\phi) = R_0 \left[1 + \sum_{n,\mu} \alpha_{n\mu} Y_{n\mu}(\theta,\phi) \right]\,, \tag{1.11}$$

where R_0 is the radius of the spherical nucleus, $Y_{n\mu}(\theta, \phi)$ are the spherical harmonics, and the parameters $\alpha_{n,\mu}$ represent the weight of the different types of deformation.

The principal deformations involved in the fission process is illustrated in Fig. 1.4, as described in [9], categorised by their multipolar order (2^n). The quadrupole deformation ($n = 2$) corresponds to elongation along one symmetry axis, while the octupole deformation ($n = 3$) results in left-right asymmetry. The hexadecapole deformation ($n = 4$) occurs when both pre-fragments are connected through a neck. An overview of the main deformation types is represented in Fig. 1.4.

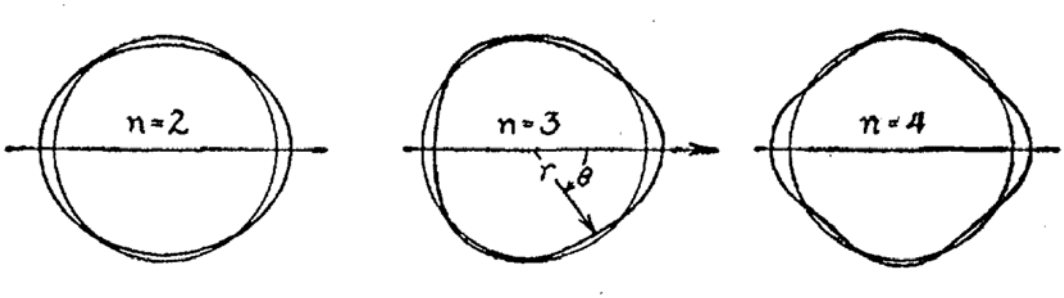

Figure 1.4: *Principal deformations involved in the fission process include quadrupole ($n = 2$), octupole ($n = 3$), and hexadecapole ($n = 4$). A value of $\mu = 0$ is assumed, indicating rotational symmetry around the axis connecting the two fragments. Adapted with permission from [9]. Copyright (1939) by the American Physical Society.*

In the context of the fission process, lower-order deformations are disregarded as they do not significantly impact the process. Additionally, the octupole deformation is not considered in the Bohr and Wheeler model, which exclusively predicts symmetric fission. It is assumed that the fission deformation exhibits rotational symmetry around the axis connecting the two fragments, resulting in a value of $\mu = 0$. The deformation of a nucleus, specifically a quadrupole deformation ϵ, affects only the surface and Coulomb terms in the semi-empirical mass formula. In the case of a nucleus with a quadrupole deformation, the surface and Coulomb terms can be expressed as:

$$E_S(\epsilon) = E_S(0) \cdot \left(1 + \frac{2}{5}\alpha_{2,0}^2\right) , \tag{1.12}$$

$$E_C(\epsilon) = E_C(0) \cdot \left(1 - \frac{1}{5}\alpha_{2,0}^2\right) , \tag{1.13}$$

where $E_S(0)$ and $E_C(0)$ represent the surface and Coulomb terms involved in the binding energy for the spherical nucleus.

Bohr and Wheeler defined the first potential surface based on the deformation energy, E_{def}. This energy represents the difference in binding energy between the deformed nucleus $B(\epsilon)$ and the spherical nucleus $B(0)$.

$$E_{def} = B(\epsilon) - B(0) = \frac{a_{2,0}}{5} \cdot (2E_S(0) - E_C(0)) . \tag{1.14}$$

A fission barrier is observed in the calculation when the deformation is low, indicating that the binding energy of the deformed nucleus is higher than that of the spherical nucleus. However, at higher deformations, there is an energy inversion that strongly favours nuclear fission. This energy inversion occurs at the called "*saddle point*", which represents the deformation of the nucleus at an unstable equilibrium. According to Eq. 1.14, the fission barrier disappears when $2E_S(0) < E_C(0)$.

In Fig. 1.5, the potential energy, calculated by Bohr and Wheeler, is depicted as a function of quadrupole deformation and secondary degrees of freedom (specifically, hexadecapole deformation in this case). The fission trajectory, denoted by "x" follows the path of lowest potential. The *saddle point* is identified as the location where equipotential lines intersect.

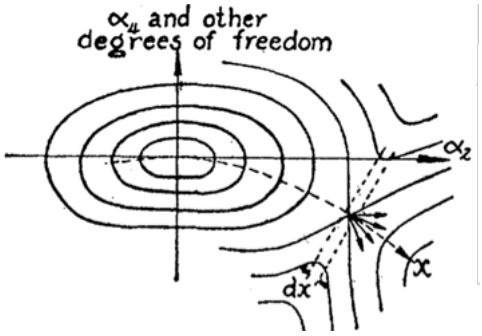

Figure 1.5: *The figure displays the potential energy plotted against the quadrupole and hexadecapole deformations. The trajectory of the system is represented by the dashed line. The saddle point, marked as "dx", represents the specific point where the two equipotential lines intersect. Adapted with permission from [9]. Copyright (1939) by the American Physical Society.*

By utilising this approach, it becomes possible to define the *fissility parameter* as a measure of nucleus stability. The existence of a fission barrier is determined when $2E_S(0) > E_C(0)$ according to Eq. 1.14. Therefore, the fissility parameter, k, can be obtained by substituting the corresponding values of surface and Coulomb terms as:

$$k = \frac{E_C(0)}{2E_S(0)} \propto \frac{Z^2}{50A}\,. \tag{1.15}$$

The early model based on the liquid-drop approach, while providing good predictions for fission barriers, requires ad-hoc corrections to reproduce measured fragment distributions. It offers a qualitative understanding of why fission is favoured by heavy nuclei and explains the main features of fission barriers. However, the asymmetric nature of fragment distributions is not explained. Nevertheless, the LDM has demonstrated success in explaining various nuclear phenomena such as nuclear stability, binding energy, and the fission process.

1.3.3 Strutinsky Model: a microscopic-macroscopic approach

When considering the behaviour of a nucleus, two different approaches come into play. In a macroscopic perspective, such as the LDM, the microscopic structure of the nucleus is not taken into account. The LDM failed to explain certain aspects, such as deformation in the ground state and asymmetric fission. It was found that the existing Shell Model could address these limitations. This model incorporates the concept of energy levels and shells filled with nucleons, governed by a central potential generated by all other nucleons. It was observed that nuclei with specific numbers of protons and/or neutrons exhibited higher binding energy than neighbouring nuclei [20]. In the microscopic approach, nucleons (protons and neutrons) are considered quantum particles moving independently under a central potential. The Shell Model, based on this microscopic view, describes the discrete energy levels and wave functions of nucleons inside the nucleus according to the Schrödinger equation. Later in 1955, Nilsson expanded the Shell Model to include deformed nuclei [21], introducing an elliptic central potential that accounted for the ground state deformations, investigating how the single-particle energy changes with deformation and revealing the emergence of new magic numbers ($Z = 52$, 56 and $N = 84$, 88) associated with deformed shells. Both approaches provide valuable insights into the behaviour of nuclei. While the macroscopic approach, represented by the LDM, offers a suitable framework for collective descriptions, the microscopic approach, represented by the Shell Model, focuses on the individual behaviour of nucleons within the nucleus and it explains phenomena such as magic numbers and the influence of deformation on energy levels.

In 1967, Strutinsky introduced a model [22] which combined the macroscopic and microscopic approaches to provide a more accurate description of asymmetric fission. This model employed the level scheme of Nilsson [21] to calculate the shell-model correction, considering the occupation number and deformation, and incorporating it into the energy of the LDM.

In the Strutinsky Model, the binding energy of the nucleus (W) is redefined as the sum of two contributions. The first contribution is the binding energy calculated using the LDM (W_{LDM}). The second contribution is the energy difference between a distribution of nucleon states described by Nilsson and a smooth distribution of states described by the LDM (δU). These contributions are summed over the number of protons and neutrons to obtain the total binding energy:

$$W = W_{LDM} + \sum_{Z,N} (\delta U(Z,A) + P)\,, \tag{1.16}$$

$$\delta U(Z,A) = U - U_{LDM}\,, \tag{1.17}$$

where P is the pairing term and U is the sum of the individual energies (single-particle energies) in a shell-model based potential:

$$U = \sum_i e_i 2n_i\,, \tag{1.18}$$

where e_i are the nucleon levels in the average potential and n_i represent the occupation numbers. U_{LDM} is obtained as the integral over all the energy states occupied in the LDM smooth distribution:

$$U_{LDM} = 2 \cdot \int_{-\infty}^{\lambda_{LDM}} e \cdot g_{LDM}(e) de\,, \tag{1.19}$$

where $g_{LDM}(e)$ represents the level density described by the LDM and λ_{LDM} represents the corresponding Fermi level. This $g_{LDM}(e)$ is defined as a Gaussian according to the Strutisky model with a width γ:

$$g_{LDM}(e) = \frac{1}{\gamma\sqrt{\pi}} \sum_i e^{\frac{-1}{\gamma^2}\cdot(E-E_i)^2}\,. \tag{1.20}$$

The theory of Strutinsky aimed to account for fluctuations in the total energy of the nucleus caused by single-particle effects. By applying this theory, the binding energy of the nucleus in its ground state could be corrected. The shell correction was computed for each deformed nuclear configuration along the fission path, corresponding to every point on the fission barrier derived from the LDM. This resulted in a refined fission barrier that adequately incorporated the effects of the shell structure.

For actinides, the incorporation of shell corrections in the LDM results in the formation of a double-humped fission barrier, where the barrier is divided into two distinct regions. An example of a one-dimensional double-humped fission barrier for a typical actinide nucleus obtained using the Strutinsky procedure is depicted in Fig. 1.6, alongside the simple fission barrier obtained from the LDM. The potential energy, plotted as a function of a parameter representing the elongation of the fissioning system along the energetically favoured path to fission, illustrates the barrier characteristics.

USC UNIVERSIDADE DE SANTIAGO DE COMPOSTELA

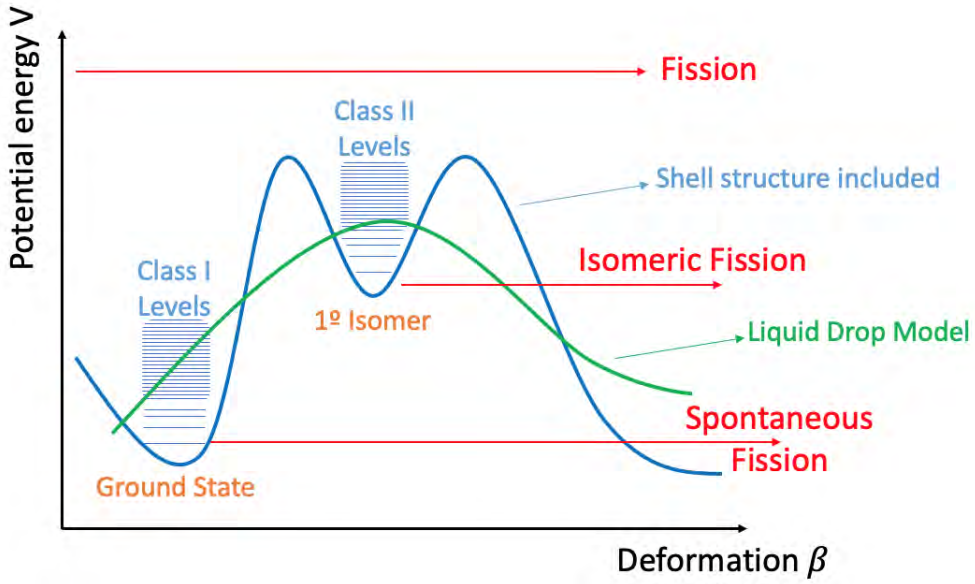

Figure 1.6: *Schematic illustration comparing the single-humped fission barrier in the Liquid Drop Model (LDM) with the double-humped fission barrier obtained by incorporating the shell structure into the LDM.*

The first minimum of the barrier corresponds to the energy levels of the deformed ground state, while the second minimum represents a more highly deformed state with higher energy, giving rise to a series of isomeric levels[3]. Within the fission barrier, various energy levels are populated, with those above the barrier maxima known as transition states and those within the minima referred to as *Class I* or *Class II* levels, depending on the respective well they are associated with.

Actinide nuclei, both in their ground and excited states are typically non-spherical. In general, an excited nucleus can decay to its ground state through processes such as (n, γ) reactions, or it can traverse the first hump of the barrier and reside in the second well. The presence of states within the second well provides a natural explanation for the existence of fissioning isomers or shape isomers, and the relatively short half-lives of these states (on the order of nanoseconds or microseconds for most actinides) indicate a high probability of undergoing fission.

The results of the calculations, depicted in Fig. 1.7, illustrate the relationship between the binding energy W and the deformation parameter β. The dashed lines represent the binding energy obtained from the LDM, while the solid line corresponds to the binding energy calculated using the Strutinsky approach. Additionally, the shell correction δU and the Fermi shell level densities g are shown separately for protons (solid line) and neutrons (crosses) in the case of ^{238}U.

These calculations reveal that the predicted ground states for the nuclei depicted in Fig. 1.7 have slightly lower energies (few MeV) compared to the spherical states predicted by the LDM, aligning well with experimental measurements. The fission thresholds for deformed transuranic nuclei are estimated to be larger than those predicted by the LDM, indicating relative stability against spontaneous fission. Furthermore, the presence of a second and even a third fission barrier naturally emerges, providing an explanation for the existence of fission isomers.

[3]The term "*isomer*" refers to nuclei that possess excited levels with half-lives ranging from 100 to 1000 times longer than the half-lives of excited nuclear states that decay through a "prompt-γ" cascade, which typically occurs on the order of 10^{-12} seconds.

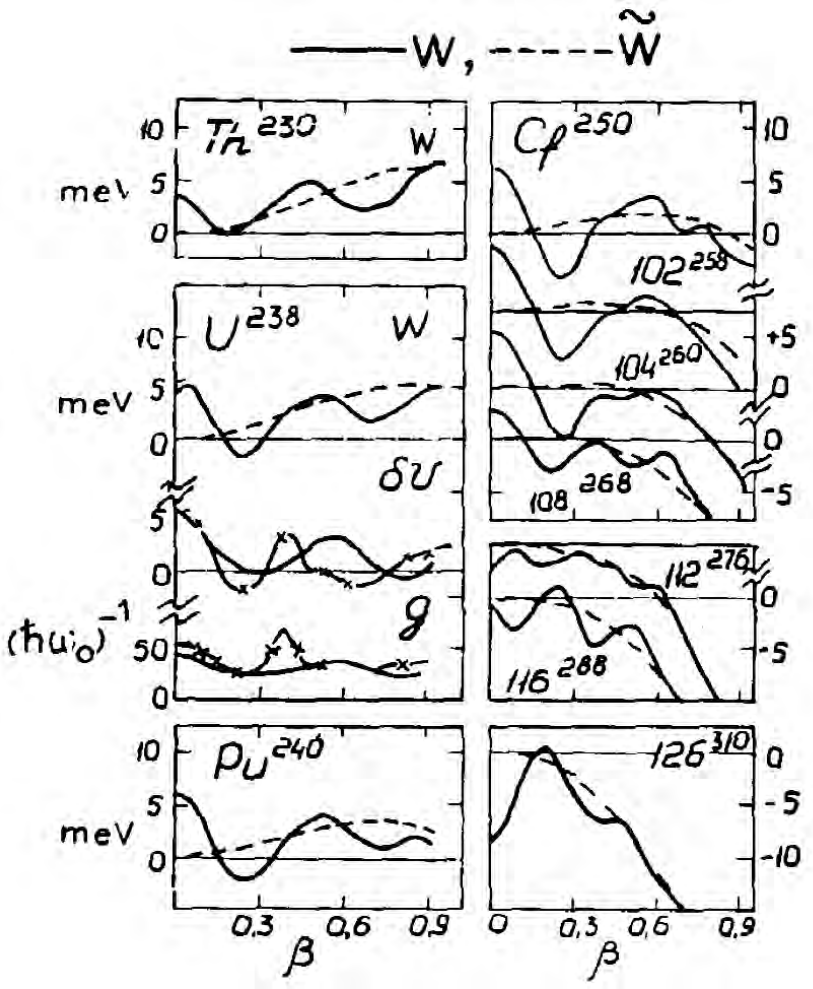

Figure 1.7: *Binding energy of heavy nuclei calculated using the Strutinsky model (W) compared to the predictions of the Liquid Drop Model (W_{LDM}) as a function of the deformation parameter (β). Additionally, for the ^{238}U system, the figure presents the calculated shell correction (δU) and the Fermi shell level densities (g) separately for protons (solid line) and neutrons (crosses). This image provides a comparison between the Strutinsky approach and LDM predictions for the binding energy of selected actinides and transactinides. Adapted with permission from [22]. Copyright (1967) by the Elsevier Science B.V.*

The Strutinsky approach successfully reproduces asymmetric fission by incorporating octupole deformation, which was not considered in the LDM by Bohr and Wheeler. As a result, the discrepancies observed between the fragment distributions predicted by the LDM and experimental data can be attributed to the effects of the nuclear shell structure.

Unlike the LDM approximation of Bohr and Wheeler, which only considers quadrupole and hexadecapole deformations, the Strutinsky model allows for the inclusion of octupole deformation, enabling the description of asymmetric fission. Fig. 1.8 illustrates the potential energy of ^{240}Pu calculated using this approach, incorporating both macroscopic and microscopic contributions (solid line), as well as solely the macroscopic contribution (dashed line). The upper image displays the potential energy as a function of quadrupole ("*symmetric*") deformation, denoted as β_2, revealing the presence of a second barrier in the micro-macro approach. The lower image illustrates the potential energy in the second barrier as a function of octupole ("*asymmetric*") deformation, denoted as β_3, where the potential minimum is notably shifted from zero, indicating the prediction of asymmetric fission.

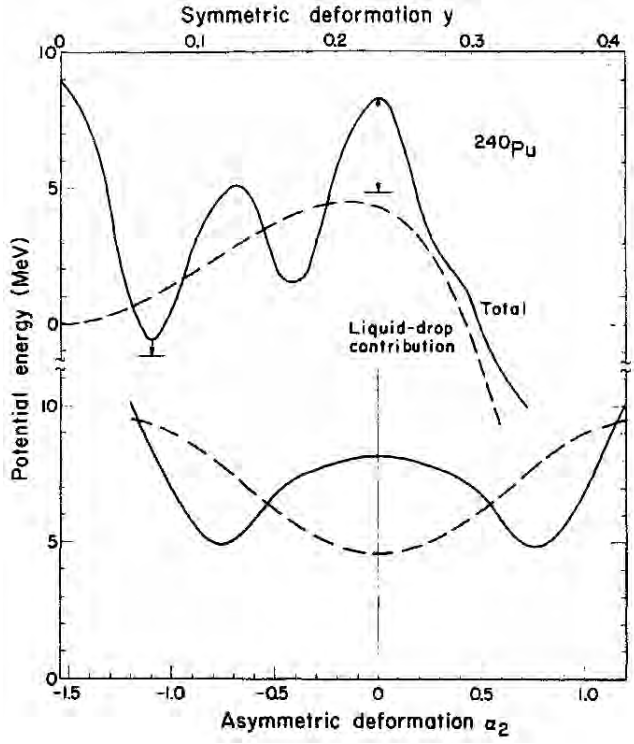

Figure 1.8: *The energy potential of ^{240}Pu, calculated using a microscopic-macroscopic model incorporating the Strutinsky approach, is depicted as a function of quadrupole deformation in the upper plot and as a function of octupole deformation in the second barrier in the lower plot. The solid line represents the potential energy considering both macroscopic and microscopic contributions, while the dashed line represents the potential energy considering only the macroscopic component. Adapted with permission from [23]. Copyright (1972) by the American Physical Society.*

The presence of a second well in the fission barrier is supported by the observation of a narrow resonance structure below the first-chance threshold in the fission cross-section. This structure was initially attributed to the *Class II* levels (related with Fig. 1.6), which are associated with the second well. Nonetheless, the existence of narrower resonances in the threshold region for certain thorium isotopes, such as ^{230}Th and ^{232}Th, posed a challenge to this explanation. It was suggested by Möller and Nix in 1974 [24] that these structures can be better understood by splitting the second hump of the fission barrier into two, creating a new narrow well populated by levels. This configuration is known as the triple-humped fission barrier. According to this model, the resonances in question would be produced by the *Class III* levels, which occupy the third well (related with Fig. 1.9).

1.3.4 Scission-Point Model

In 1976, two years after the suggestion by Möller and Nix, Wilkins *et al.* introduced the Scission-Point Model [25]. This statistical model assumes that the distributions of fission fragments are determined near or at the scission point based on the potential energies of the nascent fragments, without considering the evolution of the fissioning system before the scission point. In the Scission-Point Model, the fragments are treated as nearly touching, coaxial spheroids with a separation distance denoted as d and deformations β_1 and β_2. The potential energy at the scission point is calculated as the sum of a liquid-drop term (V_{LDM}) accounting for collective degrees of freedom, and a single-particle contribution that includes a separate shell (S) and pairing (P)

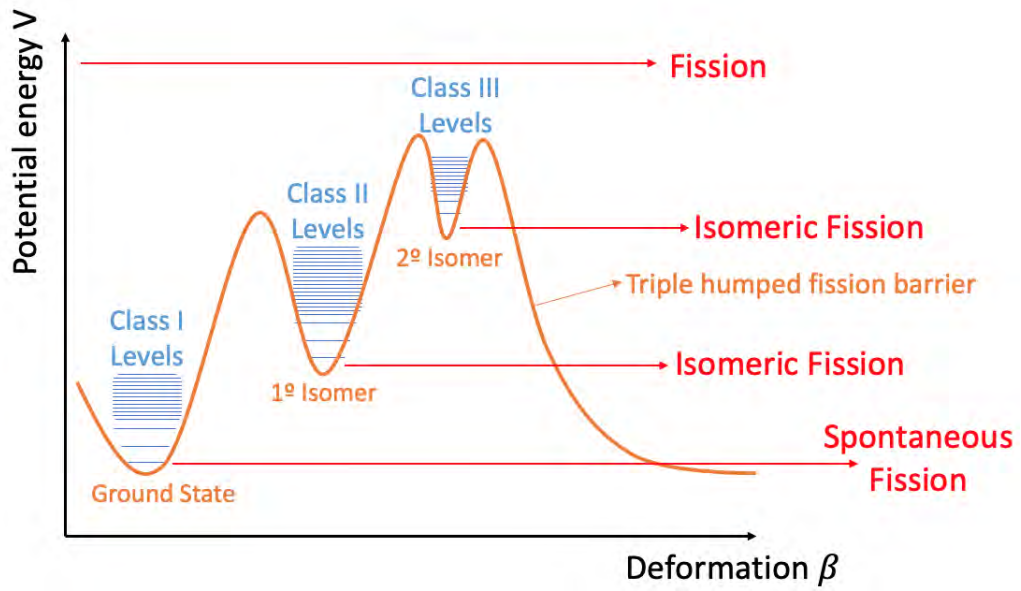

Figure 1.9: *Schematic illustration of the triple-humped fission barrier with Class I, II and III, and the comparison between spontaneous fission and isomeric fission.*

corrections for protons and neutrons in each spheroid. The interaction between the spheroids is represented by the sum of Coulomb (V_C) and nuclear (V_N) potentials. The Scission-Point Model determines the distribution of fission fragments by considering the relative potential energies of complementary pairs of nascent fragments. The deformations are defined as $R = r_0(1 + \frac{2}{3}\beta)$ and $r = r_0(1 - \frac{1}{3}\beta)$. Therefore, the total potential energy is expressed as the sum of the contributions from each fragment separately, given by:

$$\begin{aligned} V(N_1, Z_1, \beta_1, N_2, Z_2, \beta_2, \tau, d) = {} & V_{LDM_1}(N_1, Z_1, \beta_1) + V_{LDM_2}(N_2, Z_2, \beta_2) + \\ & + S_1(N_1, \beta_1, \tau) + S_1(Z_1, \beta_1, \tau) + S_2(N_2, \beta_2, \tau) + S_2(Z_2, \beta_2, \tau) + \\ & + P_1(N_1, \beta_1, \tau) + P_1(Z_1, \beta_1, \tau) + P_2(N_1, \beta_1, \tau) + P_2(Z_1, \beta_1, \tau) + \\ & + V_C(N_1, Z_1, \beta_1, N_2, Z_2, \beta_2, d) + V_N(N_1, Z_1, \beta_1, N_2, Z_2, \beta_2, d)\,. \end{aligned} \tag{1.21}$$

The shell correction (S) is calculated using the Strutinsky approach (see Section 1.3.3), which considers the deformation and intrinsic temperature to determine the occupancy of single-particle levels. The shell corrections as a function of deformation (β) for protons and neutrons separately is illustrated in Fig. 1.10, with red regions indicating the strongest corrections below -4 MeV. At small deformations, the model accurately predicts the presence of spherical magic numbers 50 and 82, while at higher deformations ($\beta \approx 0.625$), deformed shells emerge around $N \approx 66$ and $N \approx 88$ (energy levels with significantly greater energy gaps compared to the subsequent level). Additionally, the pairing correction (P) is incorporated in the model, accounting for the pairing energy of nucleons within the nucleus through the Bardeen, Cooper, and Schrieffer (BCS) standard formalism [26].

The Coulomb interaction, denoted as V_C, is computed as the repulsion between two spheroids with charges Z_1e and Z_2e, respectively. It can be expressed as:

$$V_C = \frac{Z_1 Z_2 e^2 F}{D}\,, \tag{1.22}$$

where the factor F, ranging from 1.0 to 1.1, incorporates the discrepancy between the Coulomb interaction of two uniformly charged spheroids and the interaction between two point charges separated by a distance D. Lastly, the term V_N represents the nuclear interaction between the two fragments at the scission point. Wilkins *et al.* adopted the interaction proposed by Krappe and Nix [27], where a fixed tip distance of $d = 1.4$ fm is utilised to restrict the strength of the nuclear interaction to be comparable to the binding energy of a single nucleon.

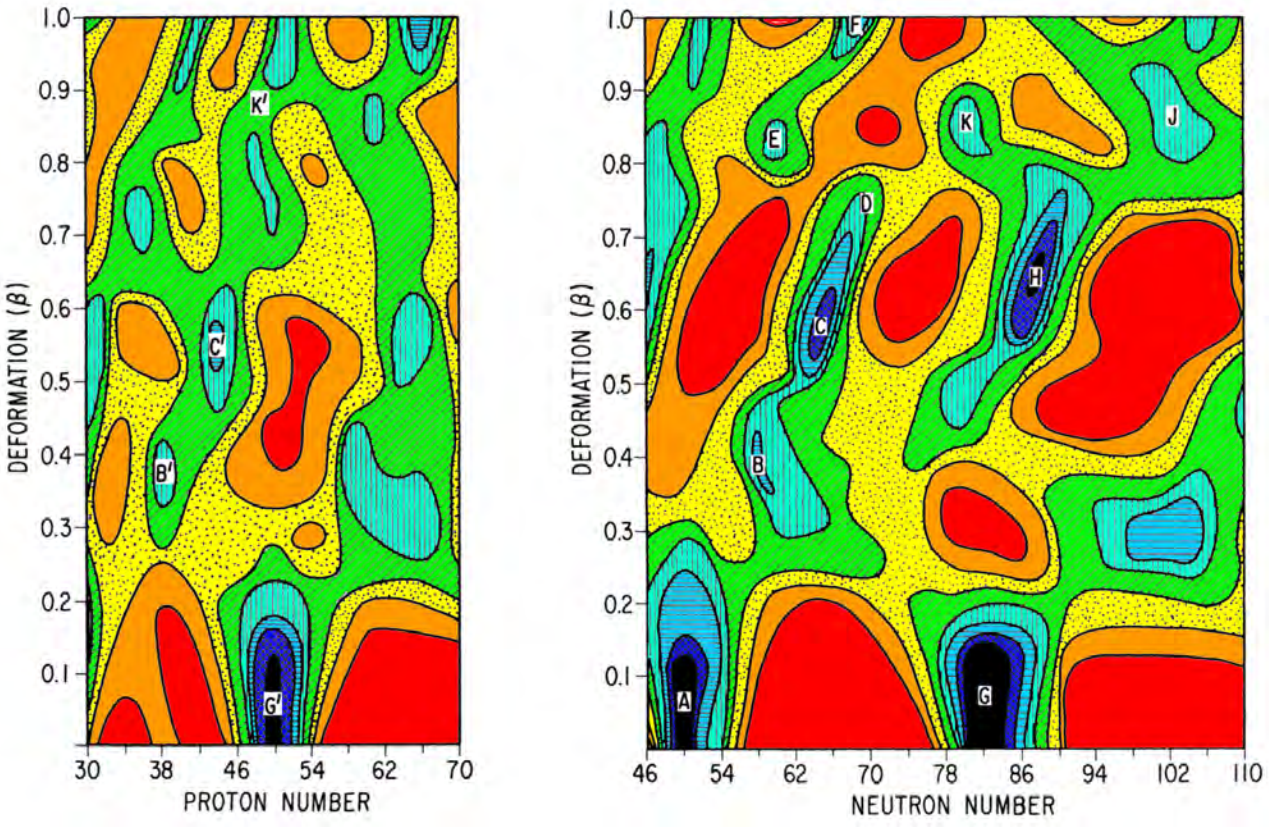

Figure 1.10: *The figures show the shell corrections (S) of the nascent fission-fragment potential as functions of the deformation parameter (β) and proton (left) and neutron (right) numbers, calculated separately using the Scission-Point model. The red regions in the figures indicate areas of strong shell effects, with values lower than -4 MeV. Thus, the independent variable is the deformation parameter (β). These representations have been modified with colour for clarity and adapted with permission from [25]. Copyright (1976) by the American Physical Society.*

The Scission-Point Model adopts an intermediate coupling between the collective and single particle levels as the system approaches scission. This scenario is characterised by introducing a collective temperature (T_{coll}) to represent the quasi-statistical equilibrium of the collective degrees of freedom, and an effective intrinsic temperature (τ) to account for the population of single-particle levels. In cases of strong coupling between the collective and single-particle motion, a statistical equilibrium is assumed across all degrees of freedom, described by a single temperature (statistical model). Conversely, when there is no coupling between the collective and single-particle motion, all energy is concentrated in the collective degrees of freedom, resulting in no single-particle excitation ($\tau = 0$). The actual fission process likely falls between these two extremes, with the nucleus exhibiting some degree of coupling between the collective and intrinsic degrees of freedom, indicating a certain level of nuclear viscosity.

The calculation of the relative probabilities of complementary fission fragment pairs formation relies on the fundamental concept of quasi-equilibrium among collective degrees of freedom, given by:

$$\Phi(N, Z, \tau, d) = \int_{\beta_1}^{\beta_{max}} \int_{\beta_2}^{\beta_{max}} e^{\frac{-V(N,Z,\beta,\tau,d)}{T_{coll}}} d\beta_1 d\beta_2 \,, \tag{1.23}$$

where β_{max} is directly equal to 1.0 in the case of Wilkins *et al.*

A comparison of the mass distributions for ^{227}Ra (a) and ^{236}U (b) is presented in Fig. 1.11. The calculated data obtained from the Scission-Point Model described in [25] are represented by dashed lines, while the experimental data [28] from the reactions ^{226}Ra(p, f) with $E_p = 13$ MeV and ^{235}U(n_{th}, f) [29] are depicted by solid lines. The Scission-Point Model shows some success in reproducing the overall features of the mass distributions, capturing the two and three-humped shapes observed experimentally. However, discrepancies arise in terms of the position and width of the distributions, suggesting possible limitations of the model in accounting for dissipation effects and accurate parameter assignments such as d, τ, or T_{coll}. Further refinements may be necessary to enhance the predictive capabilities of the model, as seen in more recent articles (see [30]).

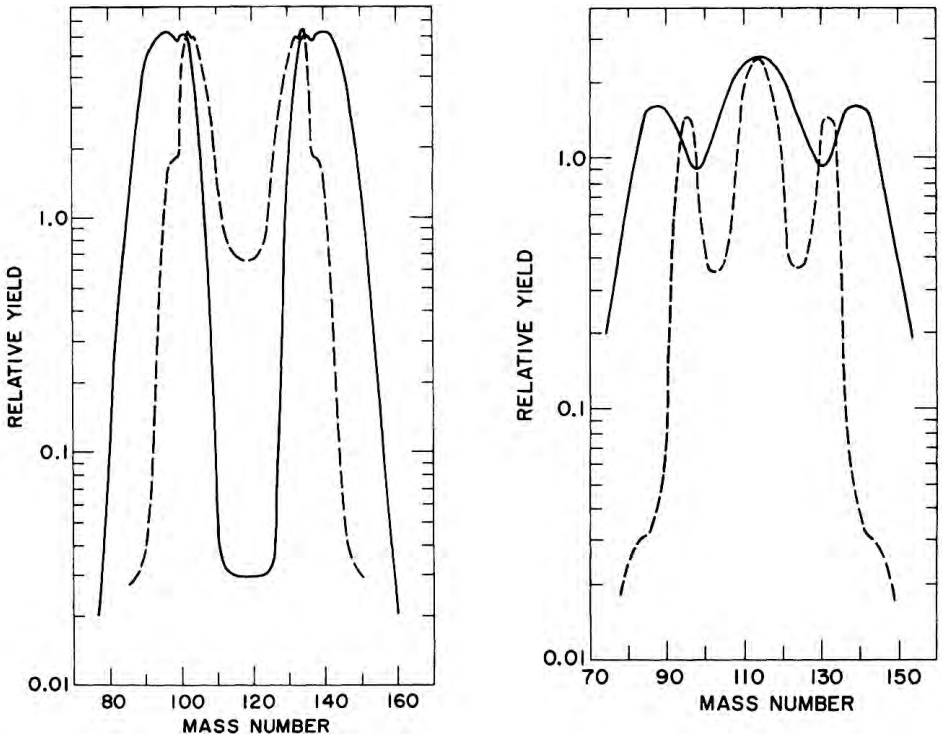

Figure 1.11: *The Scission-Point Model, as formulated in [25], is used to calculate the mass yields of ^{227}Ra (a) and ^{236}U (b). The dashed lines represent the calculated distributions, while the solid lines represent the experimental data obtained from the reactions ^{226}Ra(p, f) ($E_p = 13$ MeV) [28] and ^{235}U(n_{th}, f) [29]. Adapted with permission from [25]. Copyright (1976) by the American Physical Society.*

1.3.5 Fission modes and Random Neck Rupture Model

In 1990, Brosa, Grossmann, and Müller developed a new model aimed at describing the features observed in fission [31], such as fragment distribution, neutron evaporation, and total kinetic energy. This model consists of two main steps: the fission channels along the potential-energy surface before the scission point and the random neck rupture that occurs at

the scission stage. To construct the potential-energy surface in this model, Brosa *et al.* employed the Strutinsky method (see Section 1.3.3). Instead of calculating the full potential surface as a function of the deformation parameter, they identified specific points where the potential undergoes bifurcations. From each bifurcation, paths corresponding to distinct fission channels emerge, defining well-defined characteristics of the system at scission. In total, five fission channels are described.

The Random Neck Rupture Model (RNRM) proposed by Brosa *et al.* calculates post-fission observables, including mass distribution, kinetic energy distribution, and neutron multiplicity. According to this model, the pre-scission shape of the fissioning nucleus determines the post-fission observables. The RNRM has been successful in explaining the width of the mass distribution in both low- and medium-energy fission reactions.

The five fission channels described by Brosa *et al.* capture the different paths followed by the fissioning system along the potential-energy surface before reaching scission. These channels are associated with distinct features observed in fission:

- *Super-short channel*: This symmetric channel, observed only in nuclei heavier than ^{252}Cf, corresponds to the zero-asymmetry valley of the potential energy surface. It produces quasi-spherical fragments with similar masses, resulting in narrow mass distributions, high total kinetic energy, and negligible neutron evaporation.
- *Super-long channel*: Another symmetric channel that requires significant deformation of the fissioning system to produce equal fragments. The emitted fragments exhibit large deformations, leading to wider fragment distributions, low total kinetic energy, and high neutron evaporation.
- *Standard I channel*: An asymmetric channel influenced by the shell effect of the doubly magic nucleus ^{132}Sn. It is characterised by an almost spherical heavy fragment and a deformed light fragment. The resulting fragment distributions show a heavy component centred around $A = 135$ and $Z = 52$. A compact configuration at scission generates high total kinetic energy. The neutron evaporation is higher in the light fragment due to the excess energy stored in deformation.
- *Standard II channel*: Another asymmetric channel characterised by a deformed heavy fragment and a spherical light fragment. The fragment distributions display a heavy component centred around $A = 140$ and $Z = 54$. The total kinetic energy is lower due to a less compact configuration at scission, while neutron evaporation is significant.
- *Super-asymmetric channel*: A less common asymmetric channel with highly asymmetric mass distribution.

The scission configuration of four out of the five channels: *Super-short* (a), *Super-long* (b), *Standard I* (c), and *Super-asymmetric* (d) is illustrated in Fig. 1.12. The Figure also displays the corresponding mass distribution using dots and represents neutron evaporation with solid lines. The scission configuration plays a crucial role in understanding the final fragment observables, and the fission channels alone are insufficient to explain them. Brosa *et al.* propose a model that incorporates the concept of a random neck rupture to establish a connection between the scission configuration and the formation of the fragments.

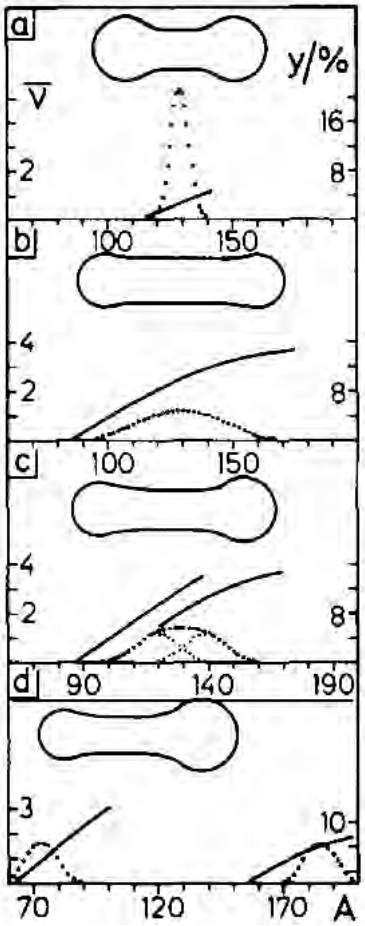

Figure 1.12: *Schematic representation of the scission point configuration for different fission channels: Super-short (a), Super-long (b), Standard I (c), and Super-asymmetric (d). The corresponding mass fragment distributions (dots) and neutron evaporation (solid line) are reported for each channel. Adapted with permission from [31]. Copyright (1990) by the Elsevier Science B.V.*

In this model, the nascent fragments at scission are represented as two spheroids connected by a hyperbolic flat neck. This scission configuration is depicted in Fig. 1.13, where the upper part represents the pre-scission stage with the nascent fragments still connected through the neck, and the lower part depicts the post-scission stage with the separated spheroid fragments. The major (a_i) and minor (b_i) axes describe the shape of the spheroids.

According to Brosa *et al.*, the system splits at a random position along the neck. The wider the neck, the greater the number of possible rupture positions, resulting in a broader distribution of fragments.

This model successfully reproduces the average mass number, measures the asymmetry of the fragments, and explains the width of the mass distribution in low- as well as medium-energy fission [32]. By considering the properties of the fissioning configuration, including the excess nucleons in the neck, the observed average mass number of $A = 140$ is obtained (see, for instance, [33]), despite the expected value being $A = 132$ based on the magic numbers $Z = 50$ and $N = 82$. This was interpreted as a consequence of the shell structure, as the heavy fragment distribution is centred near $A = 140$ (refer to Fig. 1.14). The fission fragment mass yield, according to the model of Brosa *et al.*, is influenced by the pre-scission shape, the number of evaporated neutrons, and the random position of neck rupture. When the pre-scission shape is asymmetric, with the

thinnest part of the neck off-centre, one light and one heavy fragment are produced, resulting in a double-humped mass yield distribution (refer to Fig. 1.14). Analysis of these distributions reveals that the average mass of the heavy fission fragment remains relatively constant, while the mass of the light fragment linearly increases with the mass of the fissioning system. This behaviour can be attributed to the shell structure, with the heavy fragment distribution centred around $A = 140$.

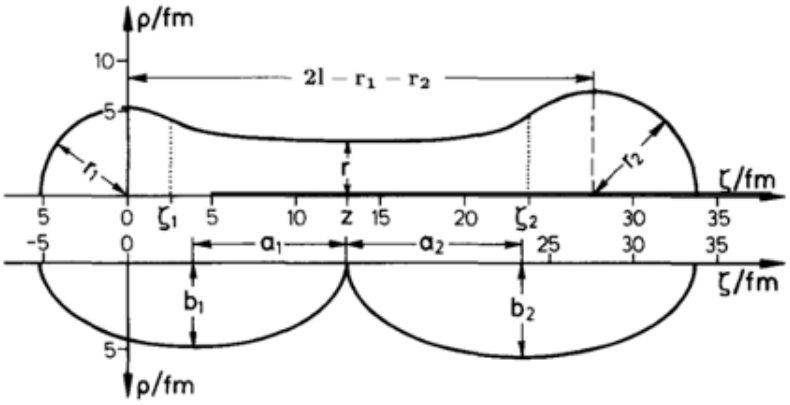

Figure 1.13: *The scission configuration, as described by Brosa et al., is illustrated [31]. The upper part depicts the pre-scission state, where the two pre-fragments are connected by a neck. In the lower part, the post-scission situation is shown, with both fragments separated after splitting. Adapted with permission from [31]. Copyright (1990) by the Elsevier Science B.V.*

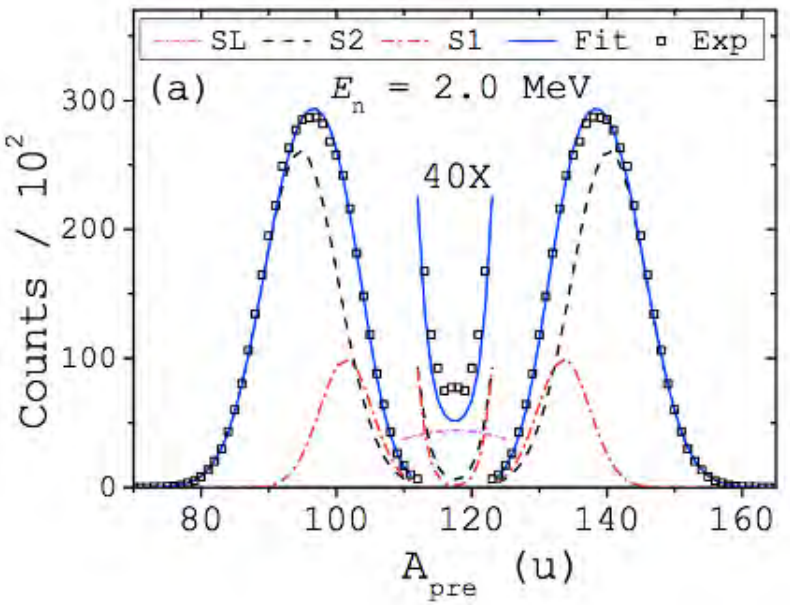

Figure 1.14: *The experimental mass yield distribution (marked data points) for the $^{234}U(n_{th}, f)$ reaction at an incident neutron energy of 2 MeV is shown, illustrating the contribution of different fission modes. Adapted with permission from [34]. Creative Commons Attribution 3.0 License (2016) by American Physical Society.*

For example, in the reaction $^{234}\mathrm{U}(n_{th}, f)$ [34], the model of Brosa *et al.* predicts three channels of mass distribution: *Superlong* (*SL*), *Standard I* (*S1*), and *Standard II* (*S2*). The *SL* mode corresponds to the symmetric scission of the nucleus, while *S1* and *S2* correspond to asymmetric division, with *S2* being more asymmetric than *S1* (see Fig. 1.14). In the energy region above the

threshold, actinide fission tends to be asymmetric. However, as the excitation energy increases, the symmetric fission component becomes more significant, resulting in a decrease in the ratio of asymmetric to symmetric yields.

The formation of fission modes was originally associated with the TKE. The generation of *Standard I* and *Standard II* fission modes, leading to systematically favoured asymmetric fission, is associated with high TKE and linked to low excitation energy and minimal energy investment in neutron emission. The *SuperLong* fission mode, which systematically favours symmetric fission, is associated with low TKE and a high energy investment in neutron emission, a preference driven by very high excitation energy. However, recent advancements in fission research have led to findings indicating that these implications are not accurate [15]; for example, *Standard II* does not necessarily exhibit high or low neutron evaporation. The random neck rupture bridged the gap between the scission configuration and the formation of the fission fragments, leading to a better understanding of the final observables.

1.3.6 Multidimensional Potential - Energy Surface Models

Nuclear fission involves nonequilibrium large-amplitude collective motion of all nucleons with complex correlation effects. To understand the transformation of a nucleus from its initial ground-state shape (fissioning system) to two separate fragments, potential energy surfaces (PESs) have been employed since the discovery of fission (see, for instance, [35]). In the current approaches, which rely on adiabatic approximation, the first step is to define relevant collective coordinates and compute the PESs.

It is worth mentioning the significant amount of energy released during the fission reaction, particularly for actinides, which can reach approximately 1 MeV per nucleon. The majority of this energy is attributed to the TKE, while the remainder is contributed by neutron and γ-ray emissions, as well as alpha and beta decays. The substantial TKE value is primarily a result of the strong repulsive Coulomb force between the two fission fragments, which can be roughly approximated by the division of the charged liquid drop. In a well-known study by Viola *et al.*, [36], a systematic relationship was proposed to describe the total kinetic energy released as a function of the Coulomb parameter $Z^2/A^{1/3}$, utilising experimental data from a wide range of fissioning nuclei. At each point on these PES, there is a certain probability of realisation, and the fissioning system must navigate them in accordance with the various variations and assumptions in the employed model. Consequently, the path with the highest probabilities dictates the primary characteristics of the calculated distribution, encompassing the most likely fragment masses and the relative intensities of the fission modes. Ultimately, the TKE distributions can be estimated using the same potential energy maps as those used for mass distributions, coupled with the underlying scission shapes parameterised based on the employed model.

Two widely used models for determining PESs are the macroscopic-microscopic (MM) approach and the energy Density Functional Theory (DFT). The MM approach considers the nucleus as a finite region of nuclear matter, with its energy parameterised based on charge, mass, and deformations, incorporating macroscopic energy, shell correction energy, and pairing energy. Various versions of the MM approach exist, employing different parameterisations of the nuclear surface within the LDM framework, such as the Five-Dimensional Finite-Range Liquid-Drop Model (FRLDM) [37], macroscopic-microscopic Woods-Saxon model [38], macroscopic-microscopic Lublin-Strasbourg Drop Model (LSD) with different parameterisations [39], and the Two-Centre

Shell Model, among others. With the multidimensional PESs obtained from these approaches, numerous methods have been developed to study the dynamical evolution in the collective space, often reproducing experimental observations.

Microscopic investigations of nuclear fission require the computation of the potential-energy surface as a function of collective coordinates. To accurately depict the topography of the surface within computational limitations, appropriate constraints on multipole moments need to be chosen. For instance, a detailed analysis of fission barriers was conducted using the self-consistent Hartree-Fock-Bogoliubov approach with the D1S parameterisation of the Gogny nucleon-nucleon interaction. Furthermore, a more comprehensive approach was proposed by Moller *et al.* in 2001 [35], wherein a potential-energy model with five parameters was utilised to describe nuclear deformation, as depicted in Fig. 1.15.

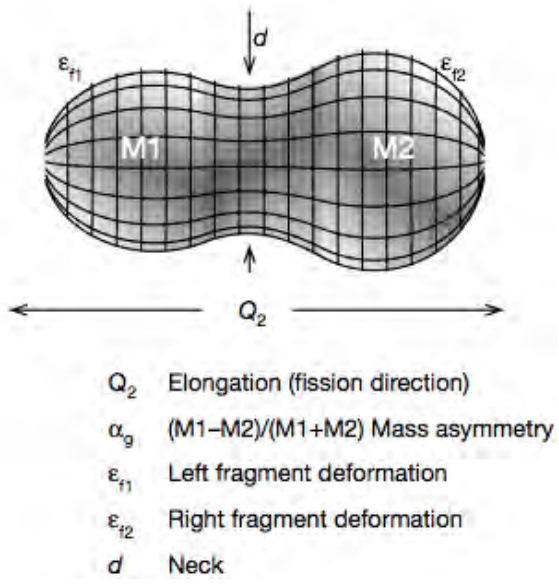

Figure 1.15: *The figure illustrates a schematic representation of a fissioning system in a five-dimensional shape parameterisation used for the PES calculation. The masses of the pre-nascent fission fragments are labelled as M1 and M2. Adapted with permission from [35]. Copyright (2001) by Nature.*

This parameterisation enables the description of potential energy as a multidimensional PES, with different fission modes, representing the transition of a nucleus from its ground state to separated fission fragments. An illustration of the potential-energy surface for the compound nucleus ^{236}U is shown in Fig. 1.2, highlighting saddle points denoted by red crossed lines and minima indicated in dark blue [13].

Nevertheless, despite the utilisation of multidimensional PES, comprehending the entirety of fission dynamics remains a profoundly intricate process that has yet to attain a fully microscopic description, despite nearly eight decades of extensive research. The formation of fission fragments has remained a contentious topic within nuclear fission phenomenology. Due to the formidable challenges posed by solving the requisite time-dependent Schrödinger equation for hundreds of strongly interacting nucleons and the absence of a comprehensive microscopic description, various phenomenological models, both quantum and classical, have been proposed over the years. Unfortunately, many of these models lack a robust microscopic foundation, and consequently, their predictive capabilities are typically confined to the processes used in their construction.

The bulk behaviour of the deformation PES is determined by the surface tension and Coulomb energy, which are rather well-known and understood, and they are the main driving force leading to fission as in liquid drop models. The underlying shell structure imprints hills and valleys on the overall charged liquid drop energy landscape. On the way to scission configuration, nucleons have to go through a large number of redistributions at the single-particle levels crossing around the Fermi level, to maintain the spherical symmetry of their local momentum distribution. As described in their article Bulgac *et al.* [12]:

> *"The deformation potential energy surface acquires a profile somewhat similar to that of an uneven mountain, with little hills and valleys and covered by trees, and the evolution of the nuclear shape is in the end similar to the erratic motion of a pinball, not straight down the hill, but rather left and right, bouncing (mostly elastically) from the many obstacles on the way to the bottom of the valley, where the pinball breaks up".*

During the final phases of this intricate development, the autonomy of nucleons within the nucleus becomes crucial once more, as the presence of magic closed shells exerts control over the evolution of nuclear shape and the ensuing division that results in the creation of fission fragments.

The transition of the nuclear shape from the ground state to the outer fission barrier occurs gradually, often described as an adiabatic process, particularly in the context of spontaneous fission. The literature approaches the description of nuclear dynamics as the nucleus traverses the outer fission barrier to reach the scission configuration in two main ways: as an adiabatic evolution, characterised by conservative dynamics, or as a damped or even overdamped motion, using similar parameters. Disagreement persists in the literature regarding the nature of these dynamics in the final stages of fission. Specifically, there is no consensus on whether it is characterised by conservative or Hamiltonian dynamics, dissipative dynamics, or even overdamped motion. Despite these diverse approaches founded on contrasting assumptions about the character of fission dynamics, they all yield reasonably accurate agreement with experimental results [40].

Two recent significant advancements have created a promising environment for achieving a microscopic understanding of nuclear fission. The first key development pertains to theory, involving the expansion of Time-Dependent Density Functional Theory (TDDFT) to superfluid fermion systems, as outlined in [41] and related references. The second advancement is computational, marked by the emergence of highly capable supercomputers equipped to address the intricate equations governing the three-dimensional time evolution of systems containing hundreds of strongly interacting nucleons without any imposed constraints. While nuclear energy density functionals (NEDFs) remain predominantly phenomenological, their accuracy is steadily improving. This progress suggests that we are approaching the capability to conduct calculations on the dynamics of nuclear fission and predict numerous properties of fission fragments.

In parallel with the Energy Density Functionals (EDF) or their functional version, upon which Bulgac *et al.* [12, 40, 41], there exist microscopic calculations that incorporate microscopic pairing correlations. These calculations involve models such as Constrained Hartree-Fock with Bardeen-Cooper Schrieffer pairing correlations (CHF+BCS) and Time-Dependent Hartree-Fock with dynamical Bardeen-Cooper Schrieffer pairing correlations (TDBCS) conducted by researchers like Scamps *et al.* [42, 43]. Based on a Time-Dependent Hartree-Fock (TDHF) model [44]. Scamps *et al.* have developed a microscopic model that provides valuable insights into nuclear

fission. Their work indicates that, in the absence of quantum shell effects, heavy nuclei predominantly undergo mass-symmetric fission, resulting in two fragments of similar mass. However, the presence of quantum shells within the fissioning nucleus can give rise to multiple scission valleys, some of which may lead to mass-symmetric fission, while others may result in mass-asymmetric fission. While recent advances have enhanced our ability to describe fission fragment mass distributions using stochastic-based methods, the theoretical characterisation of the initial fission stage, spanning from ground-state deformation to the fission barrier, remains a formidable challenge. Nevertheless, progress has been made in studying the dynamics along the fission pathways, and this is made feasible through the application of the time-dependent energy density functional approach, which accounts for nuclear superfluidity. This approach is fully quantum and microscopic in nature as it tracks the time-dependent evolution of all single-particle wave functions, whether fully or partially occupied.

Scamps *et al.* have obtained promising results with their model regarding fission asymmetry (see [42] and references therein). They reveal that the ultimate mass asymmetry of fission fragments is influenced by the enhanced stability of octupole (pear-shaped) deformations, a characteristic recently experimentally confirmed near ^{144}Ba ($Z = 56$) [45]. This nucleus is one of the rare instances exhibiting shell-stabilised octupole deformation. Utilising a contemporary quantum many-body model for superfluid fission dynamics, it has been determined that heavy fission fragments are primarily characterised by the presence of 52-56 protons, signifying substantial octupole deformation acquired during the fission process. These octupole deformations, which favour asymmetric fission, are induced by deformed shells at $Z = 52$ and $Z = 56$. In contrast, spherical "magic" nuclei are highly resistant to octupole deformation, which diminishes their occurrence as fission fragments.

1.3.7 Semi-empirical GEF code

The GEF (GEneral description of Fission observables) code developed by K.-H. Schmidt and B. Jurado, provides a comprehensive tool for simulating and describing fission observables [46]. This semi-empirical code combines theoretical principles with empirical information to achieve a global description of the fission process across a wide range of fissioning systems.

The GEF code is a valuable tool for studying spontaneous fission, neutron-induced fission, and fission of compound nuclei formed through other entrance channels. It utilises a semi-empirical approach that combines fundamental laws of physics, general properties of microscopic systems, mathematical objects, fittings tools, etc. The code parameters (around 100) are adapted to fit experimental data, covering various aspects of the fission process such as fission barriers, probabilities, fragment distributions, kinetic energies, neutron and *gamma*-ray yields, and energy spectra.

The GEF code adopts a separability principle, dividing the fission process into two distinct steps. The first step involves the deformation of the compound nucleus, driven by the macroscopic potential, while the second step incorporates the influence of nuclear shells on the fission path and the formation of fission channels.

USC UNIVERSIDADE DE SANTIAGO DE COMPOSTELA

Dynamical effects between the saddle and scission points are taken into account through the introduction of an "effective" potential energy surface. This empirically adjusted potential considers dissipative and inertial forces, which impact the distribution of specific observables.

Before the scission point, the potential energy surface influences the fission trajectory and induces memory in the fission process. The stochastic nature of this process leads to broadened distributions of observables, which are adjusted by the effective potential energy.

The potential energy surface in GEF is calculated based on the deformation of the compound nucleus and nuclear shells in the nascent fragments. The thermodynamic approach employed by GEF relies on an entropy-driven energy-sorting mechanism [17], where the entropy behaves as a linear function of energy partition, reaching its maximum when all the available excitation energy concentrates on the nucleus with the lower temperature. At low excitation energy E, nuclei exhibit distinct characteristics, marked by a transition from superfluid to normal-liquid behaviour. Consistent with first-order phase transitions, their temperature remains constant as E increases. Consequently, the phenomenon of nuclear energy segregation aligns harmoniously with the second law of thermodynamics. In asymmetric mass divisions, it has been observed that the increase in intrinsic E_{FS} of the fissioning nucleus corresponds to an increase in E solely in the heavier fission fragments. The temperature of the heavier fission fragments is typically lower than that of the lighter ones, leading to the accumulation of all the intrinsic E^*_{FS} in the heavier fragment.

The code operates as a Monte Carlo simulation, sequentially computing the decay of the system from the specified entrance channel reaction or initial compound nucleus. including the possibility of pre-equilibrium emission, and pre-scission evaporation (referred to as multi-chance fission)[4], (A, Z) production of the primary (excited) fission fragments, post-scission evaporation and γ-ray emission, (A, Z) population of the final (secondary) products and their radioactive decay wherever suited by delayed neutrons and/or γ-rays. In addition, GEF model calculates the energy of the evaporated neutrons and the energy of the emitted *gamma*-ray emission, the spin of the fission fragments before and after the scission, the multipolarity of the *gamma*-ray emission, etc.

The correlations between different quantities are preserved throughout the calculation, and no parameters need to be adjusted by the user, although some may be modified if necessary. The fixed parameters, determined through benchmark experimental data, apply to a wide range of systems and excitation energies.

1.3.7.1 Theory behind GEF

An important aspect of fission calculations is the determination of the fission probability, which defines the initial properties of the nuclei that undergo fission. In GEF, this probability is closely linked to the calculation of the fission barrier. The fission barriers in GEF are obtained using the macro-microscopic approach, incorporating the concept of the topographic theorem [47]. According to this theorem, the barrier is determined by the sum of the macroscopic barrier, derived from the extended Thomas-Fermi prescription, and the additional binding energy contributed by the empirical ground-state shell correction. Furthermore, the presence of enhanced pairing correlations at the saddle point is also taken into account. As a result, shell corrections at the saddle are neglected, as suggested by the topographic theorem. This approach avoids the uncertainties associated with theoretical shell-correction energies and allows for differentiation between various macroscopic models [48].

[4] In GEF, multi-chance fission is specifically associated with pre-fission evaporation. However, it is important to note that evaporation can still occur between the saddle and scission points, but this occurs when the nucleus is already "condemned" to fission.

Another important aspect is the partitioning of primary fragments (A, Z) at the scission point, which is a significant consideration in the modelling of fission. GEF incorporates several concepts to address this phenomenon, including the early influence of fragment shells [49], the use of quantum oscillators to represent fission modes, and the concept of dynamical freezing [50]. In GEF, the fission channels correspond to the statistical distribution of quantum oscillators in the mass-asymmetry degree of freedom, forming distinct fission valleys. Each fission channel is characterised by three parameters related to the macroscopic potential and the proton and neutron shells in both fragments, assumed to be effective near the outer saddle [49]. These shells are assumed to be the same for all fissioning systems, but their combination and interaction with the macroscopic potential lead to varying mass distributions across different systems [51]. The shape of the nascent fragments at scission, primarily quadrupole deformation, is also determined by these shells. Additionally, the charge polarisation, reflecting deviations from the N/Z ratio of the fissioning nucleus, is accounted for using the corresponding quantum oscillator [52]. The model has been adjusted to experimental data, and it has been found that four fission channels are necessary: the symmetric *SL* channel and three asymmetric channels (*S1*, *S2*, and *SA*). The empirical adjustment procedure has determined the values of all model parameters through benchmark comparisons with experimental mass and charge distributions across a wide range of nuclides [53].

The third important aspect addressed in this contribution relates to the energetics of fission, specifically the distribution of energy between the fragments at scission, which influences the decay of the primary fragments and the population of the secondary fragments. The presence of pairing correlations leads to a constant nuclear temperature below the critical pairing energy [54]. Consequently, the di-nuclear system between the saddle and scission can be viewed as two coupled microscopic thermostats [17], resulting in a sorting process of intrinsic energy and unpaired nucleons before scission. Within the thermodynamic framework implemented in GEF, the fission process follows an entropy-driven energy-sorting mechanism. For systems with excitation energies below 20 MeV, pairing correlations contribute to an effective increase in the number of degrees of freedom proportional to the excitation energy. Consequently, the temperature of the nucleus, defined as the average excitation energy per degree of freedom, remains constant [53]. Experimental studies on nuclear level densities [55] have confirmed the validity of modelling the temperature of nuclei as a function of nuclear mass, providing a satisfactory fit to the data at low excitation energies E^*_{FS}:

$$T \propto A^{-2/3}\,. \tag{1.24}$$

Actually, in a study conducted by Egidy *et al.* [55], the temperature of nuclei has been found to depend on the mass number (A) of the nucleus and the shell effects (S). This relationship was determined by fitting available data on nuclear densities, and it can be expressed as:

$$T = A^{-2/3}/(17.45 - 0.51 \cdot S + 0.051 \cdot S^2)\,, \tag{1.25}$$

with a level density that can be accurately described by the constant-temperature formula:

$$\rho(E^*_{FS}) \propto e^{E^*_{FS}/T}\,. \tag{1.26}$$

In the scission-point configuration, where the nascent fragments are considered as two separate nuclei in thermal contact through the neck, the level density of each fragment is described by the constant-temperature Eq. 1.26, with a specific value of temperature (T) assigned to each fragment. According to this equation, there is no solution where the excitation energy (E^*_{FS}) is

shared equally between the two fragments ($T_1 = T_2$). Instead, if there is remaining excitation energy in the fragment with a higher temperature (light fragment), that energy is completely transferred to the fragment with a lower temperature (heavy fragment) [55].

The transfer of excitation energy from the hot fragment to the cold fragment can be understood as a means for the entire system, consisting of the contacting pre-fragments, to maximise the number of occupied states or its entropy. Since the number of available states in the light fragment is smaller compared to the heavy fragment, the entropy is maximised when all of the excitation energy is transferred to the heavy fragment, which has a greater number of available states. This superfluid behaviour is combined with the Fermi-gas behaviour at higher excitation energy E^*_{FS}, where the total excitation energy is distributed among the fragments in proportion to their masses:

$$\frac{E^*_1}{E^*_2} = \frac{A_1}{A_2} \tag{1.27}$$

The GEF code, operating within the described framework, has demonstrated its capability to describe a wide range of observables across various nuclides [46], excitation energies, and angular momenta. Its simplicity and efficiency make it a widely used tool in the scientific community for tasks such as handling experimental data, providing guidance for theoretical models, and interpreting experimental results. However, to further validate and improve the GEF code, high-quality experimental data are essential.

1.4 Quasi-fission

The discussion will now focus on "*quasi-fission*" and the experimental signatures associated with this process, which will be explored in the subsequent Section 1.4.1. Early indications suggest that the fission fragments observed in heavy-ion bombardments can originate from a slightly different process, although certain properties justify the use of the term "fission" in its description.

In the study conducted by Heusch *et al.*, they observed one of the earliest indications that fission fragments can arise from non-equilibrium fission. They investigated the reaction of ^{132}Xe + ^{56}Fe at 5.73 MeV/u and found a fission-like cross-section of 1040 mb, corresponding to a maximum compound nuclear spin of 120$\hbar$ (according to the sharp cutoff model) [56]. This observation aligned well with fusion models of this time [57][58], suggesting that fission accounted for the total fusion cross-section. However, they also recognised that not all of these reactions could be attributed to an equilibrated compound nucleus, as the fission barrier disappears for spins larger than approximately 72$\hbar$ according to the Rotating Liquid Drop Model [59]. Consequently, the fission-like processes originating from angular momenta in the range of 72$\hbar < \ell <$ 120$\hbar$ were classified as "*fission without a barrier*". In their paper, they made the following statement:

> *"The strongly damped component which constitutes the major part of the reaction cross-section exhibits characteristics of a fusion-fission reaction with typical fission fragment kinetic energies and* $1/sin(\theta)$ *angular distributions... We tentatively conclude that an essential part of the fully damped cross-section originates from partial waves for which the compound nucleus has no fission barrier".*

USC UNIVERSIDADE DE SANTIAGO DE COMPOSTELA

Furthermore, researchers noted a significant increase in the width of the mass distribution of fission fragments in partial waves where the fission barrier disappears. Lebrun *et al.* [60] conducted a study on fission mass distributions in reactions of ^{20}Ne + ^{nat}Re and ^{40}Ar + ^{165}Ho at two different

bombarding energies. They observed a noticeable widening of the fragment mass distributions with increasing angular momentum, particularly above the partial wave where the fission barrier vanishes. This finding was further supported by Borderie *et al.* [61], who reviewed a larger dataset and concluded that "*fast fission*" occurs for $\ell-$values where the fission barrier disappears, see Fig. 1.16. Shen *et al.* provided additional evidence by analysing the mass width of fission-like reaction products in U-induced reactions [62]. They observed that while reactions involving ^{16}O and ^{24}Mg displayed the expected width, heavier targets led to broader mass distributions.

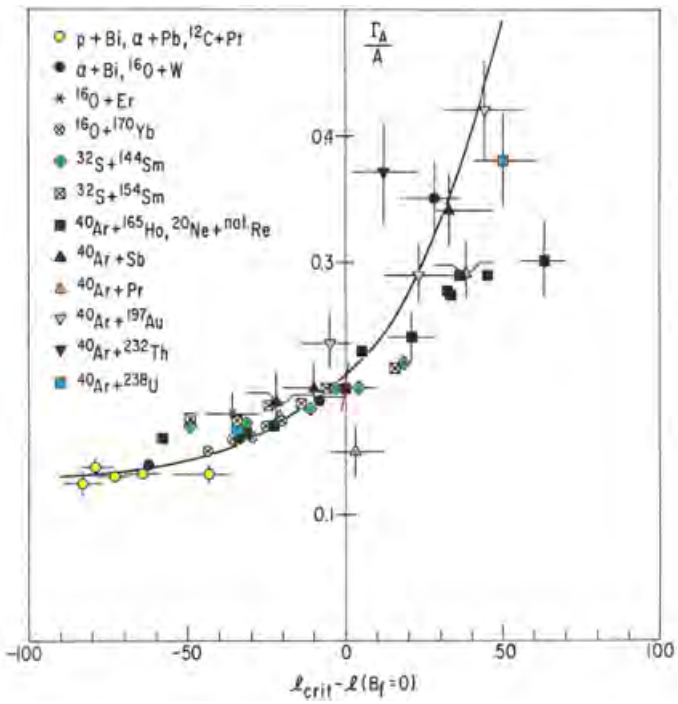

Figure 1.16: *The width of the fission fragment mass distribution is represented through the reduced mass width (FWHM of the mass distribution divided by the compound nucleus mass, denoted as Γ_A/A), is represented for different reactions to study the angular momentum characteristics of the reaction. Represented as difference in angular momentum. Specifically, the focus was on the difference between the maximum angular momentum populated during the capture phase (ℓ_{crit}) and the angular momentum at which the fission barrier completely vanishes ($\ell_{Bf} = 0$). The observed increasing width of the mass distribution was attributed to a phenomenon known as "fission without barrier" or "fast fission". This indicates that fission can occur even in the absence of a discernible barrier. The data with positive values on the abscissa indicating contributions from "fission without a barrier". Picture with permission from [63] adapted from the original in [61] with permission. Copyright (1981) by the Springer-Verlag.*

The width of the mass distribution can be estimated in a thermal model by assuming a quadratic mass asymmetry potential:

$$U(A) = \frac{1}{2} k_s \cdot (A - A_S)^2 \,, \tag{1.28}$$

where A_S is the symmetric mass, and k_s is the stiffness coefficient, which based on Liquid Drop Model [64] estimates is about $k_s = 0.0035$ MeV/u^2. A temperature T, the variance of the mass distribution is:

$$\sigma_A^2 = \frac{T}{k_s} = \frac{1}{k_s}\sqrt{\frac{8.5E^+}{A}} \,, \tag{1.29}$$

where E^+ is the nuclear excitation energy at scission given by:

$$E^+ = E^*_{FS} + Q_{sym} - TKE - E_{def} - E_{rot} \,, \tag{1.30}$$

In the given context, where E^*_{FS} represents the excitation energy of the compound system, Q_{sym} denotes the *Q-value* for symmetric fission, TKE signifies the total kinetic energy estimated using Viola systematics [36], E_{def} represents the fragment deformation energy assumed as 12 MeV, and E_{rot} corresponds to the rotational energy at scission, it is anticipated that the mass width will exhibit a weak (fourth root) increase with increasing excitation energy. This dependence aligns well with the observed data.

Fusion is the process where two nuclei merge completely, forming a new compound nucleus while conserving quantities like the total number of protons and neutrons, energy, angular momentum, and parity. When lighter nuclei (with $Z_1 \cdot Z_2 < 1000$) undergo fusion, the process is relatively straightforward. Sufficient kinetic energy overcomes the Coulomb repulsion between the nuclei, leading to an overlap of their nuclear matter distributions. This overlap generates an attractive nuclear force that overcomes the repulsion, allowing the nuclei to come closer and form a compact compound nucleus, akin to the merging of liquid droplets due to surface tension. This process is described by the inter-nuclear potential, which exhibits a peak where the nuclear and Coulomb forces balance (previously referred to as the "fusion barrier" or "Coulomb barrier"). However, for systems with larger $Z_1 \cdot Z_2$, quasi-fission may occur beyond this point, prompting the adoption of the term "capture barrier".

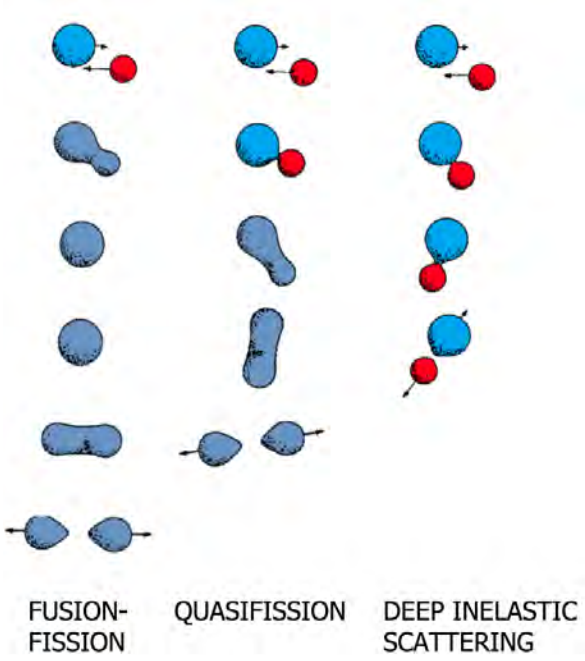

Figure 1.17: *Schematic drawing of the three competing processes when two nuclei are accelerated and collided. On the left, is the fusion-fission process with the formation of a compound nucleus. In the middle, the quasi-fission process is where the two nuclei are in contact for a very short time, exchange nucleons, and separate before completing a full rotation together. On the right, is an inelastic scattering. Picture with permission from [63] adapted from the original in [65] with permission. Copyright (1985) by the North-Holland Publishing Company.*

In reactions involving heavy nuclei, the relative angular momentum (or orbital angular momentum) $\ell\hbar$ can easily exceed $100\hbar$. At such high angular momenta, where no potential pocket is expected, the relative energy of the two nuclear surfaces can force them into close contact. This results in multiple nucleon-nucleon interactions, primarily nucleon exchange, with minimal mass drift but significant energy dissipation. These interactions are known as Deep Inelastic

Collisions (DIC) and have been extensively studied since the 1970s, representing the "energy damping mode" in heavy ion collisions (described previously). During the 1970s, experimental evidence hinted at a third process, known as quasi-fission, which exhibits intermediate properties between DIC and fusion. In the 1980s, quasi-fission was characterised as having fully damped outgoing kinetic energies, similar to fission following fusion [66]. The masses of the outgoing nuclei tended to evolve towards a symmetric mass-split, although they were not fully equilibrated as in fusion-fission. Furthermore, angular distributions deviated from the expectations for fusion fission. quasi-fission was referred to as the "mass drift mode" in heavy ion collisions [65]. A schematic representation comparing these three processes is represented in Fig. 1.17.

When heavy-ion-fusion reactions induce fission, the fusion-fission process can be accompanied by a competing quasi-fission mechanism. As explained before, quasi-fission occurs when the combined system, composed of the two colliding ions, splits into two fragments before reaching thermodynamic equilibrium and forming a compound nucleus. Nowadays, is known that the probability of quasi-fission increases with the mass of the interacting ions. One key characteristic that distinguishes quasi-fission from fusion-fission is its timescale, which represents the duration of contact between the two nuclei before they separate. The timescale of quasi-fission has been observed to be typically shorter than the rotational period of the resulting system, ranging from 10^{-21} to 10^{-20} s. In comparison, the timescale for fusion-fission falls within the range of 10^{-20} to 10^{-19} s. This difference in timescales highlights the dynamical nature of quasi-fission [65][62]. Without a fission barrier to inhibit the fission process, it should be faster than fusion-fission. The energy-damped events observed in heavy ion reactions span a continuous distribution of masses from the projectile to the target, which is inconsistent with fusion-fission. It was noticed that the cross sections around symmetry were significantly smaller than expected based on fusion models, indicating the presence of the competing process of quasi-fission, which occurred at the expense of the fusion yield.

In experimental observations, both quasi-fission and fast fission can contribute to fission-like events in the same reaction, depending on the conditions of the entrance channel. If capture occurs at high angular momenta where the fission barrier is reduced to a negligible height or zero, both processes can be present. Since the fission fragment characteristics of quasi-fission and fast fission often overlap, observed fission events typically involve contributions from both processes.

The shorter timescale of quasi-fission, in comparison to the rotation time, results in a correlation between the mass of the fragments and their emission angles. This correlation is not observed in fusion-fission. Therefore, the measurement of the Mass-Angle Distribution (MAD), which is described in the following part Section 1.4.1, offers insights into the quasi-fission process and enables its differentiation from fusion-fission.

1.4.1 Mass-Angle Distribution and Mass-Energy Distribution

As was introduced in the previous Section 1.4, when the full range of produced fragment masses is correlated with their corresponding emission angles, the mass-angle distribution (MAD) is obtained. The MADs, which are two-dimensional matrices showing the fission fragment mass (or mass-ratio $M_R = M1/(M1 + M2)$) as a function of the centre-of-mass angle, provide complementary information to the mass-energy distributions (MEDs). The MAD represents the double differential cross-section $d^2\sigma/(d\theta dA)$, where A is the deduced mass number, or $d^2\sigma/(d\theta dM_R)$, which uses M_R to avoid assumptions about the mass at scission. In heavy ion

reactions, the $d\sigma/d\phi$ for fission is constant and for that $d\sigma/d\Omega$ is generally used as $d\sigma/d\theta$ [67].

A description of the relationship between the characteristics of MADs and the dynamics of the reaction is provided in Fig. 1.18. The rotation and mass equilibration between capture and scission is illustrated for a non-zero impact parameter, with the lighter partner acting as the projectile. The change in the centre-of-mass angle theta for both the projectile-like (blue) and target-like (red) fragments is shown in Fig. 1.18(a), assuming a constant moment of inertia. Additionally, the asymptotic approach of the mass-ratio M_R towards mass symmetry is depicted in Fig. 1.18(b), indicating overdamped motion in parabolic potential energy with a minimum at symmetry [68].

The lifetime of the system before splitting and its connection to the MAD is also portrayed in Fig. 1.18. The collision between the projectile nucleus (blue) and the heavier target nucleus (red) initiates rotation and mass exchange, with the mass of the heavier nucleus decreasing over time and transferring mass to the lighter nucleus until they separate. Figure 1.18(d) showcases the variation in the shape of the dinuclear system as a function of the sticking time, while Figure 1.18(a) displays the corresponding emission angles of the fragmentation partners. The coloured areas represent different scission times, with the pink shading indicating a shorter scission time associated with fast processes like quasi-fission, and the blue shading representing a longer scission time related to equilibrium-based reaction mechanisms such as fusion-fission. Furthermore, Figure 1.18(b) illustrates the evolution of mass during the process, indicating that shorter contact times result in the less exchanged matter, whereas longer contact times lead to more similar fragments. Finally, Figure 1.18(c) presents the MAD, which combines masses and angles, displaying a clear correlation when the dinuclear system undergoes a 180° rotation (pink shading in Fig. 1.18(a) and (c)). However, after the system rotates by 360° or more, the correlation between fragment mass and angle disappears, resulting in symmetric mass sharing independent of the angle (blue shading).

The direct measurement of time in zeptoseconds (10^{-21} s) is currently not feasible. However, the emission angles of the fragments and their masses can be measured, and when plotted in the MAD, they provide valuable insights into the dynamics of the quasi-fission process.

In Fig. 1.18(c), where M_R is plotted against θ, the trajectories of the projectile-like and target-like nuclei in M_R and θ exhibit characteristic correlated evolution in both mass and angle. The yellow arrow in Fig. 1.18(c) indicates the projectile nucleus: if the heavy nucleus were the projectile, the MAD would be mirrored in θ: this is the case in Fig. 1.20. It is important to note that the correlation observed in an experiment depends on the relationship between the rotation time and the mass evolution time. Different regions in the MAD correspond to different rotation times. For short-lived events with only a fraction of a full rotation, the yellow-shaded rectangular region in Fig. 1.18 will be populated. For half a rotation, the pink region will be populated, while for a full rotation or more (blue region), the correlation between mass and angle will be minimal.

It is worth mentioning that, in a measurement, contributions from various impact parameters will be present, leading to a spread-out angular correlation. Additionally, it is important to note that Figure 1.18 does not represent the relatively small additional contribution to the observed angle of the fragments resulting from the incoming and outgoing Coulomb trajectories. Nonetheless, the MAD analysis offers valuable information about the dynamics of quasi-fission, providing insights into the relationship between mass and angle evolution in the process.

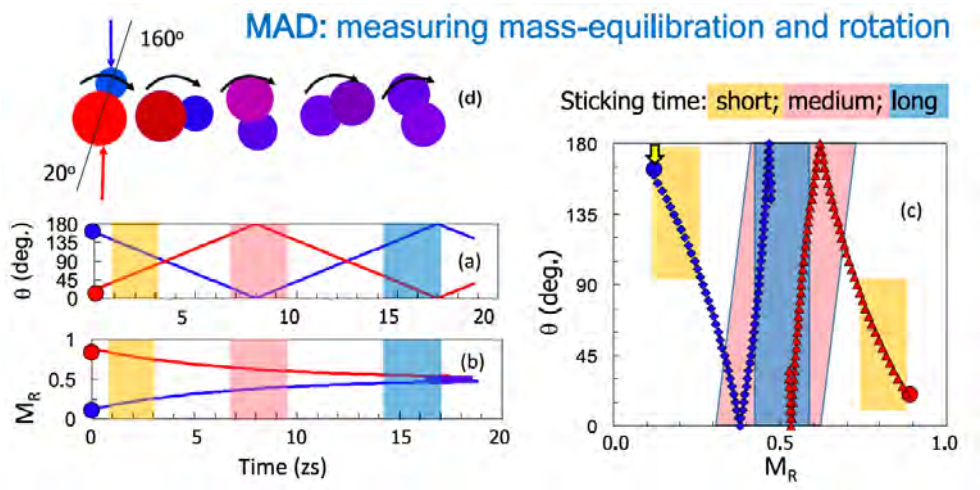

Figure 1.18: *Illustration of the fundamental principles of the mass-angle distribution (MAD). At the top, a sequence of shapes is depicted, representing the successive stages of the interaction between a light nucleus (blue) and a heavy nucleus (red) at an initial centre-to-centre contact angle of 160 degrees. Schematic diagrams (a) and (b) demonstrate the variation of the scattering angle θ and the mass-ratio M_R over time. Although the time scale is too brief for direct measurement, both θ and MR can be experimentally determined. The individual trajectories in θ and M_R are then mapped onto the MAD plot (c), which displays different outcomes corresponding to short, medium, and long sticking times. These outcomes correspond to the three categories of the MAD presented in Fig. 1.19. Adapted with permission from [63]. Copyright (2021) by the Elsevier Science B.V.*

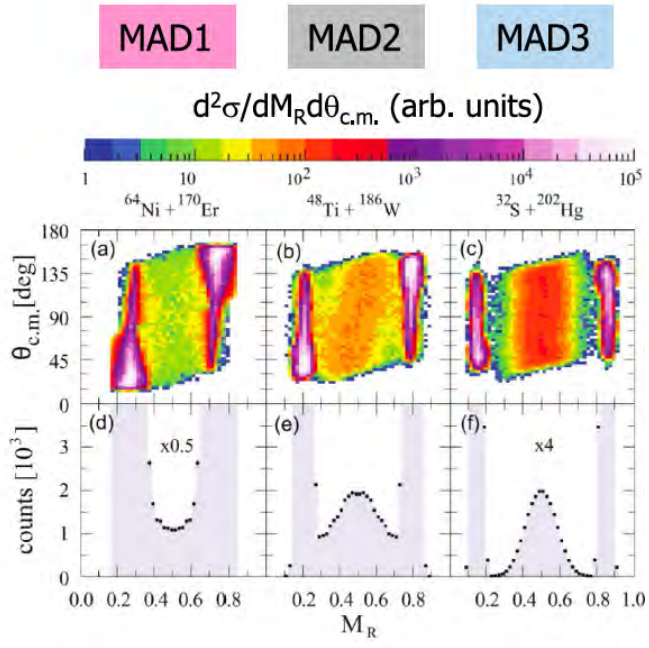

Figure 1.19: *The measured mass-angle distributions (MADs) and their corresponding projections onto the mass ratio (M_R) are displayed in panels (a) to (f) for the indicated reactions, all resulting in the formation of ^{234}Cm. The y-axis of each MAD is scaled using multiplicative factors. Each reaction exemplifies one of the three MAD categories mentioned above the yield scale at the top of the figure. Picture with permission from [63] adapted from the original in [69] with permission. Copyright (2013) by the American Physical Society.*

The MED and the MAD for the reactions ^{238}U + ^{27}Al and ^{238}U + ^{48}Ca at an incident energy per nucleon (E/A) of 6 MeV is presented in Fig. 1.20, which corresponds to approximately 10% and 25% above the respective capture barrier energies.

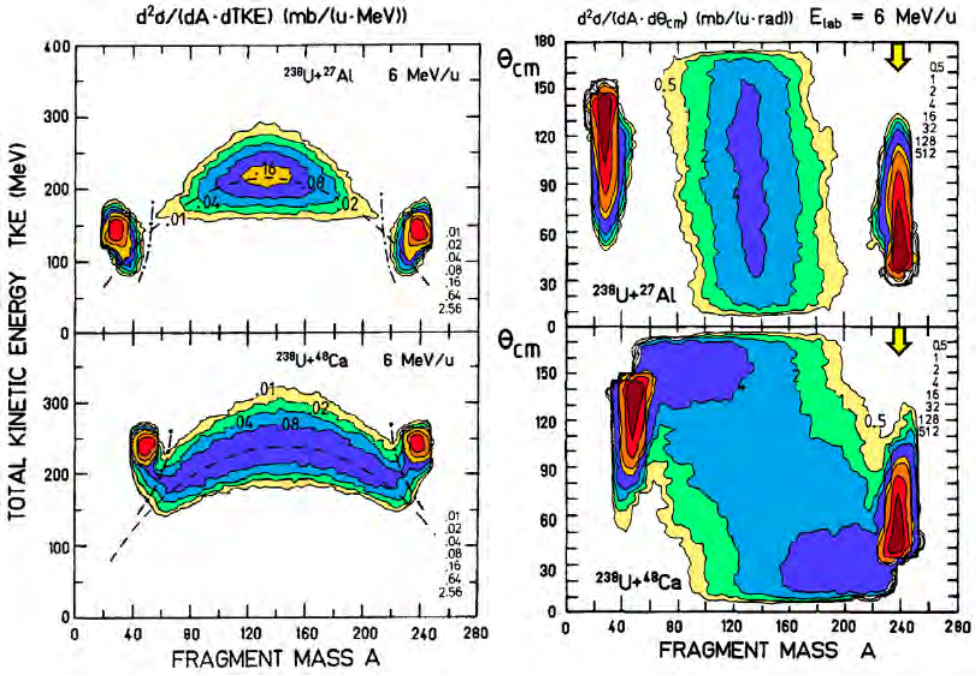

Figure 1.20: *The mass-energy distributions (MEDs) and mass-angle distributions (MADs) are presented for the reactions of ^{238}U + ^{27}Al and $^{238}U + ^{48}Ca$. The MADs are depicted with yellow arrows at the top right, indicating the mass and direction of the projectile. The total kinetic energies (TKEs) align with empirical expectations for fusion-fission, represented by dashed lines. In the case of the $^{238}U + ^{48}Ca$ reaction, the mass distribution and MAD are predominantly influenced by fast quasi-fission, characterised by a short sticking time. Conversely, for the $^{238}U + ^{27}Al$ reaction, there is no evidence of fast quasi-fission, but rather a component of slower quasi-fission that leads to a correlation between the mass centroid and angle. Picture with permission from [63] adapted from the original in [65] with permission. Copyright (1985) by the Elsevier Science B.V.*

In the case of ^{238}U + ^{27}Al, the MED exhibits a narrow mass distribution, consistent with the empirically expected reduction in TKE as the mass-asymmetry increases. Since the charges of the fragments are not directly known, it was assumed that the atomic number (Z) is proportional to the mass (A). The function $A_1A_2/(A_1^{1/3} + A_2^{1/3})$ was fitted to the TKE data for symmetric mass-splits, generating the long dashed curves shown in Fig. 1.20, which closely match the experimental data. Based on the MED, the data appear to be consistent with fusion-fission. However, the MAD reveals a clear, albeit small, correlation between mass and angle. The correlation has the opposite slope compared to the pink highlighted band labelled "*medium sticking time*" in Fig. 1.18(c). This discrepancy arises because, in these measurements, the heavier nucleus serves as the projectile (indicated by the yellow arrow) and in the case of inverse kinematics appears the angular reflection in θ.

Therefore, the fission MAD provides compelling evidence that the reaction with ^{27}Al involves, to some extent, quasi-fission with a timescale shorter than a full rotation. This observation aligns with the angular distribution for ^{238}U + ^{27}Al, which deviates significantly from the expectations for fusion-fission. The absence of highly mass-asymmetric quasi-fission events suggests that this system does not undergo immediate fragmentation after the capture stage,

unlike the ^{238}U + ^{48}Ca reaction discussed later. The slight tilt in the MAD and the pronounced angular anisotropy indicates the presence of quasi-fission with a different characteristic, later referred to as "*slow quasi-fission*" [70].

1.5 Unresolved points in fission

Numerous questions regarding the fission process remain unresolved, encompassing aspects such as the influence of nuclear structure and shell effects, and the partitioning of excitation energy among fission fragments. To address these inquiries, a comprehensive approach that combines accurate experimental data and correlations between observables is required.

One unresolved issue pertains to the sharing of excitation energy between the two fission fragments. Recent measurements and models indicate that, at very low excitation energy, the pre-fragments remain in statistical equilibrium with a constant temperature at scission, leading to an energy flux from the light fragment to the heavy fragment [17]. At higher excitation energies, a Fermi gas behaviour (see Section 1.3.7.1) is typically assumed. However, the precise boundary between these regimes and their validity is still uncertain. Experimental data on the excitation energy sharing during scission, as well as neutron evaporation, could provide valuable insights into this aspect.

As was introduced before , the stability of the heavy fragment suggests that shell effects play a significant role in the evolution of the system towards scission, but the exact nature of these effects is still uncertain. The classical explanation involved the influence of spherical shell effects at $Z = 50$ and $N = 82$, with ^{132}Sn being a leading candidate due to its strong shell effects. However, it is now known that the energy required to deform spherical nuclei favourably during the fission process poses a challenge to this explanation and the experimental data rule out this idea.

A conclusive theoretical explanation for the asymmetric modes observed in actinide fission came in 2018, when Scamps and Simenel proposed that the *Standard I* and *Standard II* fission modes may be associated with deformed shell effects near $Z = 52$ and $Z = 56$ [42]. Recent measurements have confirmed the presence of shell-stabilised octupole deformations in the ground states of two barium isotopes, ^{144}Ba and ^{146}Ba [45]. These pear-shaped deformations are believed to be essential for the formation of the neck between the fragments before scission. While these deformations are energetically costly to form with spherical fragments, the existence of a stable octupole deformation in the heavy fragment could reduce the potential energy near scission, as little energy is needed for the deformation. One significant aspect is the distribution of fission fragments at low excitation energy, which has traditionally been attributed to the influence of the spherical shell $N = 82$ and the deformed shell $N \approx 88$. The influence of closed shells on asymmetric fission has been explored in various studies, particularly focusing on the role of (doubly) magic clusters like $^{132}_{50}\mathrm{Sn}_{82}$ and neutron-deformed shell effects in fragments with a neutron count of around $N \approx 88$, as well as in the fissioning nucleus [17]. However, experimental evidence indicates that the prominent driving factor for asymmetric fission in the actinide region is the proton count of the heavy fragment (see Section 1.3.4). The observation of stabilisation in the nuclear charge of heavy fragments around $Z \approx 52$ and $Z \approx 56$ suggests that proton shell structure may also play a role, emphasising the importance of simultaneous measurements of isotopic and isobaric yields to comprehensively understand the impact of both neutron and proton shells on the fission process [71].

In 2010, Andreyev *et al.* conducted a measurement of β-delayed fission in ^{180}Tl ($Z = 79$), where the fissioning nucleus was ^{180}Hg ($Z = 80$) [72]. Surprisingly, they observed pure asymmetric fission, with the light and heavy peaks centred around $A = 80$ and $A = 100$, respectively. These results could not be explained by the potential mechanisms or spherical shell effects that typically lead to symmetric fission. The formation of two ^{90}Zr isotopes with 50 neutrons, a magic number, and a semi-magic 40 protons was expected. Considering the discrepancy with spherical shell effects, attention turned to shell structure effects arising from deformation. In 2019, Scamps and Simenel proposed a combination of octupole and quadrupole deformations in the heavy and light fragments, respectively, to explain the observed asymmetric fission [73].

Quasi-fission shares similarities with fission, as it involves the formation of two fragments moving apart with kinetic energy determined by their configuration at the scission point. However, quasi-fission can be distinguished from fission by studying the correlated mass and angular distributions of the fission fragments, which exhibit shorter contact times and non-equilibrated fragment masses (see Section 1.4.1). However, it appears that the contact times in quasi-fission are sufficiently long to induce a substantial damping of the initial relative kinetic energy through dissipation mechanisms, as evidenced by recent TDHF calculations applied to quasi-fission [74]. Furthermore, similar to fission, quasi-fission is influenced by shell effects that manifest as valleys in the potential energy surfaces. Through modern TDHF simulations [75], it appears that the shell effects responsible for the asymmetric fission mode exert a significant influence, preventing mass equilibration in each quasi-fission trajectory. Alternatively, extended contact times may be necessary for quasi-fission trajectories resulting in symmetric fragments. The dissipation and structural effects in quasi-fission continue to be subjects of speculation.

1.6 Experimental fission observables

In the domain of theoretical modelling, diverse methodologies have been developed over the past few decades for the individual reproduction of specific fission observables. Nevertheless, the simultaneous measurement of multiple observables and their interrelations could offer crucial constraints for the refinement of theoretical models, thereby enhancing their capacity to predict the intricacies of the fission process more comprehensively. The combination of precise experimental data with theoretical advancements offers the potential to pursue a deeper understanding of both fission and quasi-fission phenomena.

The VAMOS++ experimental setup encompasses a range of observables that provide insights from both the fissioning system and the generated fragments. In each fission event, the identification of the fissioning system is possible, accompanied by measurements of its excitation energy (E^*_{FS}), angle, and velocity through direct reaction reconstruction. Regarding the fission fragments, the utilization of inverse kinematics, as elaborated in the subsequent Section 1.6.1, enabled, for the first time, the isotopic identification of the complete fission fragment distribution of the fissioning systems ^{265}Db and ^{249}Bk.

This work presents novel experimental findings on diverse fission observables acquired during the 2017 campaign by the VAMOS++ collaboration. The ascertained observables encompass fission fragment yields, neutron excess, total neutron evaporation, even-odd staggering of fragment nuclear charge, angles, time-of-flight, total kinetic energy, and total excitation energy.

1.6.1 Inverse kinematics

The experimental investigation of nuclear fission has undergone significant developments over the years. Initially, neutron-induced fission experiments were conducted, where a high flux of neutrons was directed towards stable heavy nuclei to induce the fission process. This approach was primarily motivated by its application in nuclear power plants for electricity generation. However, these experiments were limited to long-lived nuclei, thereby restricting the range of fissioning systems that could be studied.

The introduction of intense ion beams paved the way for the study of fission through transfer and fusion reactions in direct kinematics. In this configuration, a light nucleus is accelerated and collided with a heavy target, resulting in a recoil fissioning system. However, the low velocities of the emitted fission fragments hindered the complete isotopic identification of the fragments, limiting the nuclear charge information to the light fragment.

To overcome these limitations, an inverse kinematics configuration was introduced by K.-H. Schmidt *et al.* in 1994 [76]. This technique involves accelerating a heavy nucleus and directing it towards a light target, leading to forward-emitted fission fragments. The two schemes of direct kinematics and inverse kinematics are illustrated in Fig. 1.21. The Lorentz boost experienced by the fissioning system in this setup results in higher velocities of the emitted fragments, enabling direct measurements of their atomic numbers. Moreover, this configuration eliminates the need for long-lived heavy nuclei as targets, allowing for the investigation of a broader range of fissioning systems, including exotic nuclei.

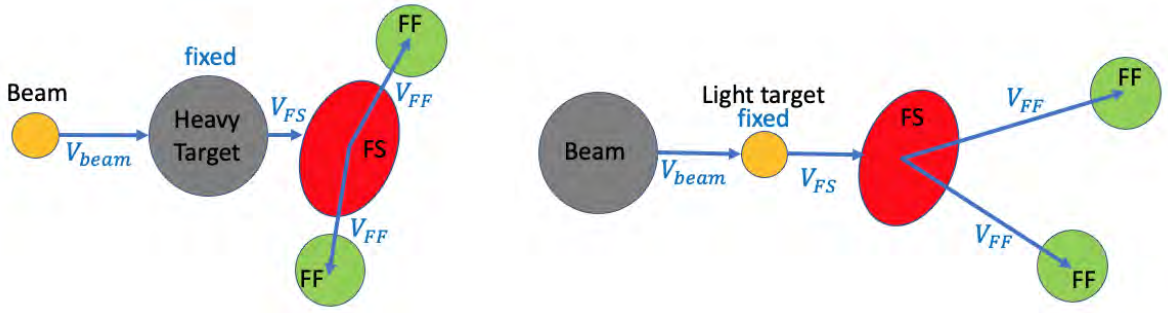

Figure 1.21: *In this figure, direct kinematics (left) allows for a low velocity of the fission fragments and incomplete access to the distributions of the fission fragments. Only a complete mass distribution could be measured, while information about the nuclear charge is partial or absent. On the other hand, inverse kinematics (right) allows for a higher velocity of the fission fragments and full access to nuclear charge information.*

By shifting the focus from neutron-induced fission to transfer and fusion reactions in direct and inverse kinematics, researchers have expanded their ability to study fission processes more comprehensively and diversely. The inverse kinematics approach, in particular, overcomes the limitations associated with low-energy fragments and offers advantages such as direct charge measurement and, typically, greater acceptance in the fissioning system reference frame than if direct kinematics were used with the same experimental setup. These advancements have opened up new avenues for understanding and characterising fission phenomena.

There are currently two collaborations that employ the inverse kinematics technique for fission research. The SOFIA collaboration at GSI (Germany) focuses on electromagnetic-induced

fission [77], while the VAMOS fission collaboration at GANIL (France) investigates transfer- and fusion-induced fission [78][79].

1.7 Objectives

The main objectives of this thesis are to obtain relevant physical observables, calculate fission fragment isotopic yields, and evaluate fission fragment velocities for the fissioning systems, ^{265}Db and ^{249}Bk, produced at high excitation energies. By achieving these objectives, this work aims to:

- Assess the role of dynamics in high-energy fission and quasi-fission reactions.
- Analyse the role of quasi-fission and its competition with fusion-fission reactions.
- Characterise the scission point (point of nuclear separation).
- Understand the role of nuclear structure in the fission process.

Experimentally, evidence suggests that nuclear structure leaves its fingerprints on several observables. Asymmetric yields, indicative of the average relative size of the emitted fragments, are known to be a product of fission from actinide nuclei. Additionally, the heaviest fragment is centred around a mass independent of the fissioning system, indicating the production of favoured numbers of protons and/or neutrons dictated by nuclear structure. However, at high excitation energies, symmetric fission is expected for the fissioning systems studied in this work, ^{265}Db and ^{249}Bk.

A developed methodology is applied to study the fission of specific fissioning systems. By analysing the isotopic yields and other observables from these systems, valuable insights can be gained into the underlying fission dynamics and the role of nuclear structure. Furthermore, fission fragments are emitted in the centre of mass of the fissioning system with a momentum that depends on their proximity and shape at the scission point. These characteristics are also expected to be governed by nuclear structure, and their effects are likely reflected in the appearance of distinctive features in the total kinetic energy of the fragments.

Another observable for studying fission properties is the relative production of odd-Z fragments compared to even-Z fragments (known as even-odd staggering). This staggering is linked to the energy dissipation throughout the process, and therefore, the sharing of energy between collective and intrinsic degrees of freedom. All these features are expected to be suppressed in high-energy fission. However, recent data suggest otherwise. This thesis will identify and study these properties in both high-energy fission systems produced with two different targets. Systematic analysis is used to identify recurring patterns and link the survival of these effects to nuclear shells.

Finally, comparing these shells with those responsible for structure effects in low-energy fission help comprehend whether shell effects are stronger than previously thought or if new effects emerge with increasing energy. In addition, using fusion-fission reactions allows studying the influence of quasi-fission channels. These are reactions where the beam and target nuclei do not fully fuse but exchange nucleons for a short time. The effects of shells in this scenario may be entirely different from those in fission and have never been measured before.

1.8 In this thesis...

In addition to this Chapter 1, this dissertation is organised into six more chapters, each addressing different aspects of the topic. These chapters are followed by the main conclusions derived from the findings of this research.

- **Chapter 2:** This part provides a comprehensive overview of the experimental setup used for fission measurements using reactions in inverse kinematics. It covers the production and acceleration of the ^{238}U beam at GANIL facilities, the capabilities of the setup for studying nuclear fission, and the detectors and configuration of the VAMOS++ spectrometer. Additionally, the electronic scheme and acquisition trigger logic employed in the experiment are discussed.

- **Chapter 3:** This part presents a detailed account of the signal treatment and calibration procedures applied to the detectors used for fission fragment identification in the VAMOS++ focal plane setup. The aligning process of the electronics of each detector channel with a pulse generator to ensure uniform output signal amplitudes is presented.

- **Chapter 4:** This part focuses on the methods utilised for precise isotopic identification of fission fragments in multi-nucleon transfer and fusion reactions involving a ^{238}U beam and various light targets (see Tab. 2.1). The identification process involves determining the mass (A), nuclear charge (Z), and charge state (q) of the fragments. The chapter concludes with a validation of fission fragment identification using γ-ray emission measurements from excited states within the fragments.

- **Chapter 5:** Focuses on determining the geometrical efficiency of fission fragment detection, denoted as $\mathcal{E}_g^{FF}$. This efficiency is influenced by the angular acceptance of the VAMOS++ spectrometer, which takes into account both the azimuthal angle and the polar angle. $\mathcal{E}_g^{FF}$ quantifies the fraction of fission fragments that are successfully accepted and identified by the spectrometer.

- **Chapter 6:** A comprehensive overview of the procedures involved in calculating the fission-fragment isotopic yields for the ^{265}Db and ^{249}Bk fissioning systems are provided in this part. The steps covered include the definition of the yields, their calculation, considering the VAMOS++ acceptance, and the intrinsic efficiency of the detectors utilised for fission-fragment identification. Finally, the study of evaluating fission fragment velocities is presented.

- **Chapter 7:** The results of the final observables and the isotopic fission-fragment yields for the fusion-produced ^{265}Db and ^{249}Bk fissioning systems are presented. Several other physical observables derived from the isotopic yields are reported, such as the distributions of fission fragment masses and nuclear charges, as well as the neutron excess, total neutron evaporation, and even-odd staggering. Additionally, the investigation and handling of the quasi-fission component in the yields of ^{265}Db is studied. Furthermore, the characterisation of the scission point for the ^{249}Bk fissioning systems is presented.

The Conclusions 7.9.6 are summarised at the end of this document, followed by the Appendices.

USC UNIVERSIDADE DE SANTIAGO DE COMPOSTELA

USC
UNIVERSIDADE
DE SANTIAGO
DE COMPOSTELA

Chapter 2

Experimental setup

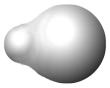

This chapter provides an overview of the experimental setup employed for the present fission measurements using transfer reactions in inverse kinematics. It begins with an introduction to the GANIL facilities, outlining the production and acceleration of the ^{238}U beam utilised in the experiment. Subsequently, the chapter discusses the capabilities of the experimental setup for investigating nuclear fission. A detailed description of the detectors used to identify the transfer reaction and the configuration of the VAMOS++ spectrometer for identifying the fission fragments is presented. Additionally, the chapter delves into the electronic scheme, including the acquisition trigger logic, employed in the experiment.

2.1 GANIL facility

GANIL (*Grand Accelerateur National d'Ions Lourds*) is one of the largest laboratories in the world dedicated to scientific research with ion beams. It has played a significant role in various fields, including radiotherapy, atomic physics, condensed matter, astrophysics, and nuclear physics[1]. Nearly 2800 unstable nuclei have been synthesised, shedding light on the properties of nuclear matter and their significance in the early stages of the universe. GANIL inaugurated in 1983 and located in Caen, Normandy, is managed by CEA[2] and CNRS/IN2P3[3].

Returning to the topic of this section, the GANIL facility consists of several components for producing and accelerating stable and radioactive beams. Stable nuclei are generated using an Electron Cyclotron Resonance (ECR) ion source and Compact Cyclotrons (C01 or C02), reaching energies of approximately 0.5 MeV/u. These nuclei are further accelerated in the coupled Separated-Sector Cyclotrons (CSS1 and CSS2), reaching average energies of 24 MeV/u and 96 MeV/u, respectively [80]. For the production of radioactive beams, GANIL employs two techniques depending on the desired energy range and the isotope. Intermediate-energy radioactive beams are generated using the In-Flight Separation technique, while low-energy radioactive beams are obtained through the Isotope Separation On Line (ISOL) technique. The combination of all these techniques opens new frontiers in the study of nuclear chart.

[1] https://www.ganil-spiral2.eu/

[2] The Atomic Energy Commission (CEA) is a state-funded research institution focusing on energy, defence, security, information technology, and health technologies.

[3] The *Institute for Nuclear Physics and Particle Physics* (IN2P3) was established to provide research support. The *Centre National de la Recherche Scientifique* (CNRS) functions as a multidisciplinary public research entity overseen by the French Ministry of Higher Education, Research, and Innovation.

Two primary techniques are employed for generating exotic radioactive beams. The first, known as "In-Flight Separation" utilises the LISE separator to fragment intense primary beams via interaction with a rotating target. The second technique, called ISOL, involves the SPIRAL facility, where radioactive products are extracted from a thick production target using the Electron Cyclotron Resonance Ion Source (ECRIS) known as Nanogan III. The extracted heavy atoms undergo ionisation within a plasma created by a radio frequency field and are then extracted using a voltage. The beams in both cases are subsequently directed to the experimental areas for research purposes.

In recent years, GANIL has undergone significant developments. In November 2016, the SPIRAL2 accelerator was inaugurated as the second-generation System for Production of Radioactive Ions Accelerated in Line. SPIRAL2 has enhanced capabilities, producing ion beams with intensities ten to one hundred times higher than previous and current installations. This advancement opens up new opportunities for studying the atomic nucleus, including its structure and thermodynamic properties, as well as heavy nuclei. The fields of nuclear physics and astrophysics stand to benefit from SPIRAL2, and its applications extend to applied research, such as the production of radioisotopes for nuclear medicine and the study of impact on materials of intense neutron fluxes. GANIL continues to serve as a hub for fundamental and applied research, welcoming scientists from diverse disciplines. The layout of the GANIL facility is depicted in Fig. 2.1.

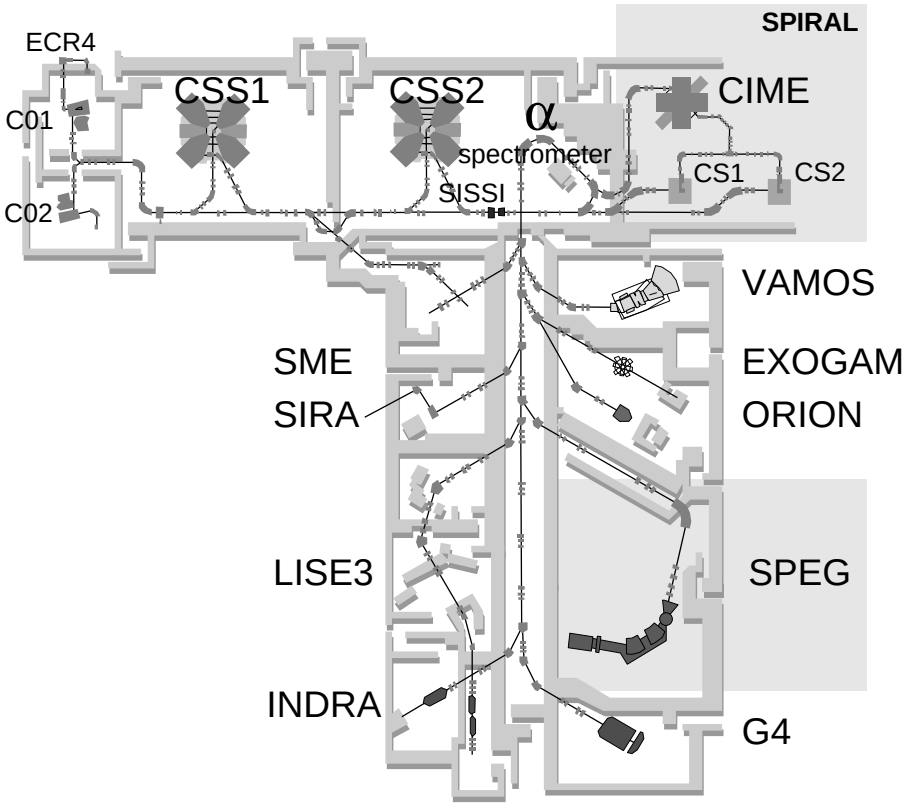

Figure 2.1: *Schematic view of the GANIL facility. The upper side corresponds to the acceleration area with the cyclotrons and α-spectrometer. In the right part, the VAMOS cavern with the VAMOS++ spectrometer and other experimental areas are depicted.*

2.2 The experiment

In this experiment, a stable $^{238}U^{31+}$ beam was generated using an Electron Cyclotron Resonance (ECR)-sputtering ion source. The ion source utilised the coupling between the electron cyclotron frequency and an externally applied microwave frequency to ionise a service gas, either oxygen or neon. The positive gas ions were then accelerated towards a negatively biased metallic uranium sample. The uranium ions were subsequently injected into the Compact Cyclotron C01 and further accelerated in the Separated-Sector Cyclotron CSS1, reaching an energy of 5.88A MeV. The beam was then directed to the α-spectrometer for emittance and energy spread diagnostics. With this spectrometer, the desired isotopes from the beam are selected by selecting them in velocity. Finally, with a final intensity of $3 \cdot 10^9$ pps, the beam was delivered to the VAMOS++ experimental area (see Fig. 2.1).

The experimental setup involved the beam colliding with a series of light targets, summarised in Tab. 2.1 along with their respective thicknesses. By assuming that all the reactions occurred at the midpoint of the target[4], the energy loss of the beam was adjusted to ensure that the centre-of-mass energy was slightly above the Coulomb barrier between ^{238}U and the specific target. The values for the Coulomb barrier (E_B), centre-of-mass energy (E_{CM}) and fissioning system excitation energy (E^*_{FS}) of each reaction can be found in Tab. 2.1. With the energy slightly above the barrier, transfer and fusion reactions, as well as elastic and inelastic scattering, were favoured channels compared to other reaction channels such as breakup reactions. The excitation of various actinides and transactinides from ^{238}U up to ^{265}Db was achieved, followed by subsequent fission decay. The boron target used is natural, ^{nat}B, implying a composition of boron isotopes, with ^{10}B and ^{11}B being the predominant isotopes at abundance percentages of 19.65% and 80.35%, respectively, both of which are stable isotopes. Consequently, the primarily generated fissioning systems were two, and among them, ^{249}Bk stands out with a significantly higher percentage. Therefore, in the notation used in this study, this fissioning system will consistently be represented, and its parameters will be employed.

Reaction	Thickness [μg/cm^2]	FS	E_{CM} [MeV]	E_B [MeV]	E^*_{FS} [MeV]
^{238}U+^{9}Be	500	^{247}Cm	50.101	45.729	43.100
^{238}U+^{nat}B	100	[^{248}Bk,^{249}Bk]	[52.210, 61.582]	[53.953, 53.368]	[47.046, 47.700]
^{238}U+^{24}Mg	500	^{262}Rf	126.073	125.037	56.520
^{238}U+^{27}Al	200	^{265}Db	142.010	133.756	61.200

Table 2.1: *List of reactions between the ^{238}U beam at 5.88A MeV and the four targets used in the experiment. The related target thickness and resulting fissioning system (FS) or compound nucleus are indicated. The corresponding energies in the centre-of-mass (E_{CM}), Coulomb barrier values (E_B) and excitation energy (E^*_{FS}) are also reported.*

Once the fission fragments are generated, they are both emitted at forward angles within a cone ranging approximately from 32° to 45° in the laboratory reference frame, due to the boost of inverse kinematics. The first detector is SPIDER, a silicon telescope consisting of two parallel disks with a hole in the centre. The fission fragments pass through this central hole (see Section 2.3.2). There are multiple possible reactions between the uranium beam and the targets, possibly a recoil is produced and provided recoil exists, it is detected and stopped by this

[4] Actually, this is not true due to the density and thickness of the targets, and the reactions probabilistically occur before the centre of the target. Specifically in the case of the aluminium target, this effect is taken into account. This correction is important for energy losses and can be seen in Section 2.8.

SPIDER telescope. The second detector they encounter is the MWPCs Start detector, comprised of two parallel multi-wire chambers, serving as a trigger (see Section 2.3.1). Only one of these fragments may continue its trajectory towards the VAMOS++ spectrometer. The fragment is focused with two quadrupoles to a dipole and is curved by the magnetic field, falling within the acceptance of the VAMOS++ spectrometer is ultimately detected reaching the detectors of the VAMOS++ spectrometer: Multi-Wire chamber MWPPAC (see Section 2.4.2.1), Drift Chambers (see Section 2.4.2.2), and Ionisation Chamber (see Section 2.4.2.3), where is stopped. The details of each detector are described in the following sections and depicted in Fig. 2.2, showcasing the complete experimental setup.

The fusion and transfer reactions introduce excitation energy into the system, leading to fissioning systems and/or recoil excitations that can decay through γ-rays emission. Similarly, the fission fragments acquire excitation energy during the fission process, which can also be released through neutron and γ-rays emission. The γ-rays emitted can be measured by the germanium crystals of the AGATA detector (see Section 2.3.3) located around the target at backward angles.

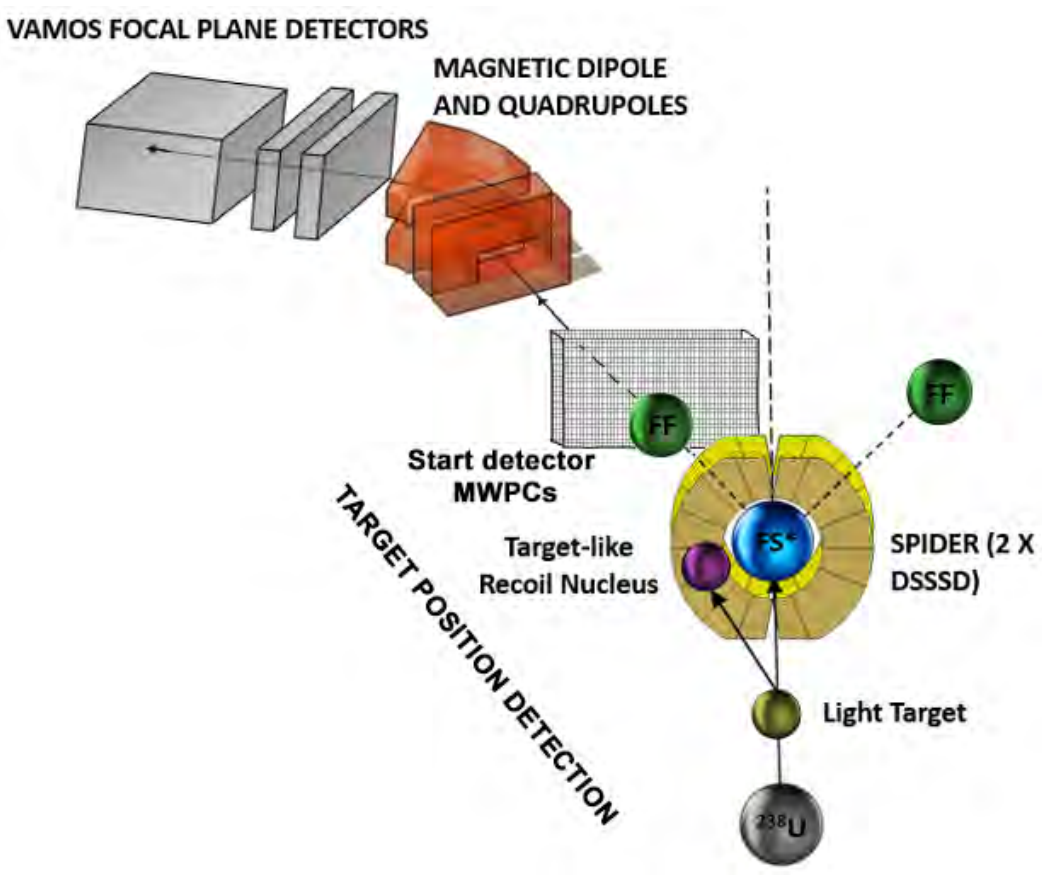

Figure 2.2: *The experimental setup of VAMOS++ spectrometer and SPIDER detector is depicted in the sketch, with the uranium beam impinged a target. In the diagram, a transfer reaction is illustrated, followed by a fission decay. The target-like recoil is represented by a purple ball, while the two fission fragments are shown in green balls. The recoil is detected and stopped by the SPIDER detector, while one of the fission fragments triggers the MWPCs Start detector and passes through the VAMOS++ spectrometer. At the focal-plane detection setup, the fragment is measured. The γ-rays emission is measured with AGATA detector placed backwards of the uranium beam but it is not shown in this sketch for clarity.*

The primary objective of this study is to analyse the data obtained from the fusion-fission process. Consequently, the events of particular interest are those in which a single fission fragment is detected with the VAMOS++ setup, in coincidence with the absence of any particle in SPIDER. In such instances, it is assumed that a fusion-fission reaction has occurred. The specific excited fissioning systems generated during these reactions are detailed in Tab. 2.1.

2.2.1 Experiment coordinate system

This experiment is comprised of two distinct detection zones, as illustrated in Fig. 2.2. The first zone, there is the "target position detection" zone, and the other one, the "VAMOS++ focal plane". Throughout this work, they will be referred to as TP and FP, respectively, to denote variables corresponding to either zone. The target position zone encompasses the SPIDER telescope, and the Start detector MWPCs. The VAMOS++ focal plane incorporates the following detectors: Multi-Wire chamber MWPPAC, Drift Chambers, and the Ionisation Chamber. To provide context on the distance between the two zones, the flight path of a fission fragment between the target and the VAMOS++ focal plane is approximately 7.6 m, with slight variations of ±0.35 m depending on the magnetic rigidity of the fragment and emission angle. All these elements can be observed in Fig. 2.4.

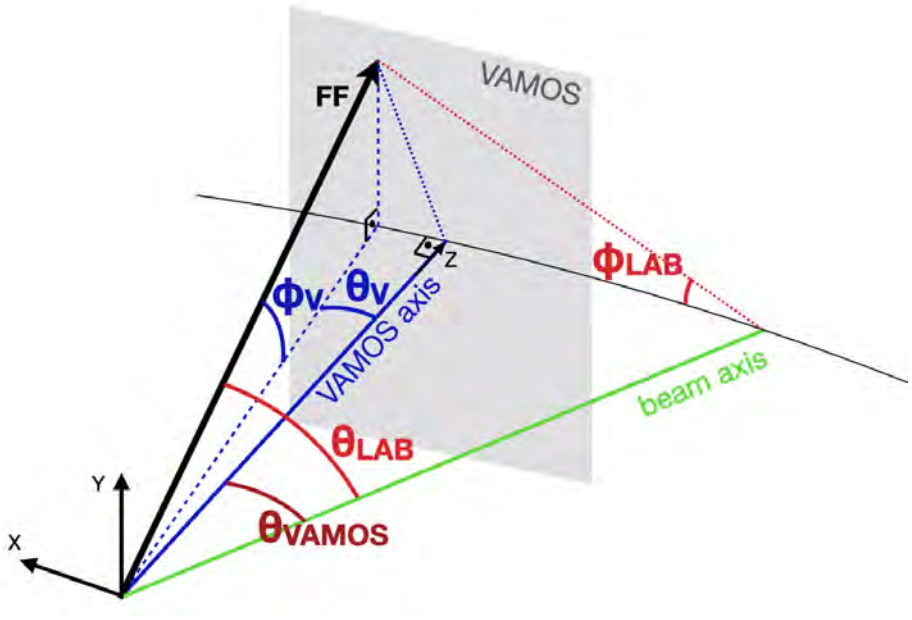

Figure 2.3: *A graphical representation illustrating the angular relations between the VAMOS++ angular system and the laboratory system is represented. This figure showcases a fission fragment, symbolised as the thick black arrow, displaying its component projections within both the laboratory system, depicted in red, (θ_{LAB}, ϕ_{LAB}), and the VAMOS++ system, represented in blue, (θ_V, ϕ_V). The angular rotation of the spectrometer, denoted as θ_{VAMOS}, thus fixing the VAMOS axis, is accentuated in dark red. The Cartesian axes utilised in the experiment are also depicted using black arrows, with the z-axis aligning with the VAMOS axis.*

Throughout the entirety of this work, reference is made to the "focal plane" of VAMOS++, though this term is used loosely. The VAMOS++ spectrometer does not possess a literal focal plane.

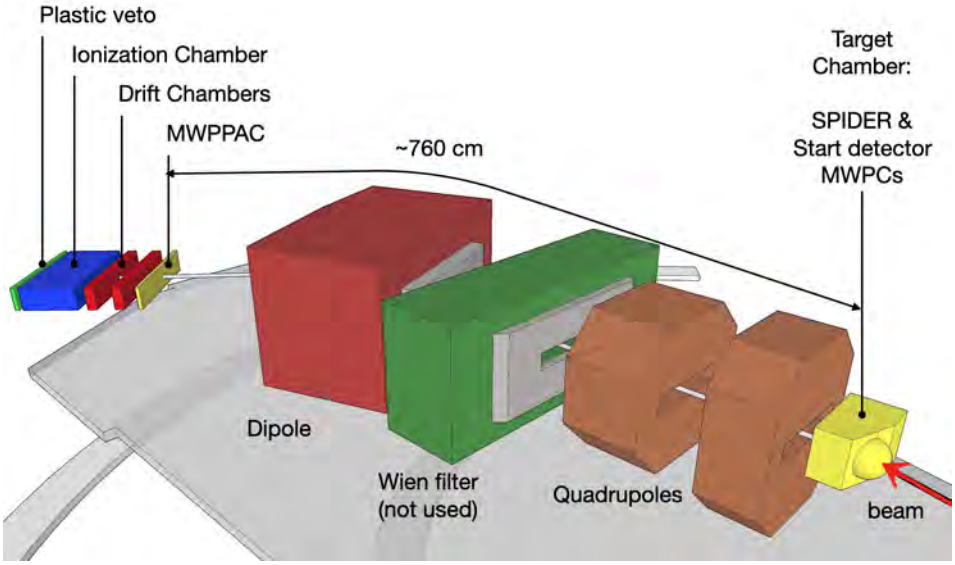

Figure 2.4: *Sketch of the e753 experiment with VAMOS++ experimental setup. The beam direction is shown in red. The target chamber zone where collisions occur, the SPIDER telescope, and the Start detector MWPCs. The VAMOS++ focal plane incorporates the following detectors: Multi-Wire chamber MWPPAC, Drift Chambers, and the Ionisation Chamber.*

Two angular systems used in the experiment and the data analysis need to be presented. The VAMOS++ angular system and the laboratory system are represented in Fig. 2.3 with their angular relations. In this representation, a fission fragment, depicted as the black arrow, exhibits its component projections in both the laboratory system, depicted in blue, (θ_V, ϕ_V) and the VAMOS++ system, represented in red, (θ_{LAB}, ϕ_{LAB}). Also, Figure 2.3 displays the rotation of the spectrometer at an angle θ_{VAMOS} with respect to the beam axis, highlighted in blue. The Cartesian axes utilised in the experiment are also depicted using black arrows, with the z-axis aligning with the VAMOS++ axis.

2.3 Target position detection

The experimental setup preceding the VAMOS++ spectrometer, situated at the target position, consists of two detector types: the Start detector and the SPIDER detector. The Start detector, a Dual Position Sensitive Multi-Wire Proportional Counter (DPS-MWPC), is responsible for initiating the Time-of-Flight (ToF) measurement of the fission fragments and provides the scattering angles through dual position measurements. The SPIDER detector is a ($\Delta E - E$) telescope comprising two annular Double-Sided Silicon Stripped Detectors designed for identifying light recoils. The SPIDER detector, MWPCs Start detector, target, and collimator are enclosed within a vacuum chamber which is tag as Target Chamber. Further details regarding each detector are provided below.

2.3.1 MWPCs Start detector

The Start detector, positioned 164 mm downstream of the target, comprises a pair of DPS-MWPC (jointly labelled MWPCs Start detector) in a common gas volume [81]. Each MWPC (labelled TMW1 and TMW2) consists of three wire planes: a central cathode for timing signal (t_1, t_2), and two external anode wire planes (X_1, X_2, Y_1, Y_2) for position measurement.

The front MWPC, i.e. TMW1, has an active area of 40×61 mm^2, the back MWPC, i.e. TMW2, has an active area of 65×93 mm^2, and the gap between their cathodes is 105 mm. Isobutane (C_4H_{10}) gas at a pressure of 6 mbar fills the detector, isolated from the beam line vacuum by aluminised Mylar windows (0.9 μm thick). Two gold-plated tungsten wires (100 μm diameter) are diagonally placed as a reference for alignment. The operation of the detector is illustrated in Fig. 2.5, showing the distances and orientations of the wire planes. The beam direction and reaction products are also indicated in the figure.

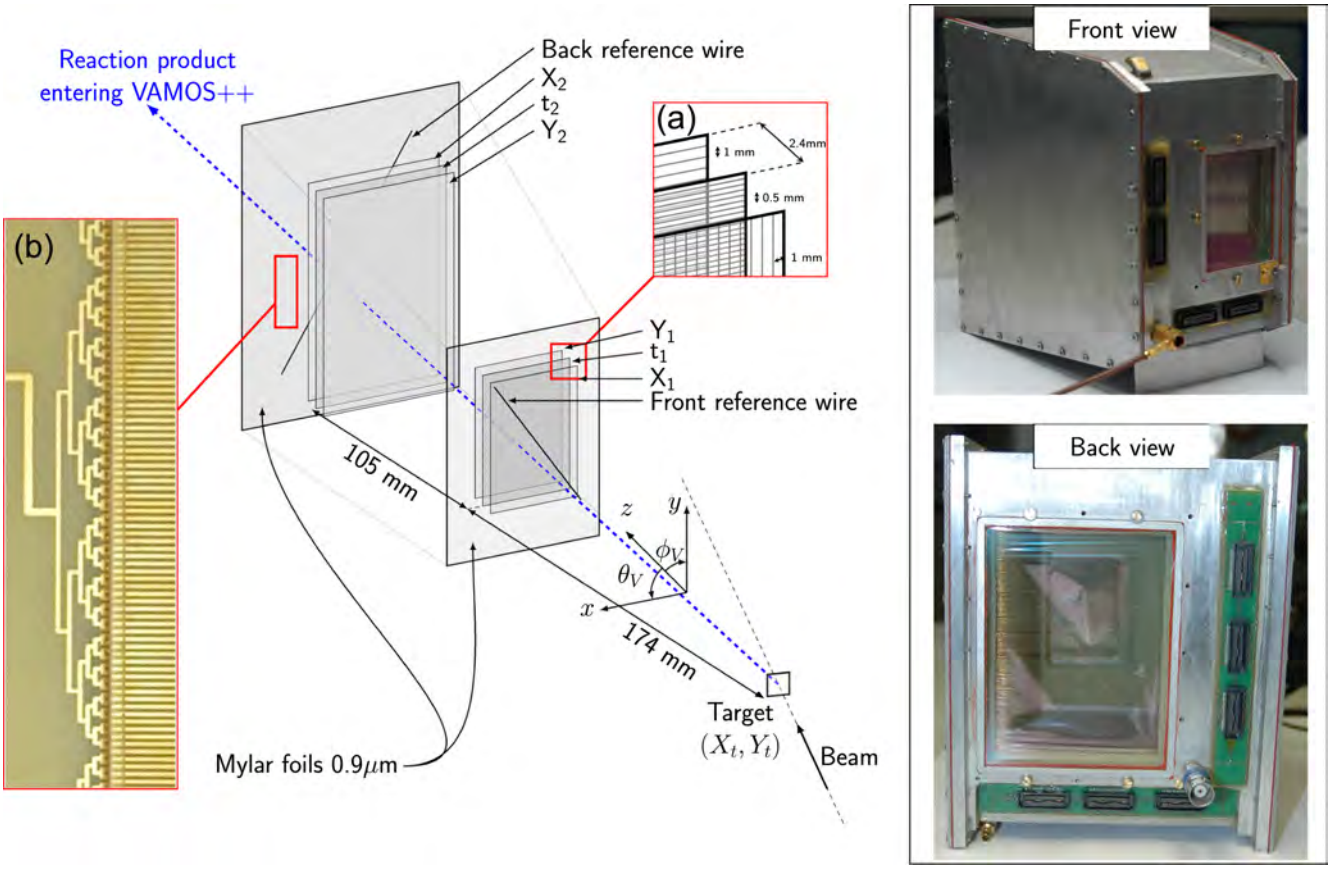

Figure 2.5: *On the left side of the figure, a schematic representation of the DPS-MWPC detector is provided, including a zoomed-in view of the wire planes to illustrate their orientations and spacing. The direction of the beam and the reaction products are also indicated in the diagram. On the right side, pictures of the detector assembly are presented, showcasing the front and back views of the detector. Inset (a): Expansion of the three wire planes illustrating the wire plane orientation and spacings. Inset (b): Picture of the equivalent path length routing of a time plane signal. Adapted with permission from [81]. Copyright (2016) by Elsevier Science B.V.*

When a fragment passes through the detector and ionises the gas, positive ions and electrons are generated. The electric field accelerates the electrons towards the anode wires, causing an avalanche, while the corresponding ions are collected at the cathode. The output signal from the cathode serves as the start signal for ToF measurement. By utilising the four spatial coordinates (X_1, Y_1, X_2, Y_2) obtained from the anode wire planes, the ion trajectory, scattering angles (θ_{TP}, ϕ_{TP}), and interaction point on the target (X_{TP}, Y_{TP}) can be reconstructed. The timing measurement has an estimated resolution of $\sim$ 216 ps, whilst the position measurement resolution has been determined as $\sim 172\,\mu$m [81].

2.3.2 SPIDER detector

The SPIDER (Silicon Particle Identification DEtector Ring) detector [82], situated 31.8 mm behind the target, is a $(\Delta E - E)$-telescope consisting of two annular Double-Sided Silicon Stripped Detectors (DSSSD). These detectors have thicknesses of 70 μm and 1042 μm, separated by 4 mm. The front side of each layer is divided into 16 rings spaced 1.5 mm apart, while the back side is segmented into 16 radial sectors and each one has an angular range of $\sim$ 0.39 rad. The central hole with a diameter of 48 mm ensures that the beam-like nuclei and fission fragments do not intercept the detector. An aluminium collimator, 0.5 mm thick and with a radius of 4 mm, is placed 3.5 mm behind the target to prevent beam particles and/or scatterings, with support from the target, from reaching SPIDER and/or entering the VAMOS++ spectrometer. Additionally, a disk-shaped shield is positioned in front of SPIDER at 24 mm behind the target to safeguard its inner ring from potential fission fragments that may reach it. The geometry of the detector and the representation of a transfer reaction followed by a fission decay are illustrated in Fig. 2.6 (the disk-shaped shield is not depicted for clarity).

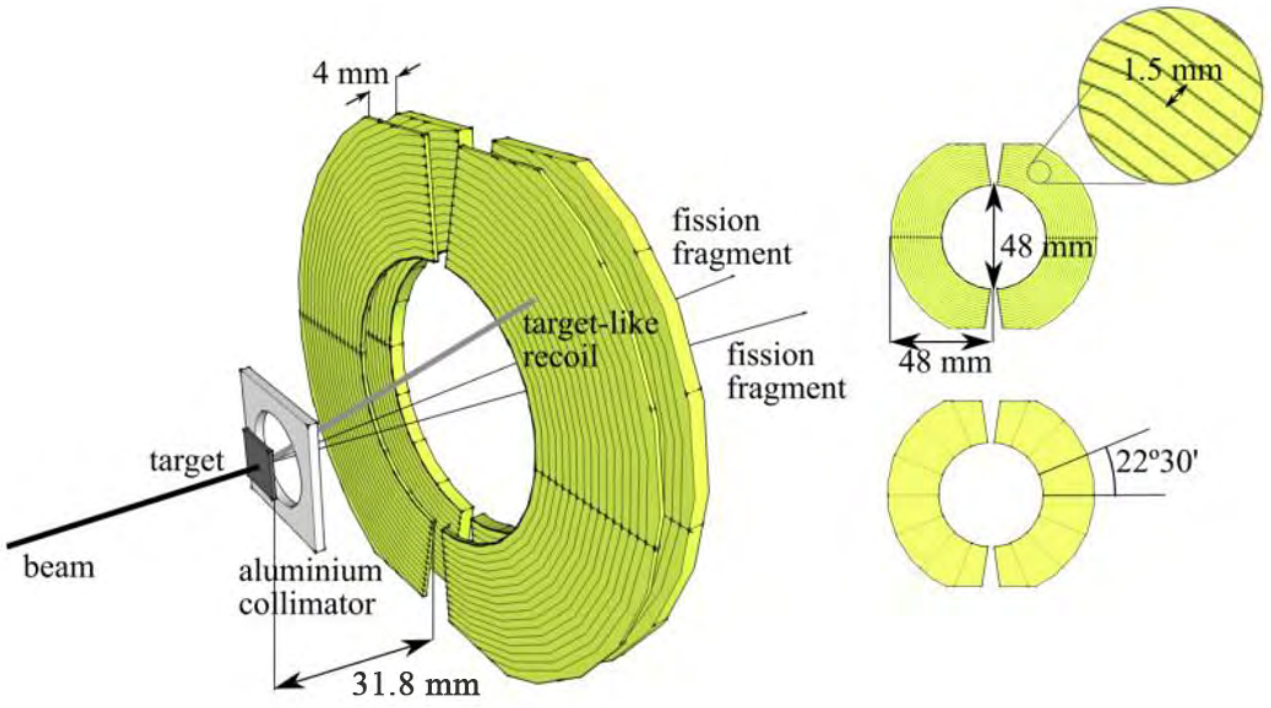

Figure 2.6: *Configuration of the SPIDER detector, including the target and aluminium collimator. The diagram illustrates a transfer-fission event, where the target-like recoil is stopped in the detector, while both fission fragments pass through the central hole.*

SPIDER is capable of measuring the energy loss and the residual energy of the target-like recoils. In the case of a transfer-induced fission reaction, the recoil passes through the first thin layer of the detector and it is fully stopped in the thicker layer. By combining the energy loss and the residual energy, SPIDER can determine the isotopic identification of the light partner involved in the reaction. Moreover, the segmentation of the detector allows for the measurement of both polar (θ_{rec}) and azimuthal (ϕ_{rec}) angles with a range below $\sim$17 mrad and below $\sim$384 mrad respectively. To mitigate the degradation of energy resolution due to increased temperature, SPIDER incorporates a cooling system that circulates liquid silicone at $-35°C$, maintaining a stable temperature of $-1°C$.

To prevent the noise and resolution degradation caused by δ electrons generated from the interaction of fast high-Z particles with matter, a magnetic field of 750 G surrounds the target, deflecting the δ electrons produced by the beam-target interaction.

2.3.3 AGATA detector

AGATA (Advanced GAmma-ray Tracking Array) is a state-of-the-art γ-ray spectrometer that offers exceptional Doppler-correction capabilities through the use of highly segmented detectors, efficient pulse-shape analysis algorithms, and an innovative γ-ray tracking concept [83].

This instrument allows the detection of γ-rays using highly segmented High Purity Germanium (HPGe) semiconductor material detectors, which interact with γ-rays through mechanisms such as the photoelectric effect, pair creation, and Compton scattering. The energy of the γ-rays is transferred to electrons or electron-positron pairs, generating signals that are proportional to the γ-ray energy. AGATA is highly segmented and can handle high counting event rates, providing precise measurements of the interaction point through pulse shape analysis.

The AGATA project is a collaborative effort funded by twelve European countries. This project, initiated in 2001 and signed by participating countries in 2002, offers advanced capabilities for event counting and can be coupled with ancillary detectors. The high segmentation of the detector and digital readout enable the measurement of induced charges in neighbouring segments, facilitating the estimation of the interaction point. The tracking algorithm reconstructs the path of the γ-rays, and sophisticated pulse-shape analysis procedures enable the determination of the γ-ray emission direction and precise interaction point localisation. By eliminating the rejections of Compton scatterings and employing advanced tracking algorithms, AGATA achieves high detection efficiency and recovers events that would be rejected in traditional spectrometers. The collaboration comprises scientists from over 40 institutions in 13 European countries, and future plans involve expanding AGATA to a 3π solid angle configuration with 135 individual Ge detectors (45 triple clusters) by 2030.

2.4 VAMOS++ spectrometer

The VAMOS++ spectrometer is a large solid angle, ray-tracing magnetic spectrometer that plays a crucial role in the complete identification of ions detected at its focal plane setup [84, 85, 86, 87, 88, 89]. Comprising a magnetic dipole, two magnetic quadrupoles, and a Wien filter (which is not utilised in this particular experiment), VAMOS++ enables precise determination of mass, charge state, velocity vector, and the atomic number of the detected ions. The quadrupoles play a key role in focusing the ion trajectory, with the first quadrupole focusing on the y-axis (perpendicular to the dispersion plane) and the second quadrupole focusing on the x-direction (the dispersion axis). Meanwhile, the dipole primarily serves to deflect and separate ions based on their momentum-charge ratio, resulting in a dispersion on the $x-z$-plane (see coordinates system in Fig. 2.3).

2.4.1 Mathematics behind VAMOS++

In a magnetic spectrometer, the magnetic field (B) generated by the dipole causes the trajectory of charged particles to deflect. This deflection is characterised by the radius of curvature (ρ), which is determined by the balance between the Lorentz force and the centrifugal

force. The magnetic rigidity ($B\rho$) is a measure of this equilibrium, reflecting the relationship between the magnetic field strength and the radius of curvature of particle trajectory, a quantity that expresses the resistance of a charged particle to the deflection caused by the magnetic field.

A particle with kinetic energy $T = (\gamma - 1)mc^2$ entering the magnetic field (see Fig. 2.7), experiences a centripetal force $F_e = \gamma m v^2/\rho$, where the orbit radius equation is given by:

$$\rho = \frac{\gamma mc\beta}{QB}\,, \tag{2.1}$$

where $\beta = v/c$ and γ is the Lorentz factor. The mass of a fragment entering the dipole can be approximated by $m = A \cdot u$, with A as its mass number and u as the atomic mass unit. Additionally, the quantisation of the charge state is applied: $Q = q \cdot e$, where $q \in \mathbb{Z}$ and e is the charge of an electron in absolute value. Solving for the charge-to-mass ratio, we have:

$$\frac{A}{q} = \frac{B\rho}{(cu/e)\cdot\gamma\beta}\,, \tag{2.2}$$

from which we obtain the dimensionless fundamental equation of the spectrometer:

$$\frac{A}{q} \approx \frac{B\rho}{(3.107[\mathrm{Tm}])\gamma\beta}\,. \tag{2.3}$$

For fixed B and velocity, the charge-to-mass ratio is directly proportional to the radius of the trajectory, meaning that ions with higher (A/q) will have greater magnetic rigidity. Therefore, if detectors are placed at the end of the magnetic field region and differently charged particles with the same velocity enter the dipole, each particle will impact different regions of the detector, allowing for the reconstruction of their trajectories and the determination of their charge-to-mass ratio.

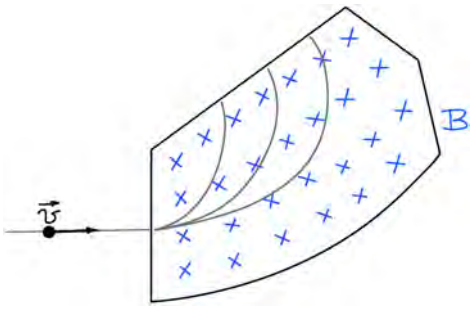

Figure 2.7: *Top view of a mass spectrometer with a charged particle with velocity $\vec{v}$ and a magnetic field B showing different trajectories in curved black lines.*

In the same vein, a magnetic rigidity $B\rho_0$ of the spectrometer can be defined as the nominal value for particles deviating along a reference path, known as the central trajectory, once the magnetic field is set. Fragments with a magnetic rigidity equal to $B\rho_0$ traverse this central trajectory, while those with higher $B\rho$ values follow more open paths and those with lower $B\rho$ values trace closer trajectories. Consequently, the position of the fragments after passing through the VAMOS++ magnetic setup directly correlates with their $B\rho$ values (see Fig. 2.8). By utilising a reconstruction method based on the ion optics of the spectrometer and $B\rho_0$, it becomes feasible to determine the $B\rho$ value of each fragment event by precisely measuring its position and angles at the VAMOS++ detection plane [87, 86].

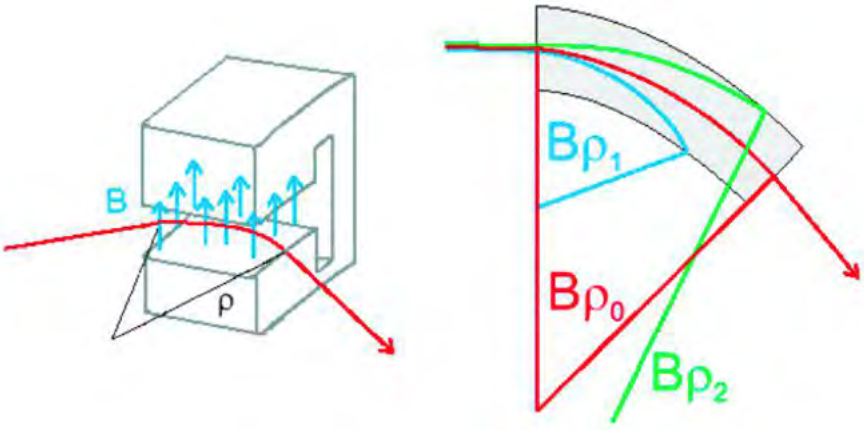

Figure 2.8: *On the left side, there is a schematic representation of a magnetic dipole. The blue lines illustrate the magnetic field (B), while the red line represents an example of an ion trajectory deflected by this field. The black line indicates the corresponding radius of curvature (ρ). On the right side, there is a comparison between ion paths with different Bρ values. The central trajectory, corresponding to the nominal value of the magnetic rigidity ($B\rho_0$), is depicted in red. The track of ions with higher Bρ values ($B\rho_2$) is shown in green, and the track of ions with lower Bρ values ($B\rho_1$) is depicted in blue.*

This reconstruction method involves simulating the ion trajectories within a mapping of the VAMOS++ magnetic field, it allows to correlate the $B\rho$ value of each ion with the measurement of its position (X_{FP}, Y_{FP}) and angles (θ_{FP}, ϕ_{FP}) at the detection setup of the focal plane, thereby enabling the extraction of its (A/q) value. The reconstruction method, which utilises the ion optics of the spectrometer and $B\rho_0$, allows for the precise determination of $B\rho$ on an event-by-event basis. A comprehensive explanation of this reconstruction method can be found in Section 2.4.3.

The mass range of the fission fragments investigated in this study spans from approximately $A = 70$ up to $A = 170$. By employing a spectrometer, it becomes feasible to achieve a certain level of resolution $(\Delta A/A)$, enabling an improved mass identification (see Section 4.3). When employing the standard calculation of mass (A) using measurements of kinetic energy (E) and velocity (v), the resolution in mass is inherently constrained by the resolution in energy and ToF measurements. This relationship can be expressed as $A \approx \frac{2E}{v^2}$, where the resolution in mass is determined by this formula:

$$\left(\frac{\Delta A}{A}\right)^2 \approx \left(\frac{\Delta E}{E}\right)^2 + 4 \cdot \left(\frac{\Delta ToF}{ToF}\right)^2 \longrightarrow \frac{\Delta A}{A} > \frac{\Delta E}{E}\,. \tag{2.4}$$

The resolution in mass determination relies on several factors. In the first case, where the ToF of the fragment is used to calculate the velocity, the resolution of the path measurement is negligible due to its small magnitude compared to the overall distance travelled. Thus, the primary limitation in mass resolution arises from the energy measurement, which typically exhibits a resolution of approximately 1% in an ionisation chamber [90]. Consequently, the calculated mass resolution is insufficient to distinguish mass values equal to or greater than 100 atomic mass units, u. However, when employing a spectrometer, the resolution is instead constrained by the magnetic rigidity $(B\rho)$ and ToF resolutions. Unlike the previous method discussed, where the energy measurement played a significant role in the resolution, the capability of the spectrometer to precisely measure the ToF and $B\rho$ values becomes the primary limiting factor for achieving

accurate mass resolution:

$$\left(\frac{\Delta A}{A}\right)^2 \approx \left(\frac{\Delta B\rho}{B\rho}\right)^2 + \left(\frac{\Delta ToF}{ToF}\right)^2 . \tag{2.5}$$

The resolution of the $B\rho$ value for fragments is determined by the resolution in the position measurement and the momentum dispersion of the spectrometer ($\delta x/\delta B\rho$). The position measurement is utilised in the reconstruction of the $B\rho$ value, thus its resolution directly affects the $B\rho$ resolution. In VAMOS++ spectrometer the magnetic rigidity is a dependence function like:

$$B\rho \approx function\left(X_{FP}, \frac{\delta x}{\delta B\rho}, \theta_{FP}, Y_{FP}, \frac{\delta y}{\delta B\rho}, \phi_{FP}\right) . \tag{2.6}$$

Nevertheless, it was demonstrated that the terms related to the vertical y-axis are negligible in the $B\rho$ reconstruction algorithm [88]. That implies a simplification:

$$B\rho \approx function\left(X_{FP}, \frac{\delta x}{\delta B\rho}, \theta_{FP}\right) . \tag{2.7}$$

Additionally, the momentum dispersion of the spectrometer, represented by the ratio $\delta x/\delta B\rho$, quantifies the deviation experienced by a charged particle when travelling through a magnetic field:

$$\left(\frac{\Delta B\rho}{B\rho}\right)^2 \approx \left(\frac{\Delta X_{FP}}{X_{FP}}\right)^2 + \left(\frac{\delta x}{\delta B\rho}\right)^2 . \tag{2.8}$$

The dispersion plays a crucial role in achieving higher $B\rho$ resolution alongside a fixed position resolution. For the VAMOS++ spectrometer, the average momentum dispersion at the focal plane was measured to be 2 cm/% [88]. This implies that a 1% difference in $B\rho$ relative to $B\rho_0$ corresponds to a 2 cm displacement from the focal plane centre. Considering the X_{FP} and Y_{FP} resolutions of 270 μm and 350 μm, respectively, and the ToF resolution of 500 ps, a mass resolution of 0.3% can be achieved, allowing the resolution of masses up to $\Delta A/A \approx 1/200$ u within the desired range, being the ToF measurement the main limitation in mass resolution [86, 88].

The acceptance of VAMOS++ is limited by the physical dimensions of the quadrupoles and by the dimensions of the detectors at the focal plane [88]. The VAMOS++ spectrometer offers an angular acceptance of ±100 mrad in the dispersive function of the relative magnetic rigidity $\Delta B\rho = (B\rho - B\rho_0)/B\rho_0$ (i.e. ±7° in θ_V) and ±160 mrad in the perpendicular plane (i.e. ±10° in ϕ_V), while the momentum acceptance is ±30% [87] (see the angular system in Fig. 2.3).

Figure 2.9 illustrates the relationship between the solid angle of the transmitted particles and the percentage relative magnetic rigidity. Although VAMOS++ offers a large acceptance, it is insufficient to cover the entire distribution of fragments. To address this limitation, two different spectrometer settings were employed for each reaction, aimed at increasing the acceptance in both magnetic rigidity and angle. These settings involve variations in the orientation of the spectrometer with respect to the beam axis (θ_{VAMOS}) and the nominal value of magnetic rigidity (see Fig. 2.3). Detailed information regarding the two settings used in this experiment and their classification can be found in Tab. 2.2.

USC UNIVERSIDADE DE SANTIAGO DE COMPOSTELA

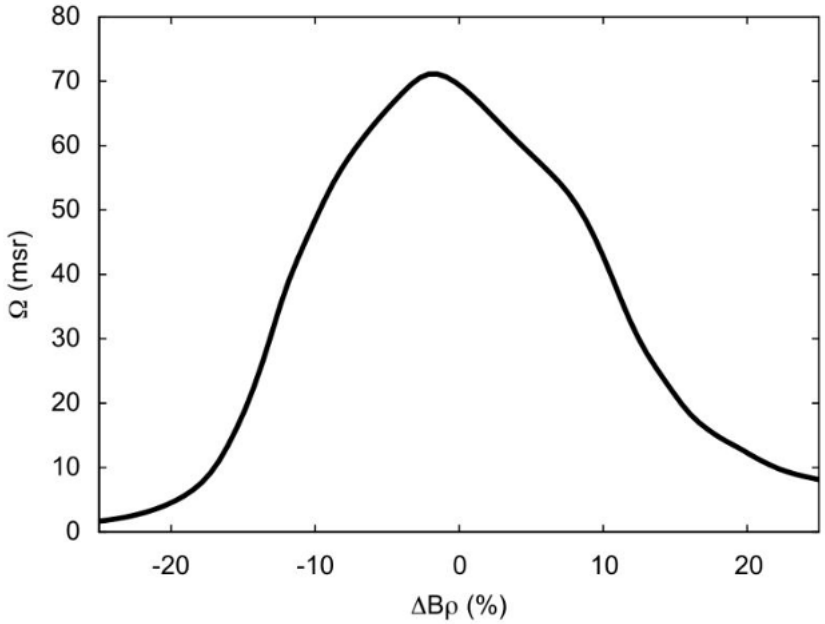

Figure 2.9: *The solid angle of VAMOS++, measured in millisteradians [msr], is shown as a function of the relative magnetic rigidity ($\Delta B\rho$) [%]. This solid angle represents the angular coverage of VAMOS++ and it is influenced by the percentage difference in magnetic rigidity $\Delta B\rho = (B\rho - B\rho_0)/B\rho_0$. Adapted with permission from [88]. Copyright (2011) by Elsevier Science B.V.*

Setting	θ_{VAMOS} [deg]	Bρ_0 [Tm]
1	14.0	1.24
2	21.5	1.10

Table 2.2: *The table is a list of VAMOS++ configurations, along with their corresponding spectrometer orientation (θ_{VAMOS}) [deg] and nominal value of magnetic rigidity ($B\rho_0$) [Tm].*

The selection of different spectrometer settings aimed to optimise the VAMOS++ acceptance in the region of highest fission fragment production. This is demonstrated in Fig. 2.10, which displays the simulated $(B\rho, \theta_{LAB})$ kinematics of fission fragments for the fissioning systems ^{249}Bk (A) and ^{265}Db (B). The acceptance boundaries for the two settings are overlaid on the plot. By utilising these two settings in combination, a wider coverage of the fragment phase space is achieved.

2.4.2 Focal plane in VAMOS++

The detection system at the focal plane of VAMOS++ allows for the comprehensive identification of fission fragments in terms of atomic number (Z), mass number (A), ionic charge state (q) and as well as the measurement of the vector velocity. This system consists of several detectors, including a Multi-Wire Parallel Plate Avalanche Counter (MWPPAC), tagged also as Multi-Wire chamber in this thesis, coupled with the MWPCs Start detector to measure the ToF, two Drift Chambers for position and angle measurements at VAMOS++ focal plane to reconstruct ion trajectories, and a segmented Ionisation Chamber for energy loss (ΔE) and residual energy (E_{res}) measurements. The active area of the focal plane setup is 1000 × 150 mm^2. The focal plane position is 7600 mm downstream from the target along the z-axis, with the y-axis perpendicular to the z-axis, and the x-axis orthogonal to both. For further details, refer to Fig. 2.11.

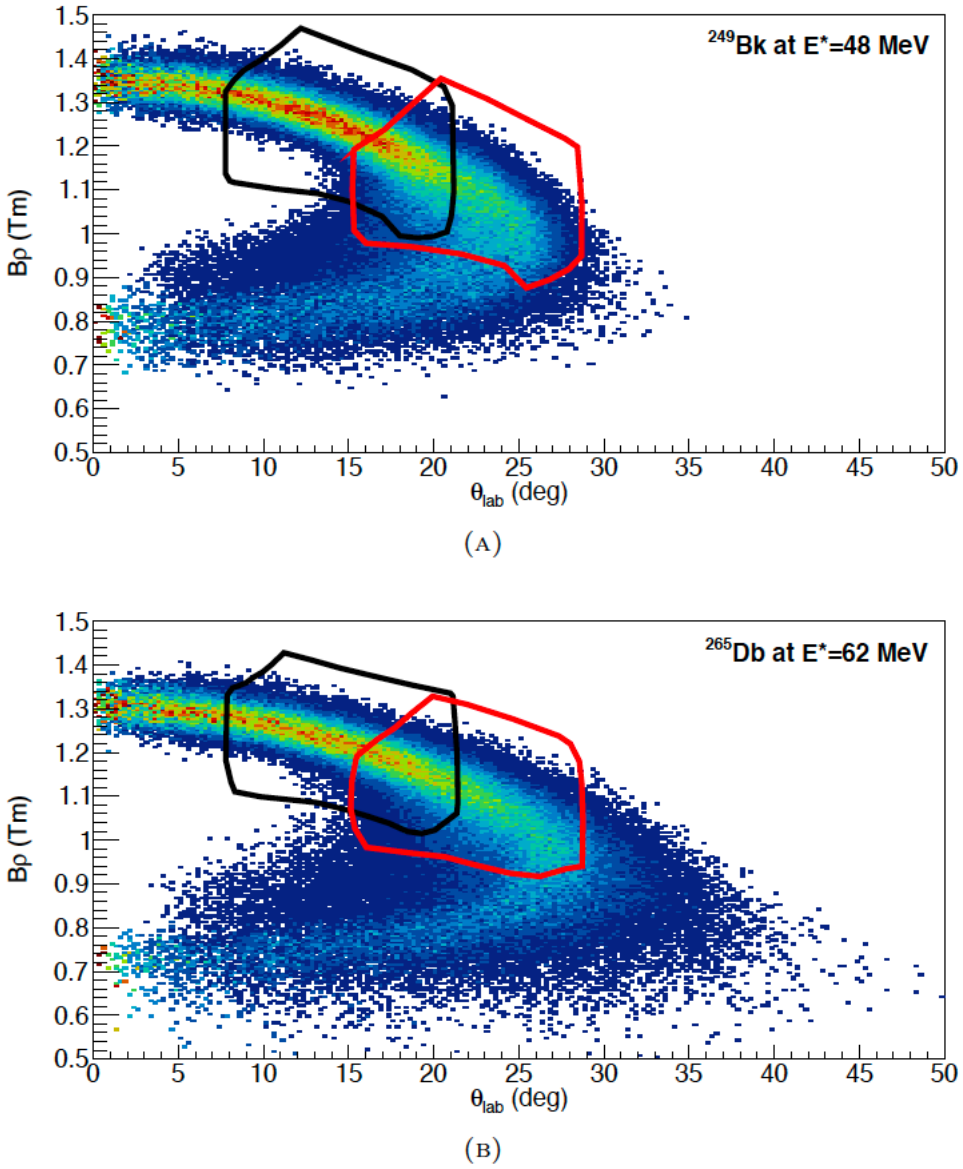

Figure 2.10: *Simulation results for the $(B\rho, \theta_{LAB})$ phase space of fission fragments are presented for two reactions: (A) $^{238}U + ^{nat}B$ reaction leading to the fissioning system ^{249}Bk, and (B) $^{238}U + ^{27}Al$ reaction producing the ^{265}Db fissioning system. The acceptance limits for the VAMOS settings are illustrated by black lines for setting 1 ($\theta_{VAMOS} = 14°$) and red lines for setting 2 ($\theta_{VAMOS} = 21.5°$). These limits define the range of $B\rho$ [Tm] and θ_{LAB} [deg] values within which the VAMOS++ spectrometer can detect and analyse the fission fragments.*

2.4.2.1 Multi-Wire Parallel Plate Avalanche Counter detector

The Multi-Wire chamber MWPPAC is a detector used in the VAMOS++ focal plane to measure the *ToF* of fission fragments [88]. It consists of a central cathode with vertical wires and two anodes, separated by 2.2 mm, with horizontal wires 1000 mm long. The cathode is polarised at −500 V, while the anodes are grounded. The detector operates with isobutane (C_4H_{10}) gas at 6 mbar and is equipped with a 0.9 μm-thick Mylar window to separate the gas volume from the vacuum. The window is supported by nylon wires with a diameter of 100 μm, placed at regular intervals every 50 mm. A scheme of the MWPPAC detector is shown in Fig. 2.12.

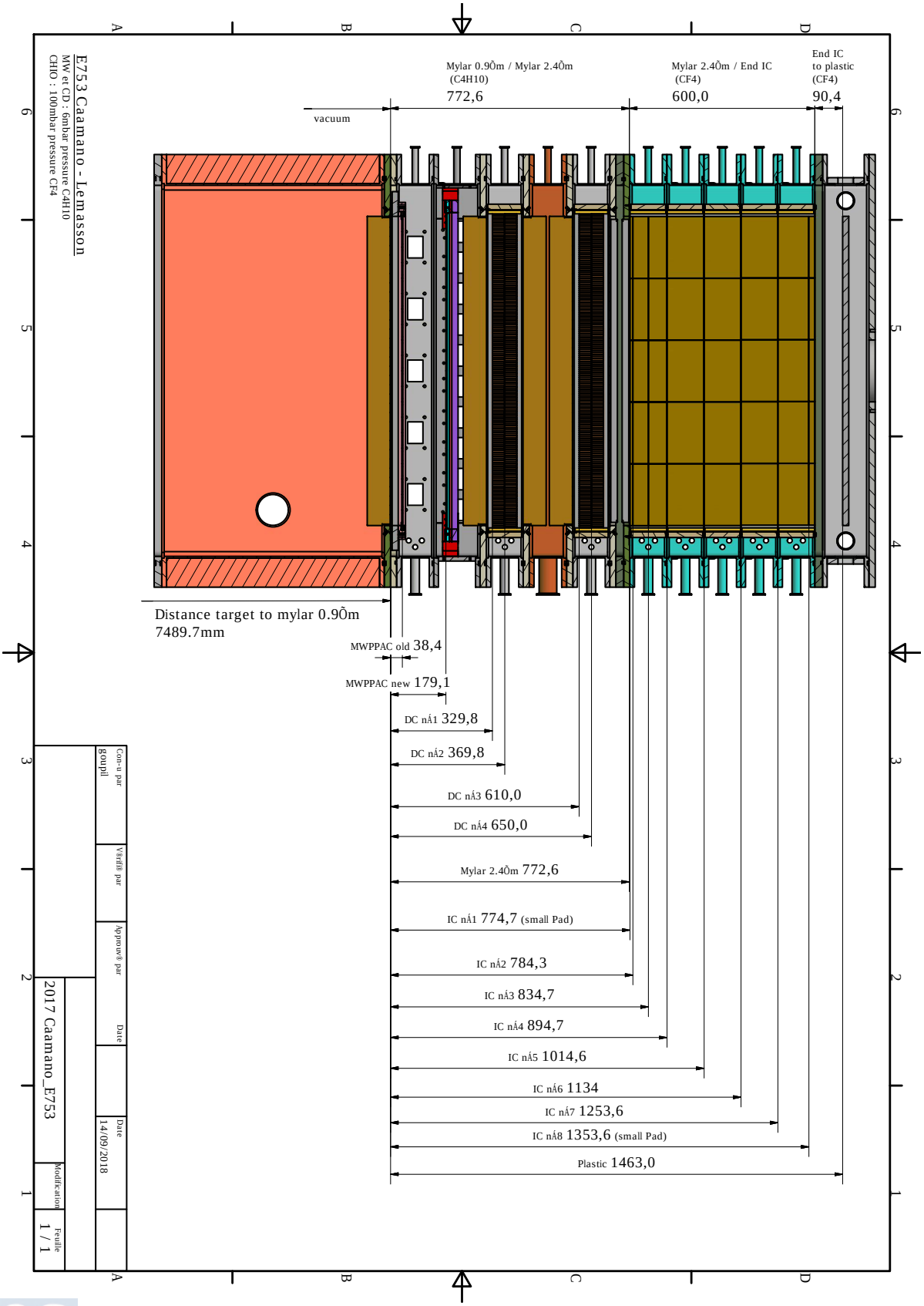

Figure 2.11: *Schematic diagram of the different detectors comprising the VAMOS++ spectrometer from the focal plane for the e753 experiment conducted in this study.*

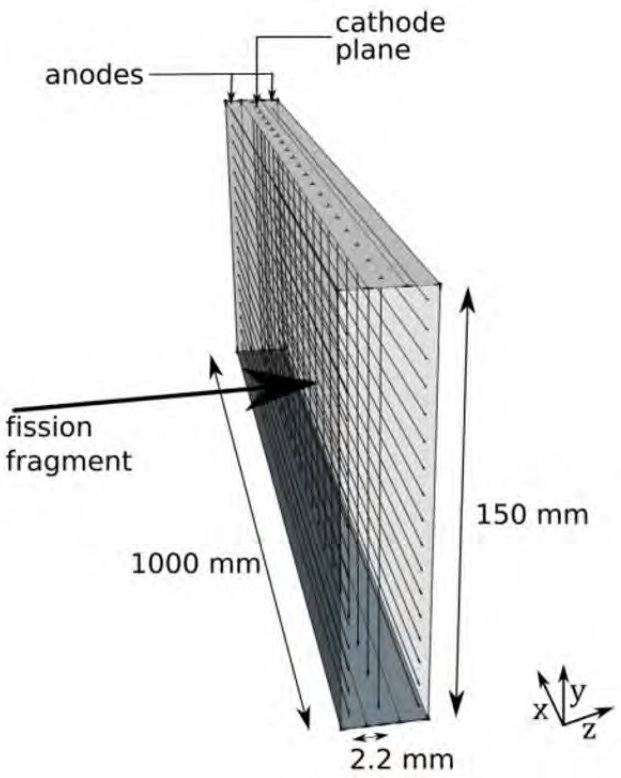

Figure 2.12: *The MWPPAC detector is illustrated in the provided sketch, showcasing the scheme and layout of the detector. The ionisation region, representing the space between the cathode and one of the anodes is indicated, although only a few wires are depicted for clarity.*

When a fission fragment passes through the MWPPAC, the resulting ionisation process generates an electron avalanche towards the anodes, while the positive ions are collected at the cathode. The cathode provides the stop signal for calculating the ToF of the fragment.

2.4.2.2 Drift Chambers

The Drift Chambers (DCs) in the VAMOS++ detection system are integral for measuring positions as well as angles: (X_{FP}, Y_{FP}, θ_V, ϕ_V). Each DC has an active volume measuring $1000 \times 150 \times 100$ mm^3, consisting of a drift region (150 mm) and an amplification region (20 mm) separated by a Frisch grid. A scheme of one DC is shown in Fig. 2.13(a) where a fission fragment direction is represented. A scheme of the corresponding cathode pads is also shown in Fig. 2.13(b). Since no separating window is placed in between the MWPPAC and the DCs, they are also filled with isobutane C_4H_{10} at 6 mbar [88].

The drift region contains a drift cathode where primary ionisation takes place in the filling gas. The Frisch grid, made of conductive wires of 50 μm diameter and a pitch of 2.54 mm, serves as an intermediate electrode to remove pulse height dependence on ionisation position. The amplification region comprises an anode with 8 wires located 15 mm below the Frisch grid and a segmented cathode positioned after the wire plane. The cathode is divided into two rows, each divided into 160 pads made of gold-plated strips, with independent signal readouts, minimising non-linearity between strips.

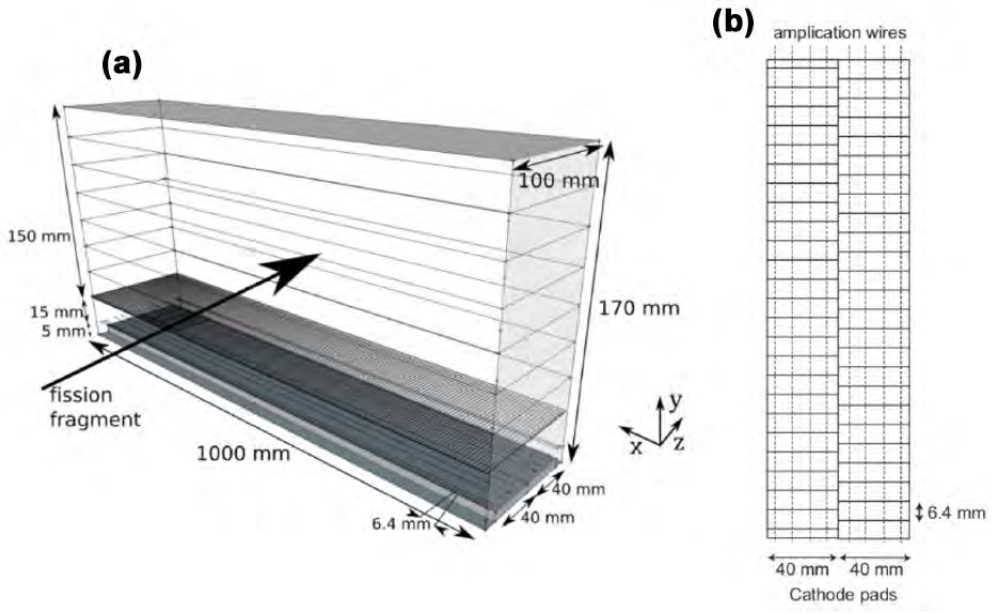

Figure 2.13: *The design of the Drift Chamber detector is illustrated in (a) with an arrow indicating the typical direction of a fission fragment. An expanded view in the $x-z$-plane of the cathode pads of the Drift Chamber detector is shown in (b).*

The DCs utilise -600 V for the drift electrode, 450 V for the amplification plane, and ground potential for the Frisch grid and segmented cathode. Metallic guard wires are placed to maintain a uniform electric field at the entrance and exit of the DCs.

Electrons produced by primary ionisation are drifted towards the amplification wires, creating an avalanche at the anode plane. Simultaneously, the electron avalanche induces a signal on the neighbouring cathode pads. The horizontal position coordinate (x) of the trajectory at the DC location is determined by applying square hyperbolic secant fit, a centre-of-gravity algorithm that takes into account the relative amplitudes of the induced charge in neighbouring pads, to the induced charge distribution on the pads (in the disperse plane). The fast signal from the amplification wires provides the drift time (t_d), which, when combined with the reference time from the Multi-Wire chamber MWPPAC, allows the position reconstruction in the vertical plane (y) with the drift velocity (v_d) of the electrons in the gas (constant velocity $v_d \approx 5.528$ cm/μs) according to the equation $y = v_d \cdot (t_d - t_0)$. The energy released inside the chambers can also be measured using the wires, although the resolution is not sufficient for its practical use. The X_{FP} and Y_{FP} coordinates at the focal plane position are finally reconstructed from the four spatial coordinates provided by the two DCs with a position resolution of 270 μm in the disperse plane and 350 μm in the drift direction.

2.4.2.3 Ionisation Chamber

The Ionisation Chamber (IC) serves the purpose of measuring the energy loss of fission fragments to determine their atomic number [86, 88]. It follows a design comprising a drift cathode at the upper part of the chamber with an active volume measuring $1000 \times 150 \times 579$ mm^3. The Frisch grid separates the drift region from the amplification region, while the amplification grid is positioned 10 mm below the Frisch grid. A segmented anode is located 20 mm below the acceleration grid. The anode consists of six segments (rows) along the flight path of the fragment (z direction), further divided into five pads along the x direction.

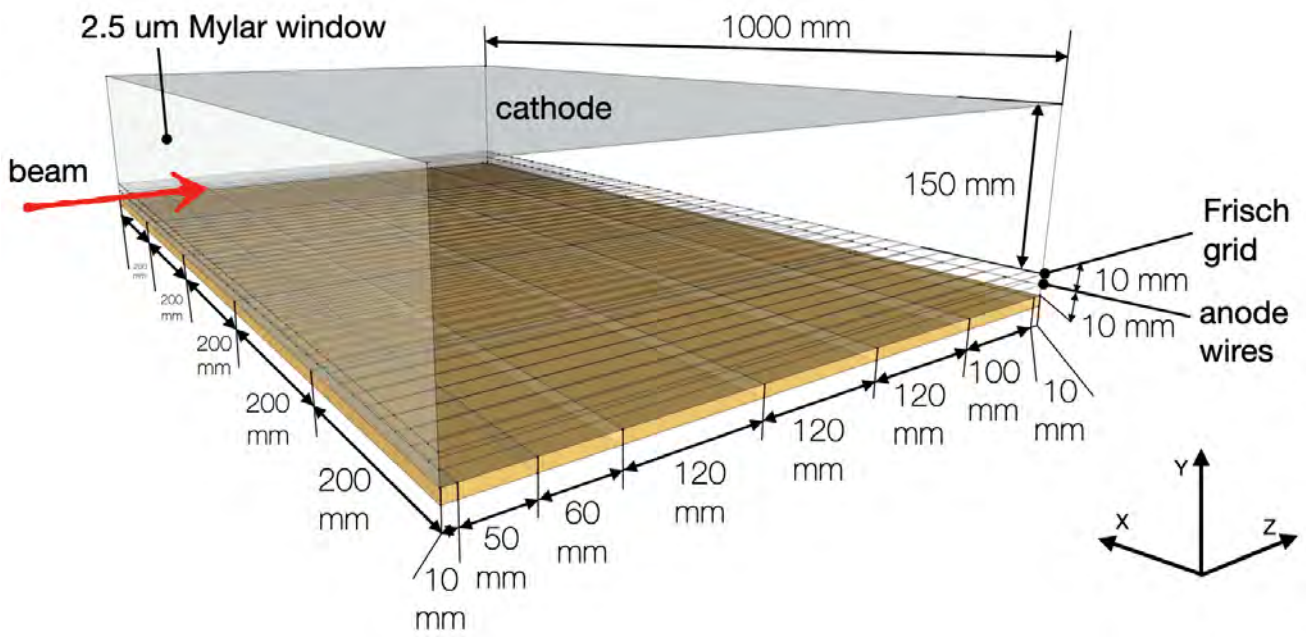

Figure 2.14: *The Ionisation Chamber detector scheme is presented in a schematic view. To provide a clear view of the full detector, the vertical grid, which ensures a homogeneous electric field at the entrance, is hidden in the illustration. A black arrow indicates the typical direction of the fission fragments.*

Figure 2.14 illustrates the design of the Ionisation Chamber. An additional guard row, is positioned at the chamber entrance with a length of 20 mm to collect δ electrons generated in the Mylar window located between the IC and the DC. The first row has an area of 1000×100 mm^2, while the second and third rows measure 1000×120 mm^2. To ensure a uniform electric field in the drift volume, a grid of wires with a pitch of 2.54 mm is placed between the cathode and the Frisch grid at the entrance of the first row and the exit of the last row.

The IC is filled with carbon tetrafluoride (CF_4) gas at 100 mbar. To prevent deformation caused by the different working pressures of the DC and the IC, a Mylar window with a thickness of 2.5 μm is supported by 32 vertical nylon wires at the IC entrance. In terms of polarisation, the cathode is negatively polarised at -2250 V, the Frisch grid is maintained at ground potential, the amplification wires are polarised at $+300$ V, and the anode pads are polarised at $+900$ V.

The Bethe-Bloch theory establishes a proportional relationship between the energy lost by a charged particle as it traverses a material and the nuclear charge. This relationship allows for the determination of the atomic number Z information of a fragment which passes through two consecutive layers of material by measuring its energy loss (ΔE) and residual energy (E_{res}). When heavy charged particles with moderate energies ($0.05 \leq \beta\gamma \leq 1$) interact with matter, their energy loss can be described using the Bethe-Bloch equation [91]:

$$-\frac{dE}{dx} = KZ^2 \frac{Z^{(m)}}{A^{(m)}} \frac{1}{\beta^2} \left[\ln \frac{2m_e c^2 \beta^2 \gamma^2}{I} - \beta^2 \right], \tag{2.9}$$

where Z and β are the charge and the velocity of the charged particle, $Z^{(m)}$ and $A^{(m)}$ are the atomic and mass numbers of the matter, I is the mean excitation energy of the matter, and $K = 4\pi N_A r_e^2 m_e c^2$, being N_A the Number of Avogadro, $r_e = 2.8179$ fm the classical electron radius, and m_e the electron mass. In the case of compound elements, such as isobutane, effective

values are defined as:

$$\left(\frac{Z^{(m)}}{A^{(m)}}\right)_{eff} = \sum_j \omega_j \frac{Z_j^{(m)}}{A_j^{(m)}}\,, \tag{2.10}$$

$$\ln I_{eff} = \frac{\sum_j \omega_j \frac{Z_j^{(m)}}{A_j^{(m)}} \ln I_j}{\sum_j \omega_j \frac{Z_j^{(m)}}{A_j^{(m)}}}\,, \tag{2.11}$$

where $\omega_j = \frac{n_j A_j^{(m)}}{\sum_k n_k A_k^{(m)}}$, being n_j the number of the j^{th} kind of atom in the compound. For the case of isobutane $(\frac{Z^{(m)}}{A^{(m)}})_{eff} = 0.586$ and $I_{eff} = 48.3$ eV.

When a fission fragment travels through the Ionisation Chamber, it undergoes a gradual loss of energy by ionising the gas molecules within the chamber. The primary ionisation generates electrons that are accelerated towards the anode pads by the electric field. The amplification region, below the drift region, provides a proportional multiplication of the number of drifted electrons and the readout of the signal they induce. The voltage settings in the IC are chosen to strike a balance between achieving significant amplification for better intrinsic resolution and maintaining proportionality between the primary ionisation energy loss and the induced charge in the pads, thus preventing gas discharges. During this process, the electrons are ultimately collected at the anode.

The number of released electrons is roughly proportional to the energy loss of the fragment, so the charge measured by each pad corresponds to the energy lost by the fragment in the area covered by that particular pad. By summing the charges collected by the pads in the same row of the IC, the energy loss (ΔE_i) of the fragment can be determined. The choice of gas pressure is crucial as it affects the Z resolution and requires a balance between achieving good Z separation and ensuring a sufficient flight path before the maximum energy release of the Bragg Peak occurs.

In this experiment, the gas pressure employed ensured the complete stopping of the fission fragments within the IC. Measuring the total energy (E_{tot}) with a single detector equipped with a segmented anode allows for offline analysis to optimise the Z identification by selecting the optimal ($\Delta E - Eres$) combination.

Through the energy relation, the determination of the atomic number Z for each interacting fragment within the IC becomes feasible. This is achieved within a narrow range of interaction, characterised by minimal variation in the velocity of the charged particle and relative constancy in the component of the Bethe-Bloch equation encapsulated by the square brackets.

In the case of this work, the concept of $Z_e = Z + q$ is introduced, where Z_e signifies the charge of the fission fragment, consisting of the sum of its atomic number and charge state, this process is known as charge exchange. This arises due to the number of electrons captured by the fission fragment. When the nearly constant velocity of the fission fragment significantly exceeds the orbital velocity of electrons, the charge remains constant. Within this context, a straightforward relationship emerges between energy loss and the charge of the fragment, as expressed by the equation:

$$-\frac{dE}{dx} \propto \frac{Z_e^2}{\beta^2}\,. \tag{2.12}$$

However, when the velocity of the fragment is not considerably high, the proportionality of the energy loss is governed by the charge and mass of the fragment. There exists a relationship between the average charge of a particle traversing a layer of matter at a specific velocity and its charge Z_e. This relationship is proportional to ΔE^2 and $Z_e^2 M \Delta x$, and although it changes within the ionisation chamber as the particles decelerate, the correlation between these quantities remains valid, except in the vicinity of the Bragg Peak.

The Bragg Peak is a low-energy region where the energy loss is at its maximum. In this region, the velocity of the particle and effective charge undergo rapid variations, making the relationship between energy loss and atomic number more complex.

Furthermore, by combining the velocity measurement obtained from the ToF and the total energy deposited in the IC, it is also possible to calculate the mass of the fragments as will be explained in Section 4.2.

2.4.3 Reconstruction algorithm

In a spectrometer, the magnetic field plays a crucial role in determining the relationship between the initial characteristics of the fragments and the final quantities measured after passing through the spectrometer. Ideally, this relationship would be described by a simple linear function, allowing for direct extraction of the initial momentum of the fragments and scattering angles from the recorded transverse positions and angles at the spectrometer focal plane. However, in the case of large acceptance spectrometers like VAMOS++, the non-homogeneity of the magnetic field complicates this relationship. Therefore, it becomes essential to reconstruct the ion trajectories within the magnets to establish the function that connects the measured positions and angles at the focal plane with the reconstructed observables, including the magnetic rigidity ($B\rho$), the polar angle (θ), azimuthal angle (ϕ), and the path length of the ion ($Path$).

The effect of the magnetic field within the spectrometer shapes the trajectory of the fragments, establishing a relationship between the characteristics of the fragments before entering the spectrometer and the transverse positions and angles measured at the focal plane detectors, that is $(X_{FP}, Y_{FP}, \theta_{FP}, \phi_{FP})$.

The first VAMOS reconstruction algorithm [87] comprised two main steps: trajectory simulation and back-tracing reconstruction. In the initial step, trajectory simulation, particle trajectories within VAMOS are simulated using *Zgoubi* [92]. This simulation is based on the magnetic field maps measured during the design stage [93]. The subsequent step, back-tracing reconstruction, involves the establishment of a 10^{th} order polynomial relationship between the measured focal plane positions and angles and the desired reconstructed observables.

Despite the complexity of the 10^{th} order polynomial method, it fails to accurately represent all aberrations with a single set of coefficients across the entire focal plane. As a result, the resolution of the reconstructed θ, $B\rho$, and $Path$ is diminished. Even attempts to enhance the atomic mass resolution by subdividing the focal plane phase space within the polynomial approach have proven ineffective. Consequently, in 2011, the two-dimensional (2D) mapping approach was introduced, accompanied by an expansion of the focal plane detection size [88, 94] and references therein.

The coordinates $m = \theta, \delta, Path$ are reconstructed solely based on the final image focal plane coordinates (X_{FP}, θ_{FP}), while keeping the reconstruction of the coordinate ϕ_{FP} following the 10^{th} order polynomial approach. The values for each of the m coordinates can be stored in the two-dimensional array M_m, with a numerical precision of 10^{-3}, 1 mrad, and 1 mm for δ, θ, and Path, respectively. The dimensions of each array M_m were chosen to be 1100×550, corresponding to steps of 1 mm and 1 mrad for the coordinates X_{FP} and θ_{FP}, respectively. For each calculated trajectory, the δ, θ, and $Path$ coordinates were stored in the M_m arrays as functions of X_{FP} and θ_{FP} coordinates, following the expressions:

$$\begin{aligned} i &= [X_{FP} + 600 + 0.5]\,, \\ j &= [\theta_{FP} + 200 + 0.5]\,, \end{aligned}$$

$$\begin{aligned} M_\delta[i][j] &= [\delta \times 1000 + 0.5]\,, \\ M_\theta[i][j] &= [\theta + 200 + 0.5]\,, \\ M_{Path}[i][j] &= [Path + 0.5]\,, \end{aligned} \tag{2.13}$$

where X_{FP} and $Path$ are in mm, and θ and θ_{FP} are in mrad. The reverse process for obtaining reconstructed parameters from measured (X_{FP}, θ_{FP}) is uncomplicated.

2.5 Electronics

In this experiment there are four possible types of reactions between the ^{238}U beam and the targets:

1. The fusion-induced fission reaction of different compound nuclei.
2. The fusion-evaporation reaction of different compound nuclei.
3. The binary reactions such transfer, elastic or inelastic scattering without fission.
4. The transfer- or inelastic-induced fission reaction.

It is necessary to design a robust trigger system in this experiment to distinguish and identify these three types of events of interest. The experiment uses three triggers, as shown in Fig. 2.15, related respectively to the three types of reactions above:

1. The **VAMOS trigger** is produced by the coincidence between a delayed signal of 600 ns from TMW1 and a 50-ns-delayed signal from Multi-Wire chamber MWPPAC. The fusion-induced fission reaction produces two fission fragments without a target-like recoil. If the acceptance allows, one of the fragments is detected at the VAMOS++ focal plane. Consequently, the VAMOS++ trigger is defined as a signal recorded by the Multi-Wire chamber MWPPAC coinciding with no signal in SPIDER. However, it is important to note that transfer-induced fission reactions, where the recoil is not detected, can also be erroneously identified with the VAMOS++ trigger. The trigger signals from Multi-Wire chamber MWPPAC and the absence of a signal in SPIDER tag the events as fusion-induced fission reactions and potentially misidentified transfer-induced fission reactions can be distinguished during the experiment.
2. The **SPIDER trigger** is generated when a signal is detected in a sector of the first detector in coincidence with no signal from the Multi-Wire chamber MWPPAC at VAMOS++. This

signal undergoes a delay of 560 ns and is then passed through a Divider module, which allows only one event every 1000 due to the high cross-section of elastic scattering. The binary reactions result in a target-like recoil emitted at a large angle, which is detected by the SPIDER detector, and a forward-emitted beam-like partner that is not measured.

3. The **SPIDER-VAMOS trigger** is defined as the coincidence between the SPIDER trigger and the VAMOS trigger. This trigger is specifically designed to identify transfer- and scattering-induced fission events. It involves the simultaneous presence of a signal from SPIDER $dE_{sectors}$ and a signal from Multi-Wire chamber MWPPAC, ensuring the detection of the recoil in SPIDER and one fragment at VAMOS++.

The electronic layout used in the experiment consists of two main components: the analogue electronic scheme and the logical electronic scheme. The analogue electronic is responsible for collecting and processing the analogue signals from the detectors. It handles receiving and manipulating the signals obtained from the detectors during the experiment. The logical electronic circuit generates the trigger signals necessary for acquiring the processed signals. It defines the logical conditions and criteria for recognising and initiating the data acquisition process based on specific events or patterns of interest. These two components work together to enable the successful acquisition and processing of the experimental data.

The synchronisation of logic trigger signals is essential to verify the coincidence and anti-coincidence of events. This is achieved by applying time delays to the initial signals. The verification of the logic trigger signals is carried out by the Ganil Master Trigger Module (GMT) module [95]. Upon receiving a trigger signal, the GMT module generates a Fast Analysis Gate (FAG) signal, which enables data processing and storage through the GANIL Data Acquisition System (DAS). Then, GMT module is responsible for defining the triggers and generating the FAG signal.

The analogue electronic scheme can be divided into two main components: the first component comprises the analogue electronics of the SPIDER detector, which is responsible for detecting the target-like recoil nucleus in scattering and transfer reactions. The second component encompasses the analogue electronics of the detectors located at the focal plane of the VAMOS++ spectrometer, primarily focused on identifying the fission fragments. The FAG signal initiated by the GMT module triggers the data readout process, which is further processed and stored by the GANIL Data Acquisition System (DAS).

The SPIDER setup, as depicted in Fig. 2.6, consists of four sources of signals: the rings (dE_{rings}) and sectors ($dE_{sectors}$) of the first detector, which measure the energy loss of the incoming ion, and the rings (E_{rings}) and sectors ($E_{sectors}$) of the second detector, which provide information about the residual energy. Each signal is initially amplified by a Pre-Amplifier (PA) module and further amplified by a Spectroscopic Amplifier (AMP) module. The analogue signals from the AMP modules are then digitised by an Analogue-to-Digital Converter (ADC) module before being sent for acquisition. In addition to the ADC process, the AMP modules generate one common logic signal and fast analogue signals that are fed into a Discriminator (DISCRI) and then transmitted to a Gate and Delay Generator module, where they undergo a 1200 ns delay. The coincidence between the delayed signal and a validated FAG initiates the readout of the ADC.

USC DE SANTIAGO DE COMPOSTELA

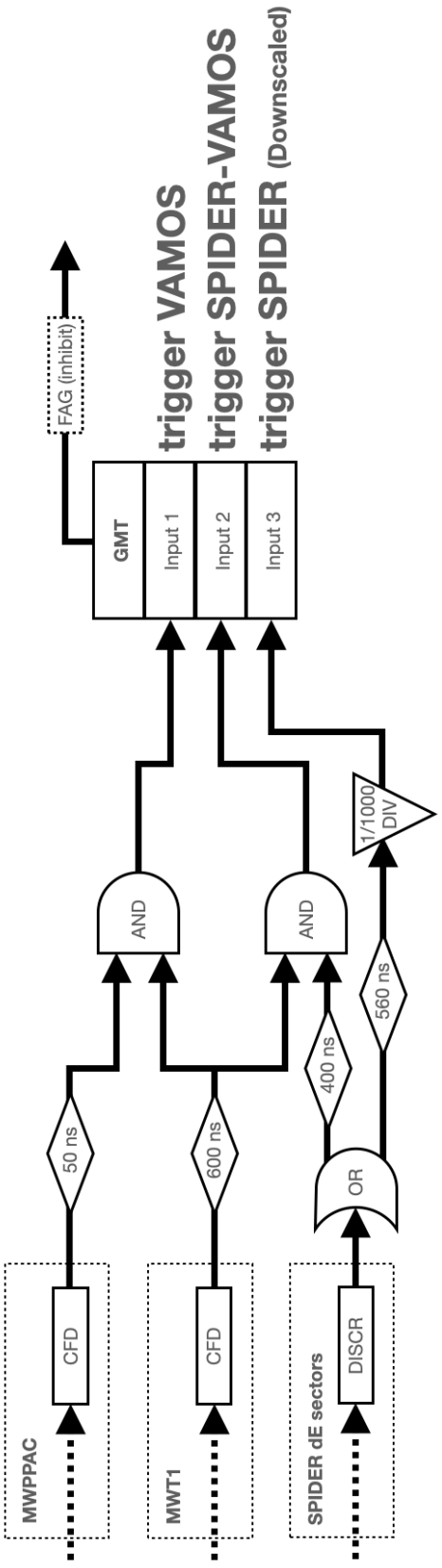

Figure 2.15: *Scheme of the logic electronic chain with the triggers diagram involved in fission fragment detection used during the experiment.*

The SPIDER trigger signal originates from the sectors of the second detector ($E_{sectors}$). The logic output from the AMP module is directed to a FAN-IN FAN-OUT module, which produces a 200 ns-width NIM signal defining the trigger signal (OR SPIDER). This trigger signal is also utilised to validate the FAG by coinciding with it after a 450 ns delay. The electronic setup of the SPIDER detector is illustrated in Fig. 2.16. The ToF measurements for the fission fragments are obtained from the MWPCs Start detector at the target position and the Multi-Wire chamber MWPPAC at the VAMOS++ focal plane. The signals from the Multi-Wire chamber MWPPAC undergo amplification in a PA and further amplification in a Timing Filter Amplifier (TFA) module. Once accepted by a Constant Fraction Discriminator (CFD), each signal is directed to a Time to Digital Converter (TDC) module for recognising events and providing a digital representation of the time they occurred. Additionally, the signals from the MWPCs Start detector trigger a logic signal in a CFD, which is delayed by 650 ns and transformed into a 40 ns-width signal serving as the gate for the TDC module.

The Drift Chambers in the experiment provide essential information for calculating the reconstructed observables, specifically the X_{FP} and Y_{FP} positions. The X_{FP} position is determined by the charge induced in the cathode pads, while the Y_{FP} position is derived from the electron drift time measured through the wire signals (see Section 2.4.2.2). The wire signal is amplified using a PA and split into two signals. One signal is further amplified in an AMP and digitised in an ADC to measure the energy loss. The other signal is amplified in a TFA and, if accepted by a CFD, is delayed by 550 ns. This delayed signal is subject to a coincidence with a FAG signal to prevent interference from other triggers during the readout process. The output of this coincidence module consists of three signals: one signal establishes a Dead Time period for pausing the acquisition, the second signal initiates the readout of the pads, and the third signal halts a Time-to-Amplitude Converter (TAC) module triggered by the validated MWFP signal from the FAG. The TAC module provides the drift time of the electrons in the chamber, which is proportional to the position of the fragment in the vertical plane.

The Drift Chambers also provide the energy loss measurement through the amplified wire signal, which is digitised in the ADC module. The charges induced on the pads in the Drift Chambers are measured using Gassiplex chips in a Track-and-hold procedure. When the signal from the wires is detected, it triggers a Track signal that instructs the chips to sequentially record the maximum charge induced in each pad. This process is controlled by the CAEN Readout for Analogue Multiplexed Signals (C-RAMS) sequencer. During the Hold time window, the chips store the recorded values and transmit them to the acquisition system. Subsequently, the chips undergo a reset procedure to clear the recorded values and prepare for the next event. The readout of the pads in the Drift Chambers, which is handled by the Ganil Acquisition Module for Electronics Resources (GAMER), contributes significantly to the Dead time ($\approx 20\,\mu s$ in total).

The Ionisation Chamber detector serves to measure both the energy loss and residual energy deposited by the fragments. The signals produced by the six rows of the IC detector are subjected to signal filtering and shaping within a PA, subsequently being further amplified within an AMP. These signals are then digitised in an ADC module and transmitted to the acquisition system. A separate AMP produces a fast trigger signal, which is accepted by a discriminator, initiating the readout of the ADC. To ensure compatibility with the ADC module, a gate generator and a translator NIM-ECL are employed to convert the discriminator output into the appropriate signal type (ECL) accepted by the ADC module. The electronic configuration of the detectors utilised in the detection of fission fragments is depicted in Fig. 2.17.

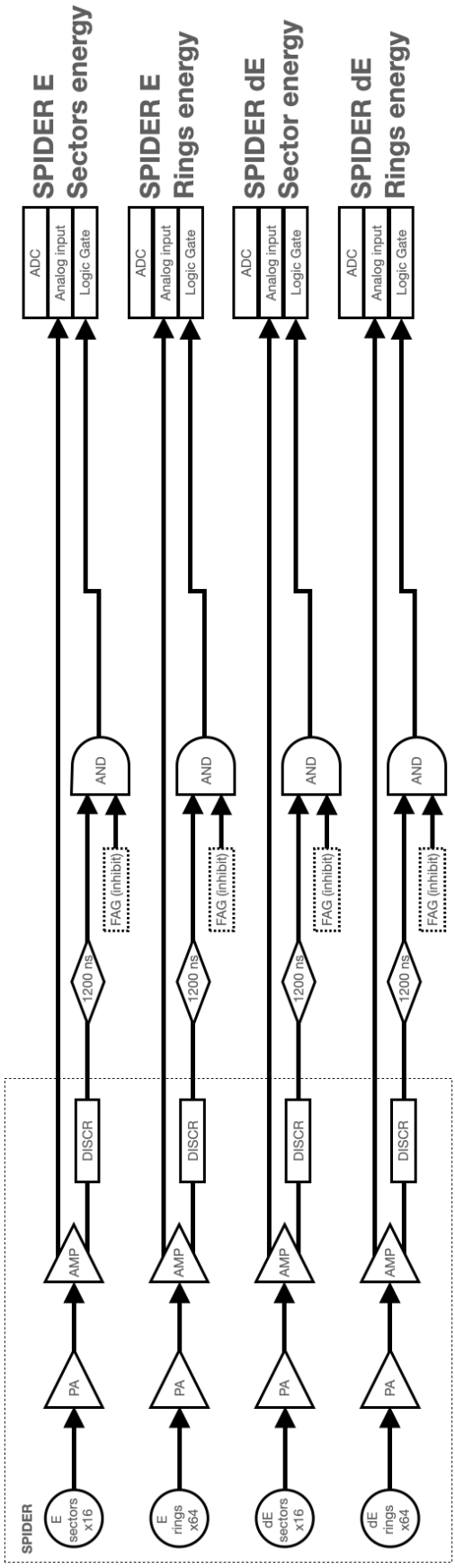

Figure 2.16: *The electronic chain of the SPIDER detector is illustrated in the diagram.*

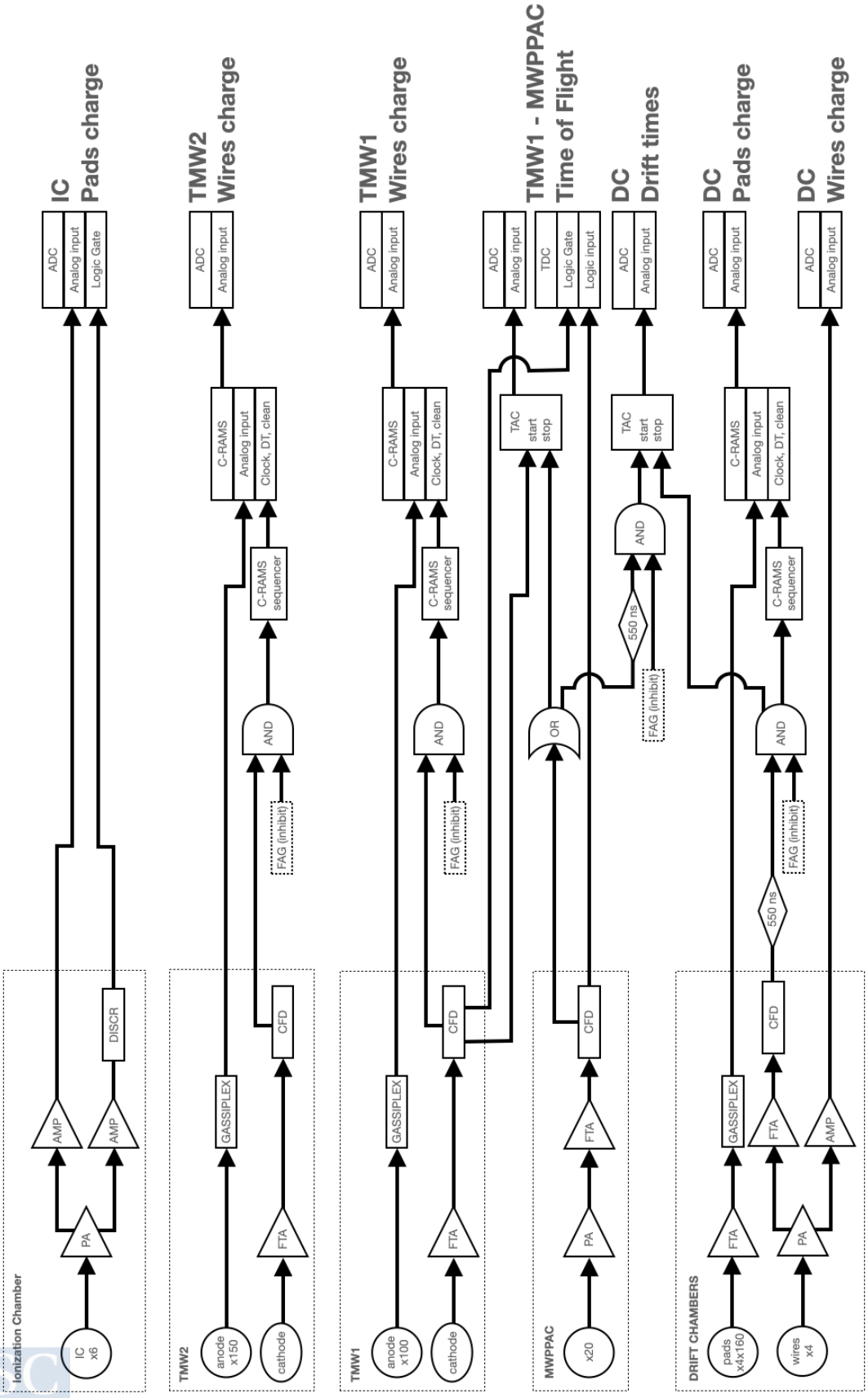

Figure 2.17: *The electronic setup diagram of the detectors involved in fission fragment detection.*

By analysing the trigger signals, the system can effectively categorise and analyse the corresponding reaction types during the experimental process.

2.6 Fissioning system tagging

A series of fissioning systems are generated through inelastic, transfer and fusion reactions, as described in Section 2.2. In the experimental setup, a transfer-fission reaction is identified when a fission fragment is detected at the VAMOS++ focal plane in coincidence with a target-like recoil in the SPIDER detector. The SPIDER telescope (see Section 2.3.2), equipped with two layers, permits the isotopic identification of the target-like recoils by measuring their energy loss and residual energy deposition (see Section 2.3.2).

Figure 2.18 illustrates the isotopic identification of light recoils resulting from transfer reactions involving different entrance channels: ^{238}U+ ^{27}Al, ^{238}U+ ^{24}Mg, ^{238}U+ ^{nat}B, and ^{238}U+ ^{9}Be. Each line on the plot represents a specific (Z, A) recoil, corresponding to a particular fissioning system. The production of target-like recoils varies with the entrance channel, with heavier targets leading to a distribution shifted towards more massive recoils. The energy resolution for the ^{238}U+ ^{24}Mg system is adversely affected by the oxidation of the target material. The presence of an oxidation layer on the target, confirmed by the significant contribution of ^{16}O in the identification plot, increases the effective thickness of the target and degrades the energy resolution. The cases of the Be and B targets there is also ^{16}O contamination as can be seen in Fig. 2.18. Nevertheless, this contamination is much less significant, being consequently negligible, affecting neither the thickness nor the yields.

In Tab. 2.3 are summarised the identified transfer reactions for the four entrance channels.

^{238}U + ^{27}Al Transfer	^{238}U + ^{24}Mg Transfer	^{238}U + ^{nat}B Transfer	^{238}U + ^{9}Be Transfer
^{27}Al(^{238}U, ^{230}Ra)^{35}Cl	^{24}Mg(^{238}U, ^{238}U)^{24}Mg	^{nat}B(^{238}U, ^{238}U)^{11}B	^{9}Be(^{238}U, ^{238}U)^{9}Be
^{27}Al(^{238}U, ^{234}Th)^{31}P	^{24}Mg(^{238}U, ^{239}Np)^{23}Na	^{nat}B(^{238}U, ^{239}U)^{10}B	^{9}Be(^{238}U, ^{239}U)^{8}Be
^{27}Al(^{238}U, ^{238}U)^{27}Al	^{24}Mg(^{238}U, ^{242}Pu)^{20}Ne	^{nat}B(^{238}U, ^{239}Np)^{10}Be	^{9}Be(^{238}U, ^{240}Np)^{7}Li
^{27}Al(^{238}U, ^{241}Np)^{24}Mg	^{24}Mg(^{238}U, ^{243}Am)^{19}F	^{nat}B(^{238}U, ^{240}Np)^{9}Be	^{9}Be(^{238}U, ^{243}Pu) ^{4}He
^{27}Al(^{238}U, ^{242}Pu)^{23}Na	^{24}Mg(^{238}U, ^{246}Cm)^{16}O	^{nat}B(^{238}U, ^{241}Np)^{8}Be	
^{27}Al(^{238}U, ^{245}Am)^{20}Ne	^{24}Mg(^{238}U, ^{247}Bk)^{15}N	^{nat}B(^{238}U, ^{242}Pu)^{7}Li	
^{27}Al(^{238}U, ^{246}Cm)^{19}F	^{24}Mg(^{238}U, ^{248}Cf)^{14}C	^{nat}B(^{238}U, ^{245}Am)^{4}He	
^{27}Al(^{238}U, ^{249}Bk)^{16}O	^{24}Mg(^{238}U, ^{249}Cf)^{13}C		
^{27}Al(^{238}U, ^{250}Cf)^{15}N	^{24}Mg(^{238}U, ^{250}Cf)^{12}C		
^{27}Al(^{238}U, ^{251}Es)^{14}C			
^{27}Al(^{238}U, ^{252}Es)^{13}C			
^{27}Al(^{238}U, ^{253}Es)^{12}C			

Table 2.3: *List of transfer reaction channels identified by SPIDER detector corresponding to the four targets used in the experiment.*

USC UNIVERSIDADE DE SANTIAGO DE COMPOSTELA

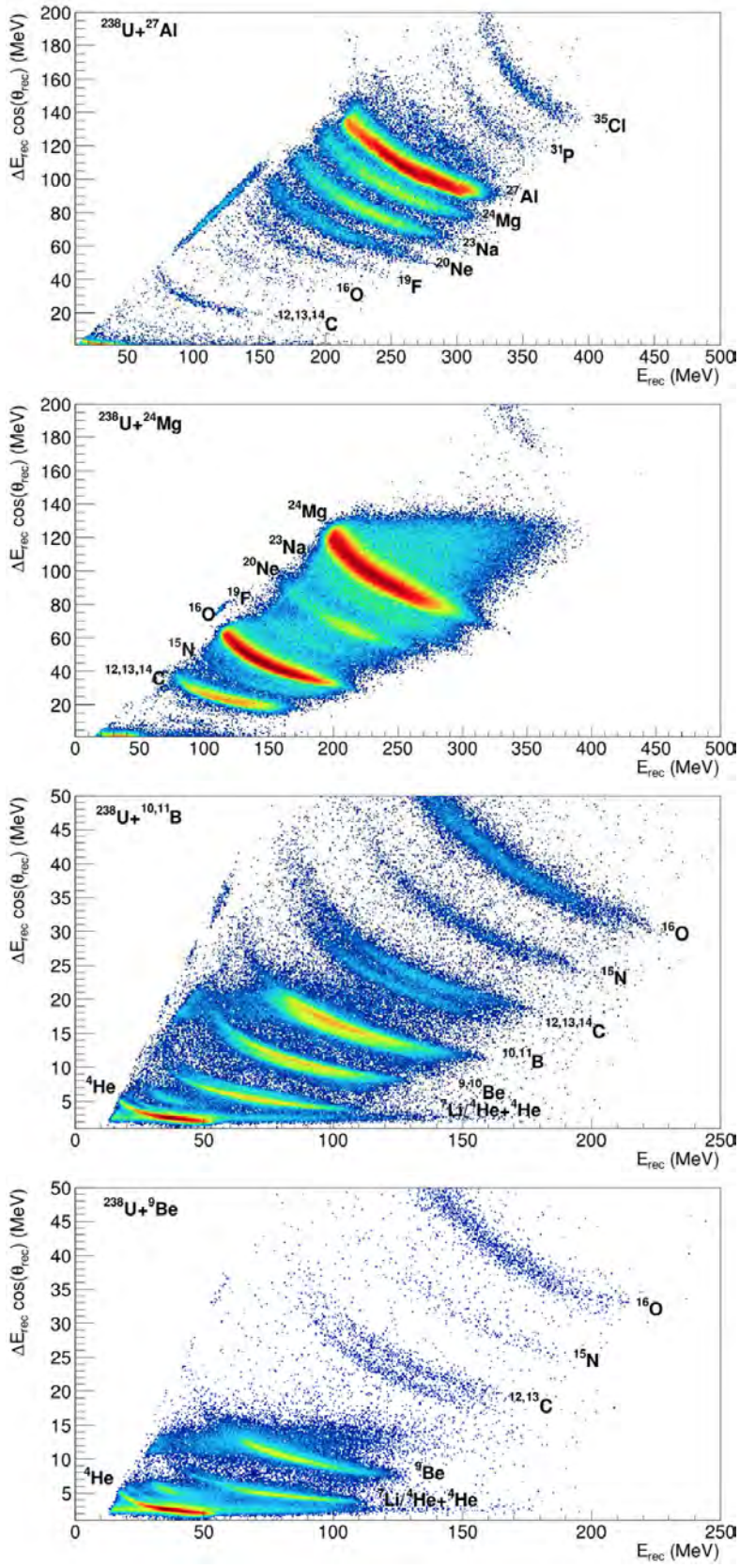

Figure 2.18: *Isotopic identification of target-like recoil nuclei produced by transfer reactions using the SPIDER detector. The systems, from top to bottom, are:* $^{238}U + {}^{27}Al$, $^{238}U + {}^{24}Mg$, $^{238}U + {}^{nat}B$, *and* $^{238}U + {}^{9}Be$.

The isotopic identification and angle measurement of the light nucleus, obtained through the segmentation of the detector, enable the calculation of the excitation energy, velocity, and angle of the fissioning system. By conserving the quadrimomentum, the binary reaction can be reconstructed, and from the measurement of energy and angle of each recoil nucleus, the excitation energy is determined according to energy-momentum conservation:

$$M_{beam} + T_{beam} + M_{target} = M_{rec} + T_{rec} + M_{FS} + T_{FS} + E^* \,, \tag{2.14}$$

$$p_{beam} = p_{rec} \cdot \cos(\theta_{rec}) + p_{FS} \cdot \cos(\theta_{FS}) \,, \tag{2.15}$$

$$0 = p_{rec} \cdot \sin(\theta_{rec}) - p_{FS} \cdot \sin(\theta_{FS}) \,. \tag{2.16}$$

In the context of the reaction, the variables M, T, p, and θ represent the ground-state mass, kinetic energy, linear momentum, and polar angle, respectively, for the nuclei involved: the beam (*beam*), the target (*target*), the recoil (*rec*), and the fissioning system (*FS*). The total excitation energy E^* is typically shared between the recoil and the fissioning system. However, due to the higher level density of the beam-like nucleus and the relatively high energy of its first excited state, the fissioning system is more likely to be excited. By rearranging Eq. 2.14 (see [82] for further details), the excitation energy of the fissioning system E^*_{FS} can be expressed as:

$$E^*_{FS} = \sqrt{(Q_{gg} + M_{FS} + T_{beam} - T_{rec})^2 - p^2_{FS}} - M_{FS} \,, \tag{2.17}$$

where Q_{gg} is the ground-state to ground-state *Q-value* of the reaction.

The fissioning system momentum, p^2_{FS}, is obtained by combining Eq. 2.15 and Eq. 2.16:

$$p^2_{FS} = p^2_{beam} + p^2_{rec} - 2p_{beam} \cdot p_{rec} \cdot \cos(\theta_{rec}) \,, \tag{2.18}$$

then, the velocity of the fissioning system, β_{FS} in units of c, is calculated as:

$$\beta_{FS} = \frac{p_{FS}}{\sqrt{p^2_{FS} + (M_{FS} + E^*_{FS})^2}} \,, \tag{2.19}$$

with a polar angle:

$$\cos(\theta_{FS}) = \frac{p_{beam} - p_{rec} \cdot \cos(\theta_{rec})}{p_{FS}} \,. \tag{2.20}$$

In the case of the fusion mechanism, the compound nucleus is formed as the fissioning system, and no target-like recoil is emitted. To identify a fusion-fission reaction experimentally, a single fission fragment is detected at the VAMOS++ focal plane in coincidence with the absence of a light recoil signal in SPIDER. In this scenario, the direction and momentum of the fissioning system correspond to those of the incident beam, resulting in well-defined values for the excitation energy and velocity of the fissioning system.

Although the excitation energy is typically shared between the recoil and scattered nuclei, the higher level density of the heavy scattered nucleus compared to the target-like recoil, along with the relatively high energy of the first excited state of the light recoil, promotes the excitation of the fissioning system. Detailed research on γ decay for the recoil nucleus with a ^{12}C target indicates a probability of approximately ≈ 0.9 for the presence of an excited heavy scattered nucleus and a cold light recoil [82].

The limited intrinsic and geometric efficiencies of the SPIDER detector result in the inability to recognise all transfer-fission events, leading to misidentification of some of them as fusion-fission events. Consequently, there exists contamination in the data identified as fusion-induced fission caused by transfer-induced fission, although the probability of such contamination is low compared to the fusion-fission mechanism, which is approximately ten times more likely. The contamination arising from the transfer-fission mechanism is subsequently eliminated by analysing the fission-fragment distributions through the contamination study with the aluminium target (see Section 6.4) and the contamination study with the boron target (see Section 6.5).

2.7 Fissioning system reference frame

The fissioning-system reference frame, referred here as the centre-of-mass (CM) reference frame, is defined as the framework in which the fissioning system is stationary. In this reference frame, the distribution of fission fragments is independent of the kinematics of the fission-inducing reaction. By measuring the velocity and angle of the fissioning system in the laboratory reference (LAB) frame, it is possible to determine the velocity and angle of the fission fragments in the CM frame. This transformation from the lab frame to the CM frame follows the Lorentz formalism, which is described in Appendix A.1. Since the velocity of the fission fragments in this experiment is $\approx 13\%$ of the speed of light, the Lorentz transformations are essential for switching between the two reference systems.

The velocity (v^{FF}_{CM}) and the polar angle (θ^{FF}_{CM}) of the fission fragments in CM are calculated as:

$$v^{FF}_{CM} = \sqrt{\left(v^{FF}_{LAB}\sin(\theta^{FF}_{LAB})\cos(\phi^{FF}_{LAB})\right)^2 + \left(v^{FF}_{LAB}\sin(\theta^{FF}_{LAB})\sin(\phi^{FF}_{LAB})\right)^2 + \left(\frac{v^{FF}_{LAB}\cos(\theta^{FF}_{LAB}) - v_{FS}}{1-\frac{v_{FS}v^{FF}_{LAB}\cos(\theta^{FF}_{LAB})}{c^2}}\right)^2} \tag{2.21}$$

$$\theta^{FF}_{CM} = \arctan\left(\frac{\sin(\theta^{FF}_{LAB})}{\gamma_{FS}\cdot(\cos(\theta^{FF}_{LAB}) - \frac{v_{FS}}{v^{FF}_{LAB}})}\right) \tag{2.22}$$

The velocity of the fissioning system denoted as v_{FS}, is derived as explained in Section 2.6, taking into account the Lorentz factor $\gamma_{FS} = 1/\sqrt{1-\beta^2_{FS}}$. The angle θ^{FF}_{LAB} is calculated using the reconstructed angles in VAMOS++ with respect to the beam axis $(\theta_{LAB}, \phi_{LAB})$ and the angle of the fissioning system (θ_{FS}, ϕ_{FS}). The definition of these angles is depicted in Fig. 2.19 in the laboratory reference frame, and it shows the relationship with the corresponding observables in the centre-of-mass reference system and the fissioning-system velocity. The calculation of $\cos(\theta^{FF}_{LAB})$ is given by the equation:

$$\begin{aligned}\cos(\theta^{FF}_{LAB}) = {} & \sin(\theta_{LAB})\sin(\theta_{FS})\cos(\phi_{LAB})\cos(\phi_{FS}) + \\ & + \sin(\theta_{LAB})\sin(\theta_{FS})\sin(\phi_{LAB})\sin(\phi_{FS}) + \\ & + \cos(\theta_{LAB})\cos(\theta_{FS})\end{aligned} \tag{2.23}$$

Furthermore, v^{FF}_{LAB} represents the velocity of the fission fragment in the laboratory system, obtained from the *ToF* measurement coupled with the reconstructed *Path*. The angles $(\theta^{FF}_{LAB}, \phi^{FF}_{LAB})$ are the polar and azimuthal angles of the fission fragments, measured with the DPS-MWPC at the Target Position described in Section 2.3.1.

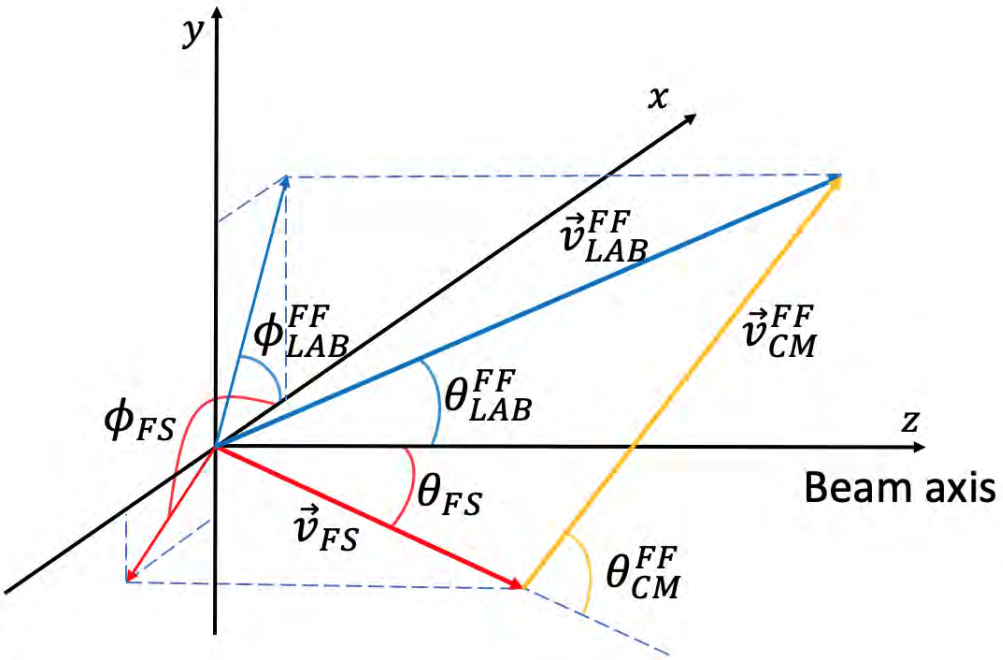

Figure 2.19: *Fission-fragments angles can be defined in two reference frames: the beam axis and the fissioning system. In the laboratory reference frame, the fission-fragment angles are represented by* $(\theta^{FF}_{LAB}, \phi^{FF}_{LAB})$*, while in the centre-of-mass frame, the polar angle is denoted as* θ^{FF}_{CM}*. To illustrate the correlation between the observables in these two frames, a sketch is provided. The fission-fragment velocity in the laboratory frame* $(\vec{v}^{FF}_{LAB})$ *and its projection on the* $x-y-$*plane are depicted in blue, while the fission-fragment velocity in the centre-of-mass frame* $(\vec{v}^{FF}_{CM})$ *is shown in yellow. The velocity of the fissioning system* $(\vec{v}_{FS})$ *is represented in red. Additionally, the angles of the fragments* $(\theta^{FF}_{LAB}, \phi^{FF}_{LAB})$ *and the fissioning system* (θ_{FS}, ϕ_{FS}) *in the laboratory reference frame are also displayed.*

The velocity distributions of Nd and Rh in the centre-of-mass frame is illustrated in Fig. 5.10 as an example. As only fusion-induced fission is considered, the fissioning system retains the direction of the beam, resulting in $\theta_{FS} = 0°$. Therefore, since the boost is solely along the z-direction, the azimuthal angle of the fragments in the centre-of-mass system is equivalent to the azimuthal angle in the laboratory frame $\phi^{FF}_{LAB} = \phi^{FF}_{CM}$.

2.8 Excitation energy reconstruction

The conservation of energy and momentum allows the reaction of the uranium beam impinging on any target to be written as U-beam$+Lt \rightarrow FS$.

$$\begin{cases} T_U + m_U + m_{Lt} = T_{FS} + (m_{FS} + E^*_{FS}) \\ |\vec{P}_U| = |\vec{P}_{FS}| \implies \gamma_U \beta_U m_U = \gamma_{FS} \beta_{FS} (m_{FS} + E^*_{FS}) \end{cases} \tag{2.24}$$

where T is the kinetic energy, m is the mass and $\vec{P}$ is the momentum. With this relations are obtained:

$$E^*_{FS} = \frac{\gamma_U \beta_U m_U}{\sqrt{(\gamma^2_{FS} - 1)}} - m_{FS} \tag{2.25}$$

USC DE COMPOSTELA

and by substituting, the following equation is obtained:

$$(T_U + m_U + m_{Lt}) = (\gamma_U \, \beta_U \, m_U) \frac{\gamma_{FS}}{\sqrt{(\gamma^2_{FS} - 1)}} \tag{2.26}$$

To determine the velocity of the fissioning system and its excitation energy, it is necessary to obtain the actual energy of the uranium beam used to generate the fissioning system. This entails evaluating the energy loss of the uranium beam as it enters the target until the reaction for the formation of the fissioning system occurs (see the diagram in Fig. 2.20).

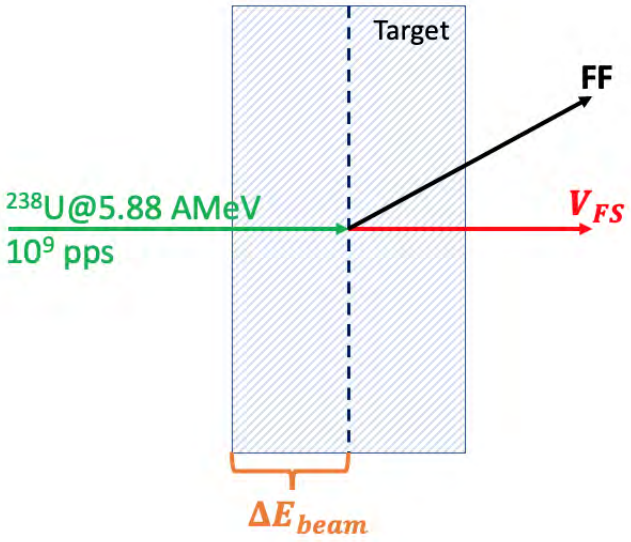

Figure 2.20: *The interaction diagram of the uranium beam with a target is depicted, illustrating the energy loss (ΔE_{beam}) experienced by uranium until reaching the midpoint of the target, resulting in the fissioning system being generated with less than 5.88A MeV.*

Fissioning systems can be generated throughout the thickness of the target, with probabilities related to the cross-section. However, it is impossible to precisely determine the location of fission system generation on an event-by-event basis. Thus, two limits must be considered: fission system generation occurs at the beginning of the target, and fission system generation occurs at the end of the target. These limits need to be studied as the fission fragment will experience greater energy loss in the former case, where the uranium beam loses energy. Additionally, it is important to note that energy losses of the fission fragment are not the same provided it traverses the target at different angles. All energy losses resulting from these limit cases, including variations in angles, have been investigated through simulations and by comparing with experimental results, accounting for corrections due to these scenarios. These studies indicate that it is impossible to distinguish differences in the centre-of-mass velocities of the fission fragments within a variation of approximately ± 0.011 ns, which is the maximum observed between scenarios. Furthermore, the width generated by the limit cases of the target on velocities is negligible compared to the velocity width in the centre-of-mass which is reconstructed in this work. Therefore, it will be assumed that the average generation of the fissioning system at the centre and the energy loss of the fragments do not take into account their inclination when traversing the target.

To account for the energy loss (ΔE_{beam}) suffered by the uranium beam in the target, a LISE++ simulation is utilised [96]. The simulation takes into consideration the thickness of each target (refer to Tab. 2.1) and assumes that the fissioning system is produced at the centre of the target. Conversely, since the fissioning system is formed and undergoes fission in an extremely short timescale of about 10^{-21} s, it is assumed that there is no energy loss. This implies that the fission fragments are assumed to be generated from the very centre of the target.

Furthermore, a significant correction had to be applied for the aluminium target due to the PACEIV cross sections, as they indicate a higher probability of the fissioning system being generated away from the ,middle of the target. This correction is illustrated in the following Fig. 2.21. However, for all other targets, this fine adjustment is negligible and has no impact on the final result.

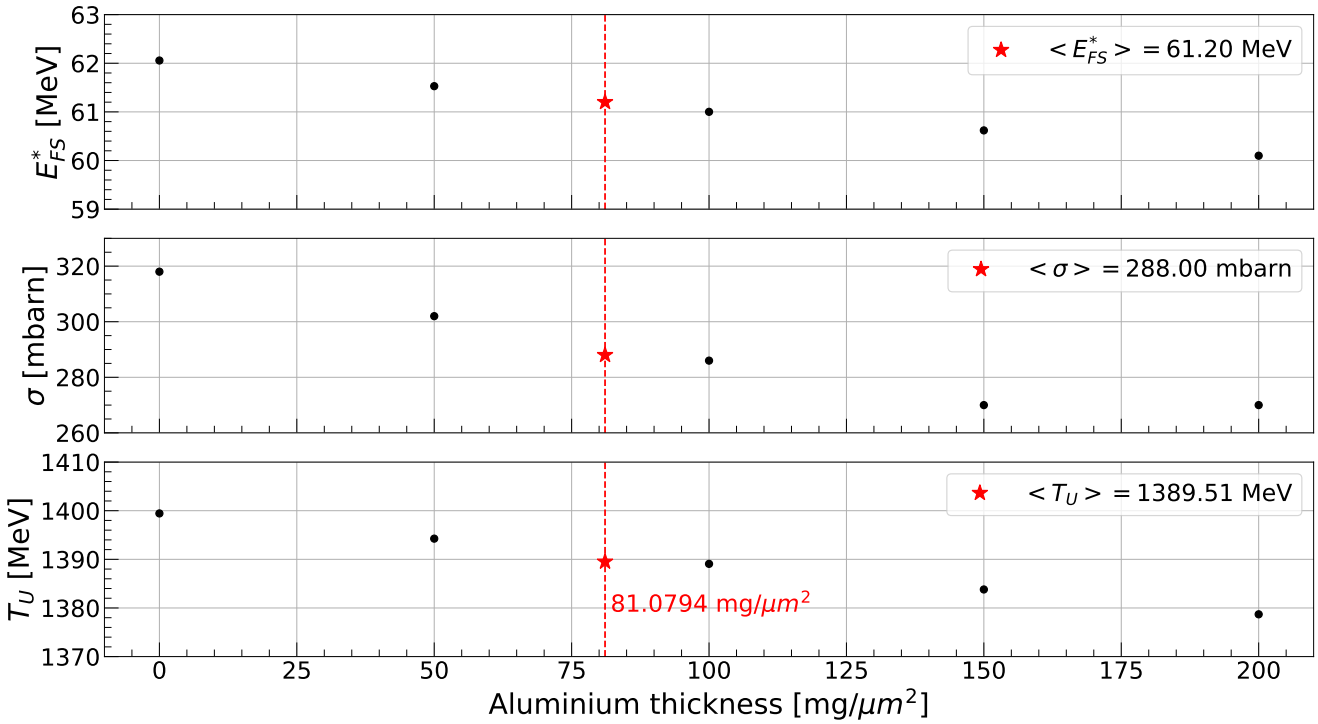

Figure 2.21: *The cross-section σ [mbarn], excitation energy E^*_{FS} [MeV], and generation location of the fissioning system in the aluminium target are estimated through simulated data with PACEIV as a function of the aluminium thickness in [mg/μm²]. The generation point of the fissioning system is indicated by a red star.*

The results summarising the fissioning system velocity, the remained energy of the uranium beam, and the excitation energy of the fissioning system for the four targets (refer to Tab. 2.1) are presented in Tab. 2.4.

	^{27}Al	^{nat}B	^{9}Be	^{24}Mg
Energy remain (T_U) [MeV]	1389.513	1393.289	1370.239	1371.865
Velocity of FS (v_{FS}) [cm/ns]	3.004	3.208	3.197	3.017
Excitation energy of FS (E^*_{FS}) [MeV]	61.201	47.710	43.100	56.520

Table 2.4: *Summary of fissioning system velocity, remaining energy of the uranium beam, and excitation energy of the fissioning system for the four targets.*

2.9 Not measured energy estimation

To evaluate the velocity of the fission fragment in the laboratory system, v^{FF}_{LAB}, and consequently obtain the angle at the centre-of-mass frame, θ^{FF}_{CM} (refer to Appendix A.1), accurate estimation of the total energy of the fragment is necessary. This total energy must consider the

energy loss in the target from the moment the fragment is generated and the losses incurred as it traverses each of the detector layers until it reaches the ionisation chamber, where it deposits the remaining energy and stops. In the following Fig. 2.22 the complete path of the fission fragment through all the detectors and across the Mylar foils is shown.

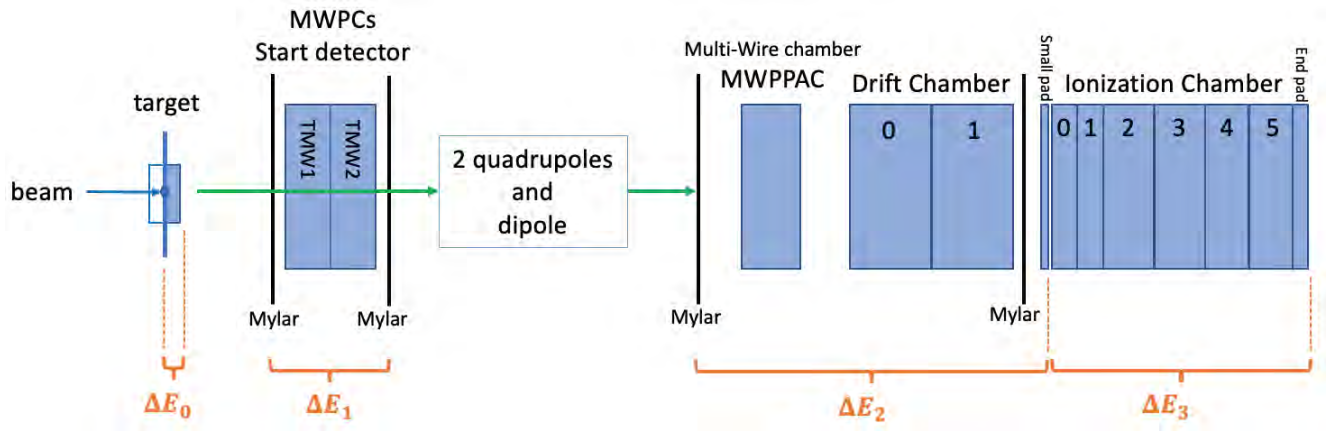

Figure 2.22: *Schematic view of the energy depositions ΔE_i, $i = 0, 1, 2, 3$, of the fission fragments as they pass through all the detectors and Mylar foils placed between them. Thus, the total energy of the fragments is $\sum \Delta E_i$.*

Thus, according to the scheme in the Fig. 2.22, the total energy of the fission fragment can be expressed as:

$$E_{tot}^{FF} = \sum_i \Delta E_i = \Delta E_0 + \Delta E_1 + \Delta E_2 + \Delta E_3 \tag{2.27}$$

where:

- ΔE_0 represents the energy lost while traversing the target.
- ΔE_1 is the energy lost while passing through the MWPCs Start detector close target position, including the two Mylar foils.
- ΔE_2 is the energy lost in the MWPPAC and Drift Chamber detectors. Including two Mylar foils and the small pad in the Ionisation Chamber.
- ΔE_3 is the total energy deposited in the Ionisation Chamber.

This energy will be reexpressed by grouping other terms Δ in Section 4.2. However, evaluating ΔE_0 and ΔE_1 is sufficient since a good measurement of the ToF ensures the reconstruction of the total energy of the fragment once the fission fragment mass is fully identified, such that:

$$E_{tot}^{FF} = \Delta E_0 + \Delta E_1 + m_{FF} \cdot c^2 \left[\frac{1}{\sqrt{1 - \beta_{FF}^2}} - 1 \right], \tag{2.28}$$

where $m_{FF} = m_{FF}[u] \cdot 931.494/c^2$ in MeV and β_{FF} is the velocity of the fission fragment that comes from the ToF measurement. The final velocity of the fission fragment in laboratory framework corrected with the not measured energy, v_{LAB}^{FF}, is calculated as:

$$v_{LAB}^{FF} = c \cdot \sqrt{1 - \frac{1}{\left(\frac{E_{tot}^{FF}}{m_{FF} \cdot c^2} + 1 \right)^2}}. \tag{2.29}$$

2.9.1 Energy lost in the target

To estimate the energy ΔE_0 lost in the target, the linear correlation between the energy lost by the ions before reaching the Ionisation Chamber and the energy released in row number zero of the chamber ($dEIC[0]$) will be used, particularly in regions far from the Bragg Peak where maximum energy release occurs:

$$\Delta E_0 = a_0 + b_0 \cdot dEIC[0] \tag{2.30}$$

The ΔE_0 can be estimated by exploiting this correlation. The procedure for the estimation is as follows: the energy loss of the fission fragments is related to the corresponding energy deposited in the zeroth row of the Ionisation Chamber $dEIC[0]$, using the code LISE++ to simulate all energy losses on the way to $dEIC[0]$. Finally, a linear fit is applied to extract the linear function. The correlation plot between ΔE_0 calculated for various heavy and light fission fragments and $dEIC[0]$ for each target is shown in Fig. 2.23. Each point corresponds to a different initial energy, and the colour represents a specific isotope. The red line represents the linear fitting function.

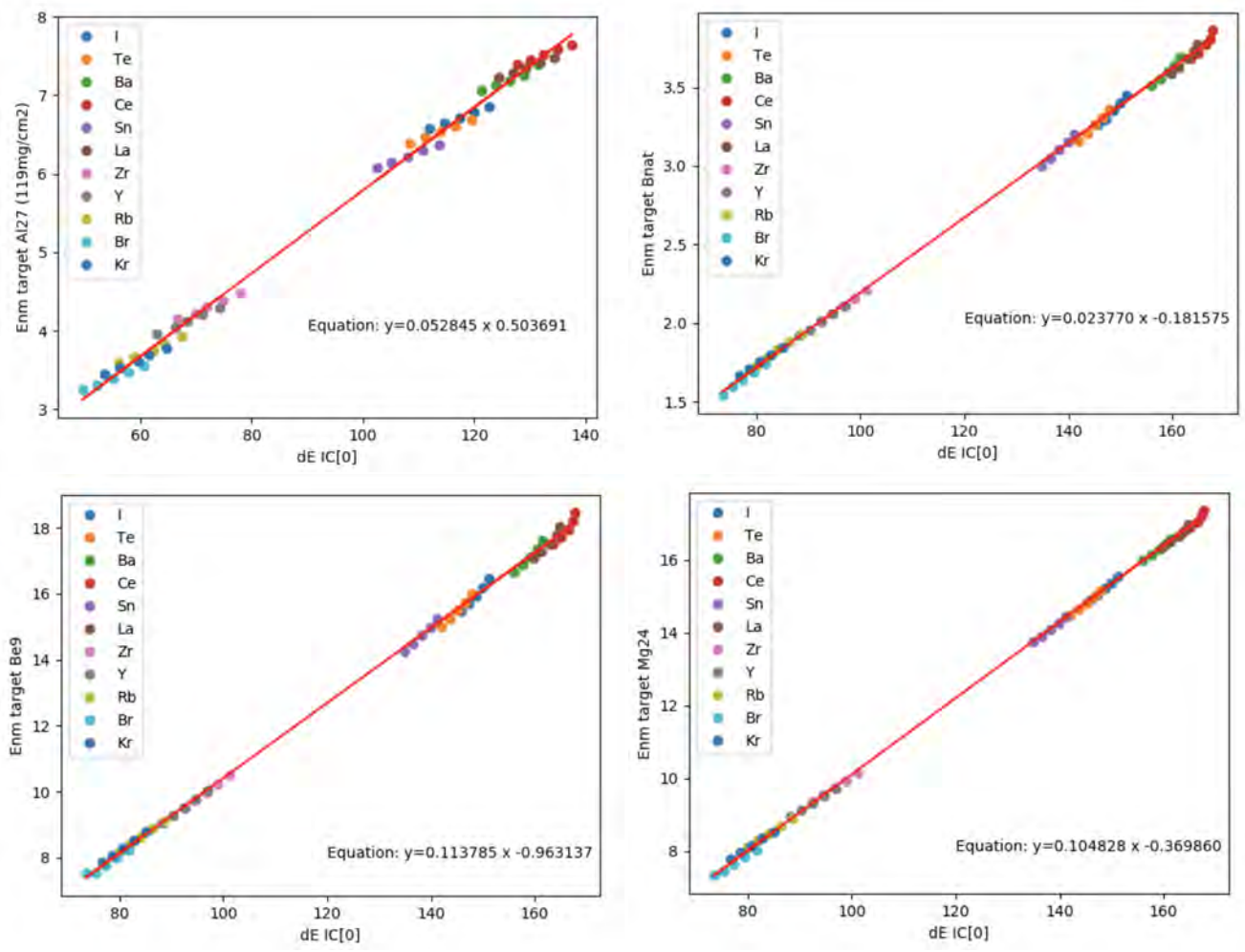

Figure 2.23: *The relation between the energy lost (ΔE_0) [MeV] by simulated fission fragments of different (Z, A) isotopes as they cross the target and the energy in the first row of the Ionisation Chamber ($dEIC[0]$) [MeV] is depicted. The linearity of this relationship is illustrated, and the linear fit is represented in red. The upper part of the figure corresponds to the Al and B targets, while the lower part represents the Be and Mg targets.*

2.9.2 Energy lost in MWPCs Start detector

The estimation of ΔE_1 can be achieved by utilising a linear correlation with row number zero of the Ionisation Chamber $dEIC[0]$, similar to the estimation of ΔE_0. The procedure for this estimation is consistent across all targets, as the MWPCs Start detector remains the same and the origin of the fission fragments does not impact the energy loss:

$$\Delta E_1 = a_1 + b_1 \cdot dEIC[0]\,. \tag{2.31}$$

Simulations were conducted in LISE++ for various combinations of (Z, A) fission fragments in the MWPCs Start detector with the two Mylar layers, and the results were compared with the corresponding values of $dEIC[0]$ [MeV]. The resulting correlation is presented in Fig. 2.24, with the linear fit represented by the red line.

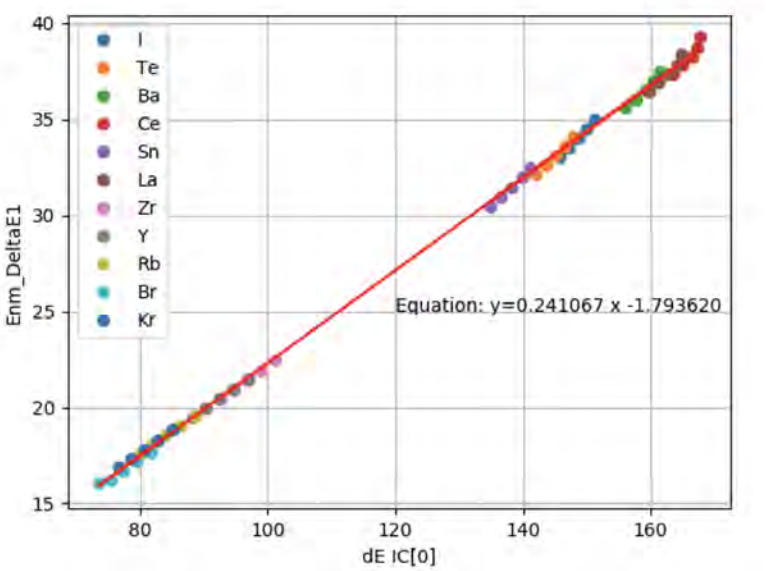

Figure 2.24: *The correlation plot between the not measured energy in MWPCs Start detector ΔE_1 [MeV] and the energy loss in the row number zero of the Ionisation Chamber $dEIC[0]$ [MeV] is displayed. Each colour represents a different element, while the red line corresponds to the linear function obtained through the fitting.*

USC
UNIVERSIDADE DE SANTIAGO DE COMPOSTELA

Chapter 3

Detectors calibration

This chapter provides a comprehensive overview of the signal treatment and calibration methods applied to the detectors involved in fission fragment identification in the VAMOS++ focal plane setup. The calibration process involves determining the physical position of the detectors using laser-aided techniques, conducted before the start of the experiment and not done for the calibrations of this thesis, followed by aligning the electronics of each detector channel using a pulse generator to simulate physical events. The goal of alignment is to ensure consistent output signal amplitudes across all channels. Furthermore, fission events are utilised to establish the relationship between the detector response and physical quantities, enabling the extraction of relevant observables from the generated signals.

3.1 Drift Chamber calibration

The Drift Chamber provides measurements in both the horizontal and vertical axes, allowing for the calculation of magnetic rigidity ($B\rho$), polar angles, and azimuthal angles of ions before reaching the spectrometer, as explained in Section 2.4.3. The horizontal position is determined based on the charge distribution induced in two rows of pads, while the vertical position relies on the drift time of electrons within the chamber. To ensure accurate results, precise calibration between neighbouring pads is essential. Additionally, an external reference is necessary to achieve an absolute measurement of vertical drift, independent of the position of the chamber.

3.1.1 Induced charge calibration

The position determination in the Drift Chamber involves both the horizontal and vertical components. For the horizontal position, it relies on the charge distribution induced on the cathode plane, which consists of two rows of 160 pads. Absolute calibration of the pads is not required, only electronic alignment is necessary. This procedure is achieved by applying a pulse generator that simultaneously sends common signals to the electronics of all pads, and then by applying an alignment function to the output signal amplitudes of the pads, ensuring that they match the amplitude of a reference pad. Using pad number 60 of the first row as an arbitrary reference, a function is defined to align the signal amplitudes of the remaining pads:

USC UNIVERSIDADE DE SANTIAGO DE COMPOSTELA

$$Q_i^{align} = A_i + B_i \cdot Q_i + C_i \cdot Q_i^2, \tag{3.1}$$

where Q_i represents the signal amplitude of pad number i, (A_i, B_i, C_i) are the alignment parameters, and Q_i^{align} represents the aligned signal amplitude of pad i. There is no significant

quadratic dependence observed for most of the pads except for those between 140 and 150, at the edge of the second DC. This equation allows for the adjustment of the signal amplitudes to ensure proper alignment within the Drift Chamber. An example of pad number 60 and the fit for Q_i^{align} are illustrated in Fig. 3.1.

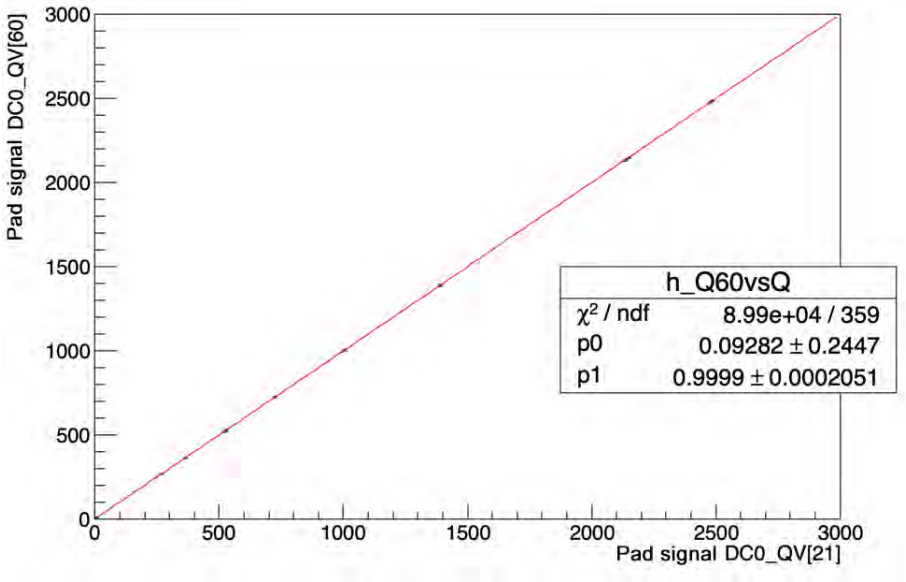

Figure 3.1: *The alignment of the pad signals of the Drift Chamber is done concerning pad number 60. As an example, the adjustment of the linear behaviour between pad number 60 and pad number 21 is illustrated for the first chamber.*

The signal outputs of each pad in the drift chambers are illustrated in Fig. 3.2. The left and right columns display the signals before and after alignment, respectively. In the right column, the logarithmically aligned real peaks stand out from the not fully aligned electronic noise signals. The top two rows correspond to the first drift chamber, whilst the bottom two rows represent the second drift chamber. Most pads exhibit a base ninth line, referred to as the pedestal, with a very low amplitude. The pedestal represents the response of the detection system in the absence of input signals and serves as the reference zero level, being necessary to subtract the pedestal from the signals. Following alignment, the pedestal becomes consistent and unique across all pads.

3.1.2 Gain-matching calibration

The amplification of the output signals is provided by each Gassiplex chip. Sixteen channels are simultaneously handled by each chip, applying the same gain to all of them. Nonetheless, variations in gain may occur from one chip to another due to distinct chip responses or slight differences in the applied bias potential for each chip. Consequently, after the initial alignment process (refer to Section 3.1.1), a gain-matching procedure becomes necessary. The gain-matching is done directly using scattering events with the aluminium target.

USC UNIVERSIDADE DE SANTIAGO DE COMPOSTELA

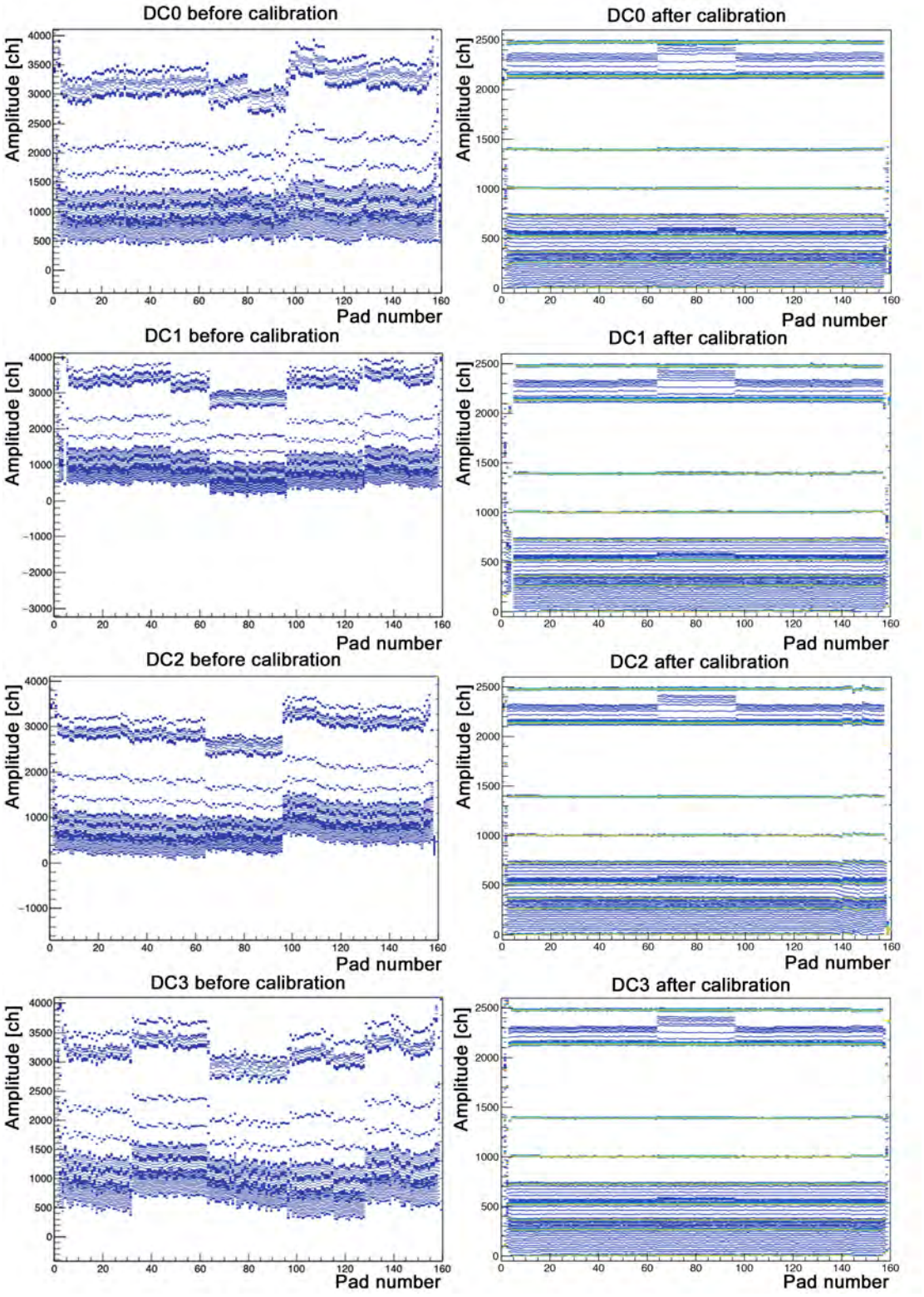

Figure 3.2: *Alignment of the pads in the Drift Chamber is achieved by comparing the output signals before and after the alignment process, as shown in the left and right columns respectively. The right column is in logarithmic scale. In the signals, a lower amplitude signal is observed, known as the pedestal, which represents the baseline response of the detection system. It should be noted that some pads in the second row do not exhibit the pedestal due to a high threshold setting. The remaining signals are generated by a pulse generator with varying attenuation factors.*

The gain-matching comprises a two-step process. The first step involves matching the charge of two consecutive pads when they are managed by different chips. Gain-matching also entails applying a single scaling factor (A^{chip_j}) to the output of the pads handled by a Gassiplex chip, ensuring that the last pad of one chip exhibits the same maximum induced charge as the first pad of the next chip:

$$A^{chip_j} = \frac{\overline{Q}_{MAX}^{chip_{j+1}}(FirstPad)}{\overline{Q}_{MAX}^{chip_j}(LastPad)}. \tag{3.2}$$

Thus, the gain-matched induced charge adheres to the following equation:

$$Q_i^{gain\,match}|_{chip_j} = A^{chip_j} \cdot Q_i^{align}|_{chip_j}\,. \tag{3.3}$$

3.1.3 Max charge calibration

After the pad alignment process (refer to Section 3.1.1), the subsequent step involves the implementation of a local smoothing method to eliminate minor fluctuations caused by field inhomogeneities, particularly in the second drift chamber. This method focuses on elastic scattering events and employs a binomial smoothing filter [97] to normalise the maximum induced charge of a single pad based on the reference provided by neighbouring pads.

$$\overline{Q_{max}^{smooth}}_i = \sum_{k=-1}^{1} b_k \cdot \overline{Q_{max}^{aligned}}_{(i-k)}\,, \tag{3.4}$$

where:

$$b_k = \binom{2}{1+k} /4\,, \tag{3.5}$$

and the term $\overline{Q_{max}^{aligned}}_{(i-k)}$ represents the average value of the maximum induced charge in the pad with index $(i-k)$ after the alignment process. Therefore, the new scaling factors which remove the fluctuations are defined as:

$$A_i^{smooth} = \frac{\overline{Q_{max}^{smooth}}_i}{\overline{Q_{max}^{aligned}}_i}\,. \tag{3.6}$$

The relationship between the maximum induced charge per event and the pad number for elastic scattering events with the aluminium target is illustrated in Fig. 3.3. The top row displays four images representing the data before the gain-matching procedure, whilst the bottom row presents the data after the procedure. In the upper-right region, events are exhibiting distinct behaviour compared to the rest. These events have been identified as direct measurements of the uranium beam, representing scattering events with very high magnetic rigidity and significantly greater mass than what the Drift Chamber registers for the 14° setting due to the small spectrometer angle.

It has been observed that the calibration parameters for the induced charge in the pads of the drift chambers are not dependent on the run number. This has been verified for all runs of the various targets in both VAMOS++ settings. As stated in Section 2.4.2.2, the charge collected by the amplification wires is not employed to quantify the energy loss in the chamber due to its significant uncertainty. Nevertheless, it serves for cross-validation purposes and, as such, is approximately calibrated by comparing it with the energy loss of simulated fragments utilising the LISE++ code [96].

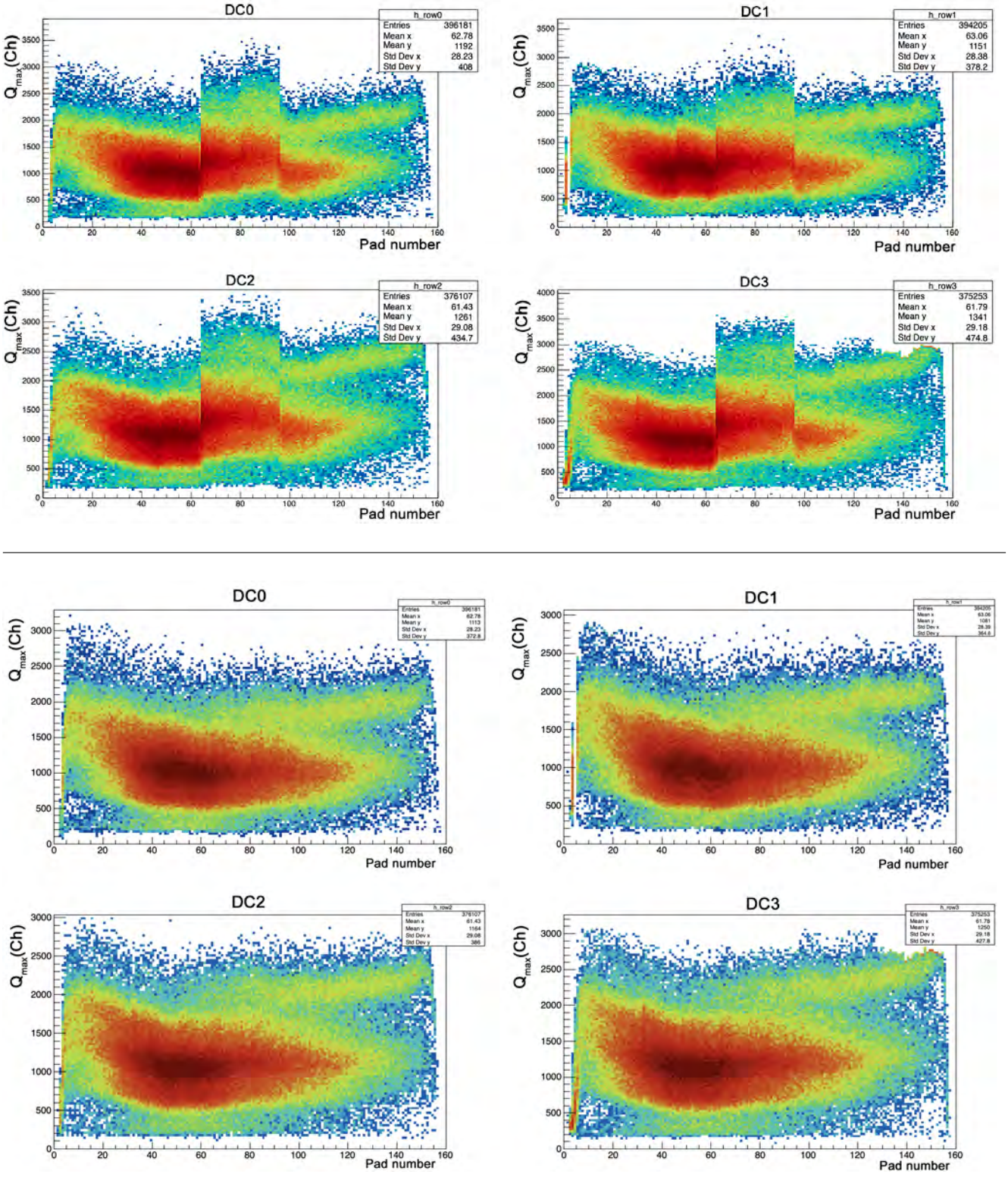

Figure 3.3: *The alignment of the Drift Chamber pads is depicted in the figure with the maximum charge deposited. The top and bottom rows display the maximum induced charge per pad before and after the gain-matching procedure, respectively, for elastic scattering events of uranium in the aluminium target.*

3.1.4 Drift time calibration

To calibrate the measurement of drift time, periodic signals are generated using a time calibrator module and sent to the four TAC modules in the Drift Chambers. The period of these signals is $\tau = 320n$ ns, where n is a randomly changing integer between 1 and 16. The TAC modules produce signals with amplitudes proportional to the period of the received signal. The calibration procedure converts the output of the TAC module, initially expressed in ADC channels, into corresponding time values using the following conversion formula:

$$t = A \cdot (Ch - Pedestal), \tag{3.7}$$

where the calibrated time (t) is obtained using the calibration factor (A), where Ch represents the TAC output in ADC channels, and the pedestal corresponds to the ADC value when no signal is present. The precise electron drift velocity is derived directly from the measurement of drift time, utilising the position of the six horizontal wires positioned at the entrance of each drift chamber. These wires, separated by a pitch of 18 mm, span the entire drift region to maintain uniform electric field conditions and ensure a consistent drift velocity.

3.2 Ionisation Chamber calibration

The Ionisation Chamber, as discussed in Subsection 2.4.2.3, serves as a gas detector for identifying the atomic number of ions by measuring their energy loss within the gas medium. When the gas undergoes ionisation, the resulting electrons generate a signal in the anode plane. The anode plane consists of thirty pads organised into six rows (refer to Fig. 3.4 for the IC pad and row layout). Each row comprises interconnected pads, forming a single electronic channel. Consequently, a unique signal is produced per row, with its amplitude proportional to the energy released immediately above by the interacting ion. To align the IC rows electronically, a pulse generator is employed, which transmits signals through the electronics chain of each row. These signals encompass various amplitudes to cover the dynamic range of the ADC module. Subsequently, the alignment is cross-validated using actual data to ensure the continuity of the energy loss distribution along the chamber.

3.2.1 Energy alignment in IC

The calibration of the Ionisation Chamber is accomplished by aligning the energy distributions in a manner that ensures accurate determination of the resulting atomic numbers (Z):

$$\begin{aligned} dE &= (dEIC[0] + dEIC[1] + dEIC[2]) \cdot \cos(\theta_{FP}) \\ E_{res} &= dE \cdot (1 - \cos(\theta_{FP})) + dEIC[3] + dEIC[4] + dEIC[5]\,. \end{aligned} \tag{3.8}$$

The projection for different intervals of residual energy (E_{res}) reveals a misalignment of the various runs, resulting in an energy shift that needs to be corrected (see upper pad of Fig. 3.5). This only occurs for the 14° setting. With the aluminium target serving as a reference projection:

$$\begin{aligned} &dE^{Mg} + 5.715/\cos(\theta_{FP}) \\ &dE^{B} + 5.35/\cos(\theta_{FP}) \\ &dE^{Be} + 3.997/\cos(\theta_{FP})\,. \end{aligned} \tag{3.9}$$

These values have been obtained by calculating the mean value by aligning peaks with projections of dE with different fixed E_{res} ranges. Gaussian fits are performed for each projection to determine, with aluminium as a reference, the correct position to place the peak (see lower pad of Fig. 3.5).

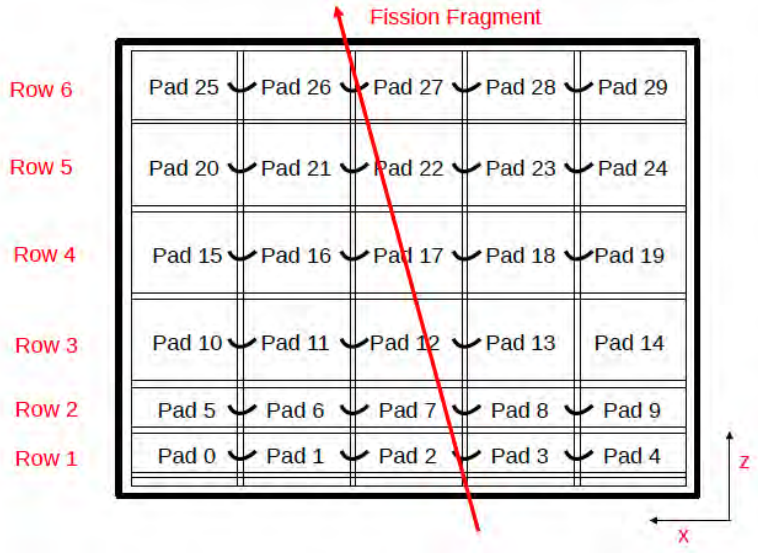

Figure 3.4: *Diagram illustrating the arrangement of pads and rows in the Ionisation Chamber. The red arrow indicates the direction of a fission fragment.*

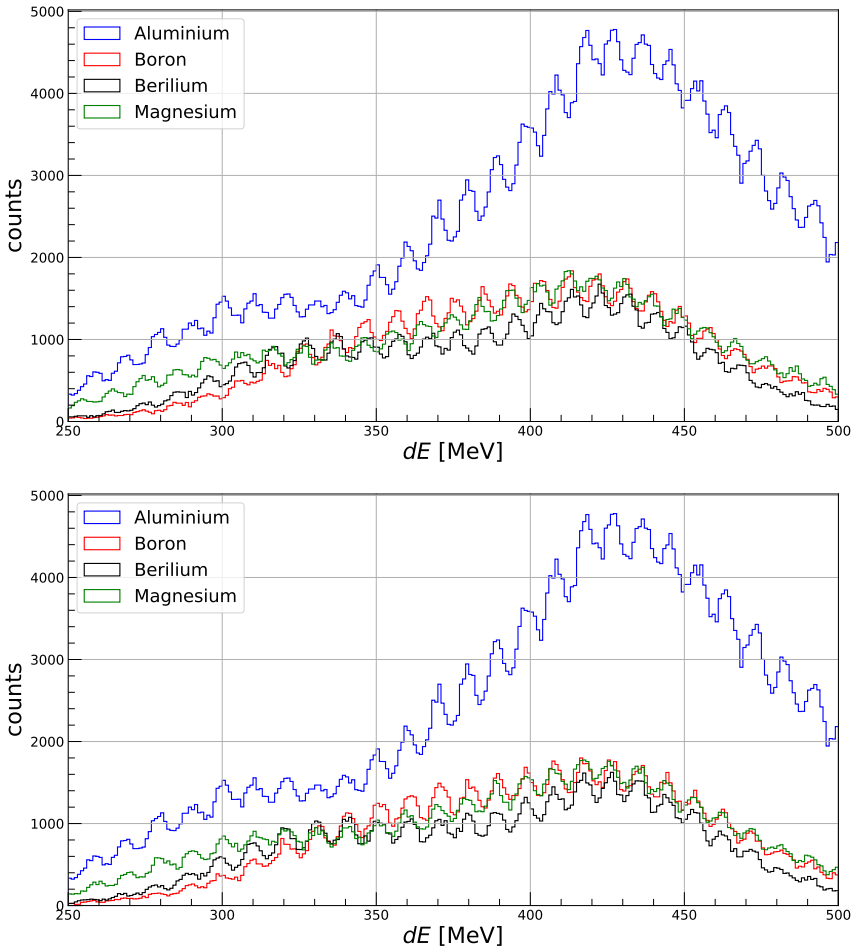

Figure 3.5: *The upper pad shows the misalignment for the energy projection in the IC within the $E_{res} \in (200, 250)$ MeV range for the targets. The lower pad shows the peaks after the alignment in the same energy region. Both panels for 14° setting.*

3.3 SPIDER calibration

The SPIDER detector plays a crucial role in isotopically identifying the light recoils emitted from transfer or inelastic-scattering reactions, as well as providing the necessary measurements for reconstructing the kinematics of the binary reaction and determining the properties of the fissioning system. To ensure accurate measurements, the electronic response of each ring and sector of SPIDER is aligned using reference signals generated by a pulser. The energy calibration is then carried out by comparing the measured $(\Delta E - E)$ matrix for target-like recoils with the expected $(\Delta E - E)$ matrix predicted by the LISE++ code [96]. The angle measurement is calibrated by comparing the output signals from reactions with well-known kinematics, such as elastic scattering or nucleon transfer, with their known emission angles. These calibration procedures ensure precise and reliable data for isotopic identification and kinematic reconstruction. The isotopic identification and the study of the transfer reactions with Spider do not fall within the scope of this analysis.

3.4 Multi-Wire chamber calibration

The Time of Flight (ToF) of the ions is determined by measuring the time difference between the MWPCs Start detector and the Multi-Wire chamber MWPPAC. It is partitioned into 20 horizontal sections, and when an ion traverses a section, it generates a signal that is transmitted to a TDC module. These signals serve as triggers for the TDC module measurement, which is halted by the delayed signal from the MWPCs Start detector. Since signals from fragments passing through this detector may not always reach the VAMOS++ focal plane, the ToF measurement is performed with the MWPPAC as the start of the TDC and the MWPC as the stop. The measured time is therefore reversed. Consequently, the ToF is computed as follows:

$$ToF = Off_{ToF} - t_{TDC}, \tag{3.10}$$

with Off_{ToF} representing the additional delay of the MWPCs Start detector.

The TDC calibration converts the output signals into scaled time values using the equation:

$$t_{TDC} = c + d \cdot Ch_{TDC}, \tag{3.11}$$

where t_{TDC} corresponds to the calibrated time values, (c, d) are the calibration parameters, and Ch_{TDC} denotes the raw TDC channels. Before commencing the experiment, the TDC was calibrated using a time calibrator in a similar way as the TAC modules were.

The offset Off_{ToF} is determined through elastic scattering, where the velocity is determined through the angle θ_{TP}:

$$Off_{ToF} = \frac{D}{v(\theta_{TP})} + t_{TDC}, \tag{3.12}$$

where $v(\theta_{TP})$ is the velocity of the scattered ion and D denotes the distance between the MWPCs Start detector and the Multi-Wire chamber MWPPAC, which is derived from the reconstructed path:

$$D = \frac{Path}{\cos(\phi_{FP})} - \frac{D_{target}^{Start}}{\cos(\theta_{TP})\cos(\phi_{TP})} + \frac{D_{FP}^{MWPPAC}}{\cos(\theta_{FP})\cos(\phi_{FP})}\,. \tag{3.13}$$

In the context of fragment trajectory measurement, the variable $Path$ represents the distance travelled by the fragment from the target to the focal plane, projected horizontally,

$D_{target}^{Start} = 17.00$ cm refers to the distance between the target and the MWPCs Start detector, and $D_{FP}^{MWPPAC} = 7.19$ cm represents the distance between the focal plane and the MWPPAC plane. The angles and the coordinate system are explained before (see Section 2.2.1).

In the Constant Fraction Discriminator (CFD), each signal is accepted, being the CFD an electronic device generating time for input signals with changing amplitudes but a constant rise time. TDC measurements have an estimated uncertainty of 10 ns. Additionally, another source of noise in ToF measurement arises from uncorrelated events between the MWPCs Start detector and the Multi-Wire chamber. When the chamber at the focal plane detects an ion that was not previously detected by the MWPCs Start detector, the TDC stop triggered by the delayed signal from the MWPCs Start detector corresponds to a subsequent ion. As a result, the measured ToF represents the time difference between two different events. This effect gives rise to similar distributions shifted by ≈ 100 ns, following the cyclotron frequency. By examining the relationship between the ToF and the residual energy, it is possible to isolate the genuine distribution for the entire range of fission fragments, more than 99% of events (refer to Fig. 3.6).

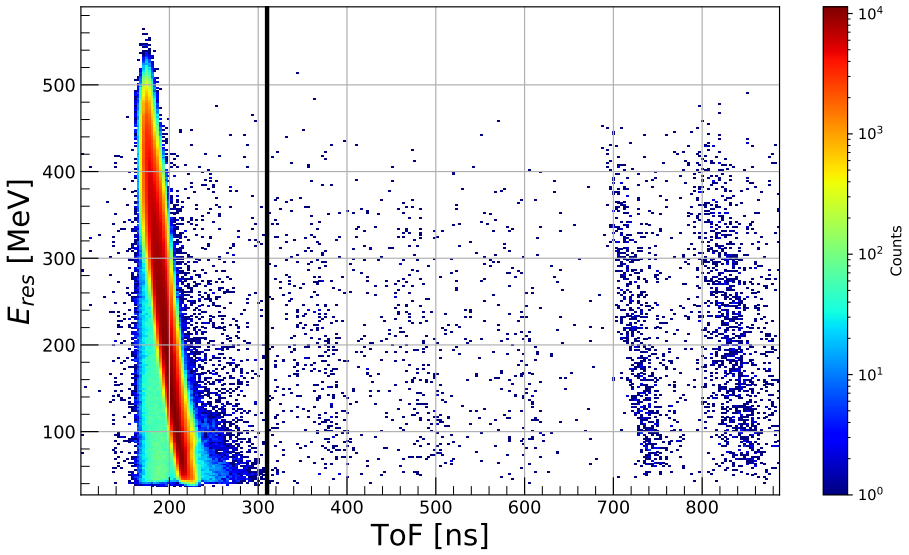

Figure 3.6: *The energy E_{res} [MeV] as a function of the ToF [ns] is depicted in the figure. Correlation loss between the Start and Stop of the ToF measurement resulted in events located beyond the black line.*

3.4.1 MWPCs Start detector angle correction

During the experiment in this work, the MWPCs Start detector encountered an issue with the connection of its signal readout module. The MWPCs Start detector has 68 vertical wires connected to 68 pins on the readout module. However, only 64 wires were connected due to the module used. As a result, there are 4 unconnected wires on one side, leading to a 2 mm displacement on the $x-$axis of the MWPCs Start detector.

This displacement causes a misalignment between the angles in the horizontal plane (see Section 2.2.1) labelled as target position angles, θ_{TP}, and the angles θ (from reconstruction) that should coincide at (0,0). The upper part of Fig. 3.7 illustrates the misalignment, resulting

in an angular deviation of approximately one degree (19 mrad). It is necessary to correct this in both VAMOS++ settings.

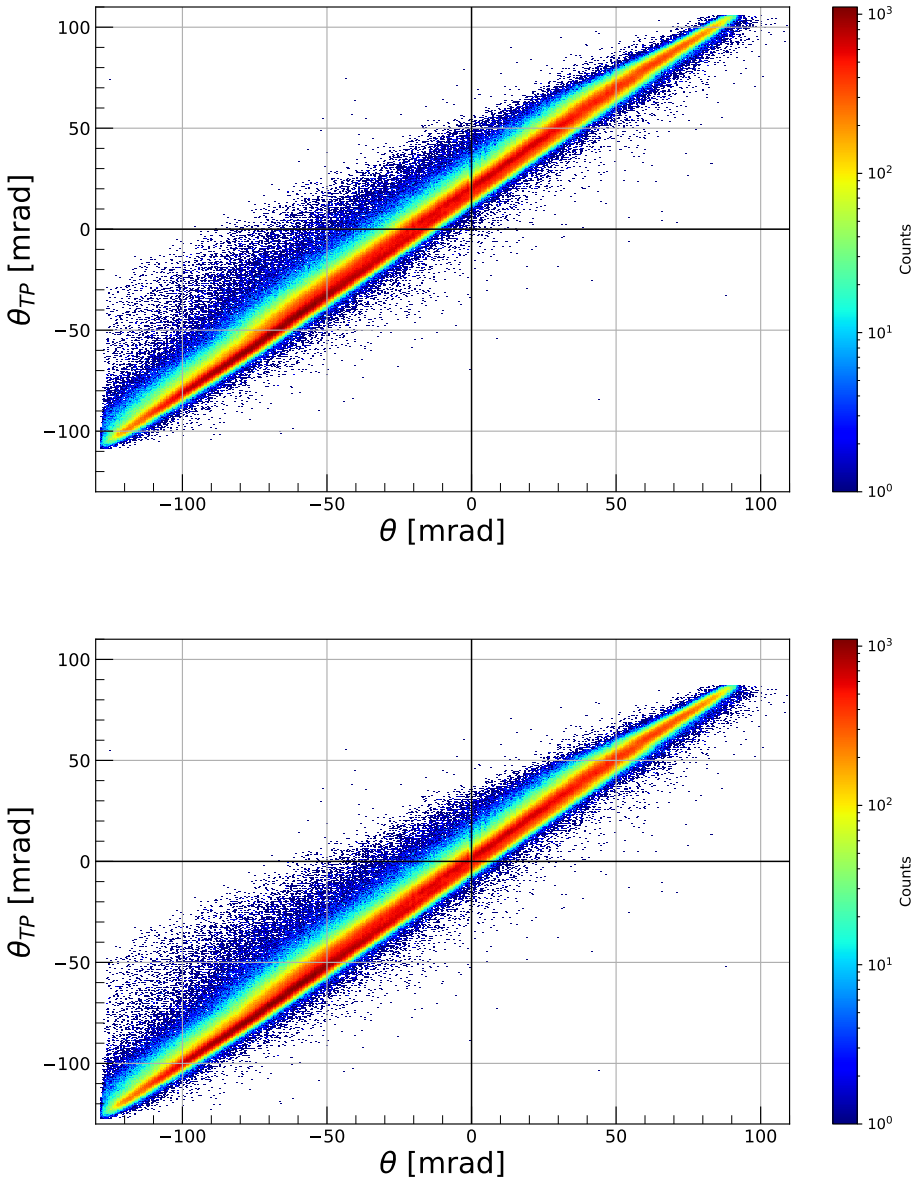

Figure 3.7: *An angular misalignment of approximately 19 mrad is observed between the angle θ [mrad] and the θ_{TP} [mrad] measured with the target position MWPCs Start detector shown in the top part, while the bottom part shows the measurement after the correction.*

By shifting the centre of the MWPCs Start detector, a coordinate transformation can align the trajectories, as follows:

$$\theta_{TP}^{corrected} = \arctan\left(\frac{TMW2_X - TMW1_X - 2\,mm}{105\,mm}\right), \tag{3.14}$$

where $TMWi_X$ represents the positions on the $x-$axis, and 105 mm is the distance between TMW1 and TMW2 on the $z-$axis. The corrected result can be seen in the lower part of Fig. 3.7.

Chapter 4

Fission-fragment identification

This chapter presents the methods employed for the isotopic identification of fission fragments generated in multi-nucleon transfer and fusion reactions involving a ^{238}U beam and various targets (see Tab. 2.1). The identification process involves determining the mass number (A), atomic number (Z), and charge state (q) of the fragments. Mass number and charge states are derived from the reconstructed magnetic rigidity, obtained by measuring the velocity vector and total energy of the fragments in the spectrometer. The atomic number is determined through the relationship between the energy loss and the residual energy deposited in the ionisation chamber. Additional corrections are applied to enhance identification resolution. The chapter concludes with the verification of fission fragment identification using γ emission measurements from excited states in the fragments.

4.1 Fragment atomic number

Identifying the atomic number Z of fission fragments relies on understanding their energy loss as they traverse matter. When ions move through a material, their primary energy loss occurs through electronic interactions with the atoms of the material. These interactions encompass processes like electron transfer, capture, or direct ionisation, leading to a net charge on the ion. The extent of energy loss, described by the Bethe-Bloch equation, depends on this net charge. This equation is valid when the velocity of the ion significantly exceeds that of the orbital electrons. As the ion progresses through the material, its charge distribution gradually reaches equilibrium after multiple collisions, wherein electron capture and loss processes balance each other. To identify the atomic number of fission fragments, this process involves correlating the energy lost in the initial three ionisation chamber layers dE with the subsequent residual energy released in the following layers, E_{res} (see details in Section 3.2 and Eq. 3.8).

The energy deposited by the fragment is projected onto θ_{FP} as shown in Eq. 3.8, with the factor $\cos(\theta_{FP})$. It is important to note that this is to maintain a nearly constant dE thickness in the first three layers of the ionisation chamber for any entry trajectory of the fission fragment.

4.1.1 dE vs E_{res}

Figure 4.1 depicts the relationship between the energy loss in the first three layers of the IC, dE, and residual energy, E_{res}, of fission fragments (see Eq. 3.8). Each atomic number is represented by a curve that spans from the Bragg Peak, associated with lower residual energy, to higher energies

reaching several hundred MeV. The curves belonging to heavier ions exhibit a higher intrinsic resolution in the region of higher residual energy.

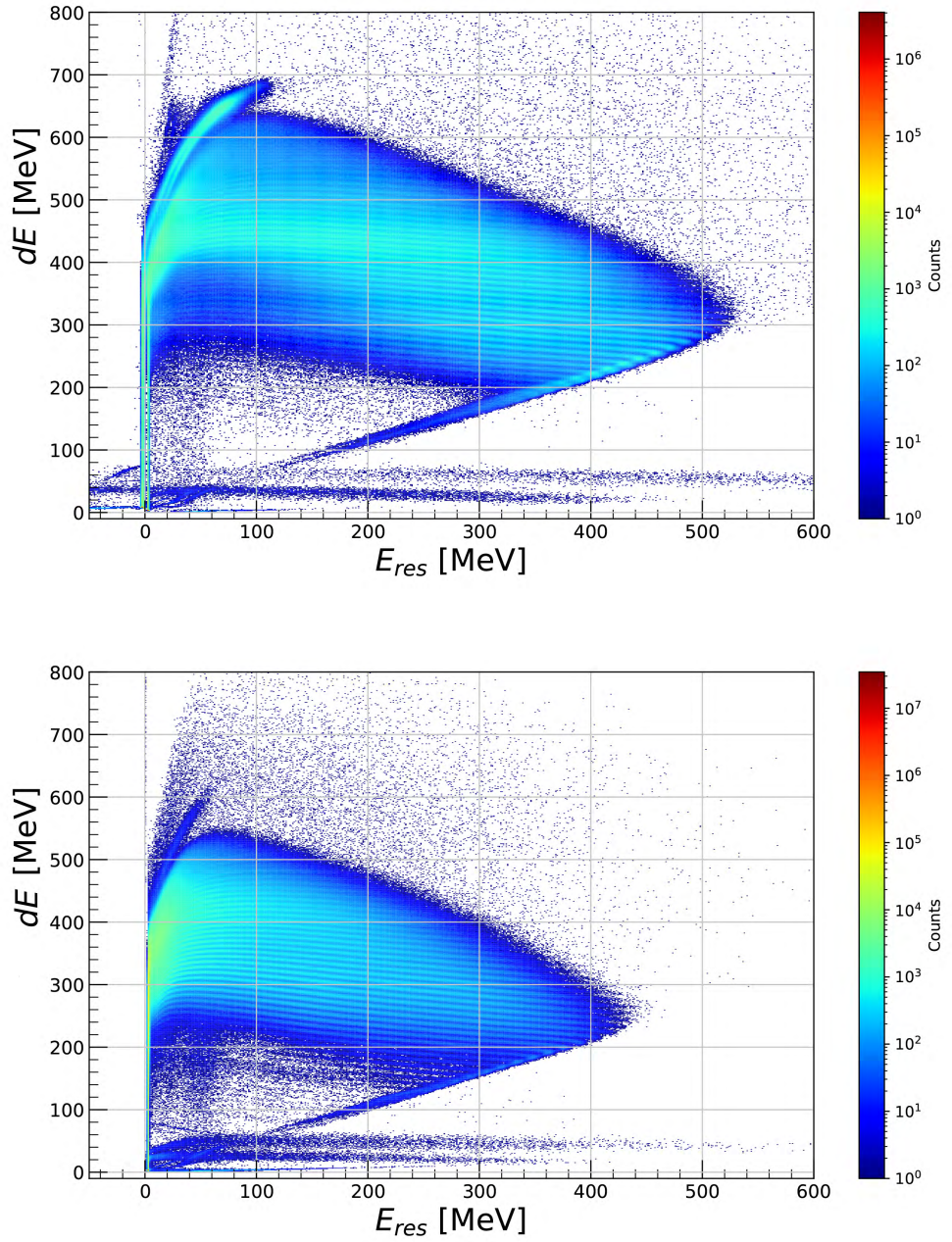

Figure 4.1: *The energy loss of fission fragments in the first layers of the IC, dE, induced in* ^{238}*U beam reactions, is presented as a function of the residual energy,* E_{res}*, in both VAMOS++ settings:* 14° *and* 21.5°*, depicted in the upper and lower panels, respectively. Each continuous line of peak values represents a curve corresponding to a specific atomic number.*

To improve the quality of the data and ensure reliable measurements, several cuts are applied in the analysis. Firstly, cuts are implemented in the lower energy loss section of the higher residual energy region and diagonal cuts are applied for higher energies. These cuts are intended to eliminate badly reconstructed events and to prevent punch-through events. The light ions with high velocities that would otherwise penetrate through the last row of the ionisation chamber are

excluded. Additionally, these cuts effectively remove heavier events, such as those related to the ^{238}U beam measurements. The resolution near the Bragg Peak is insufficient to properly identify events, and therefore, another cut is applied. The application of these cuts results in Fig. 4.2 for both 14° and 21.5° VAMOS++ settings, illustrating the impact of the cuts on the data distribution.

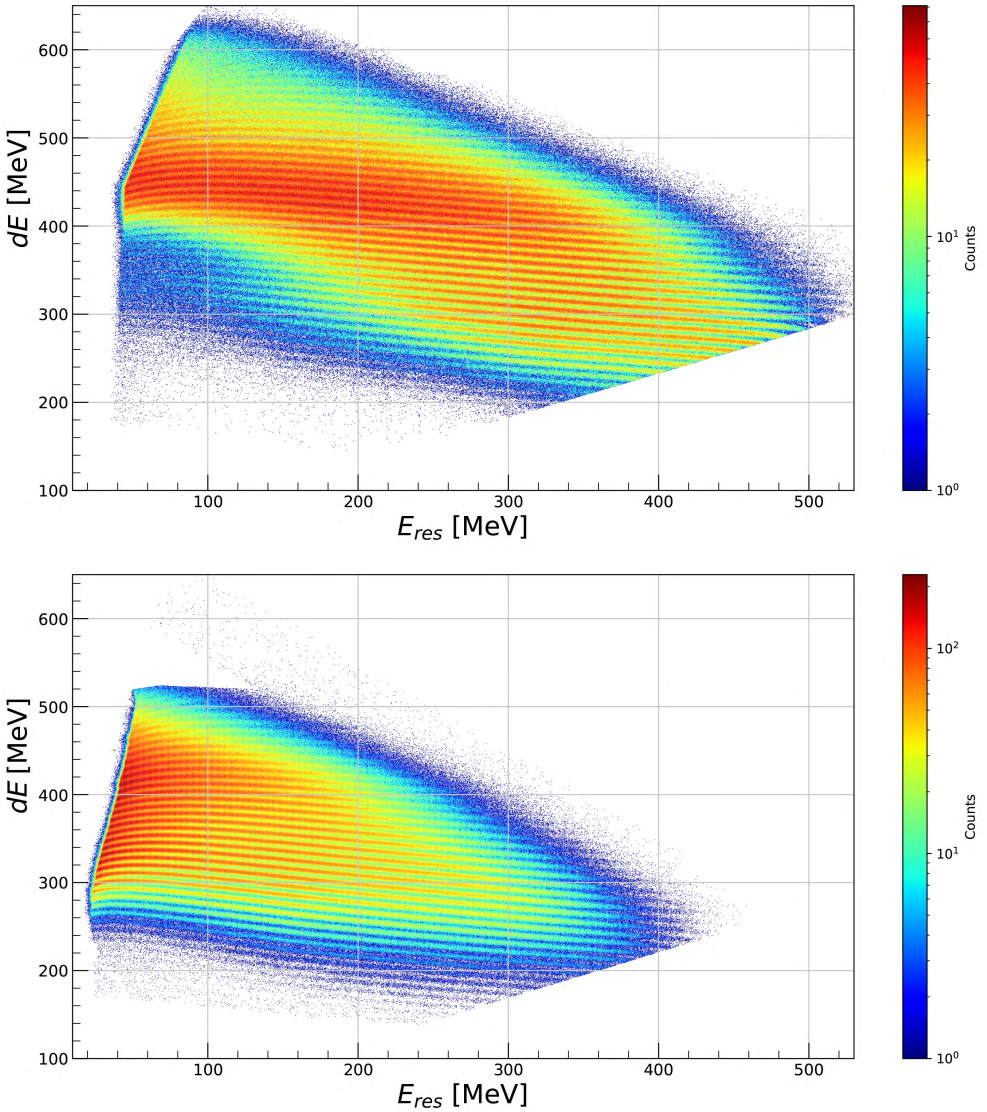

Figure 4.2: *The energy loss of fission fragments in the first layers of the IC, dE, as a function of the residual energy, E_{res} is presented after cut selections. For both VAMOS++ settings, 14° and 21.5°, are depicted in the upper and lower panels, respectively.*

4.1.2 Atomic number selection

The selection of atomic numbers is based on the (dE, E_{tot}^{IC}) space, where $E_{tot}^{IC} = dE + E_{res}$ represents the total energy deposited in the Ionisation Chamber (IC). The resulting energy curves are accurately reproduced by simulation codes such as TRIM (TRansport of Ions In Matter)[1] to ensure the correct selection of fragment atomic numbers. This selection process is applied for each target and each VAMOS++ setting.

[1] http://www.srim.org/SRIM/SRIMINTRO.htm

The atomic number selection is performed by passing each curve through the minima between the peaks of the different projections within specific intervals of E_{tot}^{IC}. Valley by valley an interpolation is used to connect all these points (see Fig. 4.4). The region enclosed by the interpolants represents a single atomic number, and the corresponding value is:

$$Z_{float} = \frac{dE_p - dE_{Z<}(E_p)}{dE_{Z>}(E_p) - dE_{Z<}(E_p)} + Z_{<}\,, \tag{4.1}$$

where each variable in the equation is shown graphically in Fig. 4.3.

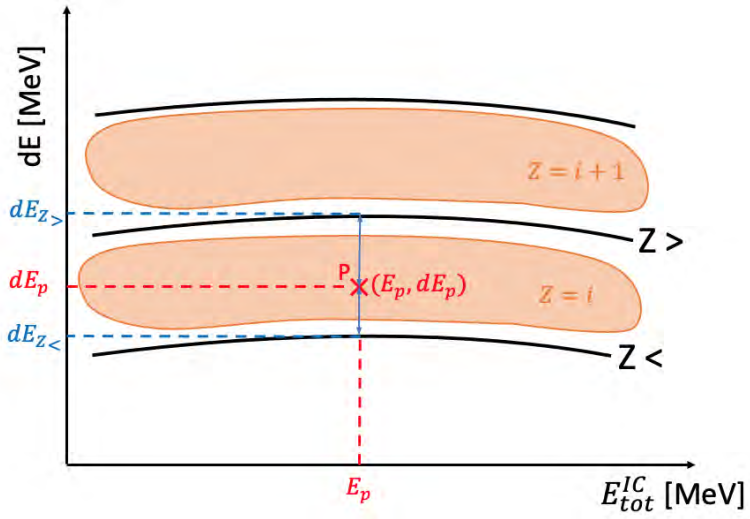

Figure 4.3: *A descriptive scheme is presented for the variables utilised to obtain Z_{float} according to Eq. 4.1 using the interpolants depicted with black lines.*

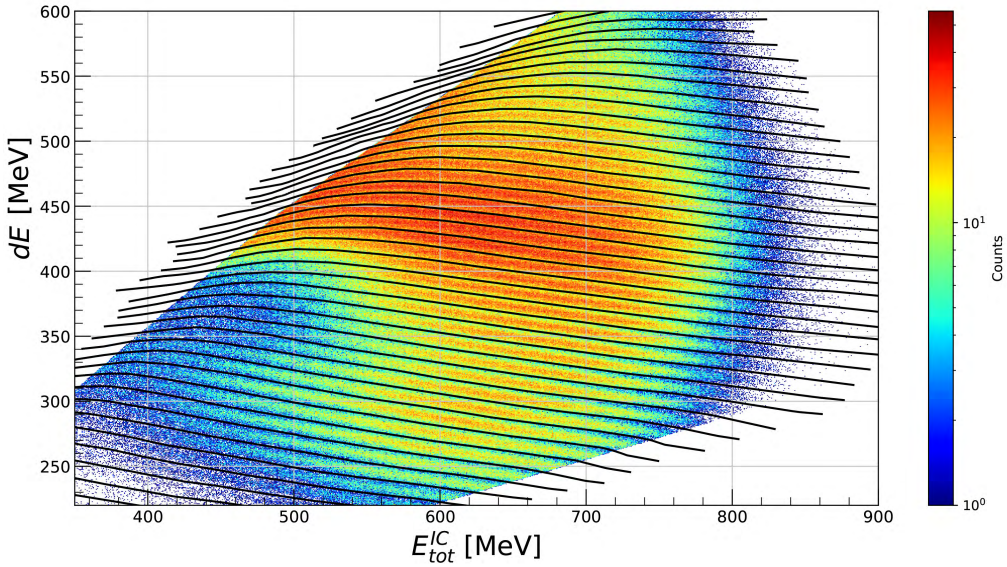

Figure 4.4: *The selection of atomic numbers in the (dE, E_{tot}^{IC}) space from the aluminium target with the 14° setting is illustrated. The interpolants, represented by black lines, traverse the valleys between the peaks of the distributions for each atomic number.*

The Z_{float} extracted from the ICs according to Eq. 4.1 as a function of E_{tot}^{IC} for aluminium runs of the 14° setting is displayed in Fig. 4.5(left) as an example. Additionally, the distribution of the Z_{float} projection is shown in Fig. 4.5(right).

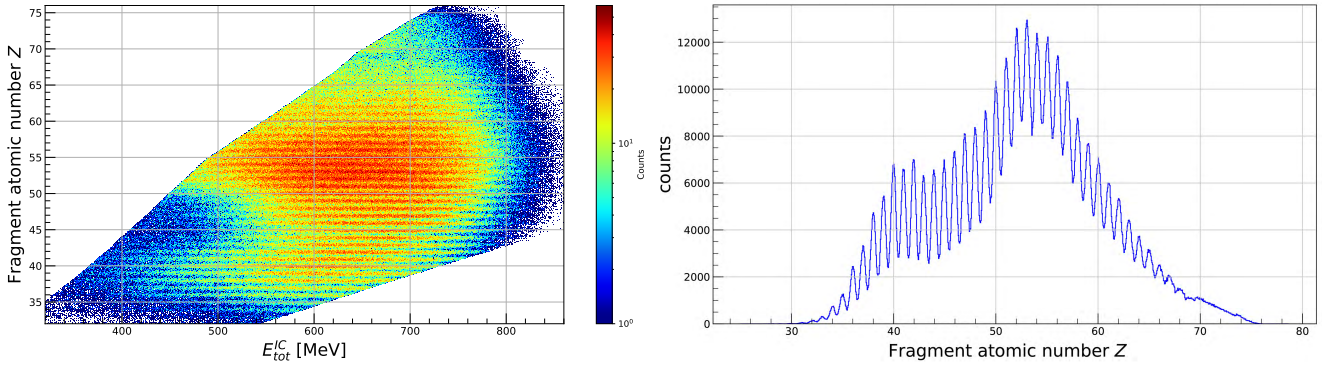

Figure 4.5: *The atomic numbers Z_{float} of the fission fragments against the total energy E^{IC}_{tot} for aluminium target with 14° setting is depicted in the left panel. The projected distribution of Z_{float} is displayed in the right panel.*

The Z_{float} behaviour exhibits a deviation from its independence from certain observables, as observed in the following Section 4.1.3. Fine corrections need to be applied to Z_{float} to improve the resolution and quality of the analysis.

4.1.3 Atomic number correction

For both VAMOS++ settings and all runs, it is necessary to correct Z_{float} with respect to Y_{FP} and X_{FP}, as curvatures and deviations from the expected constant behaviour are present.

The curvatures and misalignments of Z_{float} with respect to Y_{FP} are directly associated with the probability of collecting a reduced number of ionised electrons in the gaseous detectors when ionisation begins at higher positions. When a fission fragment enters the ionisation chamber it ionises electrons in the upper regions of the chambers. Consequently, there is an increased probability of collecting fewer electrons on the pads due to recombination processes during the drift. This phenomenon results in the generation of curvatures, as observed in the left panel of Fig. 4.6, in relation to Y_{FP}. The same technique using interpolants to define the valleys between the distributions of Z, which was previously employed along with Eq. 4.1, is applied. The projected distribution with Z aligned with respect to Y_{FP} is depicted in Fig. 4.6(right).

The curvatures and misalignment of Z_{float} with respect to X_{FP} are particularly evident at the extremes of X_{FP} because edge effects depend on the detector. This effect arises from the collection of fewer electrons in ionisations near the chamber walls compared to the central regions. Consequently, deviations occur in the accurate quantification of the electric charge as observed in Fig. 4.7(left) after applying the previous correction over Y_{FP}. Once again, the technique of using interpolants to define the valleys between the Z distributions, as previously employed along with Eq. 4.1 over Y_{FP}, is applied. The resulting projected distribution of Z_{float} with a significant improvement in the resolution after the alignment is depicted in Fig. 4.7(right).

The final corrected and aligned atomic number Z, obtained for all runs of VAMOS++ with a 14° setting, can be observed in Fig. 4.8. In the left panel, the atomic number is plotted as a function of the event entry number N_{entry}, while in the right panel, it is plotted as a function of E^{IC}_{tot}.

USC UNIVERSIDADE DE SANTIAGO DE COMPOSTELA

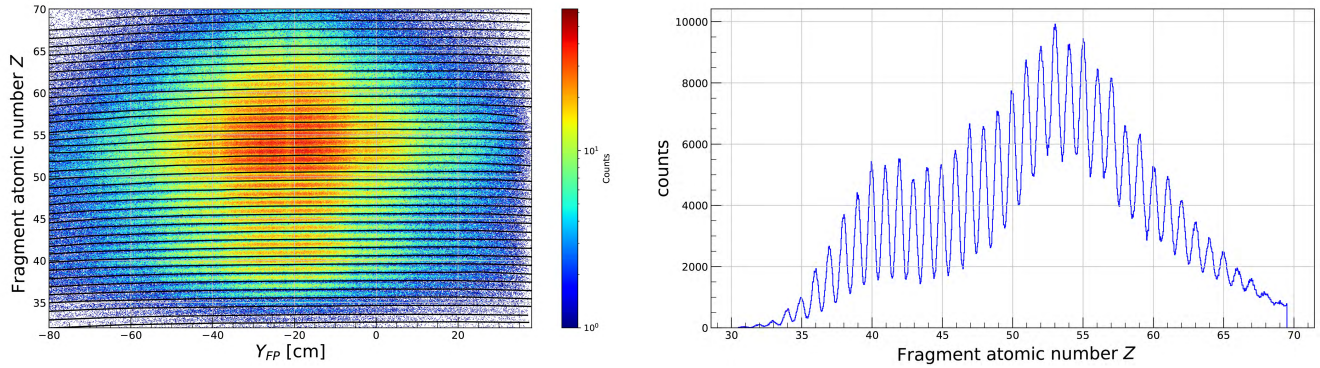

Figure 4.6: *In the left panel of the figure, the atomic number Z_{float} is plotted against the observable Y_{FP}. The black lines represent the interpolants that traverse the valleys of the distributions. The presence of curvatures and edge effects can be observed. In the right panel of the figure, the projected distribution of Z_{float} after alignment with respect to Y_{FP} is displayed. Both panels depict data from aluminium runs of VAMOS++ at 14°.*

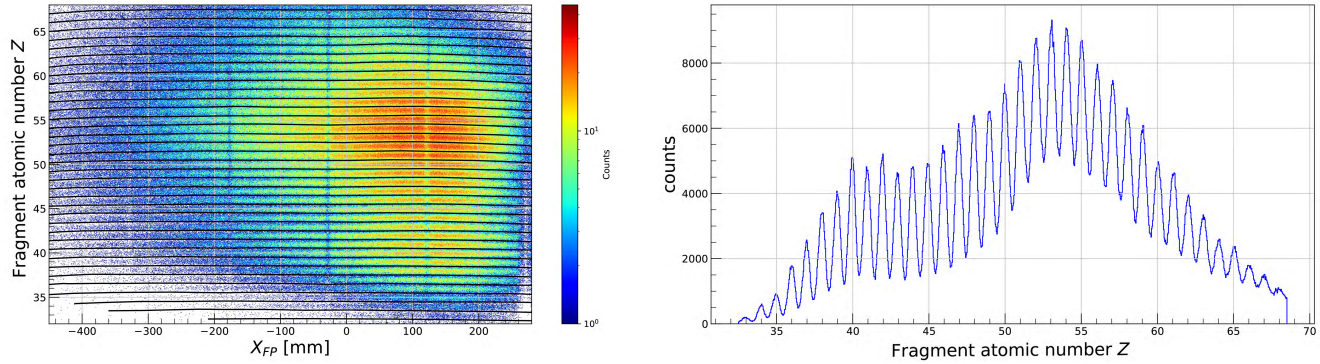

Figure 4.7: *In the left panel of the figure, the atomic number Z_{float} is plotted against the observable X_{FP} after aligning with Y_{FP}. The valleys of the distributions are represented by the black lines. The presence of curvatures and edge effects can be observed. In the right panel of the figure, the projected distribution of Z_{float} after alignment with X_{FP} is displayed. Both panels present data from aluminium runs of VAMOS++ at 14°.*

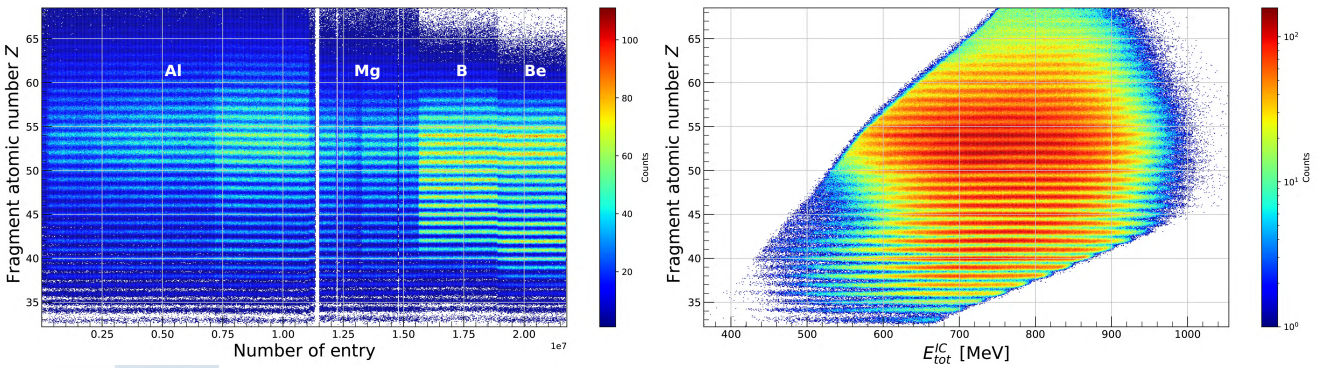

Figure 4.8: *In the left panel, the corrected and aligned Z_{float} for all the 14° runs is displayed. In the right panel, the same Z_{float} is depicted against the total energy E^{IC}_{tot}.*

4.2 Mass number and charge state

The determination of the mass number A and charge state q of the fission fragments relies on two independent measurements. The A can be obtained from the total energy E^{ToF} of the fragment when the ToF is measured, i.e. the energy that the fission fragment has after producing a signal in the Multi-Wire chamber MWPPAC. This energy is the total energy collected in the IC, E^{IC}_{tot}, plus an unmeasured energy, such as:

$$E^{ToF} \approx E^{FF}_{tot} - \Delta E_0 - \Delta E_1 \,, \tag{4.2}$$

according to Fig. 2.22 and Eq. 2.27. Then, it can be approximated that:

$$E^{ToF} \approx \Delta E_2 + \Delta E_3 \,, \tag{4.3}$$

where the energy E^{ToF} of the fragment is given by the sum of the "*Not Measured Energy*" (ΔE_{NM}), which is an estimation of the energy lost of the fragment in the layers between the ending of the dipole and the beginning of the ionisation chamber (see Section 2.9):

$$\Delta E_{NM} \doteq \Delta E_1 + \Delta E_2 \,, \tag{4.4}$$

according to Fig. 2.22 and Eq. 2.27. Rewriting the fragment energy as:

$$E^{ToF} = \Delta E_{NM} + E^{IC}_{tot} = \Delta E_{NM} + dE + E_{res} \,, \tag{4.5}$$

according to the energy deposited in the first three layers of the chamber, dE, and the residual energy E_{res} measured in the rest layers of the IC (see Eq. 3.8). The mathematical expression to obtain the mass number from ToF and the energy in the IC, A^E, is:

$$A^E = \frac{E^{ToF}}{u \cdot (\gamma - 1)} \,, \tag{4.6}$$

with u as the unified atomic mass unit, and γ as the Lorentz factor, where the velocity, β, of the fragment is determined from the ToF measurement and the distance (D) covered by the fragment within the ToF between the MWPCs Start detector and the Multi-Wire chamber MWPPAC, derived from the reconstructed *Path* (see Eq. 3.13):

$$\beta = \frac{D}{c \cdot ToF} \,. \tag{4.7}$$

The mass-to-charge state ratio $\left(\frac{A}{q}\right)$ is derived from the magnetic rigidity [85, 78, 79]. The magnetic rigidity ($B\rho$) combines the mass, charge state, and velocity of the fission fragment. The $\left(\frac{A}{q}\right)$ observable value is extracted from the velocity and the reconstructed $B\rho$ (see previous Section 2.4.1):

$$\left(\frac{A}{q}\right) = \frac{B\rho}{3.107 \cdot \beta\gamma} \,. \tag{4.8}$$

Since the mass of the fragments is independently obtained from the measurement of the total energy, the combination of A^E and $\left(\frac{A}{q}\right)$, allows for the determination of the charge state (q^{cal}) as:

$$q^{cal} = \frac{A^E}{\left(\frac{A}{q}\right)} \tag{4.9}$$

USC UNIVERSIDADE DE SANTIAGO DE COMPOSTELA

and provides a reconstructed mass, A^{rec}, as:

$$A^{rec} = int(q^{cal}) \cdot \left(\frac{A}{q}\right) , \tag{4.10}$$

where $int(q^{cal})$ is the closest integer value to a given q^{cal}. This reconstructed mass has a higher resolution compared to the mass evaluated using direct energy measurements.

After an initial analysis, additional corrections to the ToF, energy, and magnetic rigidity ($B\rho$) of the fragments are implemented to enhance the mass resolution for higher masses. To address this issue, corrections are applied. Moreover, more advanced corrections are introduced to refine the charge states, aiming to further enhance the overall mass resolution.

4.2.1 ToF correction

Being integer numbers, the correlation between the mass numbers A and charge states q exhibits a distinct pattern in the space $(A, \left(\frac{A}{q}\right))$ (see Fig. 4.9). This pattern is characterised by a distribution of $\left(\frac{A}{q}\right)$, represented with black dots in Fig. 4.9, where diagonals are the charge states (the Figure shows the cases of $q = 40$ and $q = 50$ with blue and green lines, respectively). Furthermore, by analysing the $(A, \left(\frac{A}{q}\right))$ correlation, it becomes evident that specific combinations of mass and charge produce integer values for $\left(\frac{A}{q}\right)$, resulting in vertical lines within the pattern.

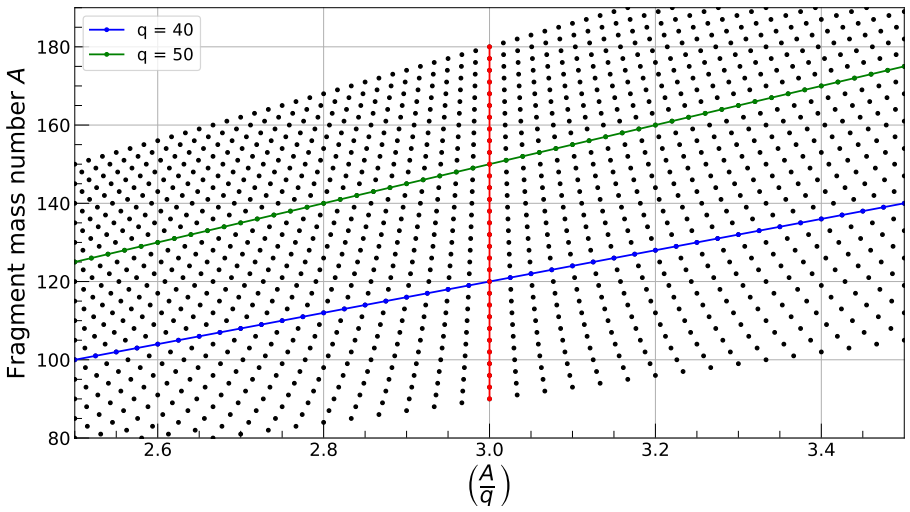

Figure 4.9: *The pattern of A versus* $\left(\frac{A}{q}\right)$ *is depicted in the figure. The red line represents the integer value of* $\left(\frac{A}{q}\right) = 3.0$. *Each diagonal line corresponds to a specific integer value of q, with the green and blue lines exemplifying* $q = 50$ *and* $q = 40$, *respectively.*

This effect is useful for cross-checking the ToF calibration and it is illustrated by the displacement of experimental data from the nominal values in Fig. 4.10(top), Figure 4.10(bottom) displays the distribution of $\left(\frac{A}{q}\right)$, revealing the presence of additional peaks caused by the finite resolution of the measurement and the limited number of produced masses. Among these peaks, the one with the lowest standard deviation is the focus of interest. Only $\left(\frac{A}{q}\right) = 3$ should not

receive the contribution of other nearby mass numbers when projected onto $\left(\frac{A}{q}\right)$. Moving away from $\left(\frac{A}{q}\right) = 3$ in the projection will result in distorted peaks due to the contribution of nearby mass numbers, which increases the width. The next value of A/q where alignment occurs again for all masses is $\left(\frac{A}{q}\right) = 4$, but this value is not reached in this experiment. It is important to note that the peak of interest in the projection is shifted from the nominal value of $\left(\frac{A}{q}\right) = 3.0$, as observed in Fig. 4.10. The shift is $= 0.00202 \pm 0.0005$ which implies an $Offset \approx -0.2$ ns.

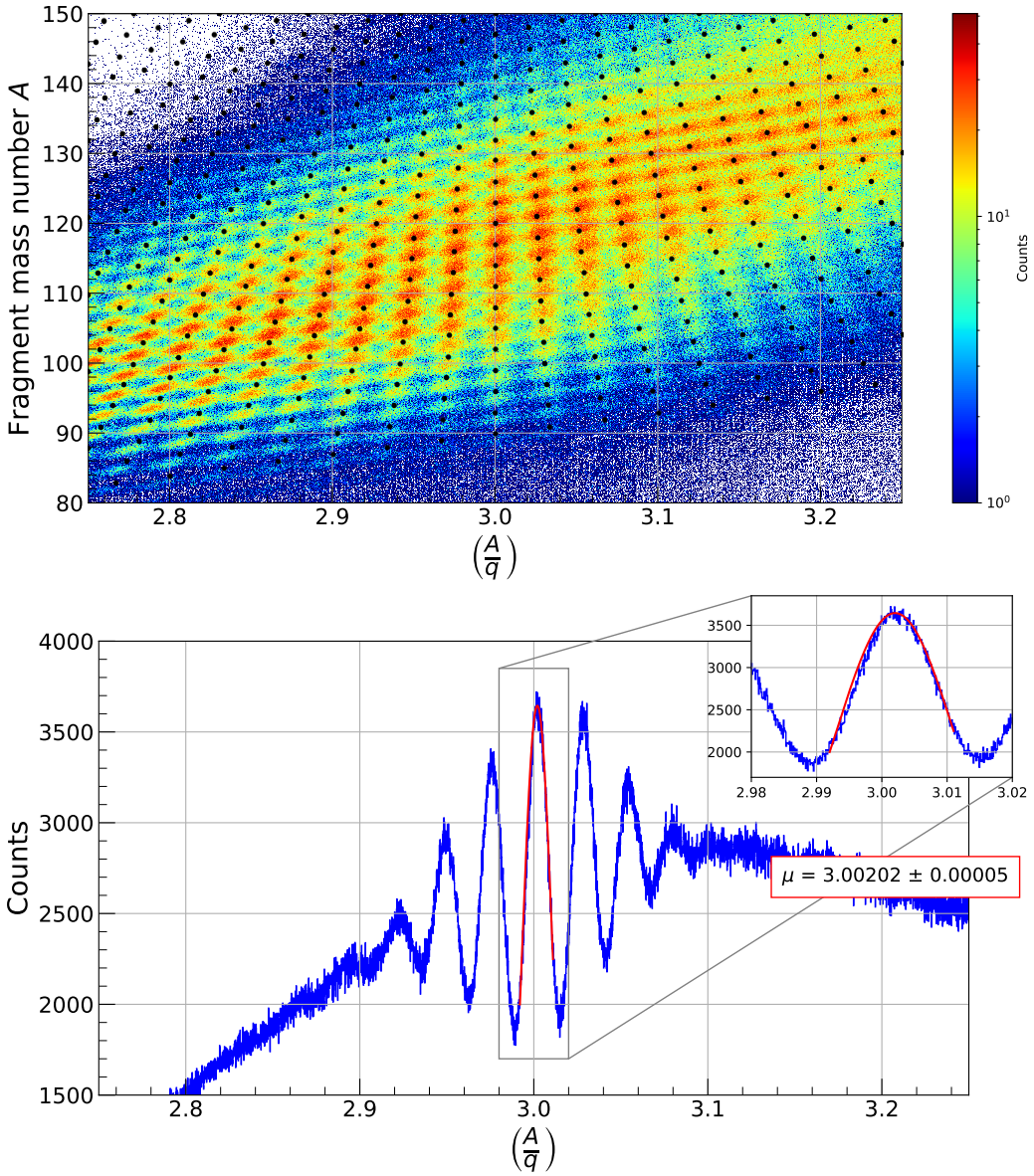

Figure 4.10: *In the top panel, the plot comparing the mass-charge state identification with the pattern of fission fragments generated from the fusion-fission process between* ^{238}U *and the four targets for the VAMOS++* 21.5° *setting is presented before corrections. In the bottom panel, the projection in* $\left(\frac{A}{q}\right)$ *is shown before ToF correction, with a specific focus on the* $\left(\frac{A}{q}\right) = 3.0$ *region. Several peaks are observed, resulting from the finite resolution of the measurement and the limited number of masses produced.*

The observed shift in $\left(\frac{A}{q}\right)$ is a result of an offset in the ToF introduced during the calibration process. It is essential to identify and correct this offset for each section of the Multi-Wire chamber MWPPAC. By expressing $\left(\frac{A}{q}\right)$ as a function of the ToF, it is possible to derive an analytical expression that relates the offset value, one value per section, to the difference between the corrected distribution $\left(\frac{A}{q}\right)_{cor}$ and the shifted distribution $\left(\frac{A}{q}\right)$:

$$\left(\frac{A}{q}\right)^2 = \left(\frac{B\rho}{3.107}\right)^2 \cdot \left[\left(\frac{ToF \cdot c}{D}\right)^2 - 1\right]^2 , \tag{4.11}$$

$$\left(\frac{A}{q}\right)^2_{corr} = \left(\frac{B\rho}{3.107}\right)^2 \cdot \left[\left(\frac{ToF_{corr} \cdot c}{D}\right)^2 - 1\right]^2 , \tag{4.12}$$

where $ToF_{corr} = ToF + Offset$ is the corrected time of flight of the fission fragments while ToF is the incorrect one. Combining the equations, the offset is obtained as:

$$Offset = -ToF + \sqrt{ToF^2 + K^2 \cdot \Delta^2} , \tag{4.13}$$

where:

$$K \doteq \frac{3.107D}{B\rho c} \tag{4.14}$$

and Δ is defined as:

$$\Delta^2 \doteq \left(\frac{A}{q}\right)^2_{corr} - \left(\frac{A}{q}\right)^2 , \tag{4.15}$$

where the value $\left(\frac{A}{q}\right)^2_{corr} = 3^2$ is imposed.

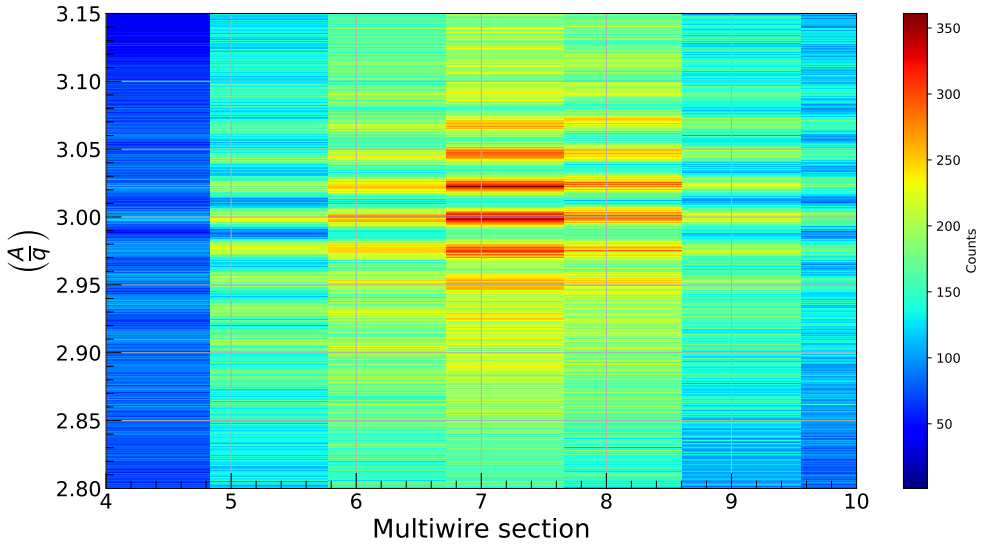

Figure 4.11: *The $\left(\frac{A}{q}\right)$ as a function of the sections of the Multi-Wire chamber MWPPAC for the fission fragments, generated from the reaction with the aluminium target with 14° setting, is shown after the offset correction.*

Therefore, by checking the $\left(\frac{A}{q}\right)$ the ToF is corrected. This procedure is applied separately for each section of the Multi-Wire chamber MWPPAC and in each setting (14°, 21.5°). In Fig. 4.11,

the $\left(\frac{A}{q}\right)$ is shown as a function of the sections of the Multi-Wire chamber MWPPAC after the alignment, for 14° setting. The previous step of the corrections is not shown because the shifts are less than 0.1 ns in ToF. This method allows for the correction of differences up to ±0.3 ns among the various sections of the Multi-Wire chamber MWPPAC. The ToF correction method over the two VAMOS++ settings is applied. Additionally, the $\left(\frac{A}{q}\right)$ measurement can be used to verify whether there is a time shift in the ToF measurement during the experiment, although in this case, no such shift is observed.

4.2.2 Correcting charge states

As mentioned previously, the determination of the fission-fragment charge state q relies on the values of A^E and $\left(\frac{A}{q}\right)$. Energy measurement plays a crucial role in calculating A^E, which is obtained from the energy and velocity of the fragments.

Obtaining the correct charge states enables the reversal of their calculation pathway and facilitates precise and accurate measurements of energy and velocity since q is derived from A^E, which is derived from energy and velocity. Simultaneously, it also provides the precise and accurate measurement of ToF and observables in the focal plane, such as X_{FP}, due to velocity; which is calculated employing these direct observables. Deviations in q with ToF, X_{FP} and Y_{FP} must be corrected, and once these deviations have been mitigated, the accurate charge states can be determined for both settings of VAMOS++.

A similar issue to the one discussed in Section 4.1 has been identified also q for both VAMOS++ settings. Figure 4.13 presents q plotted against ToF, with black solid lines representing interpolants trailing the valleys between the distributions of q. This affords the possibility of the application of the same alignment process as in the case of Z to fix the charge states:

$$q_{float} = \frac{q_p - q_{q<}(ToF_p)}{q_{q>}(ToF_p) - q_{q<}(ToF_p)} + q_{<}\,, \tag{4.16}$$

where each variable in the equation is shown graphically in Fig. 4.12.

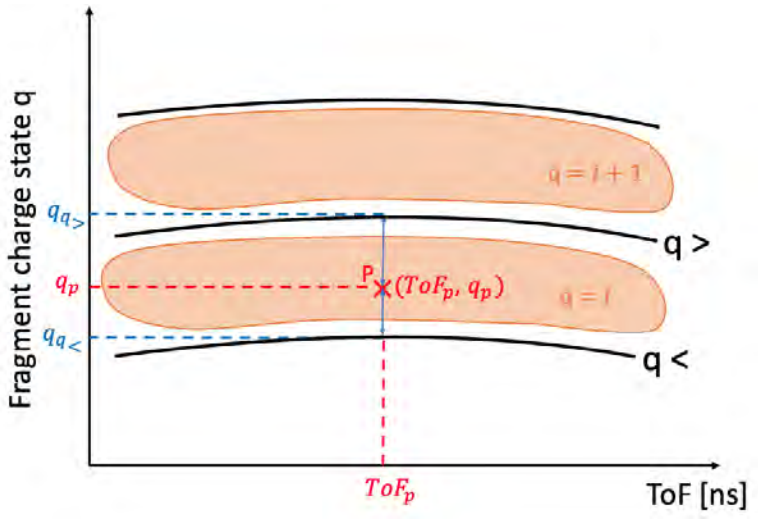

Figure 4.12: *A descriptive scheme is presented for the variables used to obtain q_{float} according to Eq. 4.16 using the interpolants depicted with black lines.*

The curvatures and misalignment of q_{float} with respect to ToF and X_{FP} are indirectly influenced by the reconstruction and corrections of $B\rho$ and D. Corrections to q_{float} must be realistic and physically grounded; therefore, these corrections are applied to ToF, where their relationship is direct, similar to the variables in the focal plane, such as X_{FP}. This phenomenon gives rise to the generation of curvatures with respect to ToF, as depicted in the left panel of Fig. 4.13.

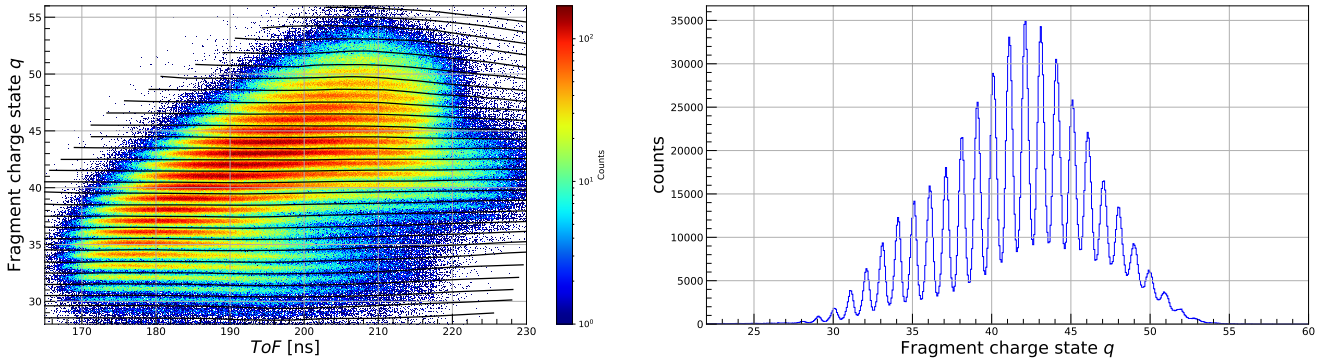

Figure 4.13: *In the left panel, the charge states q_{float} are plotted against the observable ToF. The black lines represent the interpolants that traverse the valleys of the distributions. The presence of curvatures and edge effects can be observed. In the right panel, the projected distribution of q_{float} after alignment with ToF is displayed. Both figures depict data from the aluminium target with the* 14° *setting.*

The second correction with respect to X_{FP} can be observed in the right pad of Fig. 4.14 after applying the previous correction. Once again, the technique of using interpolants to define the valleys between the q distributions, as previously employed along with Eq. 4.16, is applied. The resulting projected distribution, with q aligned with respect to X_{FP}, is depicted in the left pad of Fig. 4.14.

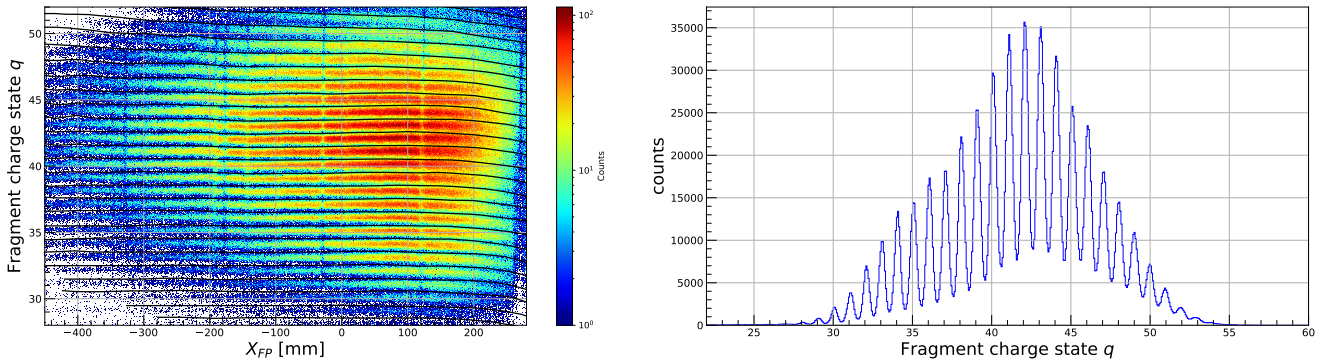

Figure 4.14: *In the left panel of the figure, the charge states q_{float} are plotted against the observable X_{FP} after aligning with ToF. The valleys of the distributions are represented by the black lines. The presence of curvatures and edge effects can be observed. In the right panel of the figure, the projected distribution of q_{float} after alignment with X_{FP} is displayed. Both panels present data from aluminium runs of VAMOS++ at* 14°.

4.2.3 Mass dependence

The identification of fragment atomic number Z is based on the correlation between energy loss and residual energy, as discussed in Section 4.1. However, it is important to consider that

the energy loss is not only dependent on velocity but also influenced by the mass of the ion (see Eq. 2.9). Consequently, ions with the same atomic number but different masses display slightly different energy loss curves. Therefore, once the mass is accurately determined, it becomes necessary to correct this dependence to refine the estimation of the fragment atomic number.

The impact of mass dependence on the identification of atomic number is depicted in Fig. 4.15 for the 14° setting. It is observed that each atomic number increases with mass. This phenomenon needs to be corrected separately for each target and both VAMOS++ settings, as the deviations and behaviours of the mass dependence vary among the different targets.

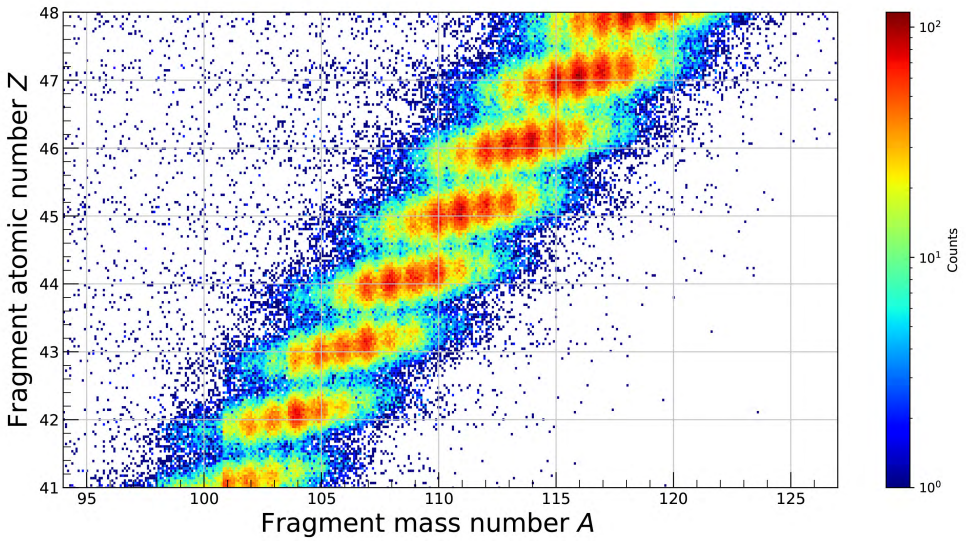

Figure 4.15: *The effect of mass dependence on the identification of fragment atomic number Z is illustrated in the zoomed-in view, which displays the fragment atomic number Z as a function of the fragment mass number A, for the 14° setting with the boron target. It can be observed that each Z increases proportionally with the mass (see Eq. 2.9), deviating from a perfectly aligned distribution.*

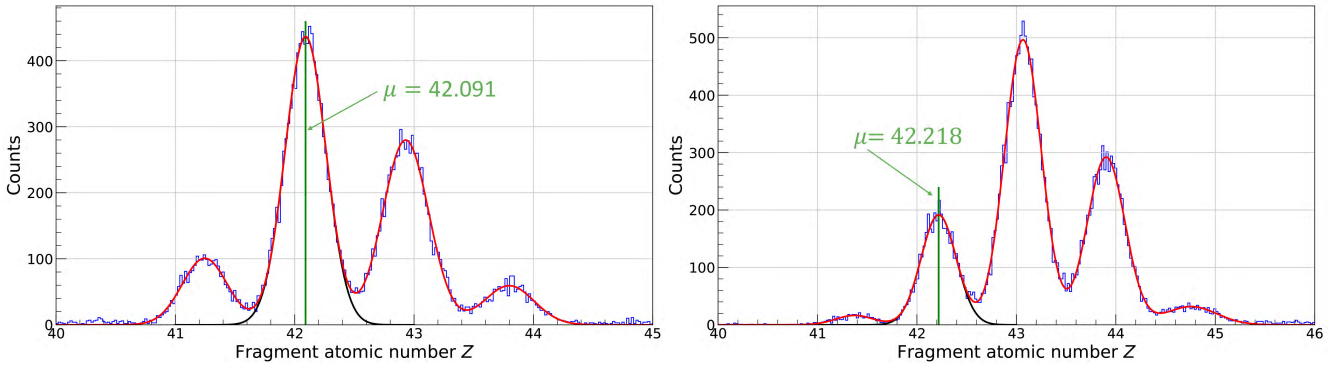

Figure 4.16: *In the right and left panels of the figure, the mean value of $Z = 42$ is calculated for two masses $A = 104$ and $A = 106$, respectively. The mean value is found to be higher for the higher mass, indicating the inclination of the mass dependence. To evaluate the mean values, a Gaussian fit is applied to all the zeta values for each mass. Both panels correspond to the 14° setting with the boron target.*

In Fig. 4.16, on both the right and left panels, the mean value of $Z = 42$ is calculated for two different masses, $A = 104$ and $A = 106$, through a Gaussian fit. Deviations from their respective integer values are revealed in the analysis. Using Gaussian fits for two extreme masses of each atomic number, the trend lines of the mass dependence can be obtained for each separate atomic number. The results, for the boron target as an example, can be observed in Fig. 4.17. The trend lines should exhibit smooth behaviour evolution as a function of Z, without sudden jumps or extreme inclinations. This is achieved through a second correction process on the slopes by plotting them against fragment atomic number Z and applying smoothing techniques.

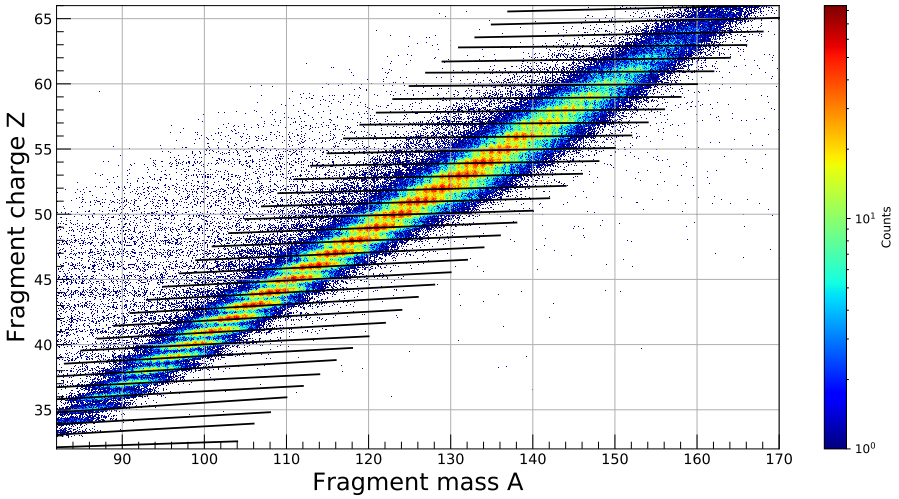

Figure 4.17: *The dependence of fragment atomic numbers Z with A is illustrated for the 14° setting with the boron target. The black lines depict the trend of each evaluated fragment atomic number Z with the average positions of extreme masses after the smoothing process.*

The accurate atomic number is determined by combining the real integer atomic number (Z_{int}) with the deviation calculated using the tendency line given by:

$$Z_{reco} = Z_{int} + \frac{Z(i) - \Delta Z_{linedown}}{\Delta Z_{lineup} - \Delta Z_{linedown}} \,. \tag{4.17}$$

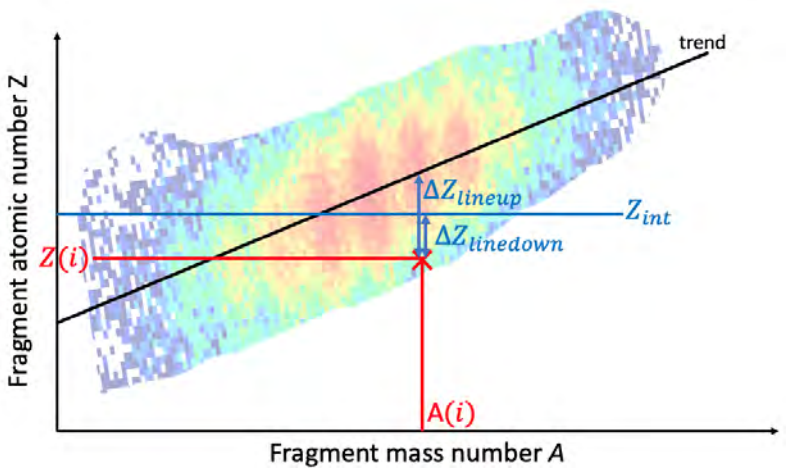

Figure 4.18: *A scheme of the variables used in the alignment of atomic numbers to correct for mass dependence with Eq. 4.17 is presented in the figure for an atomic number selection as an example.*

The differences ΔZ_{lineup} and $\Delta Z_{linedown}$ are associated with the scheme shown in Fig. 4.18. Figure 4.19 shows the atomic number distribution, after the mass dependence correction, as a function of the mass.

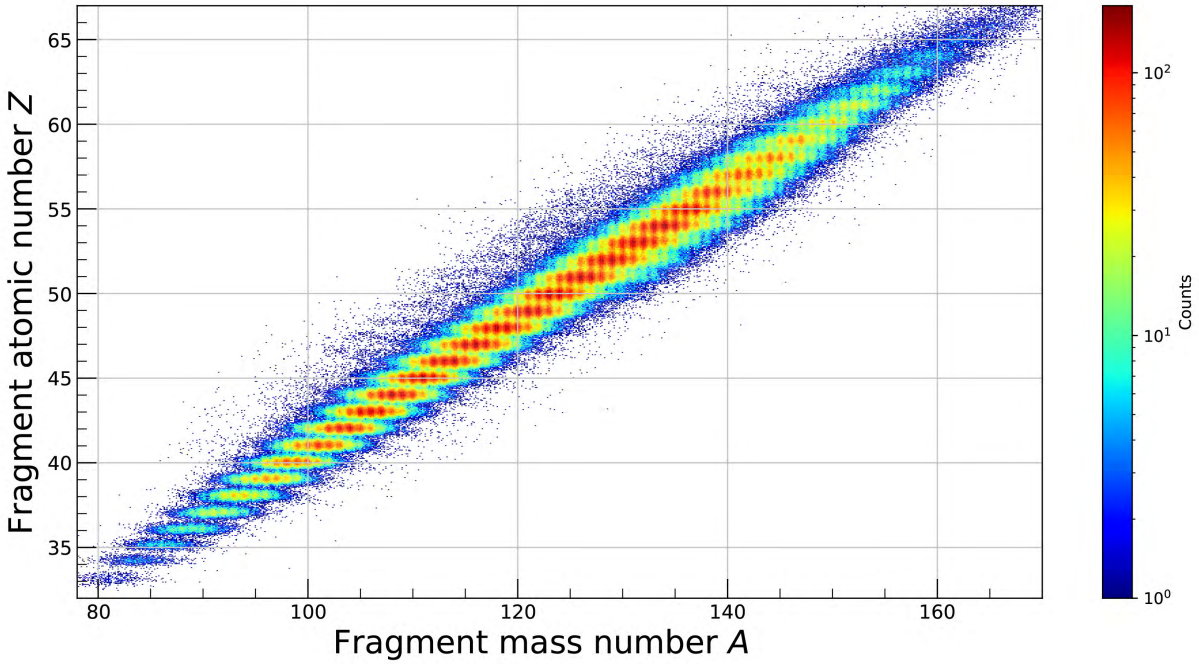

Figure 4.19: *The fragment atomic number Z distribution as a function of the fragment mass number A, after the mass dependence correction, for* 14° *setting with boron target.*

4.3 Identification resolution and accuracy

The verification of the identification of the fission fragments is achieved by analysing the energy of γ-rays released from the decay of excited states. Specifically, even-even nuclei exhibit well-defined rotational bands consisting of low-energy states that emit γ-rays sequentially. These rotational bands are extensively studied, and their γ-ray emission intensities are significant. Consequently, the γ-ray spectrum originating from rotational bands serves as a reliable cross-check for confirming the identification of fission fragments [98].

Throughout the fission process, the resulting fragments acquire energy, which is stored in the excitation of collective (deformation) and intrinsic (single-particle states) degrees of freedom. Subsequently, at the scission point (see Section 1.3.1), the accumulated energy is released through the emission of neutrons and γ-rays from excited states. The AGATA detector, as described in Section 2.3.3, is responsible for detecting and measuring the energy and angle of the γ-rays emitted during the decay of these excited states.

The fission fragments emit γ-rays while in motion, with an average velocity of 11% of the speed of light. Consequently, the measured energy of these gamma rays ($E_\gamma^{measured}$) is subject to Doppler broadening. To address this effect, a correction is applied as follows:

$$E_\gamma = \gamma \cdot (1 - \beta \cos(\alpha)) E_\gamma^{measured}\,, \tag{4.18}$$

where $\beta = v/c$ is the velocity of the fission fragment, γ is the Lorentz factor and α is the angle of emission between the fission fragment and the γ-rays.

The MWPCs Start detector is employed to determine the trajectory of the fission fragments. At the same time, the position of the AGATA crystals defines the trajectory of the γ-rays. The director vectors of these trajectories, denoted as $\overrightarrow{u_{FF}}$ for the fission fragments and $\overrightarrow{u_\gamma}$ for the γ-rays, are described by two orthogonal angles each. These angles are represented by $(\theta^v_{FF}, \phi^v_{FF})$ for the fission fragments and $(\theta_\gamma, \phi_\gamma)$ for the γ-rays:

$$\overrightarrow{u_{FF}} = \begin{pmatrix} \sin(\theta^v_{FF})\cos(\phi^v_{FF}) \\ \sin(\phi^v_{FF}) \\ \cos(\theta^v_{FF})\cos(\phi^v_{FF}) \end{pmatrix} , \tag{4.19}$$

$$\overrightarrow{u_\gamma} = \begin{pmatrix} \sin(\theta_\gamma)\cos(\phi_\gamma) \\ \sin(\theta_\gamma)\sin(\phi_\gamma) \\ \cos(\theta_\gamma) \end{pmatrix} , \tag{4.20}$$

with these vectors, the factor $\cos(\alpha)$ needed in the above equation Eq. 4.18 is obtained directly, as:

$$\cos(\alpha) = \overrightarrow{u_{FF}} \cdot \overrightarrow{u_\gamma} . \tag{4.21}$$

The angles θ^v_{FF}, ϕ^v_{FF}, θ_γ, and ϕ_γ are defined with respect to the VAMOS++ axis, as illustrated in Fig. 4.20. The angle between the fission fragments and the γ-rays is determined by calculating the scalar product of the director vectors corresponding to both trajectories.

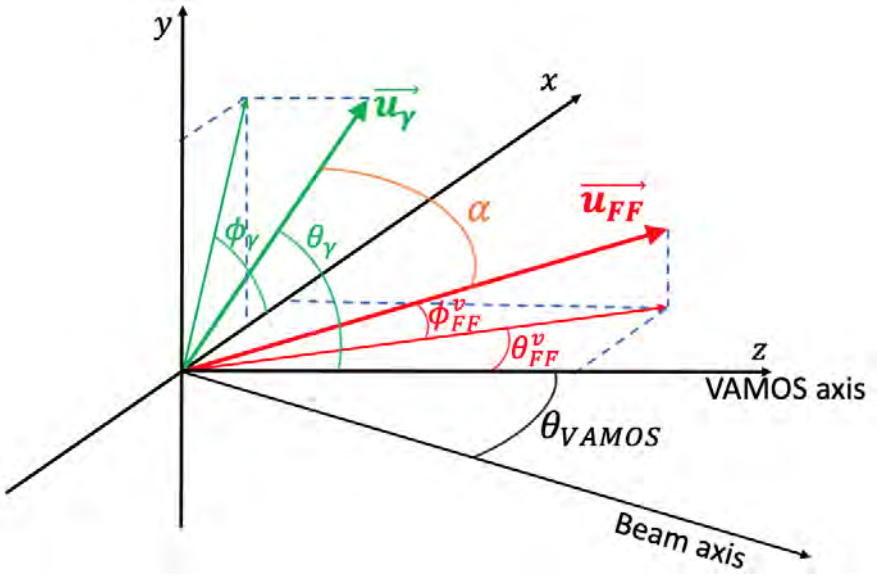

Figure 4.20: *A schematic view of the trajectories of the fission fragments and γ-rays is depicted. The angle α, which represents the angle between the two trajectories, is determined by the angles θ^v_{FF}, ϕ^v_{FF}, θ_γ, and ϕ_γ that define the orientations of the trajectories with respect to the VAMOS++ axis.*

The light fragment region exhibits distinctive rotational bands in nuclei such as ^{106}Ru and ^{108}Ru. The selection of these specific nuclei is illustrated in Fig. 4.21. By comparing the γ spectrum of each nucleus (see Fig. 4.22) with their known level schemes, the assignment of atomic number and mass for the fragments is confirmed.

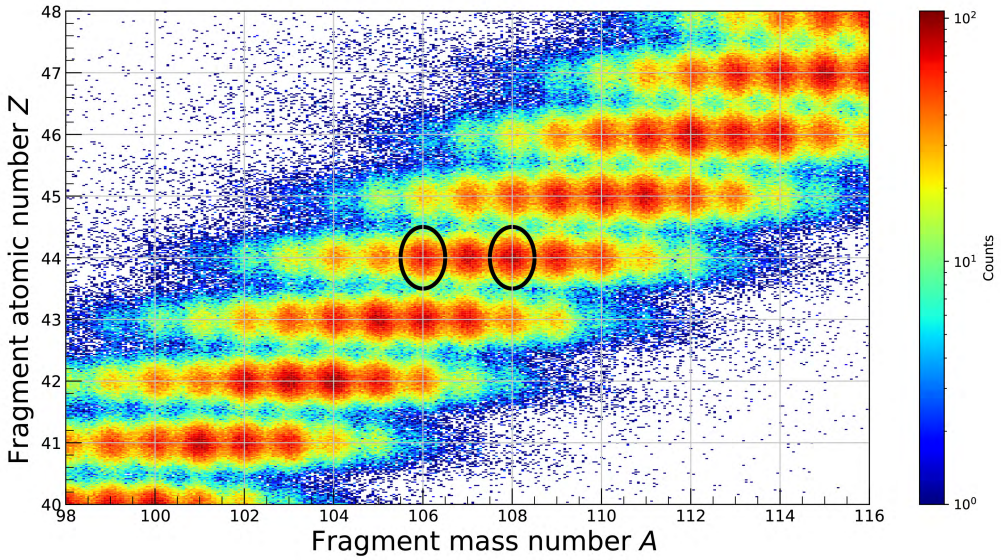

Figure 4.21: *Isotopic selection of* ^{106}*Ru and* ^{108}*Ru from fission fragment identification.*

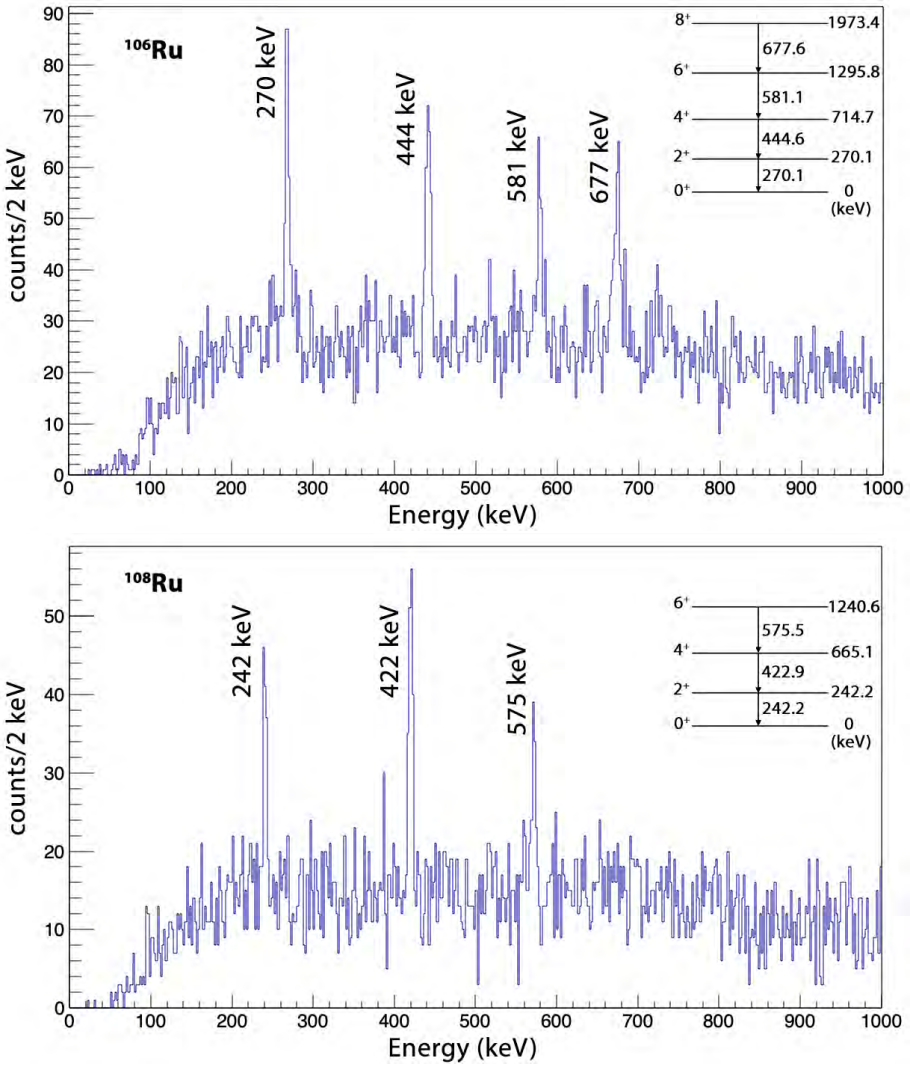

Figure 4.22: *Gamma spectra of* ^{106}*Ru and* ^{108}*Ru. The insets show the rotational level schemes, obtained from Evaluated Nuclear Structure Data File (ENSDF)* http://www.nndc.bnl.gov/ensdf.

The final resolutions achieved with the VAMOS++ spectrometer for this thesis of the fission fragment observables distributions: atomic number Z, charge state q and mass number A, are shown in Fig. 4.23, Fig. 4.24 and Fig. 4.25 respectively. All of them are depicted with data from the aluminium target after evaluating the distribution envelope with both VAMOS++ settings of 14° and 21.5°.

The resolution of the fission fragment atomic number distribution, $\left(\frac{FWHM_{Z^{float}}}{Z^{int}}\right)$, is presented in the subplot of Fig. 4.23. The $FWHM$ (full width at half maximum) on a curve of a function is given by the distance between points on the curve at which the function reaches half its maximum value. In the case of a Gaussian function the $FWHM = 2\sigma \cdot \sqrt{2\ln 2}$ where σ is the standard deviation. The determination of $FWHM_{Z^{float}}$ involves fitting Gaussian functions to the Z^{float} distribution, accounting for all the peaks. The average resolution value of the atomic number is $\left(\frac{FWHM_{Z^{float}}}{Z^{int}}\right) \approx 1.2\%$.

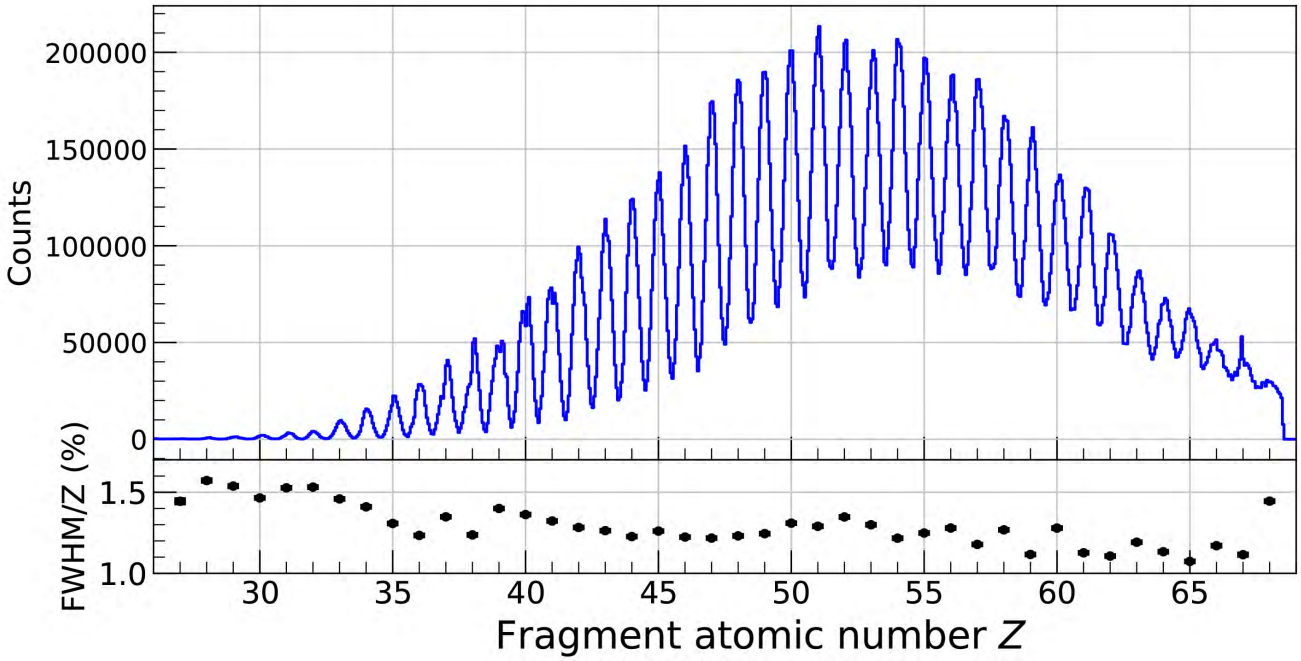

Figure 4.23: *The enveloped fission fragment atomic number Z distribution for both VAMOS++ settings is displayed for aluminium target. The Z^{float}, obtained from the direct measurement of energy in the IC after all corrections, is indicated by the blue histogram. The subplot presents the evaluation of fission fragment atomic number resolution $\left(\frac{FWHM_{Z^{float}}}{Z^{int}}\right)$ expressed in percentage.*

The resolution of the fission fragment charge state distribution, $\left(\frac{FWHM_{q^{float}}}{q^{int}}\right)$, is presented in the subplot of Fig. 4.24. The determination of $FWHM_{q^{float}}$ involves fitting Gaussian functions to the q distribution, accounting for all the peaks. The average resolution value of the mass number is $\left(\frac{FWHM_{q^{float}}}{q^{int}}\right) \approx 1.3\%$.

The resolution of the fission fragment reconstructed mass number distribution, $\left(\frac{FWHM_{A^{float}}}{A^{int}}\right)$, is presented in the subplot of Fig. 4.25. The determination of $FWHM_{A^{float}}$ involves fitting Gaussian functions to the A distribution, accounting for all the peaks. The average resolution value of the mass number is $\left(\frac{FWHM_{A^{float}}}{A^{int}}\right) \approx 0.5\%$.

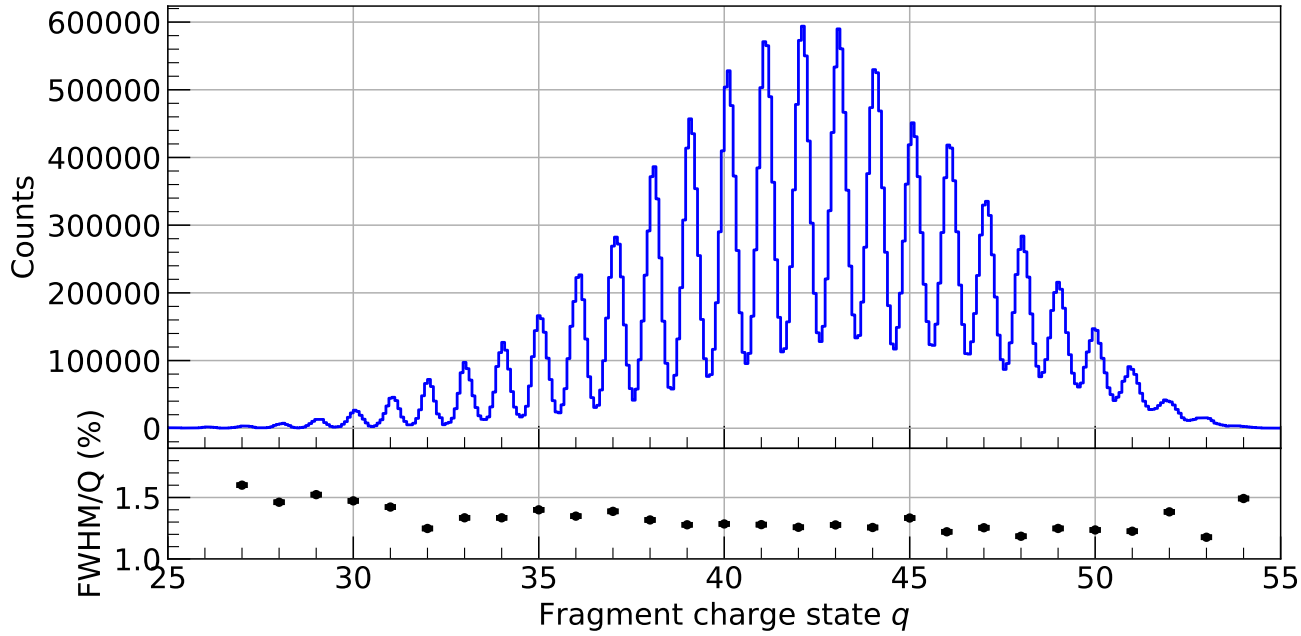

Figure 4.24: *The enveloped fission fragment charge state distribution for both VAMOS++ settings is displayed for aluminium target. The charge state distribution calibrated q^{cal}, obtained from the direct measurement A^E which comes from the energy measurement and $\left(\frac{A}{q}\right)$ after all corrections, is indicated by the blue histogram. The subplot presents the evaluation of fission fragment charge state resolution expressed in percentage.*

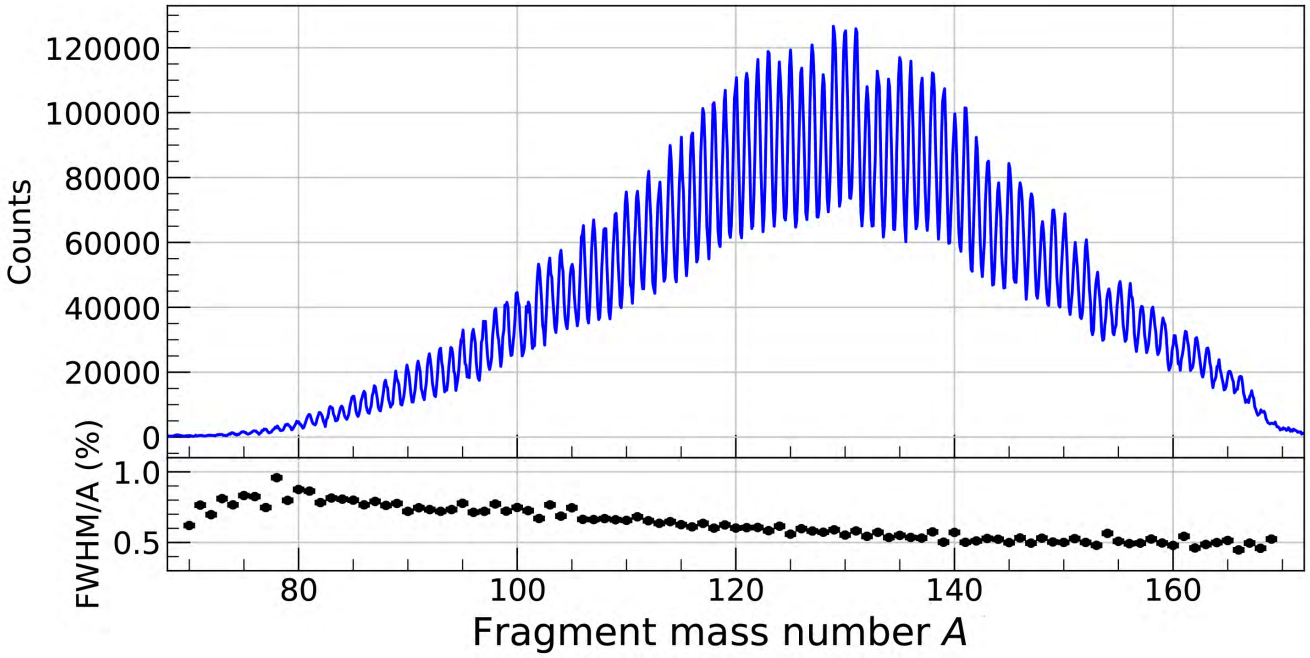

Figure 4.25: *The enveloped fission fragment mass distribution for both VAMOS++ settings is displayed is displayed for aluminium target. The reconstructed mass distribution A^{rec}, obtained from the direct measurement of energy and velocity (A^E) and the $\left(\frac{A}{q}\right)$ measurement after all corrections, is indicated by the blue histogram. The subplot presents the evaluation of fission fragment mass number resolution expressed in percentage.*

The mass resolution $\left(\frac{FWHM_{A^{float}}}{A^{int}}\right)$, depicted in the subplot of Fig. 4.25, is observed to decrease as the mass increases. This trend suggests that the resolution is limited by the precision of ToF. Heavier masses exhibit slower velocities, resulting in a smaller relative ToF precision. Additionally, the fragments accelerated by VAMOS++ at 14° attain higher velocities compared to those accelerated by VAMOS++ at 21.5°, thereby worsening both the relative ToF resolution and the mass resolution. Nonetheless, the subplot in Fig. 4.25 reveals a minimum in the resolution at higher masses, with $\left(\frac{FWHM_{A^{float}}}{A^{int}}\right) \approx 0.5\%$. This limitation is determined by the resolution in the reconstruction of magnetic rigidity (see Section 2.4.3).

The results can be compared with previous experiments. The newest one focused on other fissioning systems measured with the VAMOS++ setup [79]. A mass resolution ranging from $\approx$ 0.8% for the faster, lighter fragment to *approx*0.5% for the slower, heavier fragments, was achieved, showing remarkable similarity to the results obtained in this thesis. In the same experiment, a charge state resolution of $\approx$ 1.4% was attained, slightly worse than the result obtained in this thesis. Also, Z resolution was obtained at a rather constant value of = 1.8%, which is significantly worse than the results obtained in this work. The oldest one was the first of the experiments with the VAMOS++ setup [78]. A mass resolution ranging from $\approx$ 1% for the faster, lighter fragment to $\approx$ 0.55% for the slower, heavier fragments, was achieved. Also, an average charge state resolution of $\approx$ 2.0% was obtained, reaching minimum values of $\approx$ 1.5%. Finally, the resolution in Z around $\approx$ 1.5% was obtained.

USC
UNIVERSIDADE DE SANTIAGO DE COMPOSTELA

Chapter 5

VAMOS++ acceptance, normalisation and anisotropy

This chapter presents the determination of VAMOS++ geometrical acceptance of fission-fragment detection, $\mathcal{A}_g^{FF}$, which defines the coverage in angles (θ, ϕ) and magnetic rigidity $(B\rho)$ of the fragments. The angular acceptance is mainly defined by the size of the entrance window of VAMOS++ and the dimensions of the detectors at the focal plane [88]. That is, the geometrical acceptance of the VAMOS++ spectrometer depends essentially on three acceptances:

$$\mathcal{A}_g^{FF}(\theta, \phi, B\rho) = \mathcal{A}\theta(\phi, B\rho) \cdot \mathcal{A}\phi(\theta, B\rho) \cdot \mathcal{A}B\rho(\phi, \theta)\,, \tag{5.1}$$

where $\mathcal{A}\theta$ is the angular acceptance at θ, $\mathcal{A}\phi$ is the angular acceptance at ϕ and where $\mathcal{A}B\rho$ is the magnetic rigidity acceptance.

As $B\rho$ comes from reconstruction and it is a function of the energy, mass, and charge states of the fission fragment which in turn have complex distributions that depend on the reaction channel, the evaluation of its acceptance is highly non-trivial. Therefore, the assessment of full acceptance is restructured differently:

$$\mathcal{A}_g^{FF} = \mathcal{A}\phi_{LAB}(\theta_{LAB}^{TP}, \delta) \cdot \mathcal{A}\theta_{CM}(A, q, \theta_{FS}, \beta_{FS})\,. \tag{5.2}$$

The acceptance accounts for both the azimuthal angle ($\mathcal{A}\phi_{LAB}$) and the polar angle ($\mathcal{A}\theta_{CM}$) of the fission fragment (see Section 2.2.1).

VAMOS++ acceptance in the azimuthal angle, denoted as $\mathcal{A}\phi_{LAB}$, depends on the polar angle in the laboratory reference frame (θ_{LAB}^{TP}) and it includes the relative magnetic rigidity of the fission fragments, $\delta = B\rho/B\rho_0$. The subscript LAB in the acceptance is related to the measured angle θ. Since $\phi_{LAB}^{TP} = \phi_{CM}^{TP}$, $\mathcal{A}\phi_{LAB} \equiv \mathcal{A}\phi_{CM}$. The acceptance in the reference frame of the fissioning system, denoted as $\mathcal{A}\theta_{CM}$, is a function of the fragment mass number, the fragment charge state, as well as the angle (θ_{FS}) and velocity (β_{FS}) of the fissioning-system (see Section 2.7). Nonetheless, since this work specifically focuses on fusion-induced fission events, the $\mathcal{A}\theta_{CM}$ term is solely a function of the fragment mass number and charge state, the pre-fission neutron evaporation does not significantly alter the fissioning system velocity (β_{FS} remains constant) neither the angle ($\theta_{FS} = 0$) (see Appendix A.1).

USC DE SANTIAGO DE COMPOSTELA

5.1 Phi acceptance $\mathcal{A}\phi_{LAB}$

$\mathcal{A}\phi_{LAB}$ acceptance represents the fraction of the azimuthal angular range covered by the fission fragments, for a particular θ^{TP}_{LAB} and δ, that is accepted by VAMOS++.

$\mathcal{A}\phi_{LAB}$ is determined by the size of VAMOS++ entrance window and the dimensions of the detectors at the focal plane. The quadrupoles in VAMOS++ cause a focalization effect on the trajectories of the fission fragments, resulting in a magnification factor between the incoming azimuthal angle and the outgoing vertical angle. This magnification factor depends on the fission fragment polar angle and relative magnetic rigidity (δ). As a result, the limitations imposed by the detector size at the focal plane translate into limitations in the azimuthal angle at the entrance of VAMOS++, which vary with the fission fragment polar angle and relative magnetic rigidity.

Since the emission of fission fragments does not exhibit a preferential direction, nor is there angular anisotropy in the angle ϕ. The $\mathcal{A}\phi_{LAB}$ acceptance is defined as the ratio between the angular range $\Delta\phi(\theta^{TP}_{LAB},\delta)$ and the full range of 2π:

$$\mathcal{A}\phi_{LAB}(\theta^{TP}_{LAB},\delta) \doteq \frac{\Delta\phi(\theta^{TP}_{LAB},\delta)}{2\pi}\,, \tag{5.3}$$

where:

$$\Delta\phi(\theta^{TP}_{LAB},\delta) \doteq \phi^{TP}_{max} - \phi^{TP}_{min}\,, \tag{5.4}$$

being ϕ^{TP}_{max} and ϕ^{TP}_{min} the limits of the ϕ distribution of the fission fragments $Dist(\phi^{TP}_{LAB})$ for a given $(\theta^{TP}_{LAB},\delta)$, fully transmitted through the spectrometer.

The ideal case for the $Dist(\phi^{TP}_{LAB})$ is a rectangular distribution. The measured ϕ distribution in LAB reference frame, for a given combination of $(\theta^{TP}_{LAB},\delta)$, deviates from the ideal flat distribution inside VAMOS++ acceptance and zero outside of it. Due to the size of the selections in $(\theta^{TP}_{LAB},\delta)$ and the uncertainty measurement of ϕ, θ^{TP}_{LAB}, and δ. The resulting distribution is a *Double Error Function*. The measured ϕ-distribution in LAB reference frame for the fission fragments is modelled as:

$$Dist(\phi^{TP}_{LAB}) = C\frac{2}{\sqrt{\pi}}\left[\int_0^{A_1\cdot(\phi^{TP}-B_1)} e^{-t^2}dt - \int_0^{A_2\cdot(\phi^{TP}-B_2)} e^{-t^2}dt\right], \tag{5.5}$$

where each integral is also known as *Gaussian Error Function*, defined by the expression:

$$\mathrm{Err}(x) = \frac{2}{\sqrt{\pi}}\int_0^x e^{-t^2}dt\,. \tag{5.6}$$

The parameter C represents the amplitude of the distribution, while A_1 and A_2 correspond to the slopes of the distribution at the edges. The parameters B_1 and B_2 indicate the values at which the distribution reaches half of its maximum amplitude. The FWHM of the *Double Error Function* represents the $Dist(\phi^{TP}_{LAB})$-range accepted by VAMOS++, which implies, mathematically: $B_2 = \phi^{TP}_{min}$ and $B_1 = \phi^{TP}_{max}$. Thus,

$$\mathcal{A}\phi_{LAB} = \frac{|B_2 - B_1|}{2\pi}\,, \tag{5.7}$$

for each combination of $(\theta^{TP}_{LAB},\delta)$. This procedure is applied separately for both VAMOS++ settings.

USC UNIVERSIDADE DE SANTIAGO DE COMPOSTELA

In Fig. 5.1, the complete $(\theta^{TP}_{LAB}, \phi^{TP}_{LAB})$ space and the $(\theta^{TP}_{LAB}, \delta)$ space for the fission fragments from aluminium target runs of the 14° setting are presented. The left panel displays the $(\theta^{TP}_{LAB}, \phi^{TP}_{LAB})$ space, while the right panel shows the $(\theta^{TP}_{LAB}, \delta)$ space.

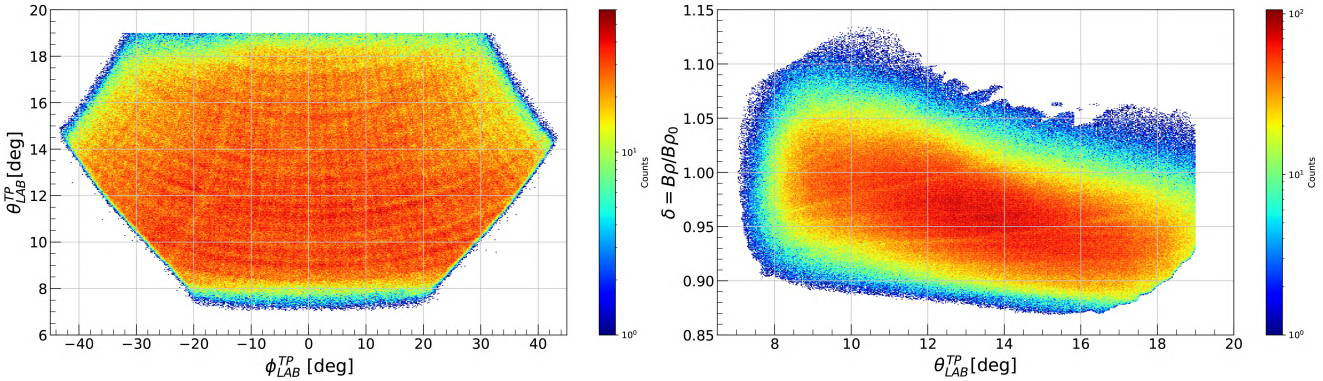

Figure 5.1: *The left panel of the figure illustrates target position $(\theta^{TP}_{LAB}, \phi^{TP}_{LAB})$ space for fission fragments measured using the 14° setting with aluminium target. In the right panel, the relative magnetic rigidity $\delta = B\rho/B\rho_0$ of the fission fragments is plotted as a function of the polar angle θ^{TP}_{LAB} for the same 14° setting.*

In Fig. 5.2 right, the correlation plot of $(\theta^{TP}_{LAB}, \phi^{TP}_{LAB})$ is presented for fission fragments with $\delta \in [1.009, 1.019]$. Fig. 5.2 left displays the corresponding projected $Dist(\phi^{TP}_{LAB})$ for $\theta^{TP}_{LAB} \in [10.918, 10.968]$ deg, which is fitted with a *Double Error Function* to extract the ϕ^{TP}_{max} and ϕ^{TP}_{min} limits, labelled as B_2 and B_1 in the legend.

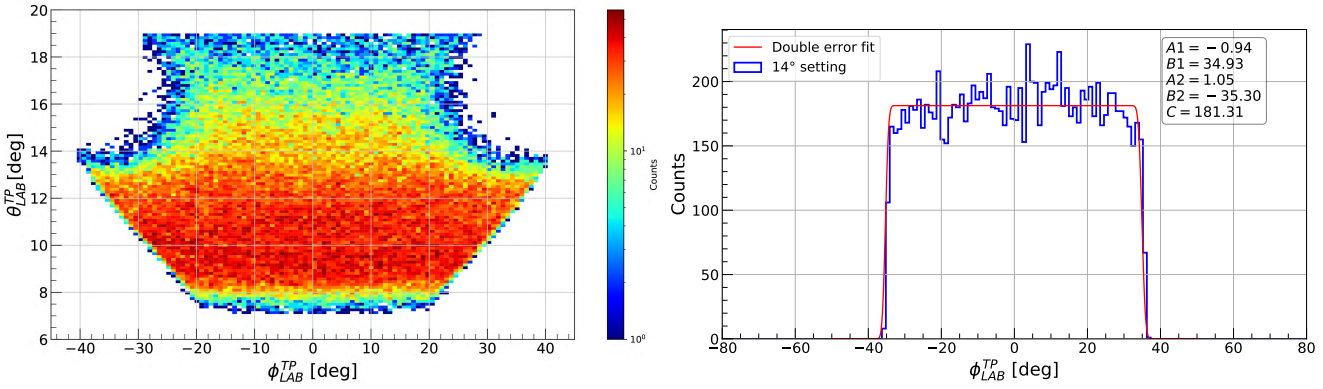

Figure 5.2: *In the left panel of the figure, the fragment polar angle (θ_{LAB}) is presented as a function of the azimuthal angle (ϕ) for $\delta \in [1.009, 1.019]$. The right panel displays the projected ϕ-distribution for $\theta_{LAB} \in [10.918, 10.968]°$. The distribution is fitted using a Double Error Function represented by the red line, enabling the extraction of the parameters corresponding to the ϕ^{TP}_{min} and ϕ^{TP}_{max} limits.*

The $\mathcal{A}\phi_{LAB}$ values obtained for each $(\theta^{TP}_{LAB}, \delta)$ combination define a 2D-acceptance grid with a step of 0.25 deg in θ^{TP}_{LAB} and 0.005 in δ. Fig. 5.3 right panel and Fig. 5.3 left panel show the $\mathcal{A}\phi_{LAB}$ surface for VAMOS++ settings 14° and 21.5° respectively.

USC UNIVERSIDADE DE SANTIAGO DE COMPOSTELA

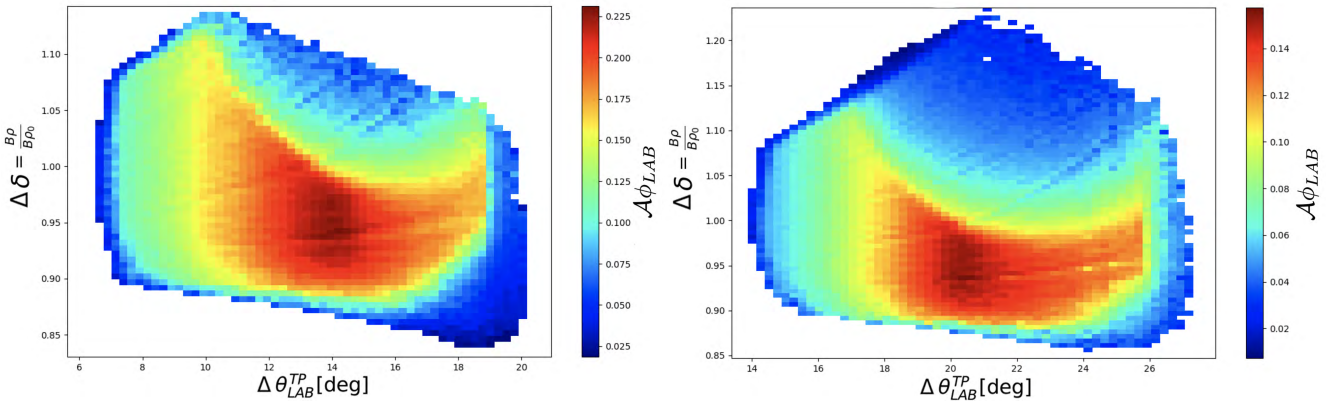

Figure 5.3: *The calculated values of $\mathcal{A}\phi_{LAB}$, indicated on the colour axis, are presented as a function of θ^{TP}_{LAB} and δ. The two-dimensional $\mathcal{A}\phi_{LAB}$ surfaces obtained for 14° (left) and 21.5° (right) settings are displayed.*

The ϕ acceptance, $\mathcal{A}\phi_{LAB}$ for any particular θ^{TP}_{LAB} and δ is determined through a local multivariate interpolation in the 2D grid:

$$\begin{aligned}\mathcal{A}\phi_{LAB} = \mathcal{A}(\theta^{TP}_{LAB}, \delta) =& \mathcal{A}(\theta^{TP}_{LAB,1}, \delta_1) \cdot \frac{(\delta_2 - \delta)}{(\delta_2 - \delta_1)} \cdot \frac{(\theta^{TP}_{LAB,2} - \theta^{TP}_{LAB})}{(\theta^{TP}_{LAB,2} - \theta^{TP}_{LAB,1})} + \\ & \mathcal{A}(\theta^{TP}_{LAB,2}, \delta_1) \cdot \frac{(\delta_2 - \delta)}{(\delta_2 - \delta_1)} \cdot \frac{(\theta^{TP}_{LAB} - \theta^{TP}_{LAB,1})}{(\theta^{TP}_{LAB,2} - \theta^{TP}_{LAB,1})} + \\ & \mathcal{A}(\theta^{TP}_{LAB,1}, \delta_2) \cdot \frac{(\delta - \delta_1)}{(\delta_2 - \delta_1)} \cdot \frac{(\theta^{TP}_{LAB,2} - \theta^{TP}_{LAB})}{(\theta^{TP}_{LAB,2} - \theta^{TP}_{LAB,1})} + \\ & \mathcal{A}(\theta^{TP}_{LAB,2}, \delta_2) \cdot \frac{(\delta - \delta_1)}{(\delta_2 - \delta_1)} \cdot \frac{(\theta^{TP}_{LAB} - \theta^{TP}_{LAB,1})}{(\theta^{TP}_{LAB,2} - \theta^{TP}_{LAB,1})} ,\end{aligned} \tag{5.8}$$

where $\mathcal{A}(\theta^{TP}_{LAB,i}, \delta_j)$ with index $i, j = 1, 2$ represent the points of the grid that are closest to the interpolation point $(\theta^{TP}_{LAB}, \delta)$, labelled as:

$$\theta^{TP}_{LAB,1} < \theta^{TP}_{LAB} < \theta^{TP}_{LAB,2} \qquad \delta_1 < \delta < \delta_2 \,. \tag{5.9}$$

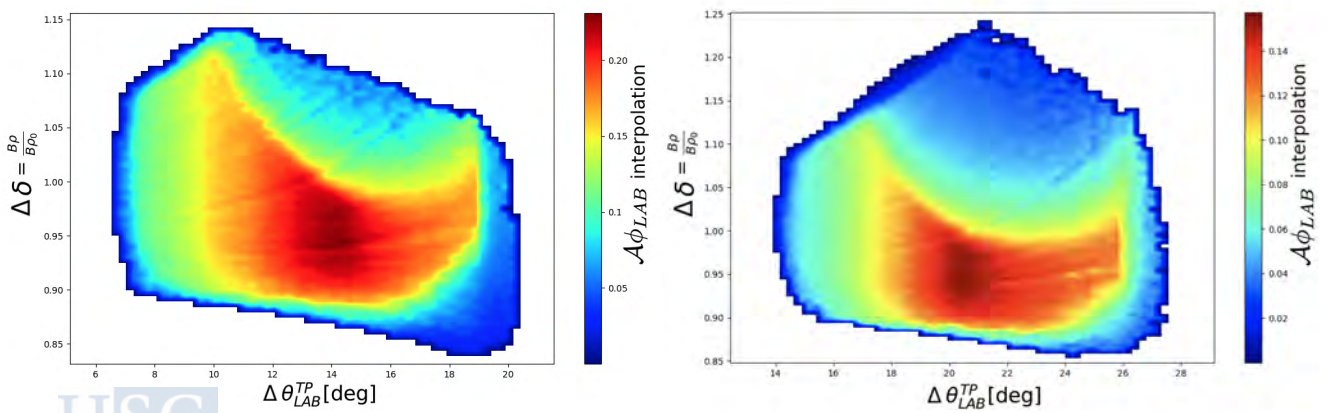

Figure 5.4: *The interpolated values of $\mathcal{A}_\phi$, indicated on the colour axis, are presented as a function of θ^{TP}_{LAB} and δ. The 2D $\mathcal{A}\phi_{LAB}$ surfaces interpolated using Eq. 5.8 for 14° (left) and 21.5° (right) settings are displayed.*

Figure 5.4 shows the interpolated surface for the two VAMOS++ settings 14° and 21.5°. This outcome closely resembles the expected and simulated result reported in [88], displayed in Fig. 5.5. The simulation depicted in Fig. 5.5 shows a region of maximum transmission resembling a parabolic shape that falls entirely within the acceptance and is symmetric in θ.

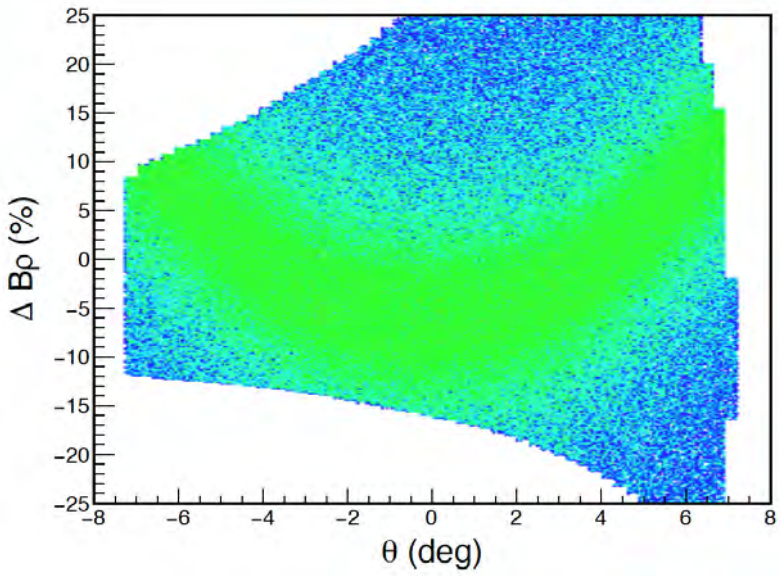

Figure 5.5: *Simulation of an isotropic distribution of $\Delta B\rho = (B\rho - B\rho_0)/(B\rho_0)$ [%] against θ [deg] of particles entering the VAMOS++ spectrometer, considering a MWPCs Start Detector size of 1000 mm × 150 mm. Adapted with permission from [88]. Copyright (2011) by Elsevier Science B.V.*

5.2 Normalisation of the settings

The recorded events vary in number between the two configurations of the VAMOS++ spectrometer (see Tab. 2.2). To merge the data from both configurations, it is necessary to normalise them. The normalisation procedure, which will be described below, is applied individually for each target.

The $(B\rho, \theta^{TP}_{LAB})$ space is plotted for both VAMOS++ settings, with a highlighted overlapping region in Fig. 5.6. It is important to note that the common region, the two settings overlap, must have consistent physics: the behaviour and integrals of the $B\rho$ and θ distributions from each setting should be the same in this region.

The normalisation factor, N_{norm}, is obtained for each target using the same process:

1. The normalisation factor is evaluated in the overlap region (see Fig. 5.6) of both VAMOS++ settings. This region selects $B\rho \in [1.1, 1.19]$ Tm and $\theta^{TP}_{LAB} \in [15.5, 18.0]$ deg to maximise statistics and avoid border effects.

2. The events within the selection are projected onto the θ^{TP}_{LAB} axis for both settings through multiple $B\rho$ selections. Specifically, projections are made with $B\rho$ steps of 0.1 Tm, 0.2 Tm, and 0.3 Tm. At this stage, the variable ϕ^{TP}_{LAB} is constrained to $[-1, 1]$ deg, ensuring a constant $\mathcal{A}\phi_{LAB}$ acceptance (see Fig. 5.7(top) with the $B\rho$ selection of 0.3 Tm between $[1.16, 1.19]$ Tm).

3. In each $B\rho$ selection from the first step, the ratio between the two projections of both settings in θ^{TP}_{LAB} is calculated. The setting at 14° is divided by the one at 21.5°. The average of this ratio is then computed.

4. To obtain N_{norm}, the 14° setting is normalised with respect to the 21.5° setting. That is, $N^{21.5^\circ}_{norm}$ is set to 1.

5. Subsequently, the obtained N_{norm} is applied to normalise all the data along with the $\mathcal{A}\phi_{LAB}$ through the weight:

$$weight = \frac{N_{norm}}{\mathcal{A}\phi_{LAB}}\,, \tag{5.10}$$

In this final step, the same projections as in the first step are selected. In this case, ϕ is not restricted and the *weight* is applied. This step is done for crosschecking and if needed, refines the normalisation factor, although it is noted that the variation with the acceptance $\mathcal{A}\phi_{LAB}$ is negligible.

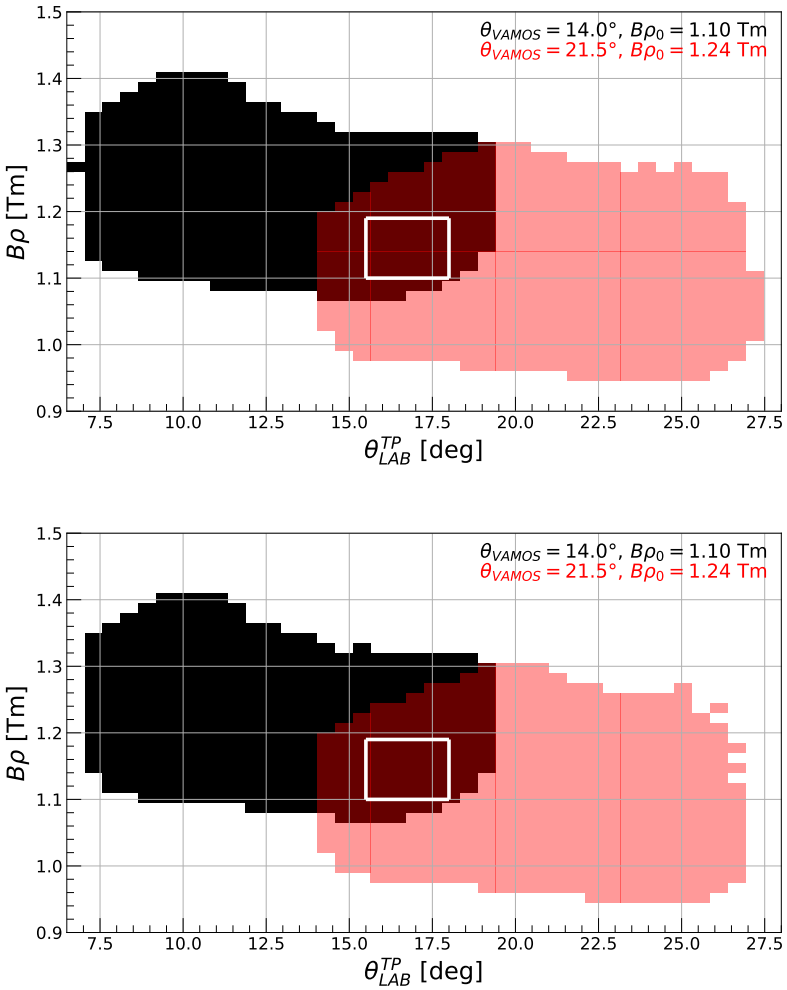

Figure 5.6: *The $(\theta^{TP}_{LAB}, B\rho)$ space for VAMOS++ settings at 14° (black) and 21.5° (red). The upper panel is for the ^{27}Al target and the lower panel is for the ^{nat}B target. In both panels, the white rectangle indicates the common region of the two settings where the normalisation factor N_{norm} is evaluated.*

A representation of the normalisation factor for the aluminium target in the same $B\rho$ region is shown in Fig. 5.7. Also is depicted the normalisation factor, before applying the acceptance with ϕ selection (top panel) and after applying it without the ϕ selection (bottom panel).

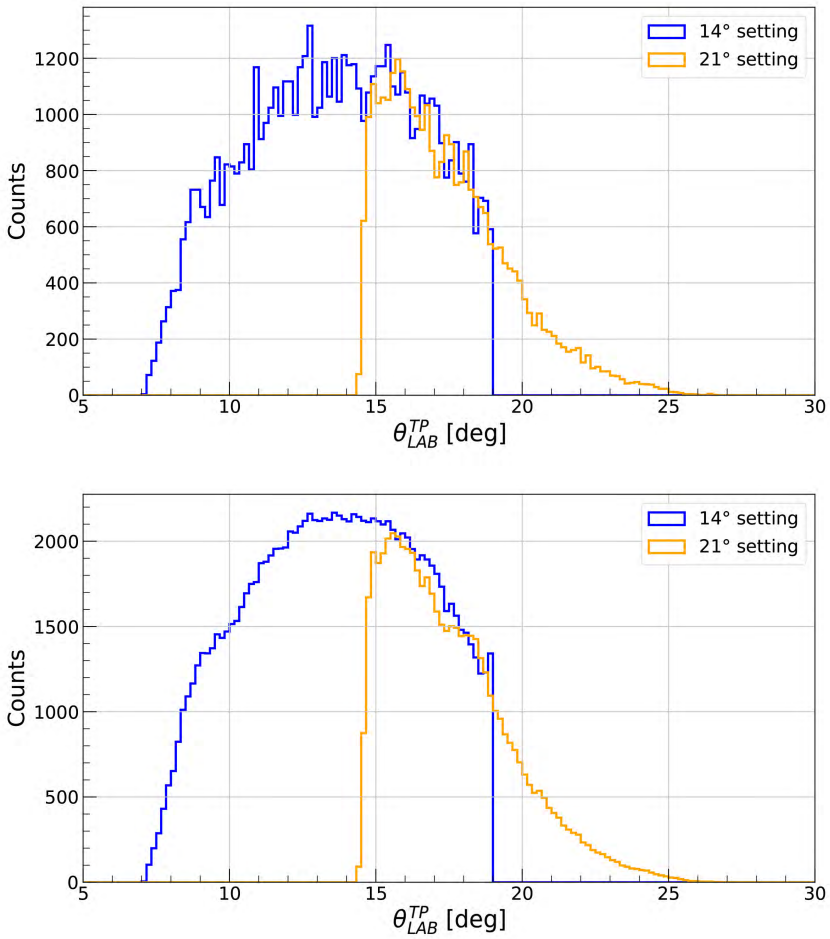

Figure 5.7: *The θ^{TP}_{LAB} angle distributions in the same $B\rho \in [1.16, 1.19]$ Tm window for the aluminium target with the two VAMOS++ settings, 14° and 21.5°, are depicted in blue and orange, respectively. The top panel displays the distribution after applying the selection $\phi \in [-1, 1]$ deg. The bottom panel shows the distribution without applying the ϕ selection and using the weight $= \frac{N_{norm}}{\mathcal{A}\phi_{LAB}}$ in order to crosscheck N_{norm}.*

The final step involves checking the homogeneity across the entire common region of the $(\theta^{TP}_{LAB}, B\rho)$ space by applying the ϕ acceptance and the corresponding N_{norm} normalisation factor for each target. By dividing the two-dimensional distributions of one set by the other, it is expected that the resulting distribution of the ratio has a mean equal to 1 with statistical dispersion. This final step can be seen in Fig. 5.8. The normalisation factors calculated for the four systems are listed in Tab. 5.1. Figure 5.9 presents $(\theta^{TP}_{LAB}, B\rho)$ for fission fragments from both VAMOS++ settings, after applying the $N_{norm}/\mathcal{A}\phi_{LAB}$ to the data and performing the two-dimensional envelope.

	Normalisation factors (N_{norm})	
Target	**14° Setting**	**21.5° Setting**
^{9}Be	4.650	1
^{nat}B	4.476	1
^{24}Mg	4.857	1
^{27}Al	3.605	1

Table 5.1: *List of the normalisation factors, N_{norm}, between the two VAMOS++ settings calculated for the four targets.*

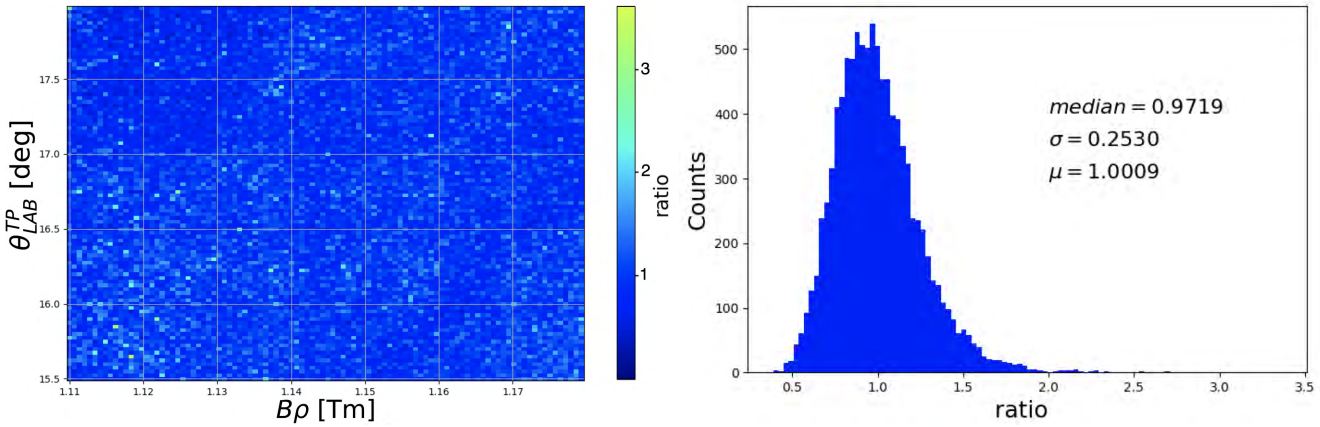

Figure 5.8: *In the left panel, the $(\theta^{TP}_{LAB}, B\rho)$ space is presented, applying the normalisation factor weight $= \frac{N_{norm}}{\mathcal{A}\phi_{LAB}}$ by dividing the two VAMOS++ settings within the common region of the aluminium target. The colourbar on the left indicates the scale. In the right panel, the distribution of the ratio between both settings is displayed, with an average value of approximately 1, indicating a reliable estimation.*

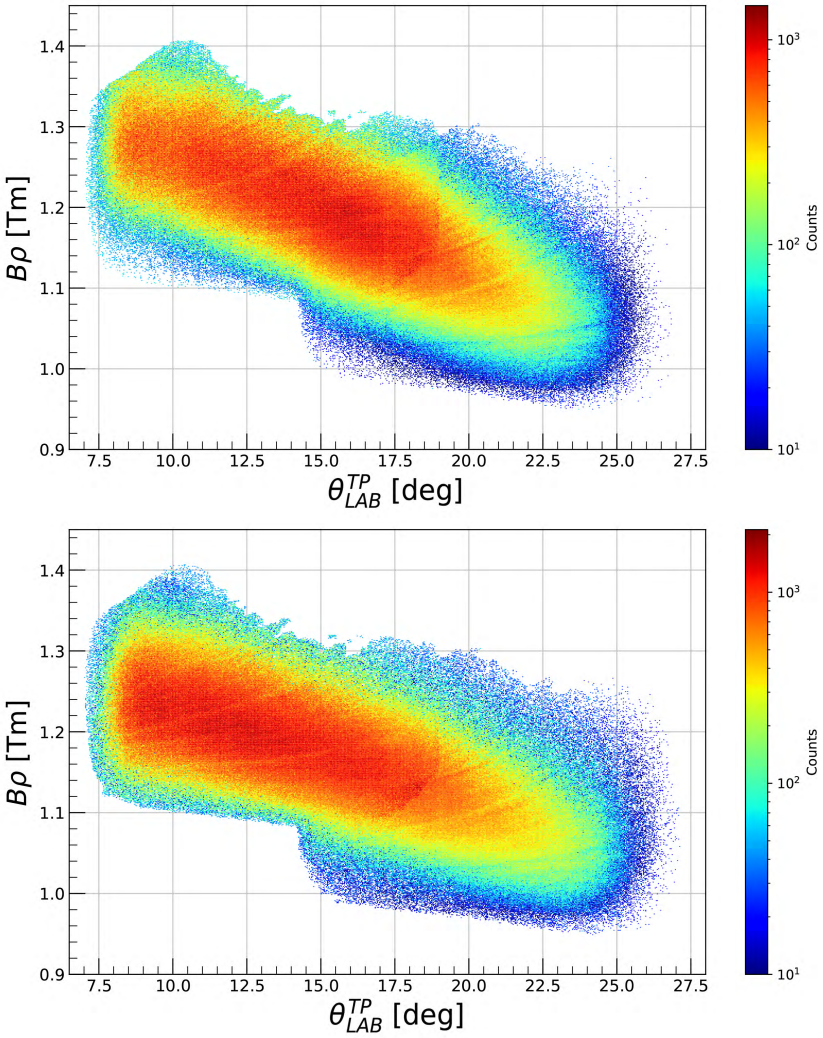

Figure 5.9: *The space distribution $(\theta^{TP}_{LAB}, B\rho)$ is presented after applying normalisation for both VAMOS++ settings and acceptance correction for two targets: boron and aluminium, shown in the top and bottom panels, respectively. Both figures are related to Fig. 2.10 of simulated events and the restrictions imposed by the acceptance window of the VAMOS++ spectrometer.*

5.3 Theta acceptance $\mathcal{A}\theta_{CM}$

VAMOS++ acceptance imposes limitations on the polar angle (θ^{TP}_{LAB}) of the measured fission fragments, which depend on the magnetic rigidity ($B\rho$) and the azimutal angle (ϕ) (see Fig. 2.10). The θ^{TP}_{LAB} distribution exhibits complex dependencies on the velocities of the fission fragments and the fissioning system. However, the acceptance in the polar angle is determined in the CM reference frame of the fissioning system (θ^{TP}_{CM}). This polar-angle acceptance $\mathcal{A}\theta_{CM}$ is evaluated and calculated in the fissioning-system reference frame, reconstructed as described in Section 2.7, ensuring that θ^{TP}_{CM} is not affected (see Section 2.2.1).

The projected velocity v^{FF}_{CM} of two complementary fission fragments ($Z_{FS} = 105$) corresponding to Nd ($Z = 60$) and Rh ($Z = 45$) from the reaction with the aluminium target are presented in Fig. 5.10. The maximum angular coverage permitted in the CM reference frame for the fission fragments is depicted in Fig. 5.11. The velocity of the fission fragments is displayed within the aperture of the spectrometer, while the limits defined by VAMOS++ at 14° and at 21.5° are indicated by the green lines. The angular range is observed to be larger for heavier fragments than lighter ones. It is important to note that the impact of charge states on the VAMOS++ acceptance should be considered, as discussed in Section 5.3.1.

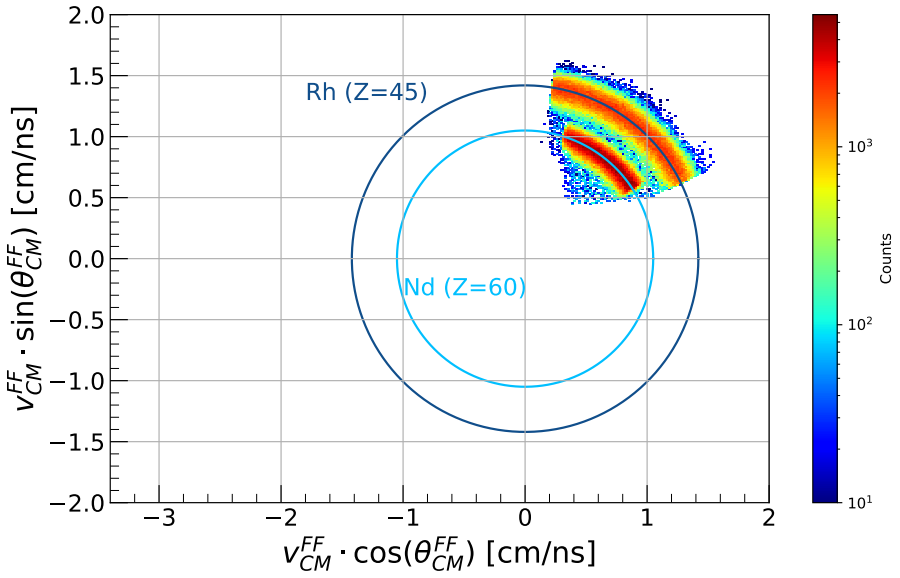

Figure 5.10: *The projection of the velocity v^{FF}_{CM} of Rh ($Z = 45$) and Nd ($Z = 60$) in the centre-of-mass reference frame are displayed for the aluminium target. The blue curves represent the complete kinematics of the fission fragment $\vec{v}^{FF}_{CM}$.*

The $\mathcal{A}\theta_{CM}$ acceptance is determined from the range of $\cos(\theta_{CM})$ distribution accepted by VAMOS++, given by:

$$\mathcal{A}\theta_{CM} = \frac{\Delta\cos(\theta^{FF}_{CM})(A, q, \theta_{FS}, \beta_{FS})}{2}\,, \tag{5.11}$$

where:

$$\Delta\cos(\theta^{FF}_{CM}) = \cos(\theta^{FF}_{CM})|_{max} - \cos(\theta^{FF}_{CM})|_{min}\,. \tag{5.12}$$

The determination of the $\cos(\theta^{FF}_{CM})$ distribution limits and their dependence on θ_{FS} and β_{FS} are elaborated in the next Section 5.3.1.

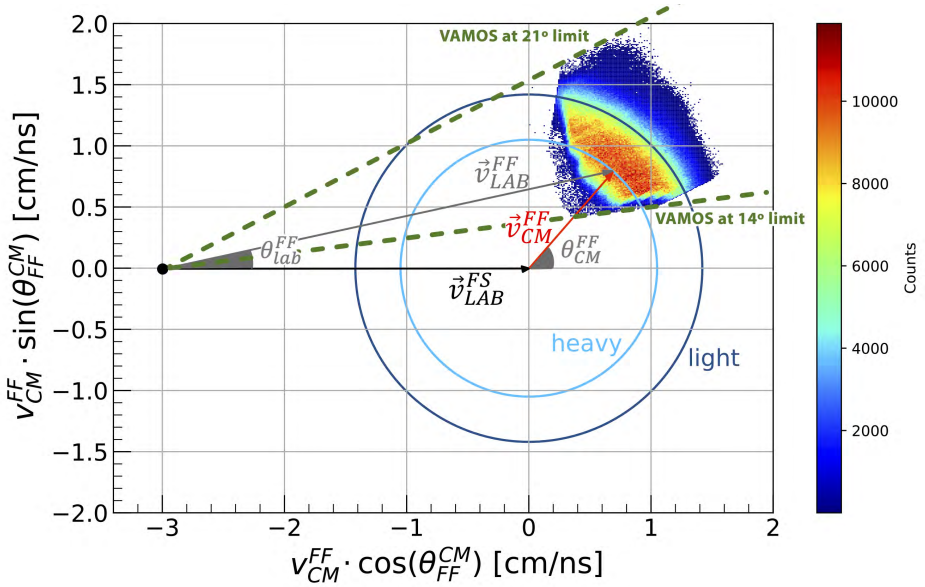

Figure 5.11: *The velocity of all fission fragments in the centre-of-mass reference frame are presented for the aluminium target. The blue curves represent the kinematics of typical light and heavy fission fragments (refer to Fig. 5.10). The data is constrained by the coverage of the acceptance spectrometer, the measurement angles θ_{VAMOS} at 14° and 21.5°, and the magnetic rigidity. The angles and kinematics in the laboratory (LAB) and centre-of-mass (CM) reference frames are depicted (see Appendix A.1). The green lines represent the measurement limits of VAMOS++ at 14° and 21.5°.*

5.3.1 Limits in $\cos(\theta^{FF}_{CM})$ distribution

The limits in $\cos(\theta^{FF}_{CM})$ are determined for each fragment mass A and each target. Moreover, the angular distribution for each A is composed of the contribution of events measured with the two VAMOS++ settings. The procedure used for the combination of the data coming from different settings is explained in the next Section 6.2. Figure 5.12 illustrates the distribution of $\cos(\theta^{FF}_{CM})$ for fission fragments with $A = 125$ with ^{27}Al target. The angular distribution of fission fragments in the CM reference frame exhibits a certain anisotropy [99, 100] (see next Section 5.4).

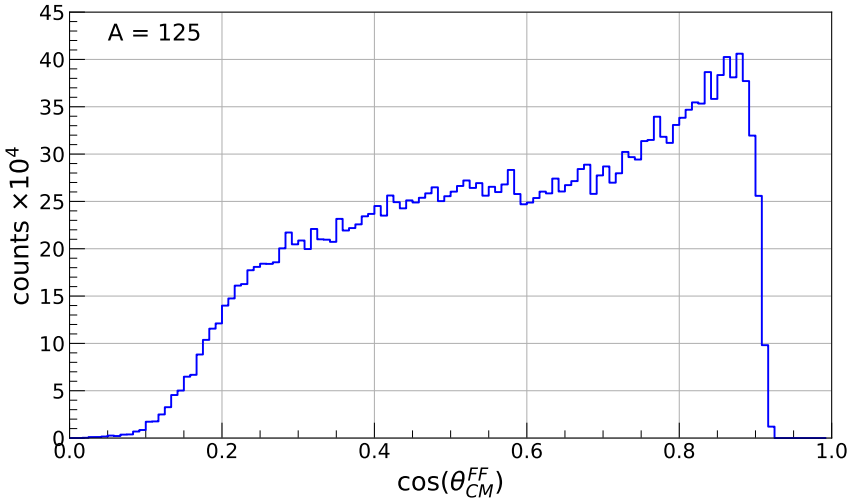

Figure 5.12: *The distribution of $\cos(\theta^{FF}_{CM})$ for fission fragments with $A = 125$ resulting from the $^{238}U + ^{27}Al$ reaction is shown.*

At 5.88A MeV, fission fragments, after their emission, obtain their charge states in interactions with the target and detectors. They are measured with different charge states depending on these interactions. Therefore, the distribution of charge states is influenced by the velocity of the fragments in the laboratory system [101]. Higher velocities result in fewer electrons remaining in the fragment, leading to a higher charge state. The production of each charge state is a probability distribution, which corresponds to an angular range in θ^{FF}_{CM} distribution.

Each (Z, A) yield is therefore distributed among multiple charge states. VAMOS++ acceptance may cut off the angular range of some charge states. It is necessary to study all charge states for each mass to exclude those that may be incomplete for isotopic yield calculations. The limits of VAMOS++ acceptance in the $(\theta^{TP}_{LAB}, B\rho)$ space defines a restricted range of $\cos(\theta^{FF}_{CM})$ distribution for each charge state, depending on the fragment mass number and the pair $(\theta_{FS}, \beta_{FS})$.

Assuming no energy losses in the target and MWPCs Start detector, the limits of $\cos(\theta^{FF}_{CM})$ distribution are calculated for each (A, q), separately for each target and each VAMOS++ setting [102]:

$$\cos(\theta^{FF}_{CM}|_{limit})(A,q) = \frac{\gamma_{FS}}{\sqrt{(\gamma^{FF}_{CM}|_{limit})^2 - 1}} \cdot \left[\mathcal{K} \cdot \cos(\theta^{FF}_{LAB}|_{limit}) - \beta_{FS}\sqrt{\mathcal{K}^2+1}\right] , \tag{5.13}$$

where $\mathcal{K} = \frac{q \cdot B\rho|_{limit}}{A \cdot 3.107}$. Therefore,

$$\gamma^{FF}_{CM}|_{limit} = \gamma_{FS} \cdot \left[\sqrt{\mathcal{K}^2+1} - \beta_{FS} \cdot \mathcal{K} \cdot \cos(\theta^{FF}_{LAB}|_{limit})\right] . \tag{5.14}$$

In fusion-induced fission, the angle of the fissioning system is fixed at zero, and its velocity is approximately the same in each event. Therefore, the limits of $\cos(\theta^{FF}_{CM})$ distribution depend on the mass number, charge state, and the limits of $B\rho$ and θ^{TP}_{LAB}, as explained earlier.

The lower limit of $\cos(\theta^{FF}_{CM})(A)$ distribution for each VAMOS++ setting is determined by selecting the lowest value among the lower limits of $\cos(\theta^{FF}_{CM})(A, q)$ distribution:

$$\cos(\theta^{FF}_{CM}|_{min})(A) = \min(\cos(\theta^{FF}_{CM}|_{min})(A,q)) . \tag{5.15}$$

Similarly, the upper limit of $\cos(\theta^{FF}_{CM})$ distribution for each VAMOS++ setting is determined by selecting the highest value among the lower limits of $\cos(\theta^{FF}_{CM})(A, q)$ distribution:

$$\cos(\theta^{FF}_{CM}|_{max})(A) = \max(\cos(\theta^{FF}_{CM}|_{max})(A,q)) . \tag{5.16}$$

The lower and upper limits of $\cos(\theta^{FF}_{CM})(A)$ distribution are presented for each target and each setting in Fig. 5.13. The combination of these limits gives the limits of $\cos(\theta^{FF}_{CM})(A)$ for each target, considering the common zone between settings and avoiding any "holes" in the combination, is shown in Fig. 5.14.

In the case of transfer-induced fission, the velocity and angle of the fissioning system define a $\Delta\cos(\theta^{FF}_{CM})$ set that changes event by event. The maximum variation of $\Delta\cos(\theta^{FF}_{CM})$ distribution, considering the maximum and minimum velocity and angle of the fissioning system, is observed to be lower than 0.1 compared to fusion-induced fission. Therefore, in transfer-induced fission, the $\Delta\cos(\theta^{FF}_{CM})$ distribution is assumed to be the same as in fusion-induced fission.

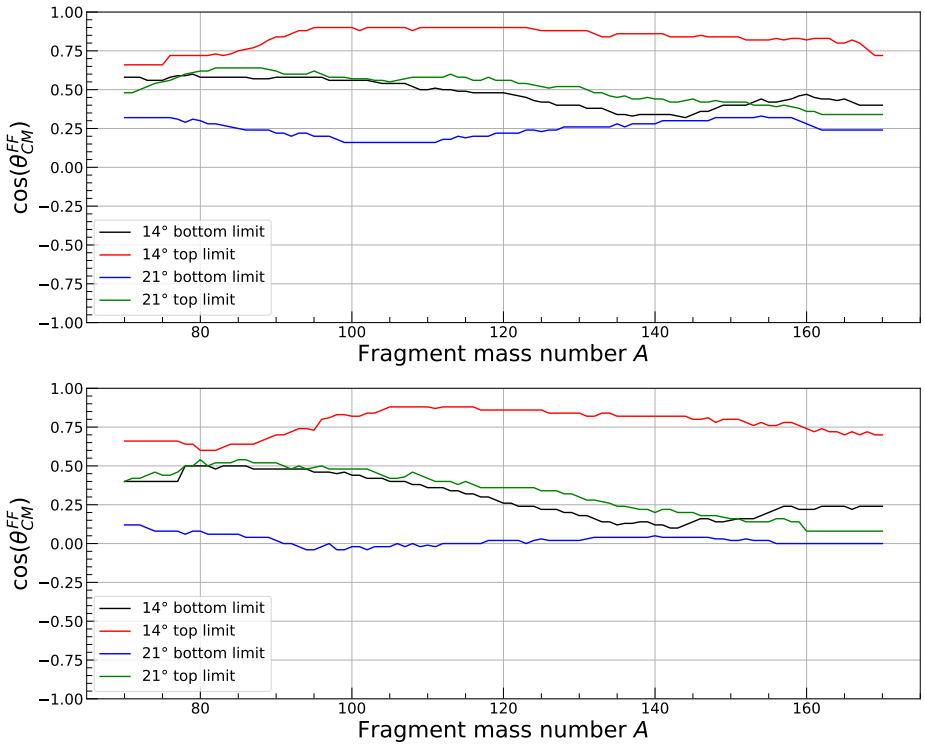

Figure 5.13: *The* $\cos(\theta^{FF}_{CM})$ *limits, calculated for the entire range of mass numbers, are shown for both settings. With the* ^{27}Al *target (top panel) and the* ^{nat}B *target (bottom panel). The bottom and top limits for the* $14°$ *setting are represented by the red and black lines, respectively, while the bottom and top limits for the* $21.5°$ *setting are represented by the blue and green lines, respectively.*

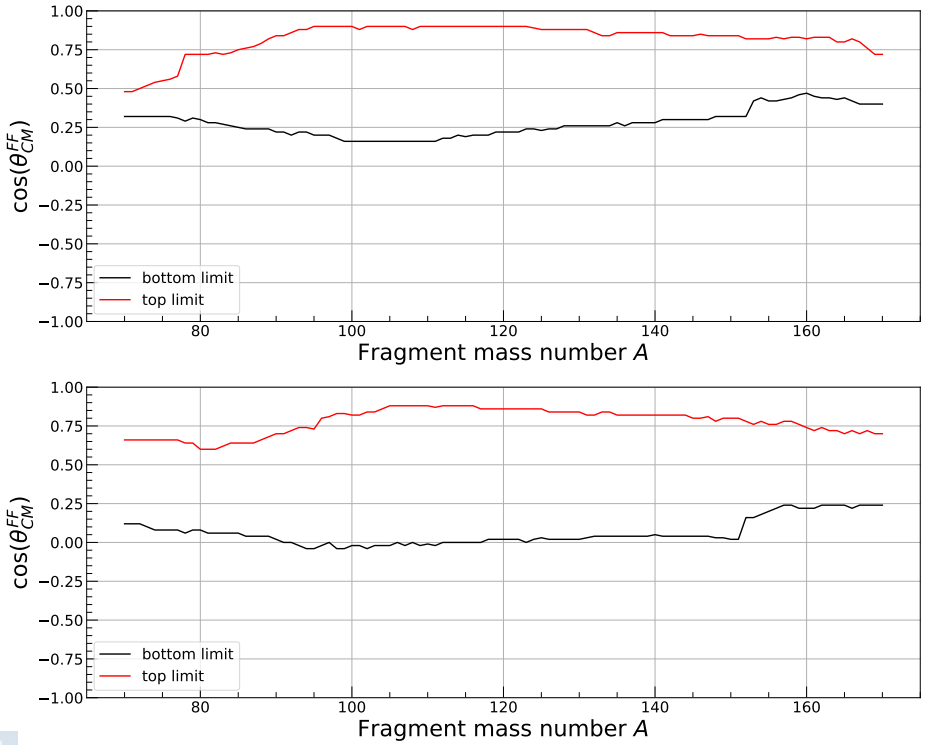

Figure 5.14: *The figure displays the* $\cos(\theta^{FF}_{CM})$ *limits, which were determined by calculating the independent limits of both settings for the entire range of mass numbers for data from the* ^{27}Al *target (top panel) and the* ^{nat}B *target (bottom panel). The black and red lines represent the lower and upper limits, respectively.*

The angular distribution as a function of θ^{TP}_{LAB} for fragments with $A = 125$ in the CM from fusion-induced fission is presented in Fig. 5.15. The limits correspond to the minimum and maximum values of $\cos(\theta^{FF}_{CM})(A = 125)$ distribution (see Fig 5.14). It can be observed that the acceptance limits restrict the majority of low or high charge states, while the central charge states are not affected.

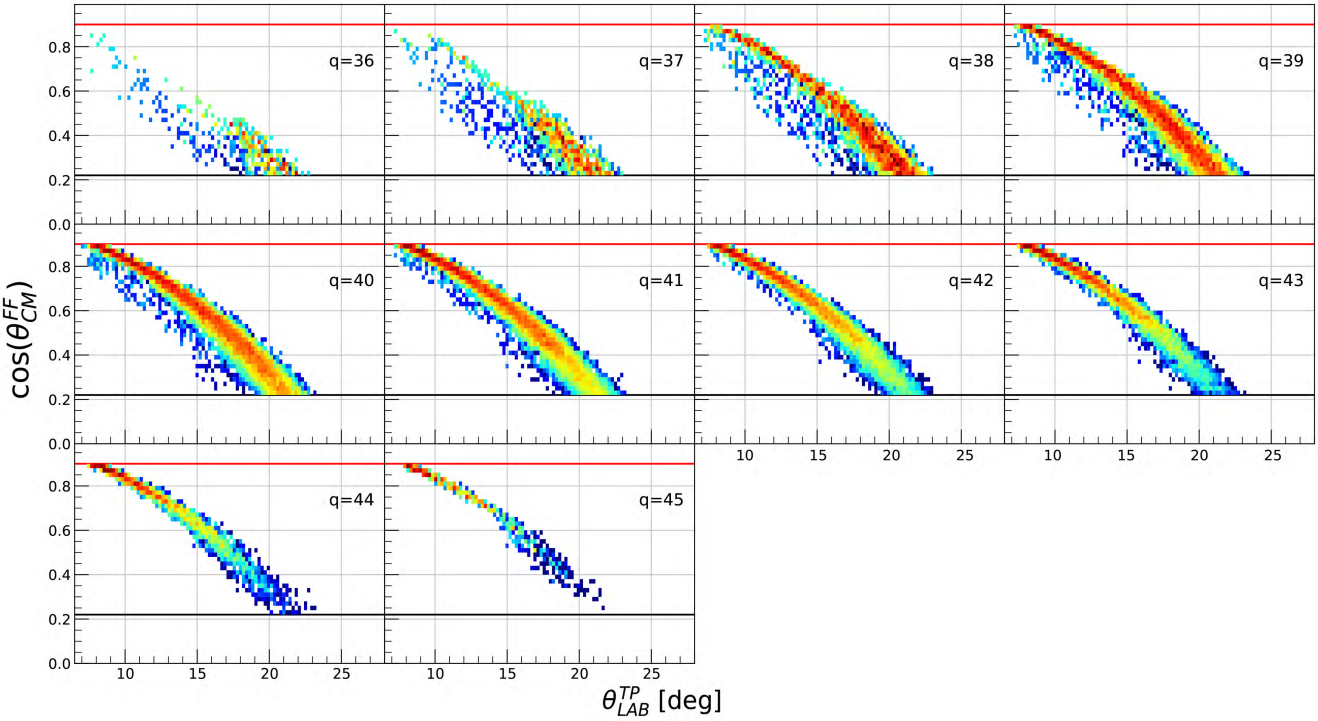

Figure 5.15: *The $\cos(\theta^{FF}_{CM})$ for fission fragment mass $A = 120$ is shown as a function of the θ^{TP}_{LAB} angle, for all charge states measured with the ^{27}Al target. The limits in $\cos(\theta^{FF}_{CM})$ distribution for each charge state are represented by the red and black lines.*

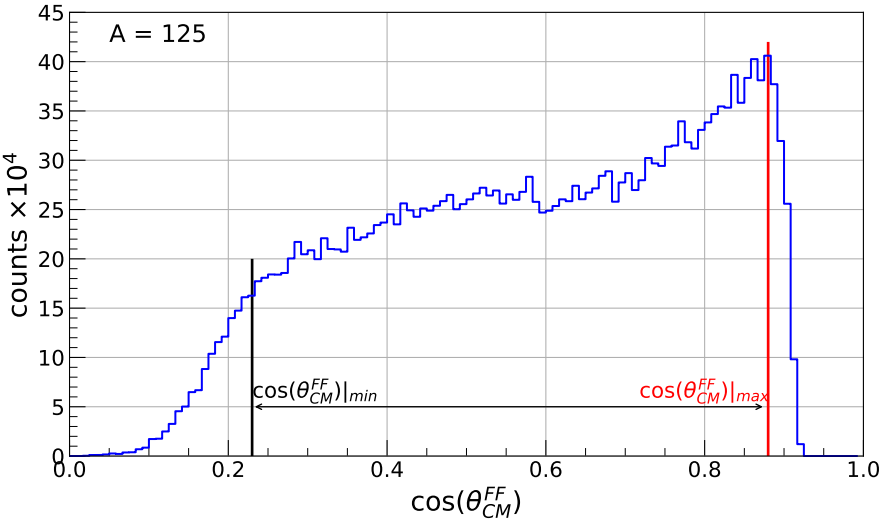

Figure 5.16: *The distribution of $\cos(\theta^{FF}_{CM})$ for fission fragments with $A = 125$ resulting from the $^{238}U + ^{27}Al$ reaction is shown. The vertical lines denote the limits of $\cos(\theta^{FF}_{CM})$ distribution which define the angular range where the charge state distribution is completely transmitted. This range is depicted by the black double arrow.*

Returning to the case of $A = 125$ with the ^{27}Al target (see Fig. 5.12), the limits for this mass are in $\cos(\theta^{FF}_{CM})$ can be depicted, with black and red lines denoting the minimum and maximum, respectively.

Having obtained the bounds on $\cos(\theta^{FF}_{CM})(A)$ distribution for each target (see Fig. 5.14), a comparison with the coverage in the previous measurement by Tōke *et al.* [65] can be done. In Fig. 5.17, the region coloured in red represents the measurement area of VAMOS++ in this experiment achieved with the aluminium target. The mass of the fission fragment on the x-axis is pre-neutron evaporation; therefore, this result is an approximation based on the neutron evaporation estimation in subsequent chapters. As observed, the measured region does not extend to the symmetry limit at $\theta_{CM} = 90°$, nor does it cover the entire quasi-fission region (see Section 1.4.1) for masses approximately $A \approx 180$ and larger. These aspects will be further discussed and analysed in the concluding chapters of this work.

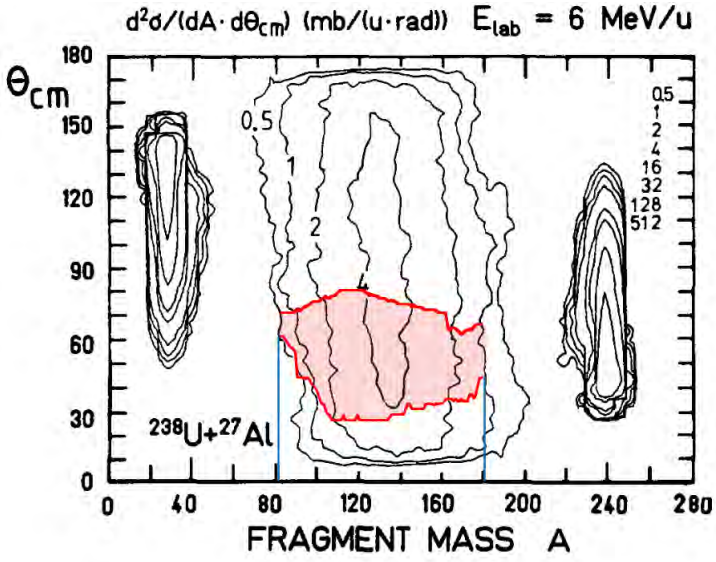

Figure 5.17: *The angle θ_{CM} [deg] versus fragment mass number A before neutron evaporation for the reaction of $^{238}U + ^{27}Al$. The VAMOS++ coverage is shown with the red shadowed region. The representation has been obtained and adapted with permission from [65] by adjusting the limits of Fig. 5.14 in the top panel. Copyright (1985) by the North-Holland Publishing Company.*

5.4 Fission fragment angular distribution

The fission fragment angular distribution is a crucial parameter in comprehending the fission mechanism, especially concerning the quantum properties of fissioning nuclei levels, particularly when examining energies close to the thresholds of various multiple-chance fission channels. In addition to its theoretical significance, the strong anisotropies observed near the thresholds of neutron emission before fission may also impact fission cross-section measurements due to limitations in detector angular coverage. Non-isotropic angular distribution of fission fragments was observed for the first time in 1952 [103] when studying the photofission of ^{232}Th where fission fragments emitted preferentially at 90° with respect to the γ-beam direction were found. Subsequent neutron-beam studies have also identified preferred emission directions for fission fragments. In these experiments, the evolution of the angular distribution with neutron energy is frequently measured using the anisotropy parameter. This parameter is defined as the ratio

between fission fragment yields measured at 0° and 90° with respect to the neutron beam direction.

In this work, the theory concerning the angular distribution of fission fragments, outlined in [104], is employed. This theory is founded on the model of axially symmetric transition states at the saddle point of the fissioning nucleus. The fissioning nucleus is conceptualised as a symmetrically spinning top, specifically a rigid body characterised by two equal moments of inertia distinct from the third one, as illustrated in Fig. 5.18. Throughout this theoretical framework, the total angular momentum vector $\vec{J}$ and its projection $\vec{M}$ onto the space-fixed z-axis (typically aligned with the beam direction) remain constant and are conserved throughout the entire fission process due to the principle of conservation of total angular momentum. Furthermore, the vector $\vec{K}$ is the projection of $\vec{J}$ onto the symmetry axis of the top, while $\vec{R}$ represents the projection of $\vec{J}$ onto any axis perpendicular to $\vec{K}$.

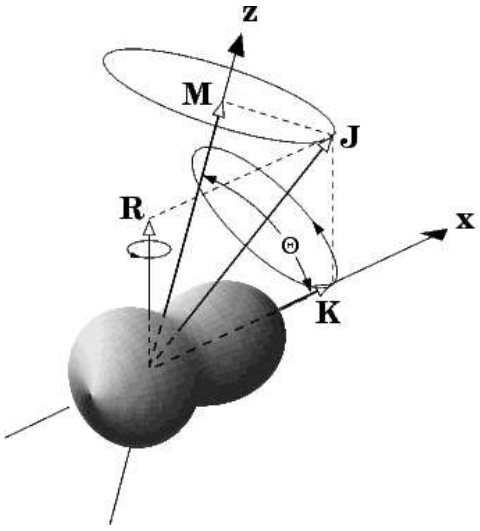

Figure 5.18: *The figure shows a typical fissioning system. $\vec{J}$ represents the total angular momentum of the compound nucleus. M, K, and R are the projections on the space-fixed z-axis, the symmetry axis of the compound nucleus, and an axis perpendicular to $\vec{K}$, respectively.*

In the fission process (see Section 1.3.1), the nucleus may experience vibrations and changes in shape, leading to a redistribution of energy and angular momentum. Consequently, the K value of the transition nucleus may not be directly linked to the initial K values of the compound nucleus. However, if K is assumed to remain a robust quantum parameter during the transition from the initial state of the nucleus to the configuration of separate fragments, the directional distribution of fission fragments resulting from a transition state with quantum numbers J, K, and M can be uniquely determined.

Fission does not exhibit isotropic emission, as previously discussed, but rather shows an angular distribution influenced by the initial conditions of the fissioning system. This distribution can be represented as a series of Legendre polynomials in terms of $\cos(\theta^{FF}_{CM})$, denoted as $W(\cos(\theta^{FF}_{CM}))$ (see Appendix A.2):

$$W(\cos(\theta^{FF}_{CM})) = \sum_{L=0}^{L_{max}} A_L P_L(\cos(\theta^{FF}_{CM}))\,. \tag{5.17}$$

The coefficients A_L and the order of the polynomial, denoted as L, are significant parameters in this context. In this specific physical scenario, only the even terms in $\cos(\theta^{FF}_{CM})$ were considered

due to the inherent backwards-forward symmetry of the emitted fragments. Considering only even terms and neglecting odd ones, the angular distribution can be reformulated as follows:

$$W(\theta^{FF}_{CM}) = A_0 \left[1 + \sum_{\substack{L=2 \\ L\,even}}^{L_{max}} A_L P_L(\cos(\theta^{FF}_{CM})) \right] . \tag{5.18}$$

In Fig. 5.19, various angular distributions of fission fragments are displayed for different combinations of quantum numbers J, K, and M with respect to the CM angle. As an example, fixing J and M while varying the projection K.

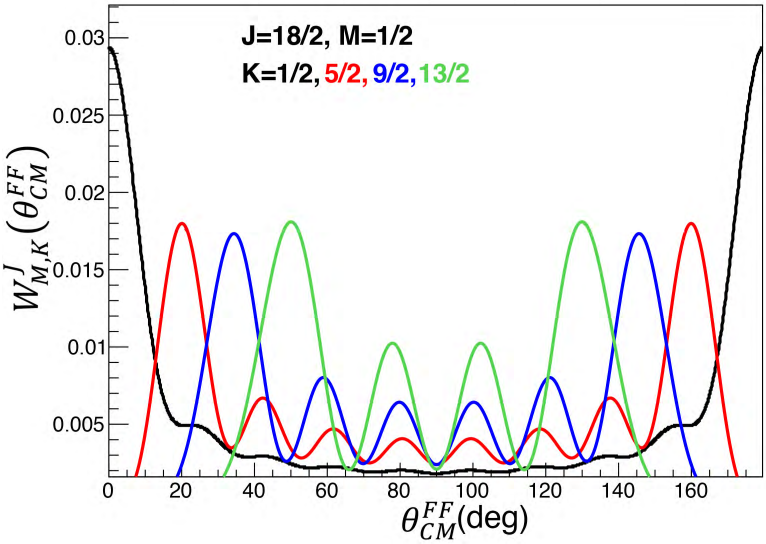

Figure 5.19: *Various angular distributions of fission fragments, $W^J_{M,K}(\theta^{FF}_{CM})$, are displayed for combinations of quantum numbers J, K, and M with respect to the angle θ^{FF}_{CM} [deg] in colours.*

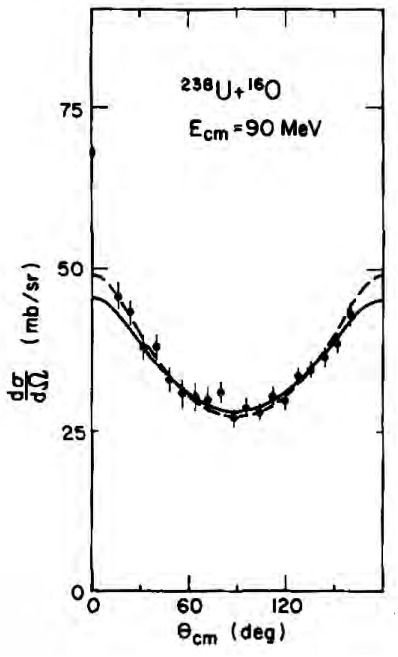

Figure 5.20: *Experimental angular distribution $W(\theta^{FF}_{CM})$ [mb/sr] versus the angle θ^{FF}_{CM} [deg] for the reaction $^{238}U + ^{16}O$ with energy $E_{CM} = 90$ MeV, fitted using a sum up to $L_{max} = 2$ in Eq. 5.18 with dashed line. Adapted with permission from [105]. Copyright (1984) by the American Physical Society.*

In Fig. 5.20, the fitting to the experimental data of the angular distribution $W(\theta_{CM}^{FF})$ with respect to the polar angle θ_{CM}^{FF} for the reaction ^{238}U + ^{16}O with energy E_{CM} = 90 MeV is presented. It is observed that the polynomial fitting (up to $L_{max} = 2$) by the equation above (see Eq. 5.18) reflects the behaviour of the distribution, considering a functional of the form $a + b \cdot \cos^2(\theta_{CM}^{FF})$.

The anisotropy parameter is customarily used to characterise the behaviour of the fission fragment angular distribution and it is defined as:

$$A_{ny} = \frac{W(0°)}{W(90°)}\,, \tag{5.19}$$

where $W(0°)$ and $W(90°)$ represent the number of fission fragments emitted at 0° and at 90°. By inserting Eq. 5.18 in this expression, and evaluating the different Legendre polynomials, given in Appendix A.2, at 0° and 90°, the following analytical expression for the anisotropy parameter A_{ny} is obtained:

$$A_{ny} = \frac{W(0°)}{W(90°)} = \frac{1 + A_2 + A_4 + A_6 + ...}{1 - \frac{1}{2}A_2 + \frac{3}{8}A_4 - \frac{5}{16}A_6 + ...}\,. \tag{5.20}$$

This expression shows how the anisotropy parameter depends only on the coefficients A_2, A_4, and A_6, given by the fits to the cosine distributions described in the previous section. This equation works for any L_{max} simply by making equal to zero the coefficients A_L of higher order than L_{max}. The anisotropy parameter itself only provides information on the ratio of the number of fragments emitted at 0° and 90°, while the behaviour at intermediate angles remains hidden. Despite this limitation, a value different from one implies an anisotropic behaviour.

USC UNIVERSIDADE DE SANTIAGO DE COMPOSTELA

USC
UNIVERSIDADE
DE SANTIAGO
DE COMPOSTELA

Chapter 6

Calculation of fission yields and fragments velocities

This chapter provides the procedures used for calculating the fission-fragment isotopic yields of the ^{265}Db and ^{249}Bk fissioning systems. It encompasses various steps, starting with the definition and the subsequent calculation using the previous VAMOS++ acceptance, and it delves into the intrinsic efficiency. Finally, the evaluation of fission fragment velocities is presented.

6.1 Fission-fragment yield definition

The isotopic identification of fission fragments enables the calculation of *fission-fragment isotopic yields* $Y(Z,A)$. These yields represent the probability that a specific fragment (Z,A) is produced in a fission event. The fission-fragment isotopic yield distribution, which can be derived from the isotopic cross-section $\sigma(Z,A)$ as:

$$Y(Z,A) = 200 \cdot \frac{\sigma(Z,A)}{\sum\limits_{Z,A} \sigma(Z,A)} \,. \tag{6.1}$$

The number of measurements of a particular fragment, $N(Z,A)$ is related to the cross-section:

$$N(Z,A) = \sigma(Z,A) \cdot N_{target} \cdot N_{beam} \cdot \mathcal{E}_{tot} \,, \tag{6.2}$$

where N_{target} and N_{beam} are the number of nuclei in the target and in the beam, respectively. The efficiency splits into:

$$\mathcal{E}_{tot} = \mathcal{A}_g^{FF} \cdot \mathcal{E}_i^{FF} \cdot \mathcal{E}_\tau \,. \tag{6.3}$$

The subindex g represents the geometric efficiency (see Eq. 5.2), while the subindex i represents the intrinsic efficiency. The subindex τ denotes the dead time of the acquisition system, which can be considered $\mathcal{E}_\tau \approx 1$ in this case due to the fast acquisition system with a time scale of tens of kHz, and the low rate of the experiment, approximately 400 Hz.

Consequently, the fission-fragment isotopic yields, $Y(Z,A)$, are computed by considering the event counts for each isotope detected during the experiment and adjusting them to account for the geometric and intrinsic efficiency of the fission fragment identification detectors.

USC UNIVERSIDADE DE SANTIAGO DE COMPOSTELA

$$Y(Z,A) = 200 \cdot \frac{N(Z,A)}{\mathcal{A}_g^{FF} \cdot \mathcal{E}_i^{FF}} \cdot \left(\sum_{Z,A} \frac{N(Z,A)}{\mathcal{A}_g^{FF}(Z,A) \cdot \mathcal{E}_i^{FF}(Z,A)} \right)^{-1} . \tag{6.4}$$

The *mass number fission yields*, $Y(A)$, and *atomic number fission yields* or *elemental yields*, $Y(Z)$, are directly derived from the fission-fragment isotopic yields:

$$Y(A) = \sum_{Z} Y(Z, A)\,, \tag{6.5}$$

$$Y(Z) = \sum_{A} Y(Z, A)\,, \tag{6.6}$$

The calculation of $\mathcal{A}_g^{FF}$, as detailed in Section 5.3.1, relies on the specific production of each fissioning system. In Section 2.7, the identification of each fissioning system and the reconstruction of its excitation energy are discussed. Additionally, the fissioning system reference frame, where the fission fragment distribution is independent of the reaction kinematics, is presented in Section 2.7. Further clarification on the determination of $\mathcal{A}_g^{FF}$, governed by the VAMOS++ acceptance, is provided in Section 5.1. Furthermore, the contribution of different charge states to the total number of events for each isotope, after correcting for $\mathcal{A}_g^{FF}$, is detailed in Section 5.2. Finally, the detection efficiency at the focal plane of VAMOS++ and the MWPCs Start detector efficiency, collectively referred to as $\mathcal{E}_i^{FF}$, are discussed in Section 6.3.

6.2 Charge-states addition and setting merging

The production of a specific charge state is affected by the fragment velocity in the laboratory reference frame, where higher velocities correspond to higher charge states due to fewer electrons remaining in the fragment. The fragment velocity is determined by its polar angle and its velocity in the centre-of-mass reference frame. The production of each charge state is confined to a specified range of velocities, which corresponds to an angular range in θ_{CM}^{FF}; in other words, the θ_{CM}^{FF} angular distribution of each fragment is composed of contributions from various charge states. The number of events of a given isotope necessary to calculate the isotopic fission-fragment yields $Y(Z, A)$ is computed as the integral of the corresponding $\cos(\theta_{CM}^{FF})$ distribution:

$$N(Z, A) = \int_{-1}^{+1} \frac{dN(Z, A)}{d(\cos(\theta_{CM}^{FF}))} \cdot d(\cos(\theta_{CM}^{FF}))\,. \tag{6.7}$$

The number of fission events per unit of $\cos(\theta_{CM}^{FF})$ of a specific isotope is calculated by summing the distributions of different charge states:

$$\frac{dN(Z, A)}{d(\cos(\theta_{CM}^{FF}))} = \sum_{q_{min}(A)}^{q_{max}(A)} \frac{dN(Z, A, q)}{d(\cos(\theta_{CM}^{FF}))}\,. \tag{6.8}$$

The angular distribution of a specific charge state of a selected isotope is obtained by merging the two VAMOS++ settings, $(14°, 21.5°)$. The merge process involves selecting the envelope of the maximum number of counts per bin of $\cos(\theta_{CM}^{FF})$ distribution after applying normalisation and weighting to the acceptance of the settings (see Section 5.2). An overlap exists between the limits of $\cos(\theta_{CM}^{FF})$ for each charge state in both settings, as exemplified in Fig. 6.1 for $q = 43^+$ and the ^{125}Te isotope. The 21.5° setting is represented in red, the 14° setting is in blue, and the envelope is depicted in dark blue.

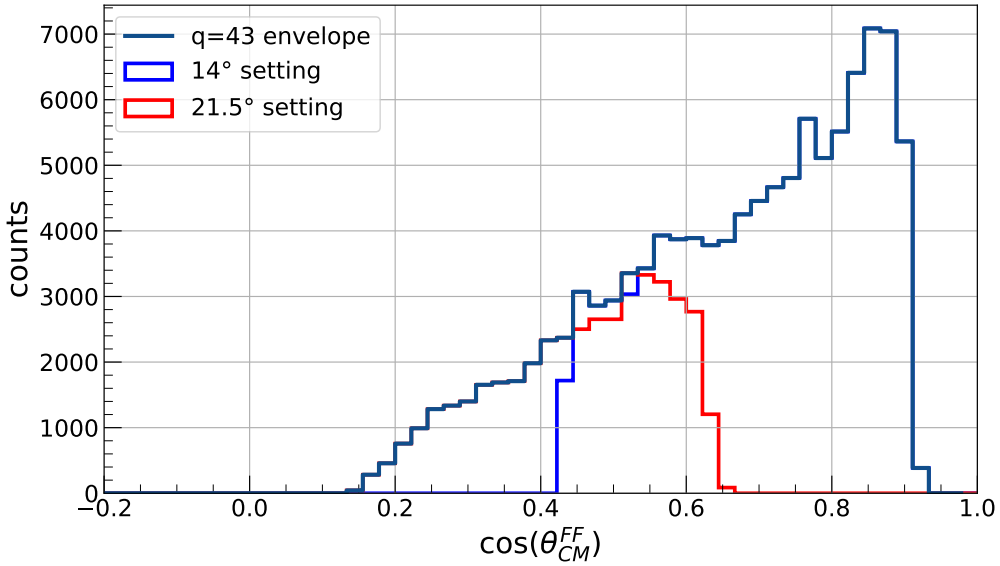

Figure 6.1: *The enveloped* $\cos(\theta^{FF}_{CM})$ *distribution for* $^{125}Te^{43+}$ *is shown in dark blue. This distribution is obtained by combining the contributions from both VAMOS++ settings. The two settings are represented in blue and red, respectively.*

Each of the charge state distributions for the isotope ^{125}Te at various $\cos(\theta^{FF}_{CM})$ angles is considered. By combining the individual charge-state contributions from both settings for each charge state (see Fig. 6.1), the complete set of individual charge-state distributions is obtained. This is depicted using different colours for the illustrative case of ^{125}Te in Fig. 6.2.

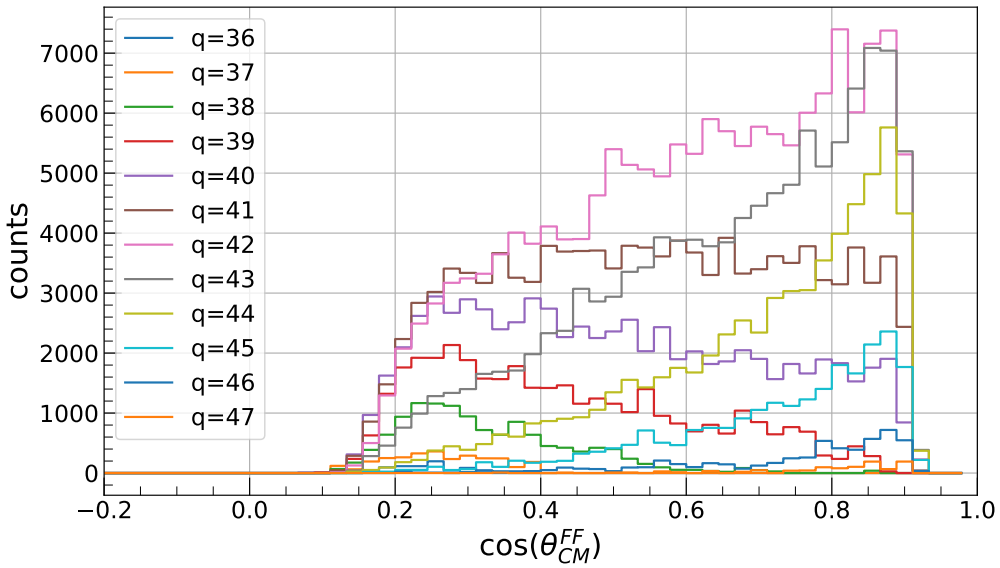

Figure 6.2: *The* $\cos(\theta^{FF}_{CM})$ *distribution for each charge-stated of* ^{125}Te *are represented in different colours. Charge states from* $q = 36$ *to* $q = 47$ *are shown.*

The final $\cos(\theta^{FF}_{CM})$ distribution of ^{125}Te, obtained by adding the individual charge-state contributions, is presented in black in Fig. 6.3. However, the angular range of θ^{FF}_{CM} is limited for specific charge states due to the acceptance of VAMOS++ (see Chapter 5), resulting in a reduction of the detected fragments per unit of θ^{FF}_{CM}. Consequently, the distributions in $\cos(\theta^{FF}_{CM})$ do not cover the entire integration range of $[-1, +1]$ in the Eq. 6.7. These distributions lie within the limits described earlier in Section 5.3.1, as clearly shown in Fig. 6.3.

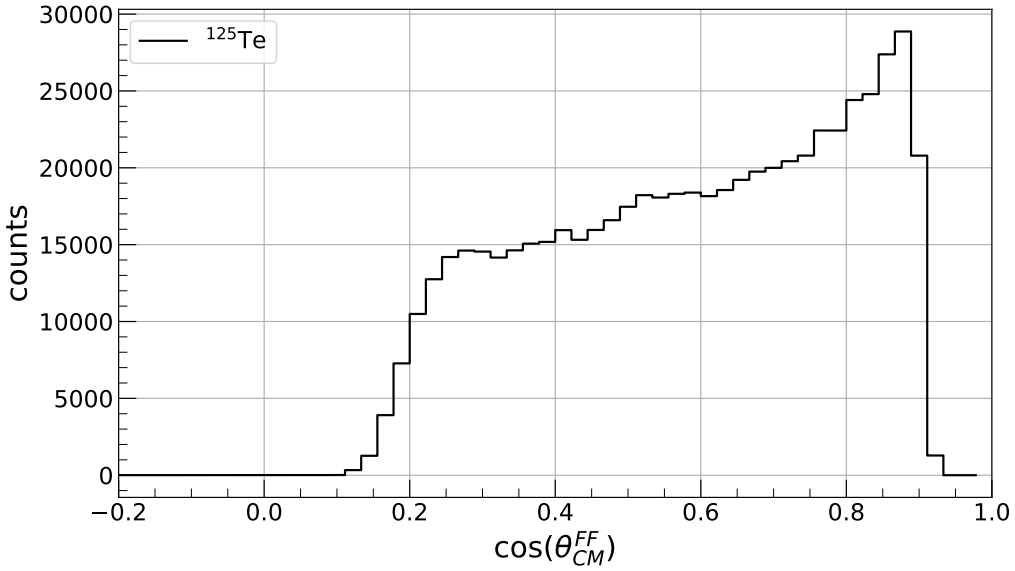

Figure 6.3: *The final* $\cos(\theta^{FF}_{CM})$ *distribution for* ^{125}*Te, obtained by combining the individual contributions from charge states* $q = 36$ *to* $q = 47$*, is shown in black.*

Hence, it is necessary to establish, for all fusion-induced fission events, a way to isotopically obtain the total counts $N(Z, A)$ for each measured isotope. In a proper approximation, the angular distributions, as previously shown in Fig. 5.20, follow a functional form: $a + b \cdot \cos^2(\theta^{FF}_{CM})$. Therefore, an isotopically fitting procedure is performed within the limits of $\cos(\theta^{FF}_{CM})$ taking into account the summing of the charge state envelopes (see Section 5.3.1). Thus, the following relationship is applied:

$$\frac{dN(Z,A)}{d\cos(\theta^{FF}_{CM})} = a + b \cdot \cos^2(\theta^{FF}_{CM}) \tag{6.9}$$

As discussed, the parameters a and b are determined through a fitting procedure over the sum of the envelopes of the charge states. In Fig. 6.4, the fitted function for the angular distribution of ^{125}Te is displayed. The red line represents the region where the fit was performed, defined by the $\cos(\theta^{FF}_{CM})$ limits discussed in Section 5.3.1. The resulting fit function with the functional form $a + b \cdot \cos^2(\theta^{FF}_{CM})$ is represented by a blue line. The integral of this function between [-1,1] is computed to recover the portion of the distribution that was cut by the VAMOS++ acceptance. This process allows estimating the total number of fission fragments by correcting the VAMOS++ angular acceptance.

USC
UNIVERSIDADE DE SANTIAGO DE COMPOSTELA

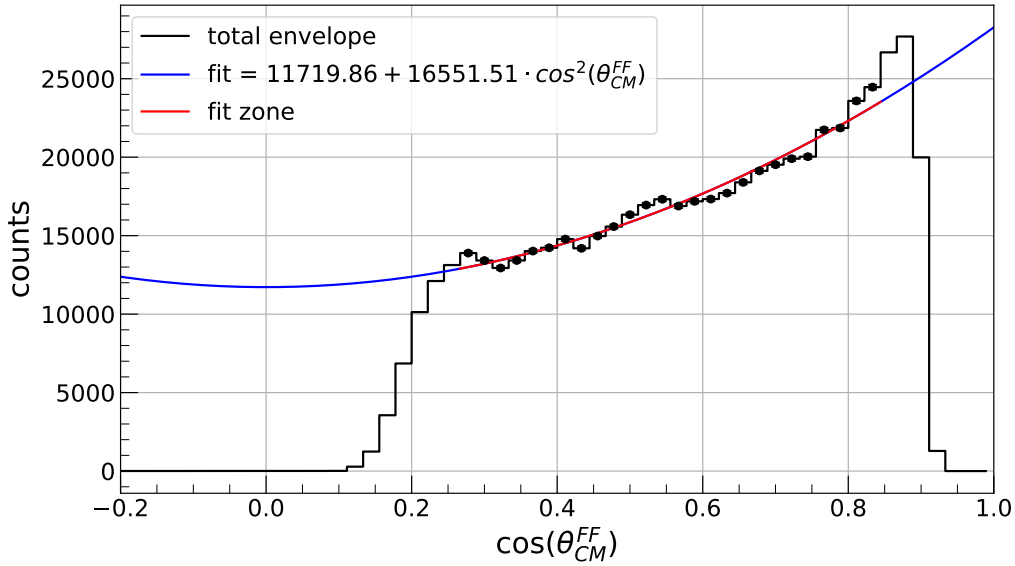

Figure 6.4: *The* $\cos(\theta_{CM}^{FF})$ *distribution for* ^{125}*Te is depicted. The red line corresponds to the region where the fitting procedure is applied to determine the parameters a and b in Eq. 6.9. The blue line represents the resulting function,* $a + b \cdot \cos^2(\theta_{CM}^{FF})$*, from the fit.*

6.3 Intrinsic efficiency

The intrinsic efficiency of fission fragment detection denoted as $\mathcal{E}_i^{FF}$, is determined by the probability of achieving isotopic identification for each fission fragment that reaches the final detector in the VAMOS++ focal plane setup. This efficiency can be divided into various contributions, each corresponding to the specific detector involved in the process:

$$\mathcal{E}_i^{FF} = \mathcal{E}_i^{DC} \cdot \mathcal{E}_i^{trigger} \cdot \mathcal{E}_i^{IC} \,. \tag{6.10}$$

Here, $\mathcal{E}_i^{DC}$ represents the intrinsic efficiency of the Drift Chamber, while $\mathcal{E}_i^{trigger}$ signifies the intrinsic efficiency of the detectors associated with the VAMOS++ trigger, specifically the MWPCs at the target position and the MWPPAC at the focal plane. In general, the intrinsic efficiency of the trigger ($\mathcal{E}_i^{trigger}$) depends on the number of electrons emitted in the detector, which is proportional to the energy loss within the filling gas. According to the Bethe-Bloch equation, $\mathcal{E}_i^{trigger}$ is then approximately proportional to $(Z/v)^2$. In Section 6.6 this efficiency is estimated and applied.

Finally, the efficiency of the IC is assumed as the reference, and defined as $\mathcal{E}_i^{IC} = 1$.

6.3.1 Drift Chamber intrinsic efficiency

The intrinsic efficiency of the drift chamber, $\mathcal{E}_i^{DC}$ is influenced by the energy loss of fission fragments inside the chamber. Small energy losses result in lower ionisation and few electrons are released, leading to lower signal amplitudes induced in the wires. If the amplitudes of these signals are small enough, they would be rejected in the discrimination modules along with the electronic noise. To estimate the fission fragment energy loss in the DC, the energy loss in the first row of the ionisation chamber ($dEIC[0]$) is used, as explained in Section 2.9:

$$\mathcal{E}_i^{DC} = function(\Delta E^{DC}) = function(dEIC[0]) \,. \tag{6.11}$$

A strong correlation exists between the energy loss in the Ionisation Chamber (IC) and the Drift Chamber (DC). Employing this correlation, the intrinsic efficiency of the DC, $\mathcal{E}_i^{DC}$, can be determined by dividing the number of events registered simultaneously in both chambers, $N_{DC\&IC}$, by the number of events registered solely in the IC, N_{IC}:

$$\mathcal{E}_i^{DC}(dEIC[0]) = \frac{N_{DC\&IC}}{N_{IC}}(dEIC[0])\,. \tag{6.12}$$

To calculate $\mathcal{E}_i^{DC}$, a plot is generated by varying $dEIC[0]$ over a range of energy values. Subsequently, the final Drift Chamber efficiency is determined through linear interpolating of this set of points. This procedure is independently applied to each of the two VAMOS++ settings.

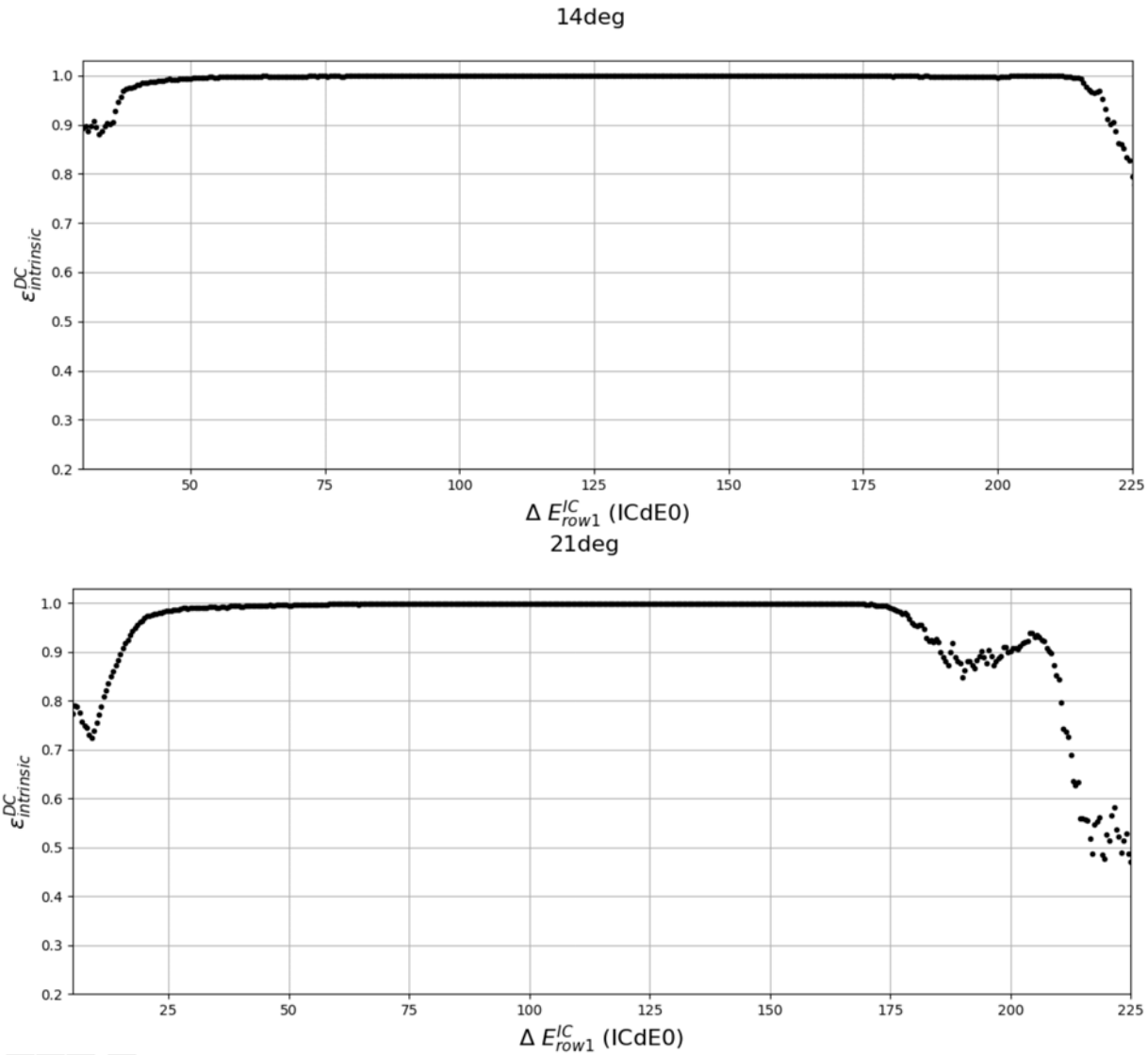

Figure 6.5: *The intrinsic efficiency of the Drift Chamber $\mathcal{E}_i^{DC}$ [MeV] is determined at discrete energy loss points in the first row of the Ionisation Chamber (dEIC[0]) for two VAMOS++ settings:* 14° *(top) and* 21.5° *(bottom). The red lines represent the boundaries where the intrinsic efficiency reaches 1, indicating the limited zone with good events.*

The resulting plot in Fig. 6.5 demonstrates that a $\mathcal{E}_i^{DC}$ value of approximately 1 is achieved in the central energy zone. However, events falling outside the energy limits, specifically $14° \rightarrow [50, 213]$ MeV and $21.5° \rightarrow [45, 177]$ MeV, are excluded from this analysis as they are

considered erroneous events due to the conditions of the border chambers. These limits are associated with the operating conditions of an IC as it is a gaseous detector and therefore exhibits different working regions based on the so-called ion pair charge collection.

For low energies deposited the fission fragments do not generate sufficient electrons in the DC and/or enough electrons do not reach the DC pads. In other words, there is a low charge collection region associated with low ion energy, leading to small generated charges. Thereby reducing intrinsic efficiency.
For high energies deposited the fission fragments generate a sufficient quantity of electrons in the DC, leading to saturation in the measurement pads of the DC. That is, the collection wires on the DC pads are unable to collect all the electrons, resulting in saturation and a region of non-linearity between charges and deposited energy. This reduction in intrinsic efficiency is observed.

To verify the absence of event loss of the IC efficiency concerning the fission fragments reaching the focal plane, the spatial coordinate X_{FP} [mm] of the Multi-Wire chamber MWPPAC is plotted against the energy deposited in the first row of the IC, $dEIC[0]$ [MeV], in Fig. 6.6. To mitigate angular dependencies, fission fragments with an angular aperture $\theta_{FP} = \pm 1$ deg are selected those entering perpendicular to the focal plane of VAMOS++. As observed in Fig. 6.6, discontinuities occur only at the locations of the structural brackets of the entrance window of Multi-Wire chamber MWPPAC, which is expected. There are no discontinuities between the pads on the x-axis of the chamber, displaying a smooth, continuous, and homogeneous distribution of fission fragments. The black lines indicate the positions of some measurement pads on the chamber as examples.

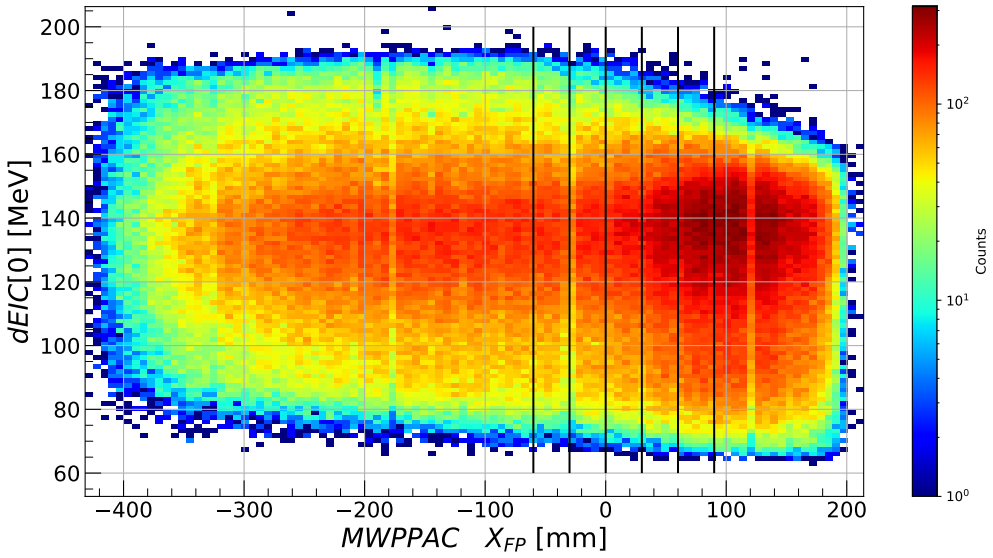

Figure 6.6: *The representation of the spatial coordinate X_{FP} [mm] of the Multi-Wire chamber MWPPAC and the energy deposited in the first row of the Ionisation Chamber ($dEIC[0]$) [MeV]. Fission fragments with an angular aperture $\theta_{FP} = \pm 1$ deg (entering perpendicularly to the VAMOS++ focal plane) are selected. The smooth and continuous distribution of fission fragments between the pads on the x-axis of the chamber is evident. Black lines represent the positions of selected measurement pads on the chamber.*

6.4 Contamination study with aluminium target

As explained in Section 6.1, the calculation of isotopic fission-fragment yields, $Y(Z, A)$, is performed through a procedure that accounts for all charge states of a specific isotope (Z, A). Therefore, the number of events for a specific isotope is determined by integrating the corresponding $\cos(\theta_{CM}^{FF})$ distribution, as discussed in Section 6.2. The geometrical efficiency $\mathcal{E}_g^{FF}$ encompasses the acceptance in azimuthal and polar angles. The intrinsic efficiency $\mathcal{E}_i^{FF}$ includes three contributions (see Eq. 6.10). Nevertheless, an important aspect that is not taken into account in this process so far is the contamination that still exists even when restricted to fusion-induced fission triggers as explained in Section 2.5.

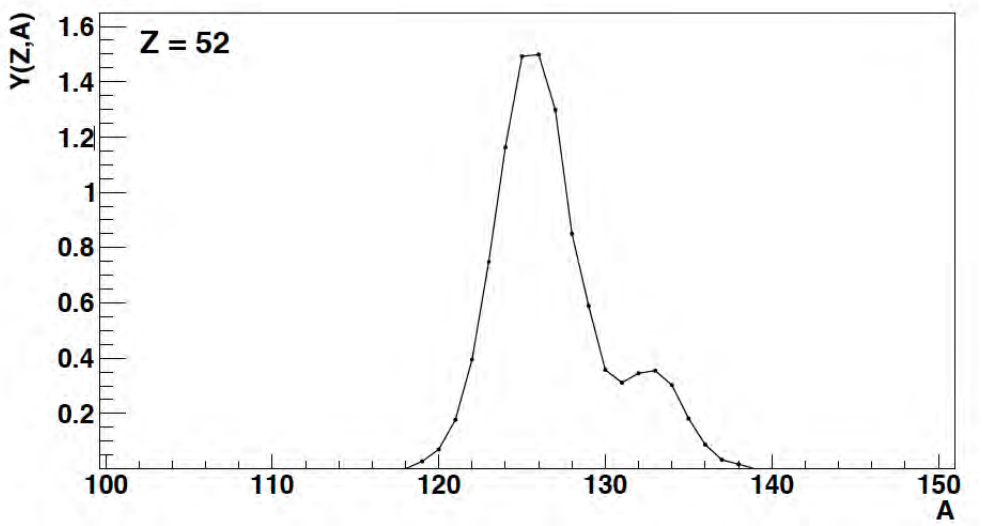

Figure 6.7: *The figure displays the isotopic fission yields of ^{265}Db for nuclear charge $Z = 52$ as a function of fragment mass number A. These yields are determined by exclusively considering fusion-induced fission events. The primary peak corresponds to fusion-induced fission events, while the secondary peak represents contamination from other sources.*

The isotopic fission yields of ^{265}Db for fragments with nuclear charge $Z = 52$ are presented in Fig. 6.7 as a function of the mass number. These yields are obtained by exclusively selecting fusion-induced fission triggers. While the yield distribution for a specific reaction mechanism is expected to exhibit an approximated Gaussian shape, a secondary smaller Gaussian peak emerges on the right side of the main distribution. This additional peak is attributed to contamination from other reaction channels, such as transfer- or inelastic scattering-induced fission. When a transfer- or inelastic-scattering-fission reaction occurs, and the target-like particle is not detected by SPIDER while the corresponding fission fragment is measured at the VAMOS++ focal plane, the event is erroneously identified as fusion-induced fission.

A calculation of the neutron excess (N/Z) of the two peaks confirms the presence of contamination. The neutron excess for the fissioning system ^{265}Db is calculated as follows: $N/Z = (262.7/105) - 1 = 1.50$, assuming the estimation of GEF model of 2.3 pre-saddle evaporated neutrons and no proton emission (see in the next chapter the Section 7.9.1 with Tab. 7.3). However, the main peak in Fig. 6.7 shows an $N/Z \approx 1.42$, while the smaller peak shows a higher $N/Z \approx 1.56$. This difference in neutron excess, which is above the fissioning system case and since at high excitation energy there is no charge polarisation (see the ^{250}Cf fissioning system with E^*_{FS}=46 MeV in [106]), supports the nature of the contamination. Fragments with

a fixed Z originating from transfer fission generally exhibit a higher neutron excess compared to those produced by the fusion-induced fission mechanism. Additional evidence supporting the identification of the contamination is obtained by examining the velocity distribution of the fragments (see Section 6.9).

As introduced earlier, due to the different kinematics of transfer reactions compared to fusion-induced fission events, it is possible to determine the number of measured contamination events that interfere with the fission events of the ^{265}Db fissioning system, allowing for partial separation of the two processes. As a recoil nucleus exists in transfer reactions, the centre-of-mass of the fissioning system has a different velocity in each reaction, resulting in a change in the angle θ^{FF}_{CM} in the centre-of-mass reference frame and causing a change in the fragment velocity in the centre-of-mass reference frame $\vec{v}^{FF}_{CM}$.

In the fusion-induced fission reactions of the fissioning system ^{265}Db, it is possible to observe contamination events in the (v^{FF}_{CM}, A) space along with fusion-fission events. By selecting the VAMOS++ trigger and the SPIDER trigger (see Section 2.5), the Fig. 6.8(left) and Fig. 6.8(right) respectively are obtained for the same nuclear charge $Z = 52$.

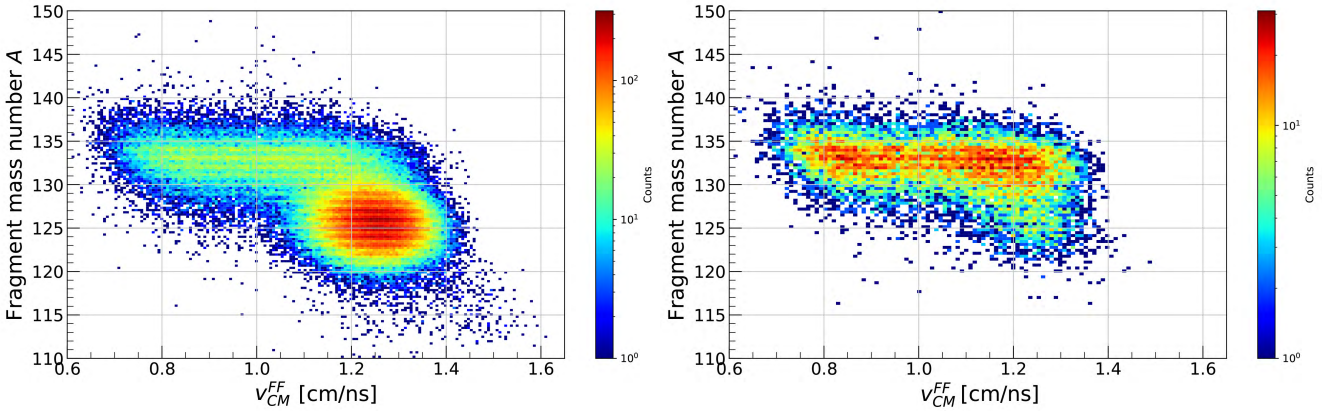

Figure 6.8: *The (v^{FF}_{CM}, A) space of fission fragments from the fissioning system ^{265}Db is shown on the right, while the left panel displays the selected transfer events with SPIDER. Both panels correspond to* 14° *and* $Z = 52$.

The displacement of N/Z and a broader velocity distribution v^{FF}_{CM} for different fragment mass number A allows for the differentiation of both reactions in each set of VAMOS++ and for each fragment element. As shown in Fig. 6.8(left), the fusion-induced fission events are localised in a two-dimensional Gaussian distribution in the (v^{FF}_{CM}, A) space, with contamination separated (see Fig. 6.9(left) for clarify). Conversely, when selecting the trigger for transfer events, contamination from fusion-induced fission events is also present Fig. 6.8(right) (see Fig. 6.9(right) for clarify).

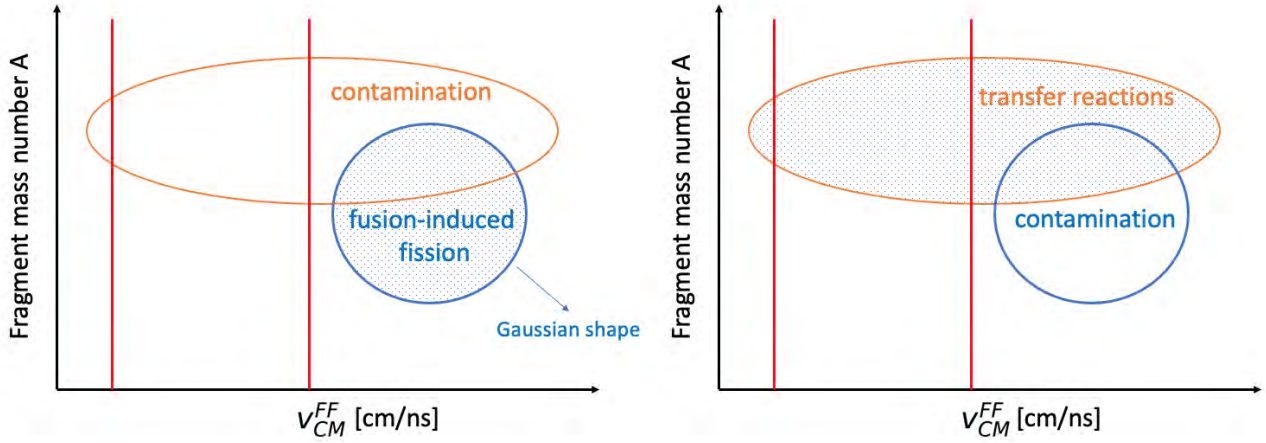

Figure 6.9: *The scheme of (v_{CM}^{FF}, A) space of fission fragments from the fusion-induced fission is shown on the right, while the left panel displays the selected transfer events scheme. The red lines schematically depict a region where reactions such as transfer can be evaluated as contamination of fusion-induced fission events.*

This separation between reaction channels enables the evaluation of contamination factors for the 14° and 21.5° settings for the aluminium target, $\mathcal{C}_{14^\circ}$ and $\mathcal{C}_{21.5^\circ}$, respectively. With these factors, the correct amount of contamination can be subtracted from the fusion-induced fission counts, as follows:

$$Env^{final} = Env^{FuFi}\left(\#(\cos(\theta_{CM}^{FF}))\right) - Env^{Cont}\left(\#(\cos(\theta_{CM}^{FF}))_{14^\circ} \cdot \mathcal{C}_{14^\circ}\,,\, \#(\cos(\theta_{CM}^{FF}))_{21.5^\circ} \cdot \mathcal{C}_{21.5^\circ}\right), \tag{6.13}$$

where Env corresponds to the envelope of the 14° and 21.5° settings for both separately selected fusion-induced fission events Env^{FuFi} and transfer events (contamination in this case) Env^{Cont}, both envelopes are evaluated with the process explained in Section 6.2, with $\#(\cos(\theta_{CM}^{FF}))$ representing the number of counts in the distribution. Env^{final} is the final envelope for each isotope (Z, A).

To evaluate the contamination factors, a window is defined in (v_{CM}^{FF}, A) space that excludes fusion-induced fission events (see red lines in Fig. 6.9). The ratio is then calculated between the distribution obtained using the VAMOS++ trigger and the SPIDER trigger for events within this window. In other words, a factor is sought for each Z such that, when multiplied within the selected window in Fig. 6.9(right), it subtracts the selected window in Fig. 6.9(left), being the window fixed. This approach allows for the elimination of contamination from fusion-induced fission events by multiplying transfer production with this factor. The procedure is carried out for each Z and for both settings separately, involving a factor for 14° that multiplies the production of contamination and a factor for 21.5° that multiplies the production of contamination before constructing the envelope of both settings.

As the width of the selection window varies for each Z, ten windows with different widths are taken into account for each Z, and the average value for the contamination factor is determined in each setting, considering that contamination is not always as well separated as observed in Fig. 6.8. The contamination factors for the aluminium target are presented in Fig. 6.10. The colour bands indicate the standard deviation of the factor distribution due to the ten windows evaluation for that specific Z.

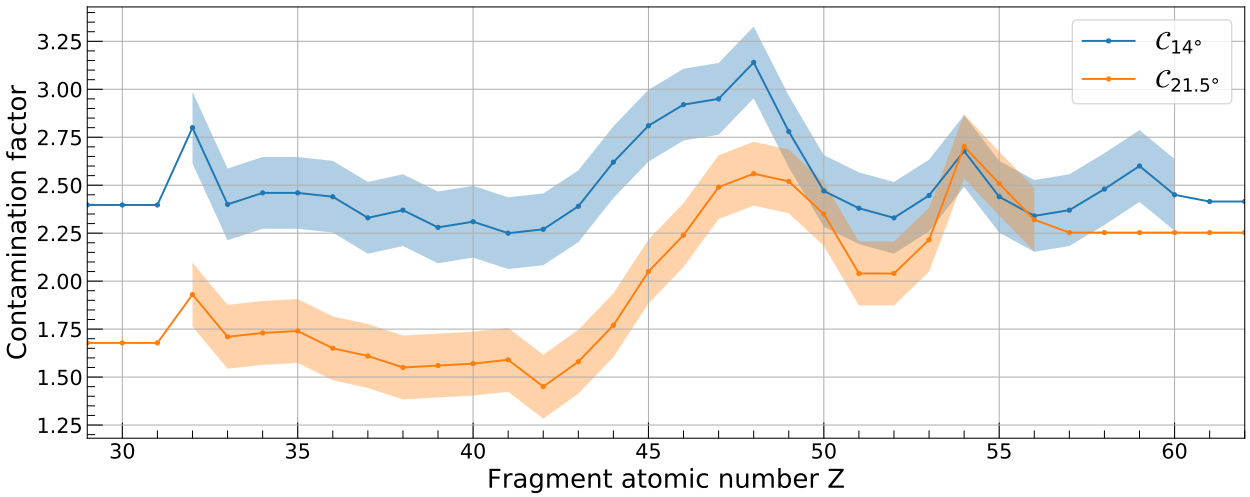

Figure 6.10: *Contamination factor evaluated for the aluminium target for each Z and for both VAMOS++ settings, 14° and 21.5°, shown in blue and orange, respectively. The colour bands represent the standard deviation of the factor for each Z.*

For very light or very heavy nuclear charges in both settings, where no contamination factor is available, the average value of nearby contamination factor values is applied.

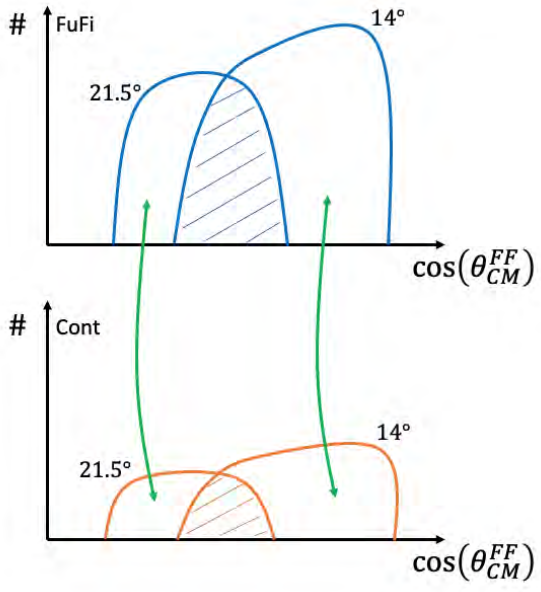

Figure 6.11: *A schematic representation of the $\cos(\theta_{CM}^{FF})$ distribution for each 14° and 21.5° settings is shown in the case of fusion-induced fission event selection (upper axes) and in the case of contamination event selection (lower axes), for an isotopic selection (Z, A). The overlapping regions between settings are indicated in both cases.*

As shown in Eq. 6.13. There are two contamination factors, $\mathcal{C}_{14°}$ and $\mathcal{C}_{21.5°}$, which had to be evaluated separately for each setting and each Z. This separation is necessary to maintain the proportionality in the contamination subtraction before generating the envelope between each setting and between fusion-induced fission and contamination events (see Fig. 6.11 and green arrows). After the envelope generation, the subtracted proportion would not remain the same due to the distinct behaviour in the common intermediate zone (hatched area in Fig. 6.11)

of overlap. In other words, the correct contamination proportion is not maintained if the contamination factor is evaluated directly on envelopes instead of settings. Ultimately, there is a global contamination factor dependent on Z, which is a function of the treatment applied by the envelope for each isotope (Z, A). This factor will depend on $\mathcal{C}_{14^\circ}$ and $\mathcal{C}_{21.5^\circ}$.

The contamination factors of each setting have different values due to the weight that each setting has on the isotope measured data (see Fig. 5.13), where the 21° setting dominates at low masses and the 14° setting dominates at high masses. Specifically, the 21° setting predominates at lower masses, while the 14° setting dominates at higher masses. Due to that, the fission fragments measured in VAMOS++ are setting-dependent, and consequently, the recoils measured in SPIDER used to assess the contamination factor are associated with them, yielding similar but different factors.

Behaviour in the bulge of the contamination factors ($Z \in [45 \rightarrow 50]$) observed in Fig. 6.10 is directly explained by the geometry of SPIDER (see Section 2.3.2). With SPIDER, only a spatial distribution of possible transfer reactions is measured (see Tab. 2.3). This occurs due to the cross-sections for specific regions of recoil excitation energy being greater within specific angular regions, such as $\theta_{LAB} \in [30°, 45°]$. In this particular region, nuclei with very high and very low excitation energy are excluded, respectively, at the specified limits. This results in a higher contamination factor for intermediate Z values, as the transfer yield distribution is asymmetric.

6.5 Contamination study with boron target

Unlike the previous case with the fissioning system ^{265}Db, the contamination factors for the fissioning system ^{249}Bk cannot be evaluated in the same way. This is because the contamination is concentrated behind the fusion-induced fission distribution in the (v_{CM}^{FF}, A) space, both for the VAMOS++ settings of 14° and 21.5°. As can be observed in Fig. 6.12, there is a big overlap between fusion-induced fission events and its contamination.

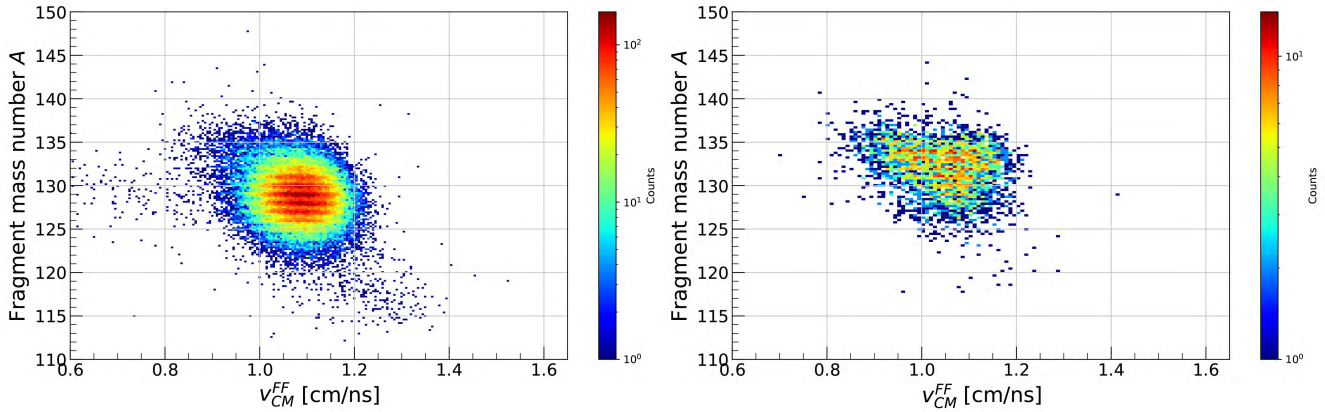

Figure 6.12: *The (v_{CM}^{FF}, A) space of fission fragments from the fissioning system ^{249}Bk is shown on the right, while the left panel displays the selected transfer events with SPIDER. Both panels correspond to* 14° *and* $Z = 52$.

The entire process of obtaining contamination factors for the boron target is outlined in the following Section 6.6, as it will be necessary to utilise the elemental yields within the process. In summary, the contamination factors ^{249}Bk for each Z are determined by employing both

the fusion-induced fission elemental yields and the contamination elemental yields, calculated separately following the procedure detailed in Section 6.2. The selection is made based on the VAMOS++ trigger and the SPIDER trigger (see Section 2.5). An initial common contamination factor for both settings is obtained using an iterative method aimed at minimising the detection efficiency. This initial contamination factor is then subjected to smoothing and a search for symmetrisation in the elemental yields. The resulting contamination factor for the boron target can be observed in the subsequent Fig. 6.13.

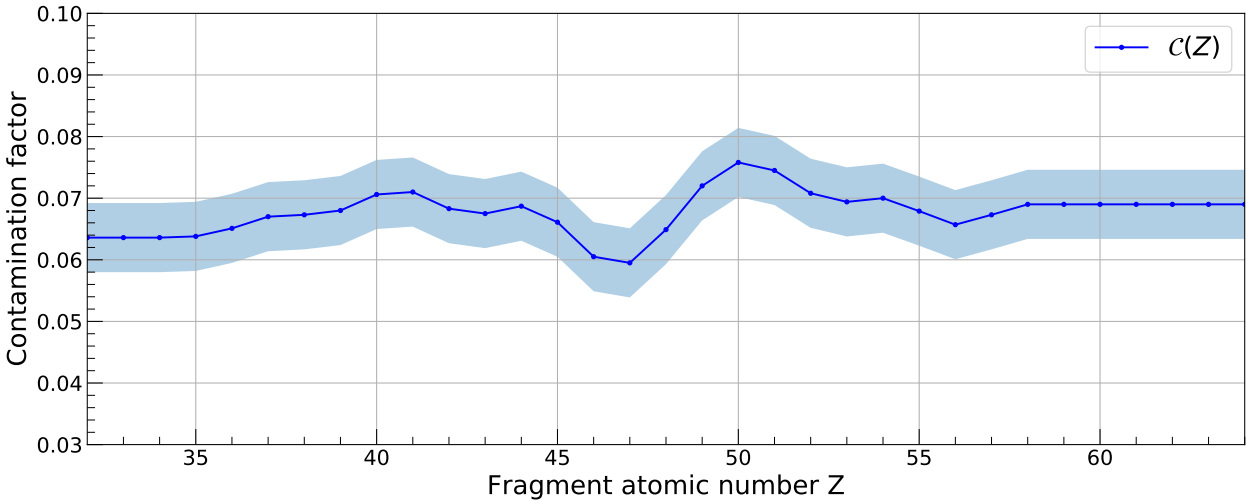

Figure 6.13: *The contamination factor $\mathcal{C}(Z)$ of the boron target as a function of the nuclear charge Z of the fission fragments is depicted in the blue line. The colour band represent the mean value of the evaluated deviation of the factor.*

The $\mathcal{C}(Z)$ factors shown in Fig. 6.13 for the boron target exhibit similar behaviour to the ones estimated for the aluminium target (see $\mathcal{C}_{14^\circ}$ and $\mathcal{C}_{21.5^\circ}$ in Fig. 6.10).

6.6 Calculation of boron target isotopic yields

The isotopic yields with the boron target are evaluated following the process outlined in Section 6.2: by fitting to a functional $a + b \cdot \cos^2(\theta^{FF}_{CM})$ for both fusion-induced fission, $Y^{FuFi}_m(Z,A)$, and transfer reactions, $Y^{Transfer}_m(Z,A)$, selected with the appropriate triggers (see Section 2.5). In the first step, the yields are evaluated with no background subtraction. In other words, $Y^{FuFi}_m(Z,A)$ that are predominantly fusion-induced fission events and with cases where a significant contribution arises from transfer events or other reactions. These isotopic yields, labelled as "*measured*" with the subscript m, will serve as the basis for the process to evaluate the contamination factor $\mathcal{C}(Z)$ and to extract the correct amount of contamination events, $Y^{Cont}(Z,A)$, contained within the $Y^{FuFi}_m(Z,A)$.

Once the yields are evaluated, $\log\left(Y^{FuFi}_m(Z,A)/Y^{FuFi}_m(Z)\right)$ is calculated and plotted against the mass deviation from the average mass: $A - \langle A \rangle$. The result can be seen in Fig. 6.14.

USC UNIVERSIDADE DE SANTIAGO DE COMPOSTELA

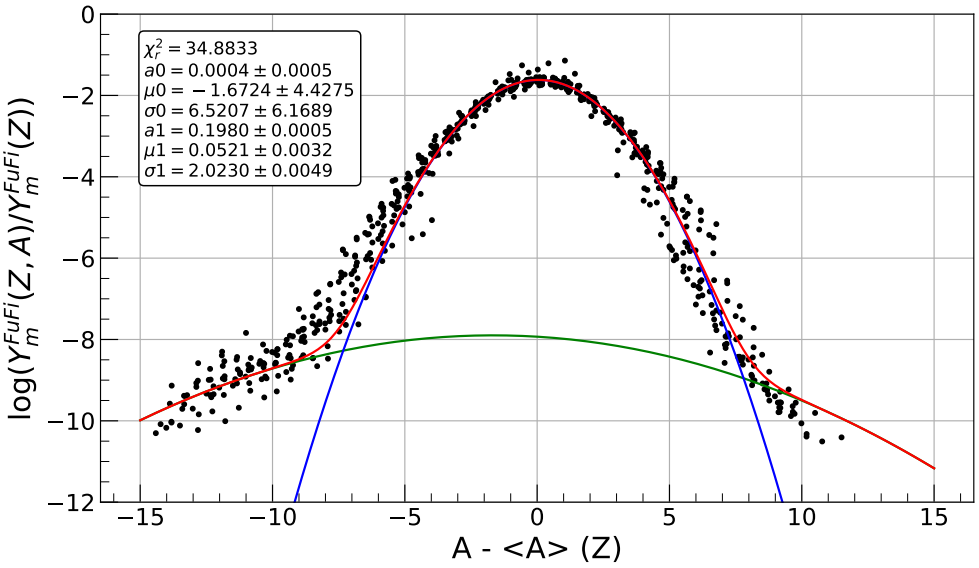

Figure 6.14: *The difference between the masses and the average mass for each elemental yield from boron target is fitted against the logarithmic ratio of $Y_m^{FuFi}(Z,A)$ and its elemental yield $Y_m^{FuFi}(Z)$ to determine the global background. The fitting process yields two Gaussian distributions, with the fusion-induced fission events represented in blue and the background depicted in green.*

A clear contribution of masses that form a Gaussian distribution (well-reconstructed fusion-induced fission yields) in Fig. 6.14 is accompanied by another background distribution with masses deviating from the average mass for very small yield contributions. These background contributions are also fitted to a Gaussian distribution and correspond to those masses related with wrong identification that would be in the tails of the isotopic distributions of the yield $Y_m^{FuFi}(Z,A)$. With both fittings, it can be assumed that the global background (green line in Fig. 6.14) must be extracted. For the boron yields $Y_m^{FuFi}(Z)$ this global background is subtracted.

Once the global background has been extracted, the resulting yields $Y_m^{FuFi}(Z,A)$ are the basis of the process to calculate the contamination factor, in such a way that employing the elemental yields (see definition in Section 6) for both fusion-induced fission and transfer reactions, it can be written:

$$Y^{FuFi}(Z) = Y_m^{FuFi}(Z) - Y_m^{Transfer}(Z)\cdot\mathcal{C}(Z) = Y_m^{FuFi}(Z) - Y^{Cont}(Z)\,. \tag{6.14}$$

Note that the superscript "*Cont*" refers to the transfer reactions which are considered as contamination when referring to events that are not fusion-induced fission. In this work, only fusion-induced fission events are studied.

The first step in obtaining the contamination factor $\mathcal{C}(Z)$ involves ensuring that the following condition is satisfied:

$$\frac{Y^{FuFi}(Z)}{Y^{FuFi}(Z_{comp})} = 1\,. \tag{6.15}$$

Here, $Z_{comp} = Z_{FS} - Z$, where the fissioning system in this case is ^{249}Bk, and assuming no proton emission, $Z_{FS} = 97$. Rewriting the above equality using the definition from Eq. 6.14, it can be expressed as follows:

$$\frac{Y_m^{FuFi}(Z) - Y_m^{Transfer}(Z)\cdot\mathcal{C}(Z)}{Y_m^{FuFi}(Z_{comp}) - Y_m^{Transfer}(Z_{comp})\cdot\mathcal{C}(Z_{comp})} = 1\,. \tag{6.16}$$

The first assumption that needs to be made is to assume that $\mathcal{C}(Z)$ is initially a constant factor. In this way, $\mathcal{C}(Z) = \mathcal{C}(Z_{comp})$, simplifying the above equality. Then, an initial contamination factor, $\mathcal{C}(Z)_{init}$, is estimated in order to evaluate the elemental yields in the next step. Multiple factors within the interval $\mathcal{C}(Z)_{init} \in [0.0, 2.0]$ are used, evaluating for each one the ratio $Y^{FuFi}(Z)/Y^{FuFi}(Z_{comp})$. In the following Fig. 6.15, the ratio for various constant factors is depicted. As observed, the elemental yields ratio is not equal to unity in any case; however, patterns of behaviour in the data can be observed as $\mathcal{C}(Z)$ increases.

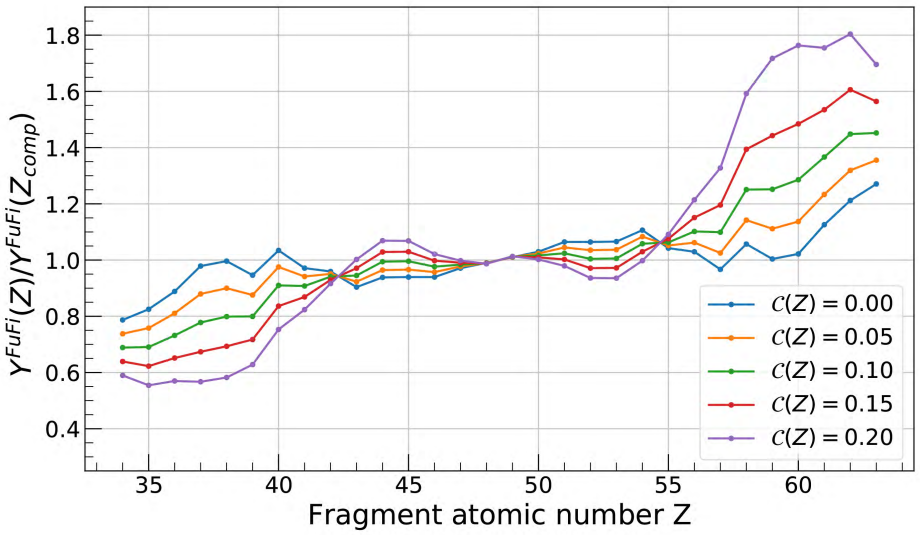

Figure 6.15: *The ratio of fusion-induced fission elemental yields for Z and its complementary partner Z_{comp} is displayed in various colours for different constant contamination factors $\mathcal{C}(Z)$ against the atomic fragment number Z. The data of 14° and 21.5° VAMOS++ settings with the boron target is used.*

At this point, the detection efficiency is introduced, labelled as intrinsic trigger efficiency: $\mathcal{E}_i^{trigger}$ (see Section 6.3):

$$Y_{corr}^{FuFi}(Z) = \frac{Y^{FuFi}(Z)}{\mathcal{E}_i^{trigger}(Z)}\,. \tag{6.17}$$

The elemental yield $Y^{FuFi}(Z)$ for each nuclear charge is corrected by $\mathcal{E}_i^{trigger}(Z)$ in order to obtain the elemental yield of fusion-induced fission corrected, $Y_{corr}^{FuFi}(Z)$. This efficiency primarily depends on the energy loss in detection layers. Therefore, as introduced in Section 6.3, there should be a linear correlation between $(Z/v_{LAB}^{FF})^2$ and Z^2. This can be observed in the following Fig. 6.16 for the boron target using Z and velocity V_{LAB}^{FF} distributions.

The intrinsic efficiency, $\mathcal{E}_i^{trigger}$, can be approximated by the following behaviour [102]:

$$\mathcal{E}_i^{trigger} \simeq 1 - a_0 \cdot exp\left(-b_0 \cdot \left(\frac{Z}{v_{LAB}^{FF}}\right)^2\right) \simeq 1 - a_0 \cdot exp(-b_0 Z^2)\,, \tag{6.18}$$

with this efficiency, the equality of the ratio of elemental yields of Eq. 6.15 can be rewritten as:

$$\frac{Y^{FuFi}(Z)}{Y^{FuFi}(Z_{comp})} = \frac{1 - a_0 \cdot exp(-b_0 Z^2)}{1 - a_0 \cdot exp(-b_0 Z_{comp}^2)}\,. \tag{6.19}$$

USC UNIVERSIDADE DE SANTIAGO DE COMPOSTELA

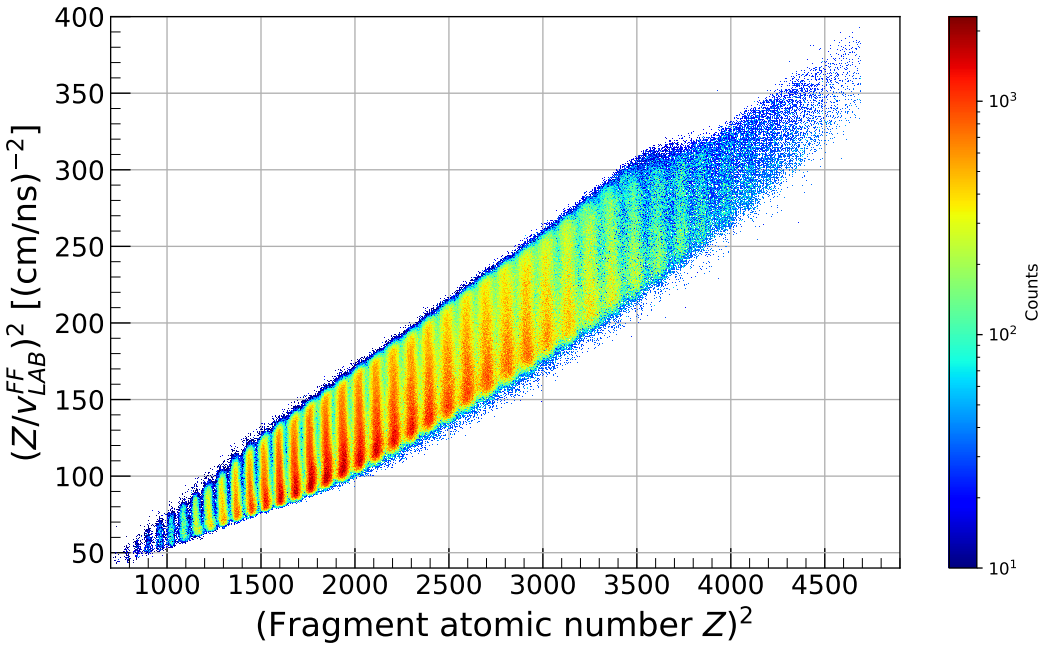

Figure 6.16: *The correlation between* $\left(Z/v^{FF}_{LAB}\right)^2$ *and* Z^2 *for fusion-induced fission events in both VAMOS++ settings is depicted for the boron target.*

Then, multiple factors $\mathcal{C}(Z)_{init} \in [0.0, 2.0]$ are applied, and the ratio of elemental yields is evaluated as done for Fig. 6.15. For each dataset, the intrinsic efficiency is fitted to Eq. 6.19. Consequently, a χ^2_r is obtained for each fit and represented alongside its corresponding constant contamination factor $\mathcal{C}(Z)_{init}$, as shown in Fig. 6.17.

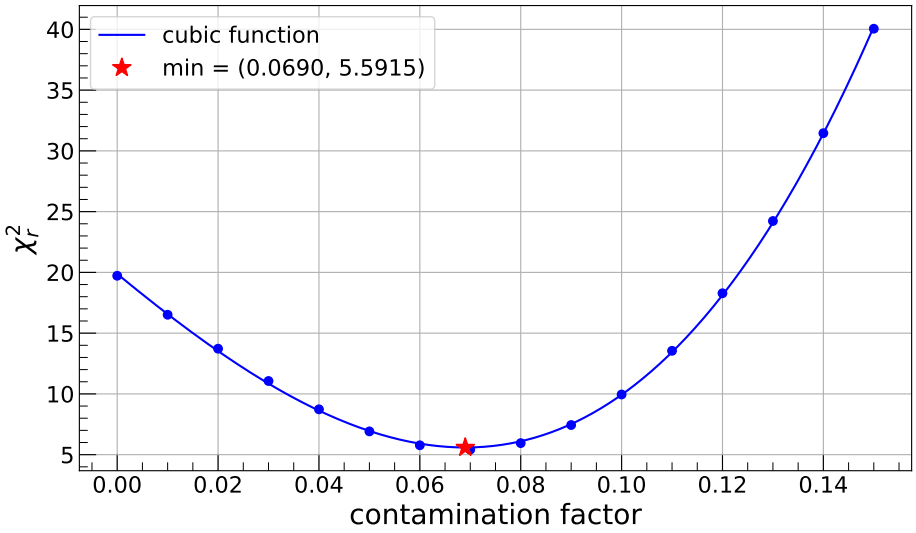

Figure 6.17: χ^2_r *values resulting from fitting the intrinsic trigger efficiency to the elemental yield ratio of* Z *and* Z_{comp} *are depicted for each employed constant initial contamination factor. The minimum is shown with a red star, obtained through fitting to a cubic polynomial shown by the blue line.*

As it can be observed in Fig. 6.17, only $\mathcal{C}(Z)_{init} \in [0.0, 0.15]$ has been represented. This is because the χ^2_r grows for higher values, making their representation impractical. It can be seen that there is a minimum χ^2_r factor when fitting to a cubic function, marked with a red star in Fig. 6.17. Based on this result, the initial factor is taken as $\mathcal{C}(Z)_{init} = 0.069$.

The intrinsic trigger efficiency is fixed with the parameters that correspond to the fit with the resulting $\mathcal{C}(Z)_{init}$. See Fig. 6.18.

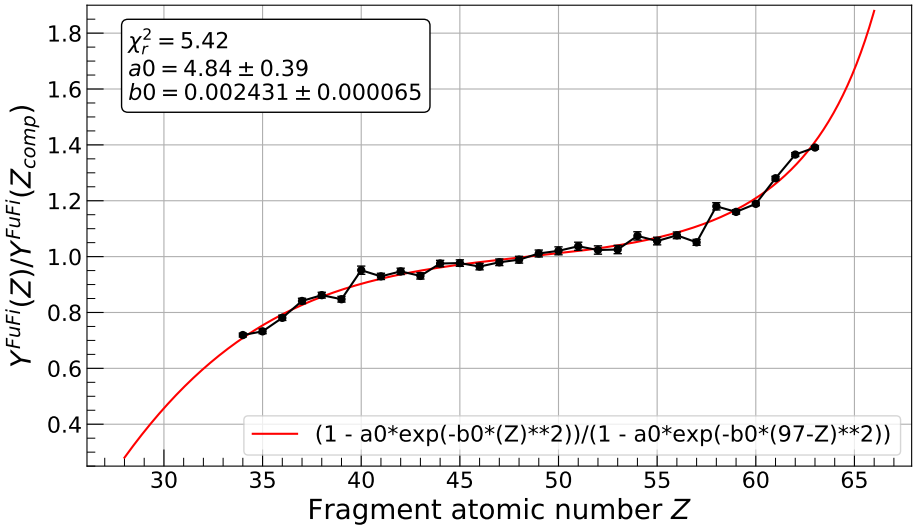

Figure 6.18: *The figure shows the fitting of the ratio $Y^{FuFi}(Z)/Y^{FuFi}(Z_{comp})$ in order to obtain the parameters a_0 and b_0 for the efficiency $\mathcal{E}_i^{trigger}$ in the ^{249}Bk fissioning system.*

The intrinsic trigger efficiency evaluated for the boron target is thus:

$$\mathcal{E}_i^{trigger} \simeq 1 - (4.84 \pm 0.39) \cdot exp(-(0.002431 \pm 0.000065) \cdot Z^2)\,. \tag{6.20}$$

It is depicted in the following Fig. 6.19 for each atomic fragment number Z.

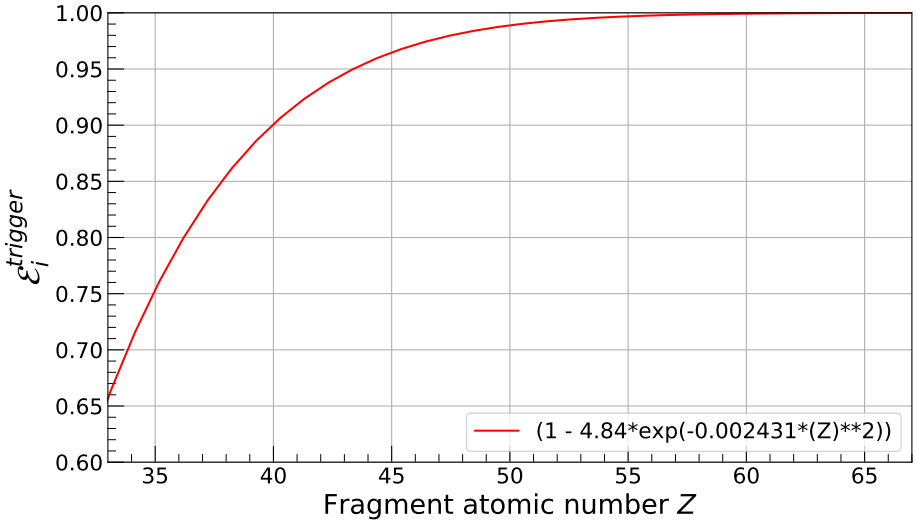

Figure 6.19: *The intrinsic efficiency $\mathcal{E}_i^{trigger}$ results for each fragment atomic number Z can be seen for the fusion-induced fission fragments using the boron target.*

The next step involves employing the initial contamination factor $\mathcal{C}(Z)_{init} = 0.069$ as a constant and constructing the corrected elemental yield $Y^{FuFi}_{corr}(Z)$ considering the intrinsic efficiency (see Eq. 6.20). Then, an iterative symmetrisation process is employed between the yields of complementary fragment Z. The aim is to find the contamination factor $\mathcal{C}(Z)$ dependent

on the atomic fragment number Z, capable of satisfying the condition: $Y_{corr}^{FuFi}(Z) = Y_{corr}^{FuFi}(Z_{comp})$.

The iterative symmetrisation process consists of applying the following equation

$$Y_{corr}^{FuFi}(Z) = \frac{Y_m^{FuFi}(Z) - Y_m^{Transfer}(Z)\cdot\mathcal{C}(Z)}{\varepsilon_i^{trigger}(Z)} = \frac{Y_m^{FuFi}(Z_{comp}) - Y_m^{Transfer}(Z_{comp})\cdot\mathcal{C}(Z_{comp})}{\varepsilon_i^{trigger}(Z_{comp})} = Y_{corr}^{FuFi}(Z_{comp}) \tag{6.21}$$

in the following manner: one-half of the elemental yields ($Z > 48.5$) is fixed and a new contamination factor is for the other half. With the new contamination factor, the other half is then fixed, and the contamination factor is reevaluated. Through multiple iterations and by enforcing the symmetry condition of fission $Y_{corr}^{FuFi}(Z) = Y_{corr}^{FuFi}(Z_{comp})$, the contamination factor for the boron target is obtained.

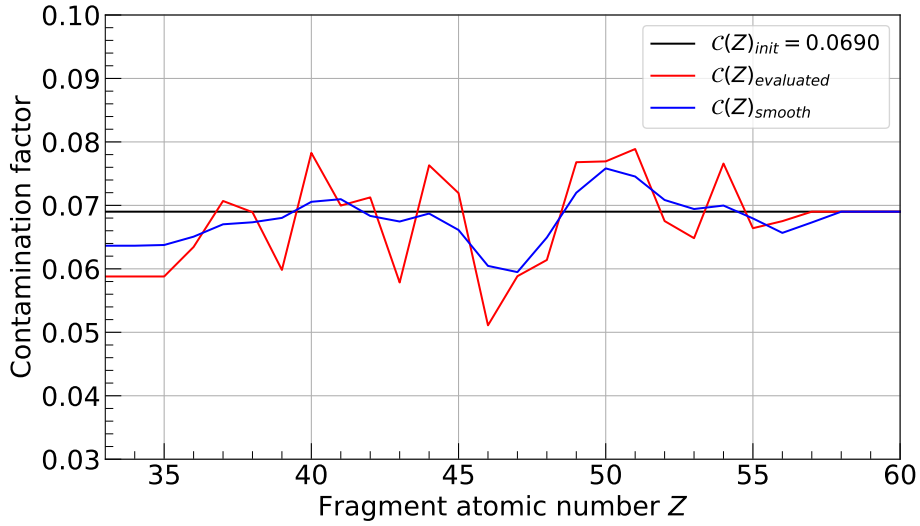

Figure 6.20: *The initial contamination factor $\mathcal{C}(Z)_{init}$, the contamination factor obtained after the iterative symmetrisation $\mathcal{C}(Z)_{evaluated}$, and the final smooth contamination factor $\mathcal{C}(Z)_{smooth}$ are depicted with black, red, and blue lines, respectively, plotted against the fragment atomic number Z for the boron target.*

The resulting contamination factor, denoted as $\mathcal{C}(Z)_{smooth}$, along with the initial and the evaluated ones, is presented in Fig. 6.20 following a smoothing process. This process is essential to address irregularities in the contamination factor arising from statistical and systematic fluctuations. The contamination factor values for $Z < 35$ and $Z > 58$ are fixed to $\mathcal{C}(Z = 35)_{smooth}$ and $\mathcal{C}(Z = 58)_{smooth}$, respectively.

The final contamination factor $\mathcal{C}(Z)_{smooth}$ for all atomic fragment numbers Z is also presented in the preceding Fig. 6.13 of Section 6.5 as $\mathcal{C}(Z)$. Throughout this procedure, numerous forms of contamination factors have been iteratively assessed. The standard deviation of the final contamination factor can be obtained using random variations falling within the uncertainties of the efficiency and fits for all prior steps. The same random variation is applied to all Z for simplicity. The constant standard deviation for all Z is depicted by a blue band in Fig. 6.13.

Once the final contamination factor for boron, $\mathcal{C}(Z)$ (see Fig. 6.13), is obtained, it is applied alongside the intrinsic efficiency (see Eq. 6.20) to derive $Y_{corr}^{FuFi}(Z)$ (see Eq. 6.17), now corrected with the appropriate contamination factor. With this elemental yield and its complement, we can

proceed to check that:

$$\frac{Y_{corr}^{FuFi}(Z)}{Y_{corr}^{FuFi}(Z_{comp})} = 1\,. \tag{6.22}$$

Fig. 6.21 shows the ratio to be nearly flat and close to 1. However, for very low Z and hence very high Z_{comp}, deviations in the behaviour are evident.

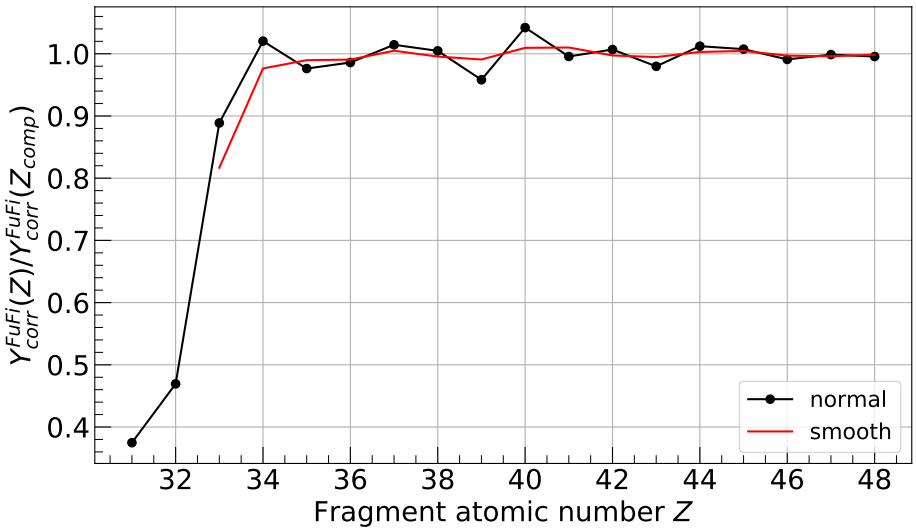

Figure 6.21: *The ratio of yields, $Y_{corr}^{FuFi}(Z)/Y_{corr}^{FuFi}(Z_{comp})$, for $Z < 48.6$ is presented alongside its respective smoothing curve depicted in red. This smoothing curve will represent the relative efficiency that will correct anomalous behaviours for low Z values.*

The fission fragments with $Z < 34$ significantly deviate from the expected behaviour. These effects are generated by the iterative method used to obtain the contamination factor and fixing its extremes to constant values. It is essential to note that this effect is not physical but a mathematical artefact. The relative efficiency applied for $Z < 34$ is fixed by the relative efficiency at $Z = 34$. The red line in Fig. 6.21 represents the smooth ratio of the yields, and this will precisely be the efficiency, $\mathcal{E}_{rel}$, being multiplied by the intrinsic trigger efficiency, giving an overall efficiency for the boron target, i.e., $\mathcal{E}^g = \mathcal{E}_i^{trigger} \cdot \mathcal{E}_{rel}$. Note that this efficiency is evaluated up to $Z_{FS}/2$ and it is applied to the same atomic fragments, as correcting one part automatically corrects the other when the yield ratio is calculated.

This ultimately defines the isotopic fission yields $Y(Z, A)$, derived from the originally measured yields, for the boron target, as follows:

$$Y(Z,A) = \frac{Y_m^{FuFi}(Z,A) - Y_m^{Transfer}(Z,A)\cdot \mathcal{C}(Z)}{\mathcal{E}_i^{trigger}(Z)\cdot \mathcal{E}_{rel}(Z)} = \frac{Y_m^{FuFi}(Z,A) - Y^{Cont}(Z,A)}{\mathcal{E}^g(Z)}\,. \tag{6.23}$$

Although this relative efficiency would not be an intrinsic efficiency *per se*, Eq. 6.10 for the boron target can be reformulated as:

$$\mathcal{E}_i^{FF} = \mathcal{E}_i^{DC}\cdot \mathcal{E}^g \cdot \mathcal{E}_i^{IC}\,. \tag{6.24}$$

It can be seen that the ratio of the final elemental yields $Y(Z)/Y(Z_{comp})$ is practically flat and equal to 1 with a standard deviation of 0.032. The result is shown in the Fig. 6.22. The elemental yields as a percentage against the fragment atomic number Z for the boron target are presented in Fig. 6.23. The measured elemental yields of fusion-induced fission $Y_m^{FuFi}(Z)$, which

contain contamination, are depicted in blue. The measured transfer yields $Y_m^{Transfer}$ are shown in purple. $Y^{Cont}(Z)$, the measured transfer yields corrected by the intrinsic trigger efficiency $\mathcal{E}_i^{trigger}$ and multiplied by the contamination factor $\mathcal{C}(Z)$, are shown in green. The fusion-induced fission yields $Y(Z)$ after correcting for the global efficiency $\mathcal{E}^g$ and subtracting the contamination yields, are shown in red.

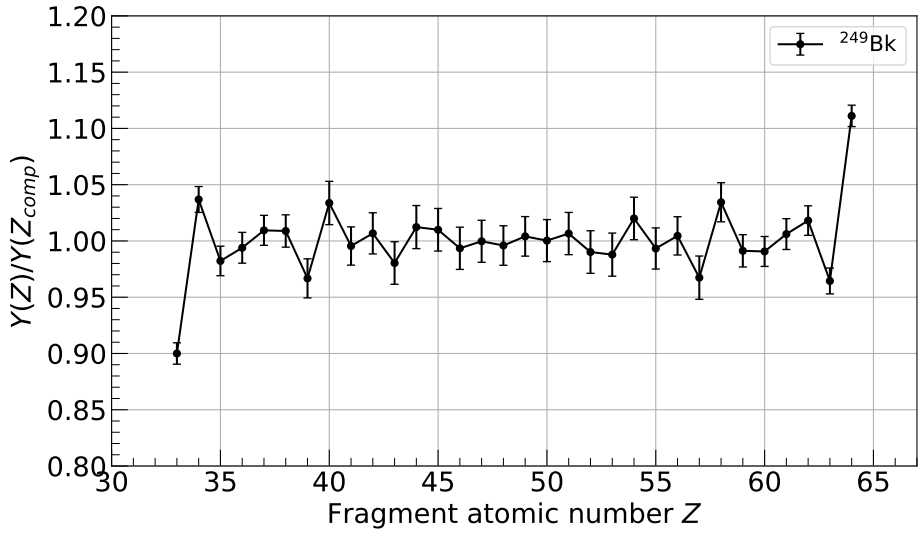

Figure 6.22: *The ratio of the final yields of fusion-induced fission to their complements, $Y(Z)/Y(Z_{comp})$, for the boron target against the fragment atomic number Z after applying all corrections and efficiencies is displayed. The behaviour remains highly constant and equals 1 with a standard deviation of* 0.032.

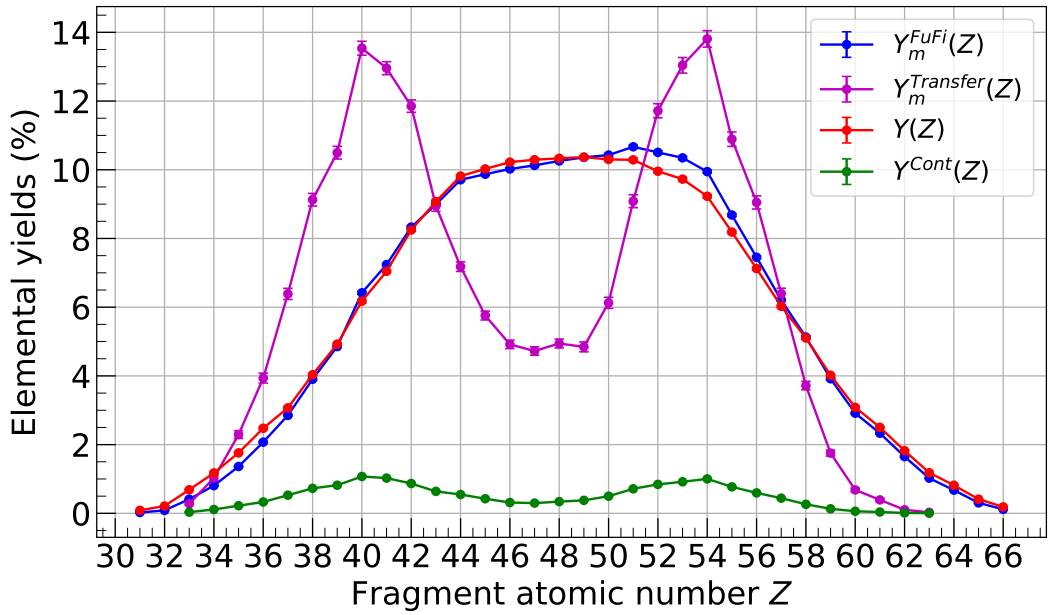

Figure 6.23: *The figure shows the measured elemental yields $Y_m^{FuFi}(Z)$ (blue line and symbols), the measured elemental transfer yields $Y_m^{Transfer}(Z)$ (purple line and symbols), the estimated elemental contamination yields $Y^{Cont}(Z)$ (green line and symbols), and the evaluated elemental fusion-induced fission yields $Y(Z)$ (red line and symbols).*

The isotopic fission yields $Y(Z, A)$ from the boron target are calculated based on the entire preceding process described. The final yields will be presented in the following chapter and are selected in masses according to Fig. 6.14 for each Z. The selection criterion involves a limit of $\langle A(Z) \rangle \pm 6$, along with a minimum in the number of counts in the $\cos(\theta_{CM}^{FF})$ distribution. This ensures that the final isotopic yields are as pure as possible without contamination.

6.7 Calculation of isotopic yields from the aluminium target

The procedure for obtaining the yields of the ^{265}Db fissioning system and estimating the contamination factor differs from the approach used for the ^{249}Bk fissioning system. Due to the known presence of quasi-fission reactions when using the aluminium target (see Section 1.4) and based on the prior measurement by Tōke *et al.* [105], the functional form of the fit is not $a + b \cdot \cos^2(\theta_{CM}^{FF})$. The left panel of Fig. 6.24 displays measurements of the centre-of-mass angle θ_{CM} against fragment mass A (before evaporation) in the ^{238}U + ^{27}Al reaction [105].

In the selected range of $\theta_{CM} \in [10°, 80°]$ and for the isotopic case of $A \approx 135$ and $Z \approx 51$, the angular projection would exhibit symmetry, suggesting an approximate functional form of $a + b \cdot \cos^2(\theta_{CM})$ (see green line in Fig. 6.24). This assumption remains valid even if only the continuous green line is measured, excluding data in the region marked by the discontinuous green line. In the same angular range $\theta_{CM} \in [10°, 80°]$, the isotopic case of $A \approx 185$ for $Z \approx 67$ is selected (see red line in Fig. 6.24). The angular projection now lacks symmetry and its distribution in $\cos(\theta_{CM})$ does not follow a functional form of $a + b \cdot \cos^2(\theta_{CM})$. Moreover, the projection is truncated by the measurement range in θ_{CM}. The green line indicates a mass primarily composed of fusion-induced fission events with angular symmetry, while the red line represents a mass predominantly composed of quasi-fission events.

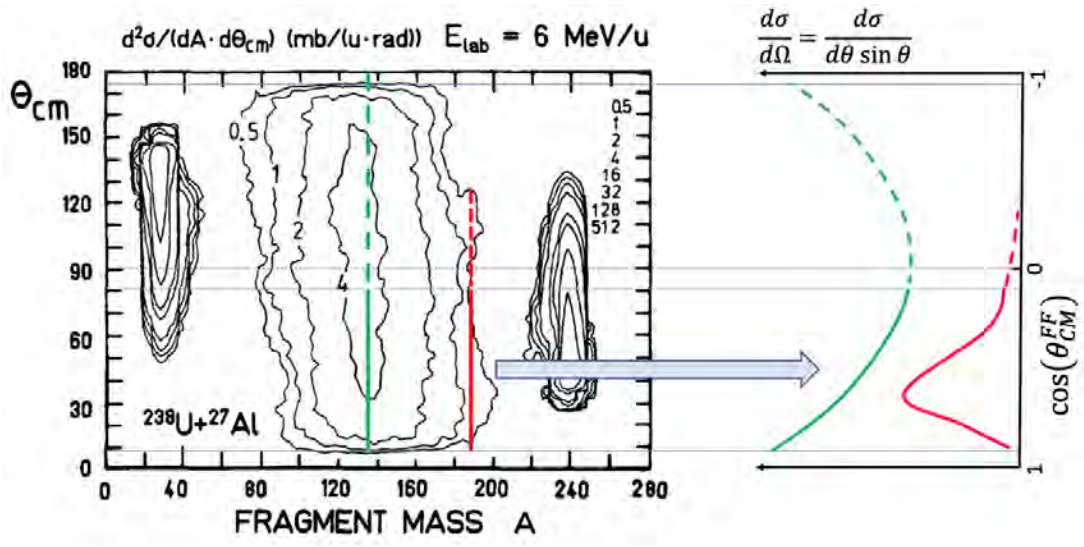

Figure 6.24: *Angular measurements in the centre-of-mass reference frame (θ_{CM} [deg]) plotted against fragment mass (A) before evaporation for the ^{238}U + ^{27}Al reaction. The green line represents a scenario where the contributions are predominantly from fusion-induced fission events, displaying angular symmetry. The red line represents a scenario dominated by quasi-fission events lacking angular symmetry. The discontinuous lines indicate the regions where measurements are not available in this example. Adapted with permission from [65]. Copyright (1985) by the North-Holland Publishing Company.*

Figure 6.25 shows the angular distribution $W(\theta_{CM}^{FF})$ [mb/sr] against the angle θ_{CM} and the fit to a sum of Legendre polynomials up to $L_{max} = 2$ with a dashed line, for ^{238}U + ^{27}Al reactions [105] (see Section 5.4). As can be observed, the dashed line does not replicate the behaviour of the data, which is instead due to continuous fluctuations in the nuclear radius (solid line). Therefore, fitting with the functional form $a + b \cdot \cos^2(\theta_{CM}^{FF})$ has a limited accuracy.

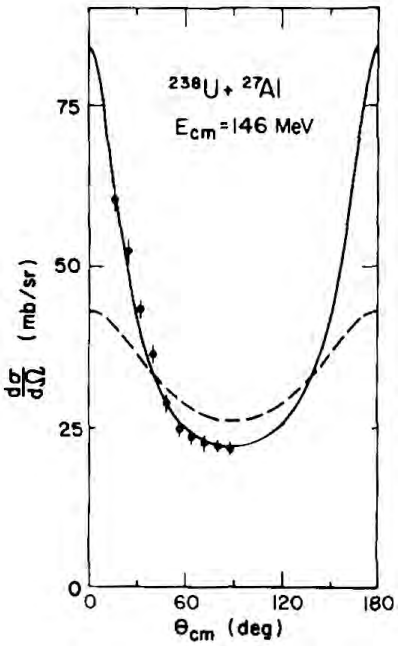

Figure 6.25: *Representation of the angular distribution $W(\theta_{CM}^{FF})$ [mb/sr] versus the polar angle θ_{CM}^{FF} [deg] for the experimental data of the reaction ^{238}U + ^{27}Al with energy E_{CM} = 146 MeV, fitted using a sum of Legendre polynomials up to $L_{max} = 2$ in Eq. 5.18. Adapted with permission from [105] where $\frac{d\sigma}{d\Omega} \equiv W(\theta_{CM}^{FF})$. Copyright (1984) by the American Physical Society.*

Therefore, the isotopic fission yields with the aluminium target are evaluated following the process outlined in Section 6.2 without fitting to a functional $a + b \cdot \cos^2(\theta_{CM}^{FF})$ and using only the total number of counts, extracting contamination for fusion-induced fission, $Y_m^{FuFi}(Z, A)$, with the contamination factors (see Section 6.4) multiplying the transfer reactions, $Y_m^{Transfer}(Z, A)$, doing the envelope subtraction (see Eq. 6.13).

Once the number of counts, $\#(Z, A)$, for each final envelope Env^{final} are obtained for each isotope (Z, A), the aluminium yields are constructed as follows doing a normalisation:

$$Y_m^{FuFi}(Z, A) = \frac{\#(Z, A)}{\sum\limits_{Z,A} \#(Z, A)} \,. \tag{6.25}$$

Similar to the procedure with boron target, in a preliminary stage to select the fraction of events that genuinely correspond to the fusion-induced fission yield and not to background, $log\left(Y_m^{FuFi}(Z, A)/Y_m^{FuFi}(Z)\right)$ is computed and plotted against the mass deviation from the average mass: $A - \langle A \rangle(Z)$. The outcome is illustrated in Fig. 6.26.

Similar to the observation in the boron target (see Fig. 6.14), the aluminium target, as shown in Fig. 6.26, exhibits a discernible presence of masses conforming to a Gaussian distribution, representing real fusion-induced fission yields. Concurrently, there exists another background distribution involving masses deviating from the mean mass, contributing insignificantly to the

yields. These background contributions are also modelled using a Gaussian distribution and are associated with wrong reconstructions in fragment mass and/or atomic number, appearing in the isotopic yield distributions $Y_m^{FuFi}(Z,A)$. By conducting both fittings, it is deduced that the overall background (depicted by the green line in Fig. 6.26) needs to be removed.

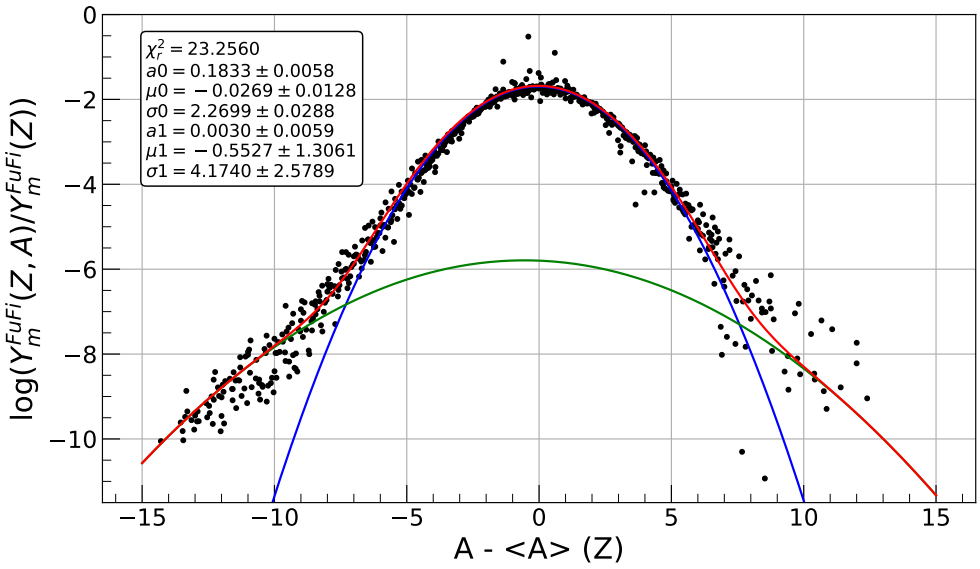

Figure 6.26: *The difference between the masses and the average mass for each elemental yield from aluminium target is fitted against the logarithmic ratio of $Y_m^{FuFi}(Z,A)$ and its elemental yield $Y_m^{FuFi}(Z)$ to determine the general background. The fitting process yields two Gaussian distributions, with the fusion-induced fission events represented in blue and the background depicted in green.*

The next step would involve assessing the intrinsic trigger detection efficiency for the aluminium target. However, as previously highlighted, due to the potential presence of quasi-fission events detected with the aluminium target, evaluating this efficiency with the same process for the fissioning system ^{265}Db is not feasible. Consequently, the efficiency evaluated for the boron target and the fissioning system ^{249}Bk will be adjusted for the aluminium target. Although the experimental setup remains consistent across both targets, and there is no distinction when evaluating fragment atomic number Z, there exists a slight dependence on velocity. To leverage this dependence, a correlation between the velocities of the fissioning systems will be implemented:

$$b_{Al} = \frac{b_0}{(v_{FS}^{Al})^2} \quad , \quad b_B = \frac{b_0}{(v_{FS}^{B})^2} \, , \tag{6.26}$$

where b_0 is the parameter of the intrinsic efficiency from Eq. 6.20 and the $v_{FS}^{Al,B}$ are displayed in Tab. 2.4. By equating these equations:

$$b_{Al} = b_B \frac{(v_{FS}^{B})^2}{(v_{FS}^{Al})^2} = 0.002768 \pm 0.000075 \, . \tag{6.27}$$

The intrinsic trigger efficiency for the aluminium target is constructed by assuming that the constant a_0 remains consistent for both boron and aluminium targets. The relative efficiency of each target, obtained from Eq. 6.17, will be employed to adjust the yields. This adjustment accounts for energy losses that primarily impact either the lighter or heavier extremities of the yields. The intrinsic trigger efficiency for the aluminium target is given by:

$$\mathcal{E}_i^{trigger} \simeq 1 - (4.84 \pm 0.39) \cdot exp(-(0.002768 \pm 0.000075) \cdot Z^2) \tag{6.28}$$

and it is depicted in the following Fig. 6.27 for each atomic fragment number Z.

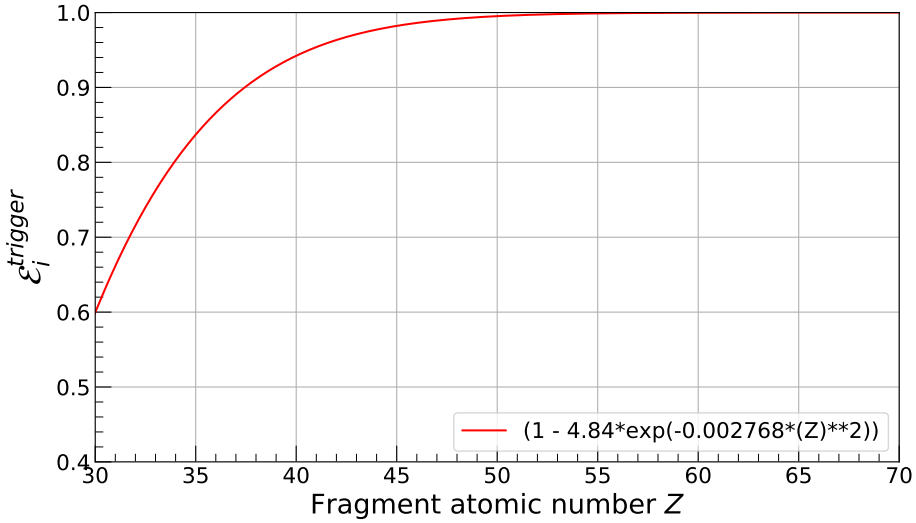

Figure 6.27: *The intrinsic efficiency $\mathcal{E}_i^{trigger}$ results for each fragment atomic number Z can be seen for the fusion-induced fission fragments using the aluminium target.*

As discussed earlier due to the absence of fitting to the functional form $a + b \cdot \cos^2(\theta_{CM}^{FF})$, the cuts in the measurement window of the (θ_{CM}^{FF}, A) space (see Fig. 5.17) need to be considered since it is not a rectangular window. Yields with a larger acceptance in $\cos(\theta)$ would increase over others that are more restricted. In other words, the isotopic fission yields must be obtained for all (Z, A) under the same conditions.

Therefore, a measurement window within the acceptance in $\cos(\theta_{CM}^{FF})$ for the aluminium target needs to be selected, in which the isotopic fission yields will be evaluated. The chosen measurement window with the widest possible mass range can be seen in green in Fig. 6.28; it corresponds to $\cos(\theta_{CM}^{FF}) \in [0.47, 0.72]$ and includes fragment mass numbers $A \in [78, 170]$.

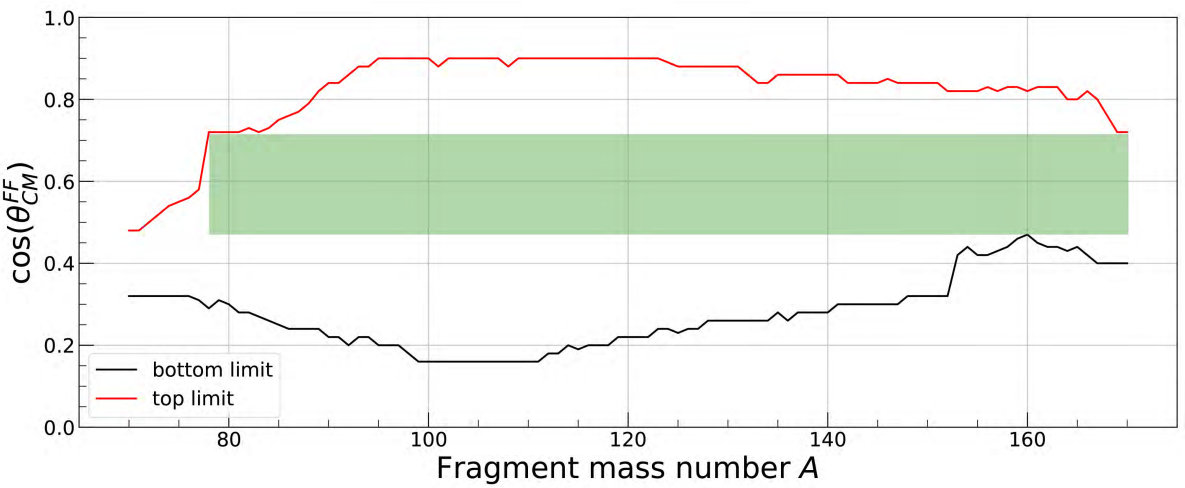

Figure 6.28: *The $\cos(\theta_{CM}^{FF})$ distribution limits are displayed with red and black lines against the fragment mass number A for the aluminium target. The green-shaded region represents the initial selection of a common region between the limits of $\cos(\theta_{CM}^{FF}) \in [0.47, 0.72]$. This window encompasses fragment mass numbers $A \in [78, 170]$.*

The isotopic fission yields $Y(Z,A)$ from the aluminium target are calculated based on the entire preceding process described. The final yields will be presented in the following chapter and are selected in masses according to Fig. 6.26 for each Z. The selection is a limit of $\langle A(Z)\rangle \pm 6$ with a minimum in the number of counts in the $\cos(\theta^{FF}_{CM})$ distribution. This ensures that the final isotopic yields are as pure as possible without contamination.

6.8 Fission yields uncertainty

The uncertainty on the fission yields is calculated as the quadratic sum of the statistical and systematic uncertainty:

$$\delta = \sqrt{\delta^2_{stat} + \delta^2_{sys}}\,. \tag{6.29}$$

6.8.1 Statistical uncertainty

The statistical uncertainty of fusion-induced fission yields is determined using the following equation:

$$\delta_{Yield} = Norm_{factor} \cdot \sqrt{4 \cdot \delta a^2 + \left(\frac{2}{3}\right)^2 \cdot \delta b^2 + 2 \cdot \frac{2}{3}\mathrm{cov}(a,b)}\,. \tag{6.30}$$

This calculation is carried out after the normalisation of the results obtained from the two VAMOS++ settings and the evaluation of the yields (see Section 6.2), with the uncertainties associated with the fit parameters of Eq. 6.9 taken into account. The value of $Norm_{factor}$ is determined as $200/N^{counts}_{total}$ for the boron target, but not for the aluminium target which is further explained in Section 6.7.

6.8.2 Systematical uncertainty

The systematic uncertainty in the determination of the VAMOS++ ϕ acceptance and the range of $\cos(\theta^{FF}_{CM})$, as well as the calculation of the intrinsic efficiency, is taken into account. This systematic uncertainty is primarily attributed to the evaluation method of the yields, considering the variations in all parameters and corrections involved. The detectors themselves contribute to further variations through their inherent variations and fluctuations, affecting the variables used in obtaining the yields. Some elements introduce systematic uncertainties which cannot be directly evaluated and quantified, but it is possible to obtain the systematic uncertainty associated with the data analysis.

The evaluation of the systematic uncertainty involves the mixture of variables which contribute to this uncertainties by combining different data samples from both settings. This is equivalent to conducting multiple independent experiments. Approximately 100 combinations of variations in the limits of $\cos(\theta^{FF}_{CM})$, the number of bins, fit conditions, and other data analysis variations that may impact the yield results are randomly performed. These combinations encompass the range of internal variables within the analysis that might contribute to the final uncertainty.

USC UNIVERSIDADE DE SANTIAGO DE COMPOSTELA

The systematic uncertainty is calculated as a normalised percentage using the formula:

$$\delta_{sys}(Y(Z))[\%] = 100 \cdot \frac{\sqrt{\overline{(\sigma_{syst})^2}}}{\sum_A \overline{Y}(Z,A)}\,. \tag{6.31}$$

The term $\overline{(\sigma^2_{syst})}$ represents the average of all squared systematic uncertainties $(\sigma^2_{syst})_i$, where the index i corresponds to a particular combination of data between the two VAMOS++ settings. The dependence of $(\sigma_{syst})^2$ on Z has been found to tend towards a constant value independent of the mass A. As a result, the average $\overline{(\sigma^2_{syst})}$ is taken. Each squared systematic uncertainty is calculated as:

$$(\sigma^2_{syst})_i = \mathcal{S}i^2 - (\overline{\sigma_i})^2\,, \tag{6.32}$$

where the mean value of the statistical errors $(\overline{\sigma i})$ for each i-combination is also calculated. Here, $\mathcal{S}i$ is the standard deviation obtained from:

$$\mathcal{S}_i = \sqrt{\frac{1}{n-1}\sum_j (Y_j - \overline{Y})^2}\,, \tag{6.33}$$

the differences between each Y_j (yield) and the mean yield $\overline{Y}$ for a specific combination of parameters within each data group i. The parameter n represents the total number of data combinations, given by $n = \sum i$, and the index j accounts for each combination of different parameters within each data group.

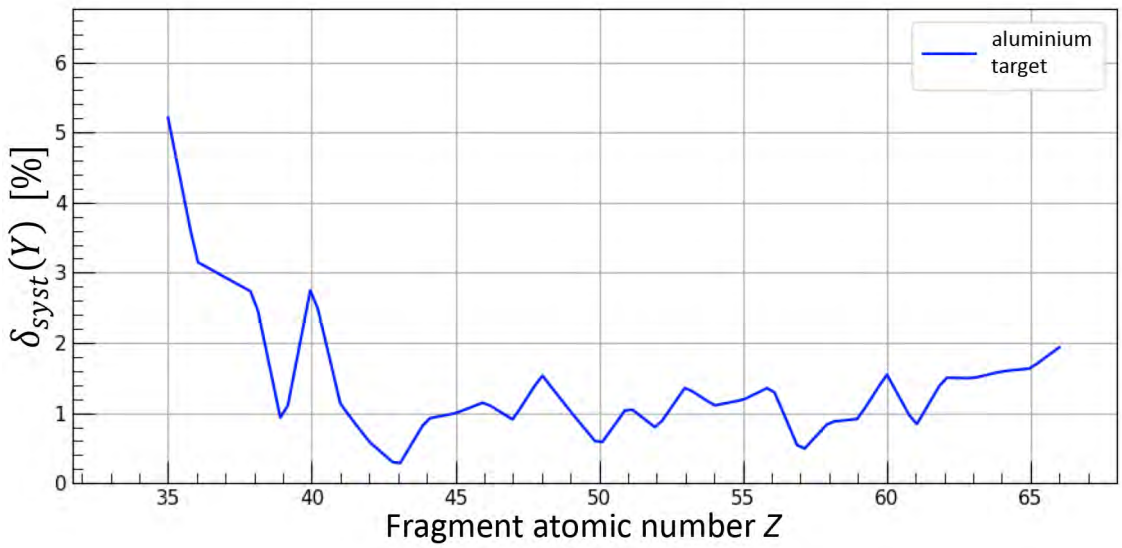

Figure 6.29: *The systematic uncertainty of the yields, $\delta_{syst}(Y)$ [%] for each Z evaluated with fusion-induced fission data from the aluminium target.*

The result of the systematic uncertainty of the yields, $\delta_{syst}(Y)$, can be observed in Fig. 6.29 for each fragment atomic number Z using fusion-induced fission data from the aluminium target. It is assumed that δ_{syst} is independent of the target employed.

The behaviour of δ_{syst} is directly influenced by relative statistics of each setting and their distribution for each fragment atomic number Z. In particular, for $Z < 40$ and light isotopes, the event count is predominantly driven by the 21.5° fit, leading to an increase in systematic error as the analysis heavily relies on the fit of a single setting. Conversely, for heavy isotopes with higher Z values, the opposite trend is observed, although the resolution is insufficient to detect the systematic error increase for $Z > 65$.

6.9 Calculation of fission fragment velocities

The determination of the velocity distributions of fission fragments at the centre-of-mass reference frame is important for assessing the dynamics of fission and obtaining indirect observables that characterise the scission point of the fissioning systems under study. This distribution, denoted as V_{CM}^{FF}, is isotopically evaluated for both ^{265}Db and ^{249}Bk fissioning systems (see Section 2.7).

6.9.1 Fragment velocities from ^{265}Db fission

The isotopic velocity distributions V_{CM}^{FF} are evaluated with both VAMOS++ settings of 14° and 21.5° using the selection of fusion-induced fission events and the selection of transfer events. An example of the fusion-induced fission distribution and the transfer production multiplied by the contamination factors (see Section 6.4) for the corresponding fragment atomic number Z, can be seen in Fig. 6.30.

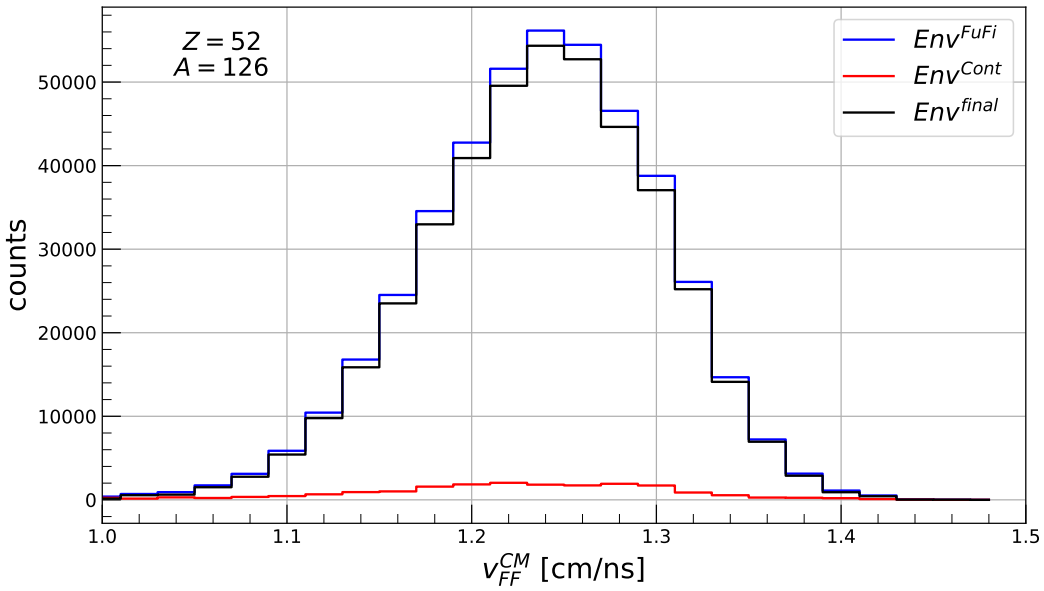

Figure 6.30: *The envelopes of the centre-of-mass velocity distributions for both VAMOS++ settings, for fusion-induced fission and transfer events, are displayed, along with the resulting envelope after the subtraction of contamination, for the fissioning system ^{265}Db and fragments with $(Z = 52, A = 126)$.*

Once the velocity distributions V_{CM}^{FF} of the fission fragments are obtained isotopically, it is necessary to verify the kinematics of the fission reactions. This can be done by checking the independence of V_{CM}^{FF} with respect to the centre-of-mass angle θ_{CM}^{FF} distribution. The scheme for a heavy fragment and a light fragment, with the angles and velocities in the laboratory framework and the centre-of-mass reference frame, can be observed in Fig. 6.31. As it can be seen, for any fragment, the module of the velocity in centre-of-mass (red vector in the figure), $|\vec{v}_{CM}^{FF}| \equiv v_{CM}^{FF}$, must be constant and, therefore, independent of the angle θ_{CM}^{FF}.

The independence can be observed by plotting the isotopic velocity v_{CM}^{FF} versus $\cos(\theta_{CM}^{FF})$. A proper reconstruction of the angle, accurate assessment of energy losses, and correct estimation and subtraction of contamination would yield a flat profile in $\cos(\theta_{CM}^{FF})$. The case $(Z = 52, A = 126)$ is shown in Fig. 6.32.

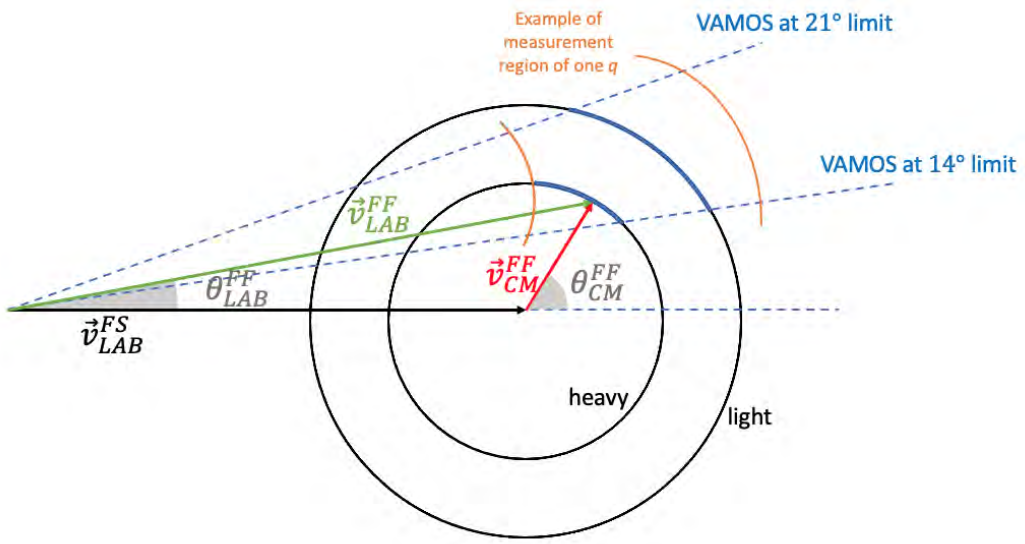

Figure 6.31: *The kinematic of the fission reaction is depicted, illustrating the relationships between the centre-of-mass reference frame and the laboratory reference frame for a non-relativistic case. Two fragments, one heavy and one light are shown. The orange lines represent an example of the measurement region for one charge state with VAMOS++ spectrometer.*

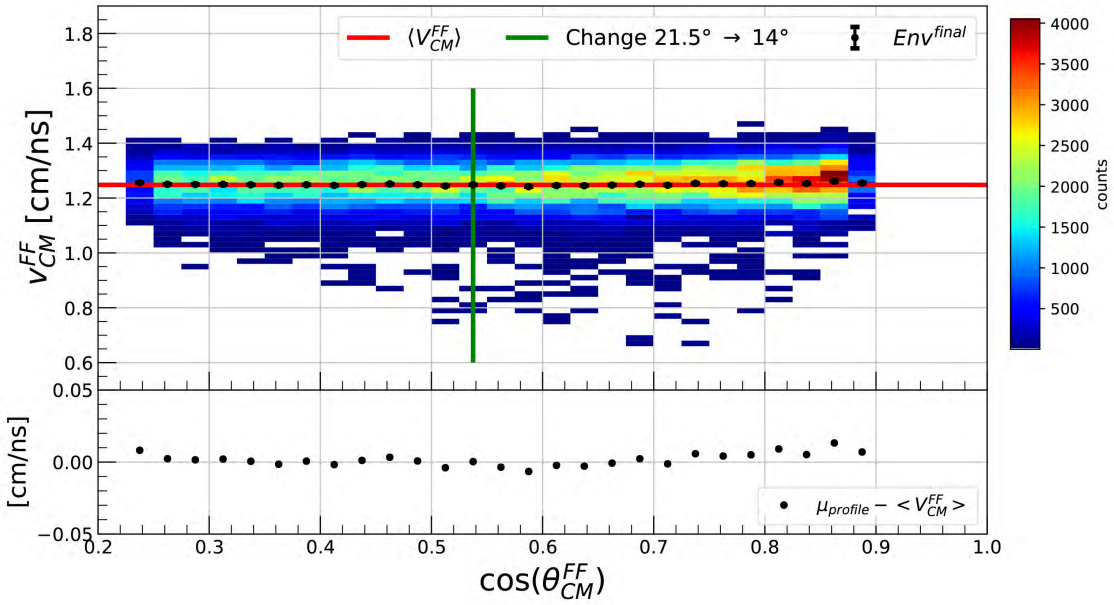

Figure 6.32: *The centre-of-mass velocity v^{FF}_{CM} is plotted against $\cos(\theta^{FF}_{CM})$ with $(Z = 52, A = 126)$ for fusion-induced fission events of the fissioning system ^{265}Db. The profile $\mu_{profile}$ for each bin in $\cos(\theta^{FF}_{CM})$ is shown with black data points, compared to the average velocity $\langle V^{FF}_{CM} \rangle$ with a red line, and the difference between the profile and the average value in the lower panel. After subtracting the contamination, the green line represents the separation between the contributions from the 21.5° and 14° settings in the final envelope.*

The alignment of velocity with respect to the centre-of-mass angle has been examined for all fission fragment isotopes of the ^{265}Db fissioning system. The centre-of-mass velocity exhibits variations of ±0.01 cm/ns, indicating alignment deviations below 1%. These variations fall within the expected differences below the precision limit in velocity.

The final result for the velocity distribution of the fission fragments in the centre-of-mass for a single isotopic selection (Z, A), depicted in Fig. 6.33, reveals a distribution with characteristics resembling a Gaussian distribution, although it does not strictly conform to this behaviour. The upper panel illustrates the average value computed from the data $\langle V_{CM}^{FF} \rangle$ and μ represented by the green and blue lines, respectively, where μ is the mean value of the Gaussian distribution fitted to the data represented with a red line. The residual is represented in the lower panel. The shape of the residual indicates a deviation from a Gaussian distribution. To obtain the velocity of the isotopic fission fragment $v_{CM}^{FF}(Z, A)$, the average value $\langle V_{CM}^{FF} \rangle$ is employed instead of the μ value, considering the existing differences with the Gaussian shape.

The velocities of both fragments are constrained by the conservation of total kinetic energy (TKE). In classical terms, TKE can be expressed as:

$$TKE = \frac{1}{2} m_{F_1} v_{F_1}^2 + \frac{1}{2} m_{F_2} v_{F_2}^2 \,. \tag{6.34}$$

The TKE is a Gaussian distribution (see for example in the context of LDM in Section 1.3.2) and therefore, these velocities do not follow Gaussian distributions. In other words, $TKE = function(V^2)$ and therefore, the fragment velocity cannot follow a Gaussian behaviour. The behaviour, while somewhat resembling a Gaussian distribution, can be observed from the oscillation of the residuals in Fig. 6.33. These oscillations indicate that the behaviour is not Gaussian and that the average value should be taken into consideration. Although in some isotopes, $\mu \approx \langle V_{CM}^{FF} \rangle$, they remain very similar.

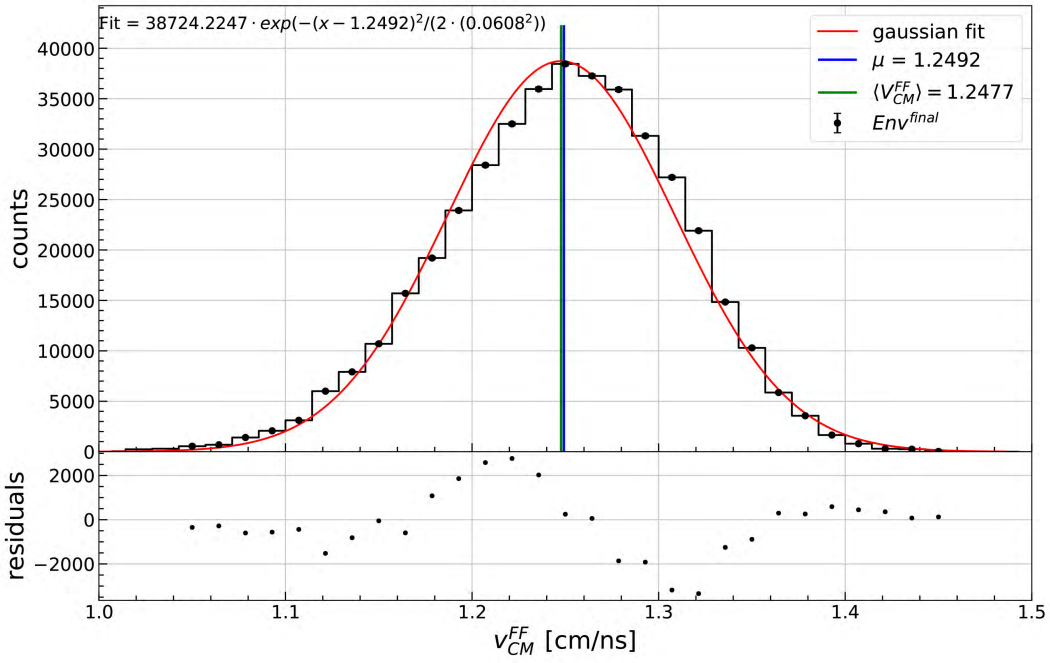

Figure 6.33: *The velocity distribution $V_{CM}^{FF}(Z, A)$ resulting from the envelope of fusion-induced fission events after subtracting the contamination for the fission fragment of $(Z = 52, A = 126)$ in the ^{265}Db fissioning system is presented. The Gaussian fit is depicted by the red line, and the residuals are shown in the bottom part of the figure. The mean value μ obtained from the Gaussian fit is represented by the blue line, while the average velocity is indicated by the green line.*

In the present experiment, the velocity resolution is enough to observe the oscillations in the residuals. As a means of comparison, the GEF model shows in Fig. 6.34 an isotopic velocity distribution akin to the experimental data presented in Fig. 6.33. However, the GEF model predicts a slightly higher velocity for the fission fragments, approximately ≈ 0.05 cm/ns, both in terms of the mean value (μ) and the average velocity. This deviation is also evident in the oscillations in the lower panel residuals.

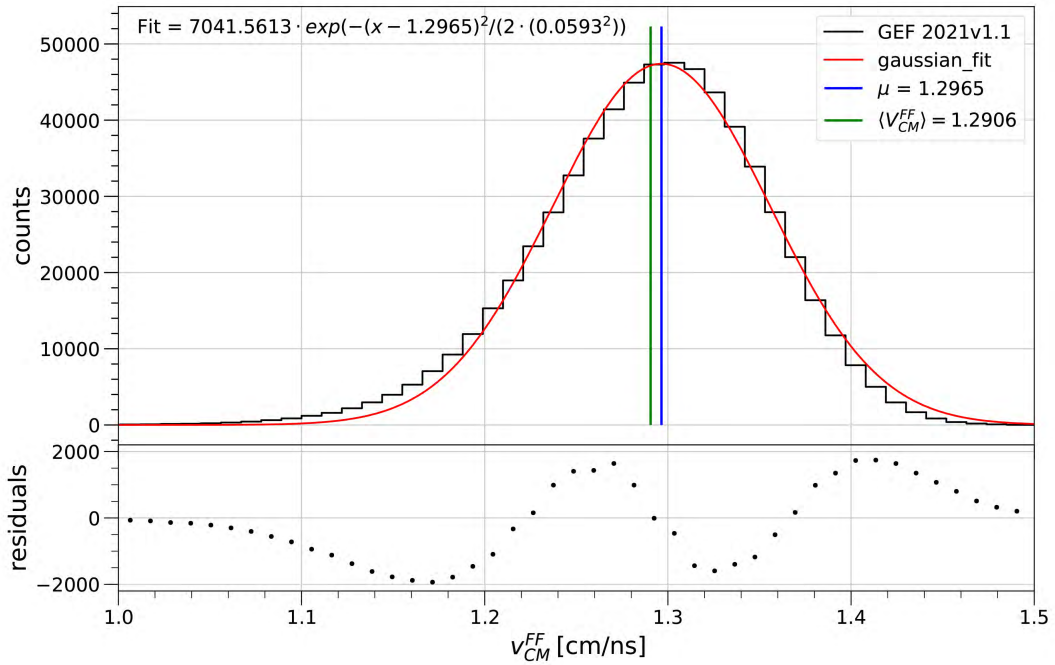

Figure 6.34: *Simulation performed by the GEF model [46] for the isotopic velocity in the centre-of-mass distribution $V_{CM}^{FF}(Z,A)$ of the fission fragments for the ^{264}Db fissioning system ($Z = 52, A = 126$). The red line represents the Gaussian fit, and the residuals are displayed in the lower section of the figure. The mean value μ, derived from the Gaussian fit, is depicted by the blue line, and the average velocity is represented by the green line.*

The average velocity of isotopically identified fragments in the centre-of-mass reference frame of the ^{265}Db fissioning system is depicted in Section 7.8.

6.9.2 Fragment velocities from ^{249}Bk fission

To assess the centre-of-mass velocity distribution of each fission fragment, similar to what was done with the aluminium target (see Fig. 6.30), it is presumed that there exists a factor that links the isotopic yields to the area of isotopic velocity distributions for both fusion-induced fission and transfer reactions. In the case of the ^{265}Db fissioning system, this factor can be directly measured for each VAMOS++ setting. However, it cannot be measured directly for the ^{249}Bk fissioning system. Thus, it can be expressed as follows:

$$V_{CM}^{FF}(Z,A) = V_{CM}^{FF}(Z,A)_{FuFi} - V_{CM}^{FF}(Z,A)_{Transfer} \cdot \mathcal{C}(Z) \cdot \frac{\mathcal{S}(Z,A)_{Transfer}}{\mathcal{S}(Z,A)_{FuFi}}, \tag{6.35}$$

where $V_{CM}^{FF}(Z,A)$, for both *FuFi* and *Transfer*, represents velocity distributions for all θ_{CM}^{FF} angles, selecting an isotope (Z,A). Here, $\mathcal{C}(Z)$ denotes the contamination factor by atomic number, as estimated in Section 6.5. The $\mathcal{S}(Z,A)_{Transfer}$ and $\mathcal{S}(Z,A)_{FuFi}$ are the scaling factors between

the area of the velocity distribution and the yield of transfer and fusion-fission production (after applying the relative efficiency), respectively:

$$Y(Z,A)_{FuFi} = \mathcal{S}(Z,A)_{FuFi} \cdot Ar(V_{CM}^{FF}(Z,A)_{FuFi})\,, \tag{6.36}$$

$$Y(Z,A)_{Transfer} = \mathcal{S}(Z,A)_{Transfer} \cdot Ar(V_{CM}^{FF}(Z,A)_{Transfer})\,. \tag{6.37}$$

The $Y(Z,A)_{Transfer}$ will be presented in the results (see Section A.4). The centre-of-mass velocity of the boron target fission fragments is calculated assuming negligible contamination from fusion-induced fission in the transfer distributions. Furthermore, due to the number of bins required to work with both fusion-induced fission and transfer distributions simultaneously, it is necessary to smooth the velocity distribution of transfer, avoiding statistical fluctuations with low statistics:

$$V_{CM}^{FF}(Z,A)_{Transfer}^{smooth} = \frac{V_{CM}^{FF}(Z,A,X_{i-1})_{Transfer} + V_{CM}^{FF}(Z,A,X_{i})_{Transfer} + V_{CM}^{FF}(Z,A,X_{i+1})_{Transfer}}{3}\,, \tag{6.38}$$

where X represents the content of the i-th bin.

Similar to the situation observed with ^{265}Db, the resulting velocity distributions stemming from fusion-induced fission in the ^{249}Bk fissioning system exhibit non-Gaussian characteristics. Once the velocity distributions have been obtained, the verification of the kinematics of fission reactions and the independence of v_{CM}^{FF} with respect to the centre-of-mass angle θ_{CM}^{FF} must be performed, as explained in the case of the ^{265}Db fissioning system. The kinematic analysis follows the same scheme as shown in Fig. 6.31, where the velocity $v_{CM}^{FF}(Z,A)$ for (Z,A) fission fragment of any fissioning system should exhibit independence with the angle θ_{CM}^{FF}. The alignment between velocity and centre-of-mass angle has been examined for all fission fragment isotopes of the ^{249}Bk fissioning system. The variations in centre-of-mass velocity are close to the deviations observed in the ^{265}Db case, with fluctuations of the order of ± 0.01 cm/ns. These results indicate alignment deviations below 1%.

As in the case of the ^{265}Db fissioning system, the measurement is precise enough to observe clearly the fluctuations of the residuals with respect to a Gaussian fit (see Fig. 6.35 for the case of $Z = 41$, $A = 101$).

The centre-of-mass velocity distribution of isotopic case $Z = 41$ and $A = 101$, simulated with GEF model [46], is presented in Fig. 6.36 for comparison. The GEF model, as depicted in the simulation found in Fig. 6.36, displays an isotopic velocity distribution resembling the experimental data presented in Fig. 6.35. Nonetheless, the GEF model predicts a slightly higher velocity for the fission fragments, approximately ≈ 0.05 cm/ns. This discrepancy is also discernible in the oscillations of the residuals shown in the lower panel. Similar discrepancies with the GEF model are observed in a manner akin to the ^{265}Db case, despite undergoing different estimation processes.

The isotopic fission fragment velocities in the centre-of-mass frame for the ^{249}Bk fissioning system are illustrated in Section 7.8. Equal to the case of ^{265}Db, the final velocity $v_{CM}^{FF}(Z,A)$ is determined by calculating the average of the velocity distribution.

USC UNIVERSIDADE DE SANTIAGO DE COMPOSTELA

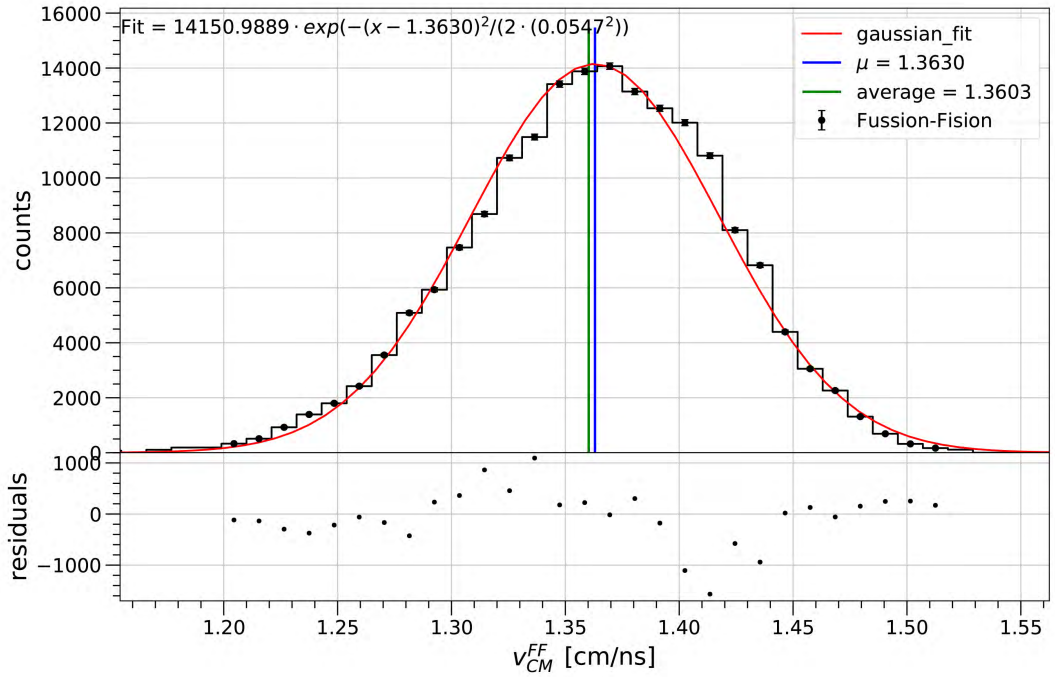

Figure 6.35: *The fragment velocities in centre-of-mass distribution V_{CM}^{FF} resulting from the subtraction of the contamination employing the relation between yields and velocities for the fission fragment of $(Z = 41, A = 101)$ in the ^{249}Bk fissioning system is presented. The Gaussian fit is depicted by the red line, and the residuals are shown in the bottom part of the figure. The mean value μ obtained from the Gaussian fit is represented by the blue line, while the average velocity is indicated by the green line.*

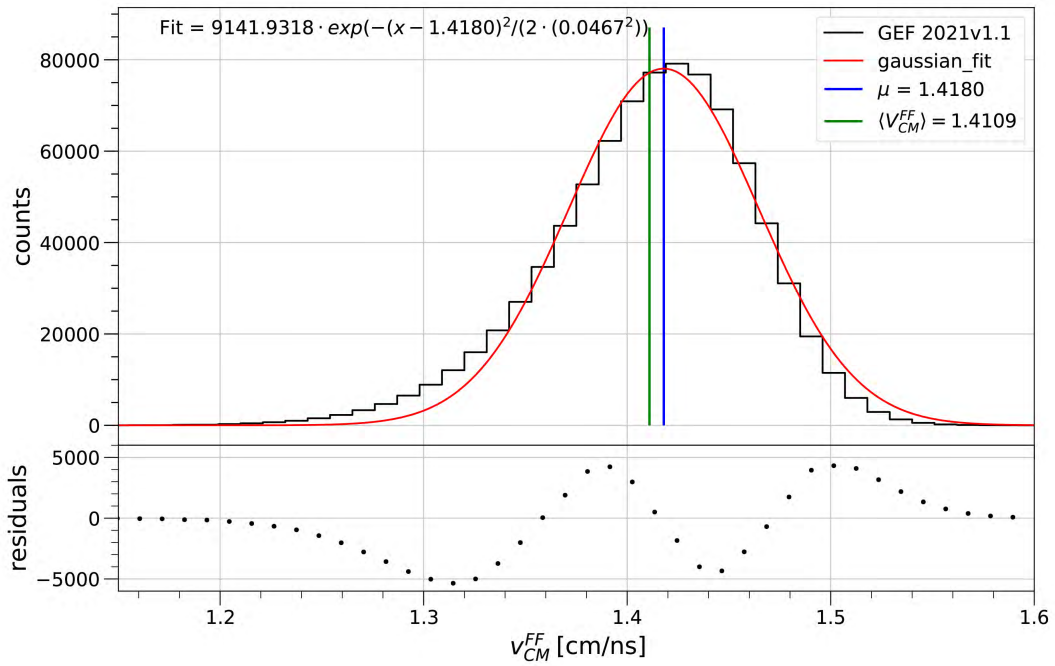

Figure 6.36: *Simulation performed by the GEF model [46] for the velocity in the centre-of-mass distribution V_{CM}^{FF} of the fission fragments for the ^{249}Bk fissioning system $(Z = 41, A = 101)$. The red line represents the Gaussian fit, and the residuals are displayed in the lower section of the figure. The mean value μ, derived from the Gaussian fit, is depicted by the blue line, and the average velocity is represented by the green line.*

Chapter 7

Results and interpretations

This chapter presents the results of the final observables and the isotopic fission-fragment yields of the ^{265}Db and ^{249}Bk fissioning systems, produced through the fusion-induced fission mechanism. These yields are calculated following the procedure discussed in Chapter 6. Additionally, various other physical observables derived from the isotopic yields are reported, including the yields of fission fragment masses and fragment atomic numbers, as well as the neutron excess, total neutron evaporation, and even-odd staggering. Furthermore, the characterisation of the scission point for the ^{249}Bk fissioning systems is presented, including the reconstruction at scission of fragment mass, post-scission neutron evaporation, total kinetic energy, and total excitation energy. The isotopic yields of the fissioning systems investigated in this study are listed in Appendix A.3. Whenever possible, the present work is compared with available previous data and calculations from the GEF semi-empirical model [46] (see Section 1.3.7). The error bars depicted in the figures correspond to the statistical errors associated with the measurements.

7.1 Final observables measurements

Throughout this investigation, a diverse set of observables, encompassing both direct and indirect measures, has been employed. Presented below is a concise compilation of the most pertinent ones. In Fig. 7.1, the left panels illustrate the final two-dimensional envelopes, showcasing the fragment mass number A plotted against the fragment mass over charge (A/q) for fusion-induced fission. Correspondingly, the right panels exhibit the relationship depicted by the final two-dimensional envelopes between the fragment atomic number Z and fragment mass-over-charge (A/q). The upper panels display data for ^{265}Db, whilst the lower panels present results for ^{249}Bk.

In Fig. 7.2, the left panels illustrate the position X_{FP} [mm] plotted against Y_{FP} [mm] at the focal plane, while the right panels display the final two-dimensional relationship between θ_{FP} [mrad] and ϕ_{FP} [mrad] at the focal plane. The upper panels showcase data for ^{265}Db, whereas the lower panels depict data for ^{249}Bk. Once again, these direct observables measured at the focal plane of VAMOS++: $(X_{FP}, Y_{FP}, \theta_{FP}, \phi_{FP})$, constitute the basis for the reconstruction of $(B\rho, Path, \theta, \phi)$ of the fission fragments.

USC UNIVERSIDADE DE SANTIAGO DE COMPOSTELA

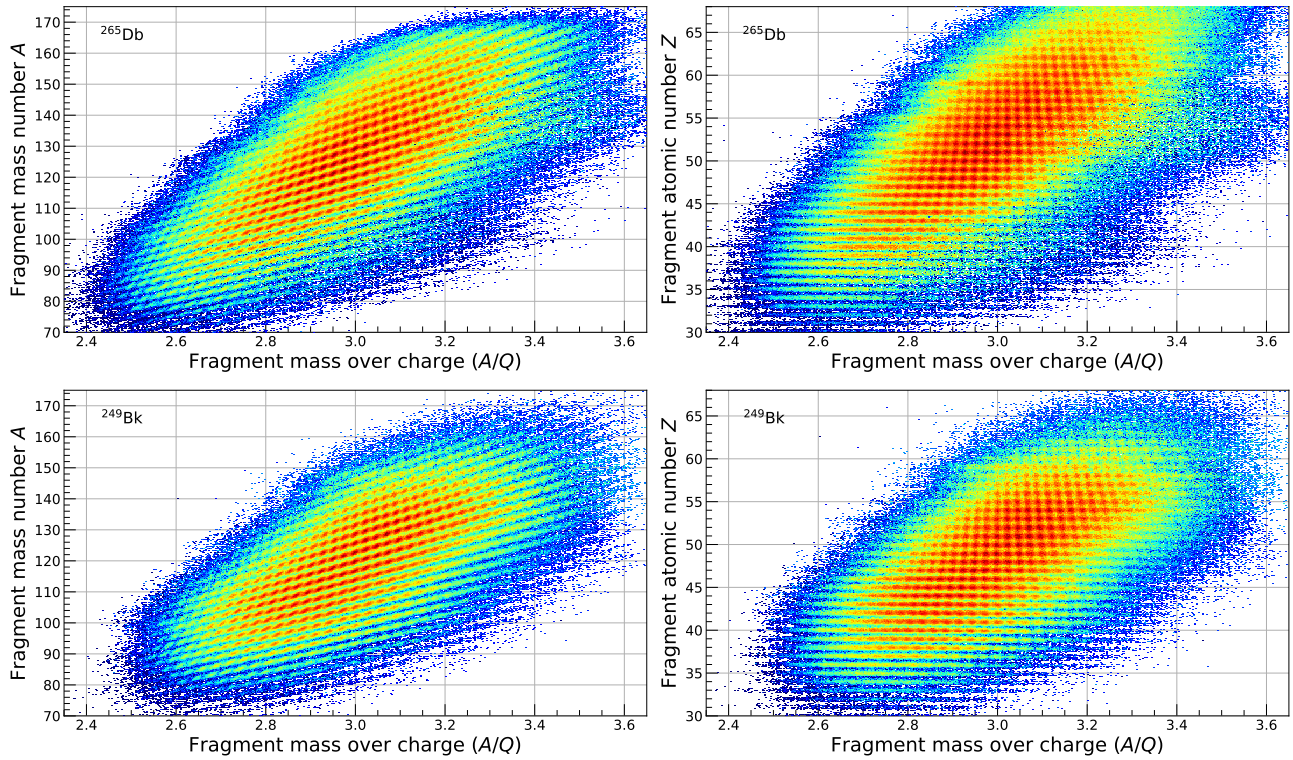

Figure 7.1: *The fragment mass number A versus mass-over-charge (A/q) in the left panels and atomic number Z versus mass-over-charge (A/q) in the right panels. ^{265}Db and ^{249}Bk are shown in the upper and lower panels respectively.*

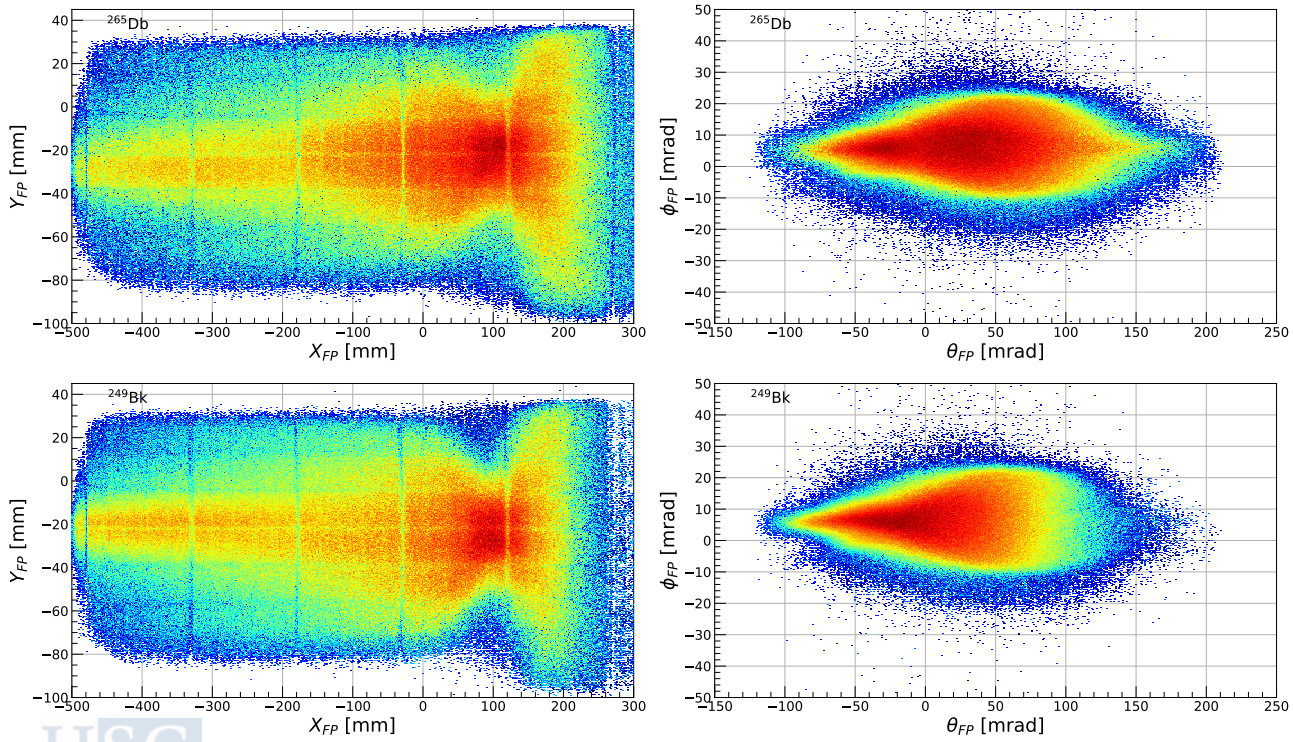

Figure 7.2: *Left panels show the position X_{FP} [mm] against the position Y_{FP} [mm], while the right panels show θ_{FP} [mrad] against ϕ_{FP} [mrad]. ^{265}Db and ^{249}Bk are shown in the upper and lower panels respectively.*

7.2 Fission fragment yields

Throughout this section, the relative fission yields of the ^{265}Db and ^{249}Bk fissioning systems are presented, each treated separately. The isotopic fission yields for each fissioning system were evaluated according to Section 6. In Fig. 7.3, isotopic distributions are depicted, illustrating fusion-induced fission yields in terms of both the fragment atomic number Z and the post-neutron-evaporation fragment mass number A. The measured isotopes for both aluminium and boron targets are presented, superimposed on the nuclear chart. The squares represent isotopes discovered to date, with the stable ones marked in black. A broad spectrum is covered in both neutrons and protons for both targets. Additionally, it can be observed that the yields for both targets are neutron-rich, agreeing with their respective fissioning systems. Finally, seemingly symmetric fission is obtained for both targets.

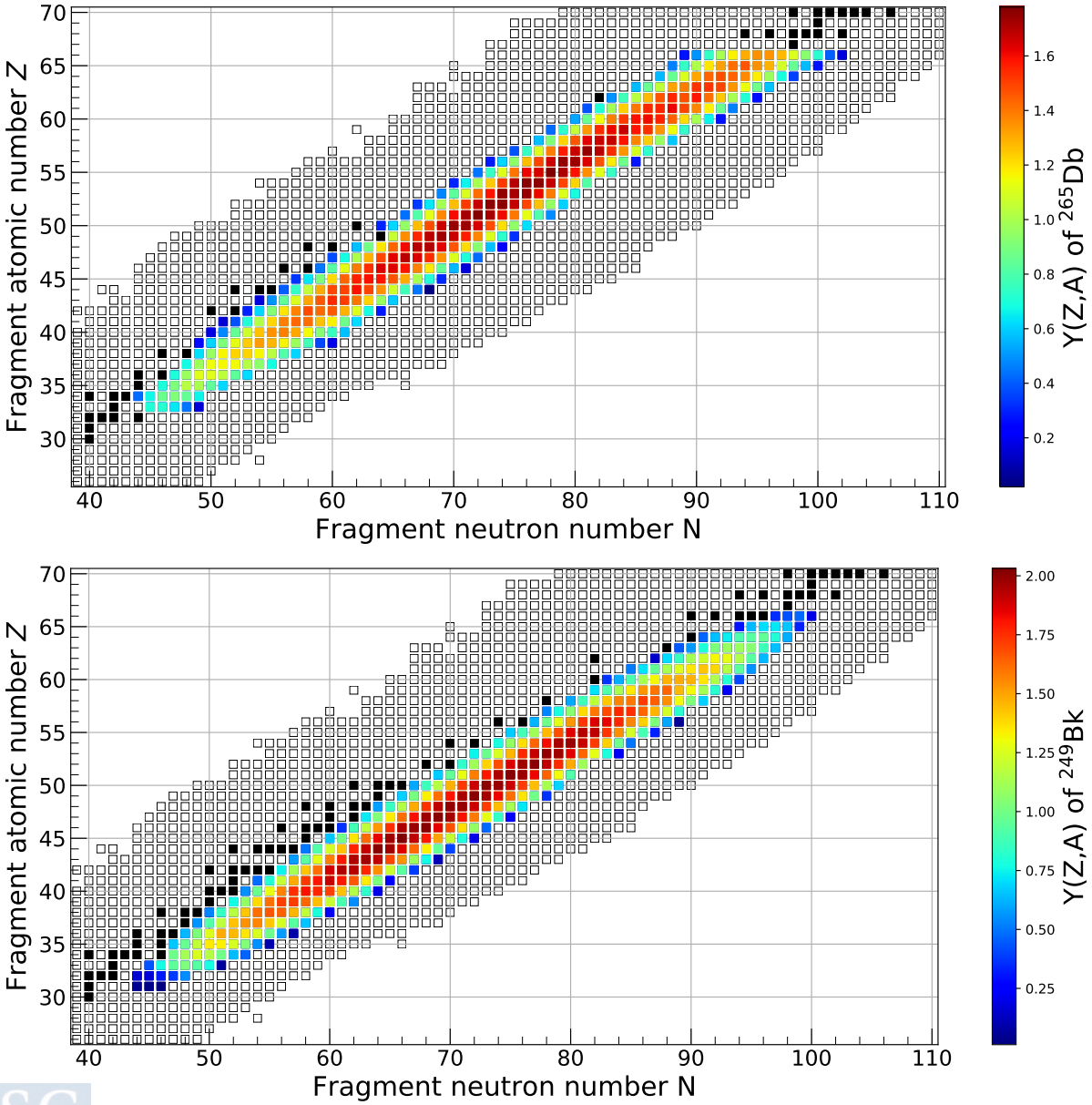

Figure 7.3: *The fission fragment yields for the fissioning systems ^{265}Db (top panel) and ^{249}Bk (bottom panel) are depicted on the nuclear chart, with the number of neutrons and protons corresponding to the fragments.*

7.2.1 Fusion-induced fission reactions with boron target

The formation of the fissioning system ^{249}Bk is achieved through fusion reactions utilising a ^{238}U beam at 5.88A MeV with a target composed of natural boron. The compound nucleus is formed with excitation energy of $E^*_{FS} = 47.7$ MeV. Under such elevated excitation conditions, the fissioning nucleus exhibits characteristics resembling those of a liquid droplet and displays a propensity for undergoing symmetric fission. These fission fragments are generated with a certain deformation and excitation, and subsequently undergo neutron and gamma emission during their deexcitation process. Consequently, the mass measurements of the fragments conducted in the experimental setup pertain to the post-neutron-evaporation mass, rather than the mass associated with the scission point (refer to Section 7.9). An angular momentum distribution (L) is also induced in the fissioning system. Following the Bass description [107], this results in $L_{RMS} \approx 1/\sqrt{2} \cdot L_{max} = 14\hbar$ where L_{max} is the grazing angular momentum estimated with $PACE_{IV}$.

The isotopic fusion-induced fission yields of ^{249}Bk are presented in Fig. 7.4. Each point corresponds to a specific fragment mass number A, and each colour represents a distinct fragment atomic number Z. Specific fission fragments such as Sr$^{Z=38}$, In$^{Z=49}$, and Ce$^{Z=58}$ are highlighted as examples.

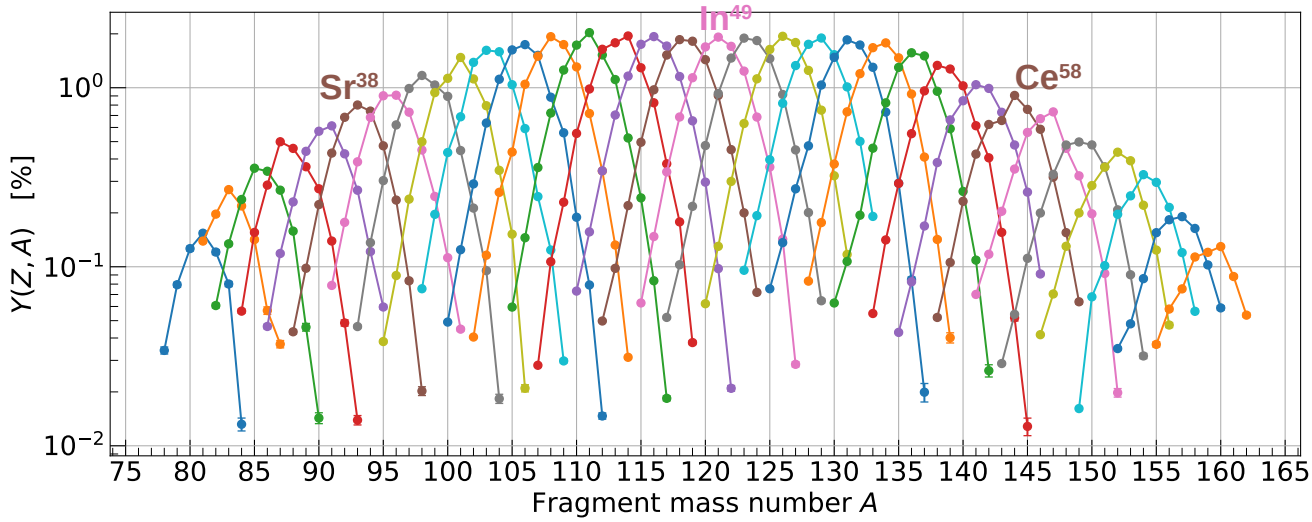

Figure 7.4: *The isotopic yields of ^{249}Bk are depicted in the figure. Each nuclear species, ranging from As$^{Z=33}$ to Gd$^{Z=64}$, is represented by a separate colour line. Each data point on the lines corresponds to a specific fragment mass A. Sr$^{Z=38}$, In$^{Z=49}$, and Ce$^{Z=58}$ are highlighted as examples.*

The ^{249}Bk fissioning system has an atomic number $Z_{FS} = 97$ and the isotopic yields have been successfully reconstructed for fragment atomic numbers $Z \in [33, 64]$ so it can be stated that the almost complete measurement of the isotopic yield distribution has been achieved.

The isotopic distributions of fission yields, $Y(Z, A)$, for ^{249}Bk in terms of fragment mass number A are depicted in Fig. 7.5 and in terms of fragment neutron number N in Fig 7.6. The red line represents the GEF semi-empirical calculations [46], while the black dots with error bars represent the current data.

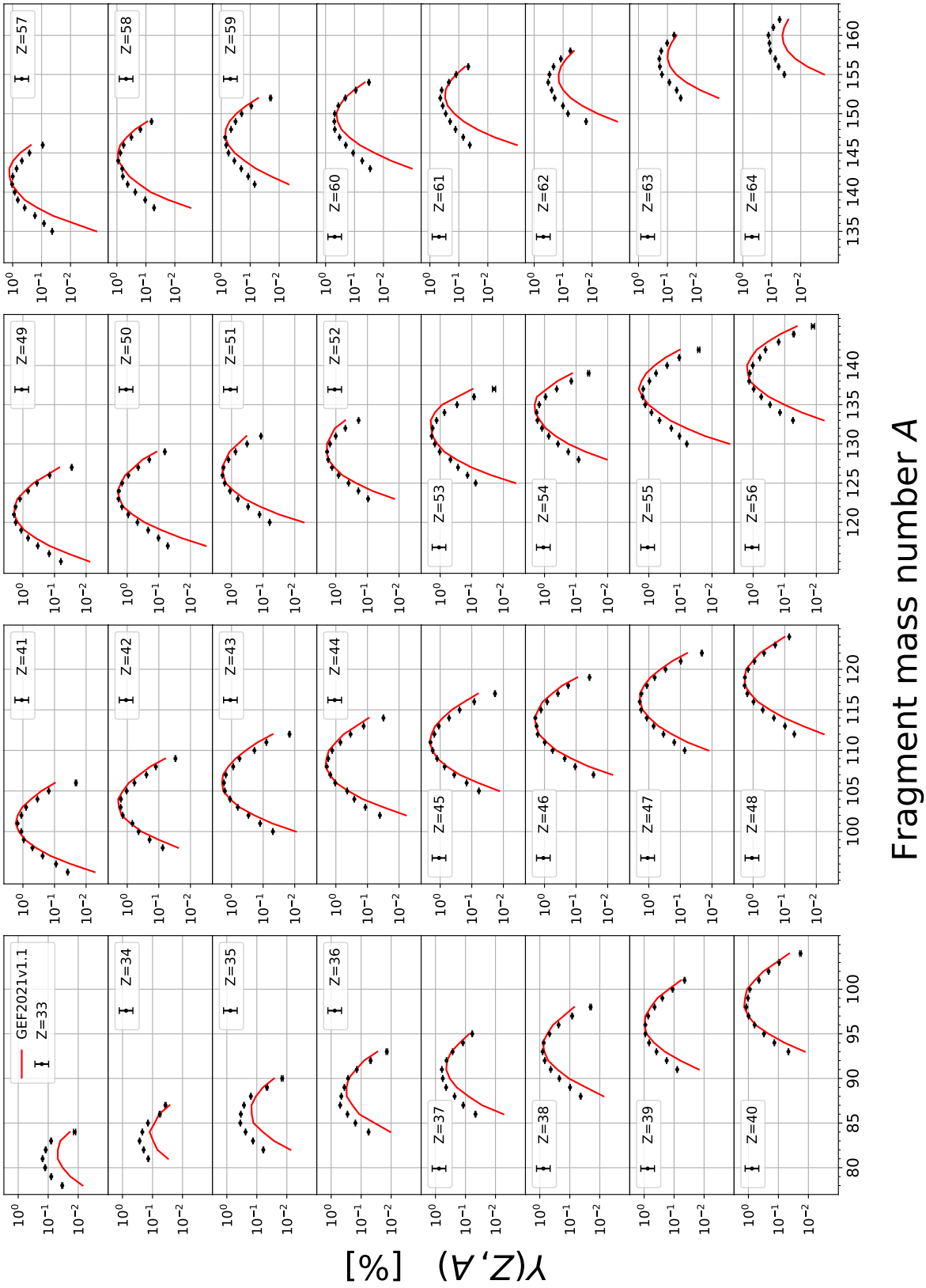

Figure 7.5: *The isotopic yield distributions in percentage as a function of the fragment mass number A for the ^{249}Bk fissioning system, with the fragment atomic number Z in the range of 33 to 64, is represented. The current data are depicted by the black dots, while the semi-empirical GEF calculations are represented by the red line [46].*

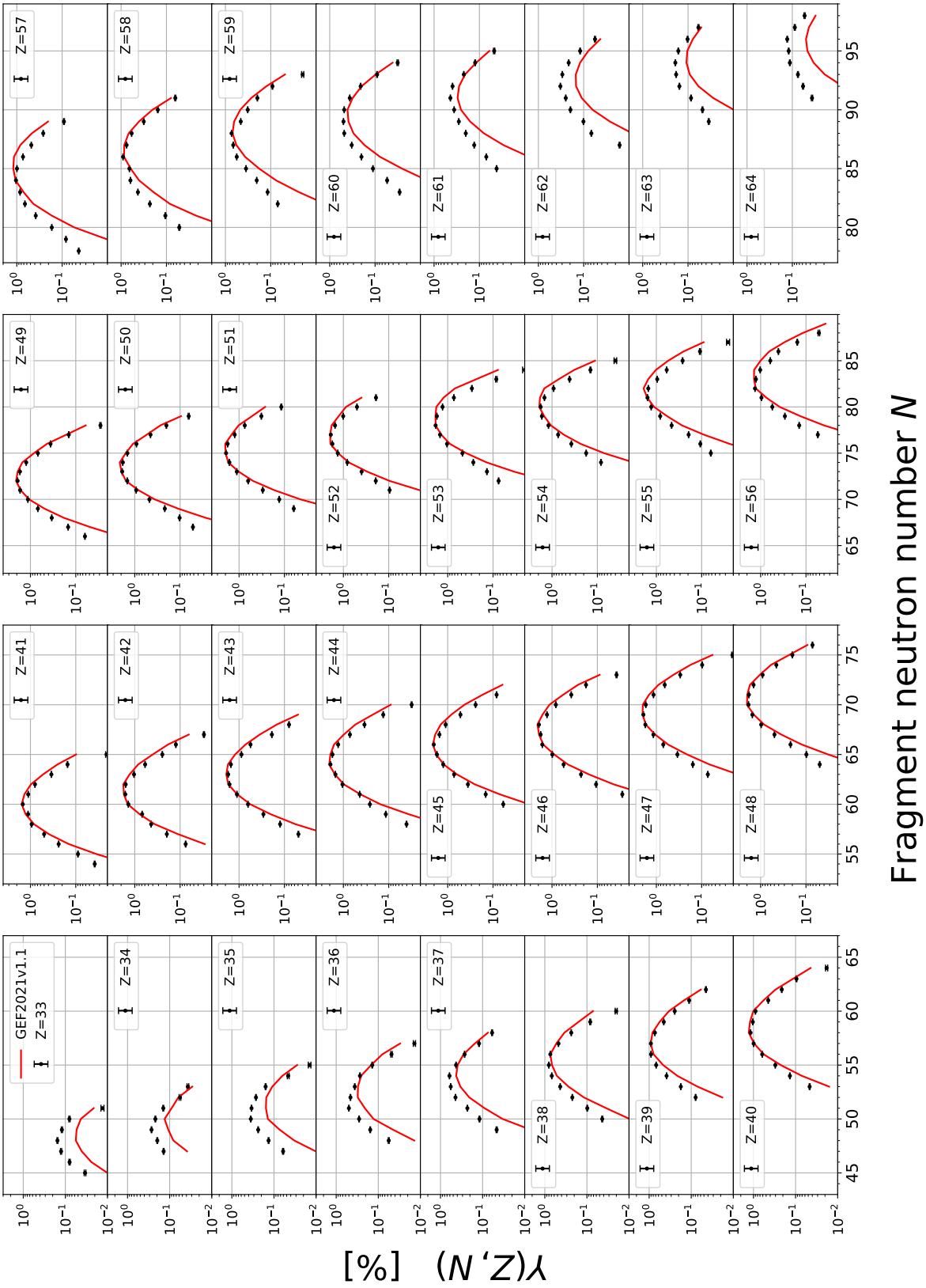

Figure 7.6: *The isotopic yield distributions in percentage as a function of the fragment neutron number N for the ^{249}Bk fissioning system, with the fragment atomic number Z in the range of 33 to 64, is represented. The current data are depicted by the black dots, while the semi-empirical GEF calculations are represented by the red line [46].*

The present data in Fig. 7.5 and in Fig. 7.6 show a generally asymmetric behaviour pronounced in the range of $Z > 47$. The GEF code exhibits a generally good agreement with the present data in the range of $Z \in [40, 52]$. However, for the rest of the atomic fragment numbers Z, the position of the experimental distributions does not agree with the GEF results.

In Fig. 7.7 the standard deviation σ of the isotopic yields $Y(Z, A)$ is presented as a function of fragment Z. For both lower and higher fragment Z, GEF appears to predict lower yield distributions, however there is a noticeable effect at $Z > 55$ where GEF has narrower distributions and at $Z \in [45, 50]$ where GEF shows constant σ but a small bulge appears in the data. The widths of the isotopic yields are a function of the excitation energy of the system and the distance of the neck, but are also related to the neutron evaporation. The standard deviation behaviour of the figure suggests that the neutron evaporation of GEF is increasing but constant and that the evaporation of the data is increasing too but with a bulge in the heavy fragments $Z > 55$. This effects is investigated in the next sections (see Section 7.9.3).

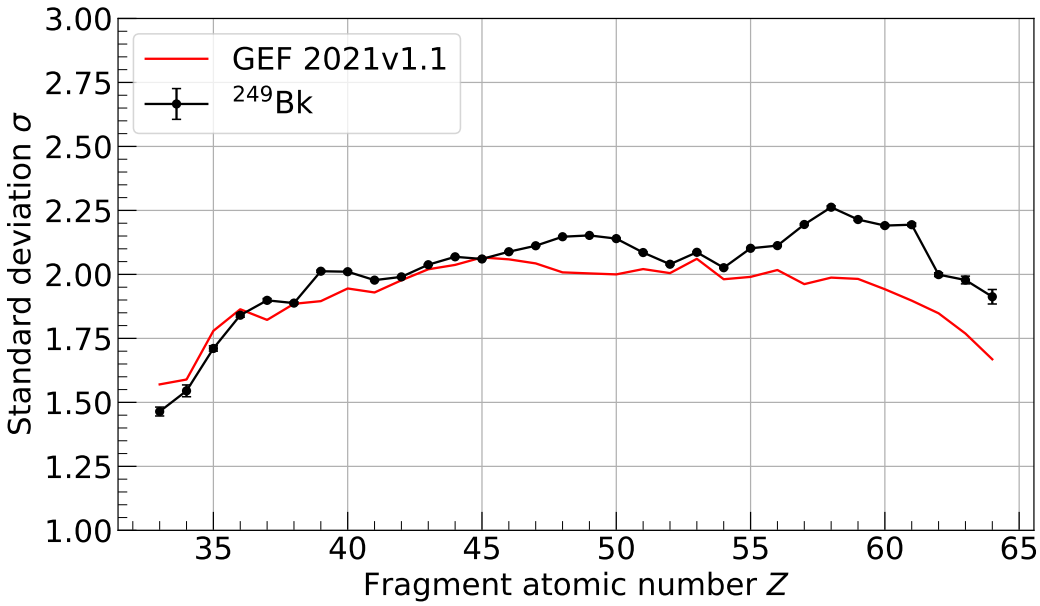

Figure 7.7: *The standard deviation of the isotopic yields $Y(Z, A)$ as a function of Z fragment of fission fragments of the ^{249}Bk fission system is shown. Experimental data with black line and dots and GEF calculations [46] with red line.*

The elemental yield $Y(Z)$ of fragment atomic number Z, for the fission fragments of the ^{249}Bk fissioning system is presented in Fig. 7.8. The current data are depicted by the black dots and it is compared from the calculations of the semi-empirical GEF model [46], represented by the red line.

The measured distribution of elemental yields, as depicted in Fig. 7.8, manifests a notable deviation when compared to the semi-empirical model GEF. On the one hand, GEF estimates a distribution characterised by asymmetric fission with peaks at approximately $Z = 45$ and $Z = 52$. On the other hand, as it can be observed, the experimental measurement indicates symmetric fission, with a peak centred at $Z_{FS}/2$ between $Z = 48$ and $Z = 49$. Nonetheless, the distribution exhibits a small central plateau. This observation suggests that some minor structural effects persist even at this high E^*_{FS}. The yields of each asymmetric-fission component are investigated in Section 7.2.2 and the shell structure effects is investigated in the next sections.

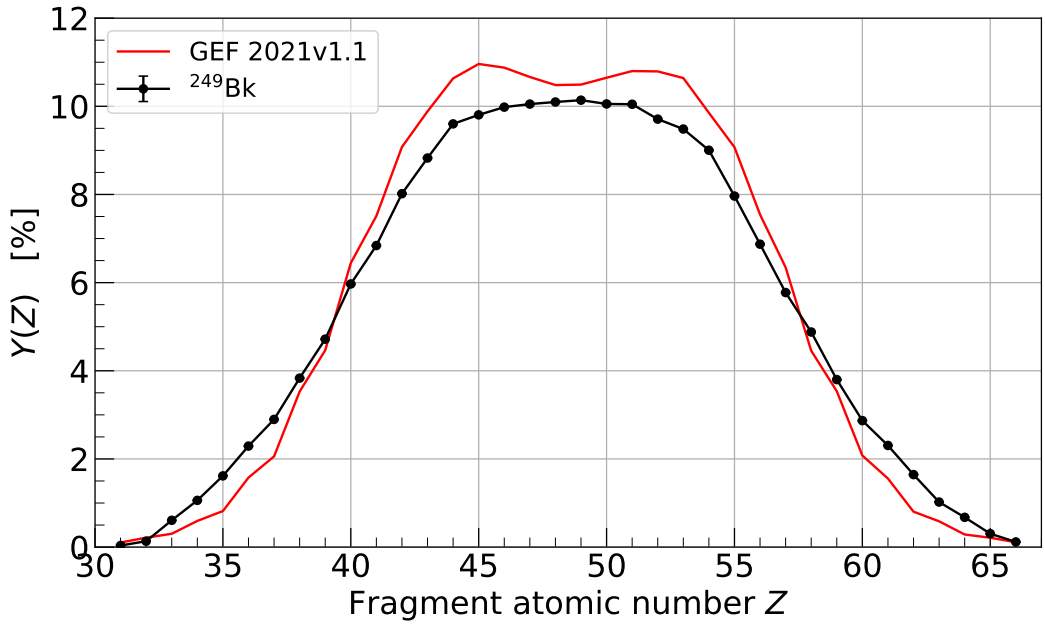

Figure 7.8: *The distribution of fragment atomic number elemental yields $Y(Z)$ of fission fragments of ^{249}Bk fissioning system at $E^*_{FS} = 47.7$ MeV is represented. The data, represented by black dots, are compared with the calculations from the semi-empirical GEF model [46], represented by the red line.*

The elemental yield $Y(A)$ of post-evaporation fragment mass for the fission fragments of the ^{249}Bk fissioning system is presented in Fig. 7.9. The current data are depicted by the black dots, compared with results from the semi-empirical GEF calculations, represented by the red line [46].

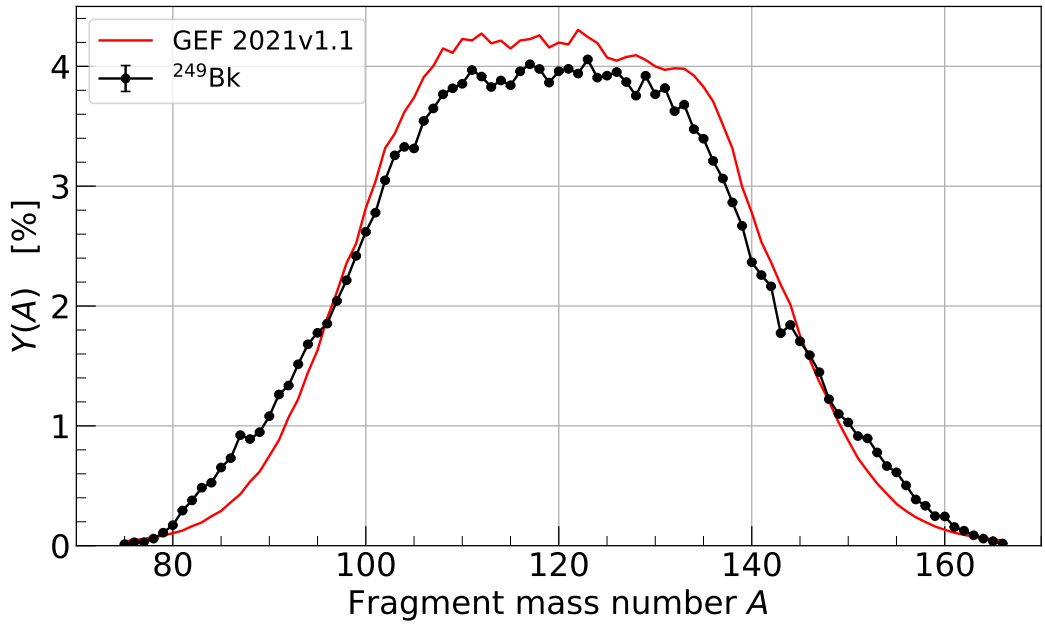

Figure 7.9: *The distribution of fragment mass elemental yields $Y(A)$ of fission fragments of ^{249}Bk fissioning system at $E^*_{FS} = 47.7$ MeV is shown. The data, represented by black dots, are compared with the calculations from the semi-empirical GEF model [46], represented by the red line.*

The post-scission neutron evaporation leads to an asymmetric distribution due to the observed increase in evaporation for heavier fragments [108]. Since neutron evaporation shifts the yields towards lower masses, heavier fragments experience a more pronounced shift in yields. A

discrepancy with the GEF model is less apparent than with the elemental yields. In contrast to the elemental yields $Y(Z)$, the prediction of GEF model shows a similar fission than the experimental data. GEF predicts that the most abundant fragments occur in a plateau between $(Z, A) = (45, 110)$ and $(Z, A) = (52, 135)$. The experimental data suggest a higher yield around $(Z, A) = (48 \leftrightarrow 49, 120)$ with a plateau towards symmetry, akin to the pattern observed in the elemental yield $Y(Z)$.

7.2.2 Fission modes in ^{249}Bk fissioning system

In this section, an investigation is conducted into the fission modes of the ^{249}Bk fissioning system in the fragment Z distributions. This analysis encompasses four fission channels, as described by Brosa *et al.* [31]: the Super-Long symmetric (SL), the Standard-I asymmetric (SI), the Standard-II asymmetric (SII), and the Super-Asymmetric channel (SA). According to the model of Brosa *et al.*, each fission channel represents a distinct pathway on the potential energy surface, relating to collective degrees of freedom, from the saddle to the scission point (refer to Section 1.3.1). These pathways exhibit well-defined characteristics in terms of elongation and asymmetry (refer to Section 1.3.5).

Each channel contributes to the overall Z distribution in the form of a Gaussian distribution. For this study, the addition of the four channels was subjected to fitting against the complete atomic number distribution of the fissioning system. It was a prerequisite that the amplitude of the SL channel remained fixed at the height of the distribution symmetry yield [106].

Figure 7.10 presents the fragment atomic number yield distributions of the ^{249}Bk fissioning system in the upper panel. Each colour line represents an individual fission channel and the solid red line is the sum of them, fitted to the distribution. The lower panel shows the residuals from the total fit. The parameters of each fission channel: position, width, and yield, are presented in Tab. 7.1.

Fission channels parameters

FS	Channel	Position	Width σ	Yield [%]	GEF Yield [%]	GEF Position
^{249}Bk	Super-Long (SL)	48.49 ± 0.04	5.6 ± 0.2	73.78 ± 1.97	71.81	48.50
	Standard I (SI)	53.5 ± 0.3	1.8 ± 0.1	8.14 ± 0.35	2.14	52.41
	Standard II (SII)	57.2 ± 0.4	2.4 ± 0.3	14.70 ± 0.72	25.77	54.20
	Super-Asymmetric (SA)	61.7 ± 0.4	1.7 ± 0.4	3.38 ± 0.06	0.28	58.80

Table 7.1: *Parameters of the fission channels, fitted to the fragment atomic number yield distributions.*

GEF estimates the yield percentages for various fission channels: a yield of 71.81% for the SL channel, 2.14% for the SI channel, 25.77% for the SII channel and 0.28% for the SA channel. When comparing the measured data with the GEF simulation, a clear discrepancy emerges. The estimation of the SL channel agrees with the actual result, deviating by < 2 percentage points. Nevertheless, the simulated fission using elemental yields $Y(Z)$ is markedly asymmetric, notably overestimating the SII channel by a significant margin. Consequently, the GEF model underestimates the asymmetric SI channel in comparison to SII. In experimental data, SII dominates over SI, yet the SI contribution of the channel is non-negligible and surpasses the prediction by GEF. Finally, attention is drawn to the SA channel or Super-Asymmetric channel. GEF model simulation dismisses it, providing a negligible yield estimation, but the data exhibit its existence with a substantial percentage.

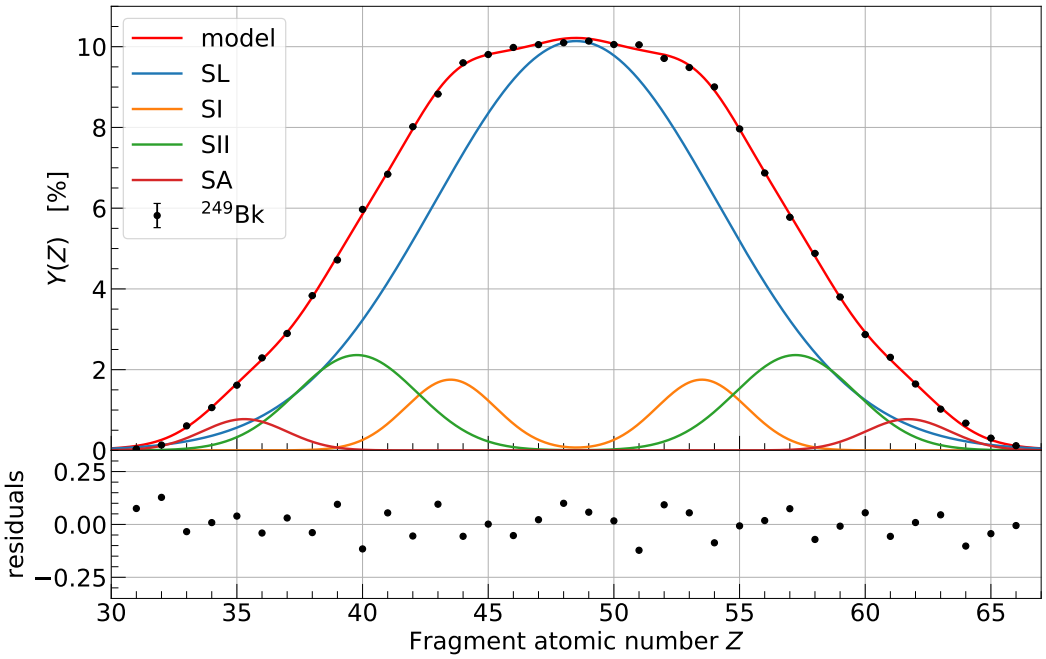

Figure 7.10: *Description of the fragment atomic number Z isotopic yield distribution in terms of fission channels for the ^{249}Bk fissioning system in the upper panel. The black dots represent experimental data with the statistical error bars, the colour solid lines reproduce each fission channels, and the solid red line indicates the sum of the four different channels. The lower panel shows the residuals of the total fit.*

A satisfactory description was achieved by employing four channels ($\chi^2_r = 0.15$). The *SI* channel is situated relatively close to the $Z = 52$ protons shell closure, particularly around masses $A = 135$ in the actinide region. The light fragment in the *SI* channel is close to $Z = 44$ protons. The *SII* channel represents an asymmetric channel centred around $Z = 57$ protons. It would be close to $Z = 56$ protons, reflecting an octupolar deformation with a deformed fission fragment. This observation of stabilisation in the nuclear charge of heavy fragments around $Z \sim 52$ and $Z \sim 56$ suggests that proton shell structure play a role in agreement with Scamps *et al.* [42]. Both channels have slightly higher values probably affected by the large contribution of the *SL* channel. The larger width of *SII* with respect to *SI* is consistent with a less compact configuration at scission. The *SL* channel corresponds to symmetry and is close to the $Z = 50$ protons shell closure. Lastly, the *SA* channel within the light fragment agrees closely with the proton shell closure at $Z = 34$. The investigation of asymmetric fission initiated from the sub-lead region is typically interpreted as an effect of octupole correlations induced by deformed shell gaps at $N = 52 \leftrightarrow 56$ neutrons within the light fission fragments in this scenario. However, it is worth noting that shell gaps associated with substantial quadrupole deformations at $Z = 34$ and $Z = 42 \leftrightarrow 46$ protons also seem to play a contributing role. With this experimental data, a plausible agreement with these premises for actinide fission is feasible, given that the *SA* of the light fragment corresponds to $Z = 35$ protons and given that the *SI* of the light fragment corresponds to $Z = 44$ protons. These findings will be extensively discussed in the ensuing sections, along with an exploration of the total kinetic energy [42]. These results will be further discussed in subsequent sections, along with the study of the total kinetic energy.

The obtained values for the positions of the four fission channels exhibit slightly higher values than expected, particularly for ^{249}Bk. However, for massive fissioning systems with $A_{FS} \geq 240$, such as ^{250}Cf, measured values of $Z_{SI} \approx 53$ and $Z_{SII} \approx 57$ have been reported [102, 79], agreeing

well with the values obtained in this study for ^{249}Bk. Additionally, the observation of *SI* and *SII* channels is coherent with the description by Brosa *et al.* and with the measurement of another highly massive system like ^{250}Cf [102, 79]. The width of the *SL* channel in ^{244}Cm and ^{250}Cf is larger than the general trend of $\sigma_{SL} \approx 4$ observed in lighter fissioning systems ($A \ll 240$), which is consistent with the measurement of $\sigma_{SL} \approx 5.6$ from these experimental data for a massive fissioning system like ^{249}Bk. The positions of the fission channels calculated by GEF exhibit similarities with the experimental data for *SL* and *SI*. However, the *SII* channel is located at $Z \approx 54$, indicating a displacement of 3 units compared to the data. This displacement is associated with the asymmetric fission calculated by GEF (see Fig. 7.8) making *SI* channel less relevant in the asymmetric fission.

7.2.3 Transfer reactions with boron target

Transfer-induced fission reactions are feasible with the boron target (see Tab. 2.3). Employing the SPIDER trigger and a similar yield construction process as for fission, the isotopic yields of transfer-induced fission reactions can be determined. Nonetheless, in this experiment, the measured fission yields of systems produced through transfer channels are contaminated by events originating from fusion-induced fission reactions. A comprehensive investigation of transfer reactions exceeds the scope of this study. Nonetheless, to obtain fusion-induced fission yields and reconstruct velocities, it is necessary to assess the transfer yields and estimate the amount of contamination present in the fusion-induced fission events. When fusion-induced fission is studied the transfer yields multiplied by the contamination factors are tagged as $Y(Z,A)^{Cont}$, but here in this section, the transfer reactions are studied, thus tagging the yields as $Y(Z,A)^{Transfer}$.

The isotopic yields of transfer reactions are presented in Fig. 7.11. Each colour corresponds to a fragment Z, and each point represents a fragment A. These yields exhibit a very small amount of contamination from fusion-induced fission events. However, this contamination is negligible, as evident in Fig. 7.11. The transfer yields have undergone a similar analysis process to that the fusion-induced fission yields. Thus, it is assumed that the intrinsic efficiency with the boron target (see Eq. 6.20) is common to both mechanisms. Nevertheless, in contrast with the fusion-induced fission yields, masses have not been selected.

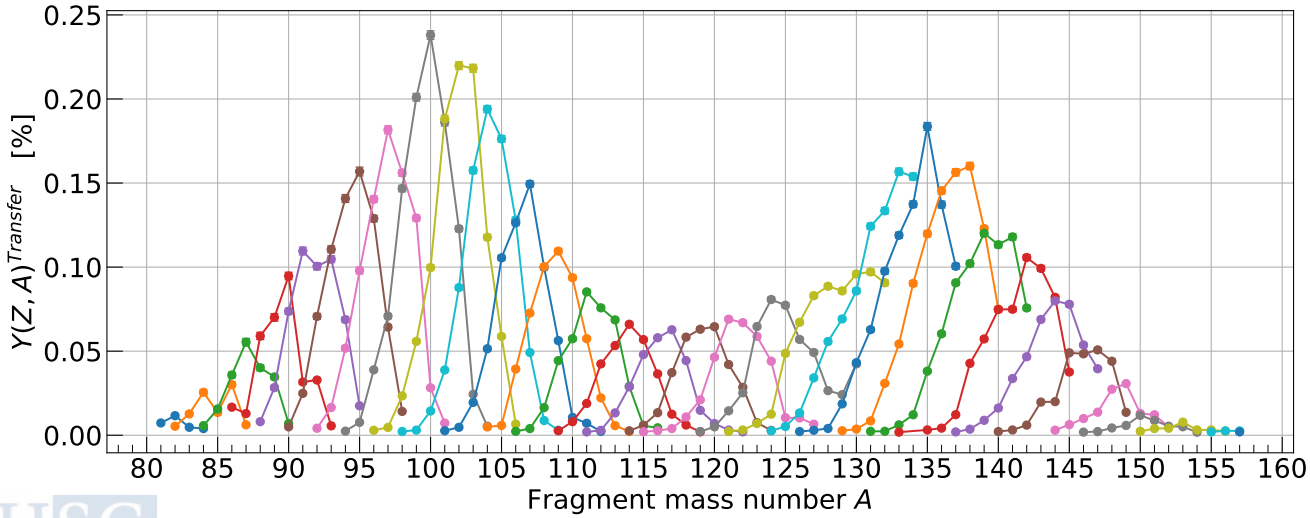

Figure 7.11: *The isotopic yields of the transfer reactions, $Y(Z,A)^{Transfer}$, with the boron target are displayed in various colours for each fragment atomic numbers Z, with the different fragment mass number A represented by data points.*

The elemental yield $Y(Z)^{Transfer}$ with the boron target is presented for each fragment Z in Fig. 7.12. The yield distribution of transfer reactions as a function of fragment mass number $Y(A)^{Transfer}$, with the boron target, is presented in Fig. 7.13. The results obtained in both figures (see Fig. 7.12 and Fig. 7.13) show that the most produced fragments have $Z = 40$ and $Z = 54$ with masses of approximately $A \approx 100$ and $A \approx 135$ respectively. These asymmetric transfer distributions are centred at $Z = 47$ and $A = 120$. It is precisely because of this shift from the symmetry centre of fusion-induced fission yields that the process of obtaining yields for the boron target can be evaluated, estimating the contamination factors as explained in Section 6.5 and Section 6.6.

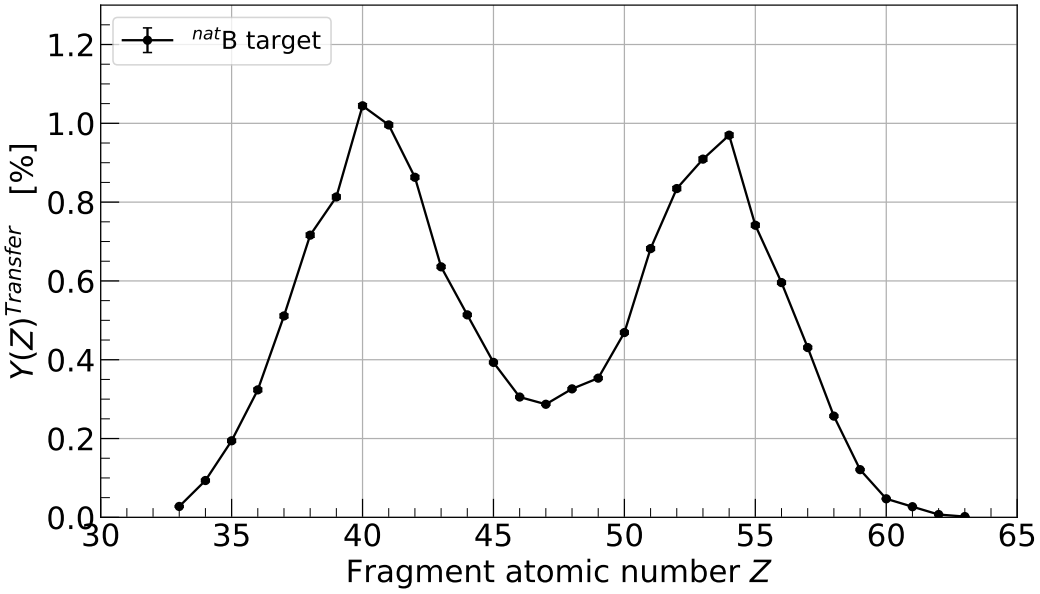

Figure 7.12: *The elemental yields of the fragment atomic number distributions $Y(Z)^{Transfer}$ of transfer reactions with the boron target are presented.*

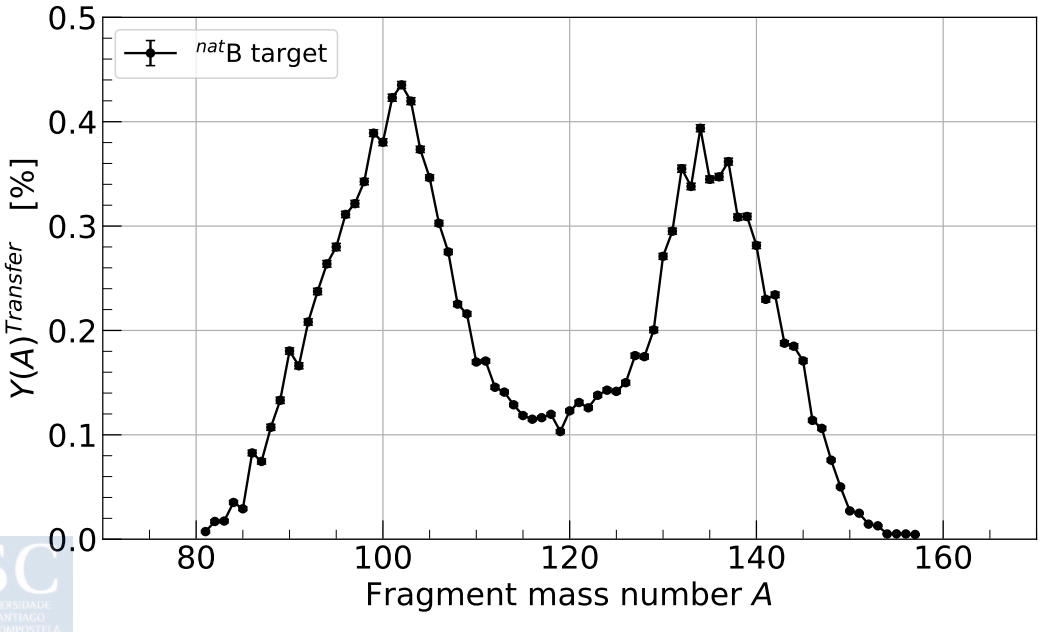

Figure 7.13: *The elemental yields of the fragment mass number distributions $Y(A)^{Transfer}$ of transfer reactions with the boron target are presented.*

Employing both the SPIDER detector and the measured energy space (E, dE) (see Section 2.3.2), the recoils generated by the interactions between the uranium beam and the boron target can be selectively identified (see Fig. 2.18). Once each recoil has been individually identified, the various possible transfer reactions are selected. The elemental yields $Y(Z)^{recoil}$ for the predominant recoils, distinguished by various colours for each resulting compound nucleus, are presented in Fig. 7.14 for reference. The compound nuclei formed are listed in Tab. 2.3.

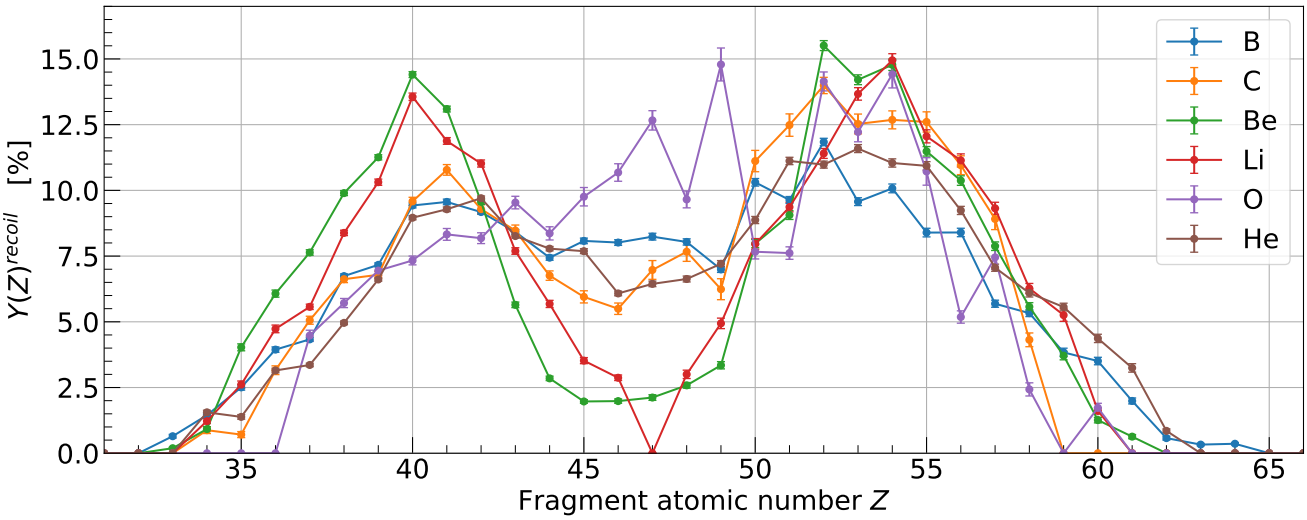

Figure 7.14: *The elemental yields $Y(Z)^{recoil}$ for each recoil selected with the SPIDER telescope detector and generated in the transfer reactions with the boron target and the uranium beam are presented as preliminary results. Each recoil is represented by different colour lines with each dot representing the atomic number Z.*

7.2.4 Fusion-induced fission reactions with aluminium target

The fusion reactions involving a ^{238}U beam at 5.88A MeV and an ^{27}Al target lead to the formation of the super-heavy ^{265}Db fissioning system. The resulting fissioning system acquires an excitation energy of $E^*_{FS} = 61.2$ MeV. Under such high excitation conditions, the fissioning nucleus exhibits characteristics reminiscent of a liquid drop and tends to undergo symmetric fission, resulting in two fragments of equal average size. These fission fragments are generated in an excited state and subsequently release neutrons. Consequently, the mass of the fragments measured in the experiment corresponds to the post-neutron-evaporation mass, rather than the mass at the scission point (see Section 7.9). An angular momentum distribution (L) is also induced in the fissioning system. Following the Bass description [107], this results in $L_{RMS} \approx 1/\sqrt{2} \cdot L_{max} = 27\hbar$ where L_{max} is the grazing angular momentum estimated with $PACE_{IV}$.

The isotopic fission yields of ^{265}Db fissioning system are presented as a function of the fragment A in Fig. 7.15. Each colour represents a distinct fragment Z. Specific fission fragments such as $Zr^{Z=40}$, $Te^{Z=52}$, and $Nd^{Z=60}$ are highlighted as examples. Isotopic yields have been successfully measured for fragment $Z \in [33, 66]$.

With the obtained isotopic yields, elemental yields are derived following the procedure explained in Section 6. The ratio of yields between $Y(Z)$ and its complementary $Y(Z_{comp})$,

where $Z_{FS} = Z + Z_{comp}$, represented as $Y(Z)/Y(Z_{comp})$, is depicted in Fig. 7.16. A noticeable increase without fluctuations is evident. This indicates a asymmetry in the yields of ^{265}Db, resulting from a phenomenon different from fusion-induced fission reactions known as quasi-fission (see Section 1.4). This process together with VAMOS++ acceptance augments the yields of higher fragment Z, hence deviating from the anticipated $Y(Z)/Y(Z_{comp}) = 1$ characteristic of fully equilibrated fusion-induced fission reactions (see Fig. 7.28). Further elaboration on this phenomenon is provided in Section 7.4. It is important to note that the GEF semi-empirical model code [46] does not include the description of the quasi-fission process.

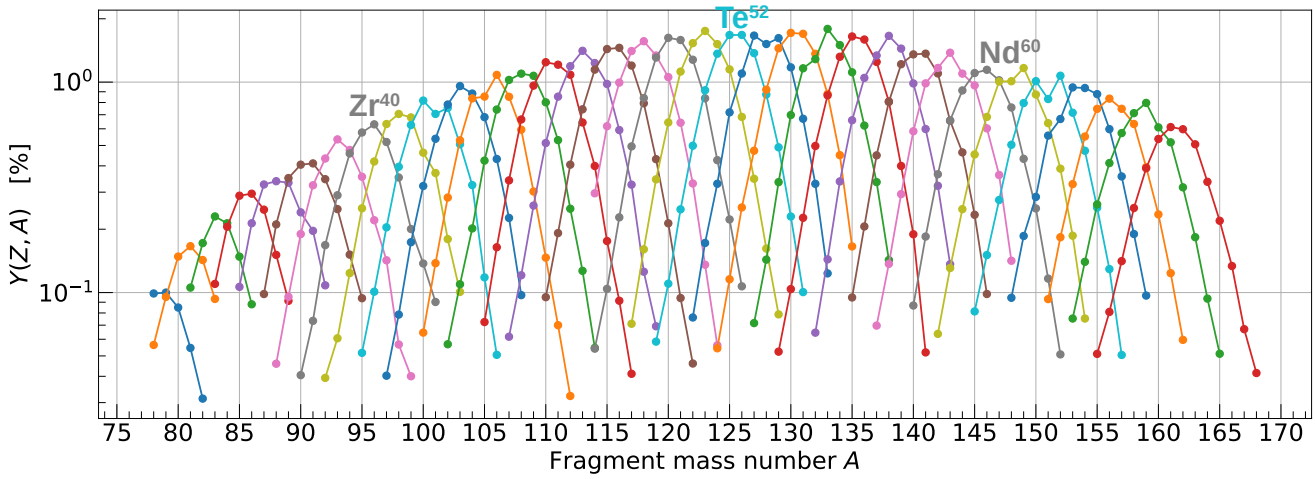

Figure 7.15: *The isotopic yields of ^{265}Db are depicted. Each nuclear species, ranging from $As^{Z=33}$ to $Dy^{Z=66}$, is represented by a separate colour line. Each data point on the lines corresponds to a specific fragment mass number A. Specific fission fragments such as $Zr^{Z=40}$, $Te^{Z=52}$, and $Nd^{Z=60}$ are highlighted as examples.*

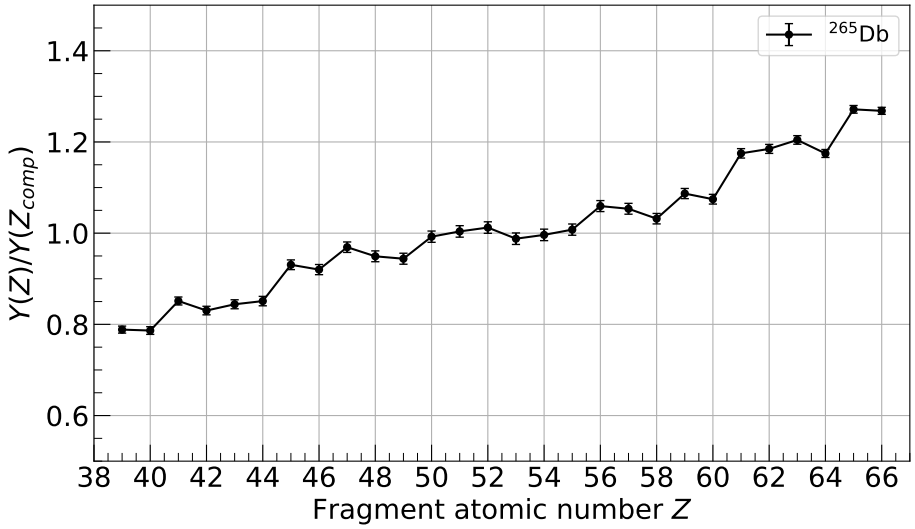

Figure 7.16: *The ratio of yields between atomic number complementary fission fragments, $Y(Z)/Y(Z_{comp})$, is shown for the ^{265}Db fissioning system.*

The distributions of fusion-induced fission isotopic yields for ^{265}Db in terms of fragment A are presented in Fig. 7.17. Similarly, the distributions of fusion-induced fission isotopic yields for ^{265}Db in terms of fragment neutron number are shown in Fig. 7.18. In both figures, the GEF semi-empirical calculations are represented by the red line, while the current data are depicted by the black dots with error bars.

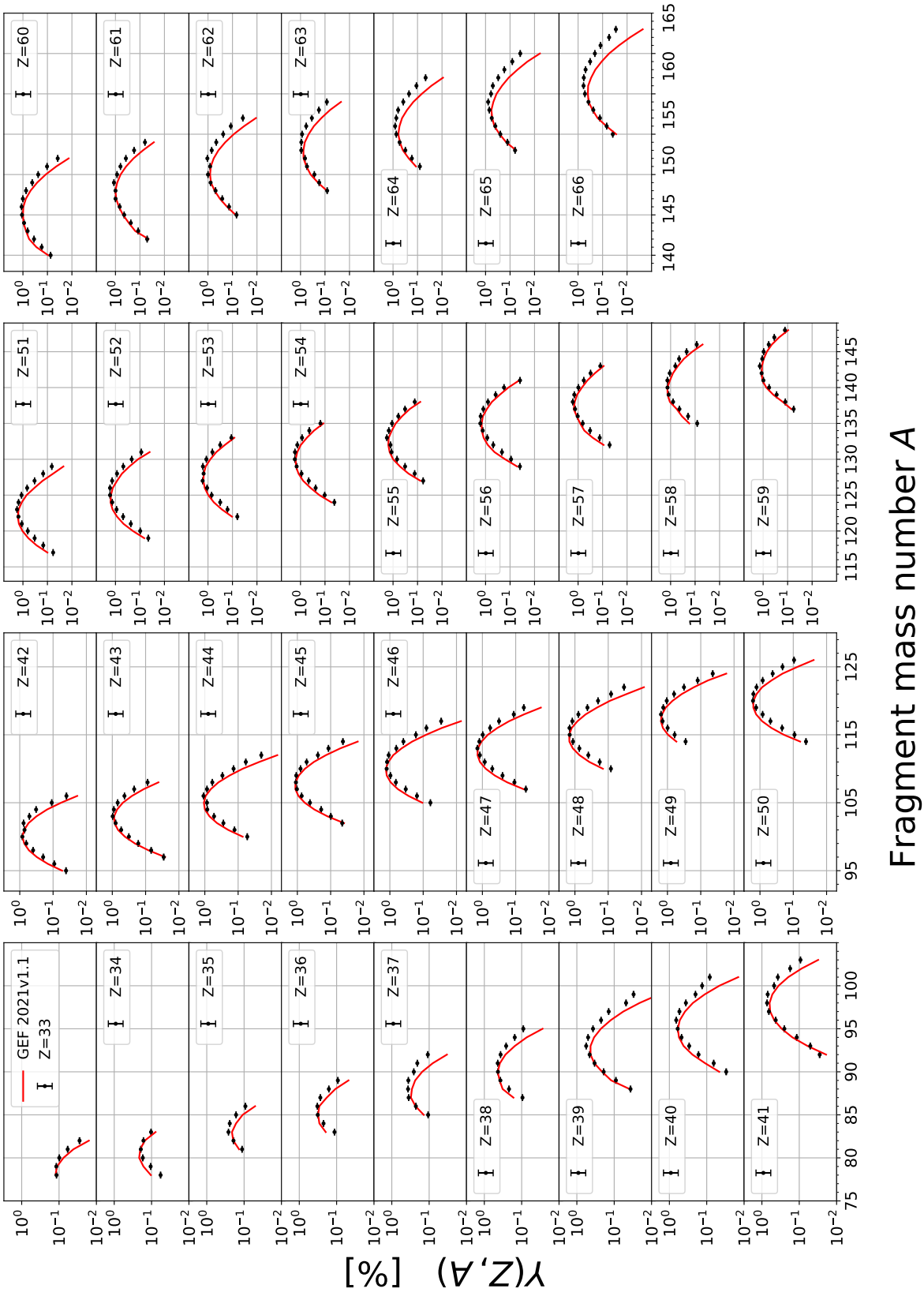

Figure 7.17: *The isotopic yield distributions in percentage as a function of the fragment A for the ^{265}Db fissioning system, for fragment Z in the range of 33 to 66, is represented. The current data are denoted by the black dots, whilst the semi-empirical GEF calculations [46] are represented by the red line.*

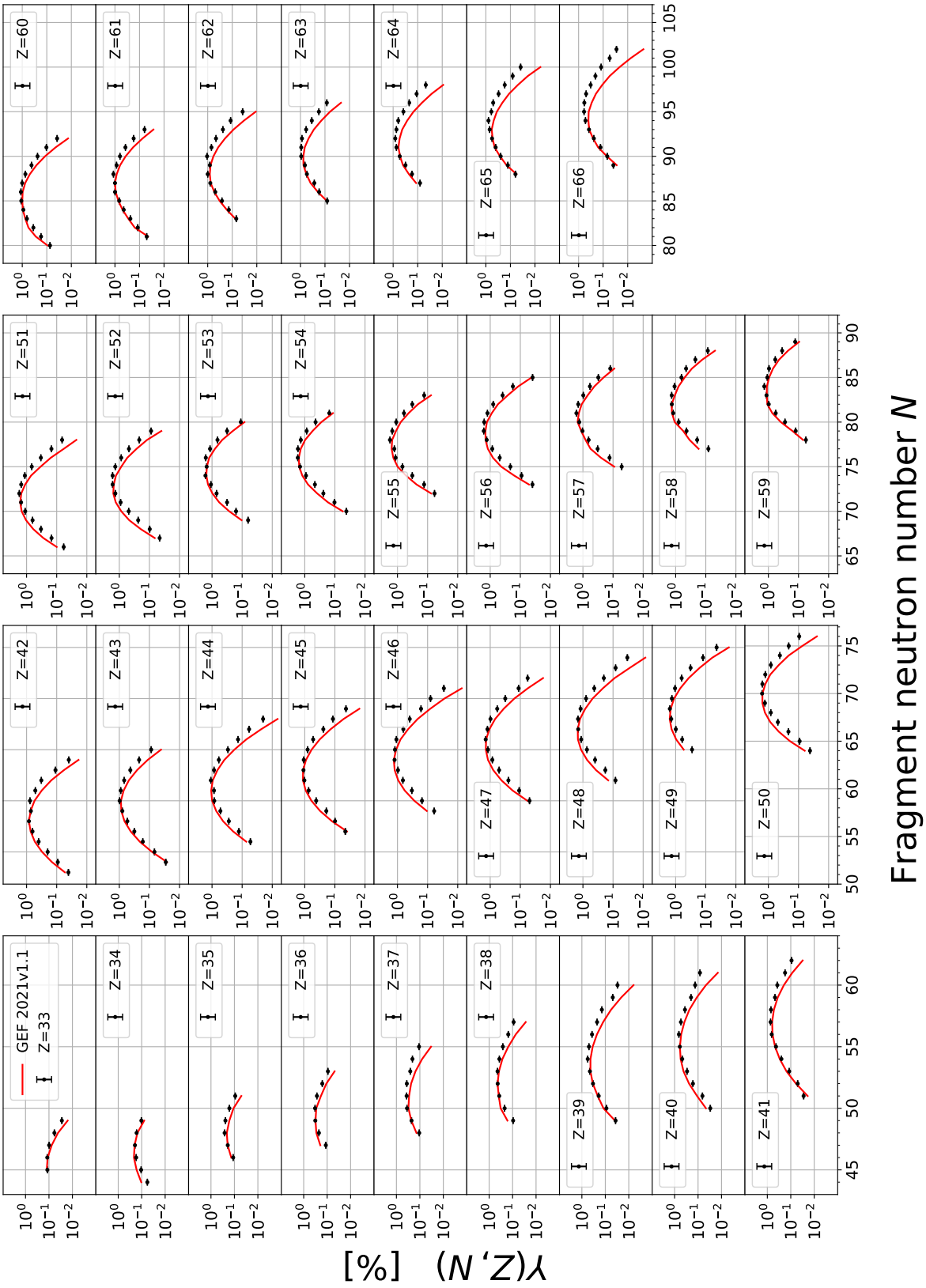

Figure 7.18: *The isotopic yield distributions in percentage as a function of the fragment neutron number N for the ^{265}Db fissioning system, focusing on fragment atomic number Z in the range of 33 to 66, is represented. The current data are denoted by the black dots, while the semi-empirical GEF calculations [46] are represented by the red line.*

As it can be seen in both figures, the experimental yield distributions are in general in good agreement with GEF semi-empirical model calculations for all fragment Z. However, it appears that the mean values of the experimental distributions do not match the GEF calculations. By combining the information from both figures, it can be observed that there is a shift on neutrons between the experimental data and the GEF model. As was done for ^{249}Bk, the widths of the isotopic yields can be calculated. In Fig. 7.19 the standard deviation σ of the isotopic yields $Y(Z, A)$ is presented as a function of fragment Z.

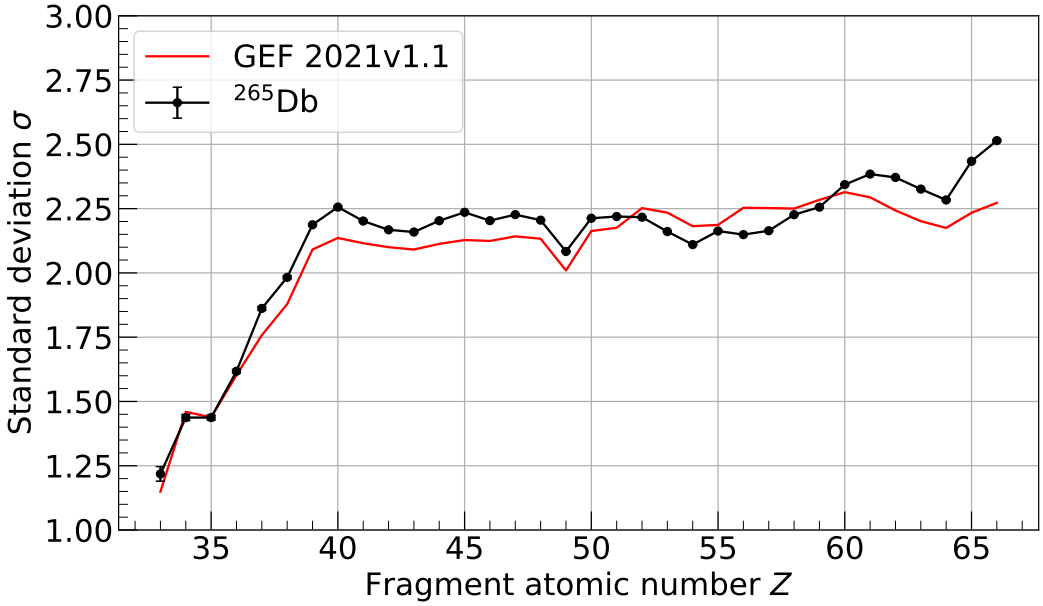

Figure 7.19: *The standard deviation of the isotopic yields $Y(Z, A)$ as a function of Z fragment of fission fragments of the ^{265}Db fission system is shown. Experimental data with black line and dots and GEF calculations [46] with red line.*

The experimental data show a larger standard deviation for $Z \in [40, 47]$ which may explain the shift on neutrons between the experimental data and the GEF model mentioned above. Despite the distributions having similar yields, GEF predicts the evaporation of more neutrons for each fragment atomic number Z compared to the experimental data of this work. The emission of one or two extra neutrons than the experimental data leads to a shift in the yield distributions. In addition to this discrepancy, the trend for fragment $Z > 60$ of the standard deviation of the isotopic yields is different between the data and the GEF prediction. The data show larger widths versus the width stability shown by GEF which may also indicate a larger neutron evaporation in the experimental data than with GEF calculations. However, this discrepancy is visible in the three figures and cannot be explained solely by the additional neutron emission from the GEF simulations. This discrepancy is attributed to the quasi-fission process, which is not accounted for in the GEF model and is prominent for higher Z values. This argument is consistent with previous measurements by Tōke *et al.* as was presented before (see Section 1.4).

The elemental yield $Y(Z)$ of fragment atomic number for the fission fragments of the ^{265}Db fissioning system is presented in Fig. 7.20. The current data are depicted by the black dots and is compared with a previous measurement conducted on the same fissioning system at GSI, represented by the dashed blue line [65], as well as calculations from the semi-empirical GEF model [46], represented by the red line.

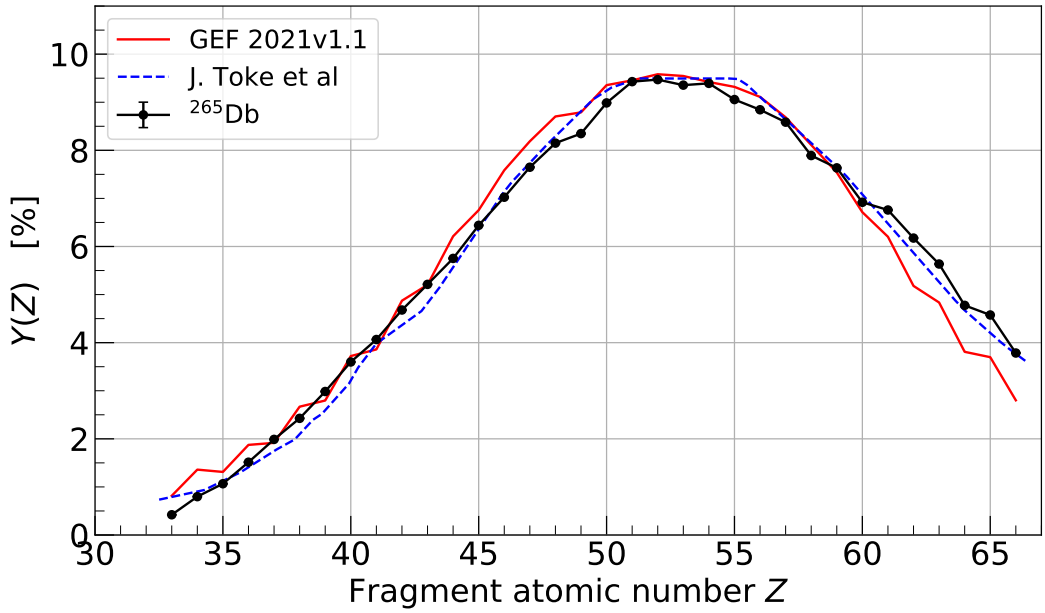

Figure 7.20: *The distribution of fragment atomic number elemental yields $Y(Z)$ of fission fragments of ^{265}Db fissioning system generated at $E^*_{FS} = 61.2$ MeV is shown. The data of this work, represented by black, are compared with the results of a previous estimation, represented by the dashed blue line from Tōke et al [65], and with the calculations from the semi-empirical GEF model [46], represented by the red line.*

The distribution of elemental yields, depicted in Fig. 7.20, measured in this study, demonstrates a clear agreement with the previous measurement, represented by the dashed blue line from Tōke *et al.*. Since the data from [65] is based on fragment mass, Fig. 7.20 shows an estimation based on an approximate N/Z. A comparison with the GEF model reveals a clear overproduction in the experimental data at higher fragment atomic numbers. Once again, the bulge for $Z > 59$ is evident, agreeing with the observed deviation in the isotopic yields (see Fig. 7.17). This disparity appears in the region where quasi-fission becomes significant, as reproduced by the previous measurement by Tōke *et al.*. This region will be a subject of investigation in subsequent sections.

The yields $Y(A)$ of post-evaporation fragment mass A for the ^{265}Db fissioning system is presented in Fig. 7.21. The current data are depicted by the black dots with error bars and it is compared with a previous estimation conducted on the same fissioning system at GSI, which is represented by the dashed blue line [65], as well as calculations from GEF, represented by the red line. The distribution of yields $Y(A)$ in Fig. 7.21 corresponds to the fragment mass after neutron evaporation (see Section 1.3.1). Neutron evaporation has been found to be higher for heavier fragments [78].

As seen in the result presented in Fig. 7.21 the data distribution deviates from the GEF model simulation. Even if the two distributions were to agree around their peaks, the measurement would still manifest a higher production in the heavy region. Once again, in connection with the preceding two figures (see Fig. 7.20 and Fig. 7.17), the phenomenon attributed to the quasi-fission mechanism comes into play. A noteworthy observation is the close agreement observed with the previous measurement [65]. The GEF model predicts an asymmetric fission in fragments, with a higher production at masses $A = 120$ and $A = 130$ approximately. Nevertheless, the experimental measurements from this work show a symmetric fission centred around $A = 130$ approximately. Starting from $A > 160$, there is not enough statistical data, hence the distribution is truncated.

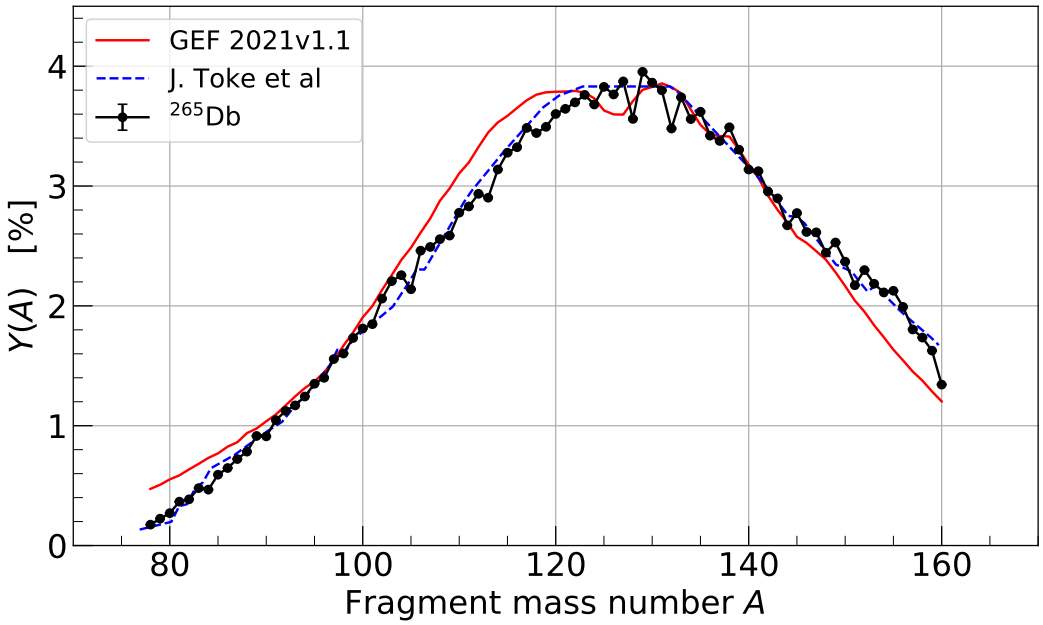

Figure 7.21: *The distribution of fragment mass elemental yields $Y(A)$ of fission fragments of ^{265}Db fissioning system at $E^*_{FS} = 61.2$ MeV is shown. The data, represented by black dots, are compared with the results of a previous estimation, represented by the dashed blue line [65], and with the calculations from the semi-empirical GEF model, represented by the red line.*

For both yield distributions, $Y(Z)$ and $Y(A)$ (see Fig. 7.20 and Fig. 7.21), no significant structure effects are anticipated given the magnitude of E^*_{FS}. Nonetheless, Figure 7.20 reveals a distribution with a central plateau, implying that structural effects persist even at this elevated E^*_{FS}. These structural or shell effects will be further examined in subsequent results sections. The yields for each asymmetric fission component are investigated in the next Section 7.2.5.

7.2.5 Fission modes in ^{265}Db fissioning system

This section delves into an investigation of the fission modes of the ^{265}Db fissioning system, focusing on their atomic number (Z) distributions. This comprehensive analysis encompasses four distinct fission channels, which were initially outlined by Brosa *et al.* [31] (see Section 1.3.5): these channels include the Super-Long symmetric (SL), Standard-I asymmetric (SI), Standard-II asymmetric (SII), and the Super-Asymmetric channel (SA). In contrast to the ^{249}Bk fissioning system, the assessment of fission channels in the case of ^{265}Db necessitates careful consideration of the quasi-fission component to ensure a more accurate estimation. It was a prerequisite that the amplitude of the SL channel remained fixed at the symmetry height of the distribution symmetry height [106].

To estimate the fission channels of the ^{265}Db system, it is crucial to consider the quasi-fission component (refer to following Section 7.4). To achieve this, an additional Gaussian function is fitted to the heavy component, obtained as illustrated in Fig. 7.29. This involves subtracting the unmeasured portion in the tail of the symmetric component, as even a small, nearly negligible area in the Gaussian tail could introduce interference. Subsequently, this component is added to the fit of all the fission channels. Figure 7.22 showcases the yield distributions of the fragment atomic numbers in the ^{265}Db fissioning system in the upper panel. Each colour line corresponds to an individual fission channel, while the red line represents their sum, fitting the distribution

while accounting for the quasi-fission component. The lower panel shows the residuals of the total fit. The parameters of each fission channel, including position, width, and yield, are presented in Tab. 7.2.

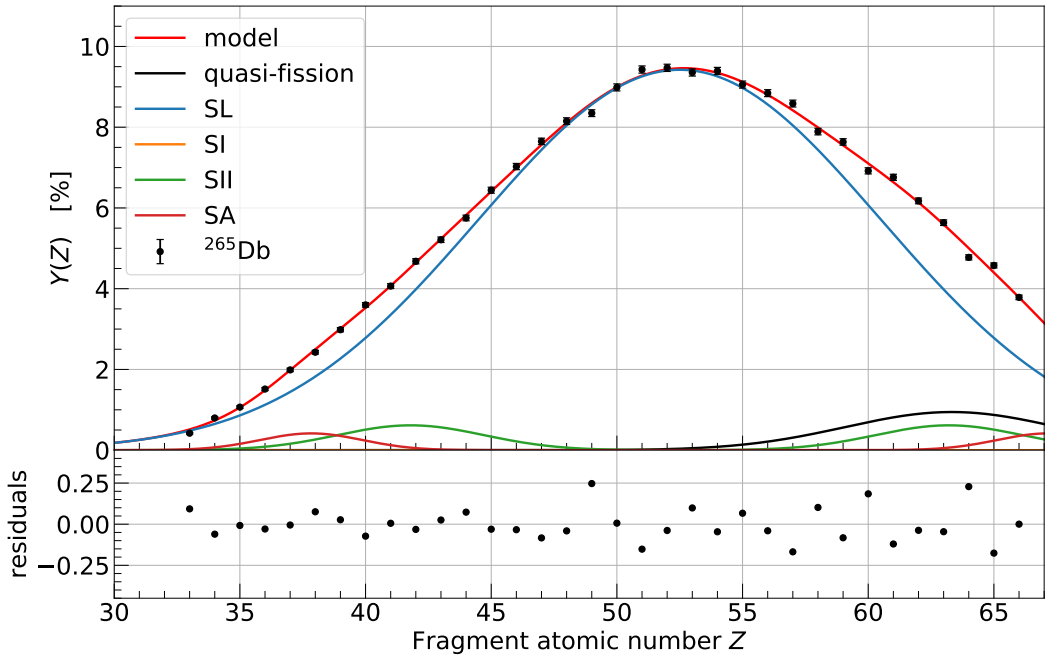

Figure 7.22: *Description of the fragment atomic number Z isotopic yield distribution in terms of fission channels for the ^{265}Db fissioning system in the upper panel. The black dots represent experimental data with the statistical error bars, the colour lines reproduce each fission channels, and the red line indicates the sum of the four different channels plus the quasi-fission component represented with black line. The lower panel shows the residuals of the total fit.*

Fission channels parameters

FS	Channel	Position	Width σ	Yield [%]	GEF Yield [%]	GEF Position
^{265}Db	Super-Long (SL)	52.51 ± 0.06	8.0 ± 0.6	93.45 ± 6.70	90.08	52.50
	Standard I (SI)	#	#	$0.00 + 0.01$	0.20	54.02
	Standard II (SII)	63.2 ± 0.4	2.9 ± 0.3	4.45 ± 0.27	9.68	55.58
	Super-Asymmetric (SA)	67.2 ± 0.4	2.0 ± 0.3	2.10 ± 0.13	0.040	60.18

Table 7.2: *Parameters of the fission channels, fitted to the fragment atomic number yield distributions.*

The quasi-fission process represents a yield of $Y_{QF} = 9.03\%$ of the total. GEF estimates the yield percentages for various fission channels: a yield of 90.08% for the *SL* channel, 0.20% for the *SI* channel, 9.68% for the *SII* channel and 0.040% for the *SA* channel. A clear discrepancy becomes evident when comparing the measured data with the GEF prediction. The estimation of the GEF model for the *SL* channel is consistent with the actual result, deviating by 3 percentage point. The GEF model computes a nearly negligible yield for the *SI* channel, which agrees well with experimental data. Considering the high excitation energies of the fissioning system, which lead to increased symmetric fission in the *SL* channel [106, 79, 109, 110], it seems reasonable that the *SL* fission channel absorbs the contribution of the asymmetric channels, specifically the *SI* channel, due to the matching symmetry at $Z = 52.5$ with the principal shells of *SI* at $Z = 52$. Therefore, GEF and experimental data appear to agree on this result. Nonetheless, the simulated fission exhibits marked asymmetry, notably overestimating the *SII* channel by

a significant margin. Consequently, the GEF model underestimates the Super-Asymmetric *SA* channel in comparison to *SII*. In experimental data, the asymmetric component is distributed between the *SII* and *SA* fission channels.

The positions of the fission channels calculated by GEF do not agree with the experimental data. The *SII* channel is situated at $Z \approx 55.5$, indicating a significant displacement compared to the experimental data. The width of the *SL* channel in the data is twice as wide as that observed in lighter fissioning systems ($A \ll 240$) with $\sigma_{SL} \approx 4$. It is also two units larger than the width of massive systems such as ^{250}Cf, which has a width of $\sigma_{SL} \approx 6$ [102, 79]. This difference may be attributed to the fact that the mass of the fissioning system ($A = 265$) is significantly higher than these cases, and its excitation energy is much greater than that of ^{250}Cf.

7.2.6 Transfer reactions with aluminium target

Transfer-induced fission reactions are feasible with the aluminium target (see Tab. 2.3). As explained earlier, employing the SPIDER trigger and a similar yield construction process as for fission, the isotopic yields of transfer-induced fission reactions can be determined. Again, a comprehensive study of transfer reactions exceeds the scope of this study. Nonetheless, to obtain fusion-induced fission yields and reconstruct velocities, it is necessary to assess the transfer yields and estimate the amount of contamination present in the fusion-induced fission events, as discussed earlier (see Section 6.4).
The isotopic yields of transfer reactions, $Y(Z,A)^{Transfer}$, are presented in Fig. 7.23 as a function of fragment A where each colour corresponds to a fragment Z. These yields exhibit a very small amount of contamination from fusion-induced fission events that cannot be subtracted but is negligible. It is assumed that the intrinsic efficiency of the aluminium target (see Eq. 6.28) is common to transfer-induced fission reactions. However, unlike the fusion-induced fission yields, masses have not been selected.

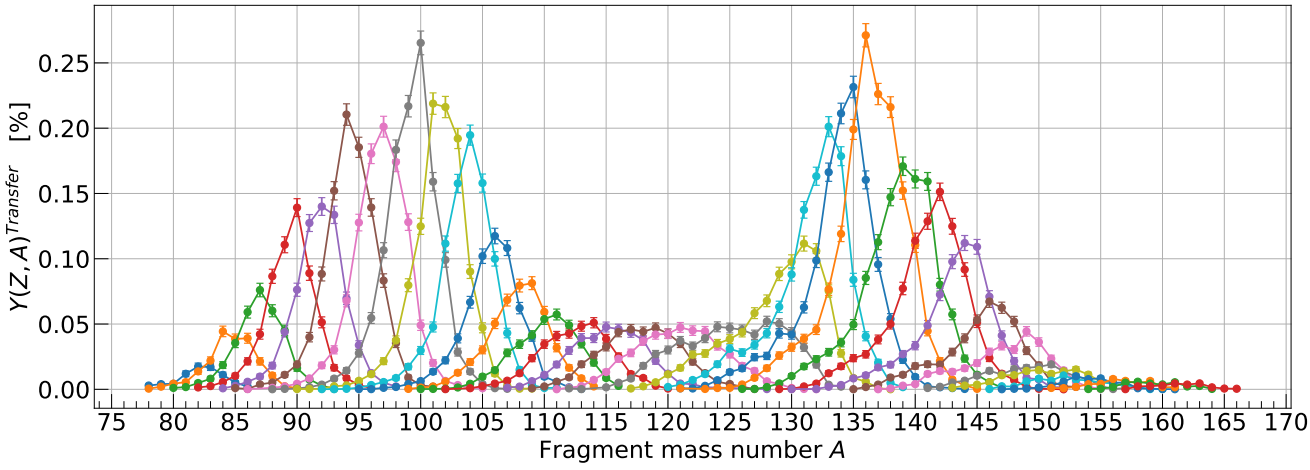

Figure 7.23: *The isotopic yields of the transfer reactions, $Y(Z,A)^{Transfer}$, with the aluminium target are displayed in various colours for each fragment atomic numbers Z, with the different fragment mass number A represented by data points.*

USC UNIVERSIDADE DE SANTIAGO DE COMPOSTELA

The elemental yield $Y(Z)^{Transfer}$ of transfer reactions with the aluminium target is presented for each fragment atomic number Z in Fig. 7.24. The yield distribution of transfer reactions as a function of fragment mass number $Y(A)$, with the aluminium target, is presented in Fig. 7.25. The results presented in both figures (see Fig. 7.24 and Fig. 7.25) indicate that the most abundant fragments possess atomic numbers of $Z = 40$ and $Z = 54$ with approximate masses of $A \approx 100$ and $A \approx 135$ respectively. These transfer distributions, which exhibit symmetry, have their centroids located at $Z = 47$ and $A = 120$ respectively. With both the aluminium and boron targets (see Fig. 7.12 and Fig. 7.13), it can be observed how the distributions closely resemble each other, yielding identical peaks in the same positions.

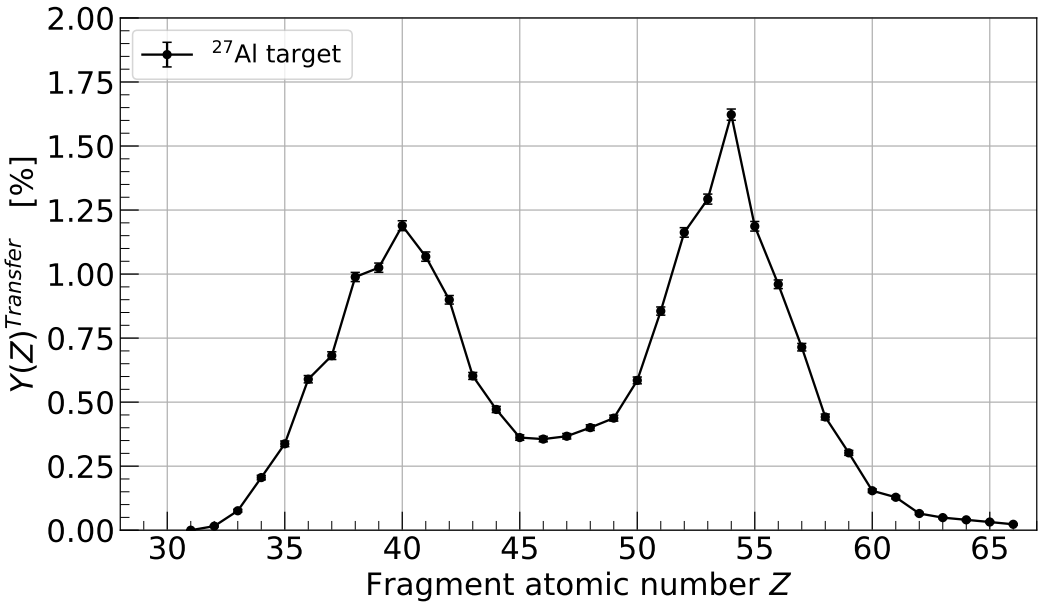

Figure 7.24: *The elemental yields of the fragment atomic number distributions $Y(Z)^{Transfer}$ of transfer reactions with the aluminium target are presented.*

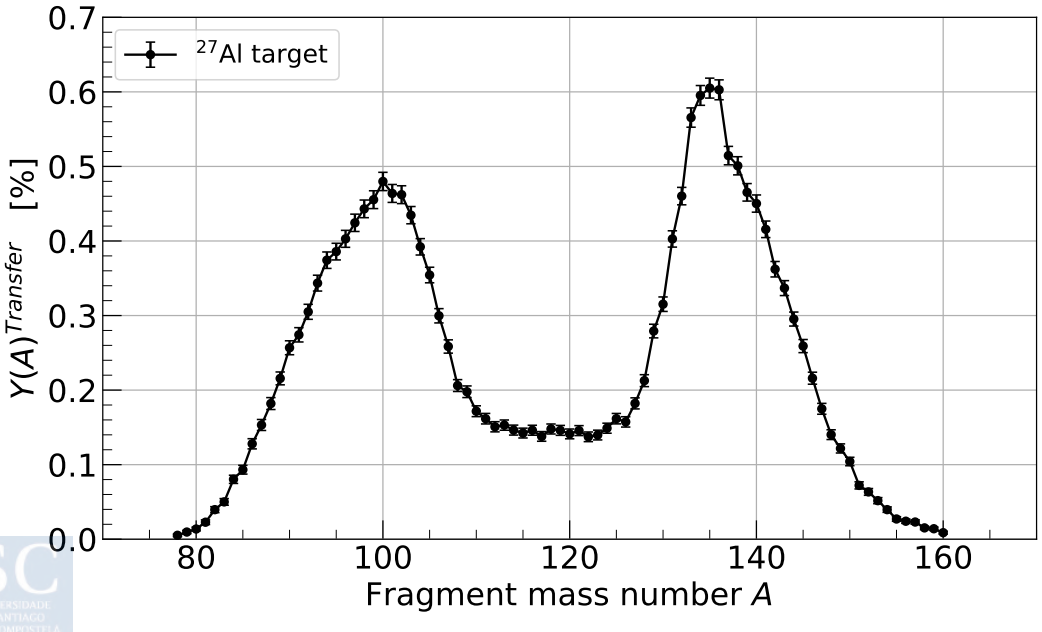

Figure 7.25: *The yields of the fragment mass number distributions $Y(A)^{Transfer}$ of transfer reactions with the aluminium target are presented.*

Similarly to the boron target, the recoils generated by the interactions between the uranium beam and the aluminium target can be selectively identified as an energy telescope by utilising the SPIDER detector and employing the measured energy space (E, dE) (see Section 2.3.2), as depicted in Fig. 2.18. When isolated individually, an estimation can be made based on the measured counts to derive the yields for these recoils or reaction products. The preliminary results of the elemental yields $Y(Z)^{recoil}$ for the predominant recoils, distinguished by various colours, are presented in Fig. 7.26. Once each recoil has been individually identified, the various possible transfer reactions must be configured, and each resulting compound nucleus examined separately. The compound nuclei formed are listed in Tab. 2.3.

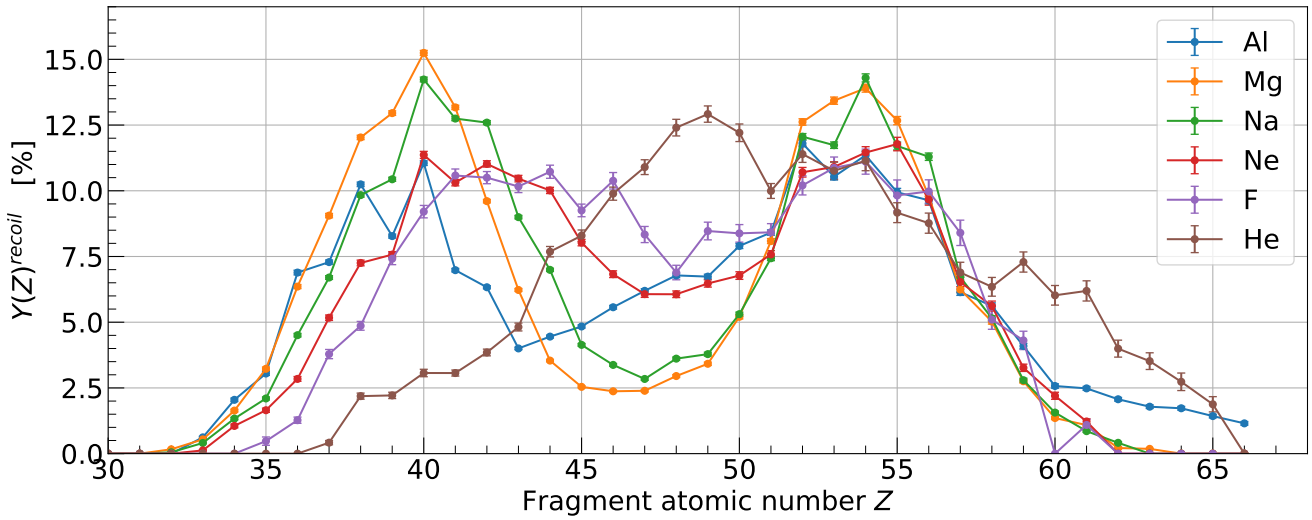

Figure 7.26: *The elemental yields $Y(Z)^{recoil}$ for each recoil selected with the SPIDER telescope detector and generated in the transfer reactions with the aluminium target and the uranium beam are presented as preliminary results. Each recoil is represented by a different colour line with each dot representing the atomic number Z.*

7.3 Angular anisotropy

The process of evaluating the yields (see Section 6) is applied to fusion-induced fission events, and in the final step, it is fitted to a functional form: $a + b \cdot \cos^2(\theta^{FF}_{CM})$ (see Eq. 6.9). It is worth noting that both target materials used in this study, ^{27}Al and ^{nat}B, required analysis with different evaluation techniques. In other words, for the aluminium target, the yields were not treated by fitting to this functional form and were obtained through an alternative method (see Section 6.7). For the boron target, the elemental yields $Y(Z)^{FuFi}$ and $Y(Z)^{Transfer}$ were calculated using the counts of the $\cos(\theta^{FF}_{CM})$ distributions. Subsequently, the contamination factor was estimated (see Fig. 6.13) employing a minimisation and symmetrization process. Once the contamination factor was obtained, it became possible to calculate the isotopic yields by fitting to the functional form: $a(Z, A) + b(Z, A) \cdot \cos^2(\theta^{FF}_{CM})$.

The anisotropy factor, A_{ny} was defined earlier (see Section 5.4 and Eq. 5.20) and is employed to describe the behaviour of a fusion-induced fission $\cos(\theta^{FF}_{CM})$ distribution. In other words, A_{ny} is the normalised curve of $\cos^2(\theta^{FF}_{CM})$ and is described as:

$$A_{ny}(Z) = \frac{W(0°)}{W(90°)} = \frac{\sum\limits_{A} a(Z,A) + b(Z,A) \cdot \cos^2(0°)}{\sum\limits_{A} a(Z,A) + b(Z,A) \cdot \cos^2(90°)} = 1 + \frac{\sum\limits_{A} b(Z,A)}{\sum\limits_{A} a(Z,A)} \,. \tag{7.1}$$

In the following Fig. 7.27, the evolution of the anisotropy factor for the fissioning systems ^{265}Db and ^{249}Bk is depicted for each fragment atomic number Z in blue and red points, respectively. As observed, the fusion-induced fission yields originating from the ^{249}Bk fissioning system approximately constant anisotropy. It appears to have a symmetric behaviour as a function of Z around $Z_{FS}/2$, which is to be expected. In the boron target, no other mechanisms are competing with fusion-induced fission yields. Fusion-induced fission yields show little to no variable anisotropy and their nearly constant evolution fluctuates slightly around $A_{ny}(Z) = 1.5$. Nonetheless, with the aluminium target, the anisotropy factor evolution increases and sharply rises beyond $Z_{FS}/2$. This effect is caused by the presence of quasi-fission in the aluminium yields, is the consequence of the estimation of the yields with the aluminium target by fitting the $\cos(\theta^{FF}_{CM})$ distributions to a functional of the form $a + b \cdot \cos^2(\theta^{FF}_{CM})$.

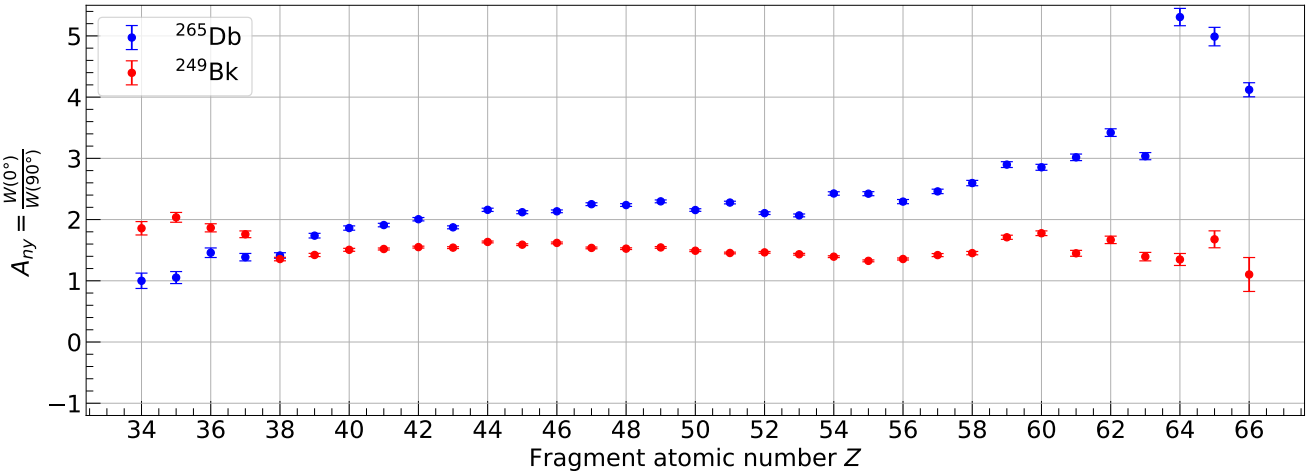

Figure 7.27: *The evolution of the anisotropy factor A_{ny} is shown for each fragment atomic number Z of the ^{265}Db and ^{249}Bk fissioning systems, represented by blue and red points, respectively.*

7.4 Quasi-fission and experimental MAD

A pure fission distribution, such as one calculated with the GEF semi-empirical model [46] is not consistent with the observed data, as discussed in Section 7.2.4 for the ^{265}Db fissioning system. The measured distribution exhibits a higher mass shift and wider fragment distributions compared to a typical fission distribution.

In this work, a portion of quasi-fission is detected by the experimental VAMOS++ setup. The acceptance of VAMOS++ is limited in terms of θ_{CM} and pre-evaporation fragment mass number A^*, as indicated by the blue region in Fig. 7.28, which represents the boundaries of the measurement window based on the Tōke *et al.* measurements [65]. Within this window, the heaviest mass component of quasi-fission, represented by the red circle line, is detected in VAMOS++. The respective light component of quasi-fission is connected to the dashed red circle line, which is also depicted in Fig. 7.28. Furthermore, the yields of ^{265}Db have been evaluated within the green window, thus further narrowing down the measurement window for the heavy quasi-fission component.

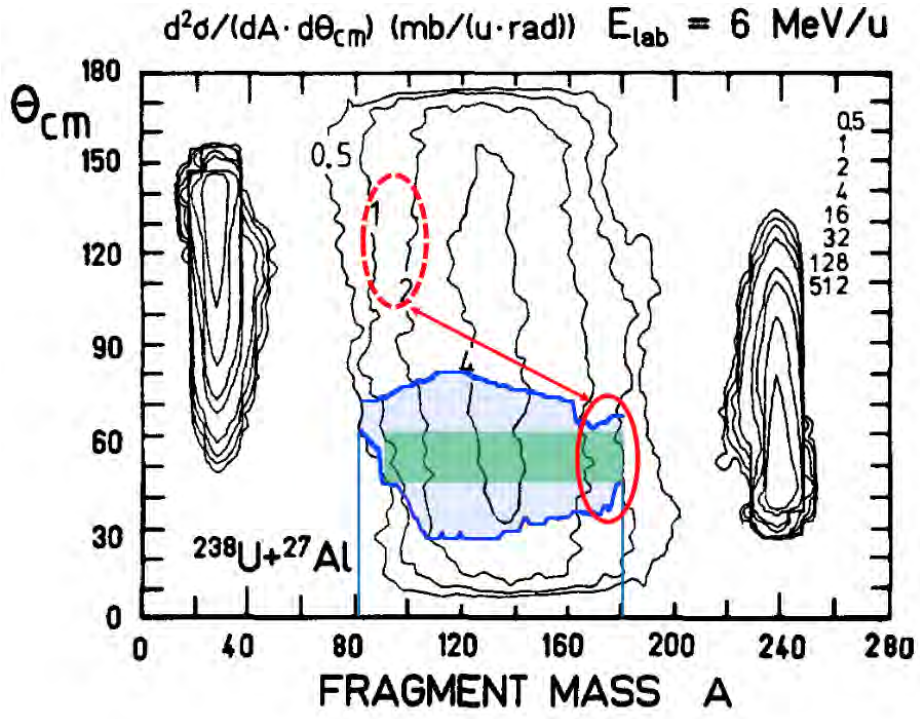

Figure 7.28: *The Mass-Angle distribution contour picture of the double differential cross section for emitted fragments from the reaction $^{238}U + ^{27}Al$, as derived by Tōke et al. [65], is represented in the (θ_{CM}, A^*) phase space. VAMOS++ limits in the θ_{CM} angle are depicted by the blue region, whilst the limits in pre-evaporation fragment mass are shown by the blue lines. The heaviest component of the quasi-fission process is indicated by the red circle line, while the lightest component is represented by the dashed red circle line. The evaluation window for the yields of ^{265}Db is confined to the green rectangle within the blue region. Adapted with permission from [65]. Copyright (1985) by the North-Holland Publishing Company.*

Consequently, the fragment mass distribution shows higher production of heavy fragments where the quasi-fission mechanism dominates over fusion-induced fission (red circle in Fig. 7.28). The observed position of the experimental distributions does not agree with the GEF simulations [46], which predict distributions shifted to lower masses for each fragment Z, which may be a consequence of the neutron evaporation calculations and/or the absence of the quasi-fission calculations, in the case of high fragment Z, in the GEF code.

In Section 1.4, the discussion revolved around the correlation between the masses and angles of the emitted fragments, resulting from the reaction time of the fission process. This correlation gives rise to a distinct pattern in the Mass-Angle Distribution (MAD) of the fragments. The experimental MAD obtained in this study differs from the MAD depicted in Fig. 1.18 due to multiple angular momenta in a real reaction. As outlined in Section 1.4.1, the fusion process, unlike quasi-fission, does not exhibit a correlation between the masses and angles of the fragments. The fission mass distribution is equal and independent of the angle at the centre-of-mass reference frame, resembling the central region shown in Fig. 7.28, which presents the MAD for the investigated system $^{238}U + ^{27}Al$. The lateral distributions, centred around the masses of the target and projectile, correspond to elastic and quasi-elastic scattering, transfer, and deep-inelastic transfer reactions.

USC UNIVERSIDADE DE SANTIAGO DE COMPOSTELA

Although the angular distribution initially appears symmetric around $\theta_{CM} = 90°$ for all masses, a closer examination of the contour lines reveals a slight forward-backwards asymmetry, indicating the presence of quasi-fission (as indicated by the red circles in Fig. 7.28). This asymmetry becomes more prominent for heavier systems, such as ^{238}U + ^{48}Ca in the right pad of Fig. 1.20. Effects of memory regarding the mass and direction of the incident particles appear in the final distributions. This suggests that the reaction times are shorter than the time required for the system to reach thermodynamic equilibrium. The increased probability of quasi-fission with the total mass of the system is attributed to the larger Coulomb repulsion, which hinders the complete fusion of the two interacting objects.

In the current study of ^{265}Db fissioning system, limitations in the angular coverage of VAMOS++ result in sensitivity primarily to the central region of pre-evaporation fragment mass number A^* and the forward-angular region. Consequently, the measured fragment atomic number distribution in the elemental yields $Y(Z)$ exhibits asymmetry. The excess of heavier fragments is not balanced by a corresponding excess in the lighter region due to the lack of angular coverage for the light-partner fragments (red dashed circle in Fig. 7.28). Therefore, the normalisation to 200 is performed using only the complete and symmetric half of the light fragment distribution ($\sum Y(Z < Z_{FS}/2) = 100$), which is reasonable to assume that it does not include quasi-fission (see Fig. 7.29). This asymmetry enables the estimation of a lower limit to the yield contribution as a function of fragment atomic number Z by subtracting the yields of two complementary fragments, as shown in Fig. 7.29. The heavy contribution of quasi-fission is represented by the solid red line. In contrast, the light contribution (which is not measured) is depicted by the dashed red line as the mirror, both related to the red circles in Fig. 7.28. The results are compared with the semi-empirical GEF model [46] in green and with the estimation by Tōke *et al.* [65] with a dashed blue line.

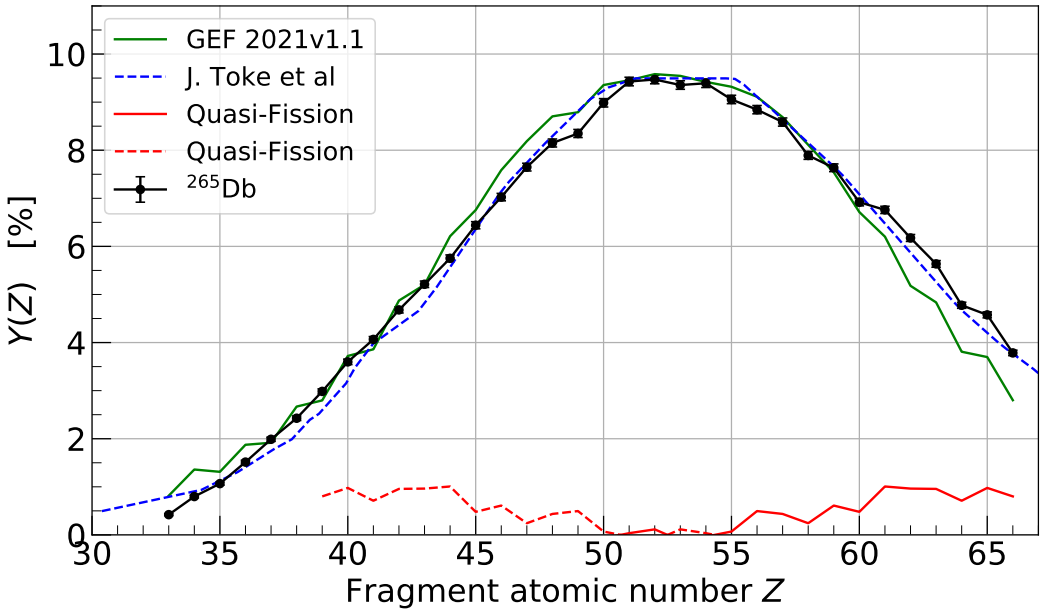

Figure 7.29: *The elemental yields $Y(Z)$ of the ^{265}Db fissioning system are presented, normalised, and compared with the semi-empirical GEF simulation [46] and the previous estimation by Tōke et al. [65], depicted in green and dashed blue lines, respectively. The extracted yield of the heavy component of quasi-fission is represented by the red line, while the light component is mirrored to the heavy component and shown as a red dashed line.*

7.5 Neutron excess

The identity of the fission fragments and their composition in terms of protons and neutrons is determined at the scission point. It is at this stage that the protons and neutrons of the fissioning system are distributed between the two newly formed fragments. To analyse the nucleon sharing it is necessary to calculate the neutron excess, represented by $\langle N \rangle / Z$. The neutron excess is defined as the average number of neutrons N per atomic number Z in the fragments. By employing the isotopic fusion-induced fission yields $Y(Z, A)$, the value of $\langle N \rangle / Z$ can be obtained, as a function of the fragment Z:

$$\frac{\langle N \rangle}{Z}(Z) = \frac{1}{Z} \sum_{N} N \cdot \frac{Y(Z,N)}{Y(Z)}\,, \tag{7.2}$$

with the elemental yield $Y(Z) = \sum_{N} Y(Z,N)$.

The neutron excess of each fragment is an observable that allows the investigation of the neutron and proton sharing between fragments during their emergence. The experimental neutron excess of the fission fragments is known to vary with the asymmetry of the fission split [111]. In the framework of unchanged charge density, both fragments keep the same neutron excess as the fissioning system.

According to a structure-less liquid drop model (see Section 1.3.2), the distribution of nucleons between the fragments at scission is governed by the interplay of Coulomb repulsion and nuclear interactions. This model predicts almost equal sharing of neutrons between the fragments, resulting in a gradual increase in the N/Z as a function of fragment atomic number (referred to as *charge polarisation*). Nonetheless, experimental data at low excitation energy deviate from this prediction [108]. In this energy regime, the heavy fragment tends to have an excess of neutrons compared to the model, whilst the light fragment is relatively less neutron-rich. Moreover, specific configurations of proton-neutron combinations are favoured, leading to an excess or deficit of neutrons for certain fragment atomic numbers.

In this work at high excitation energy, the observed neutron excess, $\langle N \rangle / Z$, is influenced by the sharing of energy at scission, which is also affected by shell effects at low energy. Therefore, the neutron excess serves as a sensitive observable to see structure effects and the distribution of protons and neutrons between the pre-fragments at the scission point (see Section 1.3.1). Figure 7.30 depicts the neutron excess $\langle N \rangle / Z$ in the fissioning systems ^{265}Db and ^{249}Bk, in the upper and lower panel respectively, along with a comparison to the GEF semi-empirical model [46], both shown as a function of fragment atomic number Z.

In the case of the ^{265}Db fissioning system, the experimental suggest that GEF predicts a greater number of evaporated neutrons, resulting in a total N/Z below the experimental data. However, it is important to note that GEF calculations effectively capture the overarching trend. In this fissioning system characterised by high excitation energy ($E^*_{FS} = 61.2$ MeV), there is a notable reduction in the shell effects impact on neutron excess. This reduction is consistent across all fragment atomic numbers Z, agreeing with a prior study [108] as mentioned earlier. The minor discrepancies with the GEF model can be elucidated by two factors. First, the presence of the quasi-fission process yields less excited fragments that tend to emit fewer neutrons and consequently exhibit a higher $\langle N \rangle / Z$. Second, the experimental setup employed in this research exclusively detects much less than of the θ^{FF}_{CM} distribution (see Fig. 7.28). This limitation restricts the ability to measure the lighter fragments produced by quasi-fission.

In the case of the ^{249}Bk fissioning system (see lower panel), characterised by an excitation energy of E^*_{FS} = 47.7 MeV, a discrepancy with the GEF calculations becomes apparent. The GEF model predicts an smooth trend, without a significant influence from nuclear shells. The experimental data do not display significant deviations in the trend, and there appear to be no structural effects, which is expected at high excitation energies.

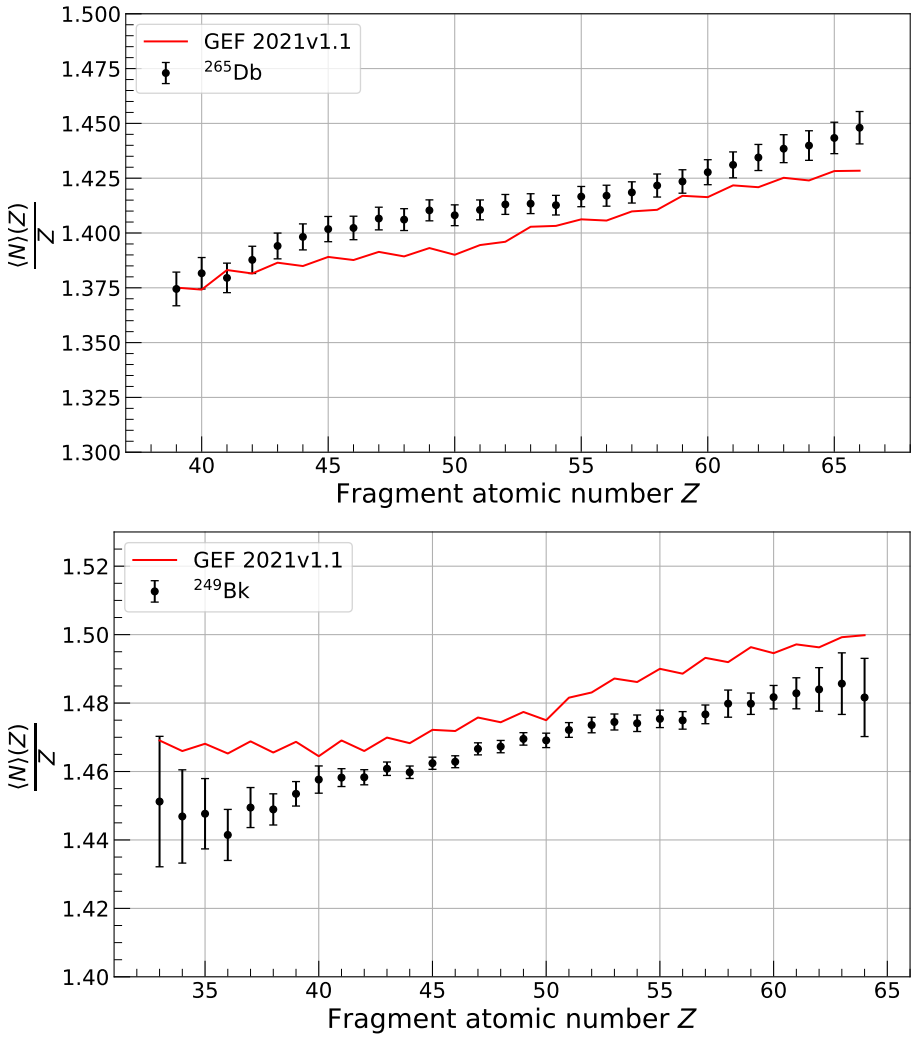

Figure 7.30: *The neutron excess, $\langle N\rangle/Z$, is shown as a function of fragment atomic number Z for the fissioning systems ^{265}Db and ^{249}Bk in the upper and lower panels, respectively. A comparison is made with the GEF semi-empirical model [46], represented by the red line.*

7.6 Neutron evaporation

The isotopic identification of fission fragments also provides valuable information for calculating the total neutron multiplicity. This multiplicity represents the combined number of neutrons that are emitted by both fragments as a result of neutron evaporation following the scission point (see Section 1.3.1). Additionally, the final identification of fission fragments allows for the estimation of the average number of neutrons evaporated during the transition from the formation of the

fissioning system to the subsequent deexcitation as:

$$\langle \nu_{total} \rangle (Z) = N_{FS} - (\langle N_{Z_1} \rangle + \langle N_{Z_2} \rangle) \ , \tag{7.3}$$

$$\langle N_{Z_1} \rangle = \sum_N N \cdot \frac{Y(Z_1, N)}{Y(Z_1)} \, , \tag{7.4}$$

$$\langle N_{Z_2} \rangle = \sum_N N \cdot \frac{Y(Z_2, N)}{Y(Z_2)} \, , \tag{7.5}$$

where N_{FS} and Z_{FS} are the number of neutrons and protons of the fissioning system at initial point, respectively. It is assumed $Z_{FS} = Z_1 + Z_2$ with no proton emission. It implies at initial point: $N_{Db} = 265 - 105$ and $N_{Bk} = 249 - 97$. Figure 7.31 shows the total neutron multiplicity measured for ^{265}Db and ^{249}Bk fissioning systems and the corresponding semi-empirical GEF model calculations [46] with a red line, as a function of fragment atomic number Z.

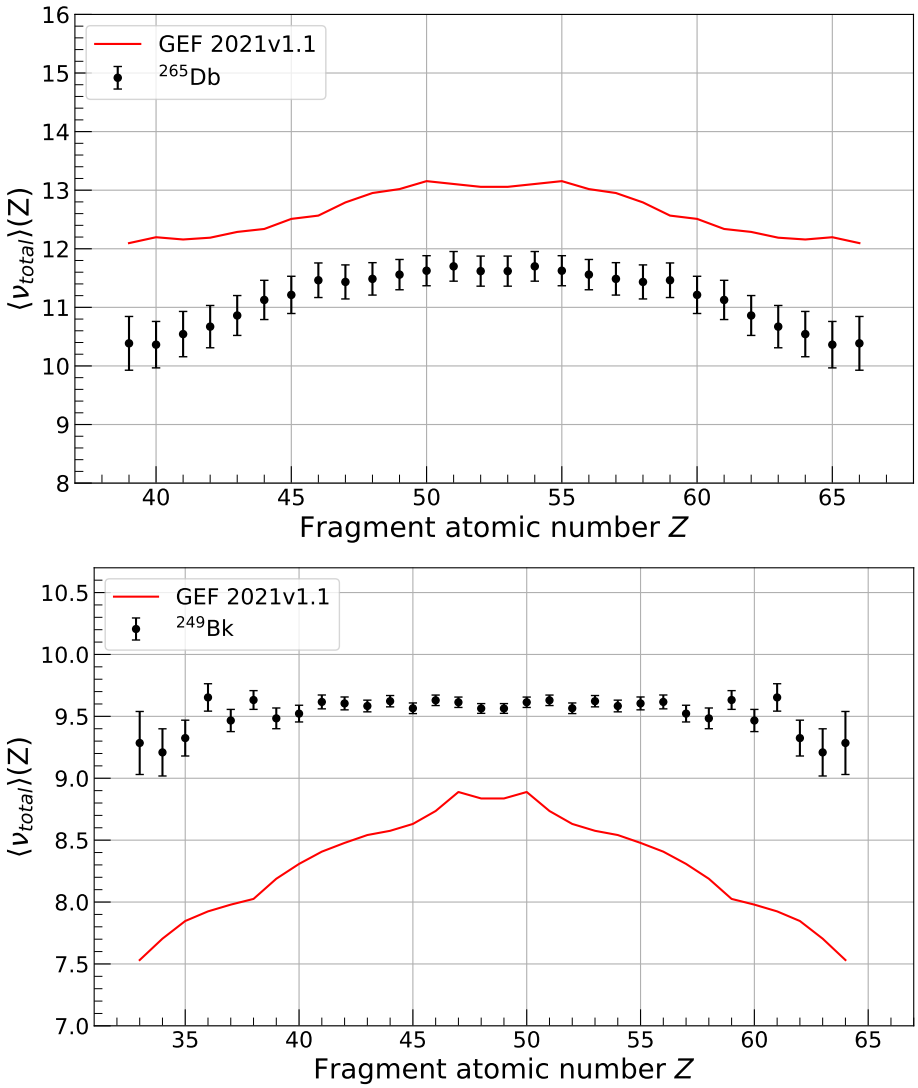

Figure 7.31: *The neutron evaporation, quantified as the total number of emitted neutrons in the fission path from the scission point, is depicted as a function of the fragment atomic number Z for the fission fragments of two systems: ^{265}Db and ^{249}Bk (upper and lower panels, respectively). The experimental data are compared with the predictions from the semi-empirical GEF model [46], shown by the red line.*

The ^{265}Db fissioning system (see Fig. 7.31 upper panel), with a high excitation energy of E^*_{FS} = 61.2 MeV, exhibits an average total neutron emission $\langle \nu_{total} \rangle$ between 10.5 and 11.5 neutrons for any fragment Z. This neutron emission agrees with other measurements, such as ^{250}Cf fissioning system with E^*_{FS} = 46 MeV which has a nearly constant emission of $\langle \nu_{total} \rangle \approx 8$ for all fragment Z [102]. Additionally, the experimental data show an arched distribution, with reduced evaporation in both light and heavy fragments and increased evaporation in fragments with $Z \in [50, 55]$. At high excitation energies, this distribution is expected to be flat; however, there is a one-neutron difference between these regions.

It seems that the ^{265}Db fissioning system displays substantial evaporation at the point of symmetry. Again, there is no clear evidence of structural effects in ^{265}Db fissioning system. The evaporation reaches a local maximum at $Z \approx 54$, however, this maximum is minimal and barely distinguishable from the rest of the values. Taking into account the statistical error bars, the structural effect remains unclear, suggesting that certain structural effects might persist at high excitation energies [102]. The GEF model predicts a higher number of evaporated neutrons, resulting in a total neutron multiplicity that does not match the experimental values numerically but agrees in terms of trends. It appears that, on average, the GEF model emits $\approx$ 1.3 more neutrons than the experimental data. When these excess neutrons are subtracted, the behaviour closely matches the measured experimental data. At this high excitation energy, it can be asserted that GEF overestimates the number of emitted neutrons. It is worth noting that quasi-fission mechanism may contribute to these discrepancies, although it cannot explain them fully. Given that access to neutron evaporation from the quasi-fission mechanism remains concealed, definitive conclusions cannot be drawn.

The ^{249}Bk fissioning system (see Fig. 7.31 lower panel), characterised by considerably high excitation energy of E^*_{FS} = 47.7 MeV, exhibits an average total neutron emission of $\langle\, \nu_{total} \,\rangle \approx 9.5$ for any fragment atomic number Z. Again, this neutron emission agrees with other measurements, such as the previously mentioned example of the ^{250}Cf fissioning system [102]. Furthermore, the experimental data present a nearly constant behaviour, as expected in high excitation energy fissioning systems [102] without nuclear structure effects. In contrast, the GEF model predicts a reduced number of evaporated neutrons, resulting in a total neutron multiplicity that does not match the experimental values both quantitatively and in terms of shape. The GEF model predicts an arched pattern with increased neutron emission at the symmetry region compared to the sides. On average, the GEF model emits $\approx 1 \rightarrow 2$ fewer neutrons than the experimental data. The neutron evaporation before the barrier, as is calculated by GEF, leads to a reduction in the E^*_{FS} excitation energy of the system. This reduction results in distributions that exhibit more pronounced nuclear structure effects compared to the experimental data. The decreased excitation energy is responsible for the lower neutron evaporation contribution of the asymmetric fission channels, which is clearly underestimated. A more detailed analysis of this behaviour will be conducted in subsequent sections, to characterise the scission point (see Section 7.9).

7.7 Even-odd staggering

The even-odd effect in fission has been observed in experimental data at low energies, where even-Z fragments are consistently produced in higher yields compared to odd-Z fragments. This effect can be attributed to the pairing energy present in atomic nuclei. The formation of odd-Z fragments from an even-Z system requires breaking proton pairs, which requires more energy compared to the formation of even-even fragments. The energy available for pair rupture comes

from the energy above the fission barrier and the energy dissipated during the fission process from the saddle to the scission point. This dissipation converts collective energy into intrinsic energy in the path from the barrier to the scission point (see Section 1.3.1).

The measurement of the even-odd staggering in atomic number provides valuable insights into the intrinsic energy at scission. Unlike neutron evaporation, proton evaporation is very small to significantly affect the even-odd effect, allowing it to directly reflect the intrinsic energy. It is observed that larger intrinsic energy results in a lower even-odd effect [33].

To estimate the local even-odd effect of the fission fragments, elemental yields $Y(Z)$ are employed. The local even-odd effect is defined as the relative difference between the production of even-Z and odd-Z fragments in a region around a particular fragment Z. The even-odd effect is known to vary with the asymmetry of the fission split. Among several formulations available, the widely-used formula by Tracy *et al.* [112] is applied in this study. The formula is given as:

$$\delta(Z+1.5) = \frac{(-1)^Z}{8} \cdot \left(\ln Y(Z) - \ln Y(Z+3) + 3\left[\ln Y(Z+2) - \ln Y(Z+1)\right]\right) , \tag{7.6}$$

To examine the even-odd staggering in the experimental data, a simulation of a completely symmetrical yield distribution, shaped like a Gaussian curve, was created. This distribution was expected to have an even-odd staggering value of $\delta(Z+1.5) = 0$. However, it was demonstrated that this was not the case. The method used to calculate the effect led to very slight variations that resulted in $\delta(Z+1.5) \approx 0$, exhibiting tiny fluctuations. In light of these findings, 10.000 random variations were applied to the initial yield distribution. These variations were used to reproduce both the statistical errors and a 2% systematic error range (see Section 6.8.2). The projection of the $\delta(Z+1.5)$ values for all Z, based on the 10.000 simulations, is depicted in Fig. 7.32.

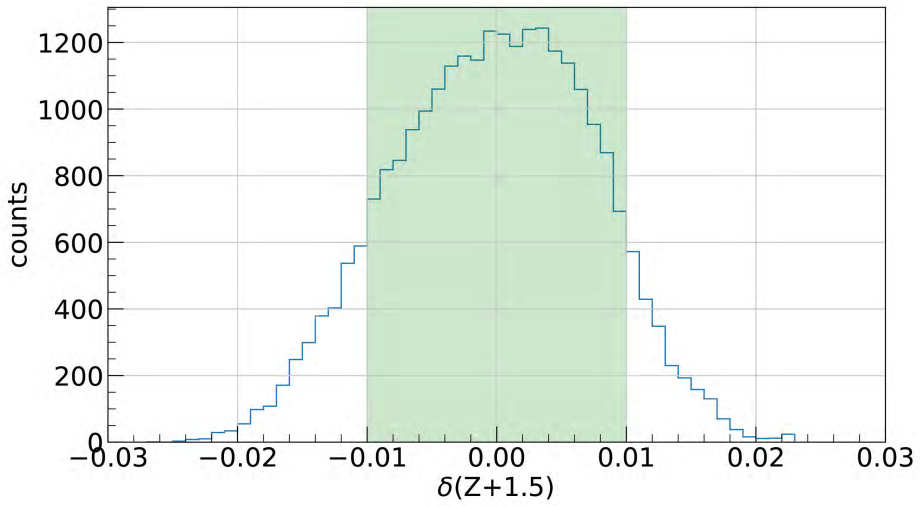

Figure 7.32: *Projection for all fragment atomic numbers Z of the even-odd staggering $\delta(Z+1.5)$ from 10.000 distributions of $Y(Z)$. These distributions were randomly generated with variations within statistical and systematic errors, based on a symmetric Gaussian distribution. The green region represents the margin in which the variation remains constant without alterations. It is assumed that $\delta(Z+1.5)$ is zero within this range, with normal and unavoidable fluctuation variations.*

This Figure 7.32 displays a distribution centred around zero, with a range of $\delta(Z+1.5) \in [-0.01, 0.01]$ related with the distribution standard deviation $\sigma \approx 0.008$, highlighted in green. Additional simulations were conducted, affecting the tails of the distribution,

occasionally making them shorter or longer with variations. Nevertheless, the distribution within the green region remained consistent. Therefore, it can be concluded that values of delta within the of $\delta(Z+1.5) = \pm 0.01$ window should not be considered significant and can be interpreted as a fluctuation of $\delta(Z+1.5) = 0$.

The results obtained for the even-odd staggering, evaluated using Eq. 7.6, are depicted in Fig. 7.33 for the ^{265}Db and ^{249}Bk fissioning systems. These results are presented in the upper and lower panels, respectively. In both cases, most of the data is within the window of $\delta(Z+1.5) = \pm 0.01$. Fissioning systems with higher E^*_{FS}, such as ^{250}Cf, exhibit an fluctuating even-odd effect with very small values, approximately centred around $\delta(Z+1.5) = 0$ [106].

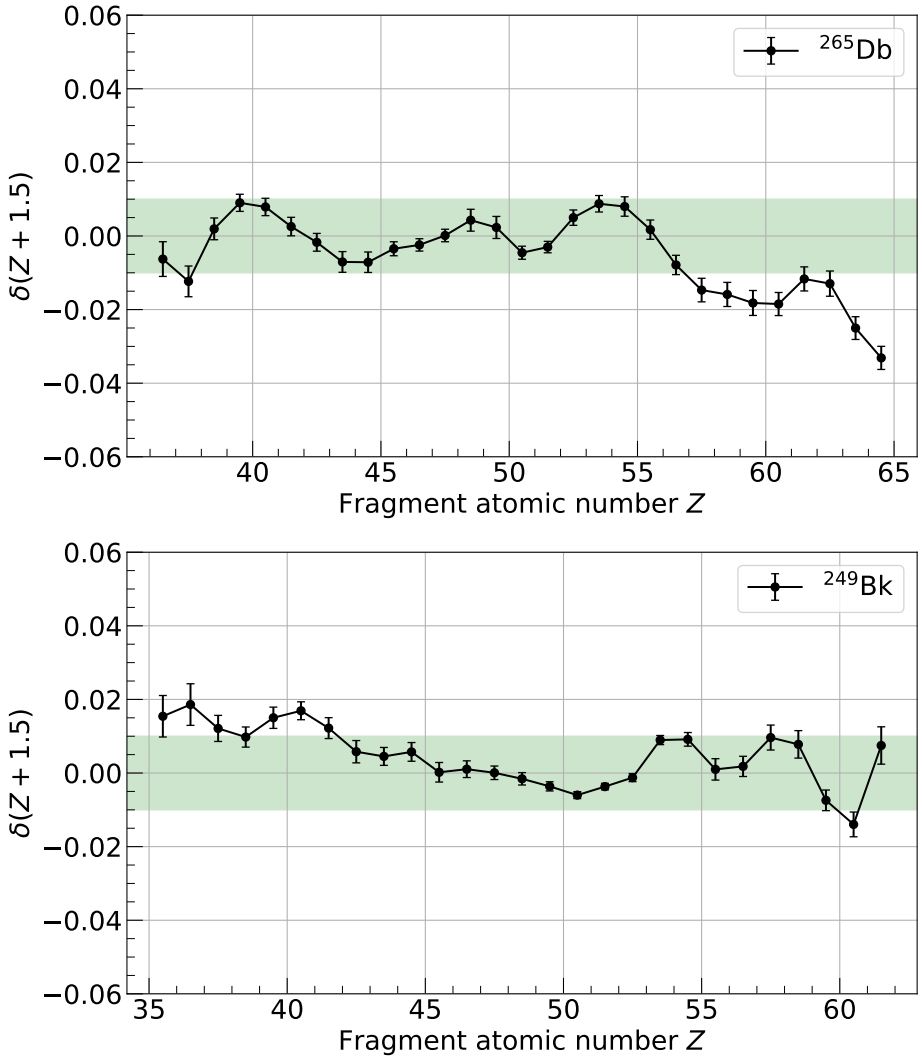

Figure 7.33: *The figure illustrates the local even-odd effect $\delta(Z+1.5)$ of $Y(Z)$ as a function of the atomic number Z for the fission fragments of two fissioning systems, ^{265}Db and ^{249}Bk. The upper panel represents the ^{265}Db system, while the lower panel represents the ^{249}Bk system. The even-odd effect is evaluated using the formula developed by Tracy et al. [112].*

In Fig. 7.33, the upper panel representing the ^{265}Db fissioning system shows that for $Z > 55$, the trend is different: the even-odd effect decreases to around $\delta(Z+1.5) = -0.04$. Precisely, this region corresponds to the measurements of quasi-fission for heavy fragments. The small amount of measured quasi-fission is influencing the local even-odd effect and tends towards a

negative even-odd effect. The lower panel, representing the ^{249}Bk fissioning system, exhibits more fluctuations within the range of $\delta(Z+1.5) = \pm 0.01$, and it can be confirmed that $\delta(Z+1.5) = 0$. There are some fluctuations outside the ± 0.01 window for very low fragment Z. This is attributed to higher uncertainties in the tails of the distribution, which extend further down for lighter fragments. It can be understood that the even-odd effect of the ^{249}Bk fissioning system is null, which is an anticipated result for massive fissioning systems at high excitation energies.

The yields of the ^{265}Db fissioning system have been estimated within the limits in $\cos(\theta_{CM}^{FF})$ (see Fig. 6.28). Maximum common region as explained in Section 6.7. However, it is possible to divide the rectangle into smaller parts to study the evolution of the yields in (θ_{CM}, A) space (see Fig. 7.28). Two divisions of the green rectangle (r_{tot}) have been made:

$$\begin{aligned} r_{tot} &\rightarrow \cos(\theta_{CM}^{FF}) \in [0.470, 0.720] \rightarrow \theta_{CM}^{FF} \in [43.95°, 61.97°]\,, \\ r2 &\rightarrow \cos(\theta_{CM}^{FF}) \in [0.470, 0.595] \rightarrow \theta_{CM}^{FF} \in [53.49°, 61.97°]\,, \\ r3 &\rightarrow \cos(\theta_{CM}^{FF}) \in [0.595, 0.720] \rightarrow \theta_{CM}^{FF} \in [43.95°, 53.49°]\,. \end{aligned} \tag{7.7}$$

The results of the elemental yields $Y(Z)$ for the three regions $(r_{tot}, r2, r3)$ can be observed in the following Fig. 7.34, represented by red, green, and blue points and lines, respectively. Additionally, as done previously (see Fig. 7.29), the heavy quasi-fission component (lower limit of the quasi-fission contribution) for each angular region can be extracted. These components, with lines of the same colours, are represented in the same figure.

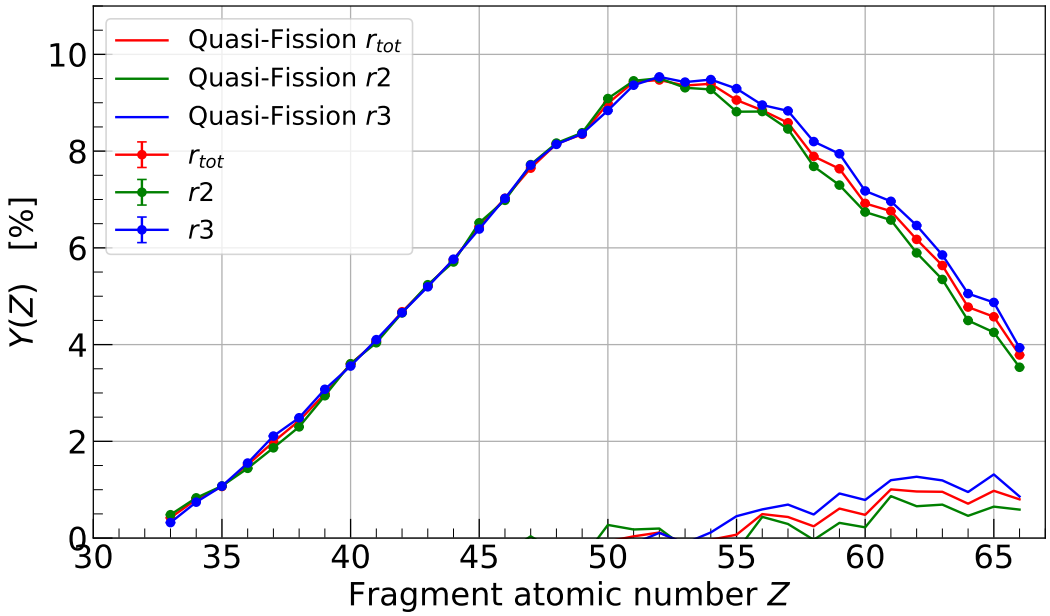

Figure 7.34: *Elemental yields $Y(Z)$ of the ^{265}Db fissioning system estimated in the measurement regions $(r_{tot}, r2, r3)$ by restricting the limits in $\cos(\theta_{CM}^{FF})$. The yields are represented with red, green, and blue lines and dots, respectively, for each measurement region. The heavy quasi-fission component has been extracted and is represented with the same colours.*

The evaluation of elemental yields $Y(Z)$ for each measurement region enables the estimation of the even-odd effect, as explained at the beginning of this section (see Eq. 7.6). The result of $\delta(Z+1.5)$ for $(r_{tot}, r2, r3)$ is presented in the following Fig. 7.35 with the same colour coding.

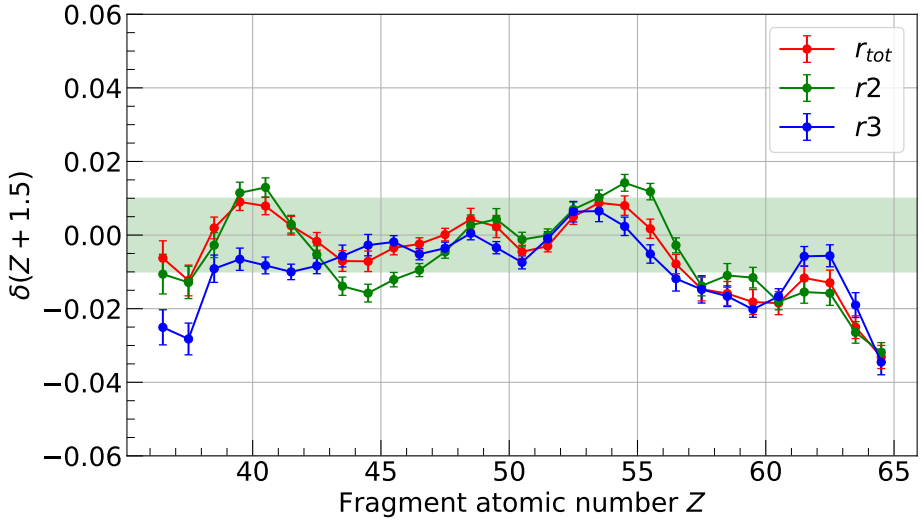

Figure 7.35: *The local even-odd effect $\delta(Z+1.5)$ of $Y(Z)$ as a function of the atomic number Z for the fission fragments of ^{265}Db within $(r_{tot}, r2, r3)$ regions in red, green and blue, respectively. The even-odd effect is evaluated using the formula developed by Tracy et al. [112].*

Figure 7.35 displays the expected behaviour in the fusion-fission region, with $\delta(Z+1.5)$ fluctuating around zero. Once again, these fluctuations agree with the anticipated behaviour and fall within the ± 0.01 window (See Fig. 7.32). However, there is a systematic negative trend for $Z > 55$. This trend is associated with the quasi-fission component. The chosen measurement region does not appear to impact this negative trend.

With the quasi-fission lower limit estimated for each measurement region (see Fig. 7.34), the estimation of the local even-odd effect becomes possible through the same procedure outlined earlier. The $\delta(Z+1.5)$ for the heavy quasi-fission component in each measurement region $(r_{tot}, r2, r3)$ is presented in Fig. 7.36 with colours red, green, and blue, respectively.

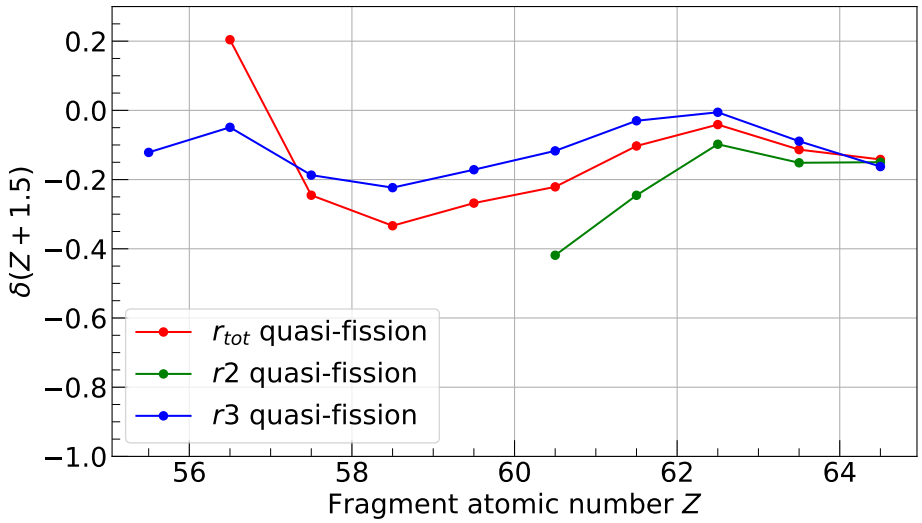

Figure 7.36: *The local even-odd effect $\delta(Z+1.5)$ of $Y(Z)$ as a function of the atomic number Z for the heavy component of quasi-fission within $(r_{tot}, r2, r3)$ regions in red, green and blue, respectively. The even-odd effect is evaluated using the formula developed by Tracy et al. [112].*

Figure 7.36 displays a consistently negative even-odd effect with $\delta(Z+1.5)$ values exceeding the typical effect in low-energy fission by an order of magnitude [106]. In the r_{tot} measurement region, this odd-even effect reaches a maximum of 30%, in the $r2$ measurement region, reaches a maximum of 40%, and in the $r3$ measurement region, a maximum of 20%. The shape of $\delta(Z+1.5)$ appears very similar between the two regions. The $r2$ region seems to exhibit a tendency toward a negative odd-even effect below that observed in r_{tot}. However, it is not possible to estimate the missing Z values in $r2$ quasi-fission green line.

The negative odd-even effect in quasi-fission is related to the dynamics of equilibration processes in quantum systems and their interplay with dissipation and fluctuation in nuclear collisions (see [113] and references therein). Atomic nuclei collisions provide an ideal setting to investigate equilibration and dissipative processes in quantum many-body systems, given their rapid nature, as seen in the case of quasi-fission, which occurs on the order of a few zeptoseconds ($1\,\mathrm{zs} = 10^{-21}$ s). The mass of the nuclei and the difference between their neutron and proton numbers are among the main collective degrees of freedom that can undergo equilibration in heavy-ion collisions. As mass and neutron-proton equilibration occur through a flow of nucleons between colliding partners, they are expected to be significantly influenced by nuclear viscosity (that means the coupling between collective motion and the intrinsic single-particle degrees of freedom). Through calculations using TDHF, Simenel *et al.* [113] aim to characterise, among other results, the timescale over which these processes occur, characterising various equilibration, dissipation, and fluctuation processes.

The contact time, denoted as τ, is typically defined by two pre-fragments connected by a neck. The equilibration of mass asymmetry is referred to as $\delta\Delta A(\tau)$, and the equilibration of the initial asymmetry between proton and neutron numbers (isospin) is referred to as $\delta I(\tau)$. Both quantities can be expressed as functions of the number of nucleons of the two fragments (A_1, N_1, Z_1) and (A_2, N_2, Z_2):

$$\begin{aligned} \delta\Delta A(\tau) &= \frac{(A_1 - A_2)}{(A_U - A_{Al})}\,, \\ \delta I(\tau) &= \frac{\frac{(N_1-Z_1)}{A_1} - \frac{(N_2-Z_2)}{A_2}}{\frac{(N_U-Z_U)}{A_U} - \frac{(N_{Al}-Z_{Al})}{A_{Al}}}\,. \end{aligned} \tag{7.8}$$

In their article, calculations by Simenel *et al.* illustrate $\delta\Delta A(\tau)$ and $\delta I(\tau)$ as functions of the contact time τ for multiple fragment systems in contact. Combining both representations results in a schematic graph as depicted in Fig. 7.37.

Although their calculations exhibit certain fluctuations, a similar pattern is observed in the behaviour of $\delta\Delta A(\tau)$ for all simulated systems, with an equilibration of mass asymmetry and an expected full symmetry around 20 zs of average contact time (see the blue line in Fig. 7.37). This indicates that mass equilibration is a relatively slow process. Reactions with such short time scales ($\tau \approx 10^{-21}$ s) are tagged quasi-fission, as fission-like fragments are produced without the formation of an intermediate compound nucleus, which would require a much longer time ($\tau \lesssim 10^{-20}$ s). Additionally, the behaviour of $\delta I(\tau)$ for all their simulated systems shows that neutron-proton equilibration is a much faster phenomenon than mass equilibration, as $\delta I(\tau)$ is approximately zero for $\tau \approx 1$ zs and above (see the blue line in Fig. 7.37). This timescale is in good agreement with a previous measurement of intermediate-energy reactions, as demonstrated in their article.

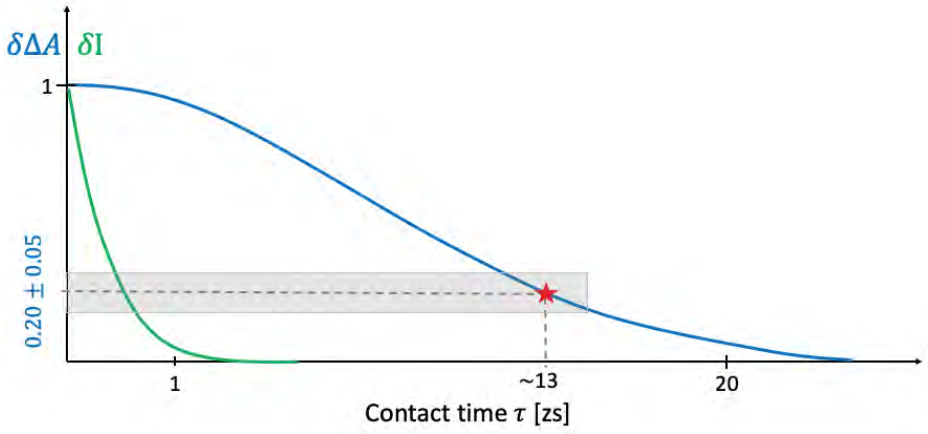

Figure 7.37: *The fragment mass asymmetry $\delta\Delta A(\tau)$ as a function of contact time τ from TDHF calculations is represented with blue line. The asymmetry between proton and neutron numbers $\delta I(\tau)$ as a function of contact time τ from TDHF calculations is represented with green line. Diagram elaborated from the calculations of Simenel et al. [113].*

The equilibration of mass asymmetry in the experimental data of quasi-fission is approximately $\delta\Delta A \approx 0.20 \pm 0.05$. According to Simenel *et al.*, this results in a contact time of $\tau \approx 13$ zs (see the red star in Fig. 7.37 and the grey dashed lines). At this contact time, the aluminium-uranium system achieves isospin equilibrium, i.e., $\delta I = 0$. However, the contact time is not sufficient to complete their mass equilibrium. This contact time indicates that it is a slow quasi-fission process, resembling in temporal scale a fusion-fission reaction. Reaching equilibrium in isospin implies that:

$$\frac{N_1 - Z_1}{A_1} = \frac{N_2 - Z_2}{A_2}\,, \tag{7.9}$$

which implies that the neutron excess of quasi-fission is equal to $N_{FS}/Z_{FS} = 1.524$ being $N_{FS} = N_1 + N_2$ and $Z_{FS} = Z_1 + Z_2$. In Fig. 7.38, the post-evaporation neutron excess of experimental fission data is shown with black dots, along with comparisons with pre- and post-evaporation GEF calculations with black and blue lines. Finally, the estimation of neutron excess of quasi-fission mechanism is depicted with a red line.

Resuming the observed negative even-odd effect in quasi-fission (see Fig. 7.36), in this specific case, the nucleus of ^{238}U ($N = 146, Z = 92$) seeks equilibration with the nucleus ^{27}Al ($N = 14, Z = 13$). Initially, both nuclei are in contact through a neck, and at that moment, the substantial mass difference between them causes the direction of the mass transfer to be from uranium to aluminium. At this initial moment, aluminium has a much smaller excess of neutrons ($N/Z = 1.08$ and $(N - Z)/A = 0.037$) than uranium ($N/Z = 1.59$ and $(N - Z)/A = 0.23$). There is a flow of protons from aluminium to uranium and a flow of neutrons from uranium to aluminium, achieving isospin equilibrium ($\delta I = 0$). Additionally, aluminium has its neutrons in pairs and one unpaired proton, unlike uranium, which has all nucleons in pairs. The experimentally observed negative even-odd effect in quasi-fission implies directly that the unpaired proton moves to uranium and has a very high probability of remaining there. Moreover, the $\delta(Z + 1.5) \sim 30\%$ is consistent with no breaking of proton pairs and the flow of protons from uranium to aluminium occurring in pairs [114].

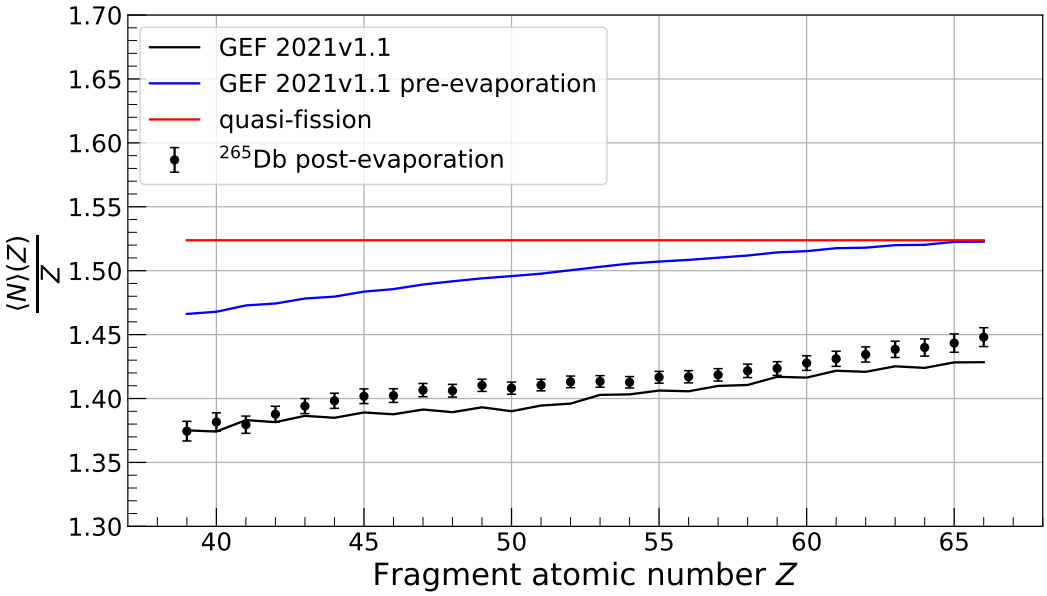

Figure 7.38: *The average neutron excess $\langle N \rangle / Z$ is shown for each fragment Z for ^{265}Db fissioning system (black dots) in comparison with GEF calculations (black line). The pre-evaporation neutron excess is estimated using GEF calculations (blue line), while the red line represents the estimation of the neutron excess for the quasi-fission mechanism.*

7.8 Fission dynamics

The entire process of calculating fragment velocities for both the ^{265}Db and ^{249}Bk fissioning systems is detailed in Section 6.9 of the previous chapter. The average velocity of isotopically identified fragments in the centre-of-mass reference frame, denoted as v_{CM}^{FF}, for the fissioning systems ^{249}Bk and ^{265}Db is illustrated in Fig. 7.39, in the upper and lower panels, respectively. Each colour corresponds to distinct fragment atomic numbers Z, while each data point represents a specific fragment mass number A.

As observed in both fissioning systems, the velocities for heavier fragments are lower than those for lighter ones, exhibiting a decreasing linear trend. In order to compare these velocities with the GEF model [46], they are represented independently for each fragment atomic number Z as a function of the fragment mass (Figs. 7.42 and 7.41) and of the fragment neutron number (Figs. 7.43 and 7.41) for the ^{265}Db or ^{249}Bk fissioning systems.

For both fissioning systems, GEF predicts isotopic centre-of-mass velocities that are higher than the velocities observed in the experimental data, with an approximate difference of +0.02 cm/ns for all fragment Z values in both fissioning systems. In the case of the ^{249}Bk fissioning system, the behaviour and trend of $v_{CM}^{FF}(Z)$ in the experimental data agree with the GEF calculations for lower fragment Z values. However, for fragment $Z > 49$, the data exhibit a slightly different curvature compared to the GEF calculations, which show more constant velocities for all masses in each fragment Z. In the case of the ^{265}Db fissioning system, the behaviour and trend of $v_{CM}^{FF}(Z)$ in the experimental data agree with the GEF calculations for fragment Z, and there is minimal difference in curvatures compared to the other fissioning system.

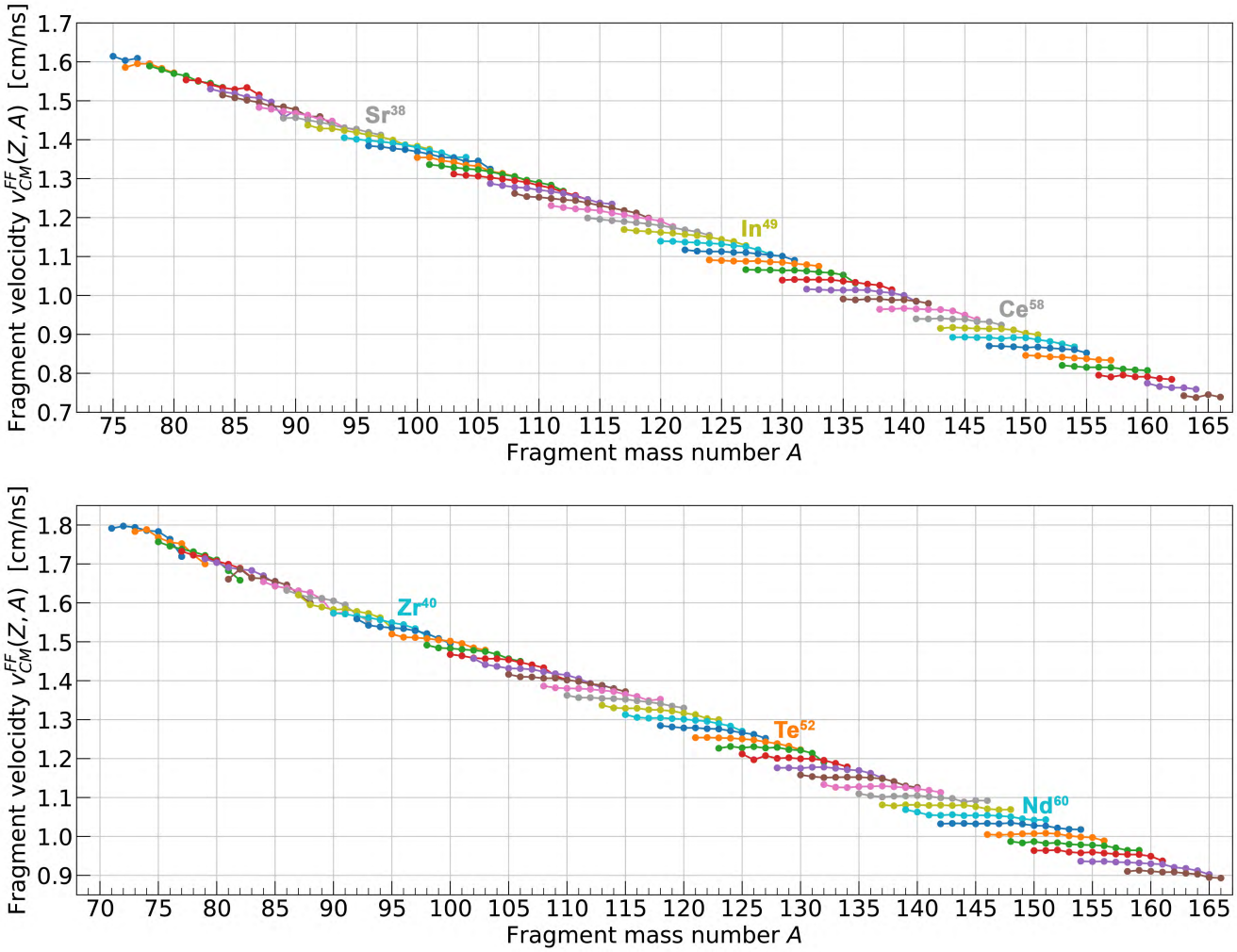

Figure 7.39: *The isotopic velocities, denoted as v_{CM}^{FF} [cm/ns], of the fission fragments from the ^{249}Bk and ^{265}Db fissioning systems are presented. The upper and lower panels correspond to the respective systems. These velocities are differentiated by various colours according to the fragment atomic numbers Z, and data points illustrate the different fragment mass numbers A. In upper panel, $Sr^{Z=38}$, $In^{Z=49}$ and $Ce^{Z=58}$ are highlighted as examples. In lower panel, $Zr^{Z=40}$, $Te^{Z=52}$ and $Nd^{Z=60}$ are highlighted as examples.*

USC
UNIVERSIDADE DE SANTIAGO DE COMPOSTELA

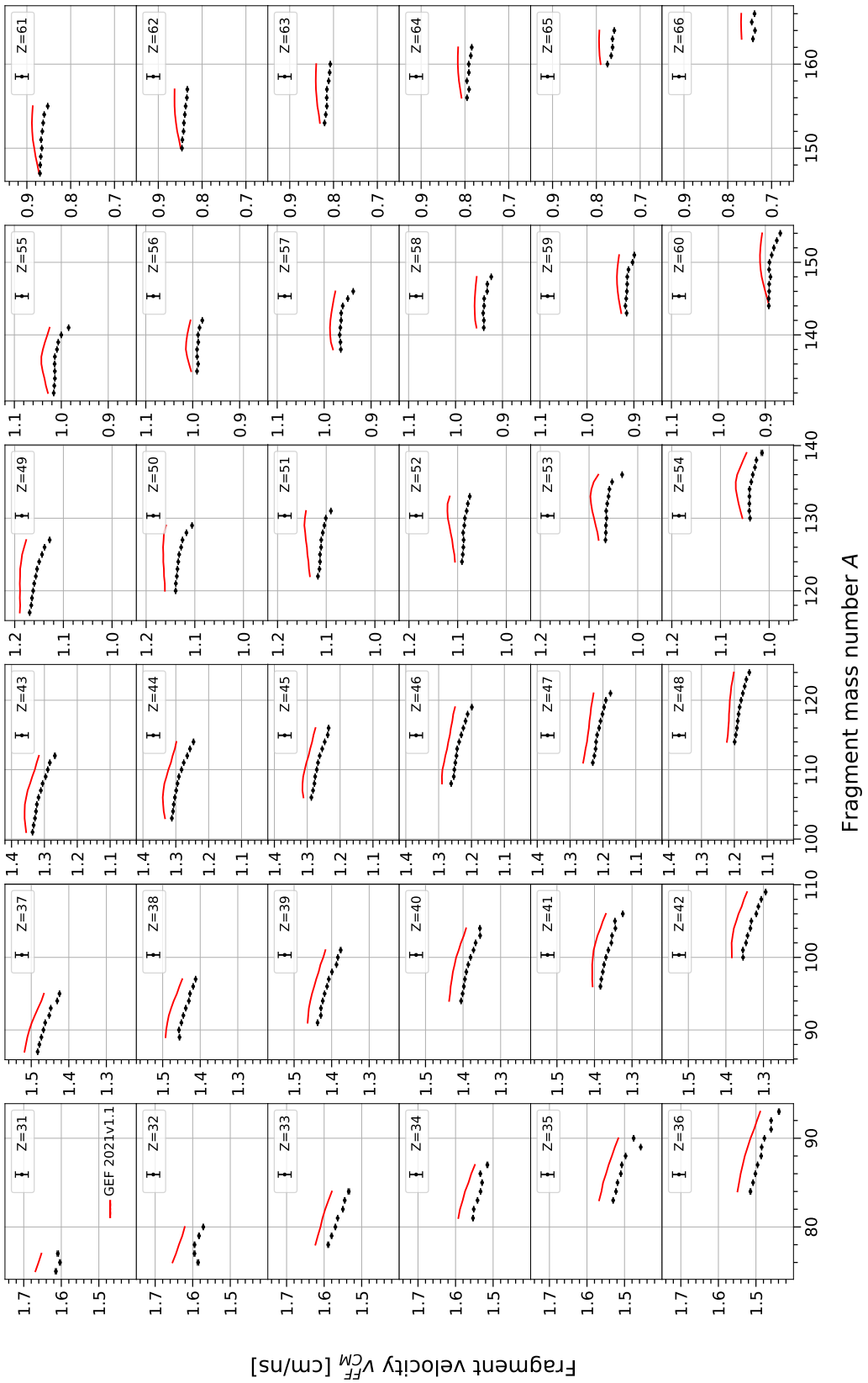

Figure 7.40: *The isotopic centre-of-mass velocities, v_{CM}^{FF} [cm/ns], for fission fragments produced in the fissioning system ^{249}Bk are presented as a function of fragment mass number A. The velocities are shown for fragment atomic number Z ranging from 31 to 66 in the pads.*

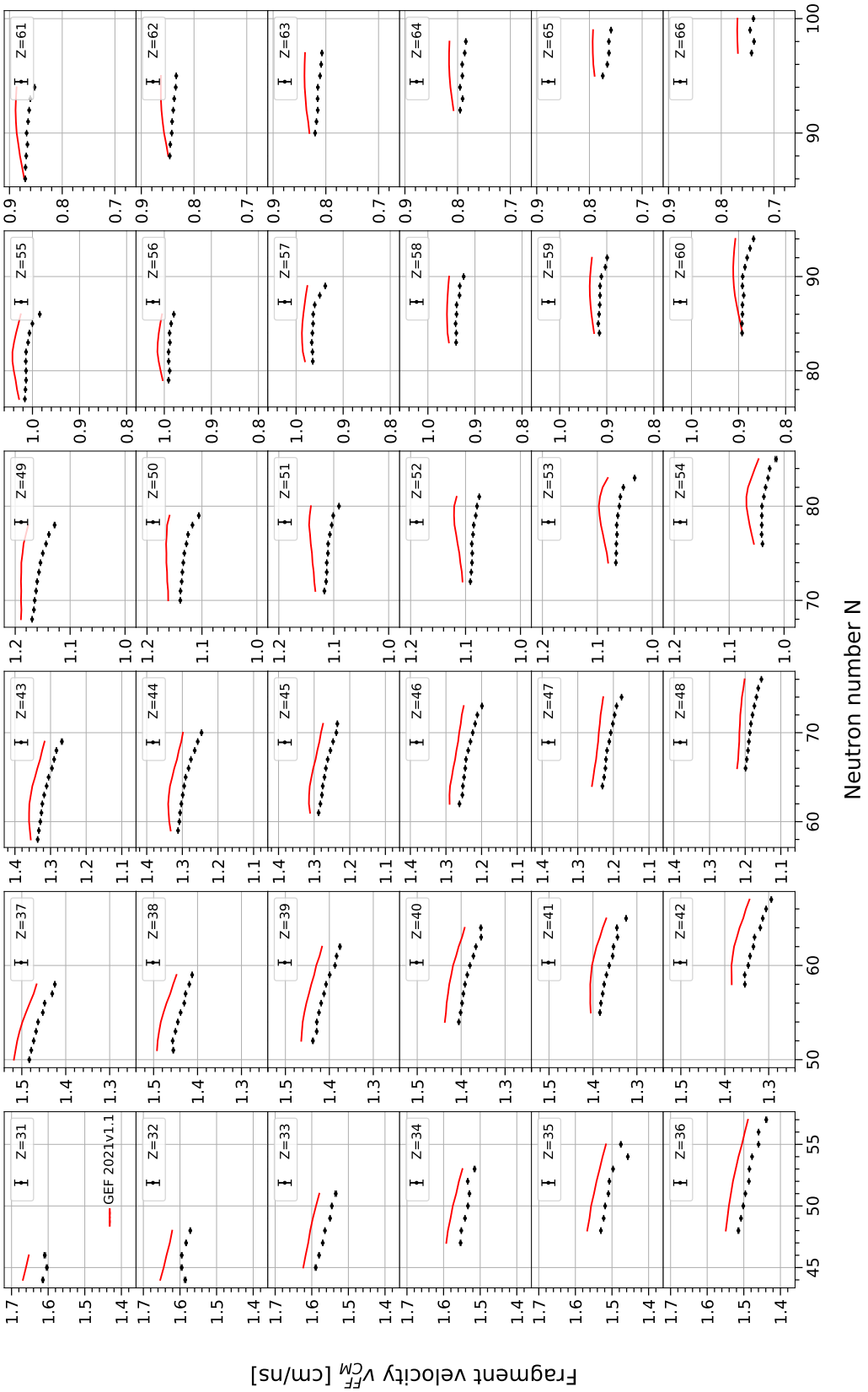

Figure 7.41: *The isotopic centre-of-mass velocities, v_{CM}^{FF} [cm/ns], for fission fragments produced in the fissioning system ^{249}Bk are presented as a function of fragment neutron number N. The velocities are shown for fragment atomic number Z ranging from 31 to 66 in the pads.*

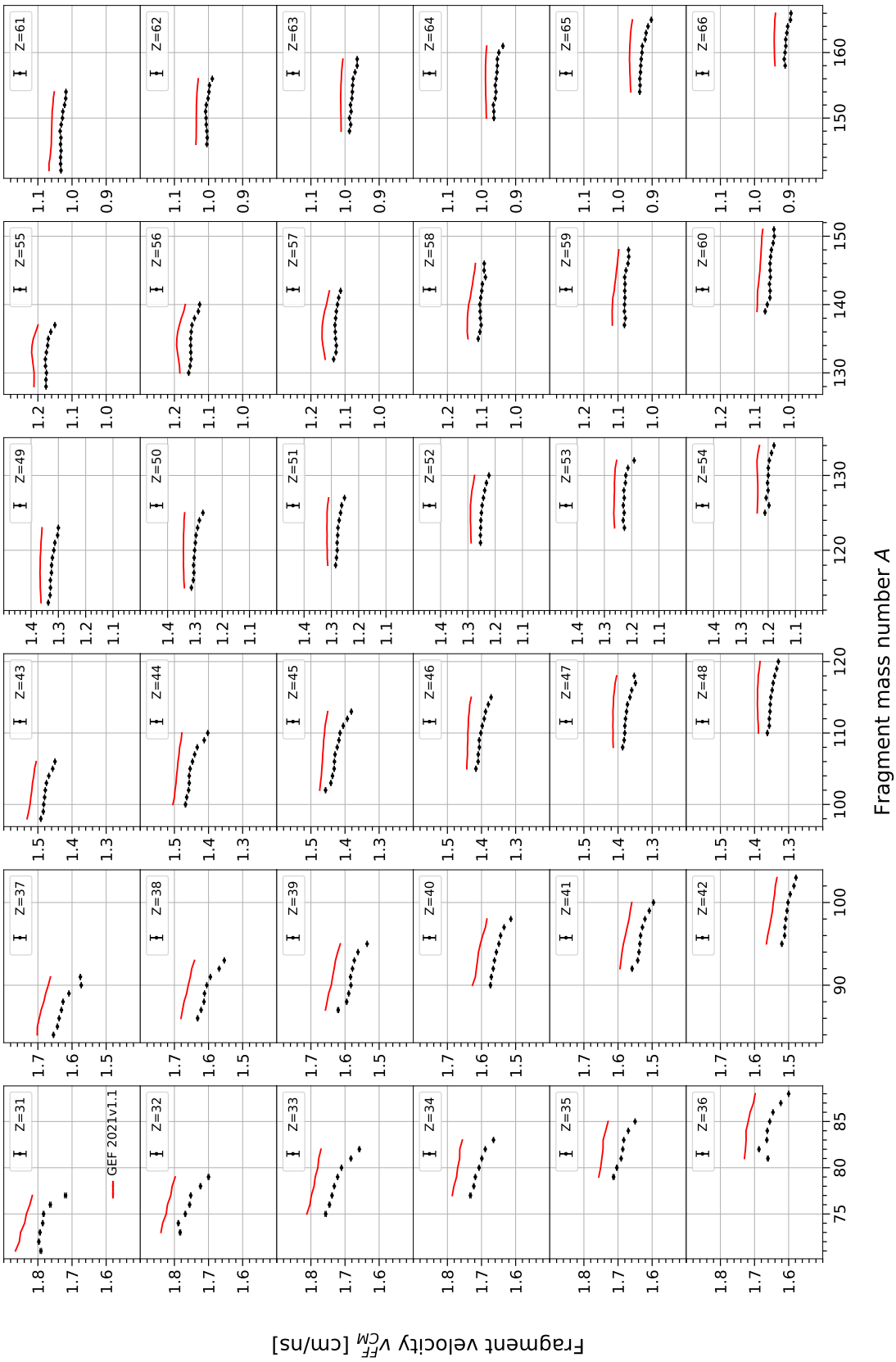

Figure 7.42: *The isotopic centre-of-mass velocities, v_{CM}^{FF} [cm/ns], for fission fragments produced in the fissioning system ^{265}Db are presented as a function of fragment mass number A. The velocities are shown for fragment atomic number Z ranging from 31 to 66 in the pads.*

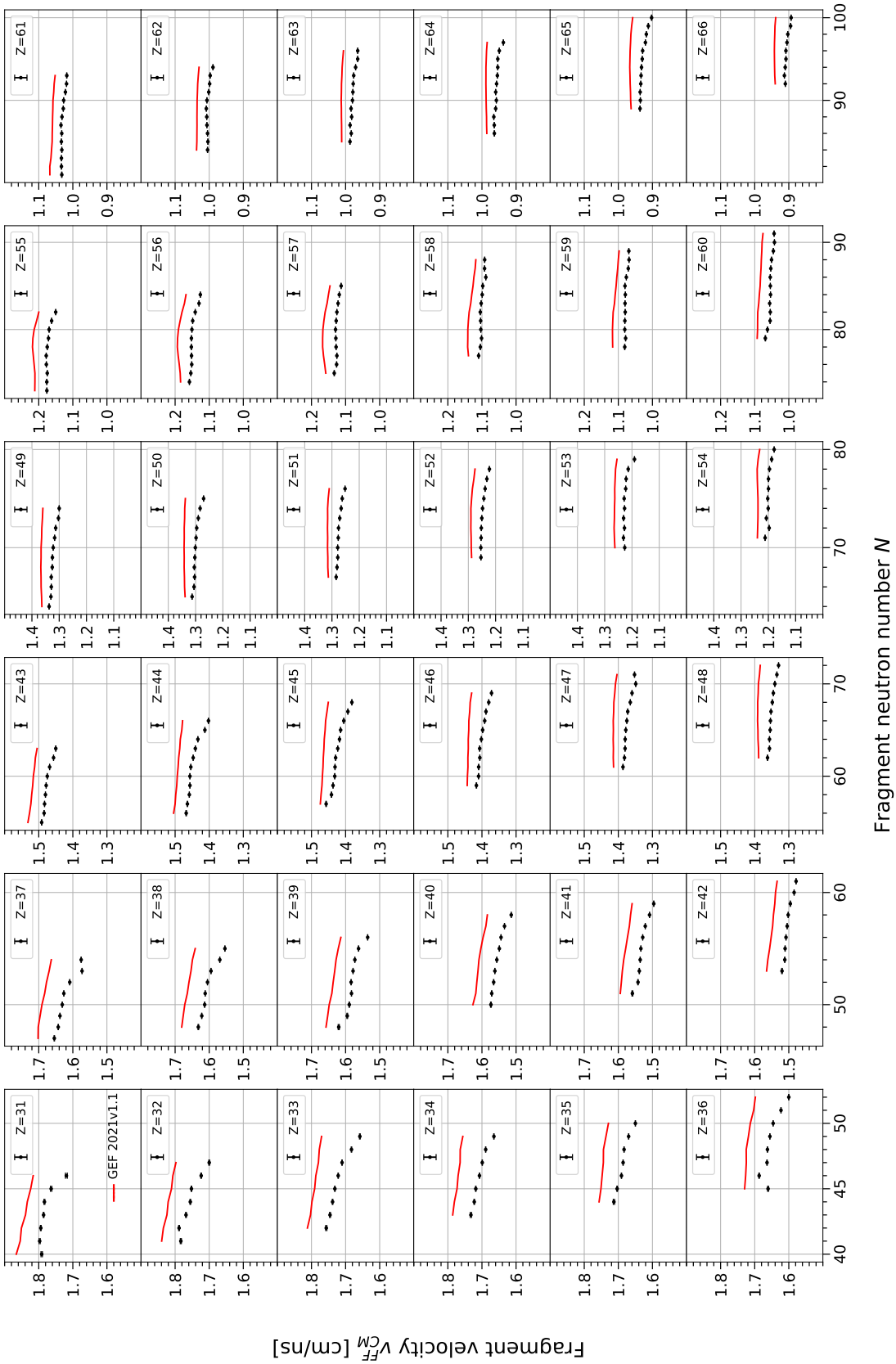

Figure 7.43: *The isotopic centre-of-mass velocities, v_{CM}^{FF} [cm/ns], for fission fragments produced in the fissioning system ^{265}Db are presented as a function of fragment neutron number N. The velocities are shown for fragment atomic number Z ranging from 31 to 66 in the pads.*

7.8.1 Average velocity

The average velocity $\langle V \rangle$ for each atomic number Z is calculated with the fragment yields $Y(Z, A)$ as:

$$\langle V \rangle(Z) = \frac{\sum_A v_{CM}^{FF}(Z, A) \cdot Y(Z, A)}{\sum_A Y(Z, A)} . \tag{7.10}$$

The average fragment velocities $\langle V \rangle$ [cm/ns] for the ^{265}Db and ^{249}Bk fissioning systems are illustrated in Fig. 7.44, presented in the upper and lower panels, respectively. As observed, the velocity decreases as the fragment Z increases. This reduction reflects the conservation of momentum, leading to slower velocities for heavier fragments.

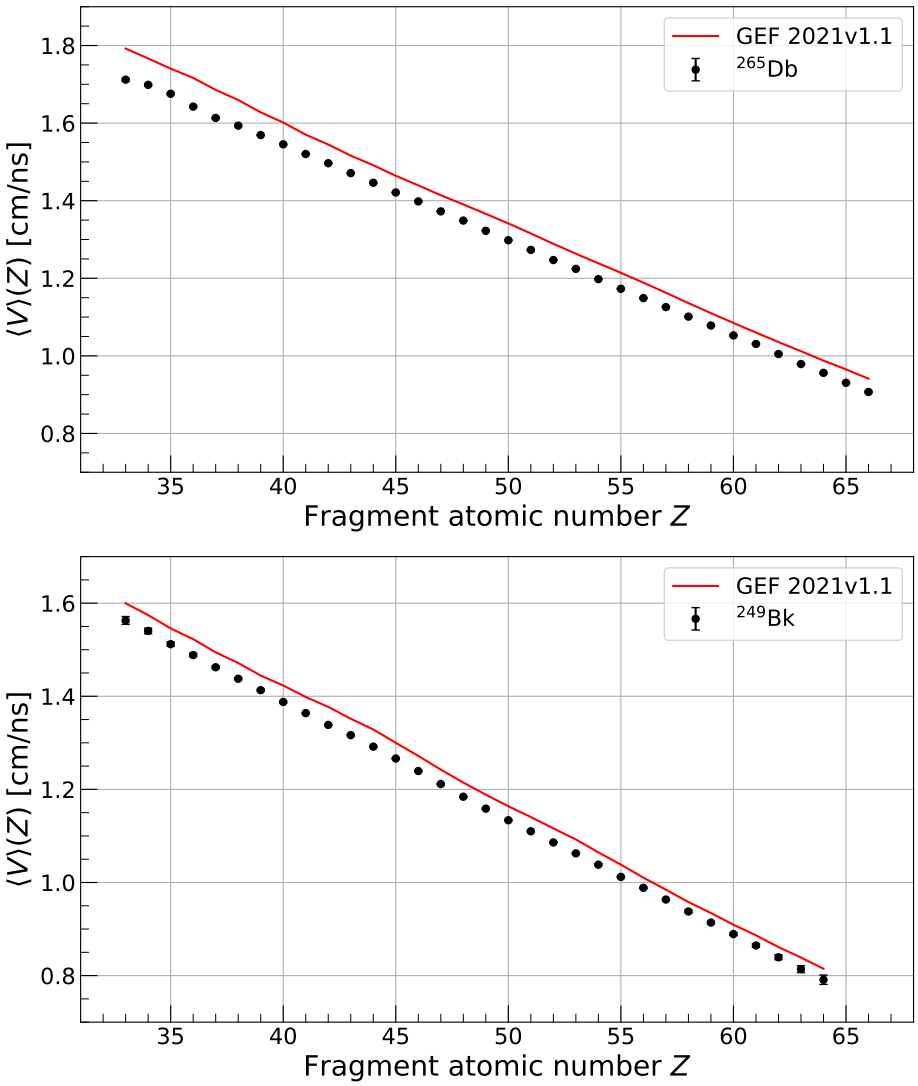

Figure 7.44: *The average fragment velocity $\langle V \rangle(Z)$ as a function of the fragment Z is shown for the fission fragments of ^{265}Db and ^{249}Bk fissioning systems, in upper and lower panel, respectively. The red lines represent the GEF semi-empirical model for comparison [46].*

In the case of the ^{265}Db fissioning system (depicted in the upper panel), the measured velocities during fission are approximately 0.1 cm/ns higher than those of ^{249}Bk. This difference can be attributed to the stronger Coulomb repulsion between the fragments, considering the heavier

mass of ^{265}Db. Comparing the average velocity $\langle V \rangle(Z)$ to the semi-empirical GEF calculation, as represented by the red line [46], differences are found, particularly in velocities for lower Z. It appears that the experimental data follows a linear trend and the GEF calculation shows a different slope. This divergence could be attributed to quasi-fission because there is a portion of the yield related with quasi-fission for high fragment Z (refer to Section 7.4), subsequently increasing $\langle V \rangle(Z)$. It is important to note that in comparisons, for $Z > 53$, the yields are a combination of fusion-induced fission yields and quasi-fission yields. For $Z < 53$ the data should have a different slope. The expected overall behaviour should not be linear, as it actually found. On the other hand, in the ^{249}Bk fissioning system (illustrated in the lower panel), the velocities exhibit a linear trend with a slope similar to the GEF model. No noticeable structural effects are observed in either of the two fissioning systems. This outcome agrees with the results of the high-excitation-energy ^{250}Cf fissioning system [108].

7.9 Characterization of the scission point

The isotopic yield distributions and kinematic properties of fragments resulting from fusion-induced fission of ^{265}Db and ^{249}Bk were experimentally measured using the VAMOS++ spectrometer in inverse kinematics. In general, this approach allowed for the investigation of neutron and proton sharing between fragments, the effect of shell structure during scission deformation, and the distribution of total kinetic and excitation energy between fragments [78, 18, 106].

In this study, the kinematic properties of fission fragments are utilised to infer information about the original split at scission. The average neutron excess of the fragments, as well as the total kinetic energy and neutron multiplicities at the scission point, are experimentally derived. These results shed light on the equilibrium of neutron and proton sharing during the elongation process up to the scission point, while also providing insights into the distance between fragments and their total excitation energy at scission. However, only this collection of results of the ^{249}Bk are presented. As previously explained (see Section 7.4), the experimental data for the ^{265}Db fissioning system exhibits a significant quasi-fission component, which interferes with the fusion-induced fission events. Due to this, it is not possible to characterise the scission point for ^{265}Db since the scission mass cannot be reconstructed without the measurement of the both complementary fragments from the quasi-fission part.

7.9.1 Reconstruction of fragment mass at scission

Information regarding important properties of the scission configuration, such as masses of the nascent fragments, is contained within the fission-fragment velocities. In the reference frame of the fissioning system, the velocities ratio between the two fission fragments is equal to the inverse ratio of the initial masses, M_1^* and M_2^*:

$$\frac{V_1\gamma_1}{V_2\gamma_2} = \frac{M_2^*}{M_1^*}\,, \tag{7.11}$$

where γ is the Lorentz factor, and the superscript asterisk (*) indicates that the magnitude is pre-neutron emission (its initial state).

USC UNIVERSIDADE DE SANTIAGO DE COMPOSTELA

However, it is not possible to evaluate this Eq. 7.11 on an event-by-event basis in the experiment of this study. The velocity of a single fragment per fission event is measured throughout the entire

fragment production process. In the investigated ^{249}Bk fissioning system, the excitation energy (E^*_{FS}) of the fissioning system (see Tab. 2.4) is sufficient to allow proton evaporation but only with a probability of less than 0.03%. Therefore, for a fissioning system with the atomic number Z_{FS}, the average characteristics of fission fragments with the atomic number Z_1 are correlated with the complementary atomic number Z_2:

$$Z_{FS} = Z_1 + Z_2\,, \tag{7.12}$$

under these conditions, momentum conservation establishes a relationship between both fragments:

$$\langle V_1\gamma_1 M_1^*\rangle = \langle V_2\gamma_2 M_2^*\rangle\,. \tag{7.13}$$

However, estimating these magnitudes independently is not possible due to the averaging in the equality. In order to extract the mass information, the average momentum can be expressed as:

$$\langle V_i\gamma_i M_i^*\rangle \approx \langle V_i\gamma_i\rangle\langle M_i^*\rangle\,, \tag{7.14}$$

with a relative error smaller than 0.4% [108].

The average values of mass excess allow expressing M_i^* as the product of the number of nucleons and the unified atomic mass unit:

$$M_i^* \approx uA_i^*\,, \tag{7.15}$$

with a deviation smaller than 0.01%. The previous Eq. 7.13 can be rewritten using this approximation:

$$\frac{\langle V_1\gamma_1\rangle}{\langle V_2\gamma_2\rangle} = \frac{\langle A_2^*\rangle}{\langle A_1^*\rangle}\,. \tag{7.16}$$

The consideration of pre-scission neutron evaporation is important in addition to the post-scission neutron evaporation from the fission fragments. The fissioning system, at high excitation energy E^*_{FS}, is able to emit neutrons before reaching the scission point. Neutrons are expected to be emitted at the pre-saddle position, reducing the effective excitation energy before the dynamical fission process (see Section 1.3.1). However, information about these neutrons cannot be obtained with the current experimental setup.

By assuming that no neutron evaporation takes place from the saddle to scission, as well as from the neck of the fissioning system at scission, and knowing the mass of the fissioning system $\langle A_{FS}\rangle$, the average masses at scission can be inferred:

$$\langle A_1^*\rangle = \langle A_{FS}\rangle \cdot \frac{\langle V_2\gamma_2\rangle}{\langle V_1\gamma_1\rangle + \langle V_2\gamma_2\rangle} \tag{7.17}$$

and consequently:

$$\langle A_2^*\rangle = \langle A_{FS}\rangle - \langle A_1^*\rangle\,. \tag{7.18}$$

In the ^{249}Bk fissioning system, neutron evaporation can take place before fission occurs due to the high excitation energy of $E^* = 47.7$ MeV. The multiplicity of evaporated neutrons depends on the available energy and the induced angular momentum in each reaction of ^{238}U + ^{nat}B. Using $PACE_{IV}$ simulation for this reaction and considering the angular anisotropy, the root-mean-squared angular momentum induced at an energy close to the Coulomb barrier was determined to be $L_{RMS} = 14\hbar$ following the Bass description [107] being L_{RMS} the $1/\sqrt{2}$ of the grazing angular momentum. Based on this angular momentum and an initial excitation energy of 47.7 MeV, the average mass of the fissioning system (A_{FS}) is calculated to be 246.707, considering

the different fission probabilities obtained from the semi-empirical model GEF predictions [46], where first-chance fission occurs in over 9.8% of events. Consequently, the GEF code predicts an average multiplicity of approximately 2.3 pre-saddle neutrons in the ^{249}Bk fissioning system.

Furthermore, despite the possibility of neutron emission during the path from the saddle to scission, resulting in a reduction of excitation energy in the fission fragments, these fragments retain significant deformations and intrinsic energy at the scission point. The release of this energy primarily occurs through neutron evaporation from the fission fragments (see Section 1.3.1). According to GEF, no neutrons in the saddle-to-scission path are emitted in the ^{249}Bk fissioning system. Probabilities for the pre-scission evaporation of a given neutron multiplicity estimated by the GEF code are reported in Tab. 7.3.

pre-saddle neutrons	protons	contribution
0	0	0.09827439
0	1	7.374117e-005
1	0	0.160886
1	1	0.000143668
2	0	0.2612885
2	1	0.000289879
3	0	0.2869348
3	1	0.0002940111
4	0	0.1658667
4	1	0.0001401717
5	0	0.02576046
5	1	4.132047e-006
6	0	4.354543e-005

Table 7.3: *The contributions of emitting pre-saddle neutrons and protons from the ^{249}Bk fissioning system with excitation energy of $E^*_{FS} = 47.7$ MeV, evaluated using the GEF semi-empirical model [46] are listed.*

In accordance with the GEF model, the ^{249}Bk fissioning system initially emits ≈ 2.3 neutron before reaching the saddle point and no emits neutrons between the saddle and the scission point. After scission, the two fission fragments release a total of $\approx 7.5 \rightarrow 8.5$ neutrons. In this study, it is not feasible to measure precise neutron emission locations or exact neutron numbers before scission. However, for comparison with the GEF model, it is assumed that the neutron emissions in GEF before scission correspond to the neutron emissions in our experimental data before scission regardless of the timing.

The standard deviation determined through a GEF calculation of $\langle A_{FS} \rangle$ is 0.27. Additionally, the average excitation energy of the fissioning system is altered by the pre-scission neutron evaporation, which is estimated using GEF. It should be emphasised that any variation in the pre-scission neutron multiplicity primarily affects the overall magnitude of the quantities presented in the subsequent sections.

7.9.2 Neutron excess at scission

The experimental neutron excess $\langle N \rangle / Z$ post-neutron evaporation was explained in Section 7.5. The experimental neutron excess at scission, $\langle N^* \rangle / Z$, can be calculated using the average fragment

masses $\langle A^* \rangle$ obtained from Eq. 7.17, expressed as:

$$\frac{\langle N^* \rangle}{Z}(Z) = \frac{\langle A^* \rangle(Z) - Z}{Z}, \tag{7.19}$$

where the asterisk denotes the time just after the split (scission). Figure 7.45 illustrates the average neutron excess for both post- and pre-neutron evaporation scenarios, for the ^{249}Bk fissioning system. The experimental data are compared with the GEF semi-empirical model [46]. It is well-known that the neutron excess varies with the asymmetry of the fission fragments, where lighter fragments exhibit a smaller neutron excess compared to heavier fragments. This phenomenon, referred to as *charge polarisation*, is observed in the presented figures (see Section 7.5).

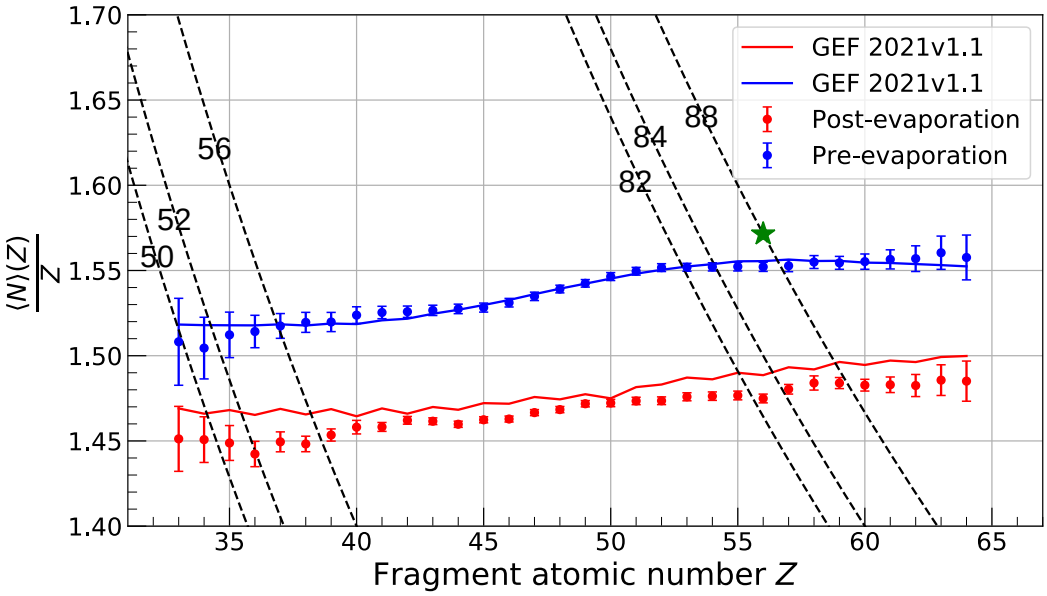

Figure 7.45: *The average neutron excess $\langle N \rangle / Z$ is shown for each fragment Z for ^{249}Bk fissioning system, for both scenarios: post-evaporation and pre-evaporation, represented with red and blue dots. The results are compared with the GEF semi-empirical model [46] with the same colours. The dashed black lines represent the nuclear neutron shells $N = [50, 52, 56, 82, 84, 88]$. The green star represents the $(Z = 56, N = 88)$ point.*

The neutron excess at scission displays a smooth behaviour with the fragment Z; however, neutron evaporation significantly alters this trend. The fragments observed after neutron evaporation exhibit a relatively smooth neutron excess with *charge polarisation*. For heavy fragments with $Z > 50$, the neutron excess at scission stabilises at approximately 1.55. This behaviour is expected at such high excitation energies, as well as being anticipated to decrease beyond $Z > 50$ at lower excitation energies. The experimental data agree with the behaviour of other studied excited fissioning systems, such as ^{250}Cf [108].

It is worth noting that the experimental data contradict the prediction of a liquid-drop scission-point (LDSP) model that considers the Coulomb interaction between the two touching fragments while neglecting their nuclear interaction. This prediction would imply a steady increase in the neutron excess of scission fragments with their atomic number Z, which would suggest the need to increase the number of neutrons to counterbalance the growing Coulomb repulsion within the heavier fragments. In contrast, the experimental data display an *S-shape*, making heavier

fragments slightly more neutron-rich and lighter fragments less neutron-rich than expected from a simple macroscopic equilibrium. This behaviour agrees with the predictions of the GEF model shown in blue. In this model configuration, the influence of the *SI* fission channel (closed shell) has disappeared. As previously mentioned, the GEF model underestimates the *Standard I* fission channel. It seems that at these high excitation energies, the octupolar-deformed shell $Z = 56$ is experimentally formed with the octupolar-deformed shell $N = 88$ (see green star in Fig. 7.45). This observation could explain why the *SII* fission channel dominates over the *SI* fission channel in the experimental data.

7.9.3 Post-scission neutron evaporation

In the case of low-energy fission, a distinct saw-tooth pattern is observed in the neutron multiplicity, which is typically measured as a function of the fragment mass in various systems [115]. This pattern is attributed to the release of excitation energy, including deformation energy when the scission fragments separate and return to ground-state deformations (see Section 1.3.1).

However, in higher-energy fission, such as ^{249}Bk at $E^*_{FS} = 47.7$ MeV, a portion of the available excitation energy and the energy gained during the fission path is shared between the nascent fission fragments and is subsequently released after scission through the emission of neutrons. Consequently, the neutron evaporation is analysed through neutron multiplicity (see Section 7.6) and it serves as an indicator of the energy distribution between the two fragments, including their respective deformations.

Access to the average neutron multiplicity $\langle\nu\rangle(Z)$ evaporated by the deformed scission fragments can be obtained through the difference between the scission mass deduced from the velocity properties (see Eq. 7.17) and the mass measured in the spectrometer:

$$\langle\nu\rangle(Z) = \langle A^*\rangle(Z) - \langle A\rangle(Z)\,. \tag{7.20}$$

Figure 7.46 displays the experimental multiplicity $\langle\nu\rangle(Z)$ of fission fragments for the ^{249}Bk fissioning system. A comparison is made with the GEF semi-empirical model [46], represented by the red line.

The experimental multiplicity, $\langle\nu\rangle(Z)$, of the fission fragments in the ^{249}Bk fissioning system, as depicted in Fig. 7.46, exhibits a consistent increase with the fragment Z. This trend agrees with measurements from comparable fusion-fission reactions, such as the ^{250}Cf fissioning system [108]. The inflection observed around $Z \approx 52$ and $Z \approx 56$ could be point fluctuations. However, the inflection around $Z \approx 36$ could be a bulge related to the *SA* fission channel of ^{249}Bk, but this effect is not shown the *S-shape* pattern observed in $\langle N^*\rangle/Z$ in Fig. 7.45.

The multiplicity indicates the formation of fragments with large excitation energy, specifically at $Z \approx 36$ and $Z \approx 62$, related to the *SA* fission channel. As was observed earlier in Fig. 7.7, the increase in the width of the yields for $Z > 55$ is reflected in the increase in neutron evaporation in this Fig. 7.46 showing the relationship between σ and $\langle\nu\rangle(Z)$. The GEF model [46] exhibits a change in the trend at $Z = 50$ and a gradual flattening, even decreasing, beyond $Z = 56$. Once again, it seems that GEF underestimates the influence of the *SA* fission channel.

USC DE SANTIAGO DE COMPOSTELA

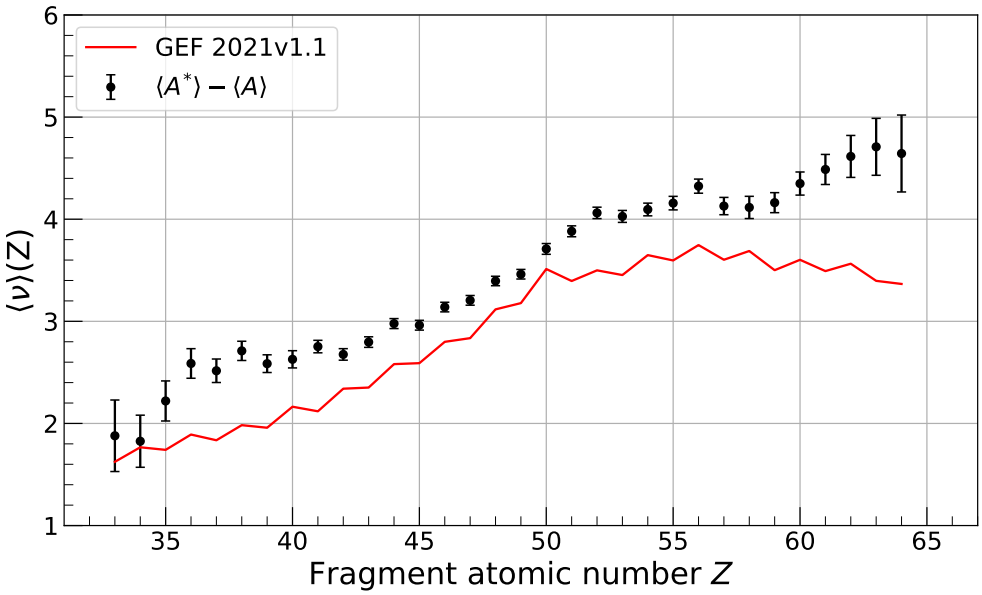

Figure 7.46: *Average neutron multiplicity $\langle\nu\rangle$ as a function of the fragment Z for the ^{249}Bk fissioning system with the comparison with the GEF model [46], represented by the red line.*

The post-scission total neutron multiplicity is determined by summing the multiplicities of fragment Z_1 and its complementary fragment $Z_2 = Z_{FS} - Z_1$. This can also be expressed as the difference in mass between the fissioning system and the detected fragments after neutron evaporation. Mathematically, it is defined as:

$$\langle\nu_{1+2}\rangle(Z) = \langle\nu_1\rangle + \langle\nu_2\rangle = \langle A_{FS}\rangle - \langle A_1\rangle - \langle A_2\rangle\,. \tag{7.21}$$

The post-scission total neutron multiplicity $\langle\nu_{1+2}\rangle(Z)$ for the fission fragments of the ^{249}Bk fissioning system are depicted in Fig. 7.47 as a function of the fragment Z. The experimental data are compared with the GEF semi-empirical model [46], indicated by the red line for $\langle\nu_{1+2}\rangle(Z)$ and the blue line for $\langle\nu_{total}\rangle(Z)$.

The structural effects identified previously are magnified in Fig. 7.47 of neutron multiplicity. The multiplicity $\langle\nu_{1+2}\rangle(Z)$ clearly reflects the impacts of the fission channels, with noticeable inflections around $Z \approx 36$ and $Z \approx 52$ (see Fig. 7.10). The inflection at $Z = 56$ appears to be a point fluctuation. The experimental data show higher neutron evaporation of approximately $1 \rightarrow 2$ neutrons more than the GEF calculations. Additionally, the GEF model presents an arc-shaped evaporation, whereas in the data, it is more flat with minor fluctuations. The experimental data agree with the behaviour of other studied excited fissioning systems, such as ^{250}Cf [108]. Mathematically, $\langle\nu_{total}\rangle(Z) = \langle\nu_{1+2}\rangle(Z) + Offset$; however, small variations in behaviour can be observed among the results of the experimental data. These variations result from the treatment of yields and the treatment of the yields plus the treatment of the distribution of velocities to obtain $\langle\nu_{1+2}\rangle(Z)$ and $\langle\nu_{total}\rangle(Z)$, respectively.

USC UNIVERSIDADE DE SANTIAGO DE COMPOSTELA

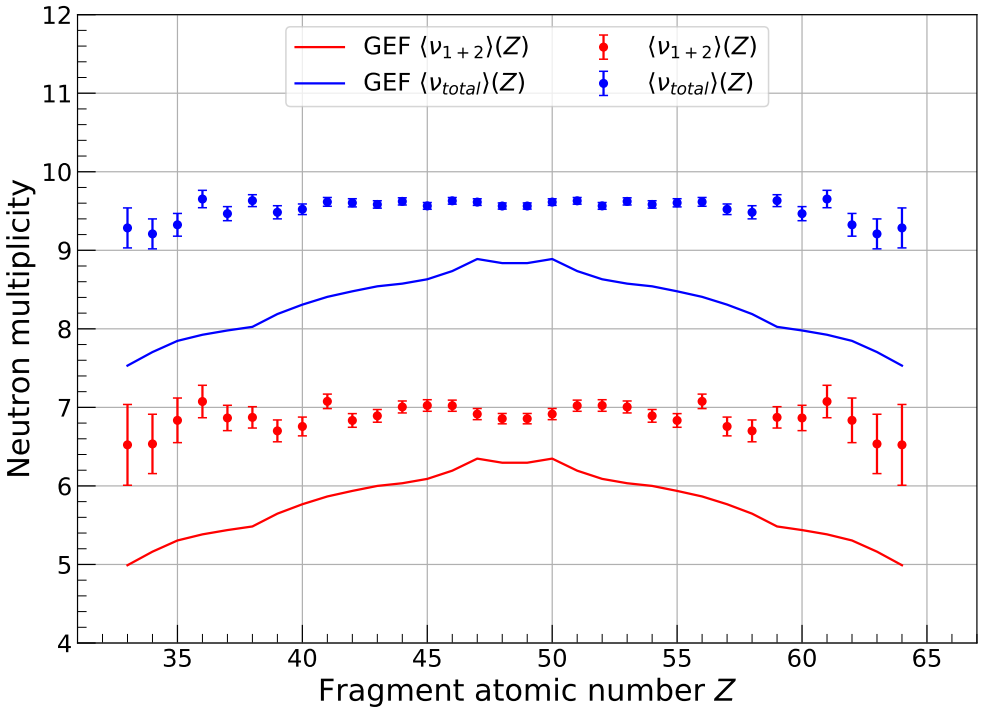

Figure 7.47: *Average total neutron multiplicity, denoted as $\langle\nu_{total}\rangle$, is depicted in blue dots as a function of the fragment atomic number Z, whereas average neutron multiplicity $\langle\nu_{1+2}\rangle$ is shown in red dots, also as a function of the fragment atomic number Z. Both sets of results are compared with the GEF model [46], represented by blue and red lines, respectively.*

7.9.4 Total Kinetic Energy at scission

The features of the total kinetic energy distribution of fully accelerated fragments are primarily influenced by the configuration of the system at scission, including factors such as mass and charge distribution, deformations, and fragment separation distance (see Section 1.3.1). Employing the fragment masses obtained through scission reconstruction (see Eq. 7.17) and their corresponding velocities, it becomes feasible to determine the Coulomb potential energy acting between the fragments. This potential energy can be then converted into the total kinetic energy at scission, denoted as $\langle TKE^{*}\rangle$, once the fragments have undergone full acceleration but before prompt-neutron emission. The average value of $\langle TKE^{*}\rangle$ can be calculated using the following equation:

$$\langle TKE^{*}\rangle = u\langle A_1^{*}\rangle \cdot (\langle\gamma_1\rangle - 1) + u\langle A_2^{*}\rangle \cdot (\langle\gamma_2\rangle - 1)\ . \tag{7.22}$$

The $\langle TKE^{*}\rangle$ at the scission point is illustrated as a function of the fragment atomic number Z for the ^{249}Bk fissioning system in Fig. 7.48 in the upper panel. The findings are compared with the GEF model [46] and the theoretical prediction of the LDM model, denoted by a red line and a blue dashed line, respectively. Furthermore, the ratio between the LDM model and the experimental data, and a comparison with the previously obtained fission channels are made (see Fig. 7.10), as observed in other fissioning systems [109], in the lower panel.

Disregarding the contribution of pre-scission velocity, the total kinetic energy at scission can be regarded as the consequence of the Coulomb repulsion between the fission fragments, taking

into account a separation distance D which is a function of the deformations and the gap between the surfaces of the fragments [25]:

$$TKE^{*} = 1.44\frac{Z_1 Z_2}{D}\,. \tag{7.23}$$

Evaluating D, this equation can be rewritten, with the consideration that the LDM model predicts the total kinetic energy at scission by taking into account the Coulomb repulsion between the fragments at a distance d. This distance d represents the separation between the surfaces of the fragments and is dependent on their deformations β_1 and β_2, and the pre-evaporation fragment masses. The parameterised equation for the LDM model prediction is as follows:

$$\langle TKE^{*}\rangle = 1.44\frac{Z_1 Z_2}{1.25\cdot(\langle A_1^{*}\rangle^{1/3}\cdot\left(1+\frac{2}{3}\beta_1\right)+\langle A_2^{*}\rangle^{1/3}\cdot\left(1+\frac{2}{3}\beta_2\right))+d}\,, \tag{7.24}$$

in the case of ^{249}Bk fissioning system, the value of d is fixed at 1.85 fm, and the deformations are $\beta_1 = \beta_2 = 0.625$ according with other publications [109]. Then, the parameter D in the case of a simplified LDM description:

$$D = 1.25\cdot\left(\langle A_1^{*}\rangle^{1/3}\cdot(1+2/3\beta_1)+\langle A_2^{*}\rangle^{1/3}\cdot(1+2/3\beta_2)\right)+d\,. \tag{7.25}$$

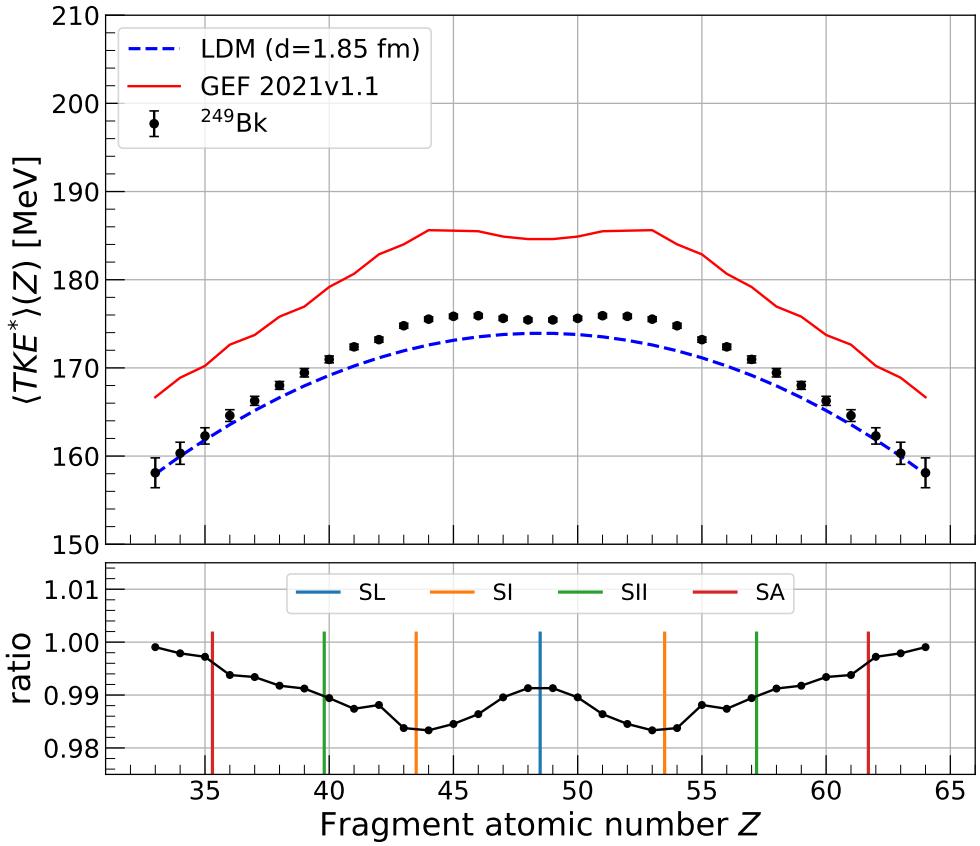

Figure 7.48: *The total kinetic energy $\langle TKE^{*}\rangle$ of the fission fragments at the scission point is presented for the ^{249}Bk fissioning system in the upper panel. A comparison is made with the semi-empirical GEF model [46] and with the LDM prediction, represented by a red line and a blue dashed line, respectively. In the lower panel, the ratio between the LDM model and the experimental data is depicted with the position of the fission channels in colours.*

In Fig. 7.48, which depicts the $\langle TKE^{*}\rangle$ of the ^{249}Bk fissioning system, structural effects are anticipated to diminish due to its relatively high excitation energy, resulting in a smoother $\langle TKE^{*}\rangle$. Nevertheless, the measured $\langle TKE^{*}\rangle$, although smoother than predicted by the GEF model, exhibits an almost uniform behaviour around symmetric splits, occurring between $Z \approx 44$ and $Z \approx 53$, implying a structural influence. Peaks emerge around $Z \approx 44$ and $Z \approx 53$, where the values of $\langle TKE^{*}\rangle$, approximately 2 MeV higher than the symmetric case, correspond to more compact configurations. This is evident in the ratio within the lower panel that highlights the positions of the asymmetric fission channels *Standard I* and *Standard II*. The ratio in the subplot is calculated by directly dividing the LDM model into the experimental data, represented by the blue dashed line. A minor contribution from the *Super-Asymmetric* fission channel also appears, albeit very limited around $Z \approx 36$.

7.9.5 Relative distance between fragments

Following Eq. 7.24, the influence of structure in the evolution can be seen and quantified more clearly considering $\langle TKE^{*}\rangle$ is contained in the distance between the fragments. It is the ratio of the actual distance parameter D (see Eq. 7.25) between the fragments at scission and their distance D_0 as spherical touching nuclei. From previous Eq. 7.24, the average of this ratio $\langle D/D_0\rangle$ as a function of the fragment split can be calculated as:

$$\langle D/D_0\rangle = 1.44\frac{Z_1 Z_2}{\langle TKE^{*}\rangle}\left(\frac{1}{r_0\cdot\langle A_1^{*}\rangle^{1/3}+r_0\cdot\langle A_2^{*}\rangle^{1/3}}\right), \tag{7.26}$$

with $r_0 = 1.25$ fm.

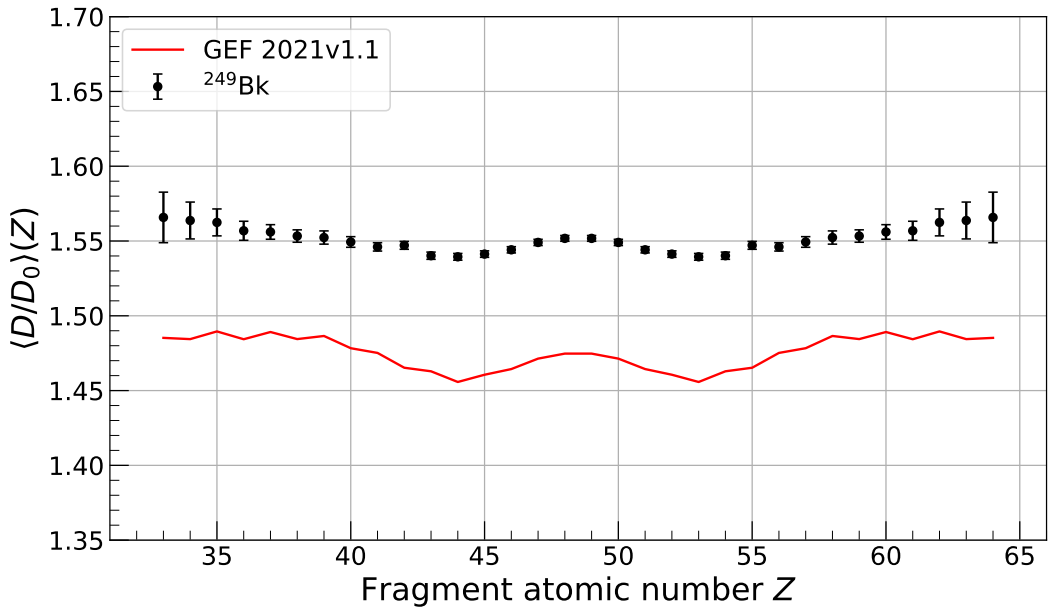

Figure 7.49: *The relative distance between fission fragments in the fission of the ^{249}Bk fissioning system is represented by the ratio of the distance between fragments at scission, denoted as D, to the distance between two spherical touching nuclei, indicated as D_0. A comparison with the GEF model [46] is illustrated by the red line.*

Figure 7.49 presents $\langle D/D_0\rangle$ data for the ^{249}Bk fissioning system. As expected, there is a correlation between $\langle TKE^{*}\rangle$ (as seen in Fig. 7.48) and $\langle D/D_0\rangle$: the most compact shapes,

characterised by the lowest $\langle D/D_0 \rangle$ value of approximately 1.54, correspond to the peaks in $\langle TKE^* \rangle$ at $Z \approx 44$ and $Z \approx 53$. The elongation remains relatively constant around $\langle D/D_0 \rangle \approx 1.55$, with a slight increase towards symmetry. As can be seen, the shape of the ratio between LDM model and experimental data shown in the lower panel of Fig. 7.48 is recovered since $\langle D/D_0 \rangle$ is equivalent to the ratio between them. Overall, the elongation behaviour remains rather flat, with no other significant features correlating with $\langle TKE^* \rangle$. The GEF model predicts a similar shape which is less smooth than the experimental data and with a clear difference in $Z > 56$ and in $Z < 41$, where the slope increase more than the experimental data. Additionally, it exhibits behaviour contrary to its prediction regarding $\langle TKE^* \rangle$ (as seen in the red line in Fig. 7.48). The discrepancy between the data and the model is approximately 0.1.

7.9.6 Total Excitation Energy at scission

The total energy available in the fission reaction E_{tot} is obtained by summing the ground state mass of the fissioning system M_{FS} and its excitation energy E^*_{FS} (see Section 1.3.1). At the moment of scission, the total energy is the sum of the masses of the pre-neutron-evaporation fragments, the total kinetic energy TKE^*, and the collective (deformations, rotations, etc.) and individual or intrinsic (excitations of individual nucleons) excitation energies of the degrees of freedom.

The determination of the total kinetic energy at scission, as evaluated in the previous Section 7.9.4, permits the determination of the portion of the total energy which is transformed into excitation energy of the fragments. Assuming no evaporation occurs along the saddle-to-scission path, energy conservation relates them as:

$$E_{tot} = M_{FS} + E^*_{FS} = \langle M^*_1 \rangle + \langle M^*_2 \rangle + \langle TKE^* \rangle + \langle TXE^* \rangle \,, \tag{7.27}$$

where $\langle M^*_i \rangle$ $(i = 1, 2)$ is the mass in the ground state of the fission fragment. The calculation of $\langle M^*_i \rangle$ uses the pre-evaporation mass (see Eq. 7.17) $\langle A^*_i \rangle$, evaluated by interpolating the mass to the nearest integer mass value:

$$\langle M^*_i \rangle = (1 - W_i) \cdot m_{0,(Z_i, int(\langle A^*_i \rangle))} + W_i \cdot m_{0,(Z_i, int(\langle A^*_i \rangle)+1)} \,, \tag{7.28}$$

where:

$$W_i = \langle A^*_i \rangle - int(\langle A^*_i \rangle) \tag{7.29}$$

and $m_{0,int}$ is the mass of the ground state tabulated in AME2021 evaluation [116], where $int(\langle A^*_i \rangle)$ represents the highest possible integer not greater than $\langle A^*_i \rangle$.

The difference between the total energy E_{tot} and the potential energy surface at scission can be regarded as the quantity $\langle TXE^* \rangle$. By subtracting E^*_{FS}, this difference can be expressed with respect to the ground state of the fissioning system as follows:

$$\langle TXE^*_{g.s} \rangle = M_{FS} - \langle M^*_1 \rangle - \langle M^*_2 \rangle - \langle TKE^* \rangle = \langle Q_{g.s} \rangle - \langle TKE^* \rangle \,, \tag{7.30}$$

where $\langle TXE^*_{g.s} \rangle$ is the portion of the energy $\langle TXE^* \rangle$ that is depicted in E^*_{def} in Fig. 1.3, whereas $\langle Q_{g.s} \rangle$ is the difference between the average masses of the fissioning system and of the fragments at scission as Eq. 1.1.

The results of the $\langle Q_{g.s} \rangle$, $\langle TKE^* \rangle$, $\langle TXE^*_{g.s} \rangle$, and the fission fragment yields for each fragment atomic charge Z for the fission of ^{249}Bk fissioning system, are depicted in the Fig. 7.50 compared

with the semi-empirical GEF model [46]. The $\langle Q_{g.s} \rangle$ behaviour in the ^{249}Bk fissioning system resembles that of $\langle TKE^* \rangle$ (refer to the upper panel in Fig. 7.50). Specifically, there is a flatter region between $Z \in [45, 53]$ within the central symmetric area. On the other hand, for the middle panel, the ^{249}Bk fissioning system exhibits a pronounced peak centred at symmetric splits, ranging from approximately ≈ 36 up to ≈ 50 MeV.

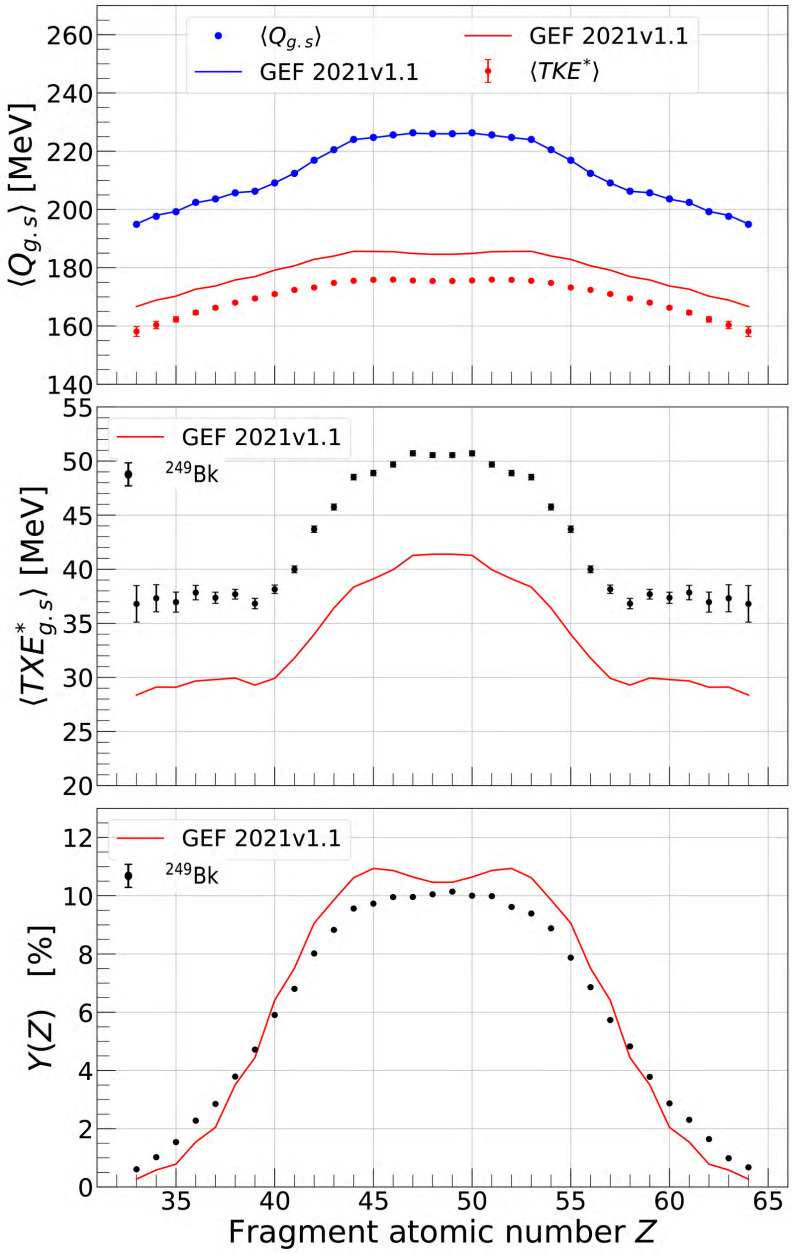

Figure 7.50: *Average differences between the ground states of the ^{249}Bk fissioning system and the fission fragments $\langle Q_{g.s} \rangle$ at scission, as well as $\langle TKE^* \rangle$ [MeV] (upper panel) indicated by blue and red dots, respectively. The total excitation energy at scission $\langle TXE^*_{g.s} \rangle$ [MeV] is presented in the middle panel. Normalized post-neutron evaporation yields $Y(Z)$ are shown in the lower panel for reference. Comparison with the semi-empirical GEF model [46] is represented by red and blue lines.*

The values presented in Fig. 7.49 for $\langle D/D_0 \rangle$ and the middle panel in Fig. 7.50 for $\langle TXE^*_{g.s} \rangle$, both as functions of the fragment atomic number Z, can be interpreted as depicting the energy potential shape experienced by the fissioning system at scission. In the ^{249}Bk system, symmetric splits are associated with elongated shapes and maxima in $\langle TXE^*_{g.s} \rangle$.

Conclusions

This thesis explores the experimental investigation of fission in heavy actinides, focusing on the ^{265}Db and ^{249}Bk. These systems are generated through fusion reactions in inverse kinematics, involving a ^{238}U beam at 5.88A MeV colliding with ^{27}Al and ^{nat}B targets. The experimental setup, utilising the SPIDER detector for fissioning system identification and the VAMOS++ spectrometer for fragment identification, enables the study of various aspects, including isotopic, isobaric, and elemental fission-fragment yields, neutron excess, total neutron evaporation and nuclear-charge even-odd staggering. Specifically, the investigation delves into fusion-induced fission in the highly excited ^{265}Db fissioning system (with E^*_{FS} = 61.2 MeV) and the onset of the quasi-fission mechanism, as well as fusion-induced fission study in the highly excited ^{249}Bk fissioning system (with $E^*_{FS} = 47.7$ MeV) accessing the characterisation of the scission point.

The VAMOS++ spectrometer, in conjunction with the SPIDER detector, enables the tagging and isotopic identification of fission fragments in super-heavy fissioning systems. In inverse kinematics, both fission fragments are emitted forward in the laboratory reference frame, confined to a cone that traverses the central hole of the SPIDER detector. The target-like recoils are detected at larger angles in the SPIDER telescope for transfer-induced fission reactions, allowing for isotopic identification and excitation energy reconstruction. Fusion-induced fission reactions are inferred when no recoils are detected. The VAMOS++ spectrometer deflects one fission fragment, which enters the focal plane setup for identification in terms of nuclear charge, mass, and charge state. By employing the SPIDER detector and the VAMOS++ spectrometer, comprehensive identification of fission fragments is achieved, facilitating the study of various fission-related observables, including isotopic and elemental fission yields, neutron excess, total neutron evaporation, and nuclear-charge even-odd staggering. Additionally, by measuring other observables such as the positions and emission angles of fission fragments, the centre-of-mass velocity of the fission fragment can be reconstructed. This enables access to intrinsic properties of the fissioning system at the scission point, such as the reconstruction of pre-evaporation fragment masses, total kinetic energy, total excitation energy, and neutron evaporation. The implementation of efficiency, normalisation, and VAMOS++ acceptance correction has been carried out for both targets employed in this research thesis.

The isotopic fission yields of ^{249}Bk have been effectively reconstructed for fragment atomic numbers $Z \in [33, 65]$. These results exhibit a substantial contribution from symmetric fission in the fissioning system, which is normal at high excitation energies. Additionally, the analysis of fission channels in terms of nuclear charge reveals the presence of asymmetric-fission contributions, notably characterised by two major and significant channels, *Standard I* and *Standard II*. The

asymmetric component for the heavy fragment is centred around $Z \approx 54$ and $A \approx 140$ and around $Z \approx 57$, respectively. Nonetheless, a contribution from the super-asymmetric channel remains observable, with a yield of approximately 3.4% centred around $Z \approx 36$ in the light fragment. These observations suggest that deformed octupole nuclear layers play a significant role in the fission of the ^{249}Bk fissioning system even at high energy.

The isotopic fission yields of ^{265}Db have been accurately reconstructed for fragment atomic numbers $Z \in [33, 66]$. These measurements reveal that the predominant contribution emanates from symmetric fission in the fissioning system, accounting approximately a yield of 93.4%. Furthermore, the examination of fission channels based on nuclear charge discloses the presence of asymmetric-fission contributions, notably characterised by two channels, *Standard II* and the *Asymmetric-Channel*, both centred at $Z \approx 63$ and $Z \approx 67$ in the heavy fragments. It is worth emphasising that the *Standard I* fission channel does not contribute.

An apparent lack of anisotropy evolution is observed in the ^{249}Bk fissioning system, with fluctuating value around $A_{ny} = W(0°)/W(90°) = 1.5$. This observation agrees with expectations, as no other mechanisms are competing with fusion-induced fission yields in this case and a symmetric behaviour as a function of Z around $Z_{FS}/2$ is expected. The fusion process, unlike quasi-fission, does not exhibit a correlation between the masses and angles of the fragments. The fission mass distribution is equal and independent of the angle at the centre-of-mass reference frame. In contrast, when utilising the aluminium target, the evolution of the anisotropy factor becomes evident, displaying a noticeable increase and a sharp rise beyond $Z_{FS}/2$. This effect is attributed to the presence of quasi-fission.

Upon obtaining the isotopic yields of fragments generated by the fissioning systems of ^{249}Bk and ^{265}Db, it becomes feasible to derive observables that are highly sensitive to structural effects. The study of nuclear structure effects at high excitation energy is one of the goals of this thesis. These observables encompass nuclear charge-yield distribution, mass-yield distribution, neutron excess, and total neutron evaporation. Furthermore, mass-angle and nuclear-charge-angle distributions, are also evaluated.

A significant portion of the component in quasi-fission is primarily detected by the experimental VAMOS++ setup when using the aluminium target. The experimental fragment mass and charge distributions exhibit an asymmetry around symmetric splits, this is a higher count in the heaviest section compared to the lightest one. This observed asymmetry is populated by the heavy fragments produced in component of quasi-fission. A lower limit for the quasi-fission yield contribution of approximately 9% is obtained by subtracting the yields of two complementary fragments.

The neutron excess, denoted as $\langle N \rangle / Z$, in the ^{265}Db fissioning system shows a nearly linear increase with the fragment atomic number, Z. However, the presence of the quasi-fission process, yielding less deformed and less excited fragments that tend to emit fewer neutrons, consequently resulting in a higher $\langle N \rangle / Z$, introduces an observable effect. In the case of the ^{249}Bk fissioning system, the $\langle N \rangle / Z$ also exhibits a nearly linear growth with the fragment atomic number Z. In the observable $\langle N \rangle / Z$ post-evaporation there appear to be no nuclear structural effects.

USC DE SANTIAGO DE COMPOSTELA

The neutron evaporation data for the ^{265}Db fissioning system reveals an average total neutron emission of approximately $\langle \nu \rangle \approx 10.5 \rightarrow 11.5$ neutrons. The experimental dataset exhibits a

distinctive, arched distribution characterised by reduced evaporation in both lighter and heavier fragments and an elevated evaporation rate from the fragments with atomic numbers in the range of $Z \in [50, 55]$. Aligning with the description of the symmetric *Super Long* fission channel. The neutron evaporation curve attains a local maximum at $Z \approx 54$, however, this maximum is barely distinguishable from the rest of values. In the case of the ^{249}Bk fissioning system, the neutron evaporation data indicates an average total neutron emission of $\langle\nu\rangle \approx 9.5$ neutrons for fragments across the entire range of atomic numbers. The experimental observations display a nearly constant pattern and, taking into account the statistical error bars, small variations are perfectly compatible with fluctuations.

The even-odd staggering is observed in both fissioning systems, with the data fluctuating within a range of $\delta(Z + 1.5) = \pm 0.01$. It has been demonstrated that this range falls within the typical statistical fluctuations of a yield distribution without any even-odd effect. Therefore even-odd staggering in the ^{249}Bk fissioning system is compatible with $\delta(Z + 1.5) = 0$. However, in the case of the ^{265}Db fissioning system, a different trend is observed for $Z > 55$. In this region, the even-odd effect decreases to approximately $\delta(Z + 1.5) = -0.04$. Specifically, this region corresponds to measurements of quasi-fission for heavy fragments suggesting that quasi-fission reactions are the source of the observed $\delta(Z + 1.5)$.
The $\delta(Z + 1.5) \sim 30\%$ values exceeding the typical effect in low-energy fission by an order of magnitude [106]. The negative odd-even effect in quasi-fission is related to the dynamics of equilibration processes in quantum systems and their interplay with dissipation and fluctuation in nuclear collisions (see [113] and references therein). This suggests a low dissipation through pair breaking (dissipation through transference of pairs would still exist). The experimentally observed negative even-odd effect in quasi-fission implies directly that the unpaired proton from aluminium moves to uranium and has a very high probability of remaining there. Moreover, the $\delta(Z + 1.5) \sim 30\%$ is consistent with no breaking of proton pairs and the flow of protons from uranium to aluminium occurring in pairs [114].

Measurements of fragment velocities and angles in the laboratory frame enable the isotopic reconstruction of the fission fragment centre-of-mass velocity. The evaluation of the average velocity $\langle V\rangle$ for each fragment Z is accomplished by employing the isotopic velocities in the centre-of-mass reference frame and the isotopic yields. A consistent trend is observed in both fissioning systems, where the average velocity decreases as the fragment Z increases. In the case of the ^{265}Db fissioning system, the average velocities are approximately 0.1 cm/ns higher than those in the case of ^{249}Bk. This difference is due to the stronger Coulomb repulsion between the fragments, given the higher Z of ^{265}Db. Within the same fissioning system, the experimental data adheres to a linear pattern with a distinct slope for higher values of $Z > 55$. This divergence may be linked to quasi-fission. In the ^{249}Bk fissioning system a linear trend is shown. No noticeable structural effects are observed in either of the two fissioning systems. This outcome agrees with the results of the high-excitation-energy ^{250}Cf fissioning system [108].

In this study, kinematic properties of fission fragments were utilised to derive information concerning the scission point in ^{249}Bk. The neutron excess at scission exhibits a gradual and smooth relationship with the fragment atomic number Z. However, the trend is significantly modified by neutron evaporation. The fragments observed post-neutron evaporation maintain a relatively stable neutron excess, with smooth observable *charge polarisation*. For heavy fragments with $Z > 50$, the neutron excess at scission stabilises at approximately 1.55. The experimental data display an *S-shaped* pattern, resulting in heavier fragments being slightly

more neutron-rich. Minor variations in this *S-shaped* trend are discernible but compatible with fluctuations. However, the potential influence of the octupolar-deformed shell $Z = 56$ formed with the octupolar-deformed shell $N = 88$ at these high excitation energies may persist.

The excitation energy of the fissioning system and that gained in the process is released post-scission through the emission of neutrons in the ^{249}Bk fissioning system, an emission that correlates with the fragment atomic number Z. The neutron multiplicity shows a consistent increase with fragment Z. The variations of the tend are compatible with fluctuations but a small bulge in the multiplicity around $Z \approx 36$ may be related with the *SA* fission channel. This would imply that, the neutron multiplicity data indicates a slightly higher excitation energy in the *SA* fission channel, which could indicate a higher deformation and/or higher dissipation.

The evaluation of the post-scission neutron multiplicities $\langle \nu_{1+2} \rangle$ and the total neutron multiplicities $\langle \nu_{total} \rangle$ for the fission fragments of the ^{249}Bk fissioning system at $E^*_{FS} = 47.7$ MeV is conducted. The behaviour of neutron multiplicities as a function of fragment Z is nearly flat with small fluctuations. This behaviour is not as expected, as indicated by the comparison with GEF calculations. However, at these high energies, the experimental data agree with the behaviour observed in ^{250}Cf fissioning system [108].

The evaluation of the Total Kinetic Energy at scission $\langle TKE^* \rangle$ in the ^{249}Bk fissioning system reveals an almost uniform pattern observed in the vicinity of symmetric fission splits (between $Z \approx 44$ and $Z \approx 53$). No signal of compact configuration due to $Z = 50$ is observed. Actually, this is expected at this high excitation energies and this is agree with GEF calculations. This suggests a diminished structural impact in this region. Peaks are discerned around $Z \approx 44$ and $Z \approx 53$, where the values of $\langle TKE^* \rangle$ are roughly 2 MeV higher than in the symmetric case, indicating more compact configurations. These peaks are typically attributed to a *SI* fission channel with the deformed proton shell $Z \approx 52$.

The determination of $\langle TKE^* \rangle$ allows for the assessment of the fraction of total energy converted into excitation energy of the fragments. The evaluation of $\langle Q_{g.s} \rangle$, $\langle TKE^* \rangle$, and $\langle TXE^*_{g.s} \rangle$ for each fragment atomic charge Z in the context of the fission of the ^{249}Bk fissioning system is conducted. The results indicate a similarity in the behaviour of $\langle Q_{g.s} \rangle$ and $\langle TKE^* \rangle$, notably featuring a relatively flat region within the central symmetric range of $Z \in [45, 53]$. In the case of $\langle TXE^*_{g.s} \rangle$, there is a prominent peak centred at symmetric splits, spanning from approximately $\approx$ 36 MeV to $\approx$ 50 MeV. In the realm of high-energy fusion-induced fission of ^{249}Bk, significant variations in $\langle TXE^*_{g.s} \rangle$ become evident. A notable 15 MeV difference in excitation energy is observed between symmetric and highly asymmetric splits.

In summary, this study contributes novel experimental insights into the distribution of fission fragments within neutron-rich actinides. It offers fresh experimental data on the fission fragment distribution within the super-heavy fissioning systems of ^{265}Db and ^{249}Bk. Structural effects have been detected in various observables for high-excitation-energy fission in the ^{249}Bk fissioning system. Additionally, this research has investigated and documented the competition between fusion-fission and quasi-fission mechanisms in the case of the ^{265}Db fissioning system. Lastly, the experimental data have been compared with the semi-empirical GEF model and with prior measurements.

USC
UNIVERSIDADE
DE SANTIAGO
DE COMPOSTELA

USC
UNIVERSIDADE
DE SANTIAGO
DE COMPOSTELA

Resumo

R.1 Limiar

A fisión nuclear, cuxo descubrimento data de 1939 grazas aos traballos de Meitner e Frisch, revelouse como un proceso altamente complexo que involucra unha serie de factores interrelacionados. Caracterízase por deformacións extremas no sistema fisionante, influencia de efectos de estrutura nuclear e fluxos de calor que determinan as propiedades das distribucións de fragmentos resultantes. Con todo, a pesar de máis de sete décadas de investigación intensiva no campo da fisión, esta aínda non se comprende completamente e a súa descripción, tanto teórica como experimental, segue sendo parcial. Dende o seu descubrimento, a fisión foi percibida como un proceso complexo onde diferentes propiedades nucleares interactúan e moldean as características das distribucións de fragmentos de fisión. Este proceso implica unha deformación extrema do sistema fisionante por mor dos movementos colectivos dos nucleóns, ao mesmo tempo que a identidade dos fragmentos se ve fortemente influenciada polos efectos de estrutura das capas nucleares. Por unha banda, a fisión nuclear a baixas enerxías de excitación representa un fenómeno nuclear que involucra tanto aspectos macroscópicos como microscópicos da estrutura nuclear. As deformacións alcanzadas polos núcleos no punto de escisión orixínanse en movementos colectivos dos nucleóns, mentres que as distribucións de fragmentos de fisión observadas non se poden explicar sen considerar o efecto da estrutura de capas dos niveis de enerxía. Doutra banda, esperaríase que a influencia dos efectos de capa diminuíse co aumento da enerxía de excitación do núcleo fisionante. Con todo, en experimentos recentes observáronse características relacionadas cos efectos de capa que persisten a altas enerxías de excitación.

Os datos experimentais en relación coas distribucións de fragmentos de fisión revelaron que o proceso de fisión de actínidos é altamente asimétrico, producindo un fragmento pesado cunha masa media constante de contorna $A \approx 140$, independentemente do sistema fisionante, e un fragmento lixeiro que completa a masa total do sistema fisionante. Os modelos teóricos que incorporan efectos de estrutura nuclear relacionan a estabilización do fragmento pesado co salto en enerxía da capa esférica $N = 82$ e a capa deformada en $N \approx 88$. Con todo, ata a última década, non se tiña acceso a información experimental detallada sobre a distribución de protóns e neutróns entre os fragmentos.

As distribucións de fragmentos de fisión desempeñan un papel crucial na modelización da fisión nuclear. Porén, acceder a estes observables foi unha tarefa desafiante ata hai pouco, xa que os datos se limitában principalmente á información de masas, onde as contribucións de protóns e neutróns entrelazábanse, dificultando a súa interpretación completa. A fisión inducida por fusión en cinemática inversa xurdiu como unha ferramenta poderosa na investigación da fisión nuclear. Este enfoque permite a identificación isotópica completa dos fragmentos de fisión, superando as limitacións inherentes ao método cinemático directo, o cal proporciona soamente información parcial. Con todo, a análise destes observables experimentais enfronta dous desafíos principais: a obtención simultánea de datos nun único experimento e a escaseza, en ocasións a ausencia, de medicións do número atómico dos fragmentos. O uso da cinemática inversa no estudo da

fisión, pioneiro por Schmidt *et al.* en GSI, presenta unha solución a estes problemas. A diferenza da cinemática directa, onde se acelera un feixe lixeiro e faise incidir sobre un albo pesado, na cinemática inversa, acelérase o núcleo pesado. Este enfoque permite que os fragmentos de fisión alcancen maiores velocidades, o que facilita a medición directa da seu número atómico. Na primeira implementación experimental desta técnica, Schmidt *et al.* observaron un valor medio constante de Z no fragmento pesado en máis de 20 sistemas fisionantes diferentes, o que suxire a importancia dos protóns no proceso de fisión. Na actualidade, dúas campañas experimentais complementarias baséanse na cinemática inversa e utilizan espectrómetros magnéticos para medir simultáneamente masa e número atómico dos fragmentos de fisión. Unha delas, SOFIA (Studies On Fission with Aladin) no Centro GSI Helmholtz para a investigación de iones pesados, de Darmstadt en Alemaña, enfócase no estudo da fisión inducida por interacción Coulombiana en sistemas coa deficiencia de neutróns. A outra, campaña de fisión co IMOS++ (Variable Mode Spectrometer) en GANIL (Grand Accélérateur National d'Ions Lourds) emprazado en Caen no norte de Francia, dedícase ao estudo de sistemas ricos en neutróns en torno ao ^{238}U, xerados mediante reaccións de fusión e transferencia de nucleóns.

Este traballo de tese forma parte de campaña de fisión co IMOS++ en GANIL, a cal utiliza reaccións de transferencia de nucleóns para investigar a evolución dos observables de fisión en función da enerxía de excitación do sistema fisionante. Ademáis da súa contribución ao estudo da fisión en si mesma, esta investigación abre oportunidades para a produción de núcleos ricos en neutróns, un tema de gran relevancia na física nuclear actual. Isto permite a análise da evolución da estrutura de capas en núcleos situados lonxe da estabilidade. Os procesos de fisión estudados nesta tese xeran fragmentos ricos en neutróns no rango de $Z = 30$ a $Z = 70$, o que amplía significativamente as posibilidades de investigar diversos núcleos neste rango.

Esta tese presenta un estudo exhaustivo da fisión inducida polo mecanismo de fusión nos sistemas fisionantes ^{265}Db e ^{249}Bk, ambos os dous xerados con alta enerxías de excitación, $E^*_{FS} = 61.2$ MeV e $E^*_{FS} = 47.7$ MeV, respectivamente. No primeiro caso, tamén se investiga a competencia coa fisión inducida por fusión, coa xeración de fragmentos de fisión a través do mecanismo de quasi-fisión. Os datos experimentais obtivéronse en GANIL mediante o bombardeo dun feixe de ^{238}U a 5.88A MeV contra un albo de ^{27}Al e un albo de ^{nat}B, respectivamente, para xerar os sistemas fisionantes. Como xa se explicou, a técnica de cinemática inversa e as capacidades do espectrómetro IMOS++ permitiron a identificación isotópica completa dos fragmentos de fisión. A información sobre os números atómicos e de masa de ambos os fragmentos é crucial para obter observables sensibles para os efectos de estrutura, como a distribución de carga nuclear, a distribución de masa, o exceso de neutróns e a evaporación total de neutróns.

No caso do albo de ^{27}Al, derívanse matrices de correlación importantes, como as distribucións de masa-ángulo e carga nuclear-ángulo, que proporcionan indicios sobre a contribución de procesos dinámicos, como o mecanismo de quasi-fisión. As distribucións de carga nuclear e masa mostran unha forma similar a unha distribución gaussiana, típica dun proceso de fisión impulsado únicamente polas propiedades da pinga líquida. Obsérvase unha sobreprodución no lado de fragmentos pesados, que non se compensa no lado dos fragmentos lixeiros, e atribúese á quasi-fisión. Tamén se realizou unha comparación dos resultados experimentais do exceso de neutróns e a evaporación total de neutróns coas predicións do código de simulación GEF (A General Description of Fission Observables).

No caso do albo de ^{nat}B, realízase un estudo exhaustivo da fisión do sistema fisionante xerado,

dende as distribucións de carga nuclear e masa ata a dinámica de alta enerxía da fisión. Isto permite avaliar observables indirectos de grande importancia para o estudo dos efectos de estrutura nuclear, como a enerxía cinética total promediada antes da evaporación de neutróns, $\langle TKE^{*}\rangle$. Nas seccións seguintes, despois da descripción da montaxe experimental, preséntanse algúns dos resultados obtidos nesta tese doutoral de investigación.

R.2 Obxectivos

Os principais obxectivos desta tese son obter observables físicos relevantes, calcular os rendementos isotópicos dos fragmentos de fisión e avaliar as velocidades dos fragmentos de fisión para os sistemas de fisión, ^{265}Db e ^{249}Bk, producidos a altas enerxías de excitación. Ao cumprir estes obxectivos, este traballo pretende:

- Avaliar o papel da dinámica nas reaccións de fisión de alta enerxía e de quasi-fisión.
- Analisar o papel da quasi-fisión e a súa competencia coas reaccións de fusión-fisión.
- Caracterizar o punto de escisión (punto de separación nuclear).
- Comprender o papel da estrutura nuclear no proceso de fisión.

Experimentalmente, evidénciase que a estrutura nuclear deixa a súa pegada en varios observables da fisión. Aplicouse unha metodoloxía para estudar estes sistemas e esperase obter información valiosa sobre a dinámica de fisión e a influencia da estrutura nuclear. A comparación coa fisión de baixa enerxía e o estudo de reaccións de fusión-fisión permiten entender mellor estes fenómenos, incluíndo os efectos da quasi-fisión, que aínda non foron completamente comprendidos.

R.3 Dispositivo experimental

O experimento levouse a cabo nas instalacións de GANIL, onde un feixe de ións de ^{238}U se aceleróu ata alcanzar unha enerxía de 5.88A MeV e dirixiuse á área experimental G1. O feixe incidente impactóu en dous albos distintos: un composto por ^{27}Al cun espesor de 200 μg/cm^2 e outro constituído por ^{nat}B cun espesor de 100 μg/cm^2. Estes albos deron lugar a unha variedade de reaccións, incluíndo fusións nucleares, transferencia de nucleóns e dispersión. No caso de que se desencadease algunha destas reaccións, o produto resultante, se a súa enerxía de excitación o permitía, podía experimentar fisión. Un aspecto relevante deste experimento é o uso da cinemática inversa. Debido a esta configuración, os dous fragmentos resultantes da fisión emitíronse cara adiante dentro dun cono cun ángulo de dispersión de 25°. Mentres tanto, o núcleo lixeiro de retroceso da reacción primaria, xa sexa de transferencia ou dispersión, emitiuse típicamente con ángulos maiores. Este núcleo de retroceso detectouse mediante un dispositivo de detección de dobre silicio coñecido como SPIDER, que consiste en dous cristais de silicio anulares. SPIDER mide a pérdida de enerxía e a enerxía residual dos núcleos lixeiros de retroceso a medida que atravesan o primeiro cristal e detéñense no segundo. Estas dúas variables permiten unha identificación isotópica precisa dos núcleos de retroceso. Ademáis, a segmentación angular do detector proporciona medicións dos ángulos polar e azimutal. Estas medidas permiten a reconstrucción da reacción binaria primaria e a determinación da energía de excitación transferida ao sistema fisionante.

Os dous produtos da fisión atravesan SPIDER por un buraco central que evita a interacción dos fragmentos co detector. Un dos fragmentos dispara o detector que dá o *Start*, unha chámase multi-fíos que proporciona a referencia de tempo, e é desviado no campo magnético do dipolo do espectrómetro IMOS++ antes de ser detectado no dispositivo experimental colocado á saída no plano focal. O percorrido nominal dos fragmentos entre o albo e o plano focal é de 7.6 m, con variacións de ±0.35 m en función da rixidez magnética e o ángulo de emisión do fragmento. O dispositivo experimental colocado no plano focal de IMOS++ permite a identificación dos fragmentos de fisión en masa, carga nuclear e estado de carga. Este conxunto de detectores está composto por: unha caixa multi-fíos, que proporciona unha medida do tempo de voo dos fragmentos; dous caixas de deriva, que miden a posición e o ángulo dos fragmentos despois do espectrómetro; unha caixa de ionización, que mide a pérdida de energía dos fragmentos; e un muro de detectores de silicio, onde os fragmentos se páran e se míde a súa enerxía residual.

Nun espectrómetro magnético as partículas cargadas desvíanse en función da súa rixidez magnética, que é unha traza de cada fragmento que relaciona o seu momento co seu estado de carga. Polo tanto, a rixidez magnética, así como o ángulo de emisión e o espazo percorrido polos fragmentos entre o albo e o plano focal, reconstrúense evento a evento a través da posición e ángulo dos fragmentos medidos no plano focal, despois de ser desviados. A rixidez magnética proporciona unha medida conxunta, con alta resolución, da masa e o estado de carga de cada fragmento cuxas contribucións se separan a través dunha medida da masa alternativa, de baixa resolución, obtida da energía e velocidade dos fragmentos. Finalmente, a identificación en carga nuclear obtense directamente da pérdida de energía combinada coa enerxía residual.

As reaccións de fusión e transferencia introducen enerxía de excitación no sistema que promociona o núcleo composto e/ou o núcleo de retroceso a estados excitados. Os fragmentos de fisión tamén adquiren enerxía de excitación durante o proceso de fisión. En ambos casos estes estados excitados poden decaer a través da emisión de gammas, detectados por AGATA, un detector composto por cristais de xermanio, que rodean ao albo proporcionando unha verificación na identificación dos fragmentos de fisión.

A gran variedade de núcleos producidos no proceso de fisión fai que o espazo de fases de fragmentos en rixidez magnética e ángulo non se poida cubrir na súa totalidade coa cobertura angular e en momento do espectrómetro. Co fin de aumentar esta cobertura empregáronse dúas configuracións angulares 14° e 21.5° con rixidez magnética de 1.24 Tm e 1.1 Tm, respectivamente.

R.4 Análise de datos

A identificación isotópica dos fragmentos de fisión permite calcular os yields de fisión para os dous sistemas fisionantes estudados neste traballo de invetsigación. As reaccións de fusión producen o sistema ^{249}Bk e ^{265}Db con enerxías de excitación ben determinadas $E^*_{FS} = 47.7$ MeV e $E^*_{FS} = 61.2$ MeV respectivamente. Os yields isotópicos de fisión $E(Z, A)$ calcúlanse en base ao número de eventos rexistrados $N(Z, A)$, corrixido pola aceptancia e a eficiencia.

$$Y(Z,A) = 200 \cdot \frac{N(Z,A)}{\mathcal{A}_g^{FF} \cdot \mathcal{E}_i^{FF}} \cdot \left(\sum_{Z,A} \frac{N(Z,A)}{\mathcal{A}_g^{FF} \cdot \mathcal{E}_i^{FF}} \right)^{-1} \tag{R.1}$$

onde $\mathcal{A}_g^{FF}$ é a aceptancia xeométrica e $\mathcal{E}_i^{FF}$ é a eficiencia intrínseca dos detectores empregados no experimento.

Os dous settings empregados $(14°, 21.5°)$ co espectrómetro IMOS++ cobren diferentes rangos en ángulo e rixidez magnética, por tanto cada configuración necesita ser normalizada pola intensidade de feixe co fin de contribuír co mesmo peso ao cálculo dos yields de fisión. Isto conséguese normalizando o número de eventos rexistrados dun settings ao outro, corrixindo pola aceptancia xeométrica.

Finalmente, o número de contas computable para o cálculo dos yields istópicos de fisión $N(Z, A)$ calcúlase como a integral da distribución de eventos en $\cos(\theta_{CM}^{FF})$ no rango na que a distribución de estados de carga se transmíte completamente:

$$N(Z,A) = \int_{-1}^{+1} \frac{dN(Z,A)}{d(\cos(\theta_{CM}^{FF}))} \cdot d(\cos(\theta_{CM}^{FF})) \tag{R.2}$$

O número de eventos de fisión por unidade de $\cos(\theta_{FF}^{deCM})$ dun isótopo específico é calculado sumando as distribucións de estados de carga diferentes:

$$\frac{dN(Z,A)}{d(\cos(\theta_{CM}^{FF}))} = \sum_{q_{min}(A)}^{q_{max}(A)} \frac{dN(Z,A,q)}{d(\cos(\theta_{CM}^{FF}))} \tag{R.3}$$

onde canda estado de carga recibe unha contribución por parte dos dous settings $(14°, 21.5°)$ do espectrómetro, as cales presentan certa superposición na rexión común de $\cos(\theta_{CM}^{FF})$, polo que o número de eventos por unidade de $\cos(\theta_{CM}^{FF})$ de cada estado de carga se tóma como a maior das contribucións.

Os yields de número de masa $E(A)$ e os yields elementais ou de número atómico $E(Z)$, derívanse directamente dos isotópicos como:

$$Y(A) = \sum_{Z} Y(Z,A) \tag{R.4}$$

$$Y(Z) = \sum_{A} Y(Z,A) \tag{R.5}$$

Os dous sistemas fisionantes estudados neste traballo deben traballarse en paralelo, debido ás súas diferenzas e semellanzas e a que os datos dun serven para estimar os do outro. Debido a que no ^{265}Db se pode avaliar a contaminación e no ^{249}Bk non se póde de forma directa e debido a que no ^{265}Db a súa anisotropía e a quasi-fisión presente non permite estimar a eficiencia de forma correcta, aplicándose a do ^{249}Bk corrixida pola velocidade do sistema fisionante, implicando que o número de contas debe ser avaliado na rexión común angular entre límites en $\cos(\theta_{CM}^{FF})$ para todas as masas dos fragmentos posibles. Deste xeito pódese comparar e traballar cunha rexión que non favoreza zonas pola anisotropía atopada.

R.5 Discusión de resultados

Neste traballo estúdase a fisión de actínidos ricos en neutróns. Os sistemas fisionantes ^{265}Db e ^{249}Bk son producidos a través de reaccións de fusión e transferencia de nucleóns, baixo cinemática inversa, cun feixe de ^{238}U a 5.88A MeV incidindo sobre albos de ^{27}Al e ^{nat}B, respectivamente. Os yields de fisión destes sistemas mostran unha forte contribución da compoñente simétrica

de fisión en ambos os dous sistemas fisionantes a alta enerxía de excitación, $E^*_{FS} = 61.2$ MeV e $E^*_{FS} = 47.7$ MeV respectivamente, centradas en $Z_{FS}/2$. Ambos sistemas fisionantes mostran certa contribución da fisión asimétrica. O estudo das canles de fisión en termos do número atómico dos fragmentos de fisión de ^{249}Bk, mostra a fisión asimétrica descrita maioritariamente por dúas canles, *SE* e *SII*, con posicións fixas en $Z_{SE} \approx 53.5$ e en $Z_{SII} \approx 57.2$, e mostra tamén unha compoñente super-asimétrica *SA* cunha porcentaxe $\approx 3.4\%$ non desprezable en $Z_{SA} \approx 61.7$. No caso do sistema fisionante ^{265}Db, o estudo das canles de fisión en termos do número atómico fíxose tendo en conta a compoñente de quasi-fisión medida, as canles de fisión asimétricos teñen posicións fixas en $Z_{SII} \approx 63.2$ e en $Z_{SA} \approx 67.2$ cunha canle *SE* absorbida pola canle simétrica que ten unha porcentaxe de yield de $\approx 90\%$.

O exceso de neutróns mostra unha clara polarización de carga, cun fragmento pesado mais rico en neutróns que o lixeiro. No caso do sistema fisionante ^{249}Bk o exceso de neutróns mostra un comportamento case lineal crecente de fragmento lixeiro a fragmento mais pesado. Aparecen efectos de estrutura en $Z \approx 36$ e $Z \approx 56$ relacionados coas capas nucleares deformadas de fisión asimétrica. No caso do sistema fisionante ^{265}Db tamén se ten un comportamento lineal crecente e non se aprecian efectos de estrutura de forma clara, a altas enerxías de excitación é o esperable.

A evaporación de neutróns crece coa enerxía de excitación do sistema fisionante E^*_{FS}. No caso do sistema fisionante ^{249}Bk a media de evaporación de neutróns está en ≈ 9.5 por fragmento de fisión, algo esperable a altas enerxías de excitación. Obsérvanse efectos de estrutura apreciables en $Z \approx 53$, $Z \approx 41$ e $Z \approx 56$ relacionada coa capa deformada de $N \approx 88$. Estas capas poden entenderse coas relacións das canles de fisión asimétricos e a canle super-asimétrica. No caso do sistema fisionante ^{265}Db a evaporación de neutróns ten unha forma de campá cun máximo de emisón de ≈ 11.5 na parte central na simetría e uns mínimos cun neutron emitido de diferenza nas colas. Esta forma suxire unha gran deformación no punto de escisión que encaixa coa canle de fisión simétrico *SL*. Hai que ter en conta que a evaporación de neutróns no caso da quasi-fisión permanece descoñecida e que este resultado debe ser interpretado con coidado.

O efecto par-impar dos sistemas fisionantes deste traballo ^{249}Bk e ^{265}Db con $Z_{FS} = 97$ e $Z_{FS} = 105$ ambos os impares mostran comportamentos moi parecidos oscilantes en cero. É dicir, en ambos casos pódese afirmar que non teñen un efecto par-impar. Con todo, en fragmentos pesados para o caso do sistema ^{265}Db hai unha tendencia negativa. Esta tendencia dáse onde a compoñente de quasi-fisión pesada cobra relevancia. Claramente, o efecto par-impar da quasi-fisión está a afectar ás oscilacións esperables entorno a cero da fisión de alta enerxía de excitación. Oscilacións que se ven no outro sistema fisionate e que non teñen mecanismo de quasi-fisión presente.

A dinámica de fisión de alta enerxía presentada neste traballo de investigación comeza co cálculo e avaliación das velocidades en centro de masas dos fragmentos de fisión dos sistemas fisionantes ^{249}Bk e ^{265}Db. Estas velocidades mostran o esperable que é a diminución lineal co aumento da masa dos fragmentos en ambos sistemas. A velocidade media pesada cos yields obtidos mostra esta linealidade. Non se aprecian cambios pola estrutura nuclear nin tampouco se ven efectos do mecanismo de quasi-fisión no caso do estudo dos fragmentos co albo de ^{27}Al. Coa dinámica de fisión pódese caracterizar o punto de escisión, algo de suma importancia que se fai na derradeira parte do traballo presentado. Hai que destacar que unicamente é posible avalialo no caso do ^{249}Bk debido ao mecanismo de quasi-fisión que afecta os resultados obtidos ao non poder acceder á parte simétrica lixeira da compoñente medida de quasi-fisión.

En conclusión, este estudo contribuíu con nova información experimental acerca da distribución de fragmentos en procesos de fisión de actínidos ricos en neutróns. Observáronse efectos de estrutura nuclear en diversos observables relacionados coa fisión a alta enerxía. Sorprendentemente, constatouse que estes efectos persisten mesmo ás elevadas enerxías de excitación estudadas, desafiando as expectativas previas do seu desmaio. Ademais, algunhas das observacións realizadas foron corroboradas mediante comparacións con datos experimentais previos. Así mesmo, levouse a cabo unha comparación entre os resultados experimentais e modelos teóricos recentes, como o modelo semiempírico GEF, o que contribuíu á súa validación e mellorou a comprensión xeral dos procesos de fisión.

USC
UNIVERSIDADE DE SANTIAGO DE COMPOSTELA

USC
UNIVERSIDADE
DE SANTIAGO
DE COMPOSTELA

Appendix

A.1 Lorentz Formalism

The Lorentz transformations play a crucial role in establishing the correlation between observables in the centre-of-mass reference frame (CM) and the laboratory system (LAB) (see Fig. A.1). In the context of a fission reaction, the centre-of-mass reference frame corresponds to the frame of the fissioning system.

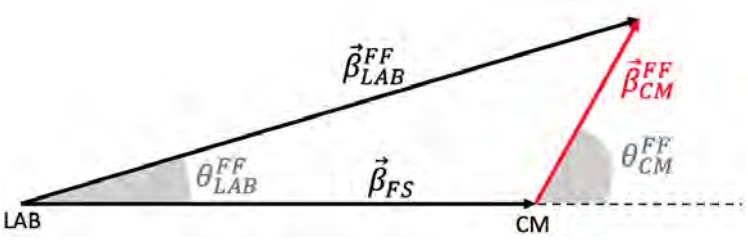

Figure A.1: *The relationship between the centre-of-mass of the fissioning system (CM) and the laboratory reference frame (LAB) is depicted in a schematic view. The transformation from the laboratory reference frame, where the fissioning system is in motion with a velocity of $\vec{\beta}_{FS}$ and a fission fragment is emitted in flight with a velocity of $\vec{\beta}^{FF}_{LAB}$, to the centre-of-mass reference frame, where the fissioning system is at rest and a fission fragment has a velocity of $\vec{\beta}^{FF}_{CM}$, is illustrated.*

By applying the Lorentz transformation to the measured energy and momentum in the laboratory frame (LAB), it becomes possible to reconstruct the corresponding energy and momentum in the centre-of-mass (CM). This allows for a consistent understanding of the fragment energy and fragment momentum between the two reference frames:

$$\begin{pmatrix} E_{FF} \\ p_{FF_\perp} \\ p_{FF_\parallel} \end{pmatrix}^{CM} = \begin{pmatrix} \gamma_{FS} & 0 & -\beta_{FS}\gamma_{FS} \\ 0 & 1 & 0 \\ -\beta_{FS}\gamma_{FS} & 0 & \gamma_{FS} \end{pmatrix} \cdot \begin{pmatrix} E_{FF} \\ p_{FF_\perp} \\ p_{FF_\parallel} \end{pmatrix}^{LAB} , \tag{A.1}$$

where E_{FF} is the total energy of the fragment, $p_{FF_\perp}$ and $p_{FF_\parallel}$ are the perpendicular and parallel components of the fragment momentum with respect to the direction of the fissioning-system velocity β_{FS} in c units and γ_{FS} is the Lorentz factor of the fissioning system, expressed as:

$$\gamma_{FS} = \frac{1}{\sqrt{1-\beta^2_{FS}}} . \tag{A.2}$$

Consequently, the components of the fragment momentum in the fissioning-system reference frame can be expressed as follows:

$$p^{FF}_{CM_\perp} = p^{FF}_{LAB_\perp} , \tag{A.3}$$

$$p^{FF}_{CM_\parallel} = \gamma_{FS} \cdot (p^{FF}_{LAB_\parallel} + \beta_{FS} E_{LAB}) . \tag{A.4}$$

The expressions for the perpendicular and parallel components of the momentum are introduced as:

$$p_\perp = p \cdot \sin(\theta) , \tag{A.5}$$

USC UNIVERSIDADE DE SANTIAGO DE COMPOSTELA

$$p_{\parallel} = p \cdot \cos(\theta)\,, \tag{A.6}$$

the following equations are derived:

$$p_{CM}^{FF} \sin(\theta_{CM}^{FF}) = p_{LAB}^{FF} \sin(\theta_{LAB}^{FF})\,, \tag{A.7}$$

$$p_{CM}^{FF} \cos(\theta_{CM}^{FF}) = \gamma_{FS} \cdot (p_{LAB} \cos(\theta_{LAB}^{FF}) + \beta_{FS} E_{LAB})\,, \tag{A.8}$$

where θ_{CM}^{FF} represents the polar angle of the fragment in the centre-of-mass frame and θ_{LAB}^{FF} corresponds to the fragment polar angle measured in the laboratory frame relative to the direction of the beam. Dividing both equations, the tangent of the fission-fragment angle in the centre-of-mass reference frame is obtained as:

$$\tan(\theta_{CM}^{FF}) = \frac{\sin(\theta_{LAB}^{FF})}{\gamma_{FS} \cdot (\cos(\theta_{LAB}^{FF}) - v_{FS}/v_{LAB}^{FF})}\,. \tag{A.9}$$

The determination of the fission-fragment velocity in the centre-of-mass frame v_{CM}^{FF} is achieved by the following expression:

$$v_{CM}^{FF} = \sqrt{(v_{CM}^{FF,x})^2 + (v_{CM}^{FF,y})^2 + (v_{CM}^{FF,z})^2}\,, \tag{A.10}$$

where the components of the fission fragment centre-of-mass velocity along the three Cartesian axes, denoted as $v_{CM}^{FF,x}$, $v_{CM}^{FF,y}$, and $v_{CM}^{FF,z}$, are defined as follows:

$$v_{CM}^{FF,x} = v_{LAB}^{FF,x} = v_{LAB}^{FF} \cdot \sin(\theta_{LAB}^{FF}) \cdot \cos(\phi_{LAB}^{FF})\,, \tag{A.11}$$

$$v_{CM}^{FF,y} = v_{LAB}^{FF,y} = v_{LAB}^{FF} \cdot \sin(\theta_{LAB}^{FF}) \cdot \sin(\phi_{LAB}^{FF})\,, \tag{A.12}$$

$$v_{CM}^{FF,z} = \frac{v_{LAB}^{FF,z} - v_{FS}}{1 - \frac{v_{FS}}{c^2} \cdot v_{LAB}^{FF,z}} = \frac{v_{LAB}^{FF} \cdot \cos(\theta_{LAB}^{FF}) - v_{FS}}{1 - \frac{v_{FS}}{c^2} \cdot v_{LAB}^{FF} \cos(\theta_{LAB}^{FF})}\,. \tag{A.13}$$

The components of the fission fragment velocity in the laboratory system, denoted as $v_{LAB}^{FF,x,y,z}$, and the azimuthal angle of the fragment ϕ_{LAB}^{FF} are involved in the expression.

USC
UNIVERSIDADE DE SANTIAGO DE COMPOSTELA

A.2 Legendre polynomials

In this work, the angular distribution of fission fragments, denoted as $W(\theta)$ (see Section 5.4), is expressed using a series of Legendre polynomials $P(\cos\theta)$. This appendix provides an overview of Legendre polynomials and some of their properties. The objective is to offer a quick reference to these polynomials and justify their suitability in this context. However, a comprehensive demonstration of their mathematical properties or the theorems mentioned here is beyond the scope of this work. Legendre polynomials find applications in various physics problems characterised by spherical symmetry. One notable instance is their role in the separation of variables within the Schrödinger wave equation for central force fields:

$$-\frac{\hbar^2}{2\mu}\nabla^2\Psi + V(r,s)\Psi = E\Psi\,, \tag{A.14}$$

In this context, the angular dependence is solely determined by the Laplacian operator. Therefore, the eigenvalue equation presented below must be fulfilled:

$$\left[\frac{1}{\sin(\theta)}\frac{\partial}{\partial\theta}\left(\sin(\theta)\frac{\partial}{\partial\theta}\right) + \frac{1}{\sin^2\theta}\frac{\partial^2}{\partial\phi^2}\right] Y = -\lambda Y\,, \tag{A.15}$$

the normalised solutions for this angular equation manifest as spherical harmonics denoted as $Y(\theta,\phi)$. They are structured as follows:

$$Y_{l,m}(\theta,\phi) = (-1)^m \left[\frac{(2l+1)(l-m)!}{4\pi(l+m)!}\right]^{1/2} e^{im\phi}\, P_l^m(\cos(\theta)\,, \tag{A.16}$$

where l and m represent integers, where $l \geq 0$ and $|m| < l$. The functions $P_{m,l}(\cos\theta)$ denote the associated Legendre polynomials of order m, encompassing the dependency on the polar angle θ. In the specific scenario where there is no reliance on the azimuthal angle ϕ (i.e., $m = 0$), the polynomials $P_{m,l}(\cos\theta)$ simplify to $P_l(\cos\theta)$, identified as Legendre polynomials. These polynomials are solutions of the Legendre equation:

$$\frac{d}{d(\cos\theta)}\left[(1-\cos^2\theta)\frac{dy(\cos(\theta)}{d(\cos\theta)}\right] + \lambda y(cos\theta) = 0\,. \tag{A.17}$$

If $\lambda = n(n+1)$, where n is a non-negative integer, the solutions to the preceding equation correspond to the Legendre polynomials $P_n(\cos\theta)$. These polynomials can be derived using Rodrigues' formula:

$$P_n(\cos\theta) = \frac{1}{2^n n!}\frac{d^n}{d(\cos\theta)^n}\left[(\cos^2\theta - 1)^n\right]\,. \tag{A.18}$$

The Legendre polynomials, denoted by $P_n(x)$, are characterised by the parameter n, which represents the degree of the polynomial. Tab. A.1 presents some of these Legendre polynomials, while Fig. A.2 visually represents them. While a rigorous demonstration is feasible, a preliminary examination of the Legendre polynomials in Tab. A.1 reveals a notable parity property they satisfy:

$$P_n(-\cos\theta) = (-1)^n P_n(\cos\theta)\,. \tag{A.19}$$

This implies that the Legendre polynomials exhibit even or odd parity concerning $(\cos\theta)$ based on whether the degree n of the polynomial is even or odd. The symmetric or antisymmetric nature is evident in Fig. A.2, showcasing separate plots for even and odd-order polynomials. This property

n	Legendre polynomials
0	$P_0(\cos\theta) = 1$
1	$P_1(\cos\theta) = \cos\theta$
2	$P_2(\cos\theta) = \frac{1}{2}(3\cos^2\theta - 1)$
3	$P_3(\cos\theta) = \frac{1}{2}(5\cos^3\theta - 3\cos\theta)$
4	$P_4(\cos\theta) = \frac{1}{8}(35\cos^4\theta - 30\cos^2\theta + 3)$
5	$P_5(\cos\theta) = \frac{1}{8}(63\cos^5\theta - 70\cos^3\theta + 15\cos\theta)$
6	$P_6(\cos\theta) = \frac{1}{16}(231\cos^6\theta - 315\cos^4\theta + 105\cos^2\theta - 5)$

Table A.1: *First Legendre polynomials.*

holds significance in quantum mechanics, particularly concerning central forces, where n serves as a quantum number associated with parity and angular momentum.

Another significant property worthy of mention is the orthogonality of Legendre polynomials. They satisfy the following relationship:

$$\int_{-1}^{+1} P_n(\cos\theta)\, P_m(\cos\theta) = \begin{cases} \frac{2}{2n+1} & \text{if } m = n \\ 0 & \text{if } m \neq n\,. \end{cases} \tag{A.20}$$

The sequence $P_0(\cos\theta)$, $P_1(\cos\theta)$, $P_2(\cos\theta)$, ..., $P_n(\cos\theta)$, ..., constitutes a set of orthogonal polynomials defined within the interval $[-1, +1]$. Furthermore, it can be proven that the Legendre polynomials constitute a comprehensive set. Consequently, any arbitrary function $f(\cos\theta)$ defined over $[-1, +1]$ can be represented through an expansion in a Legendre series:

$$f(\cos\theta) = \sum_{n=0}^{\infty} A_n P_n(\cos\theta)\,. \tag{A.21}$$

This property holds paramount importance for the objectives of the current study. By virtue of this theorem, it becomes feasible to represent any angular distribution $W(\theta)$ of emitted fission fragments through a summation of Legendre polynomials in $\cos\theta$.

The wave equation for a symmetrical top with parallel moments of inertia $J_\parallel$ and perpendicular moments of inertia $J_\perp$ is expressed as:

$$\frac{\hbar^2}{2J_\perp}\left[\frac{1}{\sin(\theta_{CM}^{FF})}\frac{\partial}{\partial\theta_{CM}^{FF}}\left(\sin(\theta_{CM}^{FF})\frac{\partial\psi}{\partial\theta_{CM}^{FF}}\right) + \frac{\left(\cos(\theta_{CM}^{FF})\frac{\partial}{\partial X} - \frac{\partial}{\partial\phi}\right)^2\psi}{\sin^2(\theta_{CM}^{FF})}\right] + \frac{\hbar^2}{2J_\parallel}\frac{\partial^2\psi}{\partial X^2} + E\psi = 0\,, \tag{A.22}$$

the solution to this equation is:

$$\psi = \sqrt{\frac{2J+1}{8\pi^2}}\cdot e^{iM\phi}\cdot e^{iKX}\cdot d^J_{M,K}(\theta_{CM}^{FF})\,. \tag{A.23}$$

The functions $d^J_{M,K}(\theta_{CM}^{FF})$ are independent by the azimuthal angle ϕ around the space-fixed axis and the rotation angle of the top around its symmetry axis. They can be expressed as:

$$d^J_{M,K}(\theta_{CM}^{FF}) = [(J+M)!\,(J-M)!\,(J+K)!\,(J-K)!]^2\cdot$$
$$\cdot\sum_X(-1)^X\frac{\left[\sin(\theta_{CM}^{FF}/2)\right]^{K-M+2X}\left[\cos(\theta_{CM}^{FF}/2)\right]^{2J-K+M-2X}}{(J-K-X)!\,(J+M-X)!\,(X+K-M)!\,X!}\,. \tag{A.24}$$

USC UNIVERSIDADE DE SANTIAGO DE COMPOSTELA

The summation is performed over $X = 0, 1, 2, 3...$, encompassing all terms wherein no negative value is present in any of the quantities within the parentheses in the denominator.

While the wave function remains independent of the moments of inertia of the symmetric spinning top, namely $J_{\parallel}$ and $J_{\perp}$, these parameters determine its level spectrum, characterised by energies:

$$E = \frac{\hbar^2 \left[J(J+1) - K^2\right]}{2J_{\perp}} + \frac{\hbar^2 K^2}{2J_{\parallel}} \,. \tag{A.25}$$

The probability of fission fragments emission from a transition state characterised by quantum numbers J, M, and K at an angle θ_{CM}^{FF} can be expressed as follows:

$$P_{M,K}^{J}(\theta_{CM}^{FF}) = \left[\frac{(2J+1)}{4\pi R^2}\right] |d_{M,K}^{J}(\theta_{CM}^{FF})|^2 2\pi R^2 \sin(\theta_{CM}^{FF})\, d\theta_{CM}^{FF} \,, \tag{A.26}$$

where θ_{CM}^{FF} represents the angle between the space-fixed axis and the symmetry axis of the fissioning system in the centre-of-mass framework. Following the equation above (refer to Eq. A.26), it can be rewritten by grouping terms as:

$$P_{M,K}^{J}(\theta_{CM}^{FF}) = W_{M,K}^{J}(\theta_{CM}^{FF})\, \sin(\theta_{CM}^{FF})\, d\theta_{CM}^{FF} \,, \tag{A.27}$$

where the angular distribution of fission fragments, denoted as $W_{M,K}^{J}(\theta_{CM}^{FF})$, is derived by dividing the probability of emitting fission fragments at an angle θ_{CM}^{FF} (as given in Eq. A.26) by $\sin(\theta_{CM}^{FF})$:

$$W_{M,K}^{J}(\theta_{CM}^{FF}) = \left[\frac{(2J+1)}{2}\right] |d_{M,K}^{J}(\theta_{CM}^{FF})|^2 \,. \tag{A.28}$$

This angular distribution can be represented as a series of Legendre polynomials in terms of $\cos(\theta_{CM}^{FF})$ according to Eq. A.21. The distribution W can be rewritten as:

$$W(\cos(\theta_{CM}^{FF})) = \sum_{L=0}^{L_{max}} A_L P_L(\cos(\theta_{CM}^{FF})) \,. \tag{A.29}$$

The emission of fission fragments exhibits symmetry concerning $\theta = 90°$, where no distinction exists between fragments emitted forward and backwards. This parity characteristic, represented by Eq. A.19, stipulates that only Legendre polynomials of even orders display this particular behaviour, a fact further illustrated in the polar representations in Fig. A.2(c,d).

USC
UNIVERSIDADE DE SANTIAGO DE COMPOSTELA

It is straightforward to confirm that a function constituted solely of the summation of even Legendre polynomials remains even. Hence, any angular distribution of fission fragments, denoted as $W(\theta)$, can be expressed as a summation exclusively involving even-order Legendre polynomials.

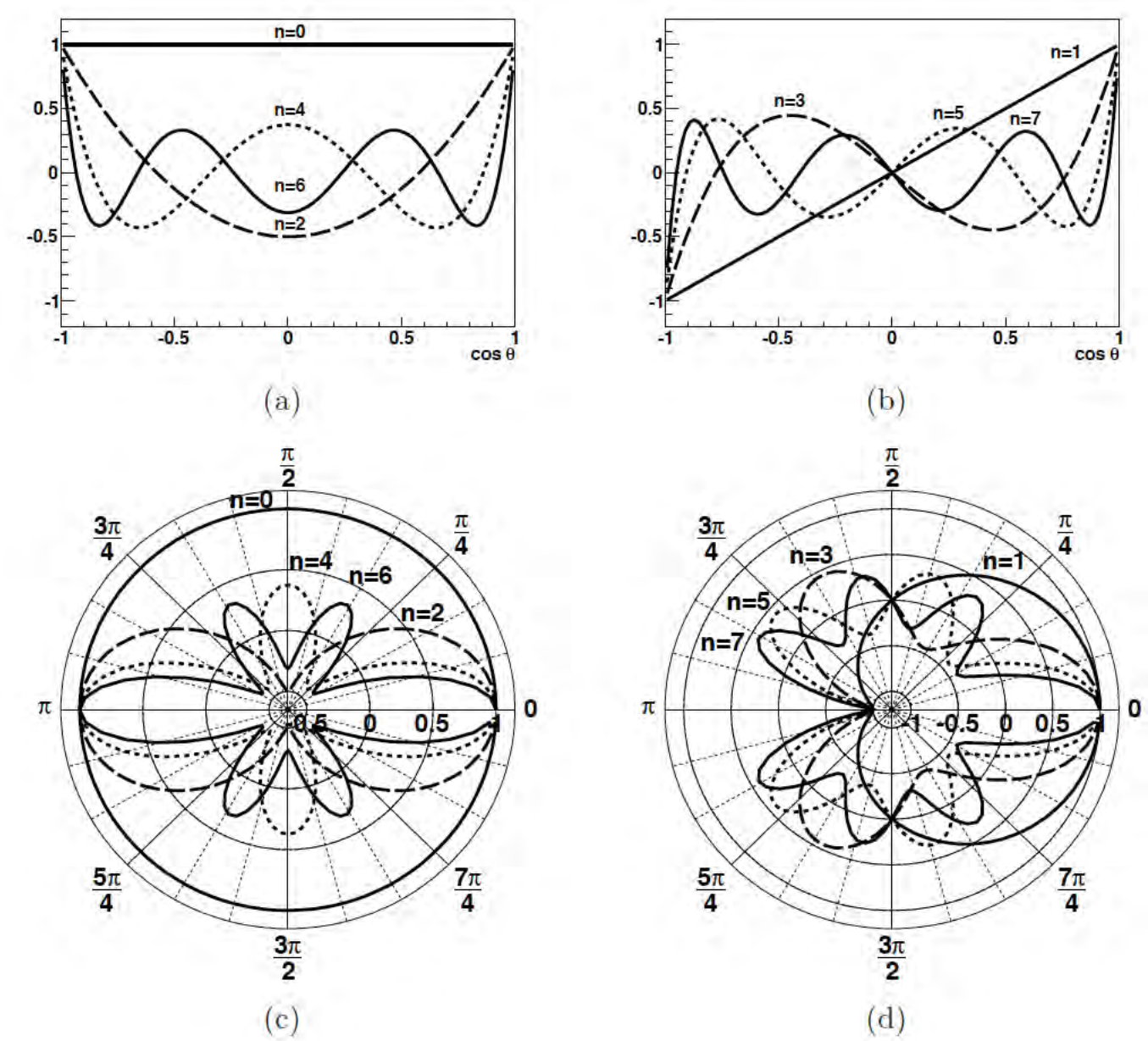

Figure A.2: *Legendre polynomials of even order in panel (a) and odd order in panel (b). Their polar representations are depicted in panel (c) and in panel (d).*

USC UNIVERSIDADE DE SANTIAGO DE COMPOSTELA

A.3 Isotopic Fission Yields

A.3.1 ^{265}Db isotopic fusion-induced fission yields

Table A.2: *^{265}Db isotopic fusion-induced fission yields*

A	Z	Y(Z, A)	Statistical error
78	33	0.0341	0.0015
79	33	0.0794	0.0025
80	33	0.1263	0.0038
81	33	0.1540	0.0041
82	33	0.1208	0.0039
83	33	0.0801	0.0027
84	33	0.0132	0.0011
81	34	0.1391	0.0033
82	34	0.1968	0.0045
83	34	0.2697	0.0050
84	34	0.2185	0.0043
85	34	0.1418	0.0032
86	34	0.0569	0.0027
87	34	0.0370	0.0017
82	35	0.0607	0.0018
83	35	0.1343	0.0030
84	35	0.2376	0.0040
85	35	0.3552	0.0050
86	35	0.3416	0.0050
87	35	0.2678	0.0050
88	35	0.1581	0.0037
89	35	0.0460	0.0023
90	35	0.0143	0.0010
84	36	0.0565	0.0015
85	36	0.1555	0.0029
86	36	0.2858	0.0042
87	36	0.4992	0.0054
88	36	0.4583	0.0055
89	36	0.3619	0.0048
90	36	0.2727	0.0041
91	36	0.1392	0.0025
92	36	0.0486	0.0019
93	36	0.0139	0.0008
86	37	0.0464	0.0014
87	37	0.1186	0.0025
88	37	0.2302	0.0034
89	37	0.4414	0.0045
90	37	0.5714	0.0049
91	37	0.6124	0.0053
92	37	0.4274	0.0044
93	37	0.2677	0.0035
94	37	0.1216	0.0026
95	37	0.0596	0.0016
88	38	0.0433	0.0012
89	38	0.0981	0.0018
90	38	0.2225	0.0027
91	38	0.4315	0.0039
92	38	0.6837	0.0049
93	38	0.8008	0.0051
94	38	0.7405	0.0051
95	38	0.4738	0.0048
96	38	0.2358	0.0031
97	38	0.0835	0.0021
98	38	0.0202	0.0011
91	39	0.0787	0.0014
92	39	0.1771	0.0021
93	39	0.3856	0.0031
94	39	0.6825	0.0043
95	39	0.9018	0.0053
96	39	0.9082	0.0048
97	39	0.7302	0.0047
98	39	0.4489	0.0036
99	39	0.2471	0.0030

Continued on next page

USC UNIVERSIDADE DE SANTIAGO DE COMPOSTELA

Table A.2 – continued from previous page

A	Z	Y(Z, A)	Statistical error
100	39	0.1123	0.0018
101	39	0.0448	0.0010
93	40	0.0463	0.0011
94	40	0.1364	0.0020
95	40	0.3029	0.0031
96	40	0.6198	0.0046
97	40	0.9900	0.0060
98	40	1.1712	0.0068
99	40	1.0361	0.0069
100	40	0.8949	0.0067
101	40	0.4459	0.0052
102	40	0.2127	0.0038
103	40	0.0952	0.0022
104	40	0.0183	0.0011
95	41	0.0382	0.0008
96	41	0.0893	0.0012
97	41	0.2386	0.0020
98	41	0.4993	0.0029
99	41	0.9393	0.0040
100	41	1.1285	0.0048
101	41	1.4757	0.0057
102	41	1.1202	0.0050
103	41	0.7934	0.0046
104	41	0.3455	0.0030
105	41	0.1520	0.0020
106	41	0.0210	0.0010
98	42	0.0754	0.0010
99	42	0.1962	0.0017
100	42	0.4345	0.0027
101	42	0.6881	0.0035
102	42	1.3856	0.0048
103	42	1.6179	0.0055
104	42	1.5884	0.0054
105	42	1.0396	0.0045
106	42	0.5915	0.0036
107	42	0.2466	0.0023
108	42	0.1240	0.0015
109	42	0.0298	0.0008
100	43	0.0491	0.0008
101	43	0.1245	0.0014
102	43	0.2903	0.0020
103	43	0.6350	0.0031
104	43	1.1154	0.0041
105	43	1.6267	0.0049
106	43	1.7411	0.0052
107	43	1.5165	0.0050
108	43	0.8853	0.0040
109	43	0.5602	0.0031
110	43	0.1890	0.0018
111	43	0.0791	0.0012
112	43	0.0147	0.0006
102	44	0.0405	0.0006
103	44	0.1160	0.0012
104	44	0.2604	0.0018
105	44	0.4374	0.0023
106	44	1.0458	0.0038
107	44	1.4995	0.0046
108	44	1.9284	0.0054
109	44	1.7421	0.0051
110	44	1.3067	0.0046
111	44	0.7179	0.0034
112	44	0.3429	0.0024
113	44	0.1322	0.0015
114	44	0.0312	0.0007
105	45	0.0595	0.0008
106	45	0.1453	0.0013
107	45	0.3583	0.0021
108	45	0.7224	0.0031
109	45	1.2554	0.0041
110	45	1.7301	0.0049
111	45	2.0311	0.0054

Continued on next page

USC UNIVERSIDADE DE SANTIAGO DE COMPOSTELA

Table A.2 – continued from previous page

A	Z	Y(Z, A)	Statistical error
112	45	1.5242	0.0048
113	45	1.1109	0.0042
114	45	0.5241	0.0029
115	45	0.2425	0.0019
116	45	0.0835	0.0012
117	45	0.0184	0.0006
107	46	0.0282	0.0005
108	46	0.1067	0.0011
109	46	0.2293	0.0016
110	46	0.5556	0.0026
111	46	0.9840	0.0036
112	46	1.6400	0.0047
113	46	1.7828	0.0049
114	46	1.9458	0.0052
115	46	1.2930	0.0044
116	46	0.8239	0.0035
117	46	0.3760	0.0025
118	46	0.1781	0.0018
119	46	0.0377	0.0010
110	47	0.0732	0.0009
111	47	0.1566	0.0014
112	47	0.3434	0.0021
113	47	0.7040	0.0030
114	47	1.1614	0.0039
115	47	1.7483	0.0049
116	47	1.9300	0.0052
117	47	1.7098	0.0051
118	47	1.1551	0.0043
119	47	0.6532	0.0032
120	47	0.2969	0.0022
121	47	0.0976	0.0013
122	47	0.0209	0.0008
112	48	0.0498	0.0007
113	48	0.0980	0.0010
114	48	0.2197	0.0016
115	48	0.4960	0.0025
116	48	0.9737	0.0036
117	48	1.5224	0.0047
118	48	1.8564	0.0053
119	48	1.8190	0.0053
120	48	1.4346	0.0048
121	48	0.9052	0.0039
122	48	0.4512	0.0029
123	48	0.2001	0.0019
124	48	0.0719	0.0012
115	49	0.0628	0.0009
116	49	0.1475	0.0013
117	49	0.3387	0.0021
118	49	0.6863	0.0031
119	49	1.1370	0.0041
120	49	1.6903	0.0050
121	49	1.9175	0.0054
122	49	1.7031	0.0052
123	49	1.2385	0.0044
124	49	0.6857	0.0035
125	49	0.3605	0.0025
126	49	0.1427	0.0018
127	49	0.0285	0.0009
117	50	0.0521	0.0010
118	50	0.1026	0.0013
119	50	0.2175	0.0020
120	50	0.4755	0.0029
121	50	0.9288	0.0041
122	50	1.4648	0.0053
123	50	1.8927	0.0061
124	50	1.8339	0.0061
125	50	1.4538	0.0055
126	50	0.9169	0.0046
127	50	0.4495	0.0034
128	50	0.2008	0.0024
129	50	0.0646	0.0017

Continued on next page

USC UNIVERSIDADE DE SANTIAGO DE COMPOSTELA

Table A.2 – continued from previous page

A	Z	Y(Z, A)	Statistical error
120	51	0.0622	0.0011
121	51	0.1301	0.0015
122	51	0.2997	0.0023
123	51	0.6313	0.0034
124	51	1.1213	0.0045
125	51	1.6365	0.0056
126	51	1.9379	0.0062
127	51	1.7888	0.0061
128	51	1.2497	0.0053
129	51	0.7496	0.0043
130	51	0.3224	0.0033
131	51	0.1172	0.0027
123	52	0.0956	0.0013
124	52	0.1930	0.0019
125	52	0.3962	0.0027
126	52	0.8187	0.0039
127	52	1.3296	0.0051
128	52	1.7481	0.0059
129	52	1.8954	0.0063
130	52	1.5293	0.0058
131	52	1.0106	0.0051
132	52	0.5015	0.0041
133	52	0.1911	0.0034
125	53	0.0754	0.0012
126	53	0.1364	0.0016
127	53	0.2725	0.0023
128	53	0.4736	0.0030
129	53	1.0357	0.0045
130	53	1.4779	0.0055
131	53	1.8509	0.0062
132	53	1.7326	0.0062
133	53	1.3008	0.0055
134	53	0.7312	0.0046
135	53	0.2927	0.0039
136	53	0.0847	0.0029
137	53	0.0199	0.0024
128	54	0.0831	0.0012
129	54	0.1766	0.0018
130	54	0.3749	0.0027
131	54	0.7335	0.0038
132	54	1.1977	0.0049
133	54	1.6737	0.0059
134	54	1.7803	0.0062
135	54	1.4691	0.0059
136	54	0.9225	0.0050
137	54	0.4100	0.0040
138	54	0.1421	0.0033
139	54	0.0401	0.0026
130	55	0.0628	0.0011
131	55	0.1071	0.0014
132	55	0.1941	0.0019
133	55	0.4596	0.0030
134	55	0.8235	0.0040
135	55	1.2991	0.0051
136	55	1.5677	0.0057
137	55	1.5055	0.0057
138	55	0.9555	0.0049
139	55	0.5903	0.0042
140	55	0.2635	0.0033
141	55	0.1089	0.0028
142	55	0.0263	0.0021
133	56	0.0548	0.0009
134	56	0.1412	0.0013
135	56	0.2921	0.0021
136	56	0.5540	0.0030
137	56	0.9601	0.0040
138	56	1.3329	0.0049
139	56	1.2721	0.0049
140	56	1.0248	0.0046
141	56	0.6136	0.0038
142	56	0.4060	0.0034

Continued on next page

USC UNIVERSIDADE DE SANTIAGO DE COMPOSTELA

Table A.2 – continued from previous page

A	Z	Y(Z, A)	Statistical error
143	56	0.1556	0.0027
144	56	0.0519	0.0021
145	56	0.0128	0.0014
135	57	0.0430	0.0007
136	57	0.0824	0.0009
137	57	0.1689	0.0015
138	57	0.3821	0.0023
139	57	0.6612	0.0032
140	57	0.8456	0.0038
141	57	1.0399	0.0043
142	57	0.9913	0.0043
143	57	0.7291	0.0040
144	57	0.4789	0.0034
145	57	0.2612	0.0030
146	57	0.0912	0.0020
138	58	0.0521	0.0013
139	58	0.1056	0.0018
140	58	0.2321	0.0027
141	58	0.4258	0.0036
142	58	0.6236	0.0044
143	58	0.6560	0.0046
144	58	0.9058	0.0054
145	58	0.7568	0.0052
146	58	0.5861	0.0047
147	58	0.3166	0.0036
148	58	0.1551	0.0028
149	58	0.0637	0.0017
141	59	0.0701	0.0008
142	59	0.1175	0.0010
143	59	0.2041	0.0013
144	59	0.3514	0.0020
145	59	0.5628	0.0029
146	59	0.6715	0.0033
147	59	0.7329	0.0035
148	59	0.4587	0.0032
149	59	0.3221	0.0027
150	59	0.1975	0.0021
151	59	0.0918	0.0015
152	59	0.0198	0.0011
143	60	0.0288	0.0005
144	60	0.0542	0.0007
145	60	0.1114	0.0010
146	60	0.1997	0.0014
147	60	0.3281	0.0017
148	60	0.4787	0.0024
149	60	0.4978	0.0027
150	60	0.4793	0.0027
151	60	0.3616	0.0025
152	60	0.2079	0.0025
153	60	0.0902	0.0017
154	60	0.0318	0.0011
146	61	0.0417	0.0006
147	61	0.0705	0.0008
148	61	0.1301	0.0011
149	61	0.1998	0.0013
150	61	0.2842	0.0016
151	61	0.3602	0.0019
152	61	0.4364	0.0035
153	61	0.3910	0.0036
154	61	0.2206	0.0026
155	61	0.1240	0.0022
156	61	0.0473	0.0015
149	62	0.0161	0.0004
150	62	0.0679	0.0008
151	62	0.1014	0.0009
152	62	0.1964	0.0023
153	62	0.2489	0.0027
154	62	0.3270	0.0031
155	62	0.2962	0.0032
156	62	0.2146	0.0029
157	62	0.1200	0.0022

Continued on next page

USC UNIVERSIDADE DE SANTIAGO DE COMPOSTELA

Table A.2 – continued from previous page

A	Z	Y(Z, A)	Statistical error
158	62	0.0564	0.0015
152	63	0.0349	0.0008
153	63	0.0480	0.0011
154	63	0.0858	0.0016
155	63	0.1550	0.0023
156	63	0.1830	0.0026
157	63	0.1905	0.0027
158	63	0.1637	0.0025
159	63	0.1024	0.0020
160	63	0.0589	0.0016
155	64	0.0369	0.0012
156	64	0.0580	0.0015
157	64	0.0752	0.0017
158	64	0.1134	0.0021
159	64	0.1204	0.0021
160	64	0.1296	0.0023
161	64	0.0882	0.0022
162	64	0.0537	0.0014
159	65	0.0242	0.0010
160	65	0.0559	0.0016
161	65	0.0677	0.0017
162	65	0.0715	0.0018
163	65	0.0593	0.0018
164	65	0.0259	0.0014
163	66	0.0276	0.0010
164	66	0.0334	0.0013
165	66	0.0372	0.0015
166	66	0.0185	0.0011

USC UNIVERSIDADE DE SANTIAGO DE COMPOSTELA

A.3.2 ^{249}Bk isotopic fusion-induced fission yields

Table A.3: *^{249}Bk isotopic fusion-induced fission yields*

A	Z	Y(Z, A)	Statistical error
75	31	0.0126	0.0009
76	31	0.0121	0.0009
77	31	0.0115	0.0009
76	32	0.0165	0.0008
77	32	0.0173	0.0012
78	32	0.0251	0.0013
79	32	0.0293	0.0016
80	32	0.0451	0.0019
78	33	0.0341	0.0015
79	33	0.0794	0.0025
80	33	0.1263	0.0038
81	33	0.1540	0.0041
82	33	0.1208	0.0039
83	33	0.0801	0.0027
84	33	0.0132	0.0011
81	34	0.1391	0.0033
82	34	0.1968	0.0045
83	34	0.2697	0.0050
84	34	0.2185	0.0043
85	34	0.1418	0.0032
86	34	0.0569	0.0027
87	34	0.0370	0.0017
82	35	0.0607	0.0018
83	35	0.1343	0.0030
84	35	0.2376	0.0040
85	35	0.3552	0.0050
86	35	0.3416	0.0050
87	35	0.2678	0.0050
88	35	0.1581	0.0037
89	35	0.0460	0.0023
90	35	0.0143	0.0010
84	36	0.0565	0.0015
85	36	0.1555	0.0029
86	36	0.2858	0.0042
87	36	0.4992	0.0054
88	36	0.4583	0.0055
89	36	0.3619	0.0048
90	36	0.2727	0.0041
91	36	0.1392	0.0025
92	36	0.0486	0.0019
93	36	0.0139	0.0008
86	37	0.0464	0.0014
87	37	0.1186	0.0025
88	37	0.2302	0.0034
89	37	0.4414	0.0045
90	37	0.5714	0.0049
91	37	0.6124	0.0053
92	37	0.4274	0.0044
93	37	0.2677	0.0035
94	37	0.1216	0.0026
95	37	0.0596	0.0016
88	38	0.0433	0.0012
89	38	0.0981	0.0018
90	38	0.2225	0.0027
91	38	0.4315	0.0039
92	38	0.6837	0.0049
93	38	0.8008	0.0051
94	38	0.7405	0.0051
95	38	0.4738	0.0048
96	38	0.2358	0.0031
97	38	0.0835	0.0021
98	38	0.0202	0.0011
91	39	0.0787	0.0014
92	39	0.1771	0.0021
93	39	0.3856	0.0031
94	39	0.6825	0.0043

Continued on next page

USC UNIVERSIDADE DE SANTIAGO DE COMPOSTELA

Table A.3 – continued from previous page

A	Z	Y(Z, A)	Statistical error
95	39	0.9018	0.0053
96	39	0.9082	0.0048
97	39	0.7302	0.0047
98	39	0.4489	0.0036
99	39	0.2471	0.0030
100	39	0.1123	0.0018
101	39	0.0448	0.0010
93	40	0.0463	0.0011
94	40	0.1364	0.0020
95	40	0.3029	0.0031
96	40	0.6198	0.0046
97	40	0.9900	0.0060
98	40	1.1712	0.0068
99	40	1.0361	0.0069
100	40	0.8949	0.0067
101	40	0.4459	0.0052
102	40	0.2127	0.0038
103	40	0.0952	0.0022
104	40	0.0183	0.0011
95	41	0.0382	0.0008
96	41	0.0893	0.0012
97	41	0.2386	0.0020
98	41	0.4993	0.0029
99	41	0.9393	0.0040
100	41	1.1285	0.0048
101	41	1.4757	0.0057
102	41	1.1202	0.0050
103	41	0.7934	0.0046
104	41	0.3455	0.0030
105	41	0.1520	0.0020
106	41	0.0210	0.0010
98	42	0.0754	0.0010
99	42	0.1962	0.0017
100	42	0.4345	0.0027
101	42	0.6881	0.0035
102	42	1.3856	0.0048
103	42	1.6179	0.0055
104	42	1.5884	0.0054
105	42	1.0396	0.0045
106	42	0.5915	0.0036
107	42	0.2466	0.0023
108	42	0.1240	0.0015
109	42	0.0298	0.0008
100	43	0.0491	0.0008
101	43	0.1245	0.0014
102	43	0.2903	0.0020
103	43	0.6350	0.0031
104	43	1.1154	0.0041
105	43	1.6267	0.0049
106	43	1.7411	0.0052
107	43	1.5165	0.0050
108	43	0.8853	0.0040
109	43	0.5602	0.0031
110	43	0.1890	0.0018
111	43	0.0791	0.0012
112	43	0.0147	0.0006
102	44	0.0405	0.0006
103	44	0.1160	0.0012
104	44	0.2604	0.0018
105	44	0.4374	0.0023
106	44	1.0458	0.0038
107	44	1.4995	0.0046
108	44	1.9284	0.0054
109	44	1.7421	0.0051
110	44	1.3067	0.0046
111	44	0.7179	0.0034
112	44	0.3429	0.0024
113	44	0.1322	0.0015
114	44	0.0312	0.0007
105	45	0.0595	0.0008
106	45	0.1453	0.0013

Continued on next page

USC UNIVERSIDADE DE SANTIAGO DE COMPOSTELA

Table A.3 – continued from previous page

A	Z	Y(Z, A)	Statistical error
107	45	0.3583	0.0021
108	45	0.7224	0.0031
109	45	1.2554	0.0041
110	45	1.7301	0.0049
111	45	2.0311	0.0054
112	45	1.5242	0.0048
113	45	1.1109	0.0042
114	45	0.5241	0.0029
115	45	0.2425	0.0019
116	45	0.0835	0.0012
117	45	0.0184	0.0006
107	46	0.0282	0.0005
108	46	0.1067	0.0011
109	46	0.2293	0.0016
110	46	0.5556	0.0026
111	46	0.9840	0.0036
112	46	1.6400	0.0047
113	46	1.7828	0.0049
114	46	1.9458	0.0052
115	46	1.2930	0.0044
116	46	0.8239	0.0035
117	46	0.3760	0.0025
118	46	0.1781	0.0018
119	46	0.0377	0.0010
110	47	0.0732	0.0009
111	47	0.1566	0.0014
112	47	0.3434	0.0021
113	47	0.7040	0.0030
114	47	1.1614	0.0039
115	47	1.7483	0.0049
116	47	1.9300	0.0052
117	47	1.7098	0.0051
118	47	1.1551	0.0043
119	47	0.6532	0.0032
120	47	0.2969	0.0022
121	47	0.0976	0.0013
122	47	0.0209	0.0008
112	48	0.0498	0.0007
113	48	0.0980	0.0010
114	48	0.2197	0.0016
115	48	0.4960	0.0025
116	48	0.9737	0.0036
117	48	1.5224	0.0047
118	48	1.8564	0.0053
119	48	1.8190	0.0053
120	48	1.4346	0.0048
121	48	0.9052	0.0039
122	48	0.4512	0.0029
123	48	0.2001	0.0019
124	48	0.0719	0.0012
115	49	0.0628	0.0009
116	49	0.1475	0.0013
117	49	0.3387	0.0021
118	49	0.6863	0.0031
119	49	1.1370	0.0041
120	49	1.6903	0.0050
121	49	1.9175	0.0054
122	49	1.7031	0.0052
123	49	1.2385	0.0044
124	49	0.6857	0.0035
125	49	0.3605	0.0025
126	49	0.1427	0.0018
127	49	0.0285	0.0009
117	50	0.0521	0.0010
118	50	0.1026	0.0013
119	50	0.2175	0.0020
120	50	0.4755	0.0029
121	50	0.9288	0.0041
122	50	1.4648	0.0053
123	50	1.8927	0.0061
124	50	1.8339	0.0061

Continued on next page

USC UNIVERSIDADE DE SANTIAGO DE COMPOSTELA

Table A.3 – continued from previous page

A	Z	Y(Z, A)	Statistical error
125	50	1.4538	0.0055
126	50	0.9169	0.0046
127	50	0.4495	0.0034
128	50	0.2008	0.0024
129	50	0.0646	0.0017
120	51	0.0622	0.0011
121	51	0.1301	0.0015
122	51	0.2997	0.0023
123	51	0.6313	0.0034
124	51	1.1213	0.0045
125	51	1.6365	0.0056
126	51	1.9379	0.0062
127	51	1.7888	0.0061
128	51	1.2497	0.0053
129	51	0.7496	0.0043
130	51	0.3224	0.0033
131	51	0.1172	0.0027
123	52	0.0956	0.0013
124	52	0.1930	0.0019
125	52	0.3962	0.0027
126	52	0.8187	0.0039
127	52	1.3296	0.0051
128	52	1.7481	0.0059
129	52	1.8954	0.0063
130	52	1.5293	0.0058
131	52	1.0106	0.0051
132	52	0.5015	0.0041
133	52	0.1911	0.0034
125	53	0.0754	0.0012
126	53	0.1364	0.0016
127	53	0.2725	0.0023
128	53	0.4736	0.0030
129	53	1.0357	0.0045
130	53	1.4779	0.0055
131	53	1.8509	0.0062
132	53	1.7326	0.0062
133	53	1.3008	0.0055
134	53	0.7312	0.0046
135	53	0.2927	0.0039
136	53	0.0847	0.0029
137	53	0.0199	0.0024
128	54	0.0831	0.0012
129	54	0.1766	0.0018
130	54	0.3749	0.0027
131	54	0.7335	0.0038
132	54	1.1977	0.0049
133	54	1.6737	0.0059
134	54	1.7803	0.0062
135	54	1.4691	0.0059
136	54	0.9225	0.0050
137	54	0.4100	0.0040
138	54	0.1421	0.0033
139	54	0.0401	0.0026
130	55	0.0628	0.0011
131	55	0.1071	0.0014
132	55	0.1941	0.0019
133	55	0.4596	0.0030
134	55	0.8235	0.0040
135	55	1.2991	0.0051
136	55	1.5677	0.0057
137	55	1.5055	0.0057
138	55	0.9555	0.0049
139	55	0.5903	0.0042
140	55	0.2635	0.0033
141	55	0.1089	0.0028
142	55	0.0263	0.0021
133	56	0.0548	0.0009
134	56	0.1412	0.0013
135	56	0.2921	0.0021
136	56	0.5540	0.0030
137	56	0.9601	0.0040

Continued on next page

USC UNIVERSIDADE DE SANTIAGO DE COMPOSTELA

Table A.3 – continued from previous page

A	Z	Y(Z, A)	Statistical error
138	56	1.3329	0.0049
139	56	1.2721	0.0049
140	56	1.0248	0.0046
141	56	0.6136	0.0038
142	56	0.4060	0.0034
143	56	0.1556	0.0027
144	56	0.0519	0.0021
145	56	0.0128	0.0014
135	57	0.0430	0.0007
136	57	0.0824	0.0009
137	57	0.1689	0.0015
138	57	0.3821	0.0023
139	57	0.6612	0.0032
140	57	0.8456	0.0038
141	57	1.0399	0.0043
142	57	0.9913	0.0043
143	57	0.7291	0.0040
144	57	0.4789	0.0034
145	57	0.2612	0.0030
146	57	0.0912	0.0020
138	58	0.0521	0.0013
139	58	0.1056	0.0018
140	58	0.2321	0.0027
141	58	0.4258	0.0036
142	58	0.6236	0.0044
143	58	0.6560	0.0046
144	58	0.9058	0.0054
145	58	0.7568	0.0052
146	58	0.5861	0.0047
147	58	0.3166	0.0036
148	58	0.1551	0.0028
149	58	0.0637	0.0017
141	59	0.0701	0.0008
142	59	0.1175	0.0010
143	59	0.2041	0.0013
144	59	0.3514	0.0020
145	59	0.5628	0.0029
146	59	0.6715	0.0033
147	59	0.7329	0.0035
148	59	0.4587	0.0032
149	59	0.3221	0.0027
150	59	0.1975	0.0021
151	59	0.0918	0.0015
152	59	0.0198	0.0011
143	60	0.0288	0.0005
144	60	0.0542	0.0007
145	60	0.1114	0.0010
146	60	0.1997	0.0014
147	60	0.3281	0.0017
148	60	0.4787	0.0024
149	60	0.4978	0.0027
150	60	0.4793	0.0027
151	60	0.3616	0.0025
152	60	0.2079	0.0025
153	60	0.0902	0.0017
154	60	0.0318	0.0011
146	61	0.0417	0.0006
147	61	0.0705	0.0008
148	61	0.1301	0.0011
149	61	0.1998	0.0013
150	61	0.2842	0.0016
151	61	0.3602	0.0019
152	61	0.4364	0.0035
153	61	0.3910	0.0036
154	61	0.2206	0.0026
155	61	0.1240	0.0022
156	61	0.0473	0.0015
149	62	0.0161	0.0004
150	62	0.0679	0.0008
151	62	0.1014	0.0009
152	62	0.1964	0.0023

Continued on next page

USC UNIVERSIDADE DE SANTIAGO DE COMPOSTELA

Table A.3 – continued from previous page

A	Z	Y(Z, A)	Statistical error
153	62	0.2489	0.0027
154	62	0.3270	0.0031
155	62	0.2962	0.0032
156	62	0.2146	0.0029
157	62	0.1200	0.0022
158	62	0.0564	0.0015
152	63	0.0349	0.0008
153	63	0.0480	0.0011
154	63	0.0858	0.0016
155	63	0.1550	0.0023
156	63	0.1830	0.0026
157	63	0.1905	0.0027
158	63	0.1637	0.0025
159	63	0.1024	0.0020
160	63	0.0589	0.0016
155	64	0.0369	0.0012
156	64	0.0580	0.0015
157	64	0.0752	0.0017
158	64	0.1134	0.0021
159	64	0.1204	0.0021
160	64	0.1296	0.0023
161	64	0.0882	0.0022
162	64	0.0537	0.0014
159	65	0.0242	0.0010
160	65	0.0559	0.0016
161	65	0.0677	0.0017
162	65	0.0715	0.0018
163	65	0.0593	0.0018
164	65	0.0259	0.0014
163	66	0.0276	0.0010
164	66	0.0334	0.0013
165	66	0.0372	0.0015
166	66	0.0185	0.0011

A.4 Transfer reactions isotopic yields

A.4.1 Aluminium target transfer reactions isotopic yields

Table A.4: *Aluminium target transfer reactions isotopic yields*

A	Z	Y(Z, A)	Statistical error
79	31	0.0000	0.0006
78	32	0.0018	0.0010
79	32	0.0036	0.0013
80	32	0.0040	0.0014
81	32	0.0037	0.0014
82	32	0.0022	0.0011
83	32	0.0004	0.0007
78	33	0.0029	0.0012
79	33	0.0040	0.0013
80	33	0.0042	0.0014
81	33	0.0119	0.0022
82	33	0.0175	0.0026
83	33	0.0171	0.0026
84	33	0.0111	0.0021
85	33	0.0052	0.0015
86	33	0.0021	0.0010
78	34	0.0005	0.0007
79	34	0.0020	0.0010
80	34	0.0044	0.0014
81	34	0.0055	0.0015
82	34	0.0137	0.0023
83	34	0.0220	0.0029

Continued on next page

USC UNIVERSIDADE DE SANTIAGO DE COMPOSTELA

Table A.4 – continued from previous page

A	Z	Y(Z, A)	Statistical error
84	34	0.0444	0.0041
85	34	0.0386	0.0038
86	34	0.0391	0.0038
87	34	0.0214	0.0028
88	34	0.0106	0.0020
89	34	0.0024	0.0011
90	34	0.0009	0.0008
80	35	0.0011	0.0008
81	35	0.0017	0.0009
82	35	0.0048	0.0014
83	35	0.0081	0.0018
84	35	0.0186	0.0026
85	35	0.0355	0.0036
86	35	0.0591	0.0046
87	35	0.0760	0.0052
88	35	0.0602	0.0046
89	35	0.0451	0.0040
90	35	0.0163	0.0024
91	35	0.0076	0.0017
92	35	0.0028	0.0011
93	35	0.0003	0.0006
82	36	0.0014	0.0009
83	36	0.0025	0.0010
84	36	0.0055	0.0015
85	36	0.0104	0.0019
86	36	0.0214	0.0027
87	36	0.0422	0.0038
88	36	0.0866	0.0054
89	36	0.1107	0.0061
90	36	0.1391	0.0069
91	36	0.0890	0.0055
92	36	0.0513	0.0042
93	36	0.0166	0.0024
94	36	0.0085	0.0018
95	36	0.0032	0.0012
96	36	0.0010	0.0008
84	37	0.0008	0.0007
85	37	0.0026	0.0011
86	37	0.0058	0.0015
87	37	0.0098	0.0019
88	37	0.0182	0.0025
89	37	0.0439	0.0038
90	37	0.0763	0.0050
91	37	0.1274	0.0065
92	37	0.1400	0.0068
93	37	0.1336	0.0066
94	37	0.0697	0.0048
95	37	0.0338	0.0034
96	37	0.0125	0.0021
97	37	0.0051	0.0014
98	37	0.0022	0.0010
85	38	0.0010	0.0007
86	38	0.0003	0.0006
87	38	0.0038	0.0012
88	38	0.0052	0.0014
89	38	0.0111	0.0019
90	38	0.0190	0.0025
91	38	0.0399	0.0036
92	38	0.0884	0.0053
93	38	0.1521	0.0070
94	38	0.2104	0.0082
95	38	0.1853	0.0077
96	38	0.1393	0.0067
97	38	0.0833	0.0052
98	38	0.0354	0.0034
99	38	0.0090	0.0018
100	38	0.0030	0.0011
101	38	0.0021	0.0010
86	39	0.0001	0.0005
88	39	0.0011	0.0008
89	39	0.0022	0.0010

Continued on next page

USC UNIVERSIDADE DE SANTIAGO DE COMPOSTELA

Table A.4 – continued from previous page

A	Z	Y(Z, A)	Statistical error
90	39	0.0043	0.0013
91	39	0.0084	0.0017
92	39	0.0183	0.0025
93	39	0.0303	0.0031
94	39	0.0678	0.0046
95	39	0.1277	0.0064
96	39	0.1804	0.0076
97	39	0.2011	0.0080
98	39	0.1741	0.0074
99	39	0.1281	0.0064
100	39	0.0491	0.0040
101	39	0.0202	0.0026
102	39	0.0064	0.0015
103	39	0.0033	0.0011
104	39	0.0011	0.0008
105	39	0.0008	0.0007
88	40	0.0001	0.0005
89	40	0.0003	0.0006
90	40	0.0006	0.0007
91	40	0.0017	0.0009
92	40	0.0036	0.0012
93	40	0.0082	0.0017
94	40	0.0144	0.0022
95	40	0.0277	0.0030
96	40	0.0546	0.0041
97	40	0.1066	0.0058
98	40	0.1834	0.0076
99	40	0.2168	0.0082
100	40	0.2653	0.0091
101	40	0.1590	0.0070
102	40	0.0991	0.0056
103	40	0.0285	0.0030
104	40	0.0136	0.0021
105	40	0.0041	0.0012
106	40	0.0009	0.0007
107	40	0.0004	0.0006
90	41	0.0002	0.0006
91	41	0.0003	0.0006
92	41	0.0005	0.0006
93	41	0.0024	0.0010
94	41	0.0030	0.0011
95	41	0.0065	0.0015
96	41	0.0116	0.0019
97	41	0.0216	0.0026
98	41	0.0375	0.0034
99	41	0.0797	0.0050
100	41	0.1248	0.0062
101	41	0.2188	0.0082
102	41	0.2162	0.0082
103	41	0.1921	0.0077
104	41	0.0902	0.0053
105	41	0.0471	0.0038
106	41	0.0120	0.0020
107	41	0.0026	0.0010
108	41	0.0005	0.0006
109	41	0.0006	0.0006
92	42	0.0002	0.0005
93	42	0.0001	0.0005
94	42	0.0004	0.0006
95	42	0.0012	0.0008
96	42	0.0033	0.0011
97	42	0.0056	0.0014
98	42	0.0087	0.0017
99	42	0.0173	0.0023
100	42	0.0297	0.0030
101	42	0.0477	0.0038
102	42	0.1116	0.0058
103	42	0.1577	0.0069
104	42	0.1947	0.0077
105	42	0.1580	0.0069
106	42	0.0999	0.0055

Continued on next page

USC UNIVERSIDADE DE SANTIAGO DE COMPOSTELA

Table A.4 – continued from previous page

A	Z	Y(Z, A)	Statistical error
107	42	0.0431	0.0036
108	42	0.0149	0.0022
109	42	0.0033	0.0011
110	42	0.0010	0.0007
111	42	0.0011	0.0008
95	43	0.0002	0.0005
96	43	0.0001	0.0005
97	43	0.0011	0.0008
98	43	0.0018	0.0009
99	43	0.0040	0.0012
100	43	0.0063	0.0015
101	43	0.0135	0.0021
102	43	0.0222	0.0026
103	43	0.0390	0.0035
104	43	0.0667	0.0045
105	43	0.1020	0.0056
106	43	0.1174	0.0060
107	43	0.1082	0.0057
108	43	0.0622	0.0044
109	43	0.0403	0.0035
110	43	0.0097	0.0018
111	43	0.0057	0.0014
112	43	0.0015	0.0008
113	43	0.0003	0.0006
99	44	0.0003	0.0006
100	44	0.0013	0.0008
101	44	0.0021	0.0009
102	44	0.0059	0.0014
103	44	0.0127	0.0020
104	44	0.0209	0.0025
105	44	0.0302	0.0030
106	44	0.0504	0.0039
107	44	0.0684	0.0045
108	44	0.0795	0.0049
109	44	0.0813	0.0050
110	44	0.0593	0.0042
111	44	0.0318	0.0031
112	44	0.0165	0.0023
113	44	0.0085	0.0017
114	44	0.0022	0.0009
100	45	0.0002	0.0005
101	45	0.0003	0.0006
102	45	0.0005	0.0006
103	45	0.0014	0.0008
104	45	0.0042	0.0012
105	45	0.0097	0.0018
106	45	0.0146	0.0021
107	45	0.0279	0.0029
108	45	0.0346	0.0032
109	45	0.0414	0.0035
110	45	0.0538	0.0040
111	45	0.0573	0.0042
112	45	0.0491	0.0038
113	45	0.0350	0.0033
114	45	0.0204	0.0025
115	45	0.0087	0.0017
116	45	0.0026	0.0010
102	46	0.0001	0.0005
104	46	0.0008	0.0007
105	46	0.0024	0.0010
106	46	0.0044	0.0012
107	46	0.0066	0.0015
108	46	0.0123	0.0020
109	46	0.0239	0.0027
110	46	0.0346	0.0032
111	46	0.0409	0.0035
112	46	0.0428	0.0036
113	46	0.0483	0.0038
114	46	0.0510	0.0039
115	46	0.0387	0.0034
116	46	0.0251	0.0028

Continued on next page

USC UNIVERSIDADE DE SANTIAGO DE COMPOSTELA

Table A.4 – continued from previous page

A	Z	Y(Z, A)	Statistical error
117	46	0.0117	0.0019
118	46	0.0087	0.0017
119	46	0.0028	0.0010
120	46	0.0006	0.0006
107	47	0.0013	0.0008
108	47	0.0021	0.0009
109	47	0.0062	0.0014
110	47	0.0111	0.0019
111	47	0.0190	0.0024
112	47	0.0298	0.0030
113	47	0.0392	0.0034
114	47	0.0392	0.0034
115	47	0.0477	0.0038
116	47	0.0461	0.0037
117	47	0.0435	0.0036
118	47	0.0377	0.0034
119	47	0.0218	0.0026
120	47	0.0120	0.0019
121	47	0.0044	0.0012
122	47	0.0039	0.0012
123	47	0.0016	0.0008
128	47	0.0002	0.0005
109	48	0.0008	0.0007
110	48	0.0022	0.0009
111	48	0.0057	0.0014
112	48	0.0092	0.0017
113	48	0.0191	0.0024
114	48	0.0263	0.0028
115	48	0.0326	0.0031
116	48	0.0439	0.0036
117	48	0.0459	0.0037
118	48	0.0441	0.0036
119	48	0.0471	0.0038
120	48	0.0427	0.0036
121	48	0.0353	0.0033
122	48	0.0212	0.0025
123	48	0.0124	0.0020
124	48	0.0057	0.0014
125	48	0.0041	0.0012
126	48	0.0019	0.0009
127	48	0.0003	0.0006
111	49	0.0001	0.0005
112	49	0.0013	0.0008
113	49	0.0024	0.0010
114	49	0.0072	0.0015
115	49	0.0132	0.0020
116	49	0.0234	0.0027
117	49	0.0279	0.0029
118	49	0.0370	0.0033
119	49	0.0420	0.0035
120	49	0.0425	0.0036
121	49	0.0474	0.0038
122	49	0.0450	0.0037
123	49	0.0445	0.0036
124	49	0.0332	0.0032
125	49	0.0269	0.0028
126	49	0.0180	0.0023
127	49	0.0141	0.0021
128	49	0.0062	0.0014
129	49	0.0040	0.0012
130	49	0.0010	0.0007
131	49	0.0003	0.0006
132	49	0.0001	0.0005
112	50	0.0007	0.0007
113	50	0.0002	0.0005
115	50	0.0015	0.0008
116	50	0.0051	0.0013
117	50	0.0083	0.0016
118	50	0.0180	0.0023
119	50	0.0269	0.0029
120	50	0.0301	0.0030

Continued on next page

USC UNIVERSIDADE DE SANTIAGO DE COMPOSTELA

Table A.4 – continued from previous page

A	Z	Y(Z, A)	Statistical error
121	50	0.0371	0.0033
122	50	0.0331	0.0032
123	50	0.0392	0.0034
124	50	0.0479	0.0038
125	50	0.0470	0.0037
126	50	0.0456	0.0037
127	50	0.0418	0.0035
128	50	0.0520	0.0039
129	50	0.0502	0.0039
130	50	0.0437	0.0036
131	50	0.0322	0.0031
132	50	0.0189	0.0024
133	50	0.0035	0.0011
134	50	0.0021	0.0009
117	51	0.0006	0.0006
118	51	0.0023	0.0009
119	51	0.0054	0.0013
120	51	0.0115	0.0019
121	51	0.0165	0.0022
122	51	0.0265	0.0028
123	51	0.0275	0.0029
124	51	0.0350	0.0032
125	51	0.0385	0.0034
126	51	0.0438	0.0036
127	51	0.0583	0.0042
128	51	0.0678	0.0045
129	51	0.0884	0.0051
130	51	0.0977	0.0054
131	51	0.1116	0.0057
132	51	0.1060	0.0056
133	51	0.0753	0.0047
134	51	0.0276	0.0029
135	51	0.0087	0.0017
136	51	0.0059	0.0014
137	51	0.0009	0.0007
138	51	0.0000	0.0005
120	52	0.0018	0.0009
121	52	0.0036	0.0011
122	52	0.0071	0.0015
123	52	0.0117	0.0019
124	52	0.0192	0.0024
125	52	0.0310	0.0031
126	52	0.0281	0.0029
127	52	0.0340	0.0032
128	52	0.0430	0.0036
129	52	0.0632	0.0043
130	52	0.0880	0.0051
131	52	0.1374	0.0064
132	52	0.1632	0.0069
133	52	0.2012	0.0077
134	52	0.1786	0.0072
135	52	0.0839	0.0050
136	52	0.0406	0.0035
137	52	0.0205	0.0025
138	52	0.0049	0.0013
139	52	0.0017	0.0008
121	53	0.0007	0.0007
122	53	0.0006	0.0006
123	53	0.0027	0.0010
124	53	0.0070	0.0015
125	53	0.0132	0.0020
126	53	0.0160	0.0022
127	53	0.0246	0.0027
128	53	0.0256	0.0028
129	53	0.0428	0.0036
130	53	0.0419	0.0035
131	53	0.0628	0.0043
132	53	0.0986	0.0054
133	53	0.1663	0.0070
134	53	0.2113	0.0079
135	53	0.2315	0.0082

Continued on next page

USC UNIVERSIDADE DE SANTIAGO DE COMPOSTELA

Table A.4 – continued from previous page

A	Z	Y(Z, A)	Statistical error
136	53	0.1604	0.0069
137	53	0.0956	0.0053
138	53	0.0540	0.0040
139	53	0.0225	0.0026
140	53	0.0095	0.0017
141	53	0.0023	0.0010
142	53	0.0015	0.0008
143	53	0.0009	0.0007
144	53	0.0003	0.0006
121	54	0.0007	0.0007
123	54	0.0003	0.0006
124	54	0.0010	0.0007
125	54	0.0011	0.0007
126	54	0.0037	0.0011
127	54	0.0088	0.0017
128	54	0.0162	0.0022
129	54	0.0259	0.0028
130	54	0.0322	0.0031
131	54	0.0388	0.0034
132	54	0.0457	0.0037
133	54	0.0767	0.0048
134	54	0.1191	0.0059
135	54	0.1990	0.0076
136	54	0.2712	0.0089
137	54	0.2261	0.0081
138	54	0.2161	0.0080
139	54	0.1522	0.0067
140	54	0.1105	0.0057
141	54	0.0446	0.0036
142	54	0.0217	0.0026
143	54	0.0075	0.0016
144	54	0.0031	0.0011
145	54	0.0004	0.0006
126	55	0.0003	0.0006
127	55	0.0002	0.0005
128	55	0.0018	0.0009
129	55	0.0045	0.0012
130	55	0.0102	0.0018
131	55	0.0175	0.0023
132	55	0.0231	0.0026
133	55	0.0284	0.0029
134	55	0.0358	0.0033
135	55	0.0496	0.0038
136	55	0.0853	0.0050
137	55	0.1127	0.0058
138	55	0.1472	0.0066
139	55	0.1708	0.0071
140	55	0.1611	0.0069
141	55	0.1592	0.0068
142	55	0.0801	0.0049
143	55	0.0574	0.0041
144	55	0.0235	0.0027
145	55	0.0112	0.0019
146	55	0.0055	0.0014
147	55	0.0014	0.0008
129	56	0.0002	0.0005
130	56	0.0004	0.0006
131	56	0.0022	0.0009
132	56	0.0044	0.0012
133	56	0.0123	0.0020
134	56	0.0176	0.0023
135	56	0.0239	0.0027
136	56	0.0268	0.0028
137	56	0.0382	0.0034
138	56	0.0500	0.0039
139	56	0.0772	0.0048
140	56	0.1138	0.0058
141	56	0.1287	0.0062
142	56	0.1513	0.0067
143	56	0.1249	0.0061
144	56	0.0917	0.0052

Continued on next page

USC UNIVERSIDADE DE SANTIAGO DE COMPOSTELA

Table A.4 – continued from previous page

A	Z	Y(Z, A)	Statistical error
145	56	0.0512	0.0039
146	56	0.0240	0.0027
147	56	0.0120	0.0019
148	56	0.0072	0.0015
149	56	0.0018	0.0009
150	56	0.0004	0.0006
152	56	0.0000	0.0005
130	57	0.0001	0.0005
132	57	0.0003	0.0006
133	57	0.0020	0.0009
134	57	0.0033	0.0011
135	57	0.0084	0.0016
136	57	0.0108	0.0018
137	57	0.0168	0.0023
138	57	0.0189	0.0024
139	57	0.0269	0.0028
140	57	0.0334	0.0032
141	57	0.0489	0.0038
142	57	0.0726	0.0046
143	57	0.0978	0.0054
144	57	0.1121	0.0057
145	57	0.1091	0.0057
146	57	0.0710	0.0046
147	57	0.0412	0.0035
148	57	0.0217	0.0026
149	57	0.0087	0.0017
150	57	0.0076	0.0016
151	57	0.0015	0.0008
152	57	0.0017	0.0008
135	58	0.0001	0.0005
136	58	0.0017	0.0009
137	58	0.0036	0.0011
138	58	0.0090	0.0017
139	58	0.0111	0.0019
140	58	0.0179	0.0023
141	58	0.0192	0.0024
142	58	0.0190	0.0024
143	58	0.0285	0.0029
144	58	0.0391	0.0034
145	58	0.0530	0.0040
146	58	0.0672	0.0045
147	58	0.0625	0.0043
148	58	0.0520	0.0039
149	58	0.0296	0.0030
150	58	0.0184	0.0024
151	58	0.0059	0.0014
152	58	0.0024	0.0010
153	58	0.0019	0.0009
137	59	0.0001	0.0005
138	59	0.0007	0.0006
139	59	0.0028	0.0010
140	59	0.0040	0.0012
141	59	0.0118	0.0019
142	59	0.0140	0.0021
143	59	0.0134	0.0020
144	59	0.0161	0.0022
145	59	0.0201	0.0025
146	59	0.0286	0.0029
147	59	0.0333	0.0032
148	59	0.0305	0.0030
149	59	0.0444	0.0036
150	59	0.0362	0.0033
151	59	0.0235	0.0027
152	59	0.0146	0.0021
153	59	0.0057	0.0014
154	59	0.0019	0.0009
155	59	0.0004	0.0006
141	60	0.0010	0.0007
142	60	0.0019	0.0009
143	60	0.0053	0.0013
144	60	0.0066	0.0015

Continued on next page

USC UNIVERSIDADE DE SANTIAGO DE COMPOSTELA

Table A.4 – continued from previous page

A	Z	Y(Z, A)	Statistical error
145	60	0.0105	0.0018
146	60	0.0142	0.0021
147	60	0.0114	0.0019
148	60	0.0156	0.0022
149	60	0.0165	0.0022
150	60	0.0172	0.0023
151	60	0.0191	0.0024
152	60	0.0137	0.0021
153	60	0.0098	0.0018
154	60	0.0078	0.0016
155	60	0.0026	0.0010
156	60	0.0002	0.0005
157	60	0.0009	0.0007
143	61	0.0012	0.0008
144	61	0.0029	0.0010
145	61	0.0036	0.0011
146	61	0.0054	0.0013
147	61	0.0108	0.0018
148	61	0.0109	0.0018
149	61	0.0141	0.0021
150	61	0.0148	0.0021
151	61	0.0118	0.0019
152	61	0.0138	0.0021
153	61	0.0152	0.0022
154	61	0.0113	0.0019
155	61	0.0060	0.0014
156	61	0.0048	0.0013
157	61	0.0021	0.0009
146	62	0.0002	0.0005
147	62	0.0023	0.0010
148	62	0.0021	0.0009
149	62	0.0061	0.0014
150	62	0.0082	0.0016
151	62	0.0066	0.0015
152	62	0.0106	0.0018
153	62	0.0074	0.0015
154	62	0.0069	0.0015
155	62	0.0052	0.0013
156	62	0.0044	0.0012
157	62	0.0031	0.0011
158	62	0.0017	0.0008
159	62	0.0002	0.0005
160	62	0.0002	0.0005
147	63	0.0001	0.0005
148	63	0.0004	0.0006
149	63	0.0006	0.0006
150	63	0.0015	0.0008
151	63	0.0027	0.0010
152	63	0.0058	0.0014
153	63	0.0100	0.0018
154	63	0.0078	0.0016
155	63	0.0084	0.0016
156	63	0.0050	0.0013
157	63	0.0053	0.0013
158	63	0.0008	0.0007
159	63	0.0005	0.0006
160	63	0.0002	0.0005
161	63	0.0001	0.0005
151	64	0.0011	0.0007
152	64	0.0009	0.0007
153	64	0.0018	0.0009
154	64	0.0039	0.0012
155	64	0.0042	0.0012
156	64	0.0079	0.0016
157	64	0.0065	0.0015
158	64	0.0046	0.0012
159	64	0.0064	0.0014
160	64	0.0017	0.0008
161	64	0.0016	0.0008
154	65	0.0002	0.0005
155	65	0.0004	0.0006

Continued on next page

USC UNIVERSIDADE DE SANTIAGO DE COMPOSTELA

Table A.4 – continued from previous page

A	Z	Y(Z, A)	Statistical error
156	65	0.0017	0.0009
157	65	0.0051	0.0013
158	65	0.0058	0.0014
159	65	0.0044	0.0012
160	65	0.0038	0.0012
161	65	0.0054	0.0013
162	65	0.0021	0.0009
163	65	0.0026	0.0010
164	65	0.0003	0.0006
157	66	0.0001	0.0005
158	66	0.0023	0.0009
159	66	0.0025	0.0010
160	66	0.0029	0.0010
161	66	0.0045	0.0012
162	66	0.0037	0.0011
163	66	0.0046	0.0012
164	66	0.0015	0.0008
165	66	0.0006	0.0006
166	66	0.0004	0.0006

A.4.2 Boron target transfer reactions isotopic yields

Table A.5: *Boron target transfer reactions isotopic yields*

A	Z	Y(Z, A)	Statistical error
82	33	0.0241	0.0028
83	33	0.0087	0.0022
83	34	0.0275	0.0025
84	34	0.0358	0.0033
85	34	0.0416	0.0034
86	34	0.0526	0.0035
87	34	0.0155	0.0024
88	34	0.0193	0.0024
85	35	0.0261	0.0026
86	35	0.0531	0.0036
87	35	0.0940	0.0045
88	35	0.0802	0.0042
89	35	0.0470	0.0026
90	35	0.0200	0.0016
91	35	0.0127	0.0014
86	36	0.0158	0.0015
87	36	0.0301	0.0026
88	36	0.0668	0.0034
89	36	0.1099	0.0041
90	36	0.1371	0.0038
91	36	0.0877	0.0024
92	36	0.0458	0.0017
93	36	0.0236	0.0015
94	36	0.0112	0.0009
88	37	0.0257	0.0020
89	37	0.0477	0.0026
90	37	0.1169	0.0035
91	37	0.1464	0.0034
92	37	0.0963	0.0023
93	37	0.0918	0.0021
94	37	0.1003	0.0021
95	37	0.0518	0.0016
96	37	0.0276	0.0021
97	37	0.0109	0.0014
91	38	0.0328	0.0016
92	38	0.0747	0.0019
93	38	0.1397	0.0023
94	38	0.1862	0.0026
95	38	0.1786	0.0026
96	38	0.1591	0.0026

Continued on next page

USC UNIVERSIDADE DE SANTIAGO DE COMPOSTELA

Table A.5 – continued from previous page

A	Z	Y(Z, A)	Statistical error
97	38	0.0775	0.0020
98	38	0.0543	0.0017
99	38	0.0198	0.0011
100	38	0.0120	0.0013
92	39	0.0087	0.0006
93	39	0.0212	0.0008
94	39	0.0585	0.0014
95	39	0.1163	0.0019
96	39	0.1743	0.0024
97	39	0.2339	0.0028
98	39	0.2135	0.0027
99	39	0.1722	0.0025
100	39	0.0647	0.0017
101	39	0.0295	0.0012
102	39	0.0160	0.0009
94	40	0.0122	0.0007
95	40	0.0117	0.0005
96	40	0.0471	0.0011
97	40	0.0915	0.0017
98	40	0.1701	0.0023
99	40	0.2226	0.0026
100	40	0.2735	0.0029
101	40	0.2331	0.0029
102	40	0.1595	0.0024
103	40	0.0558	0.0014
104	40	0.0160	0.0008
105	40	0.0113	0.0014
97	41	0.0120	0.0007
98	41	0.0218	0.0007
99	41	0.0443	0.0010
100	41	0.1074	0.0017
101	41	0.2111	0.0026
102	41	0.2395	0.0028
103	41	0.2538	0.0028
104	41	0.1437	0.0021
105	41	0.0771	0.0016
106	41	0.0250	0.0010
107	41	0.0107	0.0008
99	42	0.0094	0.0007
100	42	0.0164	0.0007
101	42	0.0330	0.0010
102	42	0.0937	0.0017
103	42	0.1794	0.0023
104	42	0.2414	0.0029
105	42	0.2208	0.0028
106	42	0.1543	0.0023
107	42	0.0678	0.0016
108	42	0.0317	0.0012
109	42	0.0185	0.0009
110	42	0.0096	0.0009
102	43	0.0118	0.0006
103	43	0.0165	0.0007
104	43	0.0389	0.0012
105	43	0.1125	0.0019
106	43	0.1504	0.0022
107	43	0.1756	0.0024
108	43	0.1421	0.0023
109	43	0.0847	0.0018
110	43	0.0295	0.0011
111	43	0.0197	0.0010
112	43	0.0119	0.0010
104	44	0.0127	0.0007
105	44	0.0149	0.0008
106	44	0.0381	0.0011
107	44	0.0772	0.0015
108	44	0.1168	0.0020
109	44	0.1312	0.0022
110	44	0.1276	0.0021
111	44	0.0736	0.0018
112	44	0.0438	0.0014
113	44	0.0310	0.0012

Continued on next page

USC UNIVERSIDADE DE SANTIAGO DE COMPOSTELA

Table A.5 – continued from previous page

A	Z	Y(Z, A)	Statistical error
114	44	0.0145	0.0010
107	45	0.0105	0.0006
108	45	0.0227	0.0009
109	45	0.0350	0.0010
110	45	0.0627	0.0014
111	45	0.0939	0.0018
112	45	0.0923	0.0018
113	45	0.0921	0.0019
114	45	0.0470	0.0014
115	45	0.0279	0.0011
116	45	0.0184	0.0011
117	45	0.0122	0.0010
109	46	0.0101	0.0007
110	46	0.0133	0.0006
111	46	0.0219	0.0008
112	46	0.0427	0.0011
113	46	0.0640	0.0015
114	46	0.0887	0.0017
115	46	0.0745	0.0015
116	46	0.0474	0.0013
117	46	0.0287	0.0011
118	46	0.0222	0.0011
119	46	0.0197	0.0012
120	46	0.0304	0.0035
112	47	0.0113	0.0007
113	47	0.0172	0.0009
114	47	0.0283	0.0010
115	47	0.0424	0.0013
116	47	0.0790	0.0017
117	47	0.0873	0.0018
118	47	0.0709	0.0016
119	47	0.0466	0.0014
120	47	0.0268	0.0012
121	47	0.0242	0.0011
122	47	0.0149	0.0010
115	48	0.0148	0.0007
116	48	0.0222	0.0010
117	48	0.0409	0.0012
118	48	0.0669	0.0015
119	48	0.0813	0.0018
120	48	0.0931	0.0019
121	48	0.0578	0.0016
122	48	0.0368	0.0013
123	48	0.0236	0.0011
124	48	0.0191	0.0010
125	48	0.0157	0.0014
117	49	0.0097	0.0006
118	49	0.0169	0.0008
119	49	0.0222	0.0009
120	49	0.0426	0.0012
121	49	0.0675	0.0016
122	49	0.0693	0.0016
123	49	0.0649	0.0016
124	49	0.0549	0.0015
125	49	0.0332	0.0013
126	49	0.0221	0.0010
127	49	0.0201	0.0010
128	49	0.0206	0.0012
129	49	0.0168	0.0011
130	49	0.0161	0.0015
131	49	0.0149	0.0018
132	49	0.0161	0.0019
120	50	0.0135	0.0007
121	50	0.0135	0.0007
122	50	0.0352	0.0011
123	50	0.0636	0.0015
124	50	0.0757	0.0016
125	50	0.0861	0.0018
126	50	0.0626	0.0016
127	50	0.0611	0.0015
128	50	0.0524	0.0014

Continued on next page

USC UNIVERSIDADE DE SANTIAGO DE COMPOSTELA

Table A.5 – continued from previous page

A	Z	Y(Z, A)	Statistical error
129	50	0.0370	0.0013
130	50	0.0375	0.0013
131	50	0.0335	0.0012
132	50	0.0247	0.0013
133	50	0.0244	0.0013
134	50	0.0162	0.0052
122	51	0.0111	0.0007
123	51	0.0143	0.0007
124	51	0.0198	0.0009
125	51	0.0394	0.0013
126	51	0.0590	0.0014
127	51	0.0834	0.0018
128	51	0.1002	0.0019
129	51	0.0840	0.0020
130	51	0.1067	0.0020
131	51	0.1079	0.0021
132	51	0.1148	0.0022
133	51	0.0923	0.0020
134	51	0.0327	0.0016
135	51	0.0231	0.0012
136	51	0.0142	0.0015
125	52	0.0111	0.0008
126	52	0.0213	0.0008
127	52	0.0289	0.0010
128	52	0.0454	0.0013
129	52	0.0648	0.0016
130	52	0.0866	0.0018
131	52	0.1250	0.0021
132	52	0.1290	0.0021
133	52	0.1725	0.0028
134	52	0.1757	0.0027
135	52	0.1057	0.0023
136	52	0.0621	0.0017
137	52	0.0177	0.0010
138	52	0.0141	0.0009
127	53	0.0081	0.0006
128	53	0.0100	0.0006
129	53	0.0186	0.0007
130	53	0.0291	0.0010
131	53	0.0412	0.0012
132	53	0.0772	0.0017
133	53	0.1075	0.0020
134	53	0.1224	0.0021
135	53	0.1875	0.0027
136	53	0.1476	0.0025
137	53	0.1118	0.0021
138	53	0.0564	0.0015
139	53	0.0313	0.0013
140	53	0.0137	0.0007
130	54	0.0078	0.0006
131	54	0.0111	0.0006
132	54	0.0188	0.0008
133	54	0.0325	0.0010
134	54	0.0518	0.0013
135	54	0.0760	0.0016
136	54	0.1055	0.0019
137	54	0.1112	0.0020
138	54	0.1286	0.0022
139	54	0.0965	0.0018
140	54	0.0687	0.0015
141	54	0.0258	0.0011
142	54	0.0132	0.0008
143	54	0.0100	0.0008
132	55	0.0074	0.0004
133	55	0.0081	0.0004
134	55	0.0156	0.0007
135	55	0.0236	0.0008
136	55	0.0372	0.0011
137	55	0.0622	0.0014
138	55	0.0652	0.0015
139	55	0.0846	0.0016

Continued on next page

USC UNIVERSIDADE DE SANTIAGO DE COMPOSTELA

Table A.5 – continued from previous page

A	Z	Y(Z, A)	Statistical error
140	55	0.0803	0.0014
141	55	0.0897	0.0017
142	55	0.0634	0.0015
143	55	0.0291	0.0011
144	55	0.0176	0.0007
145	55	0.0081	0.0008
135	56	0.0095	0.0007
136	56	0.0085	0.0006
137	56	0.0144	0.0007
138	56	0.0314	0.0010
139	56	0.0391	0.0011
140	56	0.0571	0.0013
141	56	0.0534	0.0014
142	56	0.0801	0.0017
143	56	0.0904	0.0017
144	56	0.0733	0.0016
145	56	0.0391	0.0012
146	56	0.0180	0.0007
147	56	0.0120	0.0008
138	57	0.0078	0.0006
139	57	0.0140	0.0008
140	57	0.0127	0.0006
141	57	0.0234	0.0009
142	57	0.0343	0.0011
143	57	0.0462	0.0012
144	57	0.0607	0.0015
145	57	0.0605	0.0016
146	57	0.0469	0.0013
147	57	0.0354	0.0013
148	57	0.0144	0.0007
149	57	0.0122	0.0009
141	58	0.0089	0.0007
142	58	0.0113	0.0007
143	58	0.0142	0.0008
144	58	0.0206	0.0008
145	58	0.0343	0.0012
146	58	0.0288	0.0011
147	58	0.0333	0.0011
148	58	0.0303	0.0009
149	58	0.0260	0.0011
150	58	0.0152	0.0009
151	58	0.0102	0.0009
144	59	0.0086	0.0006
145	59	0.0092	0.0006
146	59	0.0176	0.0008
147	59	0.0152	0.0007
148	59	0.0164	0.0009
149	59	0.0248	0.0010
150	59	0.0157	0.0008
151	59	0.0159	0.0009
152	59	0.0168	0.0008
153	59	0.0094	0.0007
148	60	0.0099	0.0007
149	60	0.0117	0.0007
150	60	0.0161	0.0008
151	60	0.0190	0.0010
152	60	0.0125	0.0007
153	60	0.0118	0.0007
151	61	0.0109	0.0007
152	61	0.0119	0.0007
153	61	0.0126	0.0008
154	61	0.0135	0.0008
155	61	0.0152	0.0011
156	62	0.0134	0.0014
157	62	0.0119	0.0010

USC UNIVERSIDADE DE SANTIAGO DE COMPOSTELA

USC
UNIVERSIDADE
DE SANTIAGO
DE COMPOSTELA

Bibliography

[1] J. Chadwick. "Letters to the Editor - Possible Existence of a Neutron". In: *Nature* 19.1 (1932), pp. 66–66. ISSN: 0033-8419. DOI: 10.1148/19.1.66a.

[2] E. Fermi. "Possible Production of Elements of Atomic Number Higher than 92". In: *Nature* (1934), pp. 898–899.

[3] Lise Meitner, Otto Hahn, and Fritz Strassmann. "Über die Umwandlungsreihen des Urans, die durch Neutronenbestrahlung erzeugt werden". In: *The European Physical Journal A* (1937). DOI: 10.1007/bf01340321.

[4] Curie, Irène and Savitch, Paul. "Sur les radioéléments formés dans l'uranium irradié par les neutrons. II". In: *J. Phys. Radium* 9.9 (1938), pp. 355–359. DOI: 10.1051/jphysrad:0193800909035500. URL: https://doi.org/10.1051/jphysrad:0193800909035500.

[5] O Hahn and F Strassmann. "Uber den Nachweis und das Verhalten der bei der Bestrahlung des Urans mittels Neutronen entstehenden Erdalkalimetalle". In: *Naturwissenschaften* 27.1 (1939), pp. 11–15. ISSN: 1432-1904. DOI: 10.1007/BF01488241. URL: https://doi.org/10.1007/BF01488241.

[6] Meitner L. and O. R. Frisch. "Letters to the Editor - Disintegration of Uranium by Neutrons: a New Type of Nuclear Reaction". In: 143.3615 (1939), pp. 239–240. ISSN: 0024-2527. DOI: 10.5860/lrts.49n3.150.

[7] George Gamow. "Mass Defect Curve and Nuclear Constitution". In: *Proceedings of The Royal Society A: Mathematical, Physical and Engineering Sciences* 126 (1930), pp. 632–644.

[8] Niels Bohr. "Neutron Capture and Nuclear Constitution". In: *Nature* 137 (1936), pp. 344–348. DOI: 10.1038/137344a0.

[9] Niels Bohr and John Archibald Wheeler. "The Mechanism of Nuclear Fission". In: *Phys. Rev.* 56 (5 1939), pp. 426–450. DOI: 10.1103/PhysRev.56.426. URL: https://link.aps.org/doi/10.1103/PhysRev.56.426.

[10] S. Frankel and N. Metropolis. "Calculations in the Liquid-Drop Model of Fission". In: *Phys. Rev.* 72 (10 1947), pp. 914–925. DOI: 10.1103/PhysRev.72.914. URL: https://link.aps.org/doi/10.1103/PhysRev.72.914.

[11] O. R. FRISCH. "Physical Evidence for the Division of Heavy Nuclei under Neutron Bombardment". In: *Nature* 143 (1939), pp. 276–276.

[12] Aurel Bulgac. "Fission-fragment excitation energy sharing beyond scission". In: *Phys. Rev. C* 102 (4 2020), p. 044609. DOI: 10.1103/PhysRevC.102.044609. URL: https://link.aps.org/doi/10.1103/PhysRevC.102.044609.

[13] Takatoshi Ichikawa et al. "Contrasting fission potential-energy structure of actinides and mercury isotopes". In: *Phys. Rev. C* 86 (2 2012), p. 024610. DOI: 10.1103/PhysRevC.86.024610. URL: https://link.aps.org/doi/10.1103/PhysRevC.86.024610.

USC UNIVERSIDADE DE SANTIAGO DE COMPOSTELA

[14] D.J. Hinde, D. Hilscher, and H. Rossner. "Fission timescales of excited nuclei". In: *Nuclear Physics A* 502 (1989), pp. 497–514. ISSN: 0375-9474. DOI: https://doi.org/10.1016/0375-9474(89)90684-2. URL: https://www.sciencedirect.com/science/article/pii/0375947489906842.

[15] Karl-Heinz Schmidt and Beatriz Jurado. "Review on the progress in nuclear fission experimental methods and theoretical descriptions". In: *Reports on Progress in Physics* 81.10 (2018), p. 106301. DOI: 10.1088/1361-6633/aacfa7. URL: https://doi.org/10.1088%2F1361-6633%2Faacfa7.

[16] Yusuke Tanimura, Denis Lacroix, and Guillaume Scamps. "Collective aspects deduced from time-dependent microscopic mean-field with pairing: Application to the fission process". In: *Physical Review C* 92.3 (2015). DOI: 10.1103/physrevc.92.034601. URL: https://doi.org/10.1103%2Fphysrevc.92.034601.

[17] Karl-Heinz Schmidt and Beatriz Jurado. "Entropy Driven Excitation Energy Sorting in Superfluid Fission Dynamics". In: *Phys. Rev. Lett.* 104 (21 2010), p. 212501. DOI: 10.1103/PhysRevLett.104.212501. URL: https://link.aps.org/doi/10.1103/PhysRevLett.104.212501.

[18] Manuel Caamaño and Fanny Farget. "Energy balance and deformation at scission in 240Pu fission". In: *Physics Letters B* 770 (2017), pp. 72–76. ISSN: 0370-2693. DOI: https://doi.org/10.1016/j.physletb.2017.04.041. URL: https://www.sciencedirect.com/science/article/pii/S0370269317303155.

[19] C. F. V. Weizsäcker. "Zur Theorie der Kernmassen". In: *Zeitschrift fur Physik* 96.7-8 (1935), pp. 431–458. DOI: 10.1007/BF01337700.

[20] Maria G. Mayer. "On Closed Shells in Nuclei". In: *Phys. Rev.* 74 (3 1948), pp. 235–239. DOI: 10.1103/PhysRev.74.235. URL: https://link.aps.org/doi/10.1103/PhysRev.74.235.

[21] S. G. Nilsson. "Binding states of individual nucleons in strongly deformed nuclei". In: *Kong. Dan. Vid. Sel. Mat. Fys. Med.* 29N16 (1955), pp. 1–69.

[22] V.M. Strutinsky. "Shell effects in nuclear masses and deformation energies". In: *Nuclear Physics A* 95.2 (1967), pp. 420–442. ISSN: 0375-9474. DOI: https://doi.org/10.1016/0375-9474(67)90510-6. URL: https://www.sciencedirect.com/science/article/pii/0375947467905106.

[23] M. Bolsterli et al. "New Calculation of Fission Barriers for Heavy and Superheavy Nuclei". In: *Phys. Rev. C* 5 (3 1972), pp. 1050–1077. DOI: 10.1103/PhysRevC.5.1050. URL: https://link.aps.org/doi/10.1103/PhysRevC.5.1050.

[24] P. Möller and J.R. Nix. "Proceedings of the Third IAEA Symposium on the Physics and Chemistry of fission," in: *INDC(NDS)* 245 (1974), p. 103.

[25] B. D. Wilkins, E. P. Steinberg, and R. R. Chasman. "Scission-point model of nuclear fission based on deformed-shell effects". In: *Phys. Rev. C* 14 (5 1976), pp. 1832–1863. DOI: 10.1103/PhysRevC.14.1832. URL: https://link.aps.org/doi/10.1103/PhysRevC.14.1832.

[26] J. Bardeen, L. N. Cooper, and J. R. Schrieffer. "Theory of Superconductivity". In: *Phys. Rev.* 108 (5 1957), pp. 1175–1204. DOI: 10.1103/PhysRev.108.1175. URL: https://link.aps.org/doi/10.1103/PhysRev.108.1175.

[27] H. J. Krappe and J. R. Nix. "Modified definition of the surface energy in the liquid drop formula". In: *Physics and Chemistry of Fission, Proceedings of the third IAEA Symposium* 1 (1973), p. 159. URL: https://escholarship.org/uc/item/48g4m7wt.

[28] E. Konecny and H. W. Schmitt. "Fission Energetics and Neutron Emission in 13-MeV Proton-Induced Fission of ^{226}Ra". In: *Phys. Rev.* 172 (4 1968), pp. 1213–1226. DOI: 10.1103/PhysRev.172.1213. URL: https://link.aps.org/doi/10.1103/PhysRev.172.1213.

[29] W. Reisdorf et al. "Fission fragment K x-ray emission and nuclear charge distribution for thermal neutron fission of 233U, 235U, 239Pu and spontaneous fission of 252Cf". In: *Nuclear Physics A* 177.2 (1971), pp. 337–378. ISSN: 0375-9474. DOI: https://doi.org/10.1016/0375-9474(71)90297-1. URL: https://www.sciencedirect.com/science/article/pii/0375947471902971.

[30] J.-F. Lemaître et al. "Fully microscopic scission-point model to predict fission fragment observables". In: *Phys. Rev. C* 99 (3 2019), p. 034612. DOI: 10.1103/PhysRevC.99.034612. URL: https://link.aps.org/doi/10.1103/PhysRevC.99.034612.

[31] U. Brosa, S. Grossmann, and A. Mueller. "Nuclear scission". In: *AC* 197:4 (1990). DOI: 10.1016/0370-1573(90)90114-H.

[32] U. Brosa. "Sawtooth curve of neutron multiplicity". In: *Phys. Rev. C* 32 (4 1985), pp. 1438–1441. DOI: 10.1103/PhysRevC.32.1438. URL: https://link.aps.org/doi/10.1103/PhysRevC.32.1438.

[33] C Wagemans. "The nuclear fission process". In: (1991). URL: https://www.osti.gov/biblio/6430419.

[34] Al-Adili et al. "Fragment-mass, kinetic energy, and angular distributions for ^{234}U(n, f) at incident neutron energies from $E_n = 0.2$ MeV to 5.0 MeV". In: *Phys. Rev. C* 93 (3 2016), p. 034603. DOI: 10.1103/PhysRevC.93.034603. URL: https://link.aps.org/doi/10.1103/PhysRevC.93.034603.

[35] P Möller et al. "Nuclear fission modes and fragment mass asymmetries in a five-dimensional deformation space". In: *Nature* 409.6822 (2001), pp. 785–790. ISSN: 1476-4687. DOI: 10.1038/35057204. URL: https://doi.org/10.1038/35057204.

[36] V. E. Viola, K. Kwiatkowski, and M. Walker. "Systematics of fission fragment total kinetic energy release". In: *Phys. Rev. C* 31 (4 1985), pp. 1550–1552. DOI: 10.1103/PhysRevC.31.1550. URL: https://link.aps.org/doi/10.1103/PhysRevC.31.1550.

[37] Peter Möller et al. "Nuclear ground-state masses and deformations: FRDM(2012)". In: *Atomic Data and Nuclear Data Tables* 109 (2015), pp. 1–204. URL: https://api.semanticscholar.org/CorpusID:118707897.

[38] P. Jachimowicz, M. Kowal, and J. Skalski. "Static fission properties of actinide nuclei". In: *Phys. Rev. C* 101 (1 2020), p. 014311. DOI: 10.1103/PhysRevC.101.014311. URL: https://link.aps.org/doi/10.1103/PhysRevC.101.014311.

[39] K. Pomorski and B. Nerlo-Pomorska. "Nuclear Fission Within the Lublinâ€"Strasbourg Drop Model". In: *Acta Physica Polonica B Proceedings Supplement* 6 (2013), p. 1129. DOI: 10.5506/APhysPolBSupp.6.1129.

[40] Aurel Bulgac et al. "Fission dynamics of ^{240}Pu from saddle to scission and beyond". In: *Phys. Rev. C* 100 (3 2019), p. 034615. DOI: 10.1103/PhysRevC.100.034615. URL: https://link.aps.org/doi/10.1103/PhysRevC.100.034615.

[41] Aurel Bulgac et al. "Nuclear Fission: from more phenomenology and adjusted parameters to more fundamental theory and increased predictive power". In: *arXiv: Nuclear Theory* (2017). URL: https://api.semanticscholar.org/CorpusID:119218304.

[42] Guillaume Scamps and Cédric Simenel. "Impact of pear-shaped fission fragments on mass-asymmetric fission in actinides". In: *Nature* 564.7736 (2018), pp. 382–385. ISSN: 0028-0836. DOI: 10.1038/s41586-018-0780-0. URL: https://doi.org/10.1038/s41586-018-0780-0.

[43] C. Simenel and A. S. Umar. "Formation and dynamics of fission fragments". In: *Phys. Rev. C* 89 (3 2014), p. 031601. DOI: 10.1103/PhysRevC.89.031601. URL: https://link.aps.org/doi/10.1103/PhysRevC.89.031601.

[44] Philip Goddard, Paul Stevenson, and Arnau Rios. "Fission dynamics within time-dependent Hartree-Fock: Deformation-induced fission". In: *Phys. Rev. C* 92 (5 2015), p. 054610. DOI: 10.1103/PhysRevC.92.054610. URL: https://link.aps.org/doi/10.1103/PhysRevC.92.054610.

[45] B. Bucher et al. "Direct Evidence of Octupole Deformation in Neutron-Rich ^{144}Ba". In: *Phys. Rev. Lett.* 116 (11 2016), p. 112503. DOI: 10.1103/PhysRevLett.116.112503. URL: https://link.aps.org/doi/10.1103/PhysRevLett.116.112503.

[46] K.-H. Schmidt et al. "General Description of Fission Observables: GEF Model Code". In: *Nuclear Data Sheets* 131 (2016). Special Issue on Nuclear Reaction Data, pp. 107–221. ISSN: 0090-3752. DOI: https://doi.org/10.1016/j.nds.2015.12.009. URL: https://www.sciencedirect.com/science/article/pii/S0090375215000745.

[47] W.D. Myers and W.J. Swiatecki. "Nuclear properties according to the Thomas-Fermi model". In: *Nuclear Physics A* 601.2 (1996), pp. 141–167. ISSN: 0375-9474. DOI: https://doi.org/10.1016/0375-9474(95)00509-9. URL: https://www.sciencedirect.com/science/article/pii/0375947495005099.

[48] Aleksandra KeliÄ‡ and Karl-Heinz Schmidt. "Assessment of saddle-point-mass predictions for astrophysical applications". In: *Physics Letters B* 634.4 (2006), pp. 362–367. ISSN: 0370-2693. DOI: https://doi.org/10.1016/j.physletb.2006.02.010. URL: https://www.sciencedirect.com/science/article/pii/S0370269306001717.

[49] U. Mosel and H.W. Schmitt. "Potential energy surfaces for heavy nuclei in the two-center model". In: *Nuclear Physics A* 165.1 (1971), pp. 73–96. ISSN: 0375-9474. DOI: https://doi.org/10.1016/0375-9474(71)90150-3. URL: https://www.sciencedirect.com/science/article/pii/0375947471901503.

[50] J.L. Sida et al. "Mass, charge, and energy distributions in very asymmetric thermal fission of 235U". In: *Nuclear Physics A* 502 (1989), pp. 233–242. ISSN: 0375-9474. DOI: https://doi.org/10.1016/0375-9474(89)90664-7. URL: https://www.sciencedirect.com/science/article/pii/0375947489906647.

[51] K.-H. Schmidt, A. Kelic, and M. V. Ricciardi. "Experimental evidence for the separability of compound-nucleus and fragment properties in fission". In: *Europhysics Letters* 83.3 (2008), p. 32001. DOI: 10.1209/0295-5075/83/32001. URL: https://dx.doi.org/10.1209/0295-5075/83/32001.

[52] H. Nifenecker. "A dynamical treatment of isobaric widths in fission : An example of frozen quantal fluctuations". In: *J. Physique Lett.* 41.3 (1980), "47–51". DOI: 10.1051/jphyslet:0198000410304700. URL: https://doi.org/10.1051/jphyslet:0198000410304700.

[53] Christelle Schmitt, Karl-Heinz Schmidt, and Beatriz Jurado. "The GEF model: Assessment of fission-fragment properties over an extended region". In: *EPJ Web Conf.* 169 (2018). Ed. by F. -J. Hambsch, N. Carjan, and I. Ruskov, p. 00022. DOI: 10.1051/epjconf/201816900022.

[54] Karl-Heinz Schmidt and Beatriz Jurado. "Inconsistencies in the description of pairing effects in nuclear level densities". In: *Phys. Rev. C* 86 (4 2012), p. 044322. DOI: 10.1103/PhysRevC.86.044322. URL: https://link.aps.org/doi/10.1103/PhysRevC.86.044322.

[55] T. von Egidy and D. Bucurescu. "Experimental energy-dependent nuclear spin distributions". In: *Phys. Rev. C* 80 (5 2009), p. 054310. DOI: 10.1103/PhysRevC.80.054310. URL: https://link.aps.org/doi/10.1103/PhysRevC.80.054310.

[56] B. Heusch et al. "The reaction mechanism in the system $^{132}Xe + {}^{56}Fe$ at 5.73 MeV/u: Evidence for a new type of strongly damped collisions". In: *Zeitschrift für Physik A Atoms and Nuclei* 288.4 (1978), pp. 391–400. DOI: 10.1007/BF01417723. URL: https://doi.org/10.1007/BF01417723.

[57] R. Bass. "Fusion of heavy nuclei in a classical model". In: *Nucl. Phys. A* 231 (1974), pp. 45–63. DOI: 10.1016/0375-9474(74)90292-9.

[58] J. Blocki et al. "Proximity forces". In: *Annals Phys.* 105 (1977), pp. 427–462. DOI: 10.1016/0003-4916(77)90249-4.

[59] S. Cohen, F. Plasil, and W.J. Swiatecki. "Equilibrium configurations of rotating charged or gravitating liquid masses with surface tension. II". In: *Annals of Physics* 82.2 (1974), pp. 557–596. ISSN: 0003-4916. DOI: https://doi.org/10.1016/0003-4916(74)90126-2. URL: https://www.sciencedirect.com/science/article/pii/0003491674901262.

[60] C. Lebrun et al. "Influence of angular momentum on the mass distribution width of heavy ion induced fission: What is the frontier between fission and quasi-fission?" In: *Nuclear Physics A* 321.1 (1979), pp. 207–212. ISSN: 0375-9474. DOI: https://doi.org/10.1016/0375-9474(79)90693-6. URL: https://www.sciencedirect.com/science/article/pii/0375947479906936.

[61] B. Borderie et al. "A possible mechanism in heavy ion induced reactions: Fast fission process". In: *Zeitschrift für Physik A Atoms and Nuclei* 299.3 (1981), pp. 263–271. ISSN: 0939-7922. DOI: 10.1007/BF01443944. URL: https://doi.org/10.1007/BF01443944.

[62] W. Q. Shen et al. "Fission and quasifission in U-induced reactions". In: *Phys. Rev. C* 36 (1 1987), pp. 115–142. DOI: 10.1103/PhysRevC.36.115. URL: https://link.aps.org/doi/10.1103/PhysRevC.36.115.

[63] D.J. Hinde, M. Dasgupta, and E.C. Simpson. "Experimental studies of the competition between fusion and quasifission in the formation of heavy and superheavy nuclei". In: *Progress in Particle and Nuclear Physics* 118 (2021), p. 103856. ISSN: 0146-6410. DOI: https://doi.org/10.1016/j.ppnp.2021.103856. URL: https://www.sciencedirect.com/science/article/pii/S0146641021000107.

[64] P. Möller and J. R. Nix. "Potential-energy surfaces for asymmetric heavy-ion reactions". In: *Nucl. Phys. A* 281 (1977), pp. 354–372. DOI: 10.1016/0375-9474(77)90031-8.

[65] J. Tōke et al. "Quasi-fission - The mass-drift mode in heavy-ion reactions". In: *Nuclear Physics A* 440.2 (1985), pp. 327–365. ISSN: 0375-9474. DOI: https://doi.org/10.1016/0375-9474(85)90344-6. URL: https://www.sciencedirect.com/science/article/pii/0375947485903446.

[66] S. Bjornholm and W.J. Swiatecki. "Dynamical aspects of nucleus-nucleus collisions". In: *Nuclear Physics A* 391.2 (1982), pp. 471–504. ISSN: 0375-9474. DOI: https://doi.org/10.1016/0375-9474(82)90621-2. URL: https://www.sciencedirect.com/science/article/pii/0375947482906212.

[67] R. du Rietz et al. "Predominant Time Scales in Fission Processes in Reactions of S, Ti and Ni with W: Zeptosecond versus Attosecond". In: *Phys. Rev. Lett.* 106 (5 2011), p. 052701. DOI: 10.1103/PhysRevLett.106.052701. URL: https://link.aps.org/doi/10.1103/PhysRevLett.106.052701.

[68] D. J. Hinde et al. "Disentangling Effects of Nuclear Structure in Heavy Element Formation". In: *Phys. Rev. Lett.* 100 (20 2008), p. 202701. DOI: 10.1103/PhysRevLett.100.202701. URL: https://link.aps.org/doi/10.1103/PhysRevLett.100.202701.

[69] R. du Rietz et al. "Mapping quasifission characteristics and timescales in heavy element formation reactions". In: *Phys. Rev. C* 88 (5 2013), p. 054618. DOI: 10.1103/PhysRevC.88.054618. URL: https://link.aps.org/doi/10.1103/PhysRevC.88.054618.

[70] J. Tōke et al. "Compound nucleus fission and quasi-fission in reactions of 238U with 16O and 27Al". In: *Physics Letters B* 142.4 (1984), pp. 258–262. ISSN: 0370-2693. DOI: https://doi.org/10.1016/0370-2693(84)91194-8. URL: https://www.sciencedirect.com/science/article/pii/0370269384911948.

[71] K. H. Schmidt et al. "Relativistic radioactive beams: A New access to nuclear fission studies". In: *Nucl. Phys. A* 665 (2000), pp. 221–267. DOI: 10.1016/S0375-9474(99)00384-X.

[72] A. N. Andreyev et al. "New Type of Asymmetric Fission in Proton-Rich Nuclei". In: *Phys. Rev. Lett.* 105 (25 2010), p. 252502. DOI: 10.1103/PhysRevLett.105.252502. URL: https://link.aps.org/doi/10.1103/PhysRevLett.105.252502.

[73] Guillaume Scamps and Cédric Simenel. "Effect of shell structure on the fission of sub-lead nuclei". In: *Phys. Rev. C* 100 (4 2019), p. 041602. DOI: 10.1103/PhysRevC.100.041602. URL: https://link.aps.org/doi/10.1103/PhysRevC.100.041602.

[74] V. E. Oberacker, A. S. Umar, and C. Simenel. "Dissipative dynamics in quasifission". In: *Phys. Rev. C* 90 (5 2014), p. 054605. DOI: 10.1103/PhysRevC.90.054605. URL: https://link.aps.org/doi/10.1103/PhysRevC.90.054605.

[75] C. Simenel et al. "Comparison of fission and quasi-fission modes". In: *Physics Letters B* 822 (2021), p. 136648. ISSN: 0370-2693. DOI: https://doi.org/10.1016/j.physletb.2021.136648. URL: https://www.sciencedirect.com/science/article/pii/S0370269321005888.

[76] K.-H. Schmidt et al. "Low-energy fission studies of neutron-deficient projectile fragments of 238U". In: *Physics Letters B* 325.3 (1994), pp. 313–316. ISSN: 0370-2693. DOI: https://doi.org/10.1016/0370-2693(94)90017-5. URL: https://www.sciencedirect.com/science/article/pii/0370269394900175.

[77] Martin, Julie-Fiona et al. "Studies on fission with ALADIN - Precise and simultaneous measurement of fission yields, total kinetic energy and total prompt neutron multiplicity at GSI". In: *Eur. Phys. J. A* 51.12 (2015), p. 174. DOI: 10.1140/epja/i2015-15174-0. URL: https://doi.org/10.1140/epja/i2015-15174-0.

[78] M. Caamaño et al. "Isotopic yield distributions of transfer- and fusion-induced fission from 238U+12C reactions in inverse kinematics". In: *Physical Review C* 88.2 (2013). DOI: 10.1103/physrevc.88.024605.

[79] D. Ramos et al. "Isotopic fission-fragment distributions of ^{238}U,^{239} Np,^{240} Pu,^{244} Cm, and ^{250}Cf produced through inelastic scattering, transfer, and fusion reactions in inverse kinematics". In: *Phys. Rev. C* 97 (5 2018), p. 054612. DOI: 10.1103/PhysRevC.97.054612. URL: https://link.aps.org/doi/10.1103/PhysRevC.97.054612.

[80] F. Azaiez et al. “GANIL / SPIRAL - 2001-2007 - Achievements, Highlights and Perspectives”. In: (2008).

[81] M. Vandebrouck et al. “Dual Position Sensitive MWPC for tracking reaction products at VAMOS++”. In: *Nuclear Instruments and Methods in Physics Research Section A: Accelerators, Spectrometers, Detectors and Associated Equipment* 812 (2016), pp. 112–117. ISSN: 0168-9002. DOI: https://doi.org/10.1016/j.nima.2015.12.040. URL: https://www.sciencedirect.com/science/article/pii/S0168900215016113.

[82] C. Rodríguez-Tajes et al. “Transfer reactions in inverse kinematics: An experimental approach for fission investigations”. In: *Phys. Rev. C* 89 (2 2014), p. 024614. DOI: 10.1103/PhysRevC.89.024614. URL: https://link.aps.org/doi/10.1103/PhysRevC.89.024614.

[83] S. Akkoyun, A. Algora, and B. Alikhani. “AGATAâ€”Advanced GAmma Tracking Array”. In: *Nuclear Instruments and Methods in Physics Research Section A: Accelerators, Spectrometers, Detectors and Associated Equipment* 668 (2012), pp. 26–58. ISSN: 0168-9002. DOI: https://doi.org/10.1016/j.nima.2011.11.081. URL: https://www.sciencedirect.com/science/article/pii/S0168900211021516.

[84] Herve Savajols. “VAMOS: a VAriable MOde high acceptance spectrometer”. In: *Nucl. Phys. A* 654.1 (1999), pp. 1027c–1032c. DOI: 10.1016/S0375-9474(00)88592-9.

[85] Herve Savajols. “VAMOS : a VAriable MOde high acceptance Spectrometer for identifying reaction products induced by SPIRAL beams”. In: *Nuclear Instruments and Methods in Physics Research Section B: Beam Interactions with Materials and Atoms* 204 (2003), pp. 146–153. DOI: 10.1016/S0168-583X(02)01908-0.

[86] S. Pullanhiotan et al. “Performance of VAMOS for reactions near the Coulomb barrier”. In: *Nuclear Instruments and Methods in Physics Research Section A: Accelerators, Spectrometers, Detectors and Associated Equipment* 593.3 (2008), pp. 343–352. ISSN: 0168-9002. DOI: https://doi.org/10.1016/j.nima.2008.05.003. URL: https://www.sciencedirect.com/science/article/pii/S0168900208007080.

[87] S. Pullanhiotan et al. “Improvement in the reconstruction method for VAMOS spectrometer”. In: *Nuclear Instruments and Methods in Physics Research Section B: Beam Interactions with Materials and Atoms* 266.19 (2008). Proceedings of the XVth International Conference on Electromagnetic Isotope Separators and Techniques Related to their Applications, pp. 4148–4152. ISSN: 0168-583X. DOI: https://doi.org/10.1016/j.nimb.2008.05.024. URL: https://www.sciencedirect.com/science/article/pii/S0168583X08006952.

[88] M. Rejmund et al. “Performance of the improved larger acceptance spectrometer: VAMOS++”. In: *Nuclear Instruments and Methods in Physics Research Section A: Accelerators, Spectrometers, Detectors and Associated Equipment* 646.1 (2011), pp. 184–191. ISSN: 0168-9002. DOI: https://doi.org/10.1016/j.nima.2011.05.007. URL: https://www.sciencedirect.com/science/article/pii/S0168900211008515.

[89] Carme Rodriguez-Tajes et al. “Isotopic Distributions of Fission Fragments from Transfer-induced Fission”. In: *Physics Procedia* 47 (2013), pp. 125–130. DOI: 10.1016/j.phpro.2013.06.018.

USC UNIVERSIDADE DE SANTIAGO DE COMPOSTELA

[90] H. Hotzl and R. Winkler. "Experiences with large-area frisch grid chambers in low-level alpha spectrometry". In: *Nuclear Instruments and Methods in Physics Research* 223.2 (1984), pp. 290–294. ISSN: 0167-5087. DOI: https://doi.org/10.1016/0167-5087(84)90664-1. URL: https://www.sciencedirect.com/science/article/pii/0167508784906641.

[91] K.A. Olive. "Review of Particle Physics". In: *Chinese Physics C* 38.9 (2014), p. 090001. DOI: 10.1088/1674-1137/38/9/090001. URL: https://dx.doi.org/10.1088/1674-1137/38/9/090001.

[92] Francois Méot. "The ray-tracing code Zgoubi". In: *Nuclear Instruments and Methods in Physics Research Section A: Accelerators, Spectrometers, Detectors and Associated Equipment* 427.1 (1999), pp. 353–356. ISSN: 0168-9002. DOI: https://doi.org/10.1016/S0168-9002(98)01508-3. URL: https://www.sciencedirect.com/science/article/pii/S0168900298015083.

[93] "TOSCA Static Field Analysis OPERA-3D". In: *Vector Fields, Bankside Kidlington, Oxford, England* 24 ().

[94] A. Lemasson and M. Rejmund. "Fast trajectory reconstruction techniques for the large acceptance magnetic spectrometer VAMOS++". In: *Nuclear Instruments and Methods in Physics Research Section A: Accelerators, Spectrometers, Detectors and Associated Equipment* 1054 (2023), p. 168407. ISSN: 0168-9002. DOI: https://doi.org/10.1016/j.nima.2023.168407. URL: https://www.sciencedirect.com/science/article/pii/S0168900223003972.

[95] A. Boujrad and F. Saillant. "The new GANIL data acquisition system". In: vol. 2. 2000, 12/192–12/193 vol.2. ISBN: 0-7803-6503-8. DOI: 10.1109/NSSMIC.2000.949968.

[96] O.B. Tarasov and D. Bazin. "LISE++ : design your own spectrometer". In: *Nuclear Physics A* 746 (2004). Proceedings of the Sixth International Conference on Radioactive Nuclear Beams (RNB6), pp. 411–414. ISSN: 0375-9474. DOI: https://doi.org/10.1016/j.nuclphysa.2004.09.063. URL: https://www.sciencedirect.com/science/article/pii/S0375947404010048.

[97] P. Marchand and Louis Marmet. "Binomial smoothing filter: A way to avoid some pitfalls of least-squares polynomial smoothing". In: *Review of Scientific Instruments* 54 (1983), pp. 1034–1041. DOI: 10.1063/1.1137498.

[98] Aradhana Shrivastava et al. "Prompt γ-ray spectroscopy of isotopically identified fission fragments". In: *Phys. Rev. C* 80 (2009). DOI: 10.1103/PhysRevC.80.051305.

[99] B. B. Back et al. "Angular distributions in heavy-ion-induced fission". In: *Phys. Rev. C* 32 (1985). Phys.Rev.C 33, 385–385 (1986), pp. 195–213. DOI: 10.1103/PhysRevC.32.195.

[100] H. Rossner, J. R. Huizenga, and W. U. Schroder. "Fission fragment angular distributions". In: *Phys. Rev. C* 33 (1986), pp. 560–575. DOI: 10.1103/PhysRevC.33.560.

[101] E. Baron, M. Bajard, and Ch. Ricaud. "Charge exchange of very heavy ions in carbon foils and in the residual gas of GANIL cyclotrons". In: *Nuclear Instruments and Methods in Physics Research Section A: Accelerators, Spectrometers, Detectors and Associated Equipment* 328.1 (1993), pp. 177–182. ISSN: 0168-9002. DOI: https://doi.org/10.1016/0168-9002(93)90622-O. URL: https://www.sciencedirect.com/science/article/pii/016890029390622O.

[102] Diego Ramos Doval. "Fragment Distributions of Transfer- and Fusion-Induced Fission from ^{238}U+^{12}C Reactions Measured Through Inverse Kinematics". PhD thesis. Santiago de Compostela, 2016, p. 328.

[103] E. J. Winhold, P. T. Demos, and I. Halpern. "The Angular Distribution of Fission Fragments in the Photofission of Thorium". In: *Phys. Rev.* 87 (6 1952), pp. 1139–1140. DOI: 10.1103/PhysRev.87.1139. URL: https://link.aps.org/doi/10.1103/PhysRev.87.1139.

[104] R Vandenbosch and J R Huizenga. "Nuclear fission". In: (1973). URL: https://www.osti.gov/biblio/4359815.

[105] J. Tōke et al. "Compound nucleus fission and quasi-fission in reactions of 238 U with 16 O and 27 Al". In: *Phys. Lett. B* 142 (1984), pp. 258–262. DOI: 10.1016/0370-2693(84)91194-8.

[106] D. Ramos et al. "Insight into excitation energy and structure effects in fission from isotopic information in fission yields". In: *Physical Review C* 99.2 (2019), pp. 1–11. ISSN: 24699993. DOI: 10.1103/PhysRevC.99.024615.

[107] Reiner Bass. *Nuclear reactions with heavy ions*. Berlin : Springer-Verlag, 1980.

[108] M. Caamaño et al. "Characterization of the scission point from fission-fragment velocities". In: *Phys. Rev. C* 92 (3 2015), p. 034606. DOI: 10.1103/PhysRevC.92.034606. URL: https://link.aps.org/doi/10.1103/PhysRevC.92.034606.

[109] C. Böckstiegel et al. "Nuclear-fission studies with relativistic secondary beams: Analysis of fission channels". In: *Nuclear Physics A* 802.1 (2008), pp. 12–25. ISSN: 0375-9474. DOI: https://doi.org/10.1016/j.nuclphysa.2008.01.012. URL: https://www.sciencedirect.com/science/article/pii/S0375947408000328.

[110] Tie-shuan Fan, Ji-min Hu, and Shang-lian Bao. "Study of multichannel theory for the neutron induced fissions of actinide nuclei". In: *Nuclear Physics A* 591.2 (1995), pp. 161–181. ISSN: 0375-9474. DOI: https://doi.org/10.1016/0375-9474(95)00193-5. URL: https://www.sciencedirect.com/science/article/pii/0375947495001935.

[111] J.P. Bocquet and R. Brissot. "Mass, energy and nuclear charge distribution of fission fragments". In: *Nuclear Physics A* 502 (1989), pp. 213–232. ISSN: 0375-9474. DOI: https://doi.org/10.1016/0375-9474(89)90663-5. URL: https://www.sciencedirect.com/science/article/pii/0375947489906635.

[112] Bliss L. Tracy et al. "Rb and Cs Isotopic Cross Sections from 40-60-MeV-Proton Fission of U 238 , Th 232 , and U 235". In: *Physical Review C* 5 (1972), pp. 222–234.

[113] C. Simenel, K. Godbey, and A. S. Umar. "Timescales of Quantum Equilibration, Dissipation and Fluctuation in Nuclear Collisions". In: *Phys. Rev. Lett.* 124 (21 May 2020), p. 212504. DOI: 10.1103/PhysRevLett.124.212504. URL: https://link.aps.org/doi/10.1103/PhysRevLett.124.212504.

[114] M. Caamaño. *FUSION23*. Shizuoka, Japan, 19-24 November. 2023.

[115] K. Nishio et al. "Multiplicity and energy of neutrons from 235U(nth,f) fission fragments". In: *Nuclear Physics A* 632.4 (1998), pp. 540–558. ISSN: 0375-9474. DOI: https://doi.org/10.1016/S0375-9474(98)00008-6. URL: https://www.sciencedirect.com/science/article/pii/S0375947498000086.

USC UNIVERSIDADE DE SANTIAGO DE COMPOSTELA

[116] Meng Wang et al. "The AME 2020 atomic mass evaluation (II). Tables, graphs and references". In: *Chinese Physics C* 45.3 (2021), p. 030003. DOI: 10.1088/1674-1137/abddaf. URL: https://dx.doi.org/10.1088/1674-1137/abddaf.

USC UNIVERSIDADE DE SANTIAGO DE COMPOSTELA

Erratum: High-energy fission and the onset of quasi-fission

PhD Thesis

Author: Daniel Fernández Fernández

Supervisors: Manuel Caamaño Fresco and Diego Ramos Doval

PHD PROGRAMME IN NUCLEAR AND PARTICLE PHYSICS

SANTIAGO DE COMPOSTELA

April 2024

The purpose of this Erratum is to rectify typographical and formatting errors, to complete references within the text, and to correct Table A.2 in Appendix A.3.1 ^{265}*Db isotopic fusion-induced fission yields.*

page -9- 1st paragraph: Previous: "[...] of groundstate"
Corrected: "[...] of ground state"

page -12- 4th paragraph: Previous: "[...] is depiected"
Corrected: "[...] is depicted"

page -16- 1st paragraph: Previous: "[...] with red regions"
Corrected: "[...] with black regions"

page -22- 2nd paragraph: Previous: "[...] involves nonequilibrium"
Corrected: "[...] involves non equilibrium"

page -84- 1st paragraph: Previous: "[...] by a pulser"
Corrected: "[...] by a pulse generator"

page -121- 1st paragraph: Previous: "[...] fragments, outlined in [104], is employed"
Corrected: "[...] fragments in [104] and the description in the PhD Thesis work from [1] are employed"

page -121- Figure 5.18: Previous: "[...] respectively"
Corrected: "[...] respectively. Adapted with permission from [1]"

page -123- 2nd paragraph: Previous: "[...] it is defined as:"
Corrected: "[...] it is defined as (from [1]):"

page -123- 3rd paragraph: Previous: "[...] coefficients A2, A4, and A6, given by the fits to the cosine distributions described in the previous section"
Corrected: "[...] coefficients A_{even}"

page -123- 3rd paragraph: Previous: "[...] remains hidden"
Corrected: "[...] remains hidden [1]"

page -210- Figure 7.50: Previous: "[...] Normalized post-neutron"

Corrected: "[...] Normalised post-neutron"

page -227- 1st paragraph: Previous: "[...] This appendix provides an overview of Legendre polynomials and some of their properties"
Corrected: "[...] This appendix (based on [1] and references therein) provides an overview of Legendre polynomials and some of their properties"

page -227- Figure A.2: Previous: "[...] in panel (d)"
Corrected: "[...] in panel (d). Adapted with permission from [1]"

A.3.1 ^{265}Db isotopic fusion-induced fission yields

Table A.2: ^{265}Db isotopic fusion-induced fission yields

A	Z	Y(Z, A)	Statistical error
78	33	0.0990	0.0010
79	33	0.1000	0.0010
80	33	0.0849	0.0009
81	33	0.0546	0.0007
82	33	0.0313	0.0005
78	34	0.0564	0.0007
79	34	0.0954	0.0009
80	34	0.1483	0.0012
81	34	0.1661	0.0013
82	34	0.1427	0.0012
83	34	0.0933	0.0009
81	35	0.1056	0.0010
82	35	0.1718	0.0013
83	35	0.2300	0.0015
84	35	0.2135	0.0015
85	35	0.1482	0.0012
86	35	0.0880	0.0009
83	36	0.1100	0.0010
84	36	0.2055	0.0014
85	36	0.2886	0.0017
86	36	0.2950	0.0017
87	36	0.2477	0.0016
88	36	0.1510	0.0012
89	36	0.0914	0.0009
85	37	0.1064	0.0010
86	37	0.2135	0.0015
87	37	0.3263	0.0018
88	37	0.3383	0.0019
89	37	0.3326	0.0018
90	37	0.2406	0.0016
91	37	0.1965	0.0014
92	37	0.1082	0.0010
87	38	0.0984	0.0010
88	38	0.2108	0.0014
89	38	0.3499	0.0019
90	38	0.4053	0.0020
91	38	0.4109	0.0020
92	38	0.3458	0.0019
93	38	0.2492	0.0016
94	38	0.1514	0.0012
95	38	0.0940	0.0009
88	39	0.0459	0.0006
89	39	0.0955	0.0009
90	39	0.1897	0.0014
91	39	0.3234	0.0018
92	39	0.4335	0.0021
93	39	0.5345	0.0023

Continued on next page

USC UNIVERSIDADE DE SANTIAGO DE COMPOSTELA

Table A.2 – continued from previous page

A	Z	Y(Z, A)	Statistical error
94	39	0.4758	0.0022
95	39	0.3551	0.0019
96	39	0.2207	0.0015
97	39	0.1423	0.0012
98	39	0.0567	0.0007
99	39	0.0400	0.0005
90	40	0.0405	0.0006
91	40	0.0734	0.0008
92	40	0.1681	0.0013
93	40	0.2901	0.0017
94	40	0.4582	0.0022
95	40	0.5763	0.0024
96	40	0.6300	0.0025
97	40	0.5192	0.0023
98	40	0.3522	0.0019
99	40	0.2004	0.0014
100	40	0.1375	0.0012
101	40	0.0902	0.0009
92	41	0.0393	0.0005
93	41	0.0607	0.0007
94	41	0.1237	0.0011
95	41	0.2515	0.0016
96	41	0.4196	0.0021
97	41	0.6322	0.0026
98	41	0.7059	0.0027
99	41	0.6798	0.0027
100	41	0.4620	0.0022
101	41	0.3699	0.0019
102	41	0.1795	0.0013
103	41	0.1007	0.0010
95	42	0.0517	0.0007
96	42	0.1009	0.0010
97	42	0.2042	0.0014
98	42	0.3960	0.0020
99	42	0.6255	0.0025
100	42	0.8173	0.0029
101	42	0.7060	0.0027
102	42	0.7545	0.0028
103	42	0.5069	0.0023
104	42	0.3242	0.0018
105	42	0.1181	0.0011
106	42	0.0506	0.0006
97	43	0.0403	0.0005
98	43	0.0786	0.0008
99	43	0.1735	0.0013
100	43	0.3209	0.0018
101	43	0.5380	0.0024
102	43	0.7827	0.0028
103	43	0.9576	0.0032
104	43	0.8827	0.0030
105	43	0.6815	0.0027
106	43	0.4313	0.0021
107	43	0.2263	0.0015
108	43	0.0972	0.0009
100	44	0.0645	0.0007
101	44	0.1380	0.0012
102	44	0.2828	0.0017
103	44	0.5288	0.0023
104	44	0.8370	0.0029
105	44	0.8537	0.0030
106	44	1.0822	0.0034
107	44	0.8518	0.0030
108	44	0.5942	0.0025
109	44	0.3022	0.0017
110	44	0.1465	0.0012
111	44	0.0700	0.0008
112	44	0.0323	0.0005
102	45	0.0568	0.0007
103	45	0.1095	0.0010
104	45	0.2017	0.0014
105	45	0.4237	0.0021

Continued on next page

USC UNIVERSIDADE DE SANTIAGO DE COMPOSTELA

Table A.2 – continued from previous page

A	Z	Y(Z, A)	Statistical error
106	45	0.7408	0.0028
107	45	1.0243	0.0033
108	45	1.0971	0.0034
109	45	1.0718	0.0033
110	45	0.8017	0.0029
111	45	0.5300	0.0023
112	45	0.2503	0.0016
113	45	0.1268	0.0011
114	45	0.0546	0.0007
105	46	0.0724	0.0008
106	46	0.1642	0.0013
107	46	0.3412	0.0019
108	46	0.6644	0.0026
109	46	0.9623	0.0032
110	46	1.2434	0.0036
111	46	1.2099	0.0035
112	46	1.0842	0.0034
113	46	0.6428	0.0026
114	46	0.3994	0.0020
115	46	0.1758	0.0013
116	46	0.0915	0.0009
117	46	0.0411	0.0006
107	47	0.0617	0.0007
108	47	0.1209	0.0011
109	47	0.2590	0.0016
110	47	0.5136	0.0023
111	47	0.8532	0.0030
112	47	1.1905	0.0035
113	47	1.4086	0.0038
114	47	1.2323	0.0036
115	47	0.9798	0.0032
116	47	0.5918	0.0025
117	47	0.3256	0.0018
118	47	0.1256	0.0011
119	47	0.0691	0.0008
110	48	0.0951	0.0009
111	48	0.1917	0.0014
112	48	0.4053	0.0020
113	48	0.7428	0.0028
114	48	1.1467	0.0035
115	48	1.4361	0.0039
116	48	1.4553	0.0039
117	48	1.1985	0.0035
118	48	0.7931	0.0029
119	48	0.4304	0.0021
120	48	0.2134	0.0015
121	48	0.0942	0.0009
122	48	0.0460	0.0006
114	49	0.2963	0.0017
115	49	0.6173	0.0025
116	49	0.9947	0.0032
117	49	1.4053	0.0038
118	49	1.5644	0.0040
119	49	1.3384	0.0037
120	49	1.0564	0.0033
121	49	0.6412	0.0026
122	49	0.3298	0.0018
123	49	0.1356	0.0011
124	49	0.0562	0.0007
114	50	0.0541	0.0007
115	50	0.1042	0.0010
116	50	0.2277	0.0015
117	50	0.4950	0.0023
118	50	0.8401	0.0030
119	50	1.3088	0.0037
120	50	1.6234	0.0041
121	50	1.5850	0.0041
122	50	1.2774	0.0036
123	50	0.8377	0.0029
124	50	0.4258	0.0021
125	50	0.2226	0.0015

Continued on next page

USC UNIVERSIDADE DE SANTIAGO DE COMPOSTELA

Table A.2 – continued from previous page

A	Z	Y(Z, A)	Statistical error
126	50	0.1071	0.0010
117	51	0.0711	0.0008
118	51	0.1606	0.0013
119	51	0.3451	0.0019
120	51	0.6432	0.0026
121	51	1.1221	0.0034
122	51	1.5313	0.0040
123	51	1.7507	0.0043
124	51	1.5156	0.0040
125	51	1.1496	0.0035
126	51	0.6835	0.0027
127	51	0.3474	0.0019
128	51	0.1619	0.0013
129	51	0.0788	0.0008
119	52	0.0585	0.0007
120	52	0.1102	0.0010
121	52	0.2486	0.0016
122	52	0.4987	0.0023
123	52	0.9148	0.0031
124	52	1.3644	0.0038
125	52	1.6745	0.0042
126	52	1.6754	0.0042
127	52	1.3729	0.0038
128	52	0.8734	0.0030
129	52	0.4900	0.0022
130	52	0.2299	0.0015
131	52	0.1005	0.0010
122	53	0.0761	0.0008
123	53	0.1721	0.0013
124	53	0.3288	0.0018
125	53	0.7180	0.0027
126	53	1.0987	0.0034
127	53	1.6641	0.0042
128	53	1.5172	0.0040
129	53	1.6184	0.0041
130	53	1.1755	0.0035
131	53	0.6698	0.0026
132	53	0.3286	0.0018
133	53	0.1233	0.0011
124	54	0.0544	0.0007
125	54	0.1157	0.0010
126	54	0.2538	0.0016
127	54	0.4721	0.0022
128	54	0.9209	0.0031
129	54	1.4482	0.0039
130	54	1.7136	0.0042
131	54	1.6970	0.0042
132	54	1.3633	0.0038
133	54	0.8779	0.0030
134	54	0.4498	0.0021
135	54	0.1657	0.0013
127	55	0.0716	0.0008
128	55	0.1434	0.0012
129	55	0.3348	0.0018
130	55	0.6976	0.0027
131	55	1.1633	0.0035
132	55	1.2859	0.0037
133	55	1.7900	0.0043
134	55	1.4998	0.0040
135	55	1.1136	0.0034
136	55	0.6218	0.0025
137	55	0.3349	0.0018
138	55	0.1428	0.0012
129	56	0.0524	0.0007
130	56	0.1039	0.0010
131	56	0.2266	0.0015
132	56	0.4972	0.0023
133	56	0.8654	0.0030
134	56	1.3196	0.0037
135	56	1.6481	0.0041
136	56	1.5938	0.0041

Continued on next page

USC UNIVERSIDADE DE SANTIAGO DE COMPOSTELA

Table A.2 – continued from previous page

A	Z	Y(Z, A)	Statistical error
137	56	1.2472	0.0036
138	56	0.8083	0.0029
139	56	0.3996	0.0020
140	56	0.1893	0.0014
141	56	0.0520	0.0007
132	57	0.0645	0.0007
133	57	0.1438	0.0012
134	57	0.3373	0.0019
135	57	0.6588	0.0026
136	57	1.0475	0.0033
137	57	1.3379	0.0037
138	57	1.6591	0.0042
139	57	1.4433	0.0039
140	57	0.9859	0.0032
141	57	0.5985	0.0025
142	57	0.3216	0.0018
143	57	0.1364	0.0011
135	58	0.0948	0.0009
136	58	0.2061	0.0014
137	58	0.4487	0.0021
138	58	0.8054	0.0029
139	58	1.2164	0.0036
140	58	1.3545	0.0038
141	58	1.3655	0.0038
142	58	1.0996	0.0034
143	58	0.6553	0.0026
144	58	0.4634	0.0022
145	58	0.2342	0.0015
146	58	0.0985	0.0010
137	59	0.0697	0.0008
138	59	0.1369	0.0011
139	59	0.2936	0.0017
140	59	0.5842	0.0025
141	59	0.9864	0.0032
142	59	1.1679	0.0035
143	59	1.3797	0.0038
144	59	1.0974	0.0034
145	59	0.9647	0.0032
146	59	0.6029	0.0025
147	59	0.3619	0.0019
148	59	0.1416	0.0012
140	60	0.0868	0.0009
141	60	0.1846	0.0013
142	60	0.3649	0.0019
143	60	0.6579	0.0026
144	60	0.9130	0.0031
145	60	1.1047	0.0034
146	60	1.1445	0.0035
147	60	1.0204	0.0033
148	60	0.7576	0.0028
149	60	0.4321	0.0021
150	60	0.2511	0.0016
151	60	0.1165	0.0011
152	60	0.0508	0.0006
142	61	0.0636	0.0007
143	61	0.1308	0.0011
144	61	0.2491	0.0016
145	61	0.4532	0.0022
146	61	0.6835	0.0027
147	61	1.0067	0.0032
148	61	1.0099	0.0032
149	61	1.1666	0.0035
150	61	0.8731	0.0030
151	61	0.6383	0.0026
152	61	0.3880	0.0020
153	61	0.1863	0.0014
154	61	0.0753	0.0008
145	62	0.0814	0.0009
146	62	0.1508	0.0012
147	62	0.2753	0.0017
148	62	0.5038	0.0023

Continued on next page

USC UNIVERSIDADE DE SANTIAGO DE COMPOSTELA

Table A.2 – continued from previous page

A	Z	Y(Z, A)	Statistical error
149	62	0.7953	0.0029
150	62	1.0108	0.0032
151	62	0.8312	0.0029
152	62	1.0725	0.0033
153	62	0.7155	0.0027
154	62	0.4719	0.0022
155	62	0.2530	0.0016
156	62	0.1293	0.0011
157	62	0.0505	0.0006
148	63	0.0945	0.0009
149	63	0.1857	0.0014
150	63	0.2848	0.0017
151	63	0.5571	0.0024
152	63	0.6680	0.0026
153	63	0.9438	0.0031
154	63	0.9375	0.0031
155	63	0.8770	0.0030
156	63	0.5980	0.0025
157	63	0.3563	0.0019
158	63	0.1898	0.0014
159	63	0.0968	0.0009
151	64	0.0931	0.0009
152	64	0.1832	0.0013
153	64	0.3277	0.0018
154	64	0.5516	0.0024
155	64	0.7463	0.0028
156	64	0.8349	0.0029
157	64	0.7468	0.0028
158	64	0.6326	0.0026
159	64	0.3946	0.0020
160	64	0.2352	0.0015
161	64	0.1237	0.0011
162	64	0.0596	0.0007
153	65	0.0753	0.0008
154	65	0.1400	0.0012
155	65	0.2623	0.0016
156	65	0.4124	0.0021
157	65	0.5725	0.0024
158	65	0.7122	0.0027
159	65	0.7966	0.0029
160	65	0.6094	0.0025
161	65	0.5176	0.0023
162	65	0.3163	0.0018
163	65	0.1833	0.0013
164	65	0.0936	0.0009
165	65	0.0512	0.0006
155	66	0.0511	0.0006
156	66	0.0809	0.0009
157	66	0.1411	0.0012
158	66	0.2522	0.0016
159	66	0.3898	0.0020
160	66	0.5368	0.0023
161	66	0.6116	0.0025
162	66	0.5973	0.0025
163	66	0.5064	0.0023
164	66	0.3359	0.0018
165	66	0.2193	0.0015
166	66	0.1337	0.0011
167	66	0.0670	0.0008
168	66	0.0415	0.0006

References

[1] Diego Tarrío Vilas. "Neutron-induced fission fragment angular distribution at CERN nTOF: the Th-232 case". PhD thesis. Santiago de Compostela, 2012.

This work was partially supported by the Spanish "Ministerio de Ciencia e Innovación", under the grant FPI:PRE2018-085934.

This thesis delves into nuclear fission, a complex process discovered in 1939, exploring extreme deformations, nuclear structure effects, and heat flows influencing fragment distributions.

The study focuses on fusion-induced fission in ^{265}Db and ^{249}Bk fissioning systems generated with high excitation energies employing inverse kinematics with the VAMOS++ spectrometer. Asymmetric fission channels are observed, providing insights into nuclear charge, mass, neutron excess, and neutron evaporation.

In the case of ^{265}Db, an overproduction of heavy fragments attributed to quasi-fission is observed. For ^{249}Bk, the characterization of the scission point is studied through crucial indirect observables for understanding nuclear structure effects, such as the total kinetic energy averaged before neutron evaporation.